Springer Series in Solid-State Sciences 177

Alberto Bramati
Michele Modugno *Editors*

Physics of Quantum Fluids

New Trends and Hot Topics in Atomic and Polariton Condensates

Springer

Springer Series in
SOLID-STATE SCIENCES 177

Springer Series in

SOLID-STATE SCIENCES

The Springer Series in Solid-State Sciences consists of fundamental scientific books prepared by leading researchers in the field. They strive to communicate, in a systematic and comprehensive way, the basic principles as well as new developments in theoretical and experimental solid-state physics.

Alberto Bramati • Michele Modugno
Editors

Physics of Quantum Fluids

New Trends and Hot Topics in Atomic and Polariton Condensates

Springer

ISSN 0171-1873 Springer Series in Solid-State Sciences
ISBN 978-3-642-37568-2 ISBN 978-3-642-37569-9 (eBook)
DOI 10.1007/978-3-642-37569-9
Springer Heidelberg New York Dordrecht London

Library of Congress Control Number: 2013944213

Printed on acid-free paper

Springer is part of Springer Science+Business Media (www.springer.com)

Preface

The concept of *quantum fluid*—a fluid whose properties are governed by the laws of quantum mechanics—dates back to 1926, when Madelung introduced the hydrodynamic formulation of the Schrödinger equation. This, along with the prediction of Bose-Einstein condensation (BEC) for a non-interacting gas made by Einstein in 1924, and the discovery of superfluidity in liquid helium, achieved independently by Kapitza and Allen in 1937, can be considered the early milestones of this fashinating field.

Remarkably, though the role of Bose-Einstein condensation in the superfluid behaviour of helium was soon recognized by London in 1938, it took seventy year before its first direct observation. In fact, it was only in 1995 that the groups of Cornell, Weiman, and Ketterle achieved to cool a sample of atomic gases down to temperatures of the orders of few hundreds of nanokelvins, below the critical temperature for BEC. These landmark experiments have produced a tremendous impact in the experimental and theoretical research in the field of quantum fluids. In fact, thanks to the fact that interacting Bose-Einstein condensates (BECs) are genuine superfluids and that they can be controlled and manipulated with high precision, they have made possible to investigate thorougly many of the manifestation of superfluidity, as quantized vortices, absence of viscosity, reduction of the moment of inertia, occurrence of persistent currents, to mention a few.

Very recently, in 2006, following a pioneering proposal by Imamoglou (1996), BEC was observed in a solid state system: polaritons in semiconductor microcavities, which are composite bosons arising from the strong coupling between excitons and photons. Due to their very light mass, several orders of magnitude smaller than the free electron mass, polaritons can exhibit Bose-Einstein condensation at higher temperature and lower densities compared to atomic condensates. On the other hand, polaritons constitute a new type of quantum fluid with specific characteristics coming from its intrinsic dissipative and non-equilibrium nature.

The main objective of this book is to take a snapshot of the state of the art of this fast moving field with a special emphasis on the hot-topics and new trends. Bringing together the contributions of some of the most active specialists of the two areas (atomic and polaritonic quantum fluids), we expect that this work could facilitate

the exchanges and the collaborations between these two communities working on subjects with very strong analogies. The book is organized in two distinct parts, preceded by a general introduction; the first part is focussed on polariton quantum fluids and the second one is dedicated to the atomic BEC.

In the introductory chapter, M. Wouters gives an overview of the physics of the Bose-Einstein condensates of ultracold atoms and polaritons underlining their analogies and differences. This chapter reviews the main achievements and discusses the current trends of both fields.

Chapter 2 by N.G. Berloff and J. Keeling deals with the central problem of the universal description for the non-equilibrium polariton condensates. A special attention is paid to the theoretical framework describing the pattern formation in such systems. Different equations characterizing various regimes of the dynamics of exciton-polariton condensates are reviewed: the Gross-Pitaevskii equation which models the weakly interacting condensates at equilibrium, the complex Ginsburg-Landau equation which describes the behaviour of the systems in presence of symmetry-breaking instabilities and finally the complex Swift-Hohenberg equation. The authors also show how these equations can be derived from a generic laser model based on Maxwell-Bloch equations.

In Chap. 3, A. Kavokin develops a general theory for the bosonic spin transport that can be applied to different condensed matter systems like indirect excitons in coupled quantum wells and exciton-polaritons in semiconductor microcavities. The relevance of this approach to the emerging field of Spin-optronics in which the spin currents are carried by neutral bosonic particles is discussed and fascinating perspectives like spin-superfluidity are addressed.

Chapters 4 and 5 are focussed on the theoretical description of the properties of the spinor polariton condensates with a special emphasis on the occurrence of topological excitations in these fluids. In Chap. 4 by Y.G. Rubo, a review of the spin-dependent properties of the multi-component polariton condensates is presented. Special attention is devoted to describe the effect of applied magnetic fields on the polarization properties of the condensate; fractional vortices are discussed and the spin texture of the half-vortices in presence of the longitudinal-transverse splitting is discussed in detail. In Chap. 5, H. Flayac, D.D. Solnyshkov and G. Malpuech first discuss in detail the specific behaviour of a flowing spinor polariton allowing for the generation of a new kind of topological excitations: the oblique half solitons. In the second part of the chapter the authors show that these systems are extremely promising to study exotic entities analogue to the astrophysical black holes and wormholes.

Chapters 6 and 7 deal with experimental studies of hydrodynamics of polariton quantum fluids. In Chap. 6, B. Deveaud, G. Nardin, G. Grosso and Y. Léger describe the behaviour of a flowing polariton quantum fluid perturbed by the interaction with a potential barrier: this experimental configuration is well suited to investigate the onset of quantum turbulence in a quantum fluid. The variations of the phase and density of the fluid are measured with a picosecond resolution allowing for the observation of the nucleation of quantized vortices and the decay of dark solitons into vortex streets. In Chap. 7, D. Ballarini, A. Amo, M. de Giorgi

and D. Sanvitto review the first observations of superfluidity in a polariton fluid: the most relevant manifestations of the superfluid behaviour of these systems are discussed, namely the friction-less motion with the consequent scattering suppression in the Landau picture and the establishment of persistent currents in the case of rotating condensates. Moreover, the authors discuss the interesting regime of the superfluidity breakdown when the polariton fluid hits a spatially extended obstacle that can be natural or created in a controlled way by mean of well suited optical beams. Vortex nucleation, vortex trapping as well as the formation of oblique dark solitons are analysed in detail. In the last part of the chapter the authors show that the strong non-linearities of the polariton systems, together with their specific propagation properties can be exploited to develop a new class of optoelectronic devices for the classical and quantum information processing.

Chapters 8 and 9 are focussed on the properties of polariton condensates confined in low dimensional structures. In Chap. 8, N.Y. Kim, Y. Yamamoto, S. Utsunomiya, K. Kusudo, S. Höfling and A. Forchel discuss the properties of exciton-polaritons condensates in artificial traps and lattices geometries in various dimensions (0D, 1D and 2D). They show how coherent π-state with p-wave order in one dimensional condensate array and d-orbital state in two dimensional square lattices can be obtained. The authors point out the interest of preparing high-orbital condensates to probe quantum phase transitions and to implement quantum emulation applications. In Chap. 9, J. Bloch reviews the recent experiments performed with polariton condensates in low-dimensional microstructures. The propagation properties of polariton condensates confined in 1D microwires, together with the possibility to manipulate and control these condensates by optical means, are discussed in detail. In the second part of the chapter, the author shows how the study of polariton condensates in fully confined geometries, obtained in single or coupled micropillars, allows gaining a deep physical insight in the nature of interactions inside the condensate as well as with the environment. In the final part of the chapter, the interesting perspectives opened by the confined polariton condensates for the implementation of devices with new functionalities are briefly reviewed.

While the previous chapters are mainly focussed on the polariton quantum fluids in GaAs-based microstructures where a cryogenic temperature (4K) is needed, Chaps. 10 and 11 explore the possibilities opened by other materials to achieve polariton condensates at room temperature. Chapter 10 by J. Levrat, G. Rossbach, R. Butté and N. Grandjean presents the recent observation of the polariton condensation at room temperature (340 K) in GaN-based planar microcavities and analyses in detail the threshold of the polariton condensation phase transition as a function of the temperature and detuning. The role of the spin-anisotropy in the polariton-polariton interactions and its impact on the polarization properties of the condensate are comprehensively discussed. In Chap. 11, F. Médard, A. Trichet, Z. Chen, L.S. Dang and M. Richard present the recent progresses towards polariton condensation at room temperature in large band-gap nanostructures, namely ZnO nanowires. The unusually large Rabi splitting observed in these systems allows achieving stable polariton at room temperature, strongly decoupled from thermal fluctuations coming from lattice vibrations. Despite this behaviour, the authors show several experimental indications of polariton quantum degeneracy at room temperature.

Chapter 12, by F. Piazza, L.A. Collins, and A. Smerzi, opens the second part of the book, dedicated to the properties of quantum fluids made by ultracold atoms. In this chapter the authors discuss the dynamics of superfluid dilute Bose-Einstein condensates in the regime where the flow velocity reaches a critical value above which stationary currents are impossible. They present results for two- and three-dimensional BECs in two different geometries: a torus and a waveguide configuration, and also discuss the behavior of the critical current, establishing a general criterion for the breakdown of stationary superfluid flows.

Chapters 13 and 14 are devoted to turbolence effects in atomic BECs, that are particularly appealing as quantized vortices can be directly visualized and the interaction parameters can be controlled by Feshbach resonances. In Chap. 13, M. Tsubota and K. Kasamatsu review recent important topics in quantized vortices and quantum turbulence in atomic BECs, providing an overview of the dynamics of quantized vortices, hydrodynamic instability, and quantum turbulence. In Chap. 14, V.S. Bagnato et al. discuss their recent observations of quantum turbolence with a condensate of ^{87}Rb.

In Chap. 15, Y. Castin and A. Sinatra discuss the coherence of a three-dimensional spatially homogeneous Bose-condensed gas, initially prepared at finite temperature and then evolving as an isolated interacting system. They review different theoretical approaches, as the number-conserving Bogoliubov approach that allows to describe the system as a weakly interacting gas of quasi-particles, and the kinetic equations describing the Beliaev-Landau processes for the quasi-particles. They show that the variance of the condensate phase-change at long times is the sum of a ballistic term and a diffusive term, with temperature and interaction dependent coefficients, and discuss their scaling behaviors in the thermodynamic limit.

Chapter 16, by R.P. Smith and Z. Hadzibabic, review the role of interactions in Bose-Einstein condensation, covering both theory and experiments. They focus on harmonically trapped ultracold atomic gases, but also discuss how these results relate to the uniform-system case, which may be relevant for other experimental systems, and for theory in general. Despite the fact that the phase transition to a Bose-Einstein condensate can occur in an ideal gas, interactions are necessary for any system to reach thermal equilibrium and so are required for condensation to occur in finite time. The authors discuss this point clarifying the effects of interactions both on the mechanism of condensation and on the critical temperature, and then review the conditions for measuring the equilibrium thermodynamics. They also discuss the non-equilibrium phenomena that occur when these conditions are controllably violated by tuning the interparticle-interaction strength.

In Chap. 17, T. Mukaiyama and M. Ueda provide an overview of theories and experiments on the thermodynamics of Fermi gases at unitarity, where the scattering length diverges, that is characterized by a universal behavior.

Finally, in Chap. 18, G. Barontini and H. Ott introduce the scanning electron microscopy (SEM), that represents one of the most promising techniques for probing and manipulating ultracold atomic systems with extremely high resolution and precision. Thanks to its extremely high resolution, below 100 nm, and to the single-atom sensitivity, the SEM method permits the observation of in-situ

profiles of trapped Bose-Einstein condensates and of ultracold clouds in one- and two-dimensional optical lattices. Moreover, the single lattice sites can be selectively addressed and manipulated in order to create arbitrary patterns of occupied sites.

We hope this book will be a useful introduction to a wide audience of researchers who wish to approach the physics of quantum fluids and be updated on the last fascinating achievements in this cutting-edge research field. Last but not least, we would like to thank all the contributors for their effort in making this project possible.

Paris, France — Alberto Bramati
Bilbao, Spain — Michele Modugno

Contents

Contributors

A. Amo Laboratoire de Photonique et de Nanostructures, CNRS, Marcoussis, France

G. Bagnato Instituto de Física de São Carlos, Universidade de São Paulo, São Carlos, SP, Brazil

V.S. Bagnato Instituto de Física de São Carlos, Universidade de São Paulo, São Carlos, SP, Brazil

D. Ballarini Istituto Italiano di Technologia, IIT-Lecce, Lecce, Italy; Istituto Nanoscienze – CNR, NNL, Lecce, Italy

Giovanni Barontini Research Center OPTIMAS and Fachbereich Physik, Technische Universität Kaiserslautern, Kaiserslautern, Germany

N.G. Berloff Department of Applied Mathematics and Theoretical Physics, University of Cambridge, Cambridge, UK

Jacqueline Bloch Laboratoire de Photonique et de Nanostructures, LPN/CNRS, Marcoussis, France

Raphaël Butté Institute of Condensed Matter Physics, Ecole Polytechnique Fédérale de Lausanne, Lausanne, Switzerland

M. Caracanhas Instituto de Física de São Carlos, Universidade de São Paulo, São Carlos, SP, Brazil

Yvan Castin Laboratoire Kastler Brossel, Ecole normale supérieure, CNRS and UPMC, Paris, France

Z. Chen Surface Physics Laboratory, Department of Physics, Fudan University, Shanghai, China

L.A. Collins Theoretical Division, Los Alamos National Laboratory, Los Alamos, NM, USA

L.S. Dang Institut Néel, CNRS-CEA, Grenoble, France

M. de Giorgi Istituto Italiano di Technologia, IIT-Lecce, Lecce, Italy; Istituto Nanoscienze – CNR, NNL, Lecce, Italy

Benoit Deveaud Ecole Polytechnique Fédérale de Lausanne, Lausanne, Switzerland

Hugo Flayac Clermont Université and Université Blaise Pascal, LASMEA, Nanostructure and Nanophotonics Group, CNRS, Aubière Cedex, France

Alfred Forchel Technische Physik and Wilhelm-Conrad-Röntgen-Research Center for Complex Material Systems, Universität Würzburg, Würzburg, Germany

Nicolas Grandjean Institute of Condensed Matter Physics, Ecole Polytechnique Fédérale de Lausanne, Lausanne, Switzerland

Gabriele Grosso Ecole Polytechnique Fédérale de Lausanne, Lausanne, Switzerland

Zoran Hadzibabic Cavendish Laboratory, University of Cambridge, Cambridge, UK

E.A.L. Henn Instituto de Física de São Carlos, Universidade de São Paulo, São Carlos, SP, Brazil

Sven Höfling Technische Physik and Wilhelm-Conrad-Röntgen-Research Center for Complex Material Systems, Universität Würzburg, Würzburg, Germany

Kenichi Kasamatsu Department of Physics, Kinki University, Higashi-Osaka, Japan

Alexey Kavokin Spin Optics Laboratory, St-Petersburg State University, St-Petersburg, Russia; Physics and Astronomy School, University of Southampton, Southampton, UK

J. Keeling School of Physics and Astronomy, University of St Andrews, SUPA, St Andrews, UK

Na Young Kim E. L. Ginzton Laboratory, Stanford University, Stanford, CA, USA

Kenichiro Kusudo National Institute of Informatics, Chiyoda-ku, Tokyo, Japan

Jacques Levrat Institute of Condensed Matter Physics, Ecole Polytechnique Fédérale de Lausanne, Lausanne, Switzerland

Yoan Léger Ecole Polytechnique Fédérale de Lausanne, Lausanne, Switzerland

K.M.F. Magalhães Instituto de Física de São Carlos, Universidade de São Paulo, São Carlos, SP, Brazil

Guillaume Malpuech Clermont Université and Université Blaise Pascal, LASMEA, Nanostructure and Nanophotonics Group, CNRS, Aubière Cedex, France

F. Médard Institut Néel, CNRS-CEA, Grenoble, France

Takashi Mukaiyama Institute for Laser Science, University of Electro-Communications, Chofu, Tokyo, Japan

S.R. Muniz Instituto de Física de São Carlos, Universidade de São Paulo, São Carlos, SP, Brazil

Gael Nardin Ecole Polytechnique Fédérale de Lausanne, Lausanne, Switzerland

Herwig Ott Research Center OPTIMAS and Fachbereich Physik, Technische Universität Kaiserslautern, Kaiserslautern, Germany

F. Piazza INO-CNR, BEC Center and Dipartimento di Fisica, Università di Trento, Povo, Trento, Italy

M. Richard Institut Néel, CNRS-CEA, Grenoble, France

G. Roati LENS and Dipartimento di Fisica, Università di Firenze, and INFM-CNR, Sesto Fiorentino, Italy

Georg Rossbach Institute of Condensed Matter Physics, Ecole Polytechnique Fédérale de Lausanne, Lausanne, Switzerland

Y.G. Rubo Instituto de Energías Renovables, Universidad Nacional Autónoma de México, Temixco, Morelos, Mexico

D. Sanvitto Istituto Italiano di Technologia, IIT-Lecce, Lecce, Italy; Istituto Nanoscienze – CNR, NNL, Lecce, Italy

J.A. Seman LENS and Dipartimento di Fisica, Università di Firenze, and INFM-CNR, Sesto Fiorentino, Italy

R.F. Shiozaki Instituto de Física de São Carlos, Universidade de São Paulo, São Carlos, SP, Brazil

Alice Sinatra Laboratoire Kastler Brossel, Ecole normale supérieure, CNRS and UPMC, Paris, France

A. Smerzi INO-CNR, BEC Center and Dipartimento di Fisica, Università di Trento, Povo, Trento, Italy

Robert P. Smith Cavendish Laboratory, University of Cambridge, Cambridge, UK

Dmitry D. Solnyshkov Clermont Université and Université Blaise Pascal, LASMEA, Nanostructure and Nanophotonics Group, CNRS, Aubière Cedex, France

P. Tavares Instituto de Física de São Carlos, Universidade de São Paulo, São Carlos, SP, Brazil

G. Telles Instituto de Física de São Carlos, Universidade de São Paulo, São Carlos, SP, Brazil

A. Trichet Institut Néel, CNRS-CEA, Grenoble, France

Makoto Tsubota Department of Physics, Osaka City University, Osaka, Japan

Masahito Ueda Department of Physics, University of Tokyo, Bunkyo-ku, Tokyo, Japan

Shoko Utsunomiya National Institute of Informatics, Chiyoda-ku, Tokyo, Japan

Michiel Wouters TQC, Universiteit Antwerpen, Antwerpen, Belgium

Yoshihisa Yamamoto E. L. Ginzton Laboratory, Stanford University, Stanford, CA, USA; National Institute of Informatics, Chiyoda-ku, Tokyo, Japan

Chapter 1
Quantum Fluids of Exciton-Polaritons and Ultracold Atoms

Michiel Wouters

Abstract We give an overview of the physics of quantum degenerate Bose gases of ultracold atoms and of exciton polaritons in microcavities. The physical systems are described and the main experimentally accessible observables are outlined. We give a schematic overview of recent trends in both fields.

1.1 Introduction

The physics of the quantum Bose gases took off from the theoretical side, when Einstein predicted that the bosonic statistics induces a phase transition in a noninteracting gas at low temperatures, when the interparticle distance is comparable to the de Broglie wave length [39]. Below the transition temperature, the gas enters the Bose-Einstein (BE) condensed phase, where a macroscopic number of particles occupies the lowest momentum state, leading to the coherence of the phase over macroscopic distances. The first physical example of this type of transition was superfluid Helium. Due to the strong interactions between the Helium atoms however, its theoretical description is complicate and the connection to the ideal Bose gas is not so direct. Still the macroscopic phase coherence and superfluidity are not qualitatively altered by the strength of interactions, so that the ideal Bose gas remains conceptually a good starting point to understand the remarkable behavior of superfluid Helium. It was in this context that Bogoliubov analyzed the effect of weak interactions and Pitaevskii constructed the classical theory for inhomogeneous Bose-Einstein condensates.

A physical realization of the weakly interacting Bose gas was lacking for many years. The condition of weak interactions $nR_e^3 \ll 1$ is only satisfied when the interparticle distance ($n^{-1/3}$) is much larger than the range of the interactions (R_e). No gases satisfy this condition at thermodynamic equilibrium. Several ideas were pursued to create metastable quantum gases that are in the weakly interacting limit. Both excitons in semiconductors and very dilute atomic gases were conceived to

M. Wouters (✉)
TQC, Universiteit Antwerpen, Universiteitsplein 1, 2610 Antwerpen, Belgium
e-mail: michiel.wouters@ua.ac.be

A. Bramati, M. Modugno (eds.), *Physics of Quantum Fluids*,
Springer Series in Solid-State Sciences 177, DOI 10.1007/978-3-642-37569-9_1,

be good candidates to achieve this goal. The first successful realization was obtained with dilute atoms in 1995 [13]. The condensation of excitons on the other hand proved to be much harder due to the complicated solid state environment. By coupling the exciton to a cavity photon, polariton quasi-particles are created. Because of their much lighter mass as compared to the exciton, they are much easier to condense in the ground state. Unambiguous proof hereof was obtained in 2006 [28].

The ultracold dilute atomic gases have turned out a very flexible system, and can be used as emulators for a wide variety of quantum systems and the field has witnessed a vigorous expansion. It is beyond the scope of the present introduction to cover this field. We will rather restrict ourselves to the physics of bosonic atoms in the regime of weak interactions. On the polariton side, the relative simplicity of the experiments has allowed for many milestone experiments to be performed in a relatively short time. The field being still much smaller than the cold atom one, we will cover relatively more of the polariton physics.

1.2 The Systems

In the following sections, we will start with short separate introductions to the microcavity and cold atom systems to describe their specific features.

1.2.1 The Microcavity Polariton System

1.2.1.1 Microcavity Polariton Properties

A microcavity is a solid state Fabri-Perrot cavity with a distance between the mirrors of the order of one micron. The mirrors are flat so that the photon modes have a conserved momentum in the directions parallel to the mirror plane, making them a two-dimensional (2D) system. At small momenta, their dispersion is in good approximation quadratic $\omega_C(k) = \omega_C^0 + k^2/2m_C$, where the effective mass is four orders of magnitude smaller than the free electron mass $m_C = 10^{-4}m_e$. The resonance frequency ω_C^0 is in the electron volt range, the typical energy scale of electronic transitions. The mirrors are usually Distributed Bragg reflectors (DBRs) with a quality factor of the order of 10.000, yielding photon line widths in the 0.1 meV range, corresponding to a few ps life time [15].

When a material is placed between the mirrors, that has an electronic transition in resonance with the optical mode, the electronic excitations couple to the light. Of particular interest is the coupling to an excitonic transition (bound electron hole pair) in the material, illustrated in Fig. 1.1(a). When a photon creates an exciton, the center of mass momentum of the exciton is equal to the photon momentum. The relative wave function of the exciton being fixed, the coupling between a photon and exciton at momentum $\mathbf{k}$ can be seen as the coupling in a two-level system. In

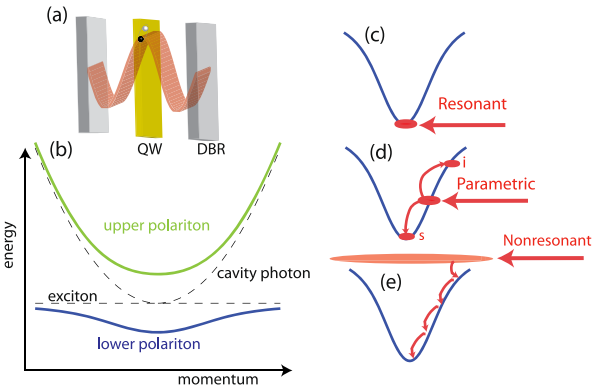

Fig. 1.1 (**a**) Overview of the microcavity polariton system. A cavity photon is strongly coupled to an exciton transition in an embedded quantum well. (**b**) The dispersion of the upper (*green*) and lower (*blue*) polaritons, compared to the bare exciton and photon dispersions (*dashed lines*). (**c**), (**d**), (**e**) comparison of the different excitation schemes: resonant (**c**), parametric (**d**) and nonresonant (**e**)

second quantization, this coupling can be described by a term in the Hamiltonian of the form

$$H_R = \frac{\Omega_R}{2} \sum_{\mathbf{k}} \psi_C^\dagger(\mathbf{k}) \psi_X(\mathbf{k}) + h.c. \tag{1.1}$$

where the coupling parameter Ω_R is the Rabi frequency and ψ_C annihilates a cavity photon. The operator ψ_C describes the annihilation of an exciton (electron-hole pair). To enhance the binding energy, the exciton is usually confined in a quantum well. The eigenstates of the full linear Hamiltonian $H = H_0 + H_R$, with the free Hamiltonian

$$H_0 = \sum_{\mathbf{k}} \left[\omega_C(k)\, \psi_C^\dagger(\mathbf{k}) \psi_C(\mathbf{k}) + \epsilon_X\, \psi_X^\dagger(\mathbf{k}) \psi_X(\mathbf{k}) \right], \tag{1.2}$$

can be obtained by diagonalizing it at fixed $\mathbf{k}$. The dispersion of the quasi-particles, the so-called lower and upper polaritons, is shown in Fig. 1.1(b). The splitting between upper and lower polariton was first experimentally seen by Weisbuch et al. in 1992 [56]. Note that in (1.2), we have neglected the momentum dependence of the exciton energy, which is well justified since its mass is around four orders of magnitude heavier than the cavity photon.

The coupling between excitons and photons is determined by the Rabi frequency Ω_R, that is of the order of a few meV in GaAs up to 50 meV in GaN (discussed in Chap. 10), 130 meV in ZnO (see Chap. 11) and even higher in organic materials [1]. A larger Rabi frequency makes the polaritons more robust with respect to temperature. Experiments with GaAs microcavities are conducted at cryogenic temperatures around 10 K, where polaritons in GaN (see Chap. 10) and organic materials can be observed at room temperature. Many experiments are however conducted with GaAs microcavities, because the growth technology for this material is much

more advanced thanks to its use in commercial opto-electronic applications. Much progress has however been made in the fabrication of GaN microcavities and many of the pioneering experiments on polariton condensation have been conducted on a CdTe microcavity [28, 33, 42].

The microcavities are structurally identical to Vertical Cavity Surface Emitting Lasers (VCSELs). The only difference is that their excitonic resonance is carefully tuned to the cavity photon. The most important consequence hereof is that unlike photons, the polaritons interact significantly with each other. Indeed, the excitons consist of electrons and holes and their (exchange dominated) interaction is responsible for the polariton-polariton interactions [11]. It is theoretically modeled by adding the interaction term

$$H_I = \frac{g}{2}\int d\mathbf{x}\, \psi_X^\dagger(\mathbf{x})\psi_X^\dagger(\mathbf{x})\psi_X(\mathbf{x})\psi_X(\mathbf{x}) \tag{1.3}$$

to the Hamiltonian. Its approximation by a contact interaction is well justified, because the range of the exciton-exciton interaction potential is of the order of 10 nm, where the polariton physics takes place on the μm length scale.

On resonance, the polariton is half exciton and half photon, so that the effective polariton-polariton interaction is $g_{LP} = g/4$. The relevant dimensionless coupling constant that characterizes the strength of interactions in a 2D gas of particles with mass m is $\tilde{g} = mg/\hbar^2$ [7]. This means that even though the excitons are in a regime of strong interactions $\tilde{g} = m_X g/\hbar^2 \sim 1$, the polaritons are in a weakly interacting regime. For example in GaAs microcavities, the dimensionless interaction constant is of the order of $\tilde{g} = m_{LP} g/\hbar^2 \approx 0.01$.

A second major difference with the bare exciton gas concerns the role of disorder. A certain degree of disorder due to growth fluctuations is inevitable. Fluctuations in the quantum well width result in an inhomogeneous effective potential for the excitons, with a correlation length on the nm scale and gives a inhomogeneous linewidth in the order of one meV. It however turns out that when the Rabi frequency is larger than this inhomogeneous broadening, the polariton modes are quite insensitive to the excitonic disorder [45]. The major source of disorder acting on the polaritons comes from the fluctuation in the distance between the two DBR mirrors. A monolayer fluctuation gives an energy shift of the order of 0.5 meV, which is of the same order of magnitude as the other polariton energy scales.

Controllable manipulation of the potential acting on the polaritons is possible by a variety of techniques, that are discussed in Chap. 8. Among the most successful strategies of creating potentials acting on the polaritons are etching (see Chaps. 8 and 9), stress induced traps [4], surface acoustic waves [10] and controlled variation of the DBR thickness (see Chap. 6).

So far, we have simplified the discussion by neglecting the polarization degree of freedom of the polaritons [47]. The photon however has two polarization states. In GaAs for example, there are four exciton polarization states. The photon only couples to the $m_z = \pm 1$ excitons. The other two states with $m_z = \pm 2$ are not coupled to the light because of angular momentum conservation. They are dark and do not form polaritons.

The single particle polariton eigenstates have a well defined linear polarization due to the splitting of both the photon and exciton linear polarization states. For what concerns the polariton-polariton interactions however, the conservation of angular momentum in collisions results in the conservation of the circularly polarized states. The interactions turn out to be anisotropic: the interactions between cocircular polarized polaritons is larger than between countercircularly polarized ones: $g_{\uparrow\uparrow} \gg |g_{\uparrow\downarrow}|$. This is due to the fact that the dominant contribution comes from the Pauli exclusion principle (exchange interaction). For countercircularly polarized excitons, both electron and hole spins are however different, so that the exchange contribution vanishes. The interactions due to higher order terms have been found to be negative $g_{\uparrow\downarrow} < 0$ [31, 54].

Discussions on the spin physics of polaritons can be found in Chaps. 3 and 4.

1.2.1.2 Experiments with Polaritons

In its ground state, the microcavity is empty. Polaritons can be injected by means of optical or electrical injection. The polariton life time is mainly limited by the finite photon life time. In state of the art microcavities, it is around 10 ps, which is of the order of the other time scales of their dynamics and thus presents a severe limitation. Therefore, polaritons are often continuously injected in order to compensate for these losses. Two different optical injection schemes should be distinguished. The first excitation scheme is *resonant* excitation (see Fig. 1.1(c)): A laser is tuned to the polariton frequency at a given wave vector. The second scheme is *nonresonant* excitation (see Fig. 1.1(e)). In this latter case, the laser is tuned to an energy above the polariton energy. High energy excitons or free electron-hole pairs are formed, that subsequently relax to the bottom of the lower polariton branch. Electrical excitation has a similar effect.

An important difference between the resonant and nonresonant excitation schemes concerns the $U(1)$ phase symmetry of the polariton field. In the case of resonant excitation, the coupling of the external laser amplitude F_L to the microcavity adds a term to the Hamiltonian

$$H_L = F_L e^{-i\omega_L t}\Psi^\dagger(\mathbf{k}_L) + h.c. \tag{1.4}$$

that explicitly breaks the $U(1)$ symmetry. The phase of the polariton field is determined by the phase of the laser and in particular its spatial and temporal coherence is determined by the coherence properties of the laser light. Under nonresonant excitation on the other hand, the $U(1)$ symmetry is not explicitly broken and polariton coherence can spontaneously form. Various models to describe this symmetry broken nonequilibrium state are discussed in Chap. 2.

An excitation scheme that is intermediate between resonant and nonresonant excitation is the so-called parametric excitation [25, 51]. The lower polariton branch is excited resonantly at an energy above the ground state carefully chosen so that polaritons can scatter into the ground state (signal) and an excited state (idler) through a single collision. The parametric scheme is illustrated in Fig. 1.1(d). Where under

parametric excitation, the phase of the pumped mode is fixed by the laser, the signal phase is chosen spontaneously, because only the sum of signal and idler phases is fixed $\phi_s + \phi_i = 2\phi_p$. Therefore, the spontaneous formation of coherence is observed when the density of polaritons in the signal mode is increased.

Finally, under pulsed resonant excitation, the polariton phase is only fixed as long as the laser pulse excites the microcavity and is free to evolve afterwards. The main limitation of this scheme is, as we mentioned earlier, the finite polariton life time that makes the density drop on the same time scale as the other time scales that are involved in the dynamics.

1.2.2 The Cold Atom System

Similar to polaritons, also the dilute clouds of ultracold alkali atoms are not in their ground state, which is the solid phase. The relaxation to a solid however needs three-body interactions, which are very slow at low densities and the gas phase is metastable with a life time that can be of the order of one minute. This is much longer than the time needed to reach thermal equilibrium and much longer than the typical time scales of the dynamics. It is therefore a good approximation to neglect the finite life time of the trapped atoms.

Since the realization of Bose-Einstein condensation, the field of ultracold atoms has witnessed an explosive growth. Nowadays, many experiments are performed on atoms of bosonic and fermionic [21] statistics, that can be combined with ions [61] and strongly coupled to light [8]. The scope of this chapter is limited to point out some aspects of the physics of ultracold bosonic gases. More extensive reviews of their properties can be found in several text books on the subject [38, 39]. Due to the three-body losses, the maximum density of the atoms is around $n = 10^{14}$ cm^{-3}. This means that the typical interatomic spacing is similar to the polariton spacing of around 1 micron. Quantum degeneracy is reached when the de Broglie wavelength reaches this value. Due to the much heavier atomic mass, the temperature requirement for the atoms is much more severe and of the order of 100 nK, eight orders of magnitude smaller than in the polariton case. Thanks to the excellent isolation of the atomic clouds from any environment, these ultralow temperatures can however be routinely achieved. While the BEC phase transition does not rely on the interactions between the atoms, the transition temperature is affected by atomic interactions (see Chap. 16).

Spin conservation laws in the collisions of atoms make that for several combinations of hyperfine states, the number of atoms in each state is conserved. Mixtures of a well defined number of atoms in each hyperfine state can thus be prepared, which allows to study atomic gases with tunable effective spin.

Interactions between ultracold atoms have a range that is of the order of 10 nm, much shorter than their spacing. The interaction can thus be well approximated by

a contact interaction, that reads in three dimensions (omitting technicalities concerning their regularization)

$$V(\mathbf{x}) = \frac{4\pi\hbar^2 a_{sc}}{m}\delta(\mathbf{r}), \tag{1.5}$$

where a_{sc} is the scattering length, that is typically of the order of the range of the interactions. Making use of so-called Feshbach resonances, the scattering length can be tuned at will. Both positive and negative signs for the scattering length can be reached. In absolute value, it can be tuned from zero to values larger than the interparticle spacing. In the latter regime, the atomic gas enters a very controlled strongly interacting regime.

An alternative route to the regime of strong interactions in bosons is by using optical lattices. These are periodic potentials generated by standing laser fields. They allow to realize a tunable bosonic Hubbard model, where the dramatic effects of interactions between bosonic particles were first evidenced in the superfluid to Mott insulator phase transition [22].

Interactions can be meaningfully compared between 2D polariton gases and 2D atomic clouds. The latter can be created by applying a standing laser field that confines the cloud in one dimension only. In experiments on the 2D Bose gas, the interaction strength is tunable and takes values in the range $\tilde{g} = 10^{-2}$–0.3 [12, 24, 26]. As discussed above, Microcavity polariton in GaAs microcavities are in the lower values of this range.

The coupling of ultracold gases to cavity photons has been achieved as well, making for a systems that is at first sight strongly analogous to the microcavity one. For example, in Ref. [8], a BEC was placed inside an optical cavity, that was tuned to an electronic transition of the atoms, a situation very similar to the quantum well embedded in a microcavity. An important difference between the two cases is the dimensionality of the photon. Where it has in the semiconductor case the same dimensionality as the exciton, in the atomic case, the photon is zero-dimensional where the condensate is 3D. A second ingredient that causes an important difference, where the motion of the Ga and As atoms is negligible for the crystalline solid state materials, the atoms move while they interact with the light, leading to optomechanical effects [8].

1.3 Observables

1.3.1 Microcavities

The measurement of the polariton state inside the microcavity is straightforward, thanks to the one-to-one correspondence between the microcavity polaritons and the light that is transmitted through the microcavity mirrors [46]. Using standard optical techniques, the polariton density can be measured in real space $n(\mathbf{x})$ or in

momentum space $n(\mathbf{k})$. Using a spectrometer, the energy spectrum is readily obtained, resulting in images of $n(\mathbf{x}, \omega)$ or $n(\mathbf{k}, \omega)$. When a streak camera is used, the time evolution of the density can be monitored with a ps resolution.

By interfering the light that is emitted at different positions, the spatial coherence $g^{(1)}(\mathbf{x}_1, \mathbf{x}_2) = \langle \psi^+(\mathbf{x}_1)\psi(\mathbf{x}_2)\rangle / \sqrt{n(\mathbf{x}_1)n(\mathbf{x}_2)}$ can be measured [28]. From the interferrograms, also the average phase difference between different regions in the condensate can be extracted. This has allowed to evidence the existence of quantized vortices in polariton condensates [32]. This interference technique to visualize vortices has been first used for atomic condensates by Inouye et al. [27].

It is important to point out that all the measurements of polariton gases are performed over times that are very long as compared to the polariton life time. For a steady state measurement, this means that actually a long time average is recorded. In practice, the cw experiments are performed with long pulses. A typical measurement takes a time that is long with respect to the pulse duration and thus averages over many realizations of the condensate. For the observation of vortices, this means that only an average phase profile is measured, that completely misses moving vortices. For pulsed experiments where the time evolution is followed, the measurements record the average over multiple realizations of the dynamics. Again, the particular trajectory of a single realization cannot be followed.

1.3.2 Ultracold Atoms

The main observable of ultracold atoms is the density: the atomic (column) density can be imaged through its absorption of laser light. It has turned out that from the density, combined with an engineered evolution of the system before recording it, an enormous wealth of information can be derived. The clearcut observation of BEC in 1995 was a density measurement performed a certain time after the trap was switched off. The free expansion maps approximately the momentum to the distance and thus gives a good estimate of the momentum distribution. A further analysis shows that the mapping of distance to momentum is modified by the interactions during the early stages of the expansion. Note that in the polariton case, the momentum distribution is also obtained by a kind of free expansion of the emitted photons. There however, interactions are always negligible, because the propagation takes fully place outside of the microcavity, where photon-photon interactions are absent.

Also from the *in situ* measurements of the atomic clouds, important information can be extracted. By using high resolution optical [48] or scanning electron microscopy (SEM) techniques, the atomic density profiles can be measured with a resolution that is better than the interparticle distance and the lattice spacing of optical lattices. Thanks to the single atom sensitivity, also higher order correlations can be measured. This technique will be described in Chap. 18.

A crucial difference between the measurements of ultracold atoms and polaritons is that in the case of the ultracold atoms information is obtained from a single

shot measurement. A picture of a single realization of the ensemble of atoms is taken. This is relevant for phase measurements. Two atomic clouds can be made to interfere with each other and a particular realization of an experiment will always show interference fringes, irrespective of whether the phases of the two clouds are related or not. This makes it straightforward to observe spontaneous vortices [24]. The presence of a vortex is signaled by a fork like dislocation in the interference pattern between the condensate and a reference condensate. By repeating such an experiment many times, the probability distribution for the number of vortices can be measured.

Spectral information on the Bose gases can be extracted by applying time-dependent laser fields. An example is Bragg spectroscopy [50]. In this type of experiments, two lasers with frequency difference $\Delta\omega$ and wave vector difference Δk are applied to the gas. A large response of the atoms is observed when $(\Delta k, \Delta\omega)$ coincides with a resonance in the structure factor. Another example is modulation spectroscopy, where the standing laser field that creates an optical lattice is modulated [52]. The excitation frequency and spectrum turns out to be a precise probe for the properties of the quantum fluid.

For the measurement of temporal coherence, Ramsey type experiments can be used. A proposal for the measurement of the temporal coherence of atomic condensates is discussed in Chap. 15.

1.4 Physical Properties

1.4.1 Condensate Shape

In contrast to conventional condensed matter systems such as the electron gas or superfluid Helium, both the ultracold atoms and polariton gases are strongly inhomogeneous. The overall trapping potential acting on cold atoms is usually well approximated by a quadratic potential. In the polariton case, not only trapping potentials can be present, but also the excitation that injects particles is inhomogeneous. The physical consequences of the inhomogeneity are very different for systems at thermodynamic equilibrium and for nonequilibrium gases.

In the case of cold atoms in equilibrium, the effect of a shallow quadratic trapping potential can in good approximation be described in the local density approximation. This means that the gas can be treated locally as homogeneous at a given chemical potential $\mu(\mathbf{r})$. This chemical potential varies in space as $\mu(\mathbf{r}) = \mu_0 - V_{ext}(\mathbf{r})$, where V_{ext} is the trapping potential. What at first sight could seem to be a complication, actually turns out to be a convenience: one has access to a range of chemical potentials in a single experiment. Measuring the local density, it is possible to extract the equation of state $\mu(n)$, from which thermodynamic quantities such as the pressure and phase space density can be extracted. A discussion on this method in the context of the unitary Fermi gas is given in Chap. 17.

In the polariton case on the other hand, the inhomogeneity induces more complicated phenomena. Due to the nonequilibrium situation, that breaks time reversal symmetry, the steady state can sustain flows of polaritons. In other terms, the superfluid phase is not guaranteed to be homogeneous in the steady state. For a general inhomogeneous potential $V_{ext}(\mathbf{r})$ and inhomogeneous injection of particles $P(\mathbf{r})$, it is not possible to find a steady state with a uniform superfluid phase. Because of these flows, it is a much harder problem to find the steady state. It has been observed that when exciting the polariton gas with a very small pump spot, the condensation mainly takes place at a finite wave vector. The physical interpretation is that most of the particles are flowing away from the region where they are created [42, 57]. It is even possible that under certain conditions, these flows appear under the form of quantized vortices [32]. Thanks to the polarization degree of freedom, even more complex topological structures such as half vortices can be generated [34].

1.4.2 Coherence

1.4.2.1 Spatial Coherence

The order parameter of the Bose-Einstein condensation phase transition is the long range phase coherence, which means that for large separation $|\mathbf{x}_1 - \mathbf{x}_2| \to \infty$, the first order coherence goes to a nonzero condensate density $\langle \psi^\dagger(\mathbf{x}_1)\psi(\mathbf{x}_2)\rangle = n_c \neq 0$. In ultracold atomic gases, the nonzero value of the condensate density in a 3D condensate was observed experimentally in Ref. [6].

For one and two dimensional systems at finite temperature, the Hohenberg-Mermin-Wagner theorem asserts that no true long range order can exist, $n_c = 0$. In two dimensions, there is still a phase transition from a normal gas at high temperatures to a superfluid phase at low temperatures, that is of the Berezinskii-Kosterlitz-Thouless (BKT) type. Above the transition temperature, the phase coherence decays exponentially $\langle \psi^\dagger(\mathbf{x}_1)\psi(\mathbf{x}_2)\rangle \sim \exp(-|\mathbf{x}_1 - \mathbf{x}_2|/\ell_c)$. Moreover, above the transition temperature, one expects to see the spontaneous formation of vortices. Below the transition temperature, the coherence decays as a power law of the distance $\langle \psi^\dagger(\mathbf{x}_1)\psi(\mathbf{x}_2)\rangle \sim 1/|\mathbf{x}_1 - \mathbf{x}_2|^{\alpha(T)}$. For $T \to 0$, the power goes to zero as well and long range order is recovered at zero temperature. In a finite size system, the gas can already show coherence over its full extent at finite temperature.

Pancake shaped clouds of bosonic atoms have been used to study the Kosterlitz-Thouless transition experimentally. The spontaneous vortices were observed and the transition in the analytic behavior of the coherence was observed when the gas was cooled through the transition. The most difficult aspect of the cold atom experiments is the finite size of the system. The BKT transition is theoretically usually studied for homogeneous systems, but the finite size effects can mask the algebraic decay of long range order [23].

As we have pointed out in the general description of polariton quantum fluids, Sect. 1.2.1.2, only in nonresonantly and parametrically excited microcavities, there

is a spontaneous formation of coherence. Due to the nonequilibrium character where the steady state is determined as a balance between driving and dissipation, the phase fluctuations of the polariton condensates are much less understood.

A fundamental question concerns how the nonequilibrium situation affects the long range decay of the coherence. Theoretical calculations based on very different formalisms predict that in the limit of slow phase decay, the coherence still falls off algebraically in 2D [53] and exponentially in 1D [59]. While this behavior is the same as the equilibrium Bose gas at finite temperature, the exponent (2D) and coherence length (1D) are now determined by the strength of the losses rather than by the temperature. Moreover, the details of the coupling to the reservoir affect the coherence [60].

Clear experimental results on the spatial decay of the coherence are not available yet, mainly because the size of the polariton gas is still limited and because in many experiments disorder is too large. In the recent experiments by Spano et al. [49] on a high quality sample, the coherence length of a parametrically excited polariton condensate, the spatial coherence was found to extend over the whole condensate, without any sign of algebraic decay.

1.4.2.2 Temporal Coherence

The coherence of a Bose gas does not only decay as a function of spatial distance, but also as a function of the time delay $t_1 - t_2$. For polariton condensates, the temporal coherence is in principle directly available from the spectrally resolved images

$$n(x,\omega) = \frac{1}{T}\int_0^T dt_1 dt_2 e^{i\omega(t_2-t_1)}\left\langle \psi^\dagger(\mathbf{x},t_1)\psi(\mathbf{x},t_2)\right\rangle. \tag{1.6}$$

The line narrowing at the threshold for condensation/parametric oscillation illustrates the expected increase in coherence time a mode gets macroscopically occupied. The same phenomenon takes place above the threshold of a normal laser.

Let us discuss briefly the main mechanisms that limit the coherence time of a laser. Far above the threshold, the temporal coherence of a laser is limited by the Shawlow-Townes phase diffusion, that predicts an exponential decay of the coherence with a decay time $\tau_{ST}^{-1} = 4N/\gamma$, where γ is the bare cavity line width and N the number of photons. The losses and gain contribute both equally to the magnitude of the decay rate. When the gain medium not only provides a gain for the photons, but also changes the refractive index and hence the cavity frequency, an additional contribution to the linewidth appears, the so-called Henry linewidth enhancement $\tau_H = \alpha^2\gamma/N$, where $\alpha = d\omega_C/dR$ is the ratio of the change in cavity frequency to the change in optical gain.

Both the Shawlow-Townes and Henry mechanisms are present in polariton condensates as well. In addition, the coherence time of polariton condensates is also limited by the polariton-polariton interactions [58].

For the case of atomic Bose-Einstein condensates, when losses are neglected, the only mechanism for phase decoherence comes from the interactions between

the atoms. The analysis by Castin and Sinatra, presented in Chap. 15, shows that the ensemble (microcanonical, canonical, grand canonical) changes the functional behavior of the temporal coherence.

1.4.3 Superfluidity

The phase coherence of a Bose-Einstein condensed gas has profound consequences on its hydrodynamic behavior and shows effects such as persistent flows and quantization of vorticity. It has turned out that the phenomena associated to superfluidity are robust with respect to particle losses so that many of the phenomena that were first studied with ^{4}He and ultracold atoms can also be observed in polariton gases.

A major consequence of Bose-Einstein condensation on an interacting system is the change in the spectrum of elementary excitations from quadratic to linear. According to the argument by Landau, this change of the excitation spectrum is responsible for the dissipationless flow of the superfluid component, because the energy cannot be lowered by creating excitations on top of the superfluid, at least for superfluid velocities below the speed of sound. When the speed of sound is exceeded, excitations are created and the superflow is dissipated.

The use of an energetic argument could suggest that the dissipationless flow is limited to systems at thermodynamic equilibrium, but this turns out not to be the case. The Landau critical velocity can be derived without relying on energetic minimization arguments. Let us limit ourselves to the case of static defects. The excitation spectrum on top of a moving condensate (in equilibrium or not) is obtained in the rest frame of the defect by a Galilean transformation. A static defect can only create excitations at the frequency of the condensate. As long as the condensate speed is below the speed of sound, no excitations can be created.

In the polariton case, this mechanism results in a strong suppression of the Rayleigh scattering when the polariton gas is in the superfluid regime. Since it is for this physics not important whether the superfluid phase coherence is spontaneous or not, the easiest experiment to observe the reduced scattering is under resonant excitation. Following the suggestion by Carusotto and Ciuti [9], this suppression was experimentally observed by Amo et al. [2], where a resonantly excited polariton condensate was collided with a natural defect on the sample. In the atomic condensate case, the experiments probing the dissipation of superfluidity were performed soon after the realization of BEC. The defect they used was created by a laser field that exerts a repulsive potential on the atoms [41].

The Landau argument being based on the linear excitation spectrum is only valid for weak perturbations that do not strongly change the condensate density and speed. For strong defects, the theoretical analysis by Frisch et al. [20] has shown that the critical velocity is lower by a factor of more than two. The physical reason is that a large defect strongly alters the density and speed of the superfluid. This implies that locally the Landau criterion can be violated when the asymptotic speed is still below the sound speed. In this case, the dissipation of the superflow does not take place

in the form of elementary phonon excitations, but rather in the periodic shedding of vortices (at lower speeds) or in the creation of a dark soliton (at higher speeds). Experimentally, both in cold atoms [37] and in polariton condensates [3, 36] (see Chaps. 6 and 7), this instability of the superflow was observed. An extensive discussion of the theory of the critical speed in atomic condensates is given in Chap. 12.

The quantization of vorticity is a key feature of superfluids. Soon after the realization of Bose Einstein condensation of ultracold atoms, quantized vortices and vortex lattices were generated by rotating the trap. The study of rotating atomic gases have allowed for a detailed study of many phenomena of rotating Bose gases, such as the Kelvin modes of vortex lines and the Tkachenko modes of vortex lattices [18]. Currently, there is a great interest in reaching the regime of ultrafast rotation where correlated quantum hall states can be created. One of the most promising techniques are artificial gauge fields created by a properly designed laser field [14].

Furthermore, when many vortices are present they can form complex tangles, a quantum turbulent state. The theory of quantum turbulence applied to ultracold atomic gases is discussed in Chap. 13, where pioneering experiments are discussed in Chap. 14.

In polariton condensates, mechanical rotation speeds needed to induce vortices are technically not achievable, but in this case the nonequilibrium situation can lead to the spontaneous formation of vortices [32] and even the formation of vortex lattices has been predicted [29].

The interplay between the polarization degree of freedom and superflows gives rise to the existence of topological defects that are more complicate than standard quantized vortices. These objects are discussed in Chaps. 4 and 5.

1.4.4 Disorder

The effect of disorder on quantum systems has proven to be very rich. The original studies were motivated by the unavoidable presence of random fluctuations when solid state structures are fabricated. The problem of a particle moving in a random potential whose magnitude is described by a statistical distribution has become an important field of research. Already on the level of single particle physics, random potentials have a dramatic impact on the behavior of quantum systems. The solutions of the wave equation are qualitatively different. As it was shown by Anderson, waves are always localized in a 1D random potential, where in 3D, there is a mobility edge, i.e. an energy above which the waves can propagate through the whole space.

In the case of ultracold atomic gases, potential fluctuations are absent, but this makes the atomic gases an almost ideal testing bed for the precise study of the effect of disorder on quantum systems, by applying an additional laser field with random intensity distribution [44]. The polariton system is rather in a standard solid state situation, where the disorder is unavoidable and often of the same order as the other energy scales.

In the cold atom gases, the Anderson localization of waves in a 1D random potential was clearly demonstrated by several groups. The disorder is made by applying a laser beam on the atoms whose intensity varies randomly in space. In the presence of such a random potential, the atoms can no longer propagate, but the density distribution at long times shows an exponential decay, characteristic for the Anderson localized states [5, 43].

When interactions enter into play, the physical picture becomes much richer. On the one hand the interactions screen out the disorder potential and thus delocalize the Bose gas, on the other hand the interactions cause dephasing that is detrimental to superfluidity. The ground state of the strictly noninteracting Bose gas is the state where all the particles are in the lowest energy state, that is exponentially localized. These exponentially localized states below to the so-called Lifshitz tail. In the thermodynamic limit where the number of particles goes to infinity, the density goes to infinity as well. An infinitesimal amount of interactions dramatically changes the ground state, that spreads over many of the low-lying localized states and forms many islands, a 'fragmented' state.

When the interaction strength is increased, the density spreads out and starts to cover space more and more homogeneously. Consequently, the coherence of the Bose gas improves. On the mean field level, the defragmentation transition coincides with the Bose glass to superfluid transition, where the spatial coherence decay goes from exponential to algebraic. Interactions can thus enhance the coherence of a disordered Bose gas. This trend is opposite to the quantum depletion of a homogeneous condensate that grows with the interaction strength. This effect of quantum fluctuations starts to dominate when the mean field theory breaks down, i.e. in the case of strong interactions when the interaction energy is of the order of the tunneling energy to go from one to the next valey in the disorder potential. The disorder potential then amplifies the effect of quantum fluctuations due to interactions in a way that is similar to a periodic potential, where the celebrated superfluid to Mott insulator phase occurs. At a critical strength of the disorder potential, a phase transition to the Bose glass phase occurs, that is in analogy with the Mott insulator phase not superfluid. The difference between the Mott insulator and Bose glass phases is that the excitation spectrum that is gapped in the Mott insulator and not gapped in the Bose glass phase [19].

1.4.5 Dynamics

An advantage of both the atom and polariton systems is that the time scales of their dynamics are slower than the temporal resolution of the measurements. This allows to study the temporal dynamics of the observables. Moreover, the external forces acting on the systems can be varied fast with respect to the dynamics.

For cold atoms, the collective excitations that are excited when the clouds are shaken have revealed a wealth of information on their properties. For example, the frequency of the breathing mode gives information on the equation of state, where

the scissor mode is very sensitive to the superfluidity of the gas [39]. Typically, the oscillation amplitude is moderate and the oscillation frequencies can be computed in linear response theory.

A more recent direction of the field concerns the study of dynamics far from equilibrium. For a review, we refer to Ref. [40]. One of the pioneering experiments on the dynamics far from equilibrium was performed in 2006 by Kinoshita et al. They created a one-dimensional Bose gas, that is a close experimental realization of the Lieb-Liniger gas. The atoms were put in a superposition of the momentum states $\pm p_0$ and it was observed that the momentum distribution remained non-Gaussian, even after thousands of collisions. This lack of thermalization was interpreted in terms of the integrability of the Lieb-Liniger gas. This experiment motivated a great body of theoretical studies on questions concerning ergodicity and integrability [40].

A second field of interest concerns quantum quenches. Here a control parameter is changed so that the system undergoes a phase transition. For classical phase transitions, this is typically the temperature; for quantum phase transitions it is rather the coupling constant that tunes the system through the quantum critical point. It is then predicted that excitations will be created through the so-called Kibble-Zurek (KZ) mechanism [30, 62]. In the case of Bose-Einstein condensation, those excitations are quantized vortices and they were observed experimentally by Weiler et al. [55]. In these experiments, the temperature was quickly lowered below the critical one and the spontaneously formed vortices were observed. Related experiments were performed with exciton-polaritons [35], where the density was suddenly increased above the critical density. The subsequent buildup of the spatial coherence was monitored, but no spontaneous vortices were observed, because so far no experimental technique exists to visualize them (see Sect. 1.3.1).

With respect to dynamics, we remind that the polariton system is intrinsically in a non-equilibrium situation when the driving compensates for the losses. One has to resort do descriptions of the dynamics to assess the properties of the stationary state. In most cases, the steady state of the ultracold atomic gases corresponds to a thermal state that can be described with statistical methods. The flexibility of ultracold atoms has however also generated proposals to study driven-dissipative dynamics with ultracold atoms, where an environment is engineered so to introduce nonequilibrium phase transitions [16] and topological states of matter [17].

References

1. V.M. Agranovich, *Excitations in Organic Solids*. International Series of Monographs on Physics (Oxford University Press, London, 2009)
2. A. Amo, J. Lefrere, S. Pigeon, C. Adrados, C. Ciuti, I. Carusotto, R. Houdre, E. Giacobino, A. Bramati, Superfluidity of polaritons in semiconductor microcavities. Nat. Phys. **5**(11), 805–810 (2009)
3. A. Amo, S. Pigeon, D. Sanvitto, V.G. Sala, R. Hivet, I. Carusotto, F. Pisanello, G. Lemenager, R. Houdre, E. Giacobino, C. Ciuti, A. Bramati, Hydrodynamic solitons in polariton superfluids. Science **332**, 1167–1170 (2011)

4. R. Balili, V. Hartwell, D. Snoke, L. Pfeiffer, K. West, Bose-Einstein condensation of microcavity polaritons in a trap. Science **316**(5827), 1007–1010 (2007)
5. J. Billy, V. Josse, Z. Zuo, A. Bernard, B. Hambrecht, P. Lugan, D. Clement, L. Sanchez-Palencia, P. Bouyer, A. Aspect, Direct observation of Anderson localization of matter waves in a controlled disorder. Nature **453**(7197), 891–894 (2008)
6. I. Bloch, T.W. Hansch, T. Esslinger, Measurement of the spatial coherence of a trapped Bose gas at the phase transition. Nature **403**(6766), 166–170 (2000)
7. I. Bloch, J. Dalibard, W. Zwerger, Many-body physics with ultracold gases. Rev. Mod. Phys. **80**, 885–964 (2008)
8. F. Brennecke, T. Donner, S. Ritter, T. Bourdel, M. Kohl, T. Esslinger, Cavity QED with a Bose-Einstein condensate. Nature **450**(7167), 268–271 (2007)
9. I. Carusotto, C. Ciuti, Probing microcavity polariton superfluidity through resonant Rayleigh scattering. Phys. Rev. Lett. **93**, 166401 (2004)
10. E.A. Cerda-Méndez, D.N. Krizhanovskii, M. Wouters, R. Bradley, K. Biermann, K. Guda, R. Hey, P.V. Santos, D. Sarkar, M.S. Skolnick, Polariton condensation in dynamic acoustic lattices. Phys. Rev. Lett. **105**, 116402 (2010)
11. C. Ciuti, V. Savona, C. Piermarocchi, A. Quattropani, P. Schwendimann, Role of the exchange of carriers in elastic exciton-exciton scattering in quantum wells. Phys. Rev. B **58**, 7926–7933 (1998)
12. P. Cladé, C. Ryu, A. Ramanathan, K. Helmerson, W.D. Phillips, Observation of a 2D Bose gas: From thermal to quasicondensate to superfluid. Phys. Rev. Lett. **102**, 170401 (2009)
13. F. Dalfovo, S. Giorgini, L.P. Pitaevskii, S. Stringari, Theory of Bose-Einstein condensation in trapped gases. Rev. Mod. Phys. **71**, 463–512 (1999)
14. J. Dalibard, F. Gerbier, G. Juzeliūnas, P. Öhberg, Colloquium: Artificial gauge potentials for neutral atoms. Rev. Mod. Phys. **83**, 1523–1543 (2011)
15. B. Deveaud, *The Physics of Semiconductor Microcavities* (Wiley, New York, 2007)
16. S. Diehl, A. Micheli, A. Kantian, B. Kraus, H.P. Buchler, P. Zoller, Quantum states and phases in driven open quantum systems with cold atoms. Nat. Phys. **4**(11), 878–883 (2008)
17. S. Diehl, E. Rico, M.A. Baranov, P. Zoller, Topology by dissipation in atomic quantum wires. Nat. Phys. **7**(12), 971–977 (2011)
18. A.L. Fetter, Rotating trapped Bose-Einstein condensates. Rev. Mod. Phys. **81**(2), 647–691 (2009)
19. M.P.A. Fisher, P.B. Weichman, G. Grinstein, D.S. Fisher, Boson localization and the superfluid-insulator transition. Phys. Rev. B **40**, 546–570 (1989)
20. T. Frisch, Y. Pomeau, S. Rica, Transition to dissipation in a model of superflow. Phys. Rev. Lett. **69**, 1644–1647 (1992)
21. S. Giorgini, L.P. Pitaevskii, S. Stringari, Theory of ultracold atomic Fermi gases. Rev. Mod. Phys. **80**, 1215–1274 (2008)
22. M. Greiner, O. Mandel, T. Esslinger, T.W. Hansch, I. Bloch, Quantum phase transition from a superfluid to a Mott insulator in a gas of ultracold atoms. Nature **415**(6867), 39–44 (2002)
23. Z. Hadzibabic, J. Dalibard, Two-dimensional Bose fluids: An atomic physics perspective, in *Nano Optics and Atomics: Transport of Light and Matter Waves*, Proceedings of the International School of Physics "Enrico Fermi", vol. CLXXIII, ed. by D. Wiersma, R. Kaiser, L. Fallani (2011)
24. Z. Hadzibabic, P. Krueger, M. Cheneau, B. Battelier, J. Dalibard, Berezinskii–Kosterlitz–Thouless crossover in a trapped atomic gas. Nature **441**, 1118 (2006)
25. R. Houdré, C. Weisbuch, R.P. Stanley, U. Oesterle, M. Ilegems, Nonlinear emission of semiconductor microcavities in the strong coupling regime. Phys. Rev. Lett. **85**, 2793–2796 (2000)
26. C.-L. Hung, X. Zhang, N. Gemelke, C. Chin, Observation of scale invariance and universality in two-dimensional Bose gases. Nature **470**(7333), 236–239 (2011)
27. S. Inouye, S. Gupta, T. Rosenband, A.P. Chikkatur, A. Görlitz, T.L. Gustavson, A.E. Leanhardt, D.E. Pritchard, W. Ketterle, Observation of vortex phase singularities in Bose-Einstein condensates. Phys. Rev. Lett. **87**, 080402 (2001)

28. J. Kasprzak, M. Richard, S. Kundermann, A. Baas, P. Jeambrun, J.M.J. Keeling, F.M. Marchetti, M.H. Szymanska, R. Andre, J.L. Staehli, V. Savona, P.B. Littlewood, B. Deveaud, L.S. Dang, Bose-Einstein condensation of exciton polaritons. Nature **443**(7110), 409–414 (2006)
29. J. Keeling, N.G. Berloff, Spontaneous rotating vortex lattices in a pumped decaying condensate. Phys. Rev. Lett. **100**(25), 250401 (2008)
30. T.W.B. Kibble, Topology of cosmic domains and strings. J. Phys. A, Math. Gen. **9**(8), 1387 (1976)
31. D.N. Krizhanovskii, S.S. Gavrilov, A.P.D. Love, D. Sanvitto, N.A. Gippius, S.G. Tikhodeev, V.D. Kulakovskii, D.M. Whittaker, M.S. Skolnick, J.S. Roberts, Self-organization of multiple polariton-polariton scattering in semiconductor microcavities. Phys. Rev. B, Condens. Matter Mater. Phys. **77**(11), 115336 (2008)
32. K.G. Lagoudakis, M. Wouters, M. Richard, A. Baas, I. Carusotto, R. Andre, L.S. Dang, B. Deveaud-Pledran, Quantized vortices in an exciton-polariton condensate. Nat. Phys. **4**(9), 706–710 (2008)
33. K.G. Lagoudakis, T. Ostatnický, A.V. Kavokin, Y.G. Rubo, R. André, B. Deveaud-Plédran, Observation of half-quantum vortices in an exciton-polariton condensate. Science **326**(5955), 974–976 (2009)
34. K.G. Lagoudakis, T. Ostatnicky, A.V. Kavokin, Y.G. Rubo, R. Andre, B. Deveaud-Pledran, Observation of half-quantum vortices in an exciton-polariton condensate. Science **326**(5955), 974–976 (2009)
35. G. Nardin, K.G. Lagoudakis, M. Wouters, M. Richard, A. Baas, R. André, L.S. Dang, B. Pięţka, B. Deveaud-Plédran, Dynamics of long-range ordering in an exciton-polariton condensate. Phys. Rev. Lett. **103**, 256402 (2009)
36. G. Nardin, G. Grosso, Y. Leger, B. Pięţka, F. Morier-Genoud, B. Deveaud-Pledran, Hydrodynamic nucleation of quantized vortex pairs in a polariton quantum fluid. Nat. Phys. **7**(8), 635–641 (2011)
37. T.W. Neely, E.C. Samson, A.S. Bradley, M.J. Davis, B.P. Anderson, Observation of vortex dipoles in an oblate Bose-Einstein condensate. Phys. Rev. Lett. **104**, 160401 (2010)
38. C. Pethick, H. Smith, *Bose-Einstein Condensation in Dilute Gases* (Cambridge University Press, Cambridge, 2002)
39. L. Pitaevskii, S. Stringari, *Bose-Einstein Condensation* (Oxford University Press, London, 2003)
40. A. Polkovnikov, K. Sengupta, A. Silva, M.V. Colloquium, Nonequilibrium dynamics of closed interacting quantum systems. Rev. Mod. Phys. **83**, 863–883 (2011)
41. C. Raman, M. Köhl, R. Onofrio, D.S. Durfee, C.E. Kuklewicz, Z. Hadzibabic, W. Ketterle, Evidence for a critical velocity in a Bose-Einstein condensed gas. Phys. Rev. Lett. **83**, 2502–2505 (1999)
42. M. Richard, J. Kasprzak, R. Romestain, R. André, L.S. Dang, Spontaneous coherent phase transition of polaritons in CdTe microcavities. Phys. Rev. Lett. **94**, 187401 (2005)
43. G. Roati, C. D'Errico, L. Fallani, M. Fattori, C. Fort, M. Zaccanti, G. Modugno, M. Modugno, M. Inguscio, Anderson localization of a non-interacting Bose-Einstein condensate. Nature **453**(7197), 895–898 (2008)
44. L. Sanchez-Palencia, M. Lewenstein, Disordered quantum gases under control. Nat. Phys. **6**(2), 87–95 (2010)
45. V. Savona, Effect of interface disorder on quantum well excitons and microcavity polaritons. J. Phys. Condens. Matter **19**(29), (2007)
46. V. Savona, C. Piermarocchi, A. Quattropani, P. Schwendimann, F. Tassone, Optical properties of microcavity polaritons. Phase Transit. **68**(1, Part B), 169–279 (1999)
47. I.A. Shelykh, A.V. Kavokin, Y.G. Rubo, T.C.H. Liew, G. Malpuech, Polariton polarization-sensitive phenomena in planar semiconductor microcavities. Semicond. Sci. Technol. **25**(1), 013001 (2010)
48. J.F. Sherson, C. Weitenberg, M. Endres, M. Cheneau, I. Bloch, S. Kuhr, Single-atom-resolved fluorescence imaging of an atomic Mott insulator. Nature **467**(7311), 68–72 (2010)

49. R. Spano, J. Cuadra, C. Lingg, D. Sanvitto, M.D. Martin, P.R. Eastham, M. van der Poel, J.M. Hvam, L. Vina, Build up of off-diagonal long-range order in microcavity exciton-polaritons across the parametric threshold (2011). arXiv:1111.4894
50. J. Stenger, S. Inouye, A.P. Chikkatur, D.M. Stamper-Kurn, D.E. Pritchard, W. Ketterle, Bragg spectroscopy of a Bose-Einstein condensate. Phys. Rev. Lett. **82**, 4569–4573 (1999)
51. R.M. Stevenson, V.N. Astratov, M.S. Skolnick, D.M. Whittaker, M. Emam-Ismail, A.I. Tartakovskii, P.G. Savvidis, J.J. Baumberg, J.S. Roberts, Continuous wave observation of massive polariton redistribution by stimulated scattering in semiconductor microcavities. Phys. Rev. Lett. **85**(17), 3680–3683 (2000)
52. T. Stöferle, H. Moritz, C. Schori, M. Köhl, T. Esslinger, Transition from a strongly interacting 1D superfluid to a Mott insulator. Phys. Rev. Lett. **92**, 130403 (2004)
53. M.H. Szymanska, J. Keeling, P.B. Littlewood, Nonequilibrium quantum condensation in an incoherently pumped dissipative system. Phys. Rev. Lett. **96**(23), 230602 (2006)
54. M. Vladimirova, S. Cronenberger, D. Scalbert, K.V. Kavokin, A. Miard, A. Lemaître, J. Bloch, D. Solnyshkov, G. Malpuech, A.V. Kavokin, Polariton-polariton interaction constants in microcavities. Phys. Rev. B **82**, 075301 (2010)
55. C.N. Weiler, T.W. Neely, D.R. Scherer, A.S. Bradley, M.J. Davis, B.P. Anderson, Spontaneous vortices in the formation of Bose-Einstein condensates. Nature **455**(7215), 948–951 (2008)
56. C. Weisbuch, M. Nishioka, A. Ishikawa, Y. Arakawa, Observation of the coupled exciton-photon mode splitting in a semiconductor quantum microcavity. Phys. Rev. Lett. **69**, 3314–3317 (1992)
57. E. Wertz, L. Ferrier, D.D. Solnyshkov, R. Johne, D. Sanvitto, A. Lemaitre, I. Sagnes, R. Grousson, A.V. Kavokin, P. Senellart, G. Malpuech, J. Bloch, Spontaneous formation and optical manipulation of extended polariton condensates. Nat. Phys. **6**(11), 860–864 (2010)
58. D.M. Whittaker, P.R. Eastham, Coherence properties of the microcavity polariton condensate. Europhys. Lett. **87**(2), 27002 (2009)
59. M. Wouters, I. Carusotto, Absence of long-range coherence in the parametric emission of photonic wires. Phys. Rev. B **74**, 245316 (2006)
60. M. Wouters, V. Savona, Stochastic classical field model for polariton condensates. Phys. Rev. B **79(16)**, 165302 (2009)
61. C. Zipkes, S. Palzer, C. Sias, M. Kohl, A trapped single ion inside a Bose-Einstein condensate. Nature **464**(7287), 388–391 (2010)
62. W.H. Zurek, Cosmological experiments in superfluid helium? Nature **317**(6037), 505–508 (1985)

Chapter 2
Universality in Modelling Non-equilibrium Pattern Formation in Polariton Condensates

N.G. Berloff and J. Keeling

Abstract The key to understanding the universal behaviour of systems driven away from equilibrium lies in the common description obtained when particular microscopic models are reduced to order parameter equations. Universal order parameter equations written for complex matter fields are widely used to describe systems as different as Bose-Einstein condensates of ultra cold atomic gases, thermal convection, nematic liquid crystals, lasers and other nonlinear systems. Exciton-polariton condensates recently realised in semiconductor microcavities are pattern forming systems that lie somewhere between equilibrium Bose-Einstein condensates and lasers. Because of the imperfect confinement of the photon component, exciton-polaritons have a finite lifetime, and have to be continuously re-populated. As photon confinement improves, the system more closely approximates an equilibrium system. In this chapter we review a number of universal equations which describe various regimes of the dynamics of exciton-polariton condensates: the Gross-Pitaevskii equation, which models weakly interacting equilibrium condensates, the complex Ginsburg-Landau equation—the universal equation that describes the behaviour of systems in the vicinity of a symmetry-breaking instability, and the complex Swift-Hohenberg equation that in comparison with the complex Ginsburg-Landau equation contains additional nonlocal terms responsible for spatial mode selection. All these equations can be derived asymptotically from a generic laser model given by Maxwell-Bloch equations. Such an universal framework allows the unified treatment of various systems and allows one to continuously cross from one system to another. We discuss the relevance of these equations, and their consequences for pattern formation.

N.G. Berloff (✉)
Department of Applied Mathematics and Theoretical Physics, University of Cambridge, Cambridge CB3 0WA, UK
e-mail: N.G.Berloff@damtp.cam.ac.uk

J. Keeling
School of Physics and Astronomy, University of St Andrews, SUPA, St Andrews KY16 9SS, UK
e-mail: jmjk@st-andrews.ac.uk

A. Bramati, M. Modugno (eds.), *Physics of Quantum Fluids*,
Springer Series in Solid-State Sciences 177, DOI 10.1007/978-3-642-37569-9_2,

2.1 Introduction

For a dissipative macroscopic system in thermal equilibrium, relaxation toward a state of minimum free energy determines the states that the system may adopt, and any possible pattern formation. In contrast, if a system is driven out of equilibrium by external fluxes, then no such simple description is possible. i.e., if a system may exchange particles and energy with multiple baths (reservoirs), then the states the system adopts depend not only on the temperatures and chemical potentials of these reservoirs, but also on the rate at which particles and energy are injected and lost from the system. This can not generally be captured by relaxation to minimise a given energy functional.

Both equilibrium and non-equilibrium systems can be characterised by mean-field variables if field fluctuations are negligible (fluctuations can however be introduced phenomenologically into the evolution equations if required). A mean-field approach leads naturally to the concept of the order parameter, and the corresponding order parameter equation. The order parameter is either a physical field or an abstract field which acquires a non-zero value in the an ordered phase (such as a Bose-condensed or lasing state), and vanishes in the normal state. When considering a spatially inhomogeneous system (with trapping, or inhomogeneous pumping), the order parameter may vary in space. When considering a non-equilibrium system, or the dynamics of a system as it approaches its equilibrium state, the order parameter may also vary in time. In such cases, the order parameter equation describes the space and time dependence of the order parameter, accounting for the generic features of the system's dynamics.

One important classification of order parameter equations distinguishes whether they describe relaxation towards an equilibrium configuration, or phase evolution in a conservative system, or a mixture of the two [33]. For a dissipative system, the dynamics may be described by using an energy functional $\mathcal{F}[\psi]$, written in terms of the order parameter ψ and its spatial derivatives. The dissipative system dynamics causes this energy functional to decay as a function of time, reaching a minimal value at equilibrium, i.e. $\partial_t \psi = -\Gamma \partial_\psi \mathcal{F}$. The dynamical critical behaviour of such systems has been extensively reviewed by Hohenberg and Halperin [15]. Such an approach is appropriate for many solid-state systems, including in particular non-equilibrium superconductivity [22]. In contrast, for isolated systems such as ultracold atomic gases, the order parameter obeys conservative dynamics, in which the energy functional does not change with time, and the order parameter instead follows Hamiltonian dynamics. We will discuss the behaviour of systems that lie between these two extremes of purely dissipative and purely conservative dynamics, a scenario that includes the non-equilibrium polariton condensate.

The structure of the energy functional, and thus of the resulting order parameter equation, is determined by the symmetries of the order parameter space. Taking into account also the fact that near a phase transition, the characteristic lengthscale of fluctuations diverges, it becomes possible to restrict the form of the energy functional by keeping the lowest order derivative terms that possess the required symmetries. This makes it possible to divide systems into universality classes, depending only on the symmetries and the nature of the dynamics [15, 17]. Identifying which

classes various system belong to allows one to draw similarities between systems that are very different in nature and to predict the behaviour of the new systems that fall into previously known universality class. For instance, symmetry under changing the phase of the order parameter restricts the energy functionals to dependence on $|\psi|$ only, and considering the lowest order form that allows for a symmetry breaking from disordered (zero) to ordered (nonzero) state gives a potential as a quartic polynomial in $|\psi|$. Including the lowest compatible order of spatial derivative terms then gives the energy functional whose dissipative dynamics correspond to the Ginzburg-Landau equation:

$$\mathcal{F} = \int dV \nabla\psi \cdot \nabla\psi^* + 1/U_0\big(\mu - U_0|\psi|^2\big)^2, \tag{2.1}$$

where μ is the control parameter that forces the system to move from the normal state $|\psi| = 0$ to the ordered state with $|\psi|^2 = \mu/U_0$. Equation (2.1) is expected to be relevant to a physical system in the vicinity of the phase transition, where the smallness of the modulus and the derivatives of the order parameter allow to keep only the leading order terms in the expansion. Higher derivatives and other higher order terms can be kept to allow for more complex forms of order and associated phase transitions.

Understanding the universality class of a given system leads to understanding of fundamentals of the behaviour of that system. The studies of vortices and vortex dynamics in superfluid helium [14] led to prediction and experimental realisation of vortices first in nonlinear optics [3], then in atomic Bose-Einstein condensates [10] and finally in nonequilibrium solid-state condensates [25, 27] all due the hydrodynamic interpretation of the order parameter equations. Spiral waves in biological and chemical systems suggested the existence of such meandering waves in class B lasers. Solitary waves in atomic systems all have their analogs in nonlinear optics. Finally, many of the experiments in solid-state condensates are now motivated by finding localised excitations similar to other system that share the same universality class [1, 11]. Pattern formation in systems that belong to the same universality class share similar properties. Patterns appear in open nonlinear systems when an amplitude distribution of the order parameter becomes unstable above a certain threshold. Linear instability gives rise to a so-called pure state that, if nonlinearities are weak, can dominate the dynamics. Strong nonlinearities may mix the eigenvalues leading to various stationary or chaotic combinations of pure states with different combinations occupying either all space or different space regions.

In this chapter we shall follow the evolution from equilibrium condensates to non-equilibrium condensates to lasers analysing their universality, emphasising similarities and differences. We will discuss in some detail the origin of the most general order parameter equation for the laser system, and comment on the relation of this order parameter equation to that for cold atoms and for non-equilibrium polariton condensation. We will then demonstrate how the various terms that may exist in the order parameter equation affect the patterns which arise, focusing on three cases: the case with homogeneous pumping and no trapping, the case with inhomogeneous pumping and no trapping, and the case with an harmonic trap.

2.1.1 Review of Physical Systems

Laser dynamics is described by coupling Maxwell equations with Shrödinger equations for N atoms confined in the cavity. Expanding the electric field in cavity modes and keeping only the leading order mode leads to the equations that couple the amplitude of this mode with the collective variables that describe the polarisation and population of the gain medium. Such coupled equations are known as Maxwell-Bloch (MB) equations. Lasers are then classified depending on the relative order of the loss rates for the electric field, compared to the decay rates of the gain medium polarisation and population. The MB equations have two homogeneous stationary solutions: nonlasing (zero order parameter) and lasing (nonzero order parameter) solutions. The instabilities of these solutions, and therefore, pattern formation, are described by universal order parameter equations: the complex Swift-Hohenberg (cSH) [40] equation for lasers with a fast relaxation of population inversion and the cSH equation coupled to a mean flow if the population inversion is slowly varying. The universal equation describing the bifurcation of lasing solution takes the form of a cSH equation coupled to a Kuramoto-Sivashinsky equation [24, 35].

Semiconductor microcavities confine photon modes, which may then interact with electronic excitations in the semiconductor, see the Introduction. If the cavity is resonant with the energy to create an exciton (a bound electron hole pair), and if the exciton-photon coupling is strong enough, then new normal modes (new quasiparticles) arise as hybrids of excitons and photons: polaritons. For low enough densities, these may be considered as bosonic quasiparticles, and so can form a condensed (coherent) state above a critical density. These are intrinsically non equilibrium systems with the steady states set by balance between pumping and losses due to the short lifetime of polaritons. Depending on whether the emission from the microcavity follows the bare photon or the lower polariton dispersion the system shows either regular lasing or polariton condensation and in this sense crosses over continuously from weak coupling at higher temperatures and pumping strengths to strong coupling at lower temperatures and lower pumping intensities. Losses in the microcavity systems can be decreased by improving the quality of dielectric Bragg mirrors. The smaller the pumping and losses become the closer polariton condensates come to resemble equilibrium Bose-Einstein condensates (BECs). It seems therefore that the unified approach should be possible to describe the transition from normal lasers to the equilibrium BECs via polariton condensates. There are some other differences between atomic or polariton condensates and normal lasers. The operation of a photon laser is based on three ingredients: a resonator for the electromagnetic field, an gain medium and a excitation mechanism for the gain medium. When excited, the gain medium will undergo stimulated emission of radiation that amplifies the electromagnetic field in the cavity. In contrast, for polariton condensates there is instead stimulated scattering within the set of polariton modes, and condensation can take place without any inversion of the gain medium, and thus potentially having a lower threshold [16]. A microscopic theory would be required to fully describe how all of these aspects cross over from polariton condensation to lasing, however given the universality of order parameter equations, one may hope to write a single order

parameter equation which captures these different regimes by varying appropriate parameters.

2.2 Derivation of Order Parameter Equations

In this section we show how various order parameter equations arise in descriptions of lasers, and how these relate to the order parameter equations relevant to ultracold atoms and polariton condensates. We start with a mean field (semiclassical) model of a laser, the MB system of equations. In Sect. 2.2.2 we show how the assumption of small relaxation times for atomic polarisation in comparison with the cavity relaxation time reduces these equations to the complex Ginzburg-Landau (cGL) equations [2] or the coupled cGL equation and the gain medium population dynamics [41]. These models have been extensively used to model non-equilibrium condensates [11, 19, 45, 47]. We discuss how the mode selection, in which a particular transverse mode grows fastest, is lost in the derivation of these models. Then, in Sect. 2.2.3 we instead follow the derivation used in [31] based on the multi-scale expansion technique to derive the cSH equations for class A and class C lasers [9]. A pedagogical review of how order parameter equations can be derived for some simple models of lasers is given in [37], but not including the multiscale analysis presented below. In Sect. 2.2.4 we then discuss how nonlinear interactions appear in these equations, and discuss the interpretation of these equations as order parameter equations for polariton condensates. If the reservoir dynamics is slow in comparison with time evolution of the order parameter these equation should be replaced by a coupled system explicitly modelling the reservoir dynamics. In the limit of the long life-time of the particles the system becomes the Gross-Pitaevskii (GP) equation aka the nonlinear Schrödinger (NLS) equation that describes atomic BECs.

2.2.1 Maxwell-Bloch Equations for a Laser

We start with the MB equations for a wide-aperture laser with an intracavity saturable absorber with multiple transverse modes in the single longitudinal mode approximation [28]

$$\frac{\partial E}{\partial t} - i\nabla^2 E = P_g - P_a - (1 + i\Delta_e)E, \tag{2.2}$$

$$\tau_{\perp g}\frac{\partial P_g}{\partial t} + (1 + i\Delta_g)P_g = EG, \tag{2.3}$$

$$\tau_{\perp a}\frac{\partial P_a}{\partial t} + (1 + i\Delta_a)P_a = EA, \tag{2.4}$$

$$\tau_g\frac{\partial G}{\partial t} = G_0 - G - \frac{1}{2}\left(E^* P_g + E P_g^*\right), \tag{2.5}$$

$$\tau_a\frac{\partial A}{\partial t} = A_0 - A - \frac{D}{2}\left(E^* P_a + E P_a^*\right), \tag{2.6}$$

where the complex field E is the envelope of the electric field, the real functions G and A are the population differences for gain and absorption media, the complex functions P_g and P_a are the envelopes of polarisation for gain and absorption media. G_0 and A_0 are the stationary values of the population difference in the absence of the laser field; they are proportional to the external gain and losses in the system. The parameter $D = \tau_{\perp a}\tau_a\mu_a^2/(\tau_{\perp g}\tau_g\mu_g^2)$ is the relative saturability of gain and loss media and μ_a and μ_g stand for the atomic dipole momenta. The parameters $\tau_{\perp a,g}$ and $\tau_{a,g}$ are the relaxation times for atomic polarisations and population differences scaled by the cavity relaxation time, the time t is also scaled by the cavity relaxation time. The parameters $\Delta_a - \Delta_e = (\omega_a - \omega_c)\tau_{\perp a}$ and $\Delta_g - \Delta_e = (\omega_g - \omega_c)\tau_{\perp g}$ are detunings between the spectral line centre and the frequency of empty cavity mode ω_c. Without loss of generality we work in rotating frame such that the fast time is eliminated via introduction of Δ_e. The spatial coordinates are rescaled by the width of the effective Fresnel zone.

2.2.2 Fast Reservoir Dephasing Limit

Following [12, 36, 37] we assume that $\tau_{\perp a}$, $\tau_{\perp g}$ are small and consider the first-order approximations to (2.2)–(2.6). Keeping up to the linear terms in these small quantities we get

$$P_g = \frac{GE}{1 + i\Delta_g} - \tau_{\perp g}\frac{\partial(GE)/\partial t}{(1 + i\Delta_g)^2}, \tag{2.7}$$

and similar for P_a. The equation on E after we substitute these expressions for P_g and P_a becomes

$$(1 + i\eta)\frac{\partial e}{\partial t} - i\left(\nabla^2 - \Delta_e\right)e = \left[(1 - i\Delta_g)g - (1 - i\Delta_a)a - 1\right]e, \tag{2.8}$$

where

$$\eta = -2\tau_{\perp g}g\Delta_g/\left(1 + \Delta_g^2\right) + 2\tau_{\perp a}a\Delta_a/\left(1 + \Delta_a^2\right), \tag{2.9}$$

and where we rescaled fields as $e = E/(1 + \Delta_g^2)$, $g = G/(1 + \Delta_g^2)$ and $a = A/(1 + \Delta_a^2)$. In writing (2.8) we kept leading order contributions in the imaginary coefficient of time derivative (which is of order $O(\tau_{\perp g}, \tau_{\perp a})$). The real coefficient of the time derivative we kept to $O(1)$ in $\tau_{\perp g}$ and $\tau_{\perp a}$. The equations for scaled gain and absorption media populations to leading order take the forms:

$$\tau_g\frac{\partial g}{\partial t} = g_0 - \left(1 + |e|^2\right)g, \tag{2.10}$$

$$\tau_a\frac{\partial a}{\partial t} = a_0 - \left(1 + d|e|^2\right)a, \tag{2.11}$$

where $a_0 = A_0/(1 + \Delta_a^2)$, $g_0 = G_0/(1 + \Delta_g^2)$ and $d = D(1 + \Delta_g^2)/(1 + \Delta_a^2)$.

2.2.2.1 Fast Reservoir Population Relaxation

The system of equations (2.8), (2.10), (2.11) can be simplified under more stringent restrictions on parameters. In the limit of fast population relaxation times $\tau_g, \tau_a \ll 1$ (class A and C lasers) (2.10), (2.11) give

$$g = \frac{g_0}{1+|e|^2}, \qquad a = \frac{a_0}{1+d|e|^2}, \tag{2.12}$$

and (2.8) becomes

$$\big(1+i\eta(e)\big)\frac{\partial e}{\partial t} - i\nabla^2 e = \left[\frac{(1-i\Delta_g)g_0}{1+|e|^2} - \frac{(1-i\Delta_a)a_0}{1+d|e|^2} - 1\right]e, \tag{2.13}$$

where the coefficient η is given by

$$\eta(e) = -2\left[\frac{\tau_{\perp g} g \Delta_g}{(1+\Delta_g^2)(1+|e|^2)} - \frac{\tau_{\perp a} a \Delta_a}{(1+\Delta_a^2)(1+d|e|^2)}\right]. \tag{2.14}$$

Close to the emission threshold $|e|^2 \ll 0$, which allows a cubic approximation for the nonlinear terms we get the complex Ginzburg-Landau equation (cGL) [2]

$$\big(i-\eta(0)\big)\frac{\partial e}{\partial t} = -\nabla^2 e + Ve + U|e|^2 e + i\big[\alpha - \beta|e|^2\big]e, \tag{2.15}$$

where we let $\alpha = g_0 - a_0 - 1$, $\beta = g_0 - a_0$, $U = da_0\Delta_a - g_0\Delta_g$, $V = g_0\Delta_g - a_0\Delta_a$.

The cGL equation is not a very accurate model of a laser since it does not take into account the selection of transverse modes. The lasers emit particular transverse modes that depend on the length of the resonator. By making the assumption that $\tau_{\perp g}, \tau_{\perp a} \to 0$, we assumed that the gain line is infinitely broad. In order to take into account the tunability of lasers that allows spatial-frequency selection a more careful derivation of the order parameter equation is required, which does not take this limit of fast polarisation relaxation.

2.2.3 Multi-Scale Analysis of the Maxwell-Bloch Equations

In this section we derive the complex Swift-Hohenberg equation capable of selecting particular transverse modes from the MB (2.2)–(2.6). A similar derivation has been done for the MB equations taking into account gain only and assuming that Δ_g is small [26]. Here we shall only assume that $\nabla^2 - \Delta_e$ is small and use it as a small parameter, $\epsilon(\nabla^2 - \Delta_e)$. We apply the technique of multi-scale expansion to E, $P_{g,a}$, G and A looking for solutions in the form of a power series expansion in ϵ, and introducing two slow time scales $T_1 = \epsilon t$, $T_2 = \epsilon^2 t$, so that $\partial_t = \epsilon\partial_{T_1} + \epsilon^2\partial_{T_2}$. Next we solve equations at equal powers of ϵ. At the leading order we get non-lasing solution $(E, P_g, P_a, G, A) = (0, 0, 0, G_0, A_0)$. At $O(\epsilon)$,

$(E_1, P_{g1}, P_{a1}, G_1, A_1) = (\psi, G_0\psi/(1+i\Delta_g), A_0\psi/(1+i\Delta_a), 0, 0)$, where ψ is a yet undetermined complex field and G_0 and A_0 are linked via $1 = G_0/(1+i\Delta_g) - A_0/(1+i\Delta_a)$. This condition specifies G_0 and A_0 at the threshold for laser emission as $G_{\text{crit}} = \Delta_a(1+\Delta_g^2)/(\Delta_a - \Delta_g)$ and $A_{\text{crit}} = \Delta_g(1+\Delta_a^2)/(\Delta_a - \Delta_g)$. We make near-threshold assumption $G_0 = G_{\text{crit}} + \epsilon^2 l_g$ and $A_0 = A_{\text{crit}} + \epsilon^2 l_a$. At $O(\epsilon^2)$ we get

$$\frac{\partial\psi}{\partial T_1} = i\big(\nabla^2 - \Delta_e\big)\psi + P_{g2} - P_{a2} - E_2, \tag{2.16}$$

$$\tau_{\perp g}\frac{\partial P_{g1}}{\partial T_1} + (1+i\Delta_g)P_{g2} = E_2 G_0, \tag{2.17}$$

$$\tau_{\perp a}\frac{\partial P_{a1}}{\partial T_1} + (1+i\Delta_a)P_{a2} = E_2 A_0, \tag{2.18}$$

$$0 = -G_2 - \frac{1}{2}\big(\psi P_{g1}^* + \psi^* P_{g1}\big), \tag{2.19}$$

$$0 = -A_2 - \frac{D}{2}\big(\psi P_{a1}^* + \psi^* P_{a1}\big). \tag{2.20}$$

From these equations we get the compatibility condition

$$(1 + \widetilde{G_0}\widetilde{\tau}_{\perp g} - \widetilde{A_0}\widetilde{\tau}_{\perp a})\frac{\partial\psi}{\partial T_1} = i\big(\nabla^2 - \Delta_e\big)\psi, \tag{2.21}$$

and expressions for P_{g2}, P_{a2}, G_2 and A_2

$$P_{g2} = -\widetilde{\tau}_{\perp g}\widetilde{G_0}\frac{\partial\psi}{\partial T_1}, \qquad P_{a2} = -\widetilde{\tau}_{\perp a}\widetilde{A_0}\frac{\partial\psi}{\partial T_1}, \tag{2.22}$$

$$G_2 = -\frac{G_0|\psi|^2}{1+\Delta_g^2}, \qquad A_2 = -\frac{A_0 D|\psi|^2}{1+\Delta_a^2}, \tag{2.23}$$

where we let $E_2 = 0$ and denoted $\widetilde{\tau}_{\perp g,\perp a} = \tau_{\perp g,\perp a}/(1+i\Delta_{g,a})$, $\widetilde{G_0} = G_0/(1+i\Delta_g)$ and $\widetilde{A_0} = A_0/(1+i\Delta_a)$. At $O(\epsilon^3)$ we get

$$\frac{\partial\psi}{\partial T_2} = P_{g3} - P_{a3} - E_3, \tag{2.24}$$

$$\tau_{\perp g}\left(\frac{\partial P_{g1}}{\partial T_2} + \frac{\partial P_{g2}}{\partial T_1}\right) + (1+i\Delta_g)P_{g3} = E_3 G_0 + \psi(G_2 + l_g), \tag{2.25}$$

$$\tau_{\perp g}\left(\frac{\partial P_{a1}}{\partial T_2} + \frac{\partial P_{a2}}{\partial T_1}\right) + (1+i\Delta_a)P_{a3} = E_3 A_0 + \psi(A_2 + l_a), \tag{2.26}$$

$$\tau_g\frac{\partial G_2}{\partial T_1} = -G_3 - \frac{1}{2}\big(\psi P_{g2}^* + \psi^* P_{g2}\big), \tag{2.27}$$

$$\tau_a\frac{\partial A_2}{\partial T_1} = -A_3 - \frac{D}{2}\big(\psi P_{a2}^* + \psi^* P_{a2}\big). \tag{2.28}$$

The compatibility condition at this order after we substitute (2.22)–(2.23) gives

$$(1+\widetilde{G_0}\widetilde{\tau}_{\perp g}-\widetilde{A_0}\widetilde{\tau}_{\perp a})\frac{\partial\psi}{\partial T_2}+\widetilde{\tau}_{\perp g}\frac{\partial P_{g2}}{\partial T_1}-\widetilde{\tau}_{\perp a}\frac{\partial P_{a2}}{\partial T_1}$$
$$=\left(\frac{l_g}{1+i\Delta_g}-\frac{l_a}{1+i\Delta_a}\right)\psi-\left(\frac{\widetilde{G_0}}{1+\Delta_g^2}-\frac{\widetilde{A_0}D}{1+\Delta_a^2}\right)|\psi|^2\psi. \quad (2.29)$$

We use (2.21) and (2.22) in (2.29), collect the derivatives as $\partial_t=\epsilon\partial_{T_1}+\epsilon^2\partial_{T_2}$, absorb ϵ into ψ and $\nabla^2-\Delta_e$ and replace $\epsilon^2 l_g$ ($\epsilon^2 l_a$) with $G_0-G_{\rm crit}$ ($A_0-A_{\rm crit}$) as expected. The result is the cSH equation

$$(1+\widetilde{G_0}\widetilde{\tau}_{\perp g}-\widetilde{A_0}\widetilde{\tau}_{\perp a})\frac{\partial\psi}{\partial t}$$
$$=i\big(\nabla^2-\Delta_e\big)\psi-\frac{(\widetilde{\tau}_{\perp g}^2\widetilde{G_0}-\widetilde{\tau}_{\perp a}^2\widetilde{A_0})}{(1+\widetilde{G_0}\widetilde{\tau}_{\perp g}-\widetilde{A_0}\widetilde{\tau}_{\perp a})^2}\big(\nabla^2-\Delta_e\big)^2\psi$$
$$+\gamma\psi-\left(\frac{\widetilde{G_0}}{1+\Delta_g^2}-\frac{\widetilde{A_0}D}{1+\Delta_a^2}\right)|\psi|^2\psi, \quad (2.30)$$

where $\gamma=(G_0-G_{\rm crit})/(1+i\Delta_g)-(A_0-A_{\rm crit})/(1+i\Delta_a)$.

We can simplify the coefficients by considering a limit $\Delta_{g,a}\ll\tau_{\perp g,a}\ll 1$, neglecting $O(\Delta_{g,a}^2)$ and $O(\tau_{\perp g,a}^2\Delta_{g,a})$ terms and keeping only the higher order terms for real and imaginary parts of the coefficients. This leads to the following general form of the cSH equation

$$(1+i\eta)\frac{\partial\psi}{\partial t}=i\big(\nabla^2-\Delta_e\big)\psi-\delta\big(\nabla^2-\Delta_e\big)^2\psi$$
$$+(\alpha-iV)\psi-(\beta+iU)|\psi|^2\psi, \quad (2.31)$$

with the energy relaxation $\eta=-2G_0\Delta_g\tau_{\perp g}+2A_0\Delta_a\tau_{\perp a}$, the coefficient of superdiffusion $\delta=\tau_{\perp g}^2G_0-\tau_{\perp a}^2A_0$, the effective pumping $\alpha=G_0-A_0-1$, the effective repulsive potential $V=G_0\Delta_g-A_0\Delta_a$, the cubic damping $\beta=G_0-A_0D$ and interaction potential $U=A_0D\Delta_a-G_0\Delta_g$.

Apart from nonlinear optics and lasers the cSH equation provides a reduced description of a variety of other systems [9], such as Rayleigh-Bernard convection [8], Couette flow [29], nematic liquid crystal [6], magnetoconvection [8] and propagating flame front [30] among others.

Similar to other universal equations the cSH equation can be derived phenomenologically from general symmetry considerations. Assuming that the system is characterised by an instability at $k_c\neq 0$, the dominating growth rate (Lyapunov exponent) can be approximated close to k_c by a parabola that takes positive values in the neighbourhood of k_c. To the lowest degree of approximation this can be modelled by

$$\lambda=\alpha-\delta\big(k^2-k_c^2\big)^2+i\big(k^2-k_c^2\big), \quad (2.32)$$

where α is a control parameter that takes $Re(\lambda)$ into the positive range of values. A linear model that has the corresponding dispersion has to be complemented with a nonlinear term in order to prevent the infinite growth of unstable modes. The simplest form of such nonlinearity that preserves the invariance of the field phase is the cubic nonlinearity $|\psi|^2\psi$. So the minimum equation that describes a class of phenomena in nonlinear optics in the lowest order approximation coincides with the cSH equation (2.31).

2.2.3.1 Slow Population Evolution

For wide aperture CO_2 and semiconductor lasers the cSH equation introduced in the previous section is not a good model. The population dynamics is slow which corresponds to the case of the stiff MB equations that occurs when the parameter $b = \tau_{\perp g,a}/\tau_{g,a}$, that measures the ratio of the polarisation dephasing to the population deenergisation rate, becomes small. The order parameter equation in this case is not a single equation and the analysis of the previous section should be revised taking into account smallness of b [26]. Instead of going through the multi-scale analysis we note that we can consider gain selection separate from population evolution and therefore rewrite (2.8), (2.10), (2.11) to include the gain selection mechanism

$$(1+i\eta)\frac{\partial\psi}{\partial t} = i\big(\nabla^2-\Delta_e\big)\psi - \delta\big(\nabla^2-\Delta_e\big)^2\psi - \psi + \big[(1-i\Delta_g)G - (1-i\Delta_a)A\big]\psi, \tag{2.33}$$

$$\tau_g\frac{\partial G}{\partial t} = G_0 - \big(1+|\psi|^2\big)G, \tag{2.34}$$

$$\tau_a\frac{\partial A}{\partial t} = A_0 - \big(1+D|\psi|^2\big)A. \tag{2.35}$$

One may note that in the limit that τ_g, τ_a are small, this equation reduces to (2.31).

2.2.4 Modelling Exciton-Polariton Condensates

The cSH order parameter equation derived above from the MB equations of a laser can also describe the polariton condensate. In this section we discuss how such an equation can arise for the polariton system, and the meaning the various terms would acquire in this context. We also make contact with the limiting cases which correspond to ultracold atomic gases. For the polariton condensate we interpret ψ in (2.33)–(2.35) as a scalar mean field of a polariton matter-wave field operator $\widehat{\Psi}(\mathbf{r},t)$. We begin by considering the basic energy functional for a polariton condensate. In addition to the kinetic energy, and any external trapping potential, one must also take into account repulsive interactions of polaritons. These interactions predominately come from the short ranged electron–electron exchange interactions (when

two excitons swap their electrons). This interaction gives rise to a cubic nonlinear term $-iU_0|\psi|^2\psi$ just as in the right-hand side of (2.31). Rather than coupling the order parameter equation to the dynamics of the gain medium, one should instead consider coupling of the order parameter equation to the equation describing the density of noncondensed polaritons (reservoir excitons), G [21, 45], that may also contain a diffusion term.

In the limit of vanishing gain and losses, the order parameter equation becomes the NLS equation also used to model a Bose-Einstein condensation of ultracold atoms:

$$\frac{\partial\psi}{\partial t} = i\nabla^2\psi - iV(\mathbf{r})\psi - iU_0|\psi|^2\psi. \tag{2.36}$$

For an ultracold atomic gas this equation can also be derived microscopically from the Heisenberg representation of the many-body Hamiltonian using the language of second quantisation. For the case of an ultracold atomic gas, one may also include the dissipation that arises from collisions of condensate atoms with non condensed thermal cloud in this equation. This process leads to energy relaxation and atom transfer between the condensate and the thermal cloud. This can be modelled by writing the quantum Boltzmann equation, i.e. kinetic equation, describing the dynamics of the populations of states [13, 32]. The net rate of atom transfer η as the result of such collision can be represented by replacing the time derivative in (2.36) as $\partial_t \to (1+i\eta)\partial_t$. This parameter η depends on the temperature and the density of the noncondensed cloud. Similar mechanism of energy relaxation exists in polariton condensates and have been phenomenologically introduced into various models of polariton condensates [46, 47]. Note that such energy relaxation follows directly from the MB equations as indicated by (2.8), (2.31). The interactions with noncondensed cloud may enhance this coefficient.

In addition to the terms mentioned so far, the polariton system differs from ultracold atoms, but is similar to the laser, in having also terms describing gain and loss, i.e. pumping and decay. Including these terms, and allowing them to potentially depend on wavevector, gives a modified cSH model that includes all possible previously discussed limits of lasers, nonequilibrium polariton condensates and equilibrium atomic BECs:

$$\begin{aligned}(1+i\eta)\frac{\partial\psi}{\partial t} &= i\left(\nabla^2-\Delta_e\right)\psi - \delta\left(\nabla^2-\Delta_e\right)^2\psi - \psi \\ &\quad + \left[(1-i\Delta_g)G - (1-i\Delta_a)\right]\psi - iU_0|\psi|^2\psi, \end{aligned}\tag{2.37}$$

$$\tau_g\frac{\partial G}{\partial t} = G_0 - \left(1+|\psi|^2\right)G, \tag{2.38}$$

$$\tau_a\frac{\partial A}{\partial t} = A_0 - \left(1+D|\psi|^2\right)A. \tag{2.39}$$

Note that $V = G\Delta_g - A\Delta_a$ gives rise to a reservoir potential which causes the blueshift in the condensate, allowing nonlinear interactions between the condensate and reservoir can further increase such a term [42].

Some limiting cases of (2.37)–(2.39) have been previously considered. Assuming $\delta \to 0$ and fast relaxation of reservoirs ($\tau_a, \tau_g \to 0$) leads to the cGL equation introduced for polariton condensates in [19, 45]. In the limit $\delta \to 0$ and assuming the slow relaxation of the noncondensed reservoir gives rise to the model of atom laser [21] that has proved effective for polariton condensates [23, 34, 45, 47]. Finally, in the limit of vanishing losses and gain all systems approach the conservative NLS equation.

2.3 Pattern Formation and Stability

Having discussed the physical origin of the order parameter equations of polariton condensates, lasers and atomic condensates, this section now discusses the consequences of the form of the order parameter equations for pattern forming and stability analysis. We discuss three cases: the entirely homogeneous case, the case in which the pumping (gain) is localised, and the case in which there is inhomogeneity of the condensate mode energy (i.e. trapping) as well as pumping. The homogeneous case is most relevant to wide aperture lasers with electrical pumping. For polariton condensates and photon condensates with external pumping, the second and third cases are more relevant. As one goes toward equilibrium systems (such as atomic condensates), the role of trapping potentials to confine the condensate becomes more important, and so the third case is most relevant in this limit.

All three cases can be written as the short population relaxation time limit of (2.37):

$$(1+i\eta)\frac{\partial\psi}{\partial t} = \big(\alpha(r) - \beta|\psi|^2\big)\psi + i\big(\nabla^2 - V(r) - U_0|\psi|^2\big)\psi + 2\delta\Delta_e\nabla^2\psi - \delta\nabla^4\psi, \tag{2.40}$$

but we will rescale the equation in different ways for the different cases.

2.3.1 Behaviour of Homogeneous Order Parameter Equation

We begin by reviewing the simplest case, of linear stability analysis about the uniform solution $\rho = \psi_0^2 = \alpha/(\beta + U_0\eta)$ in (2.40). This uniform solution should be a stable solution as long as $\delta\Delta_e < 0$. One may then consider perturbations of the Bogoliubov-de Gennes form:

$$\psi = \big(\psi_0 + ue^{i(\mathbf{k}\cdot\mathbf{x}-\omega t)} + v^* e^{-i(\mathbf{k}\cdot\mathbf{x}-\omega^* t)}\big)e^{-i\mu t} \tag{2.41}$$

where the chemical potential is $\mu = U_0\rho$. For this ansätz to solve (2.40) (at linear order in u, v) requires that:

$$\rho^2\big(U_0^2 + \beta^2\big) = |S|^2 + \omega(1-i\eta)S^* - \omega(1+i\eta)S - \omega^2\big(1+\eta^2\big), \tag{2.42}$$

where $S = (k^2 + \rho U_0) + i(2\delta\Delta_e k^2 + \delta k^4 + \rho\beta)$ (making use of the steady state values of μ and ρ). For an equilibrium condensate $\alpha = \beta = \delta = \eta = 0$ one can recover the expected Bogoliubov spectrum from (2.42):

$$\omega_B(k) = \sqrt{k^2\big(2\rho U_0 + k^2\big)}. \tag{2.43}$$

Alternatively, in the cGL regime ($\delta = 0$) with $\eta = 0$ one recovers the dissipative spectrum obtained previously [44]:

$$\omega_{cGL}(k) = -i\alpha \pm \sqrt{\omega_B(k)^2 - \alpha^2}, \tag{2.44}$$

which is imaginary for small k, and then above a critical k (set by $\omega_B(k) = \alpha$), the imaginary part becomes a constant $-\alpha$ and a real part appears. Introducing the remaining terms gives

$$\omega_{cSH}(k) = \frac{1}{1+\eta^2}\Big[-i(\alpha + \chi_k) \pm \sqrt{-\alpha^2 + \epsilon_k\big(2\rho(U_0 - \eta\beta) + \epsilon_k\big)}\Big] \tag{2.45}$$

where $\chi_k = k^2[\eta + \delta(2\Delta_e + k^2)]$ and $\epsilon_k = k^2[1 - \eta\delta(2\Delta_e + k^2)]$. Note that for $k = 0$, one always has a mode at zero frequency, as expected given the phase symmetry breaking present in the ordered phase. As long as $\eta > 0, \delta\Delta_e > 0$, the imaginary part grows for large k, since such a case describes pumping that suppresses high energy (momentum) modes. If $\eta + 2\delta\Delta_e > 0$, the modes are always decaying, but if $\Delta_e < -\eta/2\delta$, it becomes possible for the CSH term to make the uniform part unstable—the exact critical Δ_e depends in a non-trivial way on the remaining parameters. Other instabilities may also arise due to the content of the square root term.

2.3.2 *Inhomogeneous Pumping*

We next consider the effect of inhomogeneous pumping, comparing the behaviour of cSH equation and cGL equations when used to model polariton condensates. As the first example we consider a small pumping spot. This geometry has been considered extensively in experiments [7, 34, 42, 43] and theory [47]. Our starting point is to consider (2.40) that we rewrite as

$$\begin{aligned}\big(1 + i\eta(P)\big)\frac{\partial\psi}{\partial t} = \big(P(\mathbf{r}) - \gamma_c - \lambda P(\mathbf{r})|\psi|^2\big)\psi + i\big(\nabla^2 - V(P) - |\psi|^2\big)\psi \\ + 2\delta\Delta_e\nabla^2\psi - \delta\nabla^4\psi.\end{aligned} \tag{2.46}$$

We take

$$\begin{aligned} &P(\mathbf{r}) = 4\exp\big(-0.05r^2\big), \qquad \gamma_c = 0.3, \qquad \lambda = 0.075, \\ &\eta(P) = 0.025P(\mathbf{r}), \qquad V(P) = 1.25\exp\big(-0.45r^2\big)P(\mathbf{r}). \end{aligned} \tag{2.47}$$

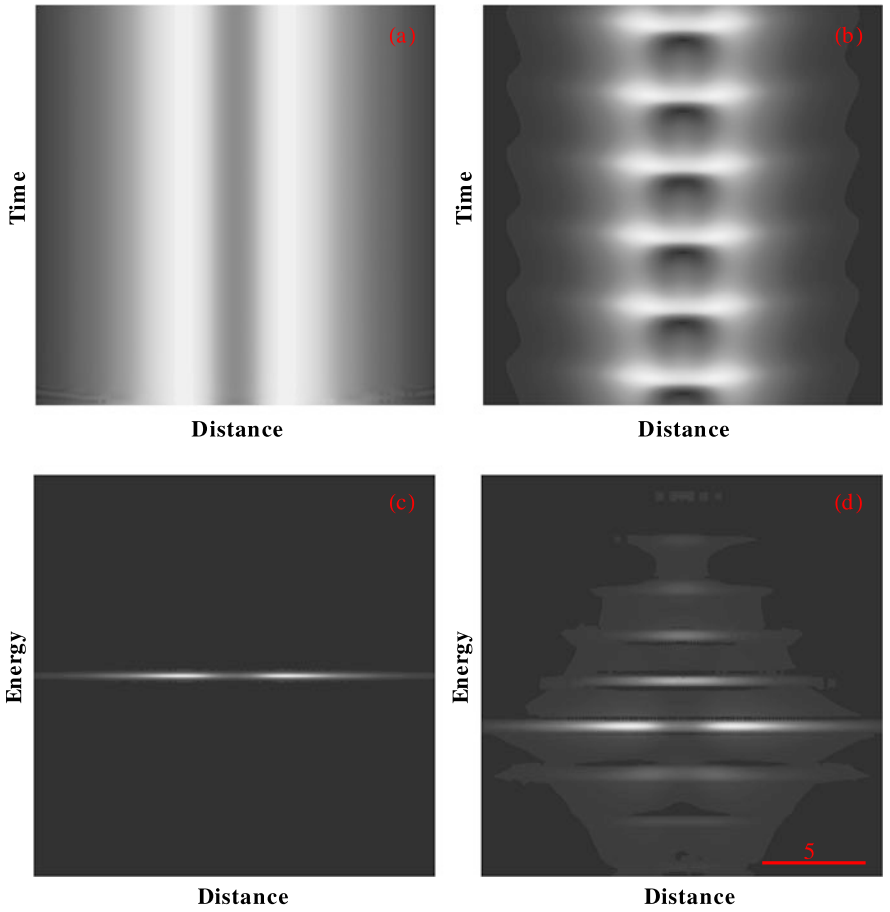

Fig. 2.1 Comparison between solutions of the cGL and cSH equations for a single pumping spot. Time evolution of the density measured across the pumping spot (**a**) for the cGL equation and (**b**) cSH equation. Energy of the solutions across the pumping spot (**c**) for the cGL equation and (**d**) cSH equation. The results of the numerical simulations of (2.46) with the parameters given in (2.47)

In writing the last two expressions we recalled that η, the energy relaxation parameter representing the rate of transfer between the noncondensed and condensed polaritons, depends on the density of the noncondensed cloud. We also assumed spatially dependent energy shifts coming from strong mutual repulsion [18], so that the repulsive force coming from potential V varies with density of the condensate.

We compare two cases: the cGL equation by letting $\delta = 0$ in (2.46) and the cSH equation with $\delta = 0.1$, $\Delta_e = -1$. In the case of the evolution according to the cGL equation the system reaches the steady state, see Fig. 2.1(a) which shows on the tomography image Fig. 2.1(c) as a single energy level. The evolution according to the cSH equation leads to periodic oscillations of the density profile shown on

Fig. 2.1(b). The corresponding tomography image on Fig. 2.1 shows several discrete energy levels. Similar behaviour has been observed in some experiments, e.g. [34].

2.3.3 Inhomogeneous Energy (Trapping)

We now turn to consider the behaviour in the presence of an harmonic trap [4, 20]. We will consider how the presence of the dissipative terms in the general order parameter equation affects the stability of known solutions of the Gross Pitaevskii equation. We will look both at linear stability analysis (where one can gain insights from analytical results found by considering the perturbative effect of dissipation), as well as full numerical time evolution to find the new steady states. Some limiting cases of these results have been presented in [5, 19].

As a starting point in the absence of dissipative terms, the Gross-Pitaevskii equation:

$$\partial_t \psi = i\left(\nabla^2 - r^2 - U_0|\psi|^2\right)\psi \tag{2.48}$$

can be approximately solved by the stationary Thomas-Fermi profile with $\partial_t \psi = -i\mu\psi$ and $|\psi|^2 = \Theta(\mu - r^2)(\mu - r^2)/U_0$. This density profile results from neglecting the kinetic energy. This is valid as long as the cloud size $r_{TF} = \sqrt{\mu}$ is large compared to the healing length $1/\sqrt{U_0}$, i.e. for $\sqrt{U_0\mu} \gg 1$. This stationary Thomas-Fermi profile gives a simple prescription for how to find the density profile in a given potential landscape. However, as will be discussed below, the stationary profile does not necessarily remain stable in the presence of the additional terms in (2.40).

2.3.3.1 Stability Analysis

Starting from (2.40) with $\alpha, \beta, \delta, \eta = 0$, we consider in turn the effects introduced by adding these dissipative terms. We restrict to considering $\Delta_e < 0$ and neglect the superdiffusion term; after rescaling parameters, we may write:

$$2\partial_t \psi - i\left(\nabla^2 - r^2 - |\psi|^2\right)\psi = \left[\tilde{\alpha} - \tilde{\beta}|\psi|^2 + \tilde{\delta}\left(2\tilde{\Delta}_e - \nabla^2\right)\nabla^2 - 2i\tilde{\eta}\partial_t\right]\psi \tag{2.49}$$

in which all dissipative terms are placed on the right hand side. We then proceed by considering normal modes around the stationary solution in an approximation where the quantum pressure terms can be neglected, this is done by writing the equations in terms of density and phase and neglecting all quantum-pressure-like terms:

$$\partial_t \rho + \nabla \cdot (\rho \nabla \phi) = \left(\tilde{\alpha} - \tilde{\beta}\rho + 2\tilde{\eta}\partial_t\phi - 2\tilde{\delta}(\nabla\phi)^2\right)\rho, \tag{2.50}$$

$$2\partial_t \phi + (\nabla\phi)^2 + r^2 + \rho = \tilde{\delta}\left(2\tilde{\Delta}_e\nabla^2 - \nabla^4\right)\phi. \tag{2.51}$$

In the absence of the dissipative terms, this problem is the two-dimensional analog of that studied by Stringari [38, 39]. Linearising these equations using

$\rho \to \rho + he^{-i\omega t}$, $\phi \to \phi + \varphi e^{-i\omega t}$ yields normal modes with frequencies $\omega_{ns} = \sqrt{2n^2 + 2(s+1)n + s}$ and density profiles given by hypergeometric functions $h(r,\theta) \propto {}_2F_1(-n, n+s+1; s+1, r^2)e^{is\theta}r^s$; here n is a radial quantum number, and s is an angular quantum number. Including dissipative terms, these normal mode frequencies acquire imaginary parts, describing either growth or decay of such fluctuations. Instability of the stationary state occurs when at least one of these fluctuation modes grows.

To account for dissipative terms perturbatively, it is enough to take the normal mode functions found in the absence of dissipation and find the first order frequency shift induced by the dissipative terms. At first order in the dissipative terms, there is no change to the density profile; however a non-zero phase gradient $\nabla\phi$ does appear at first order in the dissipative terms. Vanishing of the current at the edge of the cloud then requires $\mu = 3\tilde{\alpha}/(2\tilde{\beta} + 3\tilde{\eta})$.

Formally one may write the linearised form of (2.50) in the form $-i\omega_{s,n}\chi_{s,n}(r,\theta) = (\mathcal{L}^{(0)} + \mathcal{L}^{(1)})\chi_{s,n}$ in which $\mathcal{L}$ is a matrix of differential operators acting on the fluctuation term $\chi = (h, \varphi)^T$. By identifying the dissipative terms as $\mathcal{L}^{(1)}$, standard first order perturbation theory[1] then yields the first order correction: $\omega_{ns}^{(1)} = i\langle \chi_{ns}^{(0)}, \mathcal{L}^{(1)}\chi_{ns}^{(0)}\rangle / \langle \chi_{ns}^{(0)}, \chi_{ns}^{(0)}\rangle$ where angle brackets indicate the appropriate inner product. Following this procedure, one eventually finds

$$\omega_{ns}^{(1)} = \frac{i}{2N}\int 2\pi r dr \left[\left(h_{ns}^{(0)}\right)^2 \left(\tilde{\alpha} - \tilde{\eta}\mu - (2\tilde{\beta} + \tilde{\eta})\mu\right) + \tilde{\delta} h_{ns}^{(0)} \left(\tilde{\Delta}_e - \frac{1}{2}\nabla^2\right)\nabla^2 h_{ns}^{(0)} \right] \tag{2.52}$$

where the normalisation $N = \int 2\pi r dr h_{ns}^2$ and integration is over the area of the Thomas-Fermi profile $r^2 < \mu$. The hypergeometric form of the zero order functions $h_{ns}^{(0)}$ allows (2.52) to be evaluated analytically. The terms proportional to $\tilde{\delta}$ in fact vanishes, and the remaining term can be written (making use of the above value of μ) as:

$$\omega_{ns}^{(1)} = \frac{i\tilde{\alpha}}{4\tilde{\beta} + 6\tilde{\eta}} \left[(6\tilde{\beta} + 3\tilde{\eta}) \left(\frac{s^2 + (\omega_{ns}^{(0)})^2}{s^2 + 2(\omega_{ns}^{(0)})^2} \right) - 4\tilde{\beta} - 3\tilde{\eta} \right]. \tag{2.53}$$

Crucially, $(\omega_{ns}^{(0)})^2$ as given above grows only linearly with s. Thus, at large s the ratio in parentheses tends to one, and so $\omega_{ns}^{(1)} \to i\tilde{\beta}\tilde{\alpha}/(2\tilde{\beta} + 3\tilde{\eta}) > 0$. This positive value means that there is an instability, even for non-zero $\tilde{\eta}$. Although neither $\tilde{\eta}$ nor $\tilde{\delta}$ remove the instability in this perturbative approach, this does not prevent these terms from restoring stability via higher order corrections. This needs to be checked by numerical simulations.

[1] Some care must be taken since the operator $\mathcal{L}$ is not self adjoint and so the left and right eigenstates of $\mathcal{L}^{(0)}$ must be found separately. This is easiest if one replaces the variable φ by $u_r = \partial_r\varphi$, $u_\theta = (1/r)\partial_\theta\varphi = (is/r)\varphi$, in this case the right eigenstates (h, u_r, u_θ) corresponds to the right eigenstate $(h, 2\rho u_r, 2\rho u_\theta)$.

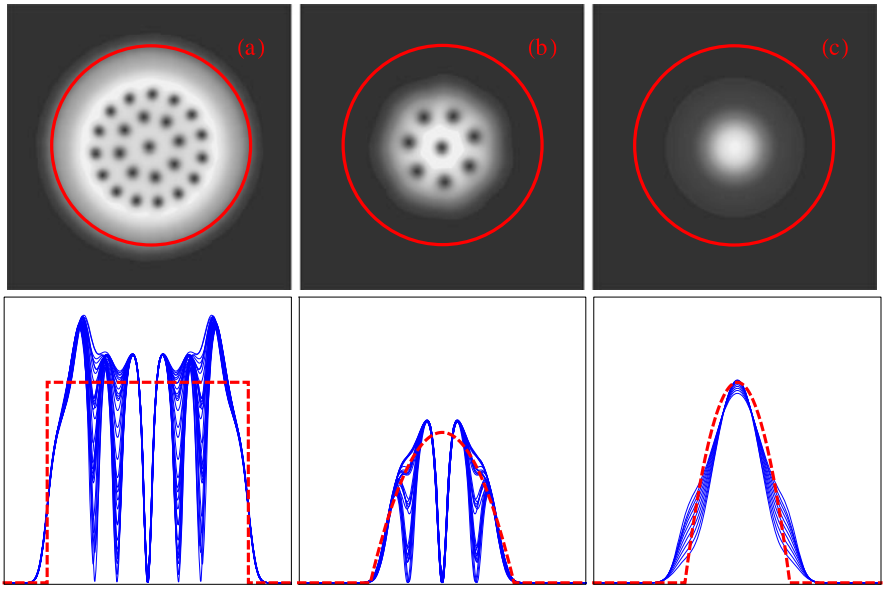

Fig. 2.2 Density plots of the polariton condensate in a harmonic trap according to the cGL equation with $\eta = 0$ (**a**), $\eta = 0.2$ (**b**) and the cSH equation with $\delta = \eta = 0.2$ and $\Delta_e = -0.5$ (**c**). *Top panels*: luminosity is proportional to density. *Red circles* show the size of the pumping spot. *Bottom panels*: (*solid lines*) density of the cross section of the condensate at various times; (*dashed lines*) analytic approximations, given for (**a**) and (**b**) by (2.58), and for (**c**) by the Thomas-Fermi profile $\Theta(\mu - r^2)(\mu - r^2)$ with $\mu = 3\tilde{\alpha}_0/(2\tilde{\beta} + 3\tilde{\eta})$

2.3.3.2 Vortex Lattices

Having seen that the stationary profile possesses an instability, we next consider the behaviour resulting from this instability. In order to reach a final configuration, it is necessary to restrict the pumping to a finite range. We thus take and $\tilde{\alpha}(\mathbf{r}) = \tilde{\alpha}_0\theta(r_0 - r)$, $\tilde{\alpha}_0 = 8$, $\tilde{\beta} = 0.6$, where the pumping is a flat top of the radius $r_0 = 7$. For $\tilde{\eta} = \tilde{\delta} = 0$, this model has been found to evolve to a rotating vortex lattice [19]. If one also includes the superdiffusion present in the cSH model, one finds that (in contrast to the linearised analysis) this may arrest the instability to vortex formation, and thus lead instead to an oscillating vortex-free state. Figure 2.2 compares the profiles that result from the numerical simulation of (2.46) for the cases of the cGL equations for $\tilde{\eta} = 0$ (Fig. 2.2(a)), $\tilde{\eta} = 0.2$ (Fig. 2.2(b)) and the cSH equation with $\tilde{\eta} = \tilde{\delta} = 0.2$ and $\tilde{\Delta}_e = -0.5$ (Fig. 2.2(c)).

Although the presence of $\tilde{\eta}$ does not remove the instability, it does significantly effect the resulting rotating profile. This can both be seen in the numerical results shown in Fig. 2.2, and can also be understood by considering the $\tilde{\delta} = 0$ limit of (2.50), written in a rotating frame. In a rotating frame, we consider solutions to

(2.49) of the form:

$$2i\frac{\partial}{\partial t}\psi = (\mu - 2i\mathbf{\Omega}\cdot\mathbf{r}\times\nabla)\psi \tag{2.54}$$

such that the time dependence has two parts: rotation with angular velocity $\mathbf{\Omega} = (0, 0, \Omega)$, and phase accumulation at rate μ. Inserting this ansätz into (2.49) and then making the Madelung transform, with neglect of quantum pressure terms, one finds:

$$\nabla\cdot\big[\rho(\nabla\phi - \mathbf{\Omega}\times\mathbf{r})\big] = \big[\tilde{\alpha} - \tilde{\beta}\rho - \tilde{\eta}(\mu + 2\mathbf{\Omega}\times\mathbf{r}\cdot\nabla\phi)\big]\rho, \tag{2.55}$$

$$-\mu + (\nabla\phi - \mathbf{\Omega}\times\mathbf{r})^2 + \big(1 - \Omega^2\big)r^2 + \rho = 0. \tag{2.56}$$

These equations can be satisfied by setting $\nabla\phi \simeq \Omega\times\mathbf{r}$ which yields:

$$0 = \tilde{\alpha} - \tilde{\beta}\rho - \tilde{\eta}\big(\mu + 2\Omega^2 r^2\big), \qquad -\mu + \big(1 - \Omega^2\big)r^2 + \rho = 0. \tag{2.57}$$

These give two equations for ρ which are both satisfied if:

$$\rho = \mu - \big(1 - \Omega^2\big)r^2 = \frac{1}{\tilde{\beta}}\big[\tilde{\alpha} - \tilde{\eta}\big(\mu + 2\Omega^2 r^2\big)\big] \tag{2.58}$$

hence $\Omega^2 = \tilde{\beta}/(\tilde{\beta} + 2\tilde{\eta})$, $\mu = \tilde{\alpha}/(\tilde{\beta} + \tilde{\eta})$. This indicates that while for $\tilde{\eta} = 0$, the lattice rotates at $\Omega = 1$, cancelling out the trapping potential, for finite η, the rotation velocity decreases, hence the density profile becomes non-flat, as seen in Fig. 2.2.

In the above, $\nabla\phi \simeq \mathbf{\Omega}\times\mathbf{r}$ would require the phase profile to mimic solid body rotation. For a condensate, this cannot be exactly satisfied, but can be approximately satisfied (on a coarse grained scale) by having a density of vortices Ω. Since increasing $\tilde{\eta}$ causes Ω to decrease, a sufficiently large value of $\tilde{\eta}$ can in effect kill any finite vortex lattice by reducing the vortex density to values so that the number of vortices falls below one.

2.4 Conclusions

We reviewed the connection between lasers, polariton condensates and equilibrium Bose condensates from a common framework based on order parameter equations. The cSH equations derived for lasers should be applicable to polariton condensates in the limit of non-negligible interactions and the stimulated scattering between polariton modes. The pattern formation in the framework of the cSH equations has been well-studied for lasers indicating a wealth of dynamics and phenomena. Some of these phenomena may be achieved in polariton condensates. At the same time the stronger nonlinearities and different external potentials (engineered or due to disorder) may lead to novel properties of the system exhibiting effects not seen in normal lasers.

References

1. A. Amo, S. Pigeon, D. Sanvitto, V.G. Sala, R. Hivet, I. Carusotto, F. Pisanello, G. Lemenager, R. Houdre, E. Giacobino, C. Ciuti, A. Bramati, Polariton superfluids reveal quantum hydrodynamic solitons. Science **332**(6034), 1167–1170 (2011)
2. I. Aranson, L. Kramer, The world of the complex Ginzburg-Landau equation. Rev. Mod. Phys. **74**(1), 99–143 (2002)
3. F. Arecchi, G. Giacomelli, P. Ramazza, S. Residori, Vortices and defect statistics in two-dimensional optical chaos. Phys. Rev. Lett. **67**(27), 3749–3752 (1991)
4. R. Balili, V. Hartwell, D. Snoke, L. Pfeiffer, K. West, Bose-Einstein condensation of microcavity polaritons in a trap. Science **316**(5827), 1007–1010 (2007)
5. M. Borgh, G. Franchetti, J. Keeling, N. Berloff, Robustness and observability of rotating vortex lattices in an exciton-polariton condensate. Phys. Rev. B **86**, 035307 (2012)
6. A. Buka, B. Dressel, L. Kramer, Direct transition to electroconvection in a homeotropic nematic liquid crystal. Chaos **14**(3), 793 (2004)
7. G. Christmann, G. Tosi, N.G. Berloff, P. Tsotsis, P.S. Eldridge, Z. Hatzopoulos, P.G. Savvidis, J.J. Baumberg, Polariton ring condensates and sunflower ripples in an expanding quantum liquid. Phys. Rev. B **85**, 235303 (2012)
8. S.M. Cox, P.C. Matthews, S.L. Pollicott, Swift-Hohenberg model for magnetoconvection. Phys. Rev. E **69**, 066314 (2004)
9. M. Cross, P. Hohenberg, Pattern formation outside of equilibrium. Rev. Mod. Phys. **65**(3), 851–1112 (1993)
10. R. Dodd, K. Burnett, M. Edwards, C.W. Clark, Excitation spectroscopy of vortex states in dilute Bose-Einstein condensed gases. Phys. Rev. A **56**(1), 587–590 (1997)
11. O. Dzyapko, V.E. Demidov, S.O. Demokritov, Ginzburg-Landau model of Bose-Einstein condensation of magnons. Phys. Rev. B **81**, 024418 (2010)
12. S.V. Fedorov, A.G. Vladimirov, G.V. Khodova, Effect of frequency detunings and finite relaxation rates on laser localized structures. Phys. Rev. E **61**, 5814 (2000)
13. C. Gardiner, P. Zoller, R. Ballagh, M. Davis, Kinetics of Bose-Einstein condensation in a trap. Phys. Rev. Lett. **79**(10), 1793–1796 (1997)
14. H.E. Hall, W.F. Vinen, The rotation of liquid helium II. II. The theory of mutual friction in uniformly rotating helium II. Proc. R. Soc. A **238**(1213), 215–234 (1956)
15. P. Hohenberg, B. Halperin, Theory of dynamic critical phenomena. Rev. Mod. Phys. **49**(3), 435–479 (1977)
16. A. Imamoğlu, R.J. Ram, Quantum dynamics of exciton lasers. Phys. Lett. A **214**(3–4), 193–198 (1996)
17. L.P. Kadanoff, *Statistical Physics: Statics, Dynamics and Renormalization* (World Scientific, Singapore, 2000)
18. J. Kasprzak, M. Richard, S. Kundermann, A. Baas, P. Jeambrun, J.M.J. Keeling, F.M. Marchetti, M.H. Szymańska, R. André, J.L. Staehli, V. Savona, P.B. Littlewood, B. Deveaud, L.S. Dang, Bose-Einstein condensation of exciton polaritons. Nature **443**(7110), 409–414 (2006)
19. J. Keeling, N.G. Berloff, Spontaneous rotating vortex lattices in a pumped decaying condensate. Phys. Rev. Lett. **100**(25), 250401 (2008)
20. J. Klaers, J. Schmitt, F. Vewinger, M. Weitz, Bose-Einstein condensation of photons in an optical microcavity. Nature **468**(7323), 545–548 (2010)
21. B. Kneer, T. Wong, K. Vogel, W. Schleich, D. Walls, Generic model of an atom laser. Phys. Rev. A **58**(6), 4841–4853 (1998)
22. N. Kopnin, *Theory of Nonequilibrium Superconductivity* (Oxford University Press, Oxford, 2001)
23. D. Krizhanovskii, K. Lagoudakis, M. Wouters, B. Pietka, R. Bradley, K. Guda, D. Whittaker, M. Skolnick, B. Deveaud-Plédran, M. Richard, R. André, L.S. Dang, Coexisting nonequilibrium condensates with long-range spatial coherence in semiconductor microcavities. Phys. Rev. B **80**(4), 045317 (2009)

24. Y. Kuramoto, T. Tsuzuki, Persistent propagation of concentration waves in dissipative media far from thermal equilibrium. Prog. Theor. Phys. **55**, 356 (1976)
25. K.G. Lagoudakis, M. Wouters, M. Richard, A. Baas, I. Carusotto, R. André, L.S. Dang, B. Deveaud-Plédran, Quantized vortices in an exciton–polariton condensate. Nat. Phys. **4**(9), 706–710 (2008)
26. J. Lega, J. Moloney, A. Newell, Swift-Hohenberg equation for lasers. Phys. Rev. Lett. **73**(22), 2978–2981 (1994)
27. T. Liew, A. Kavokin, I. Shelykh, Excitation of vortices in semiconductor microcavities. Phys. Rev. B **75**(24), :241301(R) (2007)
28. L.A. Lugiato, C. Oldano, L.M. Narducci, Cooperative frequency locking and stationary spatial structures in lasers. J. Opt. Soc. Am. B **5**(5), 879–888 (1988)
29. P. Manneville, Spots and turbulent domains in a model of transitional plane Couette flow. Theor. Comput. Fluid Dyn. **18**, 169–181 (2004). doi:10.1007/s00162-004-0142-4
30. B.J. Matkowsky, A.A. Nepomnyashchy, A complex Swift–Hohenberg equation coupled to the Goldstone mode in the nonlinear dynamics of flames. Phys. D, Nonlinear Phenom. **179**(3–4), 183 (2003)
31. J.V. Moloney, A.C. Newell, Universal description of laser dynamics near threshold. Phys. D, Nonlinear Phenom. **83**(4), 478–498 (1995)
32. A. Penckwitt, R. Ballagh, C. Gardiner, Nucleation, growth, and stabilization of Bose-Einstein condensate vortex lattices. Phys. Rev. Lett. **89**(26), 260402 (2002)
33. L.M. Pismen, *Vortices in Nonlinear Fields. From Liquid Crystals to Superfluids, From Non-equilibrium Patterns to Cosmic Strings* (Oxford University Press, Oxford, 1999)
34. G. Roumpos, W.H. Nitsche, S. Höfling, A. Forchel, Y. Yamamoto, Gain-induced trapping of microcavity exciton polariton condensates. Phys. Rev. Lett. **104**(12), 126403 (2010)
35. G.I. Sivashinsky, Nonlinear analysis of hydrodynamic instability in laminar flames–I. derivation of basic equations. Acta Astronaut. **4**, 1177–1206 (1977)
36. K. Staliunas, Laser Ginzburg-Landau equation and laser hydrodynamics. Phys. Rev. A **48**(2), 1573–1581 (1993)
37. K. Staliunas, V.J. Sanchez-Morcillo, *Transverse Patterns in Nonlinear Optical Resonators* (Springer, Berlin, 2003)
38. S. Stringari, Collective excitations of a trapped Bose-condensed gas. Phys. Rev. Lett. **77**(12), 2360–2363 (1996)
39. S. Stringari, Dynamics of Bose-Einstein condensed gases in highly deformed traps. Phys. Rev. A **58**(3), 2385–2388 (1998)
40. J. Swift, P.C. Hohenberg, Hydrodynamic fluctuations at the convective instability. Phys. Rev. A **15**, 319 (1977)
41. V. Taranenko, K. Staliunas, C. Weiss, Spatial soliton laser: Localized structures in a laser with a saturable absorber in a self-imaging resonator. Phys. Rev. A **56**(2), 1582–1591 (1997)
42. G. Tosi, G. Christmann, N.G. Berloff, P. Tsotsis, T. Gao, Z. Hatzopoulos, P.G. Savvidis, J.J. Baumberg, Sculpting oscillators with light within a nonlinear quantum fluid. Nat. Phys. **8**, 190–194 (2012)
43. E. Wertz, L. Ferrier, D.D. Solnyshkov, P. Senellart, D. Bajoni, A. Miard, A. Lemaître, G. Malpuech, J. Bloch, Spontaneous formation of a polariton condensate in a planar GaAs microcavity. Appl. Phys. Lett. **95**(5), 051108 (2009)
44. M. Wouters, Excitations and superfluidity in non-equilibrium Bose-Einstein condensates of exciton–polaritons. Superlattices Microstruct. **43**(5–6), 524–527 (2008)
45. M. Wouters, I. Carusotto, Excitations in a nonequilibrium Bose-Einstein condensate of exciton polaritons. Phys. Rev. Lett. **99**(14), 140402 (2007)
46. M. Wouters, I. Carusotto, Superfluidity and critical velocities in nonequilibrium Bose-Einstein condensates. Phys. Rev. Lett. **105**(2), 020602 (2010)
47. M. Wouters, T. Liew, V. Savona, Energy relaxation in one-dimensional polariton condensates. Phys. Rev. B **82**(24), 245315 (2010)

Chapter 3
Bosonic Spin Transport

Alexey Kavokin

Abstract Traditional spintronics relies on the spin transport by charge carriers, such as electrons in semiconductor crystals. This brings several complications: the Pauli principle prevents the carriers from moving with the same speed, Coulomb repulsion leads to rapid dephasing of electron flows. Spin-optronics is a valuable alternative to the traditional spintronics. In spin-optronic devices the spin currents are carried by electrically neutral bosonic quasi-particles: excitons or exciton-polaritons. They can form highly coherent quantum liquids and carry spins over macroscopic distances. The price to pay is a finite and usually very short life-time of the bosonic spin carriers, which breaks the flow conservation rule. In this chapter we present the theory of exciton spin transport which may be applied to a range of systems where remarkable observations of bosonic spin transport have been reported, in particular, to indirect excitons in coupled GaAs/AlGaAs quantum wells and exciton polaritons in planar microcavities. We describe the effect of spin-orbit interaction of electrons and holes on the exciton spin, account for the Zeeman effect induced by external magnetic fields, long range and short range exchange splittings of the exciton resonances. We also consider the exciton transport in the non-linear regime and discuss the definitions of exciton spin current, polarization current and spin conductivity. We address the perspective of observation of dissipationless exciton spin currents sometimes referred to as "spin superfluidity".

3.1 Introduction

Excitons are electrically neutral and have finite lifetimes. These are two obstacles which slowered the development of excitonic spintronics, or spin-optronics until

A. Kavokin (✉)
Spin Optics Laboratory, St-Petersburg State University, 1, Ulianovskaya, 198504, St-Petersburg, Russia
e-mail: A.Kavokin@soton.ac.uk

A. Kavokin
Physics and Astronomy School, University of Southampton, Highfield, Southampton, SO171BJ, UK

A. Bramati, M. Modugno (eds.), *Physics of Quantum Fluids*,
Springer Series in Solid-State Sciences 177, DOI 10.1007/978-3-642-37569-9_3,

the beginning of this century. How possibly one can speak about the current which is nearly independent on the applied bias, and whose amplitude changes dramatically with distance and time?—were the typical questions of the sceptics of exciton-based spintronics. While electrons and holes have been considered as perfectly valid spin carriers, and exotic effects like spin Hall effect [1] have been enthusiastically searched for, the spin currents carried by excitons and exciton-polaritons over tens or even hundreds of micrometers have been studied very poorly by the scientific community. There existed a huge misbalance of theoretical works on fermionic and bosonic spin transport. Fortunately, this changes now. More and more researchers invest themselves to investigations of bosonic spin current problems, and this research is paid for by beautiful recent discoveries. Several chapters of this volume address in detail the recent progress in optical studies of spin-dependent effects in excitonic systems. To summarize tens of publications in one sentence: bosonic systems bring new quantum coherent effects to the physics of spin transport. Stimulation and amplification of spin currents as well as "spin superfluidity" are possible in exciton and exciton-polariton Bose gases. The goal of this chapter is to define what the exciton spin, magnetization and polarization currents are, and to explain how they can be described within the most frequently used spin density matrix approach and mean-field approximation. We consider a very specific system, namely a planar zinc-blend semiconductor structure containing quantum wells, where excitons can be formed. This choice is dictated by recent experimental discoveries in GaAs/AlGaAs based coupled quantum wells or microcavities. However, we do not address any particular experiment. Instead, we aim at presenting a general approach which may be suitable for both exciton and exciton polariton gases in quantum wells and microcavities containing quantum wells. We limit the scope of this chapter to heavy-hole excitons, however, our approach can be easily extended to light-hole excitons or excitons in quantum wells of a different symmetry. We do not speak here about the recent experimental data and possible applications of the formalism presented here, as this would bring us too far and because these subjects have been addressed in detail in other chapters of this volume. On the other hand, we are confident that the approach formulated here is suitable for description of a great variety of excitonic spin effects in quantum wells and planar microcavities.

3.2 Spin of Propagating Excitons

In zinc-blend semiconductor quantum wells (e.g. in the most popular GaAs/AlGaAs system), the lowest energy exciton states are formed by electrons with spin projections to the structure axis of $+1/2$ and $-1/2$ and heavy holes whose quasi-spin (sum of spin or orbital momentum) projection to the structure axis is $+3/2$ or $-3/2$. Consequently, the exciton spin defined as a sum of electron spin and heavy hole quasi-spin may have one of four projections to the structure axis: -2, -1, $+1$, $+2$, see, e.g. [2]. These states are usually nearly degenerate, while there may be some splitting between them due to the short and long-range exchange interactions. Here we

derive the exciton Hamiltonian in the basis of -2, -1, $+1$, $+2$ states, accounting for the spin-orbit interaction (Dresselhaus and Rashba effects) [3], long- and short-range exchange interactions [4] and Zeeman effect, but neglecting exciton-exciton interactions, which will be discussed in the next section. We consider excitons propagating ballistically in plane of a quantum well. We shall characterize them by a fixed wave-vector $\mathbf{k}_{ex}$.

In order to build the 4×4 matrix Hamiltonian for excitons, we start with simpler 2×2 Hamiltonians describing the spin-orbit and Zeeman effects for electrons and holes.

The electron Hamiltonian in the basis of $(+1/2, -1/2)$ spin states writes:

$$H_e = \beta_e(k_{e,x}\sigma_x - k_{e,y}\sigma_y) - \frac{1}{2}g_e\mu_B B\sigma_z. \tag{3.1}$$

Here g_e is the electron g-factor, μ_B is the Bohr magneton, B is a magnetic field normal to the quantum well plane, β_e is the Dresselhaus constant describing spin-orbit interactions of electrons, the Pauli matrices are

$$\sigma_x = \begin{bmatrix} 0 & 1 \\ 1 & 0 \end{bmatrix}, \qquad \sigma_y = \begin{bmatrix} 0 & -i \\ i & 0 \end{bmatrix}, \qquad \sigma_z = \begin{bmatrix} 1 & 0 \\ 0 & -1 \end{bmatrix}.$$

Hence

$$H_e = \begin{bmatrix} -\frac{1}{2}g_e\mu_B B & \beta_e(k_{e,x} + ik_{e,y}) \\ \beta_e(k_{e,x} - ik_{e,y}) & \frac{1}{2}g_e\mu_B B \end{bmatrix} = \begin{bmatrix} -\frac{1}{2}g_e\mu_B B & \beta_e k_e e^{i\varphi} \\ \beta_e k_e e^{-i\varphi} & \frac{1}{2}g_e\mu_B B \end{bmatrix}. \tag{3.2}$$

Here φ is the angle between the electron wavevector $\mathbf{k_e}$ and the chosen x-axis. The exciton Hamiltonian needs to be written in the basis of $(+1, -1, +2, -2)$ exciton states, which correspond to $(-1/2, +1/2, +1/2, -1/2)$ electron states. The electron spin-flip couples $+1$ and $+2$ states and -1 and -2 states. For each of these two couples of states we apply the Hamiltonian (3.2), which results in the following electronic contribution to the 4×4 exciton Hamiltonian:

$$\widehat{H_e} = \begin{bmatrix} g_e\mu_B B/2 & 0 & k_e\beta_e e^{-i\varphi} & 0 \\ 0 & -g_e\mu_B B/2 & 0 & k_e\beta_e e^{i\varphi} \\ k_e\beta_e e^{i\varphi} & 0 & -g_e\mu_B B/2 & 0 \\ 0 & k_e\beta_e e^{-i\varphi} & 0 & g_e\mu_B B/2 \end{bmatrix}. \tag{3.3}$$

Note that another possible spin-orbit contribution to the Hamiltonian may came from the Rashba effect which takes place in biased quantum wells. The Rashba term to be added in (3.1) writes $\alpha_e(\sigma_x k_{e,y} - \sigma_y k_{e,x})$, where α_e is a constant proportional to the applied electric field.

The similar reasoning applies to the heavy hole contribution to the Hamiltonian: The hole Hamiltonian written in the basis of $(+3/2, -3/2)$ states is

$$H_h = \beta_h(k_{h,x}\sigma_x + k_{h,y}\sigma_y) - \frac{1}{2}g_h\mu_B B\sigma_z.$$

Here g_h is the heavy hole g-factor, μ_B is the Bohr magneton, B is a magnetic field, β_h is the Dresselhaus constant for heavy holes [5].

Hence

$$H_h = \begin{bmatrix} -\frac{1}{2}g_h\mu_B B & \beta_h(k_{h,x} - ik_{h,y}) \\ \beta_h(k_{h,x} + ik_{h,y}) & \frac{1}{2}g_h\mu_B B \end{bmatrix} = \begin{bmatrix} -\frac{1}{2}g_h\mu_B B & \beta_h k_h e^{-i\varphi} \\ \beta_h k_h e^{i\varphi} & \frac{1}{2}g_h\mu_B B \end{bmatrix}. \quad (3.4)$$

Here φ is the angle between the hole wavevector $\mathbf{k_h}$ and the chosen x-axis. The exciton Hamiltonian is written in the basis of $(+1, -1, +2, -2)$ exciton states, which correspond to $(+3/2, -3/2, +3/2, -3/2)$ hole states. The hole spin-flip couples $+1$ and -2 states and -1 and $+2$ states. For each of these two couples of states we apply the Hamiltonian (3.4), which results in the following hole contribution to the 4×4 exciton Hamiltonian:

$$\widehat{H_h} = \begin{bmatrix} -g_h\mu_B B/2 & 0 & 0 & k_h\beta_h e^{-i\varphi} \\ 0 & g_h\mu_B B/2 & k_h\beta_h e^{i\varphi} & 0 \\ 0 & k_h\beta_h e^{-i\varphi} & -g_h\mu_B B/2 & 0 \\ k_h\beta_h e^{i\varphi} & 0 & 0 & g_h\mu_B B/2 \end{bmatrix}. \quad (3.5)$$

For the translational motion of an exciton as a whole particle the exciton momentum is given by $\mathbf{P}_{ex} = (m_e + m_{hh})v_{ex}$, where m_e and m_{hh} are in-plane effective masses of an electron and of a heavy hole, respectively, v_{ex} is the exciton speed. Having in mind that the exciton translational momentum is a sum of electron and hole translational momenta given by $\mathbf{P}_{e,h} = m_{e,hh}v_{e,h}$, $v_{e,h}$ being the electron (hole) speed, one can easily see that $v_h = v_e = v_{ex}$. Having in mind that $\mathbf{P}_{ex} = \hbar\mathbf{k}_{ex}$, $\mathbf{P}_{e,h} = \hbar\mathbf{k}_{e,h}$ we have $k_{ex} = k_h + k_e$, $k_e = \frac{m_e}{m_e+m_{hh}}k_{ex}$, $k_h = \frac{m_{hh}}{m_e+m_{hh}}k_{ex}$.

Besides the contributions from electron and hole spin-orbit interactions and Zeeman splitting, there may be a purely excitonic contribution to the Hamiltonian, which is composed from the Hamiltonian for bright excitons written in the basis $(+1, -1)$:

$$H_b = E_b I - \delta_b\sigma_x = \begin{bmatrix} E_b & -\delta_b \\ -\delta_b & E_b \end{bmatrix}, \quad (3.6)$$

and the Hamiltonian for dark excitons written in the basis $(+2, -2)$:

$$H_d = E_d I - \delta_d\sigma_x = \begin{bmatrix} E_d & -\delta_d \\ -\delta_d & E_d \end{bmatrix}, \quad (3.7)$$

where I is the identity matrix. The terms with δ_b and δ_d describe the splittings of bright and dark states polarized along x and y axes in the plane of the structure due to the long-range exchange interaction. E_b–E_d is the splitting between bright ($+1$ and -1) and dark ($+2$ and -2) exciton states due to the short range exchange interaction. In microcavities, this splitting is additionally enhanced due to the vacuum field Rabi splitting of exciton-polariton modes formed by bright excitons and a confined optical mode of the cavity, see, e.g. [6].

Note that (3.6), (3.7) can be simply obtained from the exciton Hamiltonians written in the basis of (X, Y) polarizations. E.g. for the bright excitons:

$$\begin{aligned} H_{XY} &= \begin{bmatrix} E_b - \delta_b & 0 \\ 0 & E_b + \delta_b \end{bmatrix}, \\ H_b &= C^{-1} H_{XY} C, \end{aligned} \tag{3.8}$$

where $C = \frac{1}{\sqrt{2}}\begin{bmatrix} 1 & 1 \\ i & -i \end{bmatrix}$, $C^{-1} = \frac{1}{\sqrt{2}}\begin{bmatrix} 1 & -i \\ 1 & i \end{bmatrix}$ are the transformation matrices from linear to circular basis and vice versa, see e.g. [7]. The same reasoning applies to the dark excitons as well.

The sum of Hamiltonians (3.7), (3.8) in the 4×4 basis writes:

$$H_0 = \begin{bmatrix} E_b & -\delta_b & 0 & 0 \\ -\delta_b & E_b & 0 & 0 \\ 0 & 0 & E_d & -\delta_d \\ 0 & 0 & -\delta_d & E_d \end{bmatrix}. \tag{3.9}$$

Let us consider the excitons propagating with a wavevector $\mathbf{k_{ex}}$. We shall describe them by a spin density matrix $\hat{\rho} = |\Psi\rangle\langle\Psi|$, where $\Psi = (\Psi_{+1}, \Psi_{-1}, \Psi_{+2}, \Psi_{-2})$ is the exciton wave-function projected to four spin states. The elements of this density matrix ρ_{ij} are dependent on the distance from the excitation spot $r = vt$ and the polar angle φ. The elements of the upper left quarter of the density matrix are linked to the intensity of light emitted by bright exciton states I and to the components of the Stokes vector S_x, S_y and S_z of the emitted light:

$$\rho_{11} = \frac{I}{2} + S_z, \qquad \rho_{12} = S_x - iS_y, \qquad \rho_{21} = S_x + iS_y, \qquad \rho_{22} = \frac{I}{2} - S_z. \tag{3.10}$$

These expressions can be summarized using the Pauli matrices as $\begin{bmatrix} \rho_{11} & \rho_{12} \\ \rho_{21} & \rho_{22} \end{bmatrix} = \frac{I}{2}\hat{I} + \mathbf{S}\hat{\boldsymbol{\sigma}}$, where $\hat{I}$ is the identity matrix.

The components of the Stokes vector are directly proportional to the polarization degree of light measured in XY axes, diagonal axes and the circular basis. The circular polarization degree of light emitted by propagating excitons can be obtained as

$$\rho_c = \frac{2S_z}{I} = (\rho_{11} - \rho_{22})/(\rho_{11} + \rho_{22}), \tag{3.11}$$

the linear polarization degree measured in XY-axes can be found from

$$\rho_l = \frac{2S_x}{I} = (\rho_{12} + \rho_{21})/(\rho_{11} + \rho_{22}), \tag{3.12}$$

the linear polarization degree measured in the diagonal axes (also referred to as a diagonal polarization degree) is given by

$$\rho_d = \frac{2S_y}{I} = i(\rho_{12} - \rho_{21})/(\rho_{11} + \rho_{22}). \tag{3.13}$$

The dynamics of this density matrix is given by the quantum Liouville equation:

$$i\hbar\frac{d\hat{\rho}}{dt} = [\widehat{H}, \hat{\rho}], \tag{3.14}$$

where the Hamiltonian is composed from the electron, hole and exciton contributions given by (3.3), (3.5), (3.9) as follows:

$$\widehat{H} = \begin{bmatrix} E_b - (g_h - g_e)\mu_B B/2 & -\delta_b & k_e\beta_e e^{-i\varphi} & k_h\beta_h e^{-i\varphi} \\ -\delta_b & E_b + (g_h - g_e)\mu_B B/2 & k_h\beta_h e^{i\varphi} & k_e\beta_e e^{i\varphi} \\ k_e\beta_e e^{i\varphi} & k_h\beta_h e^{-i\varphi} & E_d - (g_h + g_e)\mu_B B/2 & -\delta_d \\ k_h\beta_h e^{i\varphi} & k_e\beta_e e^{-i\varphi} & -\delta_d & E_d + (g_h + g_e)\mu_B B/2 \end{bmatrix}. \tag{3.15}$$

Till now we neglected all relaxation or scattering processes in the system. The commonly used way to account for these processes is introduction of a phenomenological Lindblad superoperator (see, e.g. Ref. [6, Chap. 3]) to the Liouville equation:

$$i\hbar\frac{d\hat{\rho}}{dt} = [\widehat{H}, \hat{\rho}] - L(\hat{\rho}), \tag{3.16}$$

where the Lindblad superoperator can be introduced as

$$L(\hat{\rho}) = i\hbar \begin{bmatrix} \rho_{11}/\tau_b & \rho_{12}/\tau_b & \rho_{13}/\tau_c & \rho_{14}/\tau_c \\ \rho_{21}/\tau_b & \rho_{22}/\tau_b & \rho_{23}/\tau_c & \rho_{24}/\tau_c \\ \rho_{31}/\tau_c & \rho_{32}/\tau_c & \rho_{33}/\tau_d & \rho_{34}/\tau_d \\ \rho_{41}/\tau_c & \rho_{42}/\tau_c & \rho_{43}/\tau_d & \rho_{44}/\tau_d \end{bmatrix}, \tag{3.17}$$

where τ_b is the bright exciton lifetime, τ_d is the dark exciton lifetime, τ_c is the characteristic time of decoherence processes between dark and bright excitons.

The formalism described in this section has been successfully applied for description of the spin transport in gases of cold excitons in coupled GaAs/AlGaAs quantum wells [8].

3.3 Non-linear Spin Dynamics of Propagating Excitons and Exciton-Polaritons

In the previous section we operated with a spin density matrix which is very convenient for description of partially coherent and partially polarized exciton gases. The quantum Liouville equation (3.16) is a very efficient tool for description of linear in exciton density effects. On the other hand, one cannot straightforwardly incorporate the non-linear interaction terms in this equation. Treatment of non-linear effects in a partially coherent system is a non-trivial task. Much simpler is treatment of non-linear effects is a perfectly coherent system, such as a condensate or superfluid of excitons or exciton-polaritons. In this case, the ensemble of excitons can be described by a single 4-component wave function $\Psi = (\Psi_{+1}, \Psi_{-1}, \Psi_{+2}, \Psi_{-2})$. The

linear dynamics of this wave-function for ballistically propagating excitons having a wavevector $\mathbf{k}_{ex}$ is described by the Schrödinger equation

$$i\hbar\frac{d}{dt}|\Psi\rangle = \widehat{H}|\Psi\rangle, \tag{3.18}$$

where the Hamiltonian is the same as in (3.14). Note that this equation represents a set of four coupled linear differential equations for four exciton spin components. Non-linear effects lead to scattering of excitons in real and reciprocal space. From now on we shall consider the exciton spin dynamics in the real space, so that the wave function Ψ will become coordinate-dependent and will not be restricted to one single $\mathbf{k}_{ex}$. The non-linear interaction terms for multicomponent exciton gases are introduced and discussed in detail in the chapter "Mean-field description of multicomponent exciton-polariton superfluid" by Y.G. Rubo. Here we expand (3.18) by introducing the kinetic energy (to describe the real space dynamics) and the interaction terms. This results is a system of four non-linear Schrödinger or Gross-Pitaevskii equations:

$$\begin{aligned}
i\hbar\frac{\partial\Psi_{+1}}{\partial t} &= -\frac{\hbar^2\nabla^2}{2m_{ex}}\Psi_{+1} + \beta_e(\hat{k}_x - i\hat{k}_y)\Psi_{+2} + \beta_h(\hat{k}_x - i\hat{k}_y)\Psi_{-2} + \alpha_1|\Psi_{+1}|^2\Psi_{+1} \\
&\quad + \alpha_2|\Psi_{-1}|^2\Psi_{+1} + \alpha_3|\Psi_{+2}|^2\Psi_{+1} + \alpha_4|\Psi_{-2}|^2\Psi_{+1} + W\Psi^*_{-1}\Psi_{+2}\Psi_{-2}, \\
i\hbar\frac{\partial\Psi_{-1}}{\partial t} &= -\frac{\hbar^2\nabla^2}{2m_{ex}}\Psi_{-1} + \beta_e(\hat{k}_x + i\hat{k}_y)\Psi_{-2} + \beta_h(\hat{k}_x + i\hat{k}_y)\Psi_{+2} + \alpha_1|\Psi_{-1}|^2\Psi_{-1} \\
&\quad + \alpha_2|\Psi_{+1}|^2\Psi_{-1} + \alpha_3|\Psi_{-2}|^2\Psi_{-1} + \alpha_4|\Psi_{+2}|^2\Psi_{-1} + W\Psi^*_{+1}\Psi_{+2}\Psi_{-2}, \\
i\hbar\frac{\partial\Psi_{+2}}{\partial t} &= -\frac{\hbar^2\nabla^2}{2m_{ex}}\Psi_{+2} + \beta_e(\hat{k}_x + i\hat{k}_y)\Psi_{+1} + \beta_h(\hat{k}_x - i\hat{k}_y)\Psi_{-1} + \alpha_1|\Psi_{+2}|^2\Psi_{+2} \\
&\quad + \alpha_2|\Psi_{-2}|^2\Psi_{+2} + \alpha_3|\Psi_{+1}|^2\Psi_{+2} + \alpha_4|\Psi_{-1}|^2\Psi_{+2} + W\Psi^*_{-2}\Psi_{+1}\Psi_{-1}, \\
i\hbar\frac{\partial\Psi_{-2}}{\partial t} &= -\frac{\hbar^2\nabla^2}{2m_{ex}}\Psi_{-2} + \beta_e(\hat{k}_x - i\hat{k}_y)\Psi_{-1} + \beta_h(\hat{k}_x + i\hat{k}_y)\Psi_{+1} + \alpha_1|\Psi_{-2}|^2\Psi_{-2} \\
&\quad + \alpha_2|\Psi_{+2}|^2\Psi_{-2} + \alpha_3|\Psi_{-1}|^2\Psi_{-2} + \alpha_4|\Psi_{+1}|^2\Psi_{-2} + W\Psi^*_{+2}\Psi_{+1}\Psi_{-1}.
\end{aligned} \tag{3.19}$$

Here $k_{x,y} = -i\nabla_{x,y}$, $m_{ex} = m_e + m_{hh}$. To make this system more compact we have omitted the terms describing exchange induced exciton splittings given by the Hamiltonian (3.9). We do not discuss here the nature and value of the interaction constants $\alpha_{1,2,3,4}$ and W. In the system of indirect excitons in coupled GaAs/AlGaAs quantum wells, a zeroth approximation, one can take $\alpha_1 = \alpha_2 = \alpha_3 = \alpha_4$. Note also that in microcavities, where the lower exciton-polariton mode is strongly decoupled from dark excitons, the dark exciton states may be almost empty at low temperatures. If this is the case, the spin dynamics of the polariton condensate is given by the first two of four equations (3.19) with $\alpha_{3,4} = W = 0$.

The remaining constants $\alpha_{1,2}$ have been widely discussed in literature. We address the interested reader to the experimental and theoretical study of these constants by Vladimirova et al. [9].

The Gross-Pitaevskii (GP) equations are widely used for description of coherent propagation of exciton-polaritons in microcavities, see, e.g. [10]. They allow for studying of interesting topology effects including quantum vortices, half-quantum vortices, dark and bright solitons etc., see, e.g. [11]. The polarization of light emitted by the polariton condensate can be obtained as

$$\rho_c = \frac{2S_z}{I} = \left(\left|\Psi_{+1}^2\right| - \left|\Psi_{-1}^2\right|\right)/\left(\left|\Psi_{+1}^2\right| + \left|\Psi_{-1}^2\right|\right), \tag{3.20}$$

$$\rho_l = \frac{2S_x}{I} = 2\,\mathrm{Re}\left(\Psi_{+1}^*\Psi_{-1}\right)/\left(\left|\Psi_{+1}^2\right| + \left|\Psi_{-1}^2\right|\right), \tag{3.21}$$

$$\rho_d = \frac{2S_y}{I} = -2\,\mathrm{Im}\left(\Psi_{+1}^*\Psi_{-1}\right)/\left(\left|\Psi_{+1}^2\right| + \left|\Psi_{-1}^2\right|\right). \tag{3.22}$$

These expressions easily follow from (3.11)–(3.13) and definition of the density matrix.

It should be noted that GP equations as a theoretical tool are not universal. They fail to describe a wide range of phenomena linked with decoherence processes. To start with (3.19) are written for excitons (exciton-polaritons) with an infinite lifetime, which is never the case in real systems. Many authors introduce pumping and radiative decay terms in (3.19) phenomenologically, which strongly affects the final result. Experimentally, pumping of the polariton condensate may be either resonant (pumping laser energy matching the energy of the condensate) or non-resonant (the laser populates a reservoir of incoherent states which feeds the condensate). In both cases, it is difficult to introduce the pumping terms in (3.19) without violating the common sense in limiting particular cases. The crucial question is: should the pumping term containing the exciton wave-function be local or not? Another important issue is in which extent the features of superfluidity (including suppression of disorder scattering, vortices and solitons) obtained using GP equation may serve as a proof that exciton-polariton liquids are superfluid. Answering this question, one should bear in mind that writing GP equations one assumes that the system is fully coherent. Therefore, this equation is unsuitable for description of a phase transition towards superfluidity, which manifests itself as a build-up of spatial coherence. The density matrix formalism accounting for non-linearities would be better adapted for description of such a phase transition. On the other hand, if the superfluid is already formed, GP equation is suitable for description of superfluid currents, including the spin currents.

3.4 Exciton Spin Currents

Consider an exciton state characterized by a wavevector $\mathbf{k}_{ex}$ and described by the density matrix $\hat{\rho}$. The elements of this matrix ρ_{11}, ρ_{22}, ρ_{33}, ρ_{44} are the densities of $+1$, -1, $+2$ and -2 excitons, respectively. The current of each of these densities is

given by a product of the exciton speed and the corresponding density:

$$\mathbf{j}_{\propto} = \frac{\hbar \mathbf{k}_{ex}}{m_{ex}} \rho_{jj}, \tag{3.23}$$

with $j = 1, 2, 3, 4$ for $\alpha = +1, -1, +2, -2$, respectively. Experimentally, one can measure the magnetization current associated with the exciton density current. The magnetization carried by propagating excitons can be found as

$$\mathrm{M}_z = -\frac{\mu_B}{2\hbar}\big[(g_h - g_e)(\rho_{11} - \rho_{22}) + (g_h + g_e)(\rho_{33} - \rho_{44})\big]. \tag{3.24}$$

This expression is obtained having in mind that an electron with a spin projection to z-axis of $\pm 1/2$ contributes to magnetization projection to z-axis $\mp\frac{\mu_B}{2\hbar} g_e$, and a heavy hole with the spin projection of $\pm 3/2$ contributes to magnetization $\mp\frac{\mu_B}{2\hbar} g_h$. Hence, the magnetization (spin) current produced by the excitons having a wave-vector $\mathbf{k}_{ex}$ will be given by

$$\begin{aligned}\mathbf{j}_{\mathbf{M}}(\mathbf{k}_{ex}) = -\frac{\mu_B \mathbf{k}_{ex}}{2m_{ex}}\big[&(g_h - g_e)\big(\rho_{11}(\mathbf{k}_{ex}) - \rho_{22}(\mathbf{k}_{ex})\big) \\ &+ (g_h + g_e)\big(\rho_{33}(\mathbf{k}_{ex}) - \rho_{44}(\mathbf{k}_{ex})\big)\big].\end{aligned} \tag{3.25}$$

The total magnetization current in the exciton gas can be obtained by integration over all wave-vectors:

$$\mathbf{j}_{\mathbf{M}}^{\mathrm{tot}} = -\frac{S}{(2\pi)^2}\int d\mathbf{k}_{ex} \mathbf{j}_{\mathbf{M}}(\mathbf{k}_{ex}). \tag{3.26}$$

Here S is the area of the sample. This current may be detected e.g. by spatially resolved Kerr rotation spectroscopy.

3.4.1 Spin Currents in Exciton Condensates

The approach formulated above can be extended to description of spin currents in coherent exciton (exciton-polariton) condensates. In this case we need to replace the momentum $\hbar \mathbf{k}_{ex}$ by a momentum operator $\hat{p} = -i\hbar\nabla$ and the diagonal components of the density matrix ρ_{11}, ρ_{22}, ρ_{33}, ρ_{44} by the exciton densities $|\Psi_{+1}^2|$, $|\Psi_{-1}^2|$, $|\Psi_{+2}^2|$, $|\Psi_{-2}^2|$, respectively, in the expressions (3.24), (3.26). In this case the density currents become:

$$\mathbf{j}_{\propto} = -i\frac{\hbar}{m_{ex}} \Psi_{\propto}^* \nabla \Psi_{\alpha}, \tag{3.27}$$

and the magnetization current can be expressed as:

$$\begin{aligned}\mathbf{j}_{\mathbf{M}}^{\mathrm{tot}} = \frac{i\mu_B}{2m_{ex}}\big[&(g_h - g_e)\big(\Psi_{+1}^* \nabla \Psi_{+1} - \Psi_{-1}^* \nabla \Psi_{-1}\big) \\ &+ (g_h + g_e)\big(\Psi_{+2}^* \nabla \Psi_{+2} - \Psi_{-2}^* \nabla \Psi_{-2}\big)\big].\end{aligned} \tag{3.28}$$

One can also introduce the spin conductivity tensor linking the components of the density current (3.27) with the gradient of potential acting upon each of the exciton spin components:

$$\mathrm{j}_{\propto,l} = \sigma_{\propto,\beta}^{l,m} \nabla U_{\beta,m}, \tag{3.29}$$

where $l = x, y$ and $m = x, y$ indicate the in-plane projections of the current and potential gradient, respectively, $\beta = +1, -1, +2, -2$. One can see that $\sigma_{\propto,\beta}^{l,m}$ is a 64 component tensor in a general 2D case. The origin of the potential gradient $\nabla U_{\beta,m}$ needs to be discussed separately. As excitons are electrically neutral, the external electric field does not create a coordinate-dependent potential for them. $\nabla U_{\beta,m}$ can originate from the gradient of the quantum well width, gradient of the barrier height, or it can be induced by excitons themselves due to e.g. dipole-dipole repulsion.

3.4.2 Polarization Currents

Spatially resolved measurements of the polarization degrees ρ_c, ρ_l and ρ_d of light emitted by excitons give access to the exciton polarization currents. In terms of the density matrix formalism, they can be defined as products of the exciton speed and the corresponding polarization degree:

$$\mathbf{j}_c(\mathbf{k}_{ex}) = \frac{\hbar \mathbf{k}_{ex}}{m_{ex}} \rho_c = \frac{\hbar \mathbf{k}_{ex}}{m_{ex}} (\rho_{11} - \rho_{22})/(\rho_{11} + \rho_{22}), \tag{3.30}$$

$$\mathbf{j}_l(\mathbf{k}_{ex}) = \frac{\hbar \mathbf{k}_{ex}}{m_{ex}} \rho_l = \frac{\hbar \mathbf{k}_{ex}}{m_{ex}} (\rho_{12} + \rho_{21})/(\rho_{11} + \rho_{22}), \tag{3.31}$$

$$\mathbf{j}_d(\mathbf{k}_{ex}) = \frac{\hbar \mathbf{k}_{ex}}{m_{ex}} \rho_d = i \frac{\hbar \mathbf{k}_{ex}}{m_{ex}} (\rho_{12} - \rho_{21})/(\rho_{11} + \rho_{22}). \tag{3.32}$$

The total polarization currents can be obtained integrating the expressions (3.30)–(3.32) over the reciprocal space:

$$\mathbf{j}_{\mathrm{tot}}^{c,l,d} = -\frac{S}{(2\pi)^2} \int d\mathbf{k}_{ex} \mathbf{j}_{c,l,d}(\mathbf{k}_{ex}). \tag{3.33}$$

The polarization currents in a polariton condensate can be found from the GP equations (3.19) as

$$\mathbf{j}_c = -\frac{i\hbar}{m_{ex}} \left(\Psi_{+1}^* \nabla \Psi_{+1} - \Psi_{-1}^* \nabla \Psi_{-1}\right)/\left(\left|\Psi_{+1}^2\right| + \left|\Psi_{-1}^2\right|\right), \tag{3.34}$$

$$\mathbf{j}_l = -\frac{i\hbar}{m_{ex}} \left(\Psi_{+1}^* \nabla \Psi_{-1} + \Psi_{-1}^* \nabla \Psi_{+1}\right)/\left(\left|\Psi_{+1}^2\right| + \left|\Psi_{-1}^2\right|\right), \tag{3.35}$$

$$\mathbf{j}_d = \frac{\hbar}{m_{ex}} \left(\Psi_{+1}^* \nabla \Psi_{-1} - \Psi_{-1}^* \nabla \Psi_{+1}\right)/\left(\left|\Psi_{+1}^2\right| + \left|\Psi_{-1}^2\right|\right). \tag{3.36}$$

It is important to note that if the spin density currents (3.26), (3.27) can hardly be constant in excitonic systems, where the lifetime of each spin carrier is limited, the sum of polarization currents (3.34)–(3.36) is expected to be constant in the so-called "spin superfluidity" regime where all scattering processes causing depolarization are suppressed.

3.5 Conclusions

Bosonic spin transport is a young and promising area of solid state physics. The theories of mesoscopic transport of charge carriers and quantum transport in one-dimensional channels are among the most interesting chapters of modern physics. Substitution of fermions by bosons and of a scalar electric charge by a spin vector cannot be formally done in these theories. Basically, all mesoscopic and quantum transport effects need to be reconsidered if we speak about electrically neutral bosonic spin carriers like excitons or exciton-polaritons. Moreover, due to the finite life time of the carriers, the most basic in conventional transport theory requirements of charge and flux conservation cannot be fulfilled in the excitonic systems. This is why the area of "spin-optronics" essentially remains *terra incognita*. Experimentally, it is much easier to study the steady state of exciton or polariton condensates than their motion. Nevertheless, recent years are manifested by numbers of publications on the bosonic transport in exciton and exciton-polariton systems. The rapid progress in structure growth and experimental methods allows us to hope that very soon the new interesting bosonic spin transport effects will be discovered.

Acknowledgements This work has been supported by the Royal Society Leverhulme fellowship. The author is deeply grateful to L.V. Butov, T. Ostatnicky, Y.G. Rubo, M.R. Vladimirova, M.M. Glazov, I.A. Shelykh, T.C.H. Liew, A. Bramati for many useful discussions on the peculiarities of bosonic spin transport.

References

1. M.I. Dyakonov, V.I. Perel, Current-induced spin orientation of electrons in semiconductors. Phys. Lett. A **35**(6), 459 (1971)
2. E.L. Ivchenko, G.E. Pikus, *Superlattices and Other Heterostructures. Symmetry and Optical Phenomena* (Springer, Berlin, 1997)
3. E.I. Rashba, E.Ya. Sherman, Spin-orbital band splitting in symmetric quantum wells. Phys. Lett. A **129**, 175 (1988)
4. E.L. Ivchenko, *Optical Spectroscopy of Semiconductor Nanostructures* (Alpha Science, Oxford, 2005)
5. J.-W. Luo, A.N. Chantis, M. van Schilfgaarde, G. Bester, A. Zunger, Discovery of a novel linear-in-k spin splitting for holes in the 2D GaAs/AlAs system. Phys. Rev. Lett. **104**, 066405 (2010)
6. A.V. Kavokin, J.J. Baumberg, G. Malpuech, F.P. Laussy, *Microcavities* (Oxford University Press, Oxford, 2007)
7. M. Born, E. Wolf, *Principles of Optics* (Pergamon, London, 1970)

8. A.A. High, J.R. Leonard, A.T. Hammack, M.M. Fogler, L.V. Butov, A.V. Kavokin, K.L. Campman, A.C. Gossard, Spontaneous coherence in a cold exciton gas. Nature **483**, 584 (2012)
9. M. Vladimirova, S. Cronenberger, D. Scalbert, K.V. Kavokin, A. Miard, A. Lemaitre, J. Bloch, D. Solnyshkov, G. Malpuech, A.V. Kavokin, Polariton-polariton interaction constants in microcavities. Phys. Rev. B **82**, 075301 (2010)
10. M. Wouters, I. Carusotto, Superfluidity and critical velocities in nonequilibrium Bose–Einstein condensates. Phys. Rev. Lett. **105**, 020602 (2010)
11. A. Amo, S. Pigeon, D. Sanvitto, V.G. Sala, R. Hivet, I. Carusotto, F. Pisanello, G. Leménager, R. Houdré, E. Giacobino, C. Ciuti, A. Bramati, Polariton superfluids reveal quantum hydrodynamic solitons. Science **332**, 1167 (2011) and references therein

Chapter 4
Mean-Field Description of Multicomponent Exciton-Polariton Superfluids

Y.G. Rubo

Abstract This is a review of spin-dependent (polarization) properties of multicomponent exciton-polariton condensates in conditions when quasi-equilibrium mean-field Gross-Pitaevskii description can be applied. Mainly two-component (spin states ± 1) polariton condensates are addressed, but some properties of four-component exciton condensates, having both the bright (spin ± 1) and the dark (spin ± 2) components, are discussed. Change of polarization state of the condensate and phase transitions in applied Zeeman field are described. The properties of fractional vortices are given, in particular, I present recent results on the warping of the field around half-vortices in the presence of longitudinal-transverse splitting of bare polariton bands, and discuss the geometrical features of warped half-vortices (in the framework of the lemon, monstar, and star classification).

4.1 The Gross-Pitaevskii Equation

Currently, most theoretical descriptions of exciton-polariton condensates observed [1–5] in incoherently excited semiconductor microcavities are based on the Gross-Pitaevskii equation (GPE). When the polarization of the condensate is of interest, this equation can be generically written as

$$\mathrm{i}\hbar\frac{\partial}{\partial t}\vec{\psi}(\vec{r},t)=\frac{\delta H}{\delta\vec{\psi}^{*}(\vec{r},t)},\quad H=\int\mathcal{H}\big(\vec{\psi}^{*},\vec{\psi}\big)d^{2}r, \tag{4.1}$$

where the order parameter $\vec{\psi}(\vec{r},t)$ of the condensate is a complex 2D vector function of the 2D position in the microcavity plane $\vec{r}$ and time t. Alternatively, one can expand $\vec{\psi}$ on the circular polarization basis

$$\vec{\psi}=\frac{\hat{\vec{x}}+\mathrm{i}\hat{\vec{y}}}{\sqrt{2}}\psi_{+1}+\frac{\hat{\vec{x}}-\mathrm{i}\hat{\vec{y}}}{\sqrt{2}}\psi_{-1}, \tag{4.2}$$

Y.G. Rubo (✉)
Instituto de Energías Renovables, Universidad Nacional Autónoma de México, Temixco, Morelos, 62580, Mexico
e-mail: ygr@mazatl.cie.unam.mx

A. Bramati, M. Modugno (eds.), *Physics of Quantum Fluids*,
Springer Series in Solid-State Sciences 177, DOI 10.1007/978-3-642-37569-9_4,

and obtain the coupled GPEs for two circular components $\psi_{\pm1}$ (see (4.32a), (4.32b) in Sect. 4.4).

GPE (4.1) is used in two main flavors, strongly non-equilibrium GPE and quasi-equilibrium GPE, that treat the energy relaxation in two extreme ways. It is completely neglected in the former, and it is considered to be essential in the latter. Mathematically, these approaches differ in Hamiltonian density $\mathcal{H}(\vec{\psi}, \vec{\psi}^*)$: it is complex in the former and it is real in the latter. Each approach has its benefits and drawbacks.

The imaginary part of the Hamiltonian for non-equilibrium GPE [6–9] is given by the difference of income and escape rates of exciton-polaritons into and out of the condensate. While the escape rate is given by the reciprocal radiative lifetime of exciton-polaritons and is independent of the particle density, the income rate is a non-linear function of it. The nonlinearity is essential to stabilize the solution and it appears due to the depletion of an incoherently pumped reservoir. This approach resulted to be quite successful in modeling the experimental data on condensate density profiles for spatially nonuniform exciton-polariton condensates. On the other hand, it cannot describe the spontaneous formation of linear polarization of the condensate—the fact that is quite unfortunate since the observation of spontaneous linear polarization is one of the direct experimental evidences of Bose-Einstein condensation of exciton-polaritons [1, 2]. A workaround is to add the Landau-Khalatnikov relaxation into (4.1). But this relaxation is rather artificial because it changes the number of particles in the condensate.

In what follows, we consider the opposite limit assuming fast relaxation of exciton-polaritons, so that they reach quasi-equilibrium, even with the temperature that can be different from the lattice one. The balance of income and outcome rates produces some steady-state concentration of exciton-polaritons, that can be defined, as usual, by introducing the chemical potential μ. The coherent fraction of condensed particles can be described by the traditional GPE with real $\mathcal{H}(\vec{\psi}, \vec{\psi}^*)$,

$$\mathcal{H} = \mathcal{T} - \mu n + \mathcal{H}_{\text{int}} + \mathcal{H}'. \tag{4.3}$$

Here $\mathcal{T}$ is the density of the kinetic energy, $\mathcal{H}_{\text{int}}$ describes interaction between the particles, $\mathcal{H}'$ stands for some possible perturbations, and $n = \vec{\psi}^* \cdot \vec{\psi}$ is the exciton-polariton density.

The kinetic energy of exciton-polaritons in planar microcavities depends on the orientation of vector $\vec{\psi}$ with respect to the direction of motion. Near the bottom of lower polariton branch one has

$$\mathcal{T} = \frac{\hbar^2}{2m_l}|\vec{\nabla} \cdot \vec{\psi}|^2 + \frac{\hbar^2}{2m_t}|\vec{\nabla} \times \vec{\psi}|^2 \tag{4.4a}$$

$$= \frac{\hbar^2}{m_l}\left|\frac{\partial \psi_{+1}}{\partial z^*} + \frac{\partial \psi_{-1}}{\partial z}\right|^2 + \frac{\hbar^2}{m_t}\left|\frac{\partial \psi_{+1}}{\partial z^*} - \frac{\partial \psi_{-1}}{\partial z}\right|^2, \tag{4.4b}$$

where m_l and m_t are the longitudinal and transverse effective masses of polaritons, and the complex derivatives

$$\frac{\partial}{\partial z} = \frac{1}{2}\left(\frac{\partial}{\partial x} - \mathrm{i}\frac{\partial}{\partial y}\right), \qquad \frac{\partial}{\partial z^*} = \frac{1}{2}\left(\frac{\partial}{\partial x} + \mathrm{i}\frac{\partial}{\partial y}\right), \tag{4.5}$$

are used. The vector $\vec{\psi}$ is proportional to the in-plane electric field vector of exciton-polariton mode. According to (4.4a), (4.4b) the frequency of transverse electric (TE) mode with in-plane wave vector $\vec{k} \perp \vec{\psi}$ is $\hbar k^2/2m_t$, while for the transverse magnetic (TM) mode with $\vec{k} \| \vec{\psi}$ the frequency is $\hbar k^2/2m_l$. (The same bare frequencies of both modes at $k = 0$ are removed from (4.4a), (4.4b).)

The polariton-polariton interaction is also anisotropic: it depends on mutual orientation of $\vec{\psi}$ and $\vec{\psi}^*$. One can construct two quartic invariants from these two vectors and $\mathcal{H}_{\mathrm{int}}$ is given by

$$\mathcal{H}_{\mathrm{int}} = \frac{1}{2}(U_0 - U_1)\left(\vec{\psi}^* \cdot \vec{\psi}\right)^2 + \frac{1}{2}U_1|\vec{\psi}^* \times \vec{\psi}|^2 \tag{4.6a}$$

$$= \frac{1}{2}U_0\left(|\psi_{+1}|^4 + |\psi_{-1}|^4\right) + (U_0 - 2U_1)|\psi_{+1}|^2|\psi_{-1}|^2. \tag{4.6b}$$

It is seen that U_0 is the amplitude of interaction of polaritons with the same circular polarization (with the same spin), and $U_0 - 2U_1$ is the amplitude of interaction of polaritons with opposite circular polarizations (opposite spins). These quantities are denoted by α_1 and α_2 in some papers. The constant U_0 is positive and can be estimated as $\sim \mathcal{E}_b a_B^2$, where $\mathcal{E}_b$ is the exciton binding energy and a_B is the exciton Bohr radius. The interaction of exciton-polaritons with opposite spins depends substantially on the electron-electron and hole-hole exchange scattering and is defined by the electron and hole confinement within quantum wells and by the number of quantum wells in the microcavity. As a result, the value of U_1 is sensitive to the microcavity geometry.

To end this section it is important to mention the limitations of any GPE in application to the condensates of exciton-polaritons in microcavities, or to condensates of any other bosonic excitations that have a finite radiative life-time. Due to interference of light emitted from different parts of condensate there appears dissipative long-range coupling in the system. Most importantly, the escape rate becomes dependent on the symmetry of the condensate wave-function and this favors the formation of particular long-living many-particle states, or weak-lasing states [10]. These effects cannot be properly treated in the framework of Gross-Pitaevskii equation (4.1).

4.2 Polarization and Effects of Zeeman Field

The interaction energy (4.6a), (4.6b) of the polariton condensate is polarization dependent. While the first term in (4.6a) does not depend on polarization and is simply

proportional to the square of the polariton concentration $n = (\vec{\psi}^* \cdot \vec{\psi})$, the second term in (4.6a) is sensitive to the degree of the circular polarization of the condensate. For $U_1 > 0$ the interaction energy is minimized when the second term in (4.6a) is annulated, which is achieved for polarization satisfying $\vec{\psi}^* \times \vec{\psi} = 0$, i.e., for the linear polarization. On the other hand, in the case $U_1 < 0$ the minimum is reached for the circular polarization of the condensate, when $\vec{\psi}^* \times \vec{\psi} = \pm \mathrm{i} n$.

So, there is qualitative change in the ground state of the condensate when U_1 changes sign [11].

(i) $U_1 > 0$. The ground state is characterized by two angles, the total phase angle θ and the polarization angle η. These angles are defined from the Descartes components of the order parameter $\psi_x = \sqrt{n} e^{\mathrm{i}\theta} \cos\eta$ and $\psi_y = \sqrt{n} e^{\mathrm{i}\theta} \sin\eta$. The circular components are then $\psi_{\pm 1} = \sqrt{n/2} e^{\mathrm{i}(\theta \mp \eta)}$. There are two broken continuous symmetries and, consequently, the excitation spectrum consists of two Bogoliubov branches. The sound velocities for these branches at $m_l = m_t = m^*$ are $v_0 = \sqrt{\mu/m^*}$ and $v_1 = \sqrt{nU_1/m^*}$, where $\mu = (U_0 - U_1)n$ is the chemical potential. The presence of TE-TM splitting leads to the anisotropy of sound velocities (see [11] for details).

(ii) $U_1 < 0$. In this case one of the circular components is zero and the other is $\sqrt{n} e^{\mathrm{i}\theta}$. Since there is only one broken continuous symmetry, the excitation spectrum consists of only one Bogoliubov branch, and the other branch is gaped parabolic with the gap $2|U_1|n$. The chemical potential is $\mu = U_0 n$ in this domain, so that the sound velocity for the Bogoliubov excitations is $\sqrt{\mu/m^*}$.

The mean-field theory predicts an arbitrary polarization for $U_1 = 0$ since in this case the energy of the condensate is polarization independent. In reality, fluctuations destroy the order in this case at any finite temperature T. It can be already understood from the excitation spectrum, because, apart from the Bogoliubov branch, there is the gapless parabolic branch with dispersion $\hbar^2 k^2/2m^*$ and the condensate would evaporate completely due to excitation of these quasiparticles.[1] One can also map this case to the O(4) nonlinear sigma model, where the order is proven to be absent for $T > 0$ [14].

Note the similarity between the two-component condensates of exciton-polaritons and three-component condensates of spin-1 cold atoms [12, 13]. Due to the 3D rotational symmetry, there are also only two interaction constants in the latter case. These constants are defined by the cross-sections of scattering of two atoms with the total spin 0 and 2.[2] Two different atomic condensates can also be found depending on the sign of the scattering length with the total spin 2: ferromagnetic and anti-ferromagnetic (or polar), which are analogs of circularly and linearly polarized exciton-polariton condensates, respectively.

[1] The concentration of quasiparticles with the energy $\epsilon(k)$ is given by $\int (2\pi)^{-2} [\exp\{\epsilon(k)/T\} - 1]^{-1} d^2k$ and the integral diverges logarithmically for small k when $\epsilon(k) \propto k^2$.

[2] The case of the total spin 1 is irrelevant since the orbital wave function of colliding bosons is antisymmetric and it cannot be realized within the condensate.

It is the first case, $U_1 > 0$, that is realized in the exciton-polariton condensates observed so far. The linearly polarized condensate can be seen as composition of equal numbers mutually coherent spin-up and spin-down polaritons. Therefore, it is interesting to study the effect of applied magnetic field to this state [15]. Considering only weak fields, when the magnetic length is much greater than the exciton Bohr radius, one can study only the effects of Zeeman field, that is described by adding

$$\mathcal{H}' = \Omega\left(|\psi_{-1}|^2 - |\psi_{+1}|^2\right) \tag{4.7}$$

into Hamiltonian (4.3). Here the Zeeman field Ω is given by the half of the Zeeman splitting energy for a single polariton.

To find the order parameter for the uniform condensate in the presence of Zeeman field it is convenient to introduce the concentrations of the components $n_{\pm 1} = |\psi_{\pm 1}|^2$ satisfying $n_{+1} + n_{-1} = n$. Assuming both n_{+1} and n_{-1} to be nonzero, one can take variations of the Hamiltonian

$$\begin{aligned}\mathcal{H}_{\text{int}} + \mathcal{H}' - \mu n \\ = \frac{1}{2}U_0(n_{+1} + n_{-1})^2 - 2U_1 n_{+1} n_{-1} - (\mu + \Omega)n_{+1} - (\mu - \Omega)n_{-1}\end{aligned} \tag{4.8}$$

over $n_{\pm 1}$ to obtain

$$-2U_1 n_{\pm 1} = (\mu - U_0 n \mp \Omega). \tag{4.9}$$

The sum and the difference of (4.9) results in

$$\mu = (U_0 - U_1)n, \quad n_{\pm 1} = \frac{1}{2}\left(n \pm \frac{\Omega}{U_1}\right), \quad \text{for } |\Omega| < \Omega_c \equiv nU_1. \tag{4.10}$$

For higher Zeeman fields, $|\Omega| > \Omega_c$, one of the components becomes empty, n_{-1} for $\Omega > \Omega_c$ and n_{+1} for $\Omega < -\Omega_c$, and in this case $\mu = U_0 n - |\Omega|$.

Remarkably, for subcritical fields the chemical potential does not change at all, so that there is no change in the position of the emission line. The only effect of applied Zeeman field is the change of circular polarization degree $\varrho_c = (n_{+1} - n_{-1})/(n_{+1} + n_{-1}) = \Omega/nU_1$, that increases linearly with the field. The elliptical polarization of the condensate for subcritical fields is characterized by two angles, and in the same way as for the linearly polarized condensate, there are two Goldstone modes; only the sound velocities change with the Zeeman field. This implies the full suppression of the Zeeman splitting by polariton-polariton interactions within the condensate [15]. Note also that for subcritical fields there are two phase transitions in the left and in the right circular component of the condensate, respectively [16]. The Zeeman splitting (the gap in the exciton spectrum) appears only for supercritical fields $|\Omega| > \Omega_c$ where the condensate becomes circularly polarized. This effect, observed experimentally by Larionov et al. [17], allows to measure the spin-dependent interaction constant U_1.

4.3 Vortices in Exciton-Polariton Condensates

Vortices play a key role in various physical phenomena both on macroscopic and microscopic level. While the vortex formation is very important for description of different effects in fluid mechanics, in particular, in aerodynamics and turbulent flow motion, the understanding of properties of quantized vortices is crucial for description of phase transitions in condensed matter. The well known examples are the phase transitions in type II superconductors in applied magnetic field, which are related to the formation and melting of vortex lattices [18], and the Berezinskii-Kosterlitz-Thouless (BKT) phase transition [19–22].

As it was discussed above, the exciton-polariton condensates possess two-component order parameter (4.2) and these condensates allow half-quantum vortices (half-vortices) [23]. Moreover, the half-vortices are basic topological excitations in this case (see [24] for a review on the properties of half-quantum vortices). In spite of recent observation of both integer [25] and half-integer [26] vortices in exciton-polariton condensates, the presence of half-vortices was recently questioned [27] for the case of two-band dispersion with TE-TM splitting of polariton band given by (4.4a), (4.4b). In this section I present the details on how the vortex solutions should be found in this case (a short summary of this theory has been given in [28]). In what follows only the case of zero Zeeman field will be considered.

For a 2D system of radius R the energy of a vortex is finite but logarithmically large,

$$E_{\mathrm{vor}} = E_c + E_s \ln(R/a), \tag{4.11}$$

where $a = \hbar/\sqrt{2m^*\mu}$ is the characteristic radius of vortex core (the effective mass m^* is defined below in (4.17)). The fact that E_{vor} diverges logarithmically at $R \to \infty$ is good: it prevents the single vortices to be excited at low temperatures and thus protects the long-range order of the condensate. Knowledge of prefactor E_s allows to estimate [22] the BKT transition temperature T_c. The proliferation of single vortices appears when the free energy $E_{\mathrm{vor}} - TS$ crosses zero. The vortex core area is a^2 and the vortex can appear in R^2/a^2 places, so that the entropy $S = \ln(R/a)^2$ and this gives $T_c = E_s/2$ if one neglects the energy of the core E_c in (4.11). The energy $E_s \ln(R/a)$ is elaborated on large distances from the vortex core $r \gg a$, which we will refer to as the elastic region, and the study of vortices should begin with establishing the behavior of the order parameter in this region. When TE-TM splitting is present this behavior is, in general, nontrivial.

4.3.1 The Order Parameter on Large Distances

In the elastic region the order parameter changes within the order parameter manifold, i.e., the polarization of the condensate is linear everywhere in this domain. The circular-polarization components $\psi_{\pm 1}$ defined in (4.2) can be written in cylindrical

coordinates (r, ϕ) as

$$\psi_{\pm 1}(r \gg a, \phi) = \sqrt{\frac{n}{2}} e^{\mathrm{i}[\theta(\phi) \mp \eta(\phi)]}, \tag{4.12}$$

where n is the constant concentration of the condensate at large distances, and the phases are written in terms of total phase angle θ and polarization angle η. These angles do not depend on the radius r (such dependence would only increase the vortex energy), but they are functions of the azimuthal angle ϕ. Since the order parameters should be uniquely defined in the whole space, one has

$$\eta(\phi + 2\pi) - \eta(\phi) = 2\pi k, \qquad \theta(\phi + 2\pi) - \theta(\phi) = 2\pi m. \tag{4.13}$$

These conditions divide all possible solutions of GPE into topological sectors. Each sector is defined by two topological charges (or winding numbers), k and m. The state from one sector cannot be continuously transformed into another sector, or, in other words, any state of the condensate evolves within its own topological sector. The sector $k = m = 0$ is the ground state sector; the minimum energy here is reached for position-independent order parameter. By definition, the vortex is the state that minimizes the energy in a topological sector with at least one non-zero winding number. The energy of the (k, m)-vortex (4.11) is counted from the ground state energy, i.e., it is the difference between the minimal energy in the (k, m) sector and the minimal energy of $(0, 0)$ sector (the ground state energy). Since only the sum and the difference, $\theta \pm \eta$, enter (4.12), the winding numbers can be either both integer or both half-integer, and the corresponding vortices are referred accordingly. Note also that the vortex corresponds to a minimum of Hamiltonian H for specific boundary conditions: $\delta H / \delta \vec{\psi}^* = 0$ for the vortex solution and, therefore, it is a static solution of GPE (4.1).[3]

According to (4.13) one can add any periodic functions of ϕ to $\eta(\phi)$ and $\theta(\phi)$ without changing the topological sector. The proper functions $\eta(\phi)$ and $\theta(\phi)$ for the (k, m)-vortex should be found from minimization of Hamiltonian in elastic region. The corresponding part of Hamiltonian is related solely to the kinetic energy term $\int \mathcal{T} d^2 r$. After substitution of (4.12) into (4.4b) and use of the asymptotic behavior of the complex derivative for $r \to \infty$,

$$\frac{\partial}{\partial z} \to -\frac{\mathrm{i}}{2r} e^{-\mathrm{i}\phi} \frac{\partial}{\partial \phi}, \tag{4.14}$$

one obtains the product of integrals over r and ϕ that results in the second term of (4.11). The integral over r diverges logarithmically and should be cut by the core size a at small r, and by system radius R at large r. This gives the factor $\ln(R/a)$.

[3]Note, however, that this does not imply that a single vortex gives an absolute minimum of the H in the corresponding topological sector. For example, the integer vortex $(1, 0)$ can be unstable with respect to decay into the pair of $(\frac{1}{2}, \frac{1}{2})$ and $(\frac{1}{2}, -\frac{1}{2})$ half-vortices for $m_l < m_t$ (see Sect. 4.3.2).

The prefactor is then given by

$$E_s = \frac{\hbar^2 n}{2m^*} \int_0^{2\pi} \left\{ \left[1 + \gamma \cos(2u)\right] \left(1 + u'\right)^2 + \left[1 - \gamma \cos(2u)\right] \theta'^2 \right\} d\phi, \tag{4.15}$$

where the prime denotes the derivative over ϕ and

$$u(\phi) = \eta(\phi) - \phi. \tag{4.16}$$

The effective mass m^* and the TE-TM splitting parameter γ are defined in (4.15) by

$$\frac{1}{m^*} = \frac{1}{2}\left(\frac{1}{m_l} + \frac{1}{m_t}\right), \qquad \gamma = \frac{m_t - m_l}{m_t + m_l}. \tag{4.17}$$

Variations of the functional (4.15) over θ and u lead to the equations

$$\left[1 - \gamma \cos(2u)\right] \theta'' + 2\gamma \sin(2u) u' \theta' = 0, \tag{4.18a}$$

$$\left[1 + \gamma \cos(2u)\right] u'' + \gamma \sin(2u) \left(1 - u'^2 - \theta'^2\right) = 0. \tag{4.18b}$$

In general, the polarization will be radial at least at one specific direction and it is convenient to count the azimuthal angle from this direction and set the total phase to be zero at this direction as well. Then, the solutions of (4.18a), (4.18b) for (k, m)-vortex should satisfy the boundary conditions

$$u(0) = 0, \qquad \theta(0) = 0, \tag{4.19a}$$

$$u(2\pi) = 2(k-1)\pi, \qquad \theta(2\pi) = 2m\pi. \tag{4.19b}$$

The solutions in question are trivial for some particular vortices.

(i) *Hedgehog vortices.* These are $(1, m)$-vortices having $\theta = m\phi$ and $u \equiv 0$, so that the polarization angle $\eta = \phi$. Polarization points into the radial direction everywhere and these vortices look like hedgehogs. The solution $(1, 0)$ is similar to the magnetic monopole [29].

(ii) *Double-quantized polarization vortex* $(2, 0)$. In this special case $\theta \equiv 0$, but $u = \phi$, resulting in $\eta = 2\phi$. Polarization rotates twice when one encircles the vortex core. These vortices and experimental possibilities of their excitation in exciton-polaritons fields have been studied by Liew et al. [30].

In other cases the solutions should be found numerically. Both (4.18a) and (4.18b) can be integrated once to give

$$\left[1 - \gamma \cos(2u)\right] \theta' = C_1, \tag{4.20a}$$

$$\left[1 + \gamma \cos(2u)\right] u'^2 + \left[1 - \gamma \cos(2u)\right] \theta'^2 - \gamma \cos(2u) = C_2, \tag{4.20b}$$

and the solutions can be written as integrals of elementary functions. The constants $C_{1,2}$ should then be found, e.g., by shooting, to satisfy the boundary conditions

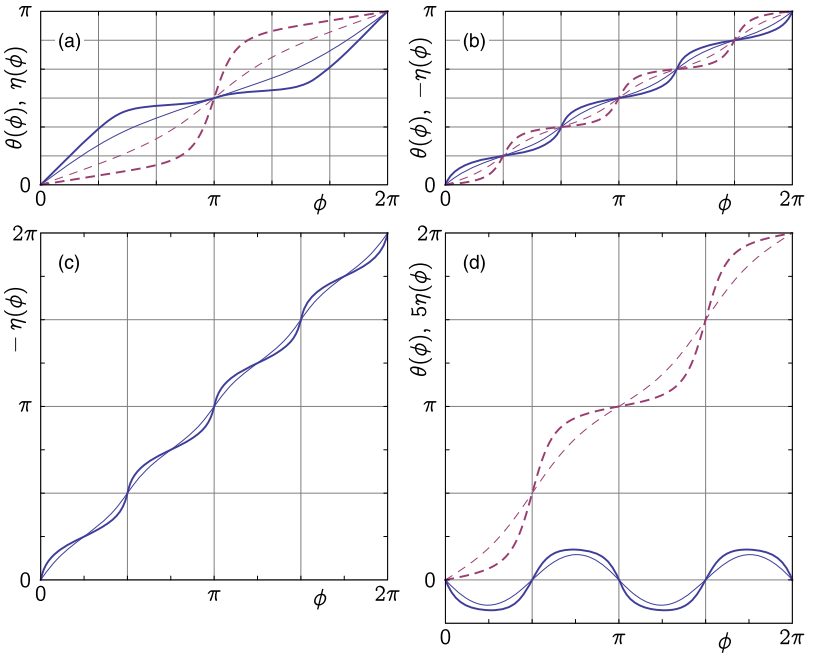

Fig. 4.1 The dependence of polarization angle η (*solid lines*) and phase angle θ (*dashed lines*) on the azimuthal angle ϕ for two values of TE-TM splitting parameter: $\gamma = -0.4$ (*thin lines*) and $\gamma = -0.9$ (*thick lines*). The panels show the behavior of the angles for the $(\frac{1}{2}, \frac{1}{2})$ half-vortex (**a**), the $(-\frac{1}{2}, \frac{1}{2})$ half-vortex (**b**), the $(-1, 0)$ polarization vortex (**c**), and the $(0, 1)$ phase vortex (**d**). In the last case the periodic function $\eta(\phi)$ has been upscaled for clarity

(4.19a), (4.19b). The functions $\theta(\phi)$ and $\eta(\phi)$ are shown in Fig. 4.1 for elementary half-vortices and for two integer vortices $(-1, 0)$ and $(0, 1)$, that also exhibit nonlinear dependencies of polarization and phase angles.

Figure 4.1 demonstrates the behavior of angles for negative values of the TE-TM splitting parameter γ. The functions $\theta(\phi)$ and $\eta(\phi)$ for positive γ can be found by the shift. Indeed, the change $u \to u + (\pi/2)$ in (4.18a), (4.18b) results in the change of the sign of γ. More precisely, to satisfy the boundary conditions (4.19a), (4.19b) the transformations can be written as

$$\gamma \to -\gamma, \tag{4.21a}$$

$$u(\phi) \to u\left(\phi + \frac{\pi}{2(k-1)}\right) + \frac{\pi}{2}, \tag{4.21b}$$

$$\theta(\phi) \to \left(\phi + \frac{\pi}{2(k-1)}\right) - \theta\left(\frac{\pi}{2(k-1)}\right), \tag{4.21c}$$

and they can be applied to all vortices except the hedgehogs with $k = 1$ (and where they are not necessary, of course, since $u(\phi) \equiv 0$).

The nonlinear change of angles seen in Fig. 4.1 becomes especially evident when γ approaches ± 1. This limit correspond to a strong inequality between effective masses, e.g., $m_l \gg m_t$ for $\gamma \to -1$. Qualitatively the strong nonlinearities can be understood if one introduces the effective masses for the phase m_θ and for the polarization m_η,

$$\frac{1}{m_\theta} = \frac{\cos^2 u}{m_t} + \frac{\sin^2 u}{m_l}, \qquad \frac{1}{m_\eta} = \frac{\sin^2 u}{m_t} + \frac{\cos^2 u}{m_l}, \tag{4.22}$$

and writes the energy (4.15) as

$$E_s = \frac{\hbar^2 n}{2} \int_0^{2\pi} \left\{ \frac{\eta'^2}{m_\eta} + \frac{\theta'^2}{m_\theta} \right\} d\phi. \tag{4.23}$$

The effective masses (4.22) depend on the orientation of polarization. Since $u(\phi)$ changes between the values specified by (4.19a), (4.19b), there are sectors where $m_\theta \approx m_l$ and $m_\eta \approx m_t$, and there are sectors where $m_\theta \approx m_t$ and $m_\eta \approx m_l$. To minimize the energy (4.23) in the case $m_l \gg m_t$, the phase angle changes rapidly and the polarization angle stays approximately constant in the former, while there is the opposite behavior in the latter.

4.3.2 The Energies and Interactions of Vortices

In the absence of TE-TM splitting the prefactors E_s of vortex energies are

$$E_{s0}^{(k,m)} = E_0\left(k^2 + m^2\right), \quad E_0 = \frac{\pi \hbar^2 n}{m^*}, \quad (\text{for } \gamma = 0). \tag{4.24}$$

It is seen that in this case the energy of an elementary half-vortex is exactly half of the energy of an elementary integer vortex. Important consequences can be drawn from this relation concerning the interactions between half-vortices. The four elementary half-vortices can be divided in two kinds, right half-vortices with $k + m = \pm 1$, and left ones with $k - m = \pm 1$. One can see from (4.12) that the right half-vortices possess the vorticity of the left-circular component of the order parameter, the amplitude of this component goes to zero and the phase of this component becomes singular in the vortex core center, and, as a result, the polarization becomes right-circular in the core center. For left half-vortices the picture is opposite. It follows from (4.24) that the left and the right half-vortices do not interact with each other. Consider, for example, the $(\frac{1}{2}, \frac{1}{2})$ and $(-\frac{1}{2}, \frac{1}{2})$ half-vortices. The elastic energy of this pair is $E_0 \ln(R/a)$ both when they are far away from each other and when they are in the same place forming the phase vortex $(0, 1)$. So, the coupling between the left and the right half-vortices is of the short range, related to the overlap of their cores and resulting change of the core energy term E_c in (4.11). As a result, the long-range coupling is present only between the half-vortices of

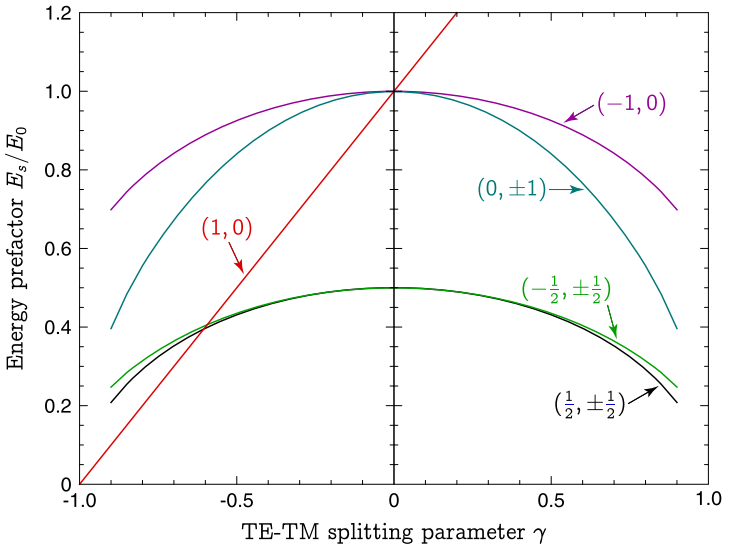

Fig. 4.2 The logarithmic prefactor of vortex energies E_s (see (4.11) and (4.15)) for half-vortices and integer vortices as functions of TE-TM splitting parameter γ (4.17). The *curves* are labeled by the winding numbers (k, m) of the vortices, and the energies are given in the units of $E_0 = \pi\hbar^2 n/m^*$

the same kind. It can be shown that identical half-vortices repel each other logarithmically, while the half-vortices and anti-half-vortices, (k, m) and $(-k, -m)$, attract each other logarithmically, as it is in the case of vortices and antivortices in one-component condensates [31]. This simple picture is changed in the presence of TE-TM splitting that leads to the long-range interaction between half-vortices of different kind.

The logarithmic prefactors $E_s^{(k,m)}$ for elementary half-vortices and elementary integer vortices are shown in Fig. 4.2. For all of them, expect the hedgehog (1,0)-vortex, these energies are even functions of γ, which can be proven using the transformations (4.21a)–(4.21c). These energies decrease with increasing γ^2. The case of hedgehog is special, as it has been discussed above. The hedgehog polarization is radial everywhere and $E_s^{(1,0)}$ is defined purely by the longitudinal effective mass,

$$E_s^{(1,0)} = \pi\hbar^2 n/m_l = E_0(1+\gamma). \tag{4.25}$$

It can be shown that when two vortices with winding numbers (k_1, m_1) and (k_2, m_2) are injected in the condensate and they are separated by distance r, such that $a \ll r \ll R$, the energy of the condensate is increased in logarithmic approximation (i.e., omitting the core energies) by

$$E_s^{(k_1+k_2,m_1+m_2)} \ln(R/a) + \left[E_s^{(k_1,m_1)} + E_s^{(k_2,m_2)} - E_s^{(k_1+k_2,m_1+m_2)}\right] \ln(r/a). \tag{4.26}$$

The second term in (4.26) gives the interaction energy of two vortices. The coupling between vortices arising due to TE-TM splitting can be analyzed analytically in the limit of small γ.

The solutions of (4.18a), (4.18b) for $k \neq 1$ are written as series in γ,

$$\theta(\phi) = m\phi + \frac{m}{2(k-1)}\gamma \sin\big[2(k-1)\phi\big] + \frac{m[(k-1)^2 - (1-m^2)]}{16(k-1)^3}\gamma^2 \sin\big[4(k-1)\phi\big] + \cdots, \tag{4.27a}$$

$$u(\phi) = (k-1)\phi - \frac{[(k-1)^2 + (m^2-1)]}{4(k-1)^2}\gamma \sin\big[2(k-1)\phi\big] + \frac{[5(k-1)^4 + 2(k-1)^2(m^2-3) + (m^2-1)^2]}{64(k-1)^4}\gamma^2 \sin\big[4(k-1)\phi\big] + \cdots. \tag{4.27b}$$

Substitution of these expression into (4.15) gives

$$\frac{E_s^{(k,m)}}{E_0} = \big(k^2 + m^2\big) - \frac{[k^2(k-2)^2 + 2[2 + 3k(k-2)]m^2 + m^4]}{8(k-1)^2}\gamma^2 - \cdots, \tag{4.28}$$

and, in particular,

$$E_s^{(-1,0)} = E_0\left[1 - \frac{9}{32}\gamma^2 - \cdots\right], \qquad E_s^{(0,\pm1)} = E_0\left[1 - \frac{5}{8}\gamma^2 - \cdots\right]. \tag{4.29}$$

There is no difference between the energies of half-vortices at this order of γ-series. The difference, however, appears in the next order. The series for the angles up to γ^4 are rather cumbersome to be presented, but they result in

$$E_s^{(\frac{1}{2},\pm\frac{1}{2})} = \frac{E_0}{2}\left[1 - \frac{\gamma^2}{2} - \frac{3\gamma^4}{16} - \cdots\right], \tag{4.30a}$$

$$E_s^{(-\frac{1}{2},\pm\frac{1}{2})} = \frac{E_0}{2}\left[1 - \frac{\gamma^2}{2} - \frac{11\gamma^4}{144} - \cdots\right]. \tag{4.30b}$$

Equations (4.25), (4.29), and (4.30a), (4.30b) can be used to find the interactions between half-vortices according to (4.26). Most important interaction that appears due to TE-TM splitting is between the $(\frac{1}{2}, \frac{1}{2})$ and $(\frac{1}{2}, -\frac{1}{2})$ half-vortices. For small γ their coupling constant is linear in γ and the interaction energy is [32]

$$V_{(\frac{1}{2},\frac{1}{2}),(\frac{1}{2},-\frac{1}{2})} \simeq -\gamma E_0 \ln(r/a). \tag{4.31}$$

It should be noted that the interrelation between m_t and m_l, i.e., the sign of γ, depends on the detuning of the frequency of the cavity photon mode from the center

of the stop-band of the distributed Bragg mirror [33]. So, one can have both attraction and repulsion of the $(\frac{1}{2}, \frac{1}{2})$ and $(\frac{1}{2}, -\frac{1}{2})$ half-vortices. The coupling of the other left and right half-vortices is quadratic in γ. The $(-\frac{1}{2}, \frac{1}{2})$ and $(-\frac{1}{2}, -\frac{1}{2})$ half-vortices repel each other with the interaction energy being $-(7/32)\gamma^2 E_0 \ln(r/a)$. The $(-\frac{1}{2}, \pm\frac{1}{2})$ and $(\frac{1}{2}, \pm\frac{1}{2})$ half-vortices attract each other with the interaction energy being $(1/8)\gamma^2 E_0 \ln(r/a)$.

In the absence of TE-TM splitting there is no coupling between the right half-vortices (with $km > 0$) and the left ones (with $km < 0$) and there are two decoupled BKT transitions, corresponding to the dissociation of pairs of left and right half-vortices [16, 23]. The transition temperature is then estimated from the energy of single half-vortex as $E_0/4$. The TE-TM splitting of polariton bands changes this picture substantially. First, because all four half-vortices become coupled and, secondly, because the energies of a vortex and its antivortex become different, so it is not clear with one should be used in the estimation of critical temperature.

One expects qualitative modifications of the BKT transition in the region of γ close to -1. In this region the attraction of the $(\frac{1}{2}, \frac{1}{2})$ and $(\frac{1}{2}, -\frac{1}{2})$ half-vortices becomes very strong and, as a result, the hedgehog is the vortex with the smallest energy in the system for $\gamma < \gamma_c \simeq -0.6$ (see Fig. 4.2). It does not mean, however, that the transition temperature can be estimated from the energy of the hedgehog in this region. In fact, the phase transition occurs due to dissociation of vortex-antivortex pairs, and the energy of the $(1, 0)$ and $(-1, 0)$ pair is still bigger than the energy of the pair of two half-vortices. One expects that when pairs of half-vortices are thermally excited in the system they will tend to form molecules consisting of the hedgehog (formed by merging of the $(\frac{1}{2}, \frac{1}{2})$ and $(\frac{1}{2}, -\frac{1}{2})$ half-vortices) with the $(-\frac{1}{2}, -\frac{1}{2})$ and $(-\frac{1}{2}, \frac{1}{2})$ half-vortices being attached to it. The proliferation of these $(-\frac{1}{2}, -\frac{1}{2}) - (1, 0) - (-\frac{1}{2}, \frac{1}{2})$ molecules defines the phase transition for $m_l \gg m_t$.

4.4 Geometry of the Half-Vortex Fields

In general, two coupled Gross-Pitaevskii equations for the circular components of the order parameter

$$\mathrm{i}\hbar\frac{\partial\psi_{+1}}{\partial t} = -\frac{\hbar^2}{2m^*}\left(\Delta\psi_{+1} + 4\gamma\frac{\partial^2\psi_{-1}}{\partial z^2}\right) - \mu\psi_{+1} + \left[U_0\left(|\psi_{+1}|^2 + |\psi_{-1}|^2\right) - 2U_1|\psi_{-1}|^2\right]\psi_{+1}, \tag{4.32a}$$

$$\mathrm{i}\hbar\frac{\partial\psi_{-1}}{\partial t} = -\frac{\hbar^2}{2m^*}\left(\Delta\psi_{-1} + 4\gamma\frac{\partial^2\psi_{+1}}{\partial z^{*2}}\right) - \mu\psi_{-1} + \left[U_0\left(|\psi_{-1}|^2 + |\psi_{+1}|^2\right) - 2U_1|\psi_{+1}|^2\right]\psi_{-1}, \tag{4.32b}$$

are not separated in cylindrical coordinates (r, ϕ). The variables are separated only in special cases of hedgehog vortices and the double-quantized polarization vortex discussed in previous section after (4.19a), (4.19b). For other vortices one needs to

solve GPEs numerically in two spacial dimensions with the boundary conditions at large distances defined by (4.12) and (4.18a), (4.18b).

Each vortex with nonzero phase winding number m is characterized by a finite superfluid current circulating around its core center. Performing numerical solutions it is important to take into account the fact that streamlines of the current are deformed with respect to perfect circles in the presence of TE-TM splitting. The circular components of the current $\vec{J}$ are given by

$$J_{+1} = \frac{\mathrm{i}\hbar}{\sqrt{2}m^*}\left\{\left(\psi_{+1}\frac{\partial\psi_{+1}^*}{\partial z} + \psi_{-1}\frac{\partial\psi_{-1}^*}{\partial z} - \psi_{+1}^*\frac{\partial\psi_{+1}}{\partial z} - \psi_{-1}^*\frac{\partial\psi_{-1}}{\partial z}\right)\right.$$
$$\left. + 2\gamma\left(\psi_{+1}\frac{\partial\psi_{-1}^*}{\partial z^*} - \psi_{-1}^*\frac{\partial\psi_{+1}}{\partial z^*}\right)\right\}, \tag{4.33}$$

and $J_{-1} = J_{+1}^*$. They are related to the radial J_r and the azimuthal J_ϕ components of the current by

$$J_r = \frac{1}{\sqrt{2}}\left(e^{\mathrm{i}\phi}J_{+1} + e^{-\mathrm{i}\phi}J_{-1}\right), \qquad J_\phi = \frac{\mathrm{i}}{\sqrt{2}}\left(e^{\mathrm{i}\phi}J_{+1} - e^{-\mathrm{i}\phi}J_{-1}\right). \tag{4.34}$$

At large distances $r \gg a = \hbar/\sqrt{2m^*\mu}$ one can use (4.12) to find

$$J_r = \frac{\hbar n}{m^* r}\gamma\sin(2u)\frac{d\theta}{d\phi}, \tag{4.35a}$$

$$J_\phi = \frac{\hbar n}{m^* r}\left[1 - \gamma\cos(2u)\right]\frac{d\theta}{d\phi}. \tag{4.35b}$$

Note that the condition of conservation of the total number of polaritons for the static vortex solution of (4.32a), (4.32b),

$$\mathrm{div}\vec{J} = \frac{1}{r}\left[\frac{\partial}{\partial r}(rJ_r) + \frac{\partial J_\phi}{\partial\phi}\right] = 0, \tag{4.36}$$

implies $\partial J_\phi/\partial\phi = 0$. So, (4.18a) obtained in the previous section is in fact the condition of conservation of the azimuthal current.

The warping of streamlines of current is shown in Fig. 4.3. The order parameter has been found numerically [34] for different values of TE-TM splitting parameter. To find the static solutions of GPE (4.32a), (4.32b), we have been choosing an initial order parameter $\vec{\psi}(\vec{r}, t = 0)$ satisfying the boundary conditions that follow from (4.18a), (4.18b) and that are shown in Fig. 4.1 for a given topological sector (k, m). Apart from this the initial functions were continuous but arbitrary. Then the functions were evolved according to (4.32a), (4.32b) in imaginary time. As a result, the order parameter relaxed to corresponding static half-vortex solution. The resulting half-vortex solutions are found to be independent of the initial shape of $\vec{\psi}(\vec{r}, t = 0)$.

In Fig. 4.3 one can see two distinct morphologies of basic half-vortices. The geometry of half-vortex solutions can be discussed in terms of singular optics [35, 36], where the polarization singularity related to a half-vortex is referred as C-point, to

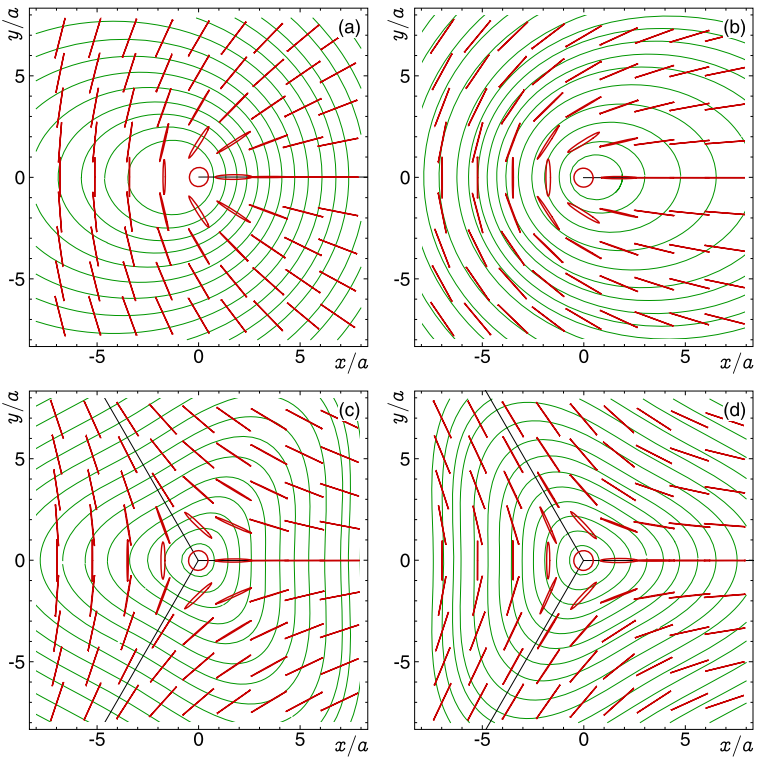

Fig. 4.3 Showing the geometry of half-vortices for different values of TE-TM splitting parameter γ (4.17). The plots are obtained from numerical solutions of GPEs (4.32a), (4.32b) [34]. The interaction constants are related as $U_1 = 0.55U_0$. The local polarization ellipses are drawn with the *thick* (*red*) *lines*. The streamlines of the current are shown by *thin* (*green*) *lines*. The *panels* demonstrate the following cases: (**a**) the half-vortices $(\frac{1}{2}, \pm\frac{1}{2})$ for $\gamma = -0.5$ (the lemon morphology); (**b**) the half-vortices $(\frac{1}{2}, \pm\frac{1}{2})$ for $\gamma = 0.5$ (the lemon morphology); (**c**) the half-vortices $(-\frac{1}{2}, \pm\frac{1}{2})$ for $\gamma = -0.5$ (the star morphology); (**d**) the half-vortices $(-\frac{1}{2}, \pm\frac{1}{2})$ for $\gamma = 0.5$ (the star morphology)

indicate that the polarization is circular at the vortex center and, therefore, the direction of the main axis of polarization ellipse is not defined. The morphologies of the field around C-points are classified by the index of associated real tensor field, and, additionally, by the number of strait polarization lines[4] that terminate at C-point [37]. The tensor index coincides with the polarization winding number k, and the number of lines could be either one or three. As a result, three different morphologies can be found. Following Berry and Hannay [38, 39], these morphologies are referred as *lemon*, *star*, and *monstar*.

[4]The tangents of polarization lines define by the direction of the main axis of polarization ellipse in each point.

The lemon configuration is characterized by $k = \frac{1}{2}$ and by only one straight polarization line terminating in the vortex center. This is the morphology of vortices in Figs. 4.3a, 4.3b with the straight polarization line being defined by $\phi = 0$. The star configuration is characterized by $k = -\frac{1}{2}$. In this case there are always three straight lines terminating in the vortex center. The stars are realized in Figs. 4.3c, 4.3d and three straight polarization lines are defined by $\phi = 0, \pm 2\pi/3$.

The change of parameter γ leads to deformation of polarization texture and to deformation of streamlines of the current, but it does not result in the change of morphologies of half-vortices. In principle, one could expect the transformation of lemon into monstar, since these morphologies possess the same topological index $k = \frac{1}{2}$. Contrary to the lemon case, however, the monstar is characterized by three straight polarization lines terminating in the vortex center, similar to the star configuration. So, from geometrical point of view the monstar has got intermediate structure between the lemon and the star, and this is why its name is constructed from "(le)mon-star".

To have the monstar configuration one needs a special behavior of polarization angle $\eta(\phi)$. Namely, it is necessary to have

$$\left.\frac{d\eta}{d\phi}\right|_{\phi=0} > 1 \quad \text{for } k = \frac{1}{2}. \tag{4.37}$$

In this case the polarization angle initially rotates faster than the azimuthal angle ϕ, but since the total rotation of η should be still π when ϕ is changing up to 2π, as it is dictated by the winding number $k = \frac{1}{2}$, there will be three roots of the equation $\eta(\phi) = \phi$. These roots, 0 and $\pm\phi_m$, define three straight polarization lines terminating in the vortex center for the monstar geometry.[5] One can see from Figs. 4.1a and 4.3a that when γ approaches -1 the derivative becomes very close to unity, but it never becomes bigger than 1, so that the monstar is not formed. The reason preventing the appearance of the monstar is that it is not energetically favorable to satisfy the condition (4.37). In fact, it is the most energetically favorable to have $\eta = \phi$, as for the hedgehog—the vortex having the smallest energy when $\gamma \to -1$ (see Fig. 4.2). The rotation of polarization of the half-vortex is also synchronous with the azimuth in rather wide sector, but the polarization never overruns the azimuth. The monstar half-vortices, however, are expected to be found in the exciton-polariton condensates out of equilibrium [9, 40, 41], where their appearance is not restricted by energetics.

4.5 Four-Component Exciton Condensates

Excitons formed by an electron and a heavy hole in the semiconductor quantum wells can be in four spin states [42]. The states with the total spin projection ± 1 are

[5] Note that for the monstar all polarization lines residing within the sector $-\phi_m < \phi < \phi_m$ terminate in the vortex center, but only three of them are straight, i.e., are having nonzero inclination at $r \to 0$ (see [37] for the details).

optically active. These bright excitons are formed by the heavy hole with the spin $+\frac{3}{2}$ and the electron with the spin $-\frac{1}{2}$, or by the $-\frac{3}{2}$ hole and the $+\frac{1}{2}$ electron. The other two states are hidden from the observer and are usually referred to as the dark excitons. The total momentum of these states is ± 2 and they are formed either by the $+\frac{3}{2}$ hole and the $+\frac{1}{2}$ electron, or by the $-\frac{3}{2}$ hole and the $-\frac{1}{2}$ electron.

The exciton-polaritons discussed in the previous sections are coupled states of quantum-well excitons and microcavity photons. Only the bright excitons are involved in this coupling, and the resulting condensates are two-component. Since the frequency of a single exciton-polariton is shifted down with respect to the single exciton frequency by a half of the Rabi frequency, the presence of dark excitons is irrelevant in this case provided the exciton-photon coupling is strong enough. Contrary, when pure exciton condensates are of interest, all four exciton spin states should be, in general, taken into account. The formation of exciton condensates is possible for cold indirect excitons in coupled quantum wells [43–47]. The life-time of these excitons is long enough, the excitons can travel coherently over long distances, and the condensates can be formed in quasi-equilibrium conditions. The presence of four-component exciton condensates has also been experimentally demonstrated recently [48].

The indirect excitons are dipoles oriented along the growth axis of the semiconductor structure, and their main interaction is spin-independent dipole-dipole repulsion. The condensate state, however, is defined by weak spin-dependent interactions arising from electron-electron, hole-hole, and exciton-exciton exchanges [49]. In what follows, I will assume the signs of these interactions to be such that they favor the distribution of excitons over all four spin states, populating both bright and dark components. This state is similar to the linearly polarized two-component condensates described above, but there is one important qualitative difference between them. The exchange scattering of two excitons can result in transformation of their spin states [50]. Namely, two bright excitons can turn into two dark ones after collision and vice versa. These processes are described microscopically by the Hamiltonian

$$\hat{\mathcal{H}}_{\rm mix} = W\big[\hat{\psi}^{\dagger}_{+2}\hat{\psi}^{\dagger}_{-2}\hat{\psi}_{+1}\hat{\psi}_{-1} + \hat{\psi}^{\dagger}_{+1}\hat{\psi}^{\dagger}_{-1}\hat{\psi}_{+2}\hat{\psi}_{-2}\big]. \tag{4.38}$$

In mean-field approximation, the creation $\hat{\psi}^{\dagger}_{\sigma}$ and annihilation $\hat{\psi}_{\sigma}$ exciton operators ($\sigma = \pm 1, \pm 2$) are replaced by the order parameter components, ψ^{*}_{σ} and ψ_{σ}, respectively. The contribution of the resulting exciton-mixing term $\mathcal{H}_{\rm mix}$ into the total energy of the exciton condensate depends on the relative phases of the components. The term of this type is absent in the two-component exciton-polariton case. Remarkably, the mixing of excitons always leads to the decrease of the condensate energy, which is achieved by fixing the proper interrelation between the phases, i.e., by the phase-locking. Denoting by θ_{σ} the phase of ψ_{σ}, one can see that the following relation holds within the order parameter manifold

$$\theta_{+2} + \theta_{-2} - \theta_{+1} - \theta_{-1} = \begin{cases} 0 \pmod{2\pi}, & \text{if } W < 0, \\ \pi \pmod{2\pi}, & \text{if } W > 0. \end{cases} \tag{4.39}$$

The mixing term (4.38) additionally favors the formation of the four-component exciton condensate with equal occupations of the components. This fact can be seen from different perspective. $\mathcal{H}_{\mathrm{mix}}$ describes the transformation of *pairs* of excitons, and, in the same way as in the BCS theory of the superconductivity, this term leads to the pairing of particles. This pairing leads to a decrease in the energy of the system and results in appearance of the gap in the excitation spectrum for one excitation branch. The other three excitation branches are Bogoliubov-like. This follows from the fact that the phase locking condition (4.39) leaves there angles to be undefined, so that there are three Goldstone modes apart from the gaped mode induced by the mixing.

The effect of applied Zeeman field on four-component exciton condensate is expected to be very spectacular [49]. The Zeeman splitting is different for dark and bright excitons: the g-factor is given by the sum of the electron and hole g-factors for the former, and by their difference for the latter. When such a field is applied to the exciton condensate its action is two-fold. On the one hand, it polarizes the bright and dark components with different degrees of circular polarization, and thus reduces the Zeeman energy of the condensate. On the other hand, the induced imbalance in the occupation of the components increases the energy of the mixing term (4.38) and suppresses the gap in the spectrum discussed above. The interplay between these two effects can lead to the first-order transitions from the four-component exciton condensate to the two- or the one-component condensates. Note also that due to the presence of $\mathcal{H}_{\mathrm{mix}}$ the system of equations defining the concentrations of the components of the exciton condensate in the Zeeman field is nonlinear, contrary to the case of two component exciton-polariton condensate (see (4.9)).

Finally, it is important to note that vortices in the four-component exciton condensate in the presence of the mixing of the component are composite: the vorticity of one component should be accompanied by the vorticity of another component to satisfy the phase-locking condition (4.39). As a result one expect twelve elementary vortices. These are four polarization vortices (two in each components), and the eight paired half-vortices in the bright and dark components.

4.6 Conclusions and Perspectives

The mean-field approximation provides simple and reliable method to study the polarization properties and topological excitations of exciton-polariton and exciton condensates that possess two and four components of the order parameter, respectively. This includes, in particular, the description of the polarization of the ground state and elementary excitations of the condensates and their change in applied Zeeman field, as well as the description of the texture of vortices and vortex interactions.

The elementary topological excitations in two-component exciton-polariton condensates are four half-vortices (k, m) with $k, m = \pm\frac{1}{2}$, characterized by half-quantum changes of polarization and phase angles. In the absence of transverse-electric-transverse-magnetic (TE-TM) splitting of the lower polariton band there is

no coupling between the left half-vortices (with $km < 0$) and the right ones (with $km > 0$), and one expects two decoupled Berezinskii-Kosterlitz-Thouless (BKT) superfluid transitions happening at the same temperature in the system. The TE-TM splitting results in two qualitative effects. First, the cylindrical symmetry of the half-vortex field is spontaneously broken that leads to warping of the polarization field around a half-vortex and to deviation of the streamlines of the supercurrent from the perfect circles. Secondly, there appears long-range interactions between left and right half-vortices. These interactions are particularly important in the case of large longitudinal polariton mass m_l when it favors the formation of hedgehog (monopole) vortices $(1, 0)$ from the $(\frac{1}{2}, \frac{1}{2})$ and $(\frac{1}{2}, -\frac{1}{2})$ half-vortices. The peculiarities of the superfluid transition in this case and related features of polarization textures of the exciton-polariton condensates are subjects of further studies. In what concerns the geometry of the half-vortex field it is shown that only two configurations, lemon and star, are realized. The monstar configuration is not energetically favorable for any value and sign of TE-TM splitting.

The essential feature of four-component exciton condensates is the presence of mixing and related phase locking between dark and bright excitons. One expects a nontrivial Zeeman-field effect resulting in a discontinuous change of the polarization state of the condensate as a result of the first-order transition. The presence of composite vortices in different components should lead to the formation of interesting polarization patterns in driven exciton condensates that provide an important topic for investigation, both experimental and theoretical.

Acknowledgements This work was supported in part by DGAPA-UNAM under the project No. IN112310 and by the EU FP7 IRSES project POLAPHEN.

References

1. J. Kasprzak, M. Richard, S. Kundermann, A. Baas, P. Jeambrun, J.M.J. Keeling, F.M. Marchetti, M.H. Szymańska, R. André, J.L. Staehli, V. Savona, P.B. Littlewood, B. Deveaud, L.S. Dang, Nature **443**, 409 (2006)
2. R. Balili, V. Hartwell, D. Snoke, L. Pfeiffer, K. West, Science **316**, 1007 (2007)
3. C.W. Lai, N.Y. Kim, S. Utsunomiya, G. Roumpos, H. Deng, M.D. Fraser, T. Byrnes, P. Recher, N. Kumada, T. Fujisawa, Y. Yamamoto, Nature **450**, 526 (2007)
4. J.J. Baumberg, A.V. Kavokin, S. Christopoulos, A.J.D. Grundy, R. Butté, G. Christmann, D.D. Solnyshkov, G. Malpuech, G.B.H. von Högersthal, E. Feltin, J.-F. Carlin, N. Grandjean, Phys. Rev. Lett. **101**, 136409 (2008)
5. E. Wertz, L. Ferrier, D.D. Solnyshkov, P. Senellart, D. Bajoni, A. Miard, A. Lemaître, G. Malpuech, J. Bloch, Appl. Phys. Lett. **95**, 051108 (2009)
6. M. Wouters, I. Carusotto, Phys. Rev. Lett. **99**, 140402 (2007)
7. M. Wouters, I. Carusotto, C. Ciuti, Phys. Rev. B **77**, 115340 (2007)
8. J. Keeling, N.G. Berloff, Phys. Rev. Lett. **100**, 250401 (2008)
9. M.O. Borgh, J. Keeling, N.G. Berloff, Phys. Rev. B **81**, 235302 (2010)
10. I.L. Aleiner, B.L. Altshuler, Y.G. Rubo, Phys. Rev. B **85**, 121301(R) (2012)
11. I.A. Shelykh, Y.G. Rubo, G. Malpuech, D.D. Solnyshkov, A. Kavokin, Phys. Rev. Lett. **97**, 066402 (2006)
12. T.-L. Ho, Phys. Rev. Lett. **81**, 742 (1998)

13. T. Ohmi, K. Machida, J. Phys. Soc. Jpn. **67**, 1822 (1998)
14. A. Pelissetto, E. Vicari, Phys. Rep. **368**, 549 (2002)
15. Y.G. Rubo, A.V. Kavokin, I.A. Shelykh, Phys. Lett. A **358**, 227 (2006)
16. J. Keeling, Phys. Rev. B **78**, 205316 (2008)
17. A.V. Larionov, V.D. Kulakovskii, S. Höfling, C. Schneider, L. Worschech, A. Forchel, Phys. Rev. Lett. **105**, 256401 (2010)
18. A.A. Abrikosov, Zh. Eksp. Teor. Fiz. **32**, 1442 (1957). Sov. Phys. JETP **5**, 1174 (1957)
19. V.L. Berezinskii, Sov. Phys. JETP **32**, 493 (1970)
20. V.L. Berezinskii, Sov. Phys. JETP **34**, 610 (1972)
21. J.M. Kosterlitz, D.J. Thouless, J. Phys. C **6**, 1181 (1973)
22. J.M. Kosterlitz, J. Phys. C **7**, 1046 (1974)
23. Y.G. Rubo, Phys. Rev. Lett. **99**, 106401 (2007)
24. G.E. Volovik, *The Universe in a Helium Droplet*. The International Series of Monographs on Physics, vol. 117 (Oxford University Press, London, 2003)
25. K.G. Lagoudakis, M. Wouters, M. Richard, A. Baas, I. Carusotto, R. André, L.S. Dang, B. Deveaud-Plédran, Nat. Phys. **4**, 706 (2008)
26. K.G. Lagoudakis, T. Ostatnický, A.V. Kavokin, Y.G. Rubo, R. André, B. Deveaud-Plédran, Science **326**, 974 (2009)
27. H. Flayac, I.A. Shelykh, D.D. Solnyshkov, G. Malpuech, Phys. Rev. B **81**, 045318 (2010)
28. M. Toledo Solano, Y.G. Rubo, Phys. Rev. B **82**, 127301 (2010)
29. R. Rajaraman, *Solitons and Instantons* (North-Holland, Amsterdam, 1989), Sect. 3.4
30. T.C.H. Liew, A.V. Kavokin, I.A. Shelykh, Phys. Rev. B **75**, 241301 (2007)
31. P.M. Chaikin, T.C. Lubensky, *Principles of Condensed Matter Physics* (Cambridge University Press, Cambridge, England, 1995), Sect. 9.3
32. M. Toledo Solano, Y.G. Rubo, J. Phys. Conf. Ser. **210**, 012024 (2010)
33. G. Panzarini, L.C. Andreani, A. Armitage, D. Baxter, M.S. Skolnick, V.N. Astratov, J.S. Roberts, A.V. Kavokin, M.R. Vladimirova, M.A. Kaliteevski, Phys. Rev. B **59**, 5082 (1999)
34. M. Toledo Solano, M.E. Mora-Ramos, Y.G. Rubo, unpublished
35. J.F. Nye, *Natural Focusing and Fine Structure of Light* (Institute of Physics Publishing, Bristol, 1999)
36. M.S. Soskin, M.V. Vasnetsov, Prog. Opt. **42**, 219 (2001)
37. M.R. Dennis, K. O'Holleran, M.J. Padgett, Prog. Opt. **53**, 293 (2009)
38. M.V. Berry, J.H. Hannay, J. Phys. A **10**, 1809 (1977)
39. J.F. Nye, Proc. R. Soc. Lond. Ser. A, Math. Phys. Sci. **389**, 279 (1983)
40. T.C.H. Liew, Y.G. Rubo, A.V. Kavokin, Phys. Rev. Lett. **101**, 187401 (2008)
41. J. Keeling, N.G. Berloff, arXiv:1102.5302
42. E.L. Ivchenko, *Optical Spectroscopy of Semiconductor Nanostructures* (Alpha Science International, Harrow, UK, 2005)
43. L.V. Butov, A.C. Gossard, D.S. Chemla, Nature (London) **418**, 751 (2002)
44. M. Hagn, A. Zrenner, G. Böhm, G. Weimann, Appl. Phys. Lett. **67**, 232 (1995)
45. L.V. Butov, A.I. Filin, Phys. Rev. B **58**, 1980 (1998)
46. Z. Vörös, R. Balili, D.W. Snoke, L. Pfeiffer, K. West, Phys. Rev. Lett. **94**, 226401 (2005)
47. L.V. Butov, J. Phys. Condens. Matter **19**, 295202 (2007)
48. J.R. Leonard, Y.Y. Kuznetsova, S. Yang, L.V. Butov, T. Ostatnicky, A. Kavokin, A.C. Gossard, Nano Lett. **9**, 4204 (2009)
49. Y.G. Rubo, A.V. Kavokin, Phys. Rev. B **84**, 045309 (2011)
50. C. Ciuti, V. Savona, C. Piermarocchi, A. Quattropani, P. Schwendimann, Phys. Rev. B **58**, 7926 (1998)

Chapter 5
Spin Effects in Polariton Condensates: From Half-Solitons to Analogues of Wormholes

Hugo Flayac, Dmitry D. Solnyshkov, and Guillaume Malpuech

Abstract Cavity exciton-polaritons are the quasiparticles formed of photons and excitons strongly coupled in microcavities. They have recently become a very convenient model system for the Bose-Einstein condensation in 2D and 1D systems as well as various related effects such as superfluidity, vortices or oblique solitons. Polaritons are bosons with only two possible spin projections on the growth axis of the sample which allows a two-component spinor condensate to form. In this chapter we will explain how one can capitalize on the unique properties of a flowing spinor exciton-polariton Bose-Einstein condensate. In the first part we will describe how the controlled generation of new types of half-integer excitations: oblique half-solitons can be achieved. In the second part, we will show that the convenience to create event horizons and thus black hole analogues in the spinor system will lead us to the modeling of wormholes.

5.1 Introduction

Bose-Einstein condensation [1, 2] has been a topic of intense research all along the 20th century, further motivated by its Nobel-prize-awarded observation in dilute atomic vapors [3]. This new state of matter, occurring at low temperature, possesses unique and fascinating properties due to the collective behavior of particles. The superfluidity, being undoubtedly the most famous among them, is the possibility for the Bose-Einstein condensate to propagate without friction (dissipation) below a certain critical velocity, given by the speed of sound. The latter is defined by the

H. Flayac · D.D. Solnyshkov · G. Malpuech
Clermont Université and Université Blaise Pascal, LASMEA, Nanostructure and Nanophotonics Group, CNRS, 63177, Aubière Cedex, France

H. Flayac
e-mail: Hugo.Flayac@EPFL.ch

D.D. Solnyshkov
e-mail: Dmitry.Solnyshkov@Univ-BPClermont.fr

G. Malpuech (✉)
e-mail: malpuech@univ-bpclermont.fr

A. Bramati, M. Modugno (eds.), *Physics of Quantum Fluids*,
Springer Series in Solid-State Sciences 177, DOI 10.1007/978-3-642-37569-9_5,

slope of the linear dispersion of the elementary excitations of the BEC at small momenta [4]. A BEC is a dilute macroscopic quantum object, carrying interacting entities in their ground state which share the same macroscopic wavefunction. Such object is called a quantum fluid [5].

Apart from the small amplitude excitations (bogolons), a significant perturbation of the BEC allows the appearance of nontrivial modifications of its wavefunction, such as topological defects [6]. Depending on the dimensionality of the system and on the nature of the interactions between particles, these defects can be of various types. In one-dimensional (1D) systems they manifest themselves as solitons that are density dips/humps for the case of repulsive/attractive interactions correspondingly, accompanied with a maximum phase shift of π. Such objects are stable thanks to the interplay between nonlinear interactions and the dispersion that compensate each other. However, since a soliton can be continuously unfolded into a homogeneous solution, it should be rather called a pseudo-topological defect. A vortex, the soliton's counterpart in two-dimensional (2D) systems, carries a quantum of angular momentum and the circulation of the velocity around its core (zero density region) is quantized in units of h/m where h is the Planck's constant and m the mass of the particles. On a loop around the vortex core, the phase is allowed to gain an integer multiple of 2π because of the degeneracy of the phase of the wave function. Vortices (at least in scalar condensates) cannot be continuously transformed into a vortex-less solution and are topologically stable. Soliton excitations such as rarefaction pulses [7], ring solitons [8], and oblique solitons [9] can also occur in 2D.

After the first observation of scalar condensates, even richer multicomponent (spinor) BECs [10] have been created by separating hyperfine states of the atoms. Polariton condensates, which will be in the focus of this chapter, are naturally spinor, and not scalar ones. They can accommodate various spin-dependent excitations. In the case of the two-component BEC that we will be dealing with, the elementary topological excitations are half-solitons (HSs) [11], half-vortices (HVs) [12], or skyrmions [13]. These half-quantum topological defects correspond to their integer counterparts occurring in only one of the two components of the BEC. The circulation of the velocity around a HV core is quantized in units of $h/2m$ and the global phase of the BEC is shifted only up to $\pi/2$ through a HS. These entities are especially interesting as their core is filled by the other component and thus they represent localized spin-polarized regions, a very promising property in the framework of spin-(op)tronics. We will see that such defects are stabilized in the polaritonic system by the interactions.

Besides being interesting on their own, BECs have shown to be a very convenient model tool for the study of a system that seems to have, at first sight, nothing in common: black holes and their event horizons. Indeed, the analogy between the equations describing the excitations of a BEC (as a quantum fluid) and the metrics of the curved space-time has been noticed a decade ago [14]. Since then, the scientists have managed to experimentally observe event horizons in atomic BECs [15]. Sound waves (phonons) propagation on top of a quantum fluid in a hydrodynamic (low momentum) approximation correspond to the propagation of an electromagnetic field in the curved space-time. Changing the speed of the flow and the speed of

sound one can construct the so-called sonic (dumb) hole. To do so, one needs to create a region in space from where the excitations of the BEC, propagating at the speed of sound, are not able to escape after they have crossed the event horizon. The horizon itself appears at the transition from superfluid to supersonic flow. One of the goals of this research was the better understanding of the Hawking Radiation [16] which is the mechanism for the black hole evaporation and explosion. Given the theoretical temperature of this radiation it looks hardly possible to extract it from the background emission. Thus, having a desktop version of a black hole could provide all the required data. In what follows, we will show the convenience that offers the decaying polaritonic quantum fluid for the generation of acoustic black holes.

Exciton-polaritons are the mixed states between cavity photons and quantum well excitons coupled by the strong light-matter interaction within microcavities [17]. They have recently become a model system for studying Bose-Einstein condensation in 2D [18] and 1D systems [19], and various associated effects such as superfluidity [20], vortex formation [21] and evolution [22] or nucleation of oblique solitons [23, 24]. They carry fascinating properties, mixing those of light (small effective mass) and matter (self-interactions and thermalization with phonons). Their spin structure is especially interesting: polaritons are bosons with only two allowed spin projections ± 1 on the growth axis of the sample. A key feature of polaritons in the view of this chapter is the strong spin-anisotropy of their interactions [25]. Indeed, the exciton-exciton interaction constant in the triplet configuration α_1 is repulsive and approximately twenty times larger than in the singlet configuration α_2 [26] (at least in multiple quantum well cavities), whereas the latter interaction is attractive. Consequently, the interaction energy of the polariton condensate is minimized when the latter is linearly polarized [27]. It gives a chemical potential at least twice smaller than in the case of circular polarization. The spin-anisotropy of interactions also makes the condensate stable against small in-plane effective magnetic fields which are acting on the polariton pseudo-spin [25]. As noted above, the two spin components of the polariton BEC make possible the existence of half-vortices [28], observed for the first time in 2009, [29] and half-solitons [30].

In this chapter we will first explain how to capitalize on the unique properties of a flowing spinor polariton BEC. In the first part we will describe how the controlled generation of new types of half-integer excitations, oblique half-solitons as well as half-vortex molecules, can be achieved. Their nucleation is provided by the presence of a defect in the flow of polaritons [23]. Because a momentum-dependent effective magnetic field (due to the spin-orbit coupling of exciton-polaritons) is present in the plane of the microcavity [31, 32], the symmetry of the flow is broken not only with respect to the density but also with respect to the polarization. The resulting excitations are strongly spin-polarized at their core and can be considered as real spin-optronic entities, while being fascinating fundamental objects by themselves.

In the second part, we will show the possibility to create the acoustic analogues of astrophysical black holes thanks to the finite lifetime of the particles. Indeed, the finite lifetime provides a natural and unavoidable transition from a superfluid injection region to a supersonic region with the decay of the density. This transition is an inevitable horizon. We will then discuss the stimulated Hawking emission seeded by disorder in a 1D microwire. The two-component spinor nature of

the BEC allows us to imagine even more [33]: The creation of artificial wormholes (coupled black and white holes), connecting the two spin components of the condensate that embody parallel universes. We consider the propagation of a signal (a 1D half-soliton) through these wormholes. We will discuss the inter-universe wormhole, where a half-soliton is captured by a black hole, being then expelled out of the wormhole by a white hole. We will also describe an intra-universe configuration and demonstrate that it allows a faster-than-sound travel of the half solitons, in analogy with the faster-than-light travel expected to occur through Einstein-Rosen bridges [34].

5.2 Oblique Half-Solitons and Their Generation in Exciton-Polariton Condensates

Let us begin this section with a necessary background on 1D solitons and vortices/oblique solitons in 2D BECs and review the state of art in polariton condensates. We will then turn to two-component BECs and define the concepts of half-soliton, half-vortices, and oblique half-solitons. Finally, we will show how such objects can be generated and observed in the spinor polariton BEC.

5.2.1 1D Solitons in Bose-Einstein Condensates

A BEC is a system of bosonic particles occupying at low temperature the same lowest energy (ground) state. These particles have the property to share the same single-particle wave function. One consequently talks about a macroscopic wavefunction or order parameter of the condensate which reads:

$$\psi(\mathbf{r},t) = \sqrt{n(\mathbf{r},t)}e^{i\theta(\mathbf{r},t)} \tag{5.1}$$

This wavefunction is in the general case complex-valued and thus possesses a phase θ which can possibly contain a propagation term $\mathbf{k}\cdot\mathbf{r}$, while its amplitude is governed by the density $n = |\Psi|^2$ of particles of mass m in the BEC. The evolution of the wave function in the mean-field approximation is well described by the Gross-Pitaevskii equation (GPE):

$$i\hbar\frac{\partial\Psi}{\partial t} = -\frac{\hbar^2}{2m}\Delta\Psi + \alpha_1|\Psi|^2\Psi \tag{5.2}$$

which adds a nonlinear interaction term to the Schrödinger equation with a particle-particle interaction constant α_1 (which can be found in the Born approximation). It what follows we will concentrate on the case $\alpha_1 > 0$ which corresponds to repulsive interaction between particles. The GPE assumes the normalization condition:

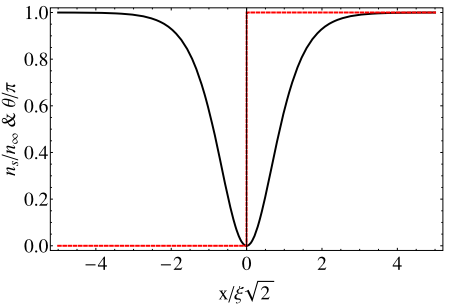

Fig. 5.1 1D dark soliton's normalized density profile $n_s(x) = |\Psi_s(x)|^2$ (*solid black line*) together with its step-like phase (*dashed red line*)

$\int |\Psi|^2 d\mathbf{r} = N$ where N is the total number of particles in the system. The most famous property of the BEC is the superfluidity allowed by the linear dispersion of its elementary excitations (bogolons) at small momenta. The slope of the linear part of the dispersion defines a speed of sound, $c = \sqrt{\mu/m}$, where $\mu = \alpha_1 n$ is the chemical potential. The small-amplitude excitations of the condensate propagate with this velocity. The Landau criterion [35] allows a propagating BEC to remain superfluid at subsonic velocities $0 < v < c$. In this range there is no final state for the Rayleigh scattering of the propagating BEC [see Fig. 5.2]. The BEC would therefore ignore any defect crossing its flow. For $v > c$, the BEC is said to be supersonic, and the Rayleigh scattering becomes possible again.

In the 1D system ($\mathbf{r} \to x$) the GPE allows special solutions to occur: the gray solitons, namely dips in the density that remain stable (do not spread with time) even if they propagate. This dip is associated with a shift of the phase through it. The soliton solution reads:

$$\Psi_S(x,t) = \sqrt{n_\infty}\left[\sqrt{1-\frac{{v_s}^2}{c^2}}\tanh\left(\frac{x-v_s t}{\xi\sqrt{2}}\sqrt{1-\frac{{v_s}^2}{c^2}}\right)+i\frac{v_s}{c}\right] \tag{5.3}$$

Here n_∞ is the density far away from the soliton's core, v_s is the speed of the soliton related to its depth via $v_s = c\sqrt{n(0)/n_\infty}$ and $\xi = \hbar/\sqrt{2m\mu}$ is the healing length of the BEC which defines the size of the soliton's core. The phase shift through the soliton is $\Delta\theta = \arccos(v_s/c)$ varying between 0 and π. For $v_s = 0$, the wavefunction is real valued, the density at the soliton's core is exactly zero and the phase is a Heaviside function of amplitude π, undefined at $x = 0$. This solution is called "dark soliton". Gray solitons remain stable in the system because interactions are present and compensate the dispersion that would show a wave packet evolving in the linear Schrödinger equation. However, from the mathematical point of view, nothing prevents this kind of solution from being continuously transformed to a homogeneous solution, and thus, strictly speaking, a gray soliton is only a pseudo-topological defect. One should by the way note that the Lorentz factor $1/\gamma = \sqrt{1-{v_s}^2/c^2}$ appears in (5.3) because the energy of BEC solitons is described by a relativistic expression (at least at low wavevectors). Figure 5.1 shows the dark soliton's normalized density profile together with its phase.

5.2.2 Vortices and Oblique Solitons in 2D Bose-Einstein Condensates

In two-dimensional superfluids, the elementary topological excitations are the quantized vortices [1] well-known in superconductors [36]. These objects are nontrivial modifications of the wavefunction of the condensate that reveal a breakdown of the superfluidity. Like dark solitons, vortices are characterized by a vanishing density as well as a singular phase at their core. But thanks to the dimensionality of the system they also possess an angular momentum, particles rotate faster and faster while approaching the density minimum like in classical whirlpool. The difference with classical fluids arises from the phase of the condensate. Indeed, the phase is defined up to a 2π factor for any wavefunction, therefore the circulation of the velocity of the superfluid on a closed loop encircling the vortex is quantized: $\oint \mathbf{v} \cdot \mathbf{dl} = lh/m$ where the quantum l is the so-called winding number. Given that $\mathbf{v} = \hbar/m\nabla\theta$, one also sees that $\theta = l\phi$ where ϕ is the polar angle. Vortices and vortex lattices were nucleated in experiments putting an atomic BEC into rotation [37] above a critical velocity with a stirring laser, following the prediction of Williams and Holland [38]. In polariton condensates spontaneously generated vortices have been first observed at deterministic positions pinned to disorder [21, 22]. Next, an artificial phase-imprinting method was proposed, based on a Gauss-Laguerre probe in the optical parametric oscillator regime [39, 40]. More recently, vortices have been detected in turbulences in a polariton fluid propagating past an obstacle [24, 41, 42]. We will focus on this kind of configuration for the discussion on oblique half-solitons. Such a large number of experimental observations reflects the convenience offered by the polaritonic system for the investigation of hydrodynamic-related effects. One of the advantages is that the vortices are much larger in spatial size than in atomic condensates: $\xi \sim 1$ μm for polaritons. The other advantage is that using the techniques of classical optics it is possible to reconstruct the entire wavefunction of the condensate, namely its density—from the intensity of light escaping from the microcavity, and its phase up to a 2π factor—from interferograms. Furthermore, the control of the condensate parameters such as its density or its wave vector can be performed by simply changing the pump intensity and the angle of the excitation laser, for example.

As mentioned in the introduction, in addition to vortices, various types of solitonic wavefunctions are realizable in two-dimensional BECs. Especially, in 2006, G.A. El et al. proposed to analyze theoretically the impact of a defect (potential barrier) crossing the flow of a supersonic BEC [9]. This experiment, quantum analogue of the one involving e.g. a jet aircraft flying at supersonic velocity in a classical fluid (air), revealed considerable differences between the two systems. Under the assumption that the defect is large enough with respect to the healing length ξ of the condensate to perturb the fluid on length scales comparable to ξ, (pseudo-) topological defects can be nucleated in a quantum fluid. The prediction of Ref. [9] was that a pair of oblique solitons would be generated in the wake of the obstacle and that they would extend without deformation. One can expect that this kind of solitonic solution in 2D should become unstable against perturbations. While the

stability analysis performed later showed that the soliton is indeed unstable [43], the instability is only convective, which means that the latter is damped while being dragged away downstream from the defect. The oblique solitons are nucleated from the shock waves because of the dispersion of the excitations (which is not linear), and because of the interactions between the particles, which favor the formation of solitons as stable structures. Another way to describe the generation of solitons is the following: The fluid tends to accelerate locally close to the defect, and since the velocity field and the phase of the fluid are related via $\mathbf{v} = \hbar/m\nabla\theta$, an important local phase shift is acquired, giving birth to negative interference producing density dips which are nothing but solitons. Increasing the size of the defect leads to larger phase shifts and then more than one pair of solitons can appear to accommodate these phase shifts, leading to multiplets of oblique solitons.

The properties of an oblique soliton can be derived analytically within the quantum hydrodynamic picture. Let $\mathbf{v} = (v_x(x, y), v_y(x, y))$ be the velocity field of the flow in Cartesian coordinates, the oblique soliton is then completely defined by the following set of equations:

$$v_x = \frac{M(1 + a^2 n)}{(1 + a^2)n} \tag{5.4}$$

$$v_y = -\frac{aM(1 - n)}{(1 + a^2)n} \tag{5.5}$$

$$n(\alpha) = 1 - (1 - p)\,\mathrm{sech}\left[\frac{\sqrt{1 - p}}{\sqrt{1 + a^2}}\alpha\right]^2 \tag{5.6}$$

where $\alpha = x - ay$ is a tilted coordinate perpendicular to the oblique soliton (with a the slope of the soliton with respect to the y-axis), $M = v/c$ is the so-called Mach number and $p = M^2/(1 + a^2)$. In 1D systems we have seen that the speed of a soliton is related to its depth and it is still true in 2D. Indeed, at fixed value of M, increasing a increases the depth of the soliton and thus reduces its speed. In other words, the more the soliton is tilted with respect to the x-axis, the faster it moves with respect to the condensate, and the shallower and larger it becomes.

5.2.3 *Topological Excitations in a Polariton Quantum Fluid*

The very first experimental evidence of oblique soliton was obtained in an exciton-polariton condensate in 2011 [24] thanks to the high degree of control offered by the system. The experiment involved a propagating polariton fluid scattered by an immobile structural defect in the microcavity, following the proposal of Ref. [23] analyzed in Ref. [44]. An exciton-polariton condensate has finite lifetime, photons are continually injected through the microcavity Bragg reflectors by the pump laser to compensate the decay. The energy of the pump laser can be tuned in resonance with the polariton branch. One can easily change the momentum of injected particles by varying the laser angle with respect to the growth axis of the sample. So,

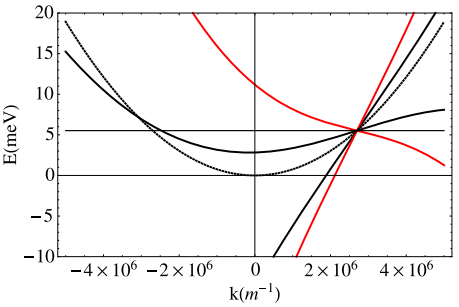

Fig. 5.2 Dispersions of elementary excitations at finite excitation momentum. The *solid red* (*black*) *line* shows a superfluid (supersonic) spectrum, the *dotted black line* is the bare dispersion of polaritons in a linear regime and the *solid* (*thin*) *horizontal black line* guides the eye to available backscattering points. As one can see, no Rayleigh scattering is possible in the superfluid regime

in principle, any point of the particle dispersion can be excited. One crucial point is that the configuration described is in fact a strongly nonlinear driven-dissipative system, for which the dispersion of elementary excitations can strongly differ from the equilibrium case [45]. Indeed, diffusive regions with flat dispersion can appear and the Bogoliubov spectrum is recovered only when the detuning δ between the laser energy and the dispersion is exactly compensated by the interaction-induced blueshift μ of the pumped state. Such a situation is depicted in Fig. 5.2. To accurately describe the driven/dissipative polariton BEC, one needs to separate the photonic mean field $\phi(\mathbf{r}, t)$ from the excitonic one $\chi(\mathbf{r}, t)$ with a set of modified Schrödinger and GP equations respectively coupled via the light matter interaction given by the Rabi splitting Ω_R:

$$i\hbar\frac{\partial\phi}{\partial t} = -\frac{\hbar^2}{2m_\phi}\Delta\phi + \Omega_R\chi + D\phi + Pe^{i(\mathbf{k}_P\cdot\mathbf{r}-\omega_P t)} - \frac{i\hbar}{2\tau_\phi}\phi \tag{5.7}$$

$$i\hbar\frac{\partial\chi}{\partial t} = -\frac{\hbar^2}{2m_\chi}\Delta\chi + \Omega_R\phi + \alpha|\chi|^2\chi - \frac{i\hbar}{2\tau_\chi}\chi \tag{5.8}$$

$m_{\phi,\chi}$ and $\tau_{\phi,\chi}$ are respectively the masses and the lifetimes of the particles, P is the amplitude of the pump laser of frequency ω_P and wavevector $\mathbf{k}_P$. $D(\mathbf{r})$ accounts for the defect that acts on the photonic part of the wavefunction. The interactions in the BEC arise from the excitonic part of the wavefunction.

As we have already seen, topological excitations are created by significant local phase shifts. The problem with the configuration we consider is that a resonant continuous wave (cw) pumping scheme imposes a specific phase at any time under the pump spot. Therefore, it is impossible to generate topological defects using a large homogeneous pumping spot extending over the whole sample. Pigeon et al. [23] proposed to use a localized pump spot with finite momentum upstream from the defect, so that the polariton fluid would be already propagating freely around the

defect and its phase would evolve without being imposed by the pump. However, because of the finite lifetime of the particles involved, the density is decaying with the propagation distance.

The authors of Ref. [23] managed to obtain numerically three regimes with different condensate densities (controlled by the laser detuning). At low density (obtained at large laser detuning) the system is in the supersonic regime and dark solitons are generated downstream from the defect. In this case, solitons appear as stable stationary solutions, however, their shape depends on the distance from the defect. Actually, due to the density decay, the healing length increases with the distance from the defect $\xi = \xi(x - x_D)$ and the oblique soliton adapts itself to the local density, becoming larger, shallower, and curved. One extra feature of the polaritonic oblique solitons is that they are able to survive even at subsonic velocities, namely in regimes where no Ćerenkov radiation (ship waves) is visible upstream from the defect. The oblique soliton is further stabilized by the lifetime induced density decay [46].

When one reduces the detuning or increases the density, the oblique solitons tend to disappear with the development of snake instabilities. They are replaced by a train of vortex dipoles (vortex streets) as predicted in Ref. [43]. This happens at a lower critical velocity than in the undamped BEC [47]. One should note here that vortices survive in subsonic regimes thanks to the local acceleration of the fluid close to the defect [48] which does not violate Landau's criterion. Increasing the density further should allow to enter the superfluid regime where no perturbations are induced by the presence of the defect. Nevertheless in that case the position of the pump spot becomes determinant. Indeed, if the latter is too much overlapping with the defect then the pump phase will be imprinted, hiding potential perturbations, if it is too far, then the density will have decayed too much arriving at the defect's position. The approximate condition for superfluidity is: $E_{int} \geq 2E_{kin}$ where $E_{int} = \mu = \alpha n$ is the interaction energy and $E_{kin} = m^* v^2/2$ is the kinetic energy, with m^* an effective mass. In brief: the polaritonic system allows the investigation of various hydrodynamic regimes ranging from oblique soliton generation to a superfluid flow, passing by emission of vortices, all observed experimentally [20, 24]. Figure 5.3 shows an example of pair of oblique solitons generated in a subsonic (no visible ship waves) regime accounting for the lifetime of the polaritons.

5.2.4 Half-Integer Topological Excitations in Spinor Bose-Einstein Condensates

Multicomponent (spinor) condensates allow even more complex topological excitations [10]. Solitons in spinor 1D condensates [49, 50] (vector solitons) and oblique solitons in spinor 2D systems have been considered theoretically [51]. In one dimension, many possible configurations were described, depending on the strength and type of the particle interactions (repulsive or attractive). In particular, a solution

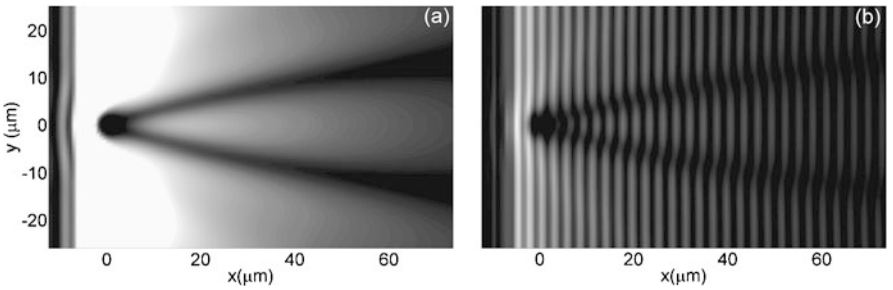

Fig. 5.3 Numerical solution showing stationary 2D oblique solitons appearing in the wake of the obstacle. (**a**) Photonic density $n_\phi(x, y)$ and (**b**) interference pattern revealing the characteristic phase shifts through the solitons

where the kink lies in only one component was reported: The dark-antidark soliton or half-soliton (HS) [11]. The counterpart of such a defect in 2D is the so-called half-vortex (HV), first reported in Ref. [12].

Exciton-polaritons have two allowed spin projections $\sigma_\pm = \pm 1$ on the growth axis of the sample [25] (other excitons are dark and do not couple with photons to form polaritons), and therefore the polariton condensates are composed of only two spin components, instead of three components expected for an atomic spin-1 condensate. The polariton BEC is strongly spin-anisotropic: the inter-component interactions are weak and therefore the BEC forms spontaneously with a linear polarization, namely with equal density of σ_+ (right circularly polarized) and σ_- (left circularly polarized) condensed particles. A case apart is that of bulk GaN, where the spin interactions may be isotropic, as shown by the random (including circular) spontaneous polarization of the condensate [52].

The elementary topological excitations of 2D polariton condensates were shown to be HVs [28], that carry twice less energy than an integer vortex, and, consequently, their interaction is twice weaker. HVs have already been observed in experiments [29], spontaneously appearing in the currents imposed by the disordered landscape in the microcavity. Their appearance requires the splitting between the linear polarizations [25] to be weak as it tends to merge HVs into an integer vortex [53, 54]. The HVs are of crucial importance for both fundamental and applied aspects. First, the superfluid transition in 2D has an universality class of Berezinskii-Kosterlitz-Thouless transition [1] and is accompanied with the binding of vortex-antivortex pairs in the vicinity of a critical temperature [55]. Therefore, this temperature would be twice smaller if half-vortex pairs are involved instead. Second, the HVs are local, strongly circularly polarized objects and are very promising information carriers in the context of spin-optronics. We will see now how the HVs and oblique half-solitons (OHSs) can be generated in a flowing spinor polariton fluid.

A two-component polariton condensate at 0K can be described by a vectorial macroscopic wave function $\mathbf{\Psi} = (\Psi_+, \Psi_-)^T$, whose evolution follows a set of (coupled) GPEs. Assuming first a parabolic dispersion with an effective mass m^* and an

infinite lifetime of the particles, one has

$$i\hbar\frac{\partial\Psi_+}{\partial t} = -\frac{\hbar^2}{2m^*}\Delta\Psi_+ + \left(\alpha_1|\Psi_+|^2 + \alpha_2|\Psi_-|^2\right)\Psi_+ \tag{5.9}$$

$$i\hbar\frac{\partial\Psi_-}{\partial t} = -\frac{\hbar^2}{2m^*}\Delta\Psi_- + \left(\alpha_1|\Psi_-|^2 + \alpha_2|\Psi_+|^2\right)\Psi_- \tag{5.10}$$

Time-independent solutions are found upon expressing the BEC's wave functions as $\Psi_\pm(\mathbf{r},t) = \psi_\pm(\mathbf{r})\exp(-i\mu t)$, where $\mu = (\alpha_1+\alpha_2)n_0/2$ is the chemical potential related to the density of the homogeneous condensate $n_{0+} = n_{0-} = n_0/2$, consistent with the linearly polarized ground state for a spin anisotropy $\alpha_2 \sim -0.1\alpha_1$. For a single-kink solution such as a vortex or a soliton, the asymptotic behavior can be found analytically. For this, let us assume that far away from the defect the condensate density is unperturbed by the presence of this defect and is therefore constant in each component.

The order parameter can be written in two distinct representations [28, 53]. On the basis of circular polarizations discussed previously, each component possesses its own phase $\theta_\pm(\mathbf{r})$ and $(\psi_+,\psi_-)^T = \sqrt{n_0}/2(\mathrm{e}^{i\theta_+},\mathrm{e}^{i\theta_-})^T$. In the linear polarization basis, the polarization angle $\eta(\mathbf{r})$ and the global phase of the condensate $\theta(\mathbf{r})$ can be separated: $(\psi_x,\psi_y) = \sqrt{n_0}(\mathrm{e}^{i\theta}\cos(\eta),\mathrm{e}^{i\theta}\sin(\eta))^T$. The transformation from one to another is obtained via $\psi_\pm = (\psi_x \mp i\psi_x)/\sqrt{2}$ and $\theta_\pm = \theta \mp \eta$. In the linear basis, HVs are characterized by two half-integer winding numbers (k,m) for both the phase and the polarization angles, which leads to integer shifts of π around their core as described in Ref. [28].

Similar considerations can be applied to solitons. Indeed, in one dimension the normalized scalar dark soliton solution [see (5.3)] is simply given by $\psi_S(x) = \sqrt{n_0}\tanh(x)$ and its phase is a Heaviside function of amplitude π. In the circular polarization (σ_+,σ_-) basis and, in the simplest case where $\alpha_2 = 0$, a half-soliton (HS) is nothing but a usual soliton appearing in one component (let's say ψ_-) while the other remains homogeneous. Thus, the associated order parameter reads $(\psi_+^{HS},\psi_-^{HS}) = \sqrt{n_0/2}(1,\tanh(x))$. Rewriting the latter on the linear polarization basis leads to $(\psi_x^{HS},\psi_y^{HS}) = \sqrt{n_0}/2(1+\tanh(x), i - i\tanh(x))^T$. Looking for the asymptotic values at infinity, one can construct the following identities:

$$\psi_x^{HS}(+\infty) = \sqrt{n_0}e^{2ih\pi}\cos(2s\pi) \tag{5.11}$$

$$\psi_y^{HS}(+\infty) = \sqrt{n_0}e^{2ih\pi}\sin(2s\pi) \tag{5.12}$$

$$\psi_x^{HS}(-\infty) = \sqrt{n_0}e^{ih\pi}\cos(s\pi) \tag{5.13}$$

$$\psi_y^{HS}(-\infty) = \sqrt{n_0}e^{ih\pi}\sin(s\pi) \tag{5.14}$$

with h and s—half-integer numbers, which can be seen as topological charges. Basic HSs appear for $(h,s) = \{(\pm1/2,\pm1/2),(\pm1/2,\mp1/2)\}$ and their phase and polarization angle change from 0 to $\pi/2$ going from $-$ to $+\infty$, while the center is fully circularly polarized, just like the half-vortex core. This topological defect can also

be seen as a domain wall with respect to x- and y-polarized particles [30]. A plot of the normalized HS density profiles is proposed in Fig. 5.4(a).

Let us now focus on the possibility of creating 2D oblique half-solitons. First of all, it is clear that in the case where the two components of the spinor BEC do not interact ($\alpha_2 = 0$), if they are initially equally populated, a significant perturbation in only *one* of the components will lead to the formation of half-integer topological excitations. Next, what happens if the interaction between the two components is no longer negligible? To answer this question following Ref. [51], we turn back to (5.1) and (5.2), rescale them, look for stationary solutions and switch to the hydrodynamic picture, where the phase of each components is expressed by means of their stationary and irrotational velocity fields via $\mathbf{v}_\pm(\mathbf{r}) = \hbar/m^*\boldsymbol{\nabla}\theta_\pm(\mathbf{r})$, with $\mathbf{r} = (x, y)$. We look for oblique solutions that depend only on the tilted coordinate $\chi = (x - ay)/\sqrt{1+a^2}$, which leads to the following set of equations

$$\left(n_+'^2/4 - n_+ n_+''/2\right) + 2n_+^2(\Lambda_1 n_+ + 2\Lambda_2 n_-) = (q + 2\mu)n_+^2 - qn_0^2 \tag{5.15}$$

$$\left(n_-'^2/4 - n_- n_-''/2\right) + 2n_-^2(\Lambda_1 n_- + 2\Lambda_2 n_+) = (q + 2\mu)n_-^2 - qn_0^2 \tag{5.16}$$

where $\Lambda_{1,2} = \alpha_{1,2}/(\alpha_1 + \alpha_2)$ and $q = U^2/(1 + a^2)$ (U is the velocity of the flow). This system has to be solved numerically, but we can first consider some simple arguments. The density profile of an integer oblique soliton in a spinor fluid is given by $n_{ODS} = 1 - (1 - q/\mu)\,\mathrm{sech}\,[\chi\sqrt{\mu - q}]^2$ with $\mu = (\Lambda_1 + \Lambda_2)n_0/2 = \Lambda n_0/2$. Now, for the case of the OHS, the density notch in the σ_- component, that contains the defect, is seen as an external potential by the initially unperturbed σ_+ component, because of the interactions between the particles of different spins. We suppose that the σ_+ component fits the shape of this potential which is nothing but $\Lambda_2 n_-$. Then, this perturbation creates in turn a potential for the σ_- component given by $-\Lambda_2 n_+ = -\Lambda_2^2 n_-$. Therefore, the density profile is modified as $\widetilde{n}_- \leftarrow (\Lambda n_- - \Lambda_2^2 n_-)/\Lambda$. Iterating this procedure leads to a geometric series and to a renormalization of the interaction constant seen by the component containing the soliton $\widetilde{\Lambda} \leftarrow \Lambda - \Lambda_2^2/(\Lambda - \Lambda_2)$. Consequently, the OHS solution is approximated by

$$n_{OHS} = 1 - (1 - q/\widetilde{\mu})\,\mathrm{sech}\,[\chi\sqrt{\widetilde{\mu} - q}]^2 \tag{5.17}$$

with $\widetilde{\mu} = \widetilde{\Lambda} n_0$. In this description, the sound velocity is changed like $c_s \to \widetilde{c}_s = \sqrt{\widetilde{\mu}/m^*}$ and the healing length like $\xi \to \widetilde{\xi} = \hbar/\sqrt{2m^*\widetilde{\mu}}$. In the case where $\Lambda_2 < 0$ (>0), which corresponds to an attractive (repulsive) interaction, c_s is slightly increased (decreased) and inversely for ξ. The component without a soliton obviously presents a minimum (maximum) [30]. This argumentation is compared to direct numerical solutions of (5.4) and (5.5) in Fig. 5.4(b) showing a remarkable accuracy for small values of Λ_2.

Now let us see how HVs and OHSs can be generated in a propagating exciton-polariton fluid. The setup is basically the same as the one required to generate integer topological defects described previously [23, 24, 44], namely a continuous and resonant pumping scheme locally upstream from a defect. However, we will now focus on the spin degree of freedom of the condensate namely the polarization of the

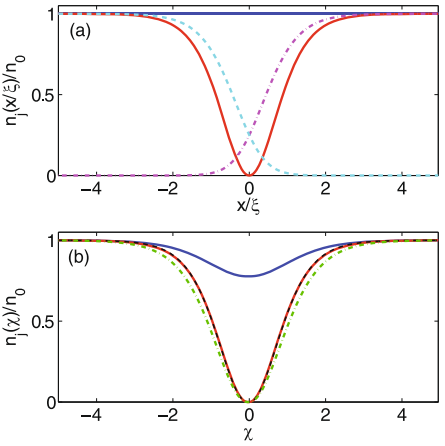

Fig. 5.4 (**a**) HS density profiles scaled to n_0 and ξ. The *solid blue* and *red curves* represent the n_+ and n_- density profiles while the *dashed-dotted purple* and *dashed cyan curves* show n_x and n_y respectively. (**b**) OHS density slice normal to its axis. The *solid blue* and *red curves* show numerical profiles, the *dashed black curve* is the perturbative solution described in the text and the *dashed dotted green curve* show the scalar soliton solution

pump and the polarization of the emission along the propagation. To describe more accurately the spinor polariton BEC, we take into account the real non parabolic dispersion of the particles, their decay and injection via a set of four coupled spin-dependent equations, similarly to spinless (5.7).

$$i\hbar\frac{\partial\phi_\pm}{\partial t} = -\frac{\hbar^2}{2m_\phi}\Delta\phi_\pm + \Omega_R\chi_\pm + D_\pm\phi_\pm + \beta\left(\frac{\partial}{\partial x} \mp i\frac{\partial}{\partial y}\right)^2\phi_\mp + P_\pm e^{i(\mathbf{k}_P\cdot\mathbf{r}-\omega_P t)} - \frac{i\hbar}{2\tau_\phi}\phi_\pm \tag{5.18}$$

$$i\hbar\frac{\partial\chi_\pm}{\partial t} = -\frac{\hbar^2}{2m_\chi}\Delta\chi_\pm + \Omega_R\phi_\pm + \left(\alpha_1|\chi_\pm|^2 + \alpha_2|\chi_\mp|^2\right)\chi_\pm - \frac{i\hbar}{2\tau_\chi} \tag{5.19}$$

The novelties that appear with respect to (5.7) are: The pump terms of amplitudes $P_\pm$ which allow to choose the polarization of injected photons and thus of polaritons, the impenetrable potential barrier $D_\pm$ that can affect independently each component, and a $\mathbf{k}$-dependent coupling between the σ_+ and σ_- components of strength $\beta = \hbar^2/2(m_l^{-1} - m_t^{-1})$ which models the polarization splitting between the TE and TM-polarized optical eigen modes of the microcavity [25], associated with effective masses m_t and m_l. The effective mass m_ϕ is therefore approximated by $m_\phi = m_t m_l/(m_t + m_l)$. To generate half-integer topological defects past the obstacle we need to be able to break the symmetry of the flow not only with respect to the density (integer topological defects) but also with respect to the polarization of the flow. In what follows, we present 2 different schemes for the generation of OHSs.

The first alternative is to find a way to perturb only one of the two components. This could be done experimentally if the defect is created optically by a circularly polarized pulse [42, 56]. This scheme is however far from being ideal since it would bring of lot of unwanted perturbations to the system and it should rather be seen as a model experiment. In this framework, one needs to impose $D_- = 0$ and to inject

linearly polarized photons upstream from the defect which requires $P_+ = P_-$ and creates equal population of polaritons with spin $+1$ and -1. In that case OHS pairs (or HV at higher densities) obviously appear in the component containing the defect and a weak density minimum is imposed in the other component due to the fact that $a_2 < 0$ [see Ref. [30] for a figure]. The unavoidable action of the TE-TM splitting (see below) can unfortunately make the situation more complex in experiments.

The second alternative, that we will discuss in more details is, on the other hand, completely realistic. The impenetrable defect is restored in both components and we will this time *benefit* from the polarization separation brought by the TE-TM splitting. The TE and TM eigen modes in planar microcavities, which correspond to particles linearly polarized perpendicular or parallel to the propagation direction, are non-degenerate for any finite wavevector. As a result, any polarization state that would differ from them would oscillate between the two. This oscillation can be associated with the action of an effective magnetic field

$$\mathbf{\Omega}_{LT}(\mathbf{k}) = \omega_x(\mathbf{k})\cos(2\phi)\mathbf{u}_{k_x} + \omega_y(\mathbf{k})\sin(2\phi)\mathbf{u}_{k_y} \tag{5.20}$$

which makes a double angle with respect to the wavevector $\mathbf{k}$ and whose strength depends on the magnitude of $\mathbf{k}$ in a nontrivial way because of the photon-exciton mixing [57]. A convenient representation for the polarization of the polaritonic system is the three dimensional pseudospin vector [25] (analogue of the Stokes vector) $\mathbf{S} = (S_x, S_y, S_z)$ on the Poincaré sphere. This vector is defined as the decomposition of the 2×2 spin-density matrix ρ_s of polaritons on a set consisting of the unity matrix $\mathbf{I}$ and the three Pauli matrices $\sigma_{x,y,z}$: $\rho_s = \mathbf{I}N/2 + \mathbf{S}\cdot\boldsymbol{\sigma}$ with N the total number of particles in the system. The pseudospin completely defines the polarization of the system: the S_x and S_y components describe the linear polarization states while the S_z component accounts for the circular polarization the particles. Moreover, it allows us to map the system to a magnetic one, namely the pseudospin responds to (effective) magnetic fields like usual magnetic moments and evolves according to the precession equations of the type $\partial_t \mathbf{S} = \mathbf{\Omega} \times \mathbf{S}$. It is the action of $\mathbf{\Omega}_{LT}$ on $\mathbf{S}$ that leads to the so-called optical spin-Hall effect [24, 31, 58]—$\mathbf{k}$-dependent polarization splitting. The normalized pseudospin vector of the emitted light can be defined via the photonic wave functions:

$$S_0 = \sqrt{S_x^2 + S_y^2 + S_z^2} \tag{5.21}$$

$$S_x = \Re\left(\phi_+\phi_-^*\right)/S_0 \tag{5.22}$$

$$S_y = \Im\left(\phi_+^*\phi_-\right)/S_0 \tag{5.23}$$

$$S_z = \left(|\phi_+|^2 - |\phi_-|^2\right)/2S_0 \tag{5.24}$$

We note that given the normalization to unity, S_z is nothing but the degree of circular polarization $\rho_c = (n_{\phi_+} - n_{\phi_-})/(n_{\phi_+} + n_{\phi_-})$ of the emission. Accounting for the TE-TM splitting, we need to carefully select the polarization of the pump laser to avoid pseudospin rotation before the fluid reaches the defect. We choose the latter

to be linear in a TM state which corresponds to a polarization along the direction of propagation (x-axis) and to $\mathbf{S}$ pointing along $\mathbf{\Omega}_{LT}$.

Arriving at the obstacle, the fluid is split into two parts propagating in opposite oblique directions around the obstacle. Before the defect, the pseudospin was aligned with the effective field, but when the propagation direction changes, the angle between the pseudospin and the field starts to increase. It induces an antisymmetric rotation of the pseudospin: the particles going up (down) will gain a σ_+ (σ_-) component, providing the seed for the OHS/HV generation. The mechanism of nucleation of the OHSs, however, is not as trivial as in the case of the polarized defect. If no TE-TM splitting is present, our experiment would lead to a pair of integer oblique solitons and each of them can be seen as a superposition of two perfectly overlapping OHSs. With the splitting turned on, the OHSs do not overlap perfectly anymore, becoming slightly shifted because of the antisymmetry of the flow with respect to circular polarizations, σ_+ and σ_-.

Downstream from the defect the flows are complex, but globally the fluid is moving along the x-axis. The core of each OHS is strongly circularly polarized because it is filled with the other component, which corresponds to a pseudospin with a strong S_z projection. As a result, $\mathbf{\Omega}_{LT}$ which lies in the plane of the microcavity, will act strongly at these positions and in an opposite way for each OHS providing their separation: one of them is bent slightly towards the axis of symmetry of the flow, becoming deeper, while the other one is moved in the opposite direction, becoming shallower and larger and possibly hardly visible for larger values of Ω_{LT} (larger $\mathbf{k}_P$). The situation is obviously totally inverse for the lower oblique soliton. Moreover, this separation effect is emphasized if α_2 is negative. Indeed, in that case the presence of a HS in one component induces a density minimum at the same position in the other component, in such a way that minimums and solitons repel each other within the same component.

On should make an important remark here. Due to the nonlinearities in the system, a population imbalance between σ_+ and σ_+ induces an energy splitting between the corresponding modes. Consequently, an imbalance-dependent effective magnetic field $\mathbf{\Omega}_L = (\alpha_1 - \alpha_2)/2n_\chi \mathbf{u}_z$ appears along the growth axis which leads to the so-called self-induced Larmor precession [59]. The total effective field $\mathbf{\Omega}_L + \mathbf{\Omega}_{LT}$ gains a z component especially strong at the cores of HV/OHS, where the circular polarization degree S_z is large. The strength of $\mathbf{\Omega}_L$ depends crucially on the value of α_2 and it is zero for $\alpha_1 = \alpha_2$ (typical case for atomic BECs). In that context, the spin-anisotropic polariton BEC offers a clear advantage: half-integer topological defects are protected against weak in-plane magnetic fields. Therefore, HV/OHS are stabilized with respect to the TE-TM splitting or other effective fields [60].

1D HSs are the domain walls between linear polarizations, which means that the polarization angle η rotates by $\pi/2$ and the in-plane projection of $\mathbf{S}\| = (S_x, S_y)^T$ by π going through the HS. This rotation of η is also expected for a the 2D system, nevertheless, the *oblique* half-solitons are usually oblique, and therefore have nonzero density in the center. Thus, the rotation of η as well as the shift of the global phase θ are slightly smaller than $\pi/2$. The HV generation at higher densities

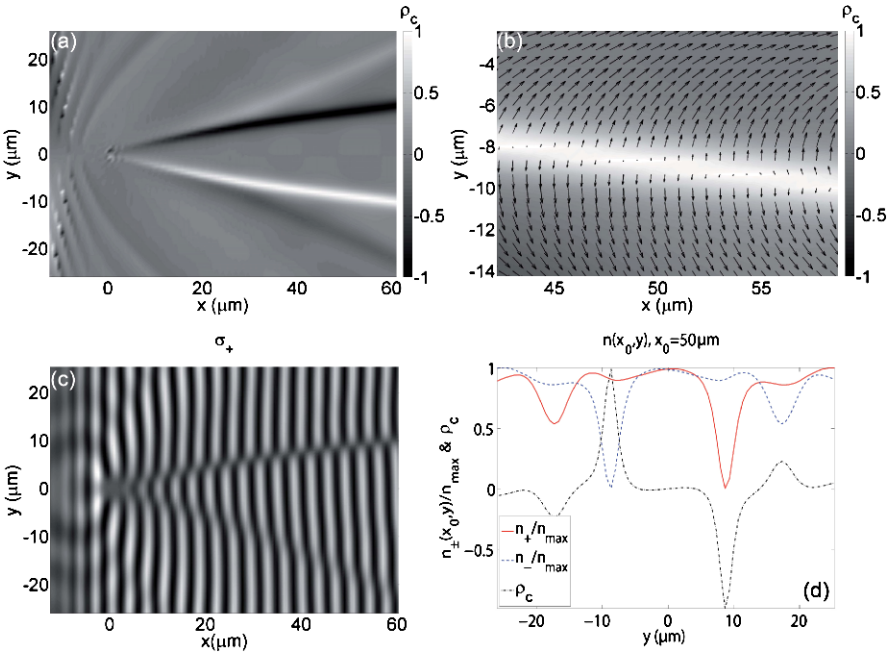

Fig. 5.5 Stationary 2D OHSs. (**a**) Degree of circular polarization ρ_c: one clearly sees the antisymmetric pattern imposed by the effective field's geometry and the OHS separation. (**b**) Zoom on the lower σ_- soliton (white one in (**a**)) with the in plane pseudospin component $\mathbf{S}\| = (S_x, S_y)$ (*black arrows*) exhibiting a rotation of almost π through the OHS ($\pi/2$ rotation of η). (**c**) Interference pattern in the σ_+ component showing the phase shifts at the OHSs position the situation is obviously antisymmetric in the other component (not shown). The repelled soliton is shallower which corresponds to smaller phase shifts. (**d**) Density slices 50 μm downstream from the defect together with ρ_c

can be understood in a similar way: integer vortices are split into HVs by the effective magnetic field. The difference is that vortices cannot be more or less shallow like solitons, they can only appear or not, being real topological defects, which explains why only one species of half-vortices appears in each half-plane. We show the corresponding numerical stationary solutions in Figs. 5.5 and 5.6, demonstrating the three density dependent hydrodynamic regimes: OHSs [Fig. 5.5], streets of HV dipoles [Fig. 5.6(a), (b)], and finally a superfluid regime [Fig. 5.6(c), (d)].

5.2.5 Conclusion

In this section we have discussed the half-integer topological excitations in exciton-polariton condensates, paying particular attention to their generation in flowing polariton condensates. Such excitations remain stable against an in-plane effective magnetic field thanks to the spin anisotropy of the polariton system. This feature

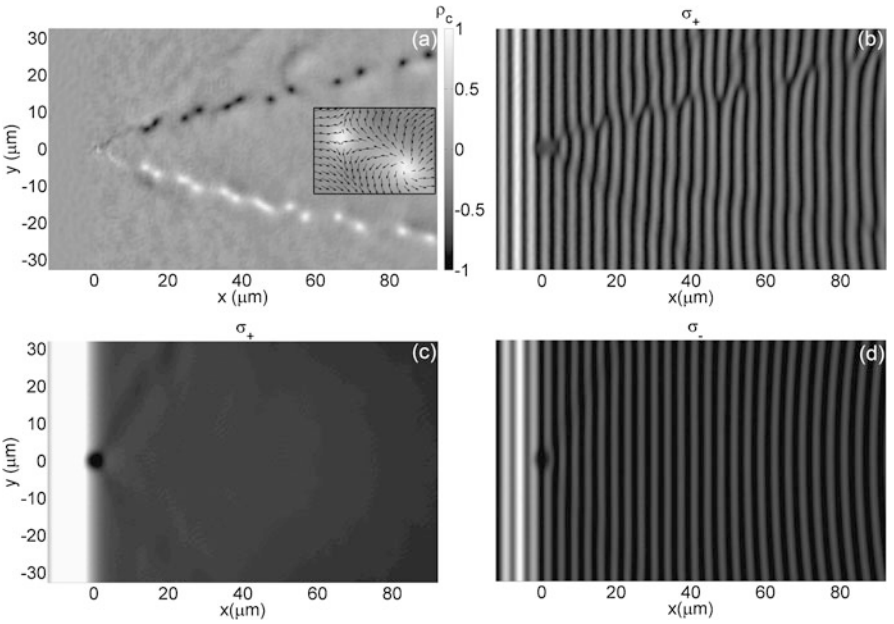

Fig. 5.6 (**a**) Degree of circular polarization: HV trains generation increasing the pump intensity with respect to Fig. 5.5. The *inset* displays $\mathbf{S}\|$ for a σ_- HV pair (*black arrows*) and shows the opposite winding of the polarization around the HVs core. (**b**) The interference pattern in the σ_+ component shows the typical forklike dislocations at the HV position. The positions corresponding to σ_- vortices show no phase modification. (**c**) Superfluid regime: The flow ignores the presence of the obstacle and shows no phase perturbation as one can see in the panel (**d**) showing the complementary antisymmetric σ_- component

allows the control of their trajectory tuning the polarization splittings in the microcavity. Therefore, half-vortices and half-solitons behave as magnetic charges accelerated by an effective field and embody the analogues of magnetic monopoles [60].

5.3 Sonic Black Holes and Wormholes in Spinor Polariton Condensates

In this second part of the chapter we will show that the polariton BEC is an excellent candidate for the construction of 1D and 2D sonic black holes thanks to the finite lifetime of the particles. Once again, the spinor nature of the BEC allows to expect even more interesting features. Indeed, mapping the two spin components to two parallel universes allows the construction of wormholes or Einstein-Rosen bridges [34] connecting these universes. To test the wormhole structure one needs to study the propagation of a signal through it. This signal has to be intrinsically stable and to initially exist in only one of the two universes. Here half-integer topological defects come into play: a half-soliton appears perfectly suitable for this task. We will

describe inter- and intra-universe wormholes, the latter offering the possibility of a "faster than sound" travel.

5.3.1 Sonic Black Holes in the Polariton Condensate

It happens quite often in physics that striking similarities are found between systems, which from the first glance have absolutely nothing in common. Sometimes, such similarities can be exploited to perform laboratory studies on accessible objects similar to inaccessible ones. One of the most recent example is that of Klein tunneling in graphene [61]: The quasi-particles in a solid-state object obey the same mathematical equations as very high-energy relativistic particles. Astrophysics allows even less laboratory studies than high-energy physics: scientists are restrained to the objects in the universe proposed by the Nature, these are studied from very far and the consideration of gravitational fields require to manipulate very large masses. Thus, having a desktop version of a black hole would be even more useful. Once again, the physics of the small comes to the aid of the physics of the large. The analogy between the equations describing the excitations of a Bose-Einstein condensate and the metrics of the curved space-time has been noticed about a decade ago [14]. Since then, the scientists have managed to experimentally observe the event horizons in atomic BECs [15].

However, such atomic condensates are still a bit far from being a convenient laboratory tool, because they require ultra-low temperatures for their formation, the measurements of the distributions inside the condensates are relatively complex to carry out and the construction of the event horizon is provided by artificial external potentials. Here the solid-state physics comes into play with the exciton-polariton condensates: The finite lifetime of polaritons in the range of tens of picoseconds turns into an important advantage, simplifying all measurements, because the decay of the condensate means the emission of photons from the cavity, and the distribution of emitted photons gives direct information on the polariton distribution function, on their dispersion and spatial evolution. Finally, the spin structure of polaritons [25] implies possible new effects due to the vectorial nature of the condensates. These particularities favor polaritons with respect to other systems proposed for the simulation of black holes, including the optical ones based on metamaterials [62–64].

5.3.2 Theoretical Description of Sonic Black Holes

It has been understood quite a long time ago in hydrodynamics, that an event horizon can appear if the flow speed increases and becomes larger than the speed of sound [65]. Indeed, the excitations in the flowing medium propagate with the speed of sound (in the linear approximation, that is, long-wavelength limit), and therefore in

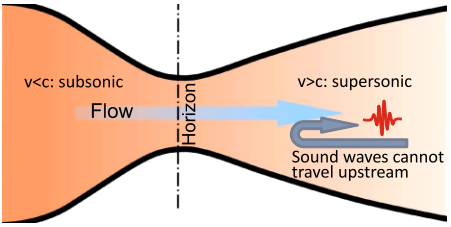

Fig. 5.7 Scheme of a de Laval nozzle

the laboratory frame they are unable to go against the flow if its speed is too high. A great research effort in this domain has recently culminated with the observation of stimulated Hawking emission in a water tank [66]. A most widespread example of a structure exhibiting an event horizon is the de Laval nozzle [see Fig. 5.7] used in jet engines. In order to have the exhaust gas velocity higher than the limit allowed by the Bernoulli's principle, the gas is accelerated from subsonic to supersonic speed. No sound waves are able to propagate backwards in the supersonic part of the flow, which is therefore separated from the subsonic part by what can be called an event horizon.

The work of W. Unruh [65] has laid down the foundations for this domain of research by showing how the hydrodynamic equations can be rewritten using the metrics to obtain exactly the Schwarzschild's metric of a black hole. Starting from the equations of motion for an irrotational fluid:

$$\nabla \times \mathbf{v} = 0 \tag{5.25}$$

$$n\big(\partial \mathbf{v}/\partial t + (\mathbf{v}\cdot\nabla)\mathbf{v}\big) = -\nabla p - n\nabla\Phi \tag{5.26}$$

$$\partial n/\partial t + \nabla\cdot(n\mathbf{v}) = 0 \tag{5.27}$$

and considering weak perturbations about a stationary solution, one can obtain the equations for a massless scalar field with a metric

$$ds^2 = \frac{n_0}{c(n_0)}\big(\big(c^2(n_0) - \mathbf{v}_0\cdot\mathbf{v}_0\big)dt^2 + 2dt\,\mathbf{v}_0\cdot d\mathbf{r} - d\mathbf{r}\cdot d\mathbf{r}\big) \tag{5.28}$$

where $c_0 = g'\ln(n_0)$ is the local velocity of sound. For a spherically symmetric converging flow in the region where the speed of the flow becomes equal to the sound velocity, this metric takes exactly the form of the Schwarzschild's metric of a black hole at the horizon:

$$ds^2 \approx \frac{n_0(R)}{c}\left(2c\alpha(r-R)d\tau^2 - \frac{dr^2}{2\alpha(r-R)}\right) \tag{5.29}$$

where α is the first coefficient of the development of $v(r)$ around R, that is $\alpha = \partial v_r^0/\partial r|_{r=R}$.

The seminal work of Unruh considered an arbitrary irrotational fluid, defined by $\mathbf{v} = \hbar/m\nabla\theta$, without detailing its nature. An application for BEC has logically come

20 years later [14], where θ was interpreted as the phase of the order parameter of the condensate and

$$\Psi(\mathbf{r}, t) = \sqrt{n(\mathbf{r})} e^{i\theta(\mathbf{r})} e^{-i\mu t/\hbar} \tag{5.30}$$

In order to discuss the hydrodynamic approximation for BEC let us rewrite the stationary Gross-Pitaevskii equation using the phase-density representation of the wavefunction:

$$\hbar \frac{\partial \theta}{\partial t} + \left(\frac{1}{2} m \mathbf{v}_s^2 + V_{ext} + \alpha n - \frac{\hbar^2}{2m\sqrt{n}} \nabla^2 \sqrt{n} \right) = 0 \tag{5.31}$$

The last term in this equation is the quantum pressure term, which scales as R^{-2} and becomes negligible if the typical density variations occur at scales much larger than the characteristic length ξ. When quantum pressure is neglected, one obtains what is called the Thomas-Fermi limit or hydrodynamic approximation, because the equation of motion for the condensate becomes simply the Euler's equation for potential flow of a nonviscous liquid.

Considering the density and phase perturbations n' and θ' for the BEC (as in the general case of Unruh [65]) and performing the linearization, one obtains the following first-order equation for the phase:

$$\partial_\mu \left(\sqrt{-g} g^{\mu\nu} \partial_\nu \theta' \right) = 0 \tag{5.32}$$

with the metric g given by

$$g_{\mu\nu} = \begin{pmatrix} -(c^2 - v^2) & -v^T \\ -v & 1 \end{pmatrix} \tag{5.33}$$

As one can see, the condition $v = c$ imposes a diagonal element to be zero, which defines the position of the event horizon.

5.3.3 Hawking Emission

The most important goal of the research activity centered on the acoustic black holes has been to verify the famous S. Hawking's prediction [16], which described cosmological black holes and showed that vacuum fluctuations producing particle/antiparticle pairs would behave in a singular way at the event horizon position. The huge gravitational fields that reign past the event horizon would absorb one of the photons towards the black hole which it could not escape, while the other one would propagate away from the horizon. The consequence of such events would lead to a loss of mass or evaporation of the black hole with time until its explosion. However, no detection of such Hawking photons was reported so far, because anyway they can hardly be extracted from the warmer cosmic background. Consequently, a quantitative study of such a phenomenon required model systems [67] and among them are the very promising BECs [14, 68, 69].

The small amplitude excitations in a BEC, called bogolons, can also exhibit linear dispersion in the long-wavelength limit, defining a speed of sound [see Sect. 5.2.1]. The finite lifetime of polaritons provides a natural way to vary the speed of sound. A propagating condensate can be injected locally via non-resonant [19] or resonant [24] pumping. Its density is bound to decrease with the distance from the pumping spot, and c will therefore decrease as well, whereas the propagation speed will remain constant or may even increase, if the condensate is accelerated by a potential ramp (for example, by its own self-interactions). At some point the two speeds become equal, defining the position of the event horizon of the black hole.

The spinor polariton condensate is described by the set of equations (5.18)–(5.19). Here $D(x,t)$ becomes a total potential that can encompass: disorder in the microcavity, potential barriers and time dependent potentials to impose excitations in the system. An extra $\mathbf{k}$-independent polarization coupling (conversion) term $i\hbar\partial_t\phi_\pm = H_0(\mathbf{r},t)\phi_\mp$ should be added to photonic parts to account for the extra longitudinal-transverse polarization splitting that occurs in 1D wires at $\mathbf{k}=\mathbf{0}$ [70].

5.3.4 1D Sonic Holes

First, let us consider a 1D configuration neglecting the spin degree of freedom. The polariton flow is resonantly and locally injected by a pumping laser located close to $x=0$ on Fig. 5.8(a). The medium is assumed to exhibit small structural disorder mainly due to the etching of the 1D wire cavities. It is modeled by a random series of delta-peaks separated by 1 μm on average. All results shown in Fig. 5.8 are averaged over 100 disorder realizations. Figure 5.8(a) shows the polariton density $n_\phi(x)$, the visible decay is mainly due to the finite lifetime of polaritons. The speed of the sound $c(x)$ decreases together with the density. On contrary, the speed of the flow $v(x)$ is increasing because of the self-interactions within the condensate. In the left part, the flow is subsonic and cannot be scattered by the disorder (superfluid). In the right part, the flow is supersonic. The exponential decay is induced not only by the life time but also because of the Anderson like-localization in the disorder. The two regions are separated by an event horizon at $v=c$. In the supersonic region no excitation can propagate towards the horizon. The generation of Hawking emission on the horizon is demonstrated in Fig. 5.8(b). Indeed, as recently proposed in Refs. [71, 72], emission of Hawking phonons means correlated density perturbations propagating on both sides of the horizon. Hawking emission can therefore be detected using the following density-density correlation matrix:

$$g^{(2)}\left(x,x'\right)=\frac{\langle n(x)n(x')\rangle}{\langle n(x)\rangle\langle n(x')\rangle} \tag{5.34}$$

This matrix is in our case averaged on many realization of disorder, and is shown at in Fig. 5.8(b). Indeed, as expected, characteristic “Hawking tongues”, indicating

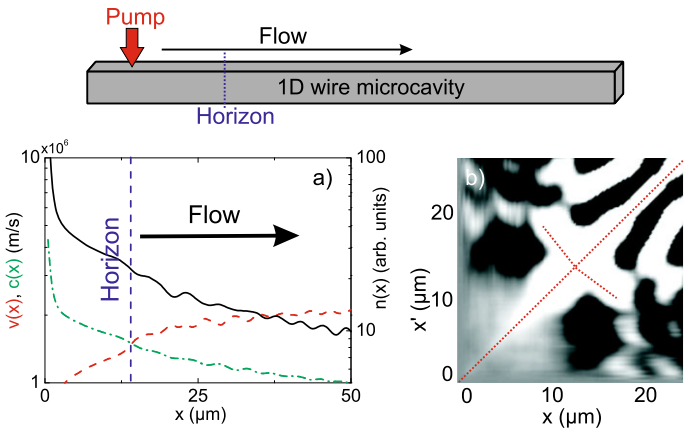

Fig. 5.8 (**a**) Propagation of a polariton condensate in 1D: density (*black solid line*), flow speed (*red dashed line*), sound speed (*green dash-dotted line*). The horizon is indicated by a *blue dashed vertical line*. (**b**) Density-density correlation matrix $g^{(2)}(x, x')$ at $t = 200$ ps. *Dotted red lines* are a guide for the eyes, indicating the Hawking tongues (positive correlations) extending from the main diagonal

positive correlations, are extending from the horizon position, marked by the red dotted lines. We underline that there is no need to introduce quantum fluctuations to seed Hawking emission thanks to the presence of the disorder potential and to the finite lifetime which broaden the states in momentum and frequency.

5.3.5 *Closed 2D Sonic Holes*

The finite lifetime of polaritons allows to organize persistent flows, as shown in Refs. [21, 73, 74] for the cases of quasi-resonant or non-resonant pumping. This particular property makes the formation of closed event horizon in 2D possible. This is much more complicated with atomic condensates, where only 1D configurations have been considered [15]. With polaritons, one needs to pump in a regime allowing the superfluidity to arise, around a large-scale defect in the microcavity mirrors possessing a lower quality factor. Polariton-polariton repulsive interactions will then create a persistent flow converging into the defect region, where the density is always lower due to the shorter lifetime. The boundary between the superfluid and supersonic regions forms a circular event horizon.

Figure 5.9 shows the results of a realistic 2D simulation with pulsed spatially homogeneous pumping. The photon density n_ϕ at the time $t = 8$ ps is plotted as a function of coordinates [panel (a)]. The defect region with a shorter lifetime is located at the origin $[(x, y) = (0, 0)]$, while the disorder is neglected. The density inside the defect region decreases faster than outside, and the repulsive interactions make polaritons propagate towards the center of the figure. The event horizon at

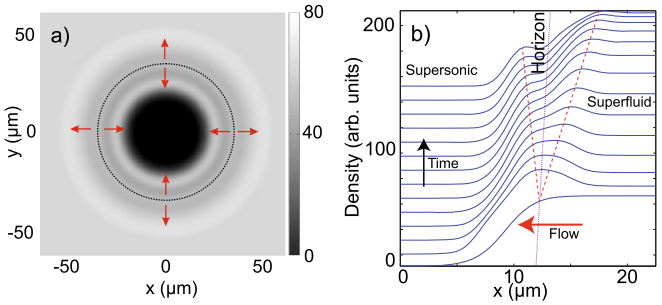

Fig. 5.9 (**a**) 2D black hole around a defect (*dark region*) in a polariton condensate. The *dashed black circle* shows the event horizon, and *red arrows* point the directions of the propagation of the Hawking radiation on both sides of the horizon (*purple dotted line*). (**b**) Waterfall density plot at different times. Propagating Hawking phonons are marked by the *red dashed lines* (Color figure online)

that time is marked with a dashed blue line. The Hawking radiation is in that case seeded by the non-equilibrium spatial distribution that populates excited states. It can be observed on the panel (b) as density waves propagating inwards inside and outwards outside the horizon (red arrows).

5.3.6 Wormholes Analogue in the Spinor Polariton Condensate

If a single scalar condensate is a model of a universe which might contain black holes, it seems natural to map two spinor components to two different universes. They can be completely decoupled from each other if there are no interactions between the particles of different spins. Adding a magnetic field can provide a coupling between these two universes, making possible simulation of wormholes [76].

In astrophysics, inter-universe wormholes are the pairs of singularities located in different universes and connected together. Using such wormhole, one could pass from one universe to the other. A more interesting situation, when both holes connected together are in the same universe, is called an intra-universe wormhole. Such wormhole can connect two distant regions of space with a tunnel much shorter than the distance between the two, which might allow faster-than-light travel [77].

Inter-Universe Wormhole Let us start with the simpler case of an inter-Universe wormhole. We consider a 1D quantum wire, as in Ref. [19]. The idea is to first create a closed black hole bordered by two event horizons and to connect it with a white hole in the other spin component using a local effective magnetic field H_0, induced by the energy splitting existing between linearly polarized (TE or TM) eigen modes. H_0 can be controlled by varying the width of the wire [70], or by applying an electric field [78].

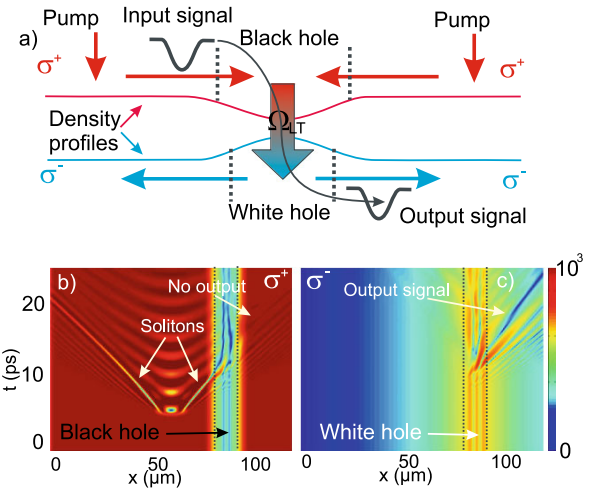

Fig. 5.10 (**a**) Scheme of a wormhole between the σ_+ (*red*) and σ_- (*blue*) universes. *Arrows* show the directions of the flow in the two components. *Dashed lines* mark the event horizons in both components. (**b**) Results of numerical simulation: $n_\phi(x,t)$ for both spin components with *black dotted lines* showing the boundaries of the black/white holes and *white arrows* indicating the propagation of signals

In general relativity, a key concept is the propagation of signals, whose speed can never exceed that of light in the vacuum. The propagation of phonon wavepackets across the event horizons in BECs has already been studied, for example in Refs. [71, 75]. In our model system, we need a "signal" that appears in only one spin component (e.g. σ_+, representing our universe), that is stable and able to propagate. The perfect candidate for this task appears to be the 1D HS. As already mentioned in Sect. 5.2.1, solitons have a lot of properties similar to those of relativistic particles [1, 79], except that their mass is negative (because they are actually holes rather than particles): $m_s = m_0/\sqrt{1 - v_s^2/c^2}$; their size is given by $l_s = \xi/\sqrt{1 - v_s^2/c^2}$ where v_s is their velocity. For attractive interactions, the mass can of course be positive. Pairs of half-solitons are created thanks to a short time-dependent pulsed potential acting on a single spin component

$$U(x,t) = U_0 e^{-(x-x_0)^2/w_x^2} e^{-(t-t_0)^2/\tau^2} \tag{5.35}$$

As the speed of a soliton is related to its depth by $v = cn(0)/n_\infty$ where $n(0)$ is the density at its center and n_∞ in its surrounding [1], we need a weak enough potential U to excite shallow solitons that will be able to travel at speeds close to c in both spin components (marked as c_1, c_2 below).

Figure 5.10 shows the scheme of a numerical experiment with a single wormhole [panel (a)] and the results of the simulations [panels (b), (c)]. A 1D polariton wire is cw-pumped by two spatially separated, quasi-resonant, σ_+ polarized lasers allowing the formation of a steady state flow and convenient density distribution sketched on the panel (a). Polaritons flow away from the pumping regions and a closed black hole is formed in the middle. A local effective magnetic field converting σ_+ to σ_- is present in the black hole region. The σ_- density therefore shows a maximum expelling excitations outside from the central region which corresponds to the formation of a white hole, in which no excitation can enter, in the σ_- universe.

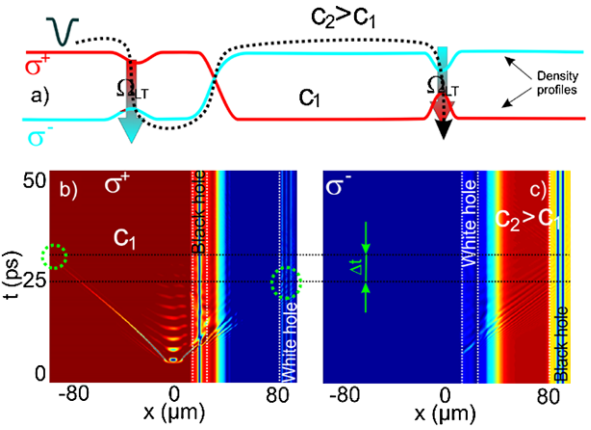

Fig. 5.11 Faster-than-sound signal propagation with two wormholes. (**a**) Scheme with two wormholes showing density profiles; (**b**) σ_+ density; (**c**) σ_- density. *Dashed horizontal lines* mark the arrival of the two signals (*green dashed circles*), with Δt the time difference between them

After the steady state is obtained, a pulsed potential is applied in the σ_+-component [panel (b)] at $t = 5$ ps at the left of the left horizon, creating propagating half-solitons. The continuity of the phase imposes the creation of solitons by pairs. One of these propagates freely to the left, whereas the other enters the black hole and remains partly guided inside. The effective magnetic field converts a part of this soliton into the other spin component: σ_- [panel (c)]. The soliton is then able to cross the horizon of the white hole, propagating away together with the flowing condensate. One can also see that short-wavelength (corresponding to nonlinear parts of the spectrum) perturbations are still able to cross the horizon of the black hole in any direction. The holes possess an internal structure. The speed of the flow is zero at the center and the black hole is in fact composed by two narrower black holes surrounding a subsonic region.

Intra-Universe Wormhole In the last part, we will discuss a scheme for an intra-universe wormhole allowing for the transfer of a HS with an apparent velocity faster than the speed of sound of its original universe. Such intra-universe wormhole is based on two inter-universe wormholes similar to the ones previously described, but connecting the Universes in opposite directions. The scheme at the figure 4(a) shows the proposed $\sigma_\pm$ density profiles with the two wormholes. Dashed line indicates the propagation of a half-soliton. A σ_+ half-soliton is generated at the left. It enters in the σ_+ black hole where it is converted in a σ_- soliton, which is ejected by the white hole part of the wormhole. Then, it travels in the σ_- component between the two wormholes with a velocity close to c_2. It then reaches the second wormhole, which is a black hole in the σ_- component, where it is captured and converted to a σ_+ soliton ejected from the white hole. The average velocity of this soliton is close to c_2 which can be larger than c_1, the speed of sound in the σ_+ universe. The results of corresponding simulations are presented in panels (b) and (c).

The pumping is *cw* quasi-resonant with inhomogeneous elliptical polarization, providing the density profiles close to Fig. 5.11(a). A pair of half-solitons is created at $t = 5$ ps in the σ_+-component at $x = 0$ [panel (b)]. The "reference" half-soliton

propagates to the left with the speed limited by c_1 and arrives to the edge at around $t = 30$ ps. The half-soliton falling inside the black hole converts into the σ_- component, gets out of the white hole in σ_- [panel c] and propagates with a higher speed, limited by $c_2 > c_1$. This half-soliton arrives to the second wormhole and is converted back into the σ_+-component, appearing there at $t = 25$ ps (marked by the dashed green circle). The two events are marked with black horizontal lines, and the time difference between them is $\Delta t \approx 5$ ps.

5.3.7 Conclusions

Spinor polariton condensates, being relatively easy to produce and manipulate, can be used for the simulation of astrophysical objects, such as black holes and wormholes. A 2D black hole with a closed event horizon can be simulated. Effective magnetic fields, well known as the cause of non-trivial spin dynamics of polaritons, can be used to organize the coupling between the black holes and white holes in the two spin components. Half-integer topological defects allow to test the propagation of signals through the wormhole structures. A system of two separated and complementary wormholes allows one to organize "faster-than-sound" signal propagation.

5.4 General Conclusion

The polariton quantum fluid has shown to have an incredible potential for the analysis of topological defects and hydrodynamic regimes. The resonant injection of particles allows to organize flows in an unprecedented manner and the finite lifetime of the particles is a key ingredient towards the creation of event horizons. The spinor nature of the polariton condensate, which allows a mixing of both phase and spin topologies, together with polarization splittings that couple the two components enrich the physics even further, and make possible the organization of fascinating structures such as oblique half-solitons, half-vortices or wormholes. The whole domain combines fundamental effects with the applied ones.

References

1. L.P. Pitaevskii, S. Stringari, *Bose-Einstein Condensation* (Oxford University Press, Oxford, 2003)
2. H. Smith, C.J. Pethick, *Bose-Einstein Condensation in Dilute Gases* (Cambridge University Press, Cambridge, 2002)
3. M.H. Anderson, J.R. Ensher, M.R. Matthews, C.E. Wieman, E.A. Cornell, Science **269**, 5221 (1995)
4. N.N. Bogoliubov, J. Phys. USSR **11**, 23 (1947)
5. J. Leggett, *Quantum Liquids* (Oxford University Press, Oxford, 2008)

6. P.G. Kevrekidis, D.J. Frantzeskakis, R. Carretero-González, *Emergent Nonlinear Phenomena in Bose-Einstein Condensates* (Springer, Berlin, 2002)
7. C.A. Jones, P.H. Roberts, J. Phys. A **15**, 2599 (1982)
8. G. Theocharis, D.J. Frantzeskakis, P.G. Kevrekidis, B.A. Malomed, Y.S. Kivshar, Phys. Rev. Lett. **90**, 120403 (2003)
9. G.A. El, A. Gammal, A.M. Kamchatnov, Phys. Rev. Lett. **97**, 180405 (2006)
10. M. Ueda, Y. Kawaguchi, Preprint (2010). arXiv:1001.2072
11. M.M. Salomaa, G.E. Volovik, J. Low Temp. Phys. **4**, 319 (1988)
12. G.E. Volovik, V.P. Mineev, JETP Lett. **24**, 561 (1976)
13. C.M. Savage, J. Ruostekoski, Phys. Rev. Lett. **91**, 010403 (2003)
14. L.J. Garay, J.R. Anglin, J.I. Cirac, P. Zoller, Phys. Rev. Lett. **85**, 4643 (2000)
15. O. Lahav, A. Itah, A. Blumkin, C. Gordon, S. Rinott, A. Zayats, J. Steinhauer, Phys. Rev. Lett. **105**, 240401 (2010)
16. S.W. Hawking, Nature **248**, 30–31 (1974)
17. A.V. Kavokin, J. Baumberg, G. Malpuech, F.P. Laussy, *Microcavities* (Oxford University Press, Oxford, 2007)
18. J. Kasprzak et al., Nature **443**, 409 (2006)
19. E. Wertz et al., Nat. Phys. **6**, 860 (2010)
20. A. Amo et al., Nature **457**, 291 (2009)
21. K.G. Lagoudakis, Nat. Phys. **4**, 706–710 (2008)
22. K.G. Lagoudakis et al., Phys. Rev. Lett. **106**, 115301 (2011)
23. S. Pigeon, I. Carusotto, C. Ciuti, Phys. Rev. **83**, 144513 (2011)
24. A. Amo et al., Science **3**, 1167 (2011)
25. I.A. Shelykh, A.V. Kavokin, Y.G. Rubo, T.C.H. Liew, G. Malpuech, Semicond. Sci. Technol. **25**, 013001 (2010)
26. P. Renucci et al., Phys. Rev. B **72**, 075317 (2005)
27. I.A. Shelykh et al., Phys. Rev. Lett. **97**, 066402 (2006)
28. Y.G. Rubo, Phys. Rev. Lett. **99**, 106401 (2007)
29. K.G. Lagoudakis et al., Science **326**, 974 (2009)
30. H. Flayac, D.D. Solnyshkov, G. Malpuech, Phys. Rev. B **83**, 193305 (2011)
31. A. Kavokin et al., Phys. Rev. Lett. **95**, 136601 (2005)
32. C. Leyder et al., Nat. Phys. **3**, 628 (2007)
33. D.D. Solnyshkov, H. Flayac, G. Malpuech, Phys. Rev. B **84**, 233405 (2011)
34. A. Einstein, N. Rosen, Phys. Rev. **48**, 73–77 (1935)
35. L.D. Landau, J. Phys. USSR **5**, 71 (1941)
36. A.A. Abrikosov, Zh. Eksp. Teor. Fiz. **32**, 1442 (1957)
37. K.W. Madison, F. Chevy, W. Wohlleben, J. Dalibard, Phys. Rev. Lett. **84**, 806 (1999)
38. J. Williams, M. Holland, Nature **401**, 568 (1999)
39. F.M. Marchetti et al., Phys. Rev. Lett. **105**, 063902 (2010)
40. G. Tosi et al., Phys. Rev. Lett. **107**, 036401 (2011)
41. G. Nardin et al., Nat. Phys. **7**, 635 (2011)
42. D. Sanvitto et al., Nat. Photonics **5**, 610 (2011)
43. A.M. Kamchatnov, L.P. Pitaevskii, Phys. Rev. Lett. **100**, 160402 (2008)
44. E. Cancellieri et al., Phys. Rev. B **82**, 224512 (2010)
45. D.D. Solnyshkov, I.A. Shelykh, N.A. Gippius, A.V. Kavokin, G. Malpuech, Phys. Rev. B **77**, 045314 (2008)
46. A.M. Kamchatnov, S.V. Korneev, Preprint (2011). arXiv:1111.4170v1
47. A.M. Kamchatnov, S.V. Korneev, Preprint (2011). arXiv:1105.0789v1
48. T. Frisch, Y. Pomeau, S. Rica, Phys. Rev. Lett. **69**, 1644 (1992)
49. P. Öhberg et al., Phys. Rev. Lett. **86**, 2918 (2000)
50. P.G. Kevrekidis et al., Eur. Phys. J. D **28**, 181 (2004)
51. Y.G. Gladush et al., Phys. Rev. A **79**, 033623 (2009)
52. J.J. Baumberg et al., Phys. Rev. Lett. **101**, 136409 (2008)
53. H. Flayac, D.D. Solnyshkov, G. Malpuech, I.A. Shelykh, Phys. Rev. B **81**, 045318 (2010)

54. M. Toledo Solano, Y.G. Rubo, J. Phys. Conf. Ser. **210**, 012024 (2010)
55. Z. Hadzibabic et al., Nature **441**, 1118 (2006)
56. A. Amo et al., Phys. Rev. B **82**, 081301(R) (2010)
57. W. Langbein, I. Shelykh, D. Solnyshkov, G. Malpuech, Yu. Rubo, A. Kavokin, Phys. Rev. B **75**, 075323 (2007)
58. A. Amo et al., Phys. Rev. B **80**, 165325 (2009)
59. D.N. Krizhanovskii et al., Phys. Rev. B **73**, 073303 (2006)
60. D.D. Solnyshkov, H. Flayac, G. Malpuech, Phys. Rev. B **85**, 073105 (2012)
61. A.F. Young, P. Kim, Nat. Phys. **5**, 222 (2009)
62. K. Muamer, D. Guillaume, T.M. Chang, S. Guenneau, S. Enoch, Preprint (2011). arXiv: 1102.0900
63. H. Chen, R.X. Miao, M. Li, Opt. Express **18**, 15183 (2010)
64. A. Greenleaf, Y. Kurylev, M. Lassas, G. Uhlmann, Phys. Rev. Lett. **99**, 183901 (2007)
65. W.G. Unruh, Phys. Rev. Lett. **46**, 1351 (1981)
66. S. Weinfurtner et al., Phys. Rev. Lett. **106**, 021302 (2011)
67. M. Visser et al., *Artificial Black Holes* (World Scientific Publishing, New Jersey, 2002)
68. J. Macher, R. Parentani, Phys. Rev. A **80**, 043601 (2009)
69. R. Schutzhold, W.G. Unruh, Phys. Rev. D **78**, 041504(R) (2008)
70. G. Dasbach et al., Phys. Rev. B **71**, 161308 (2005)
71. R. Balbinot et al., Phys. Rev. A **78**, 021603(R) (2008)
72. I. Carusotto et al., New J. Phys. **10**, 103001 (2008)
73. K.G. Lagoudakis et al., Nat. Phys. **4**, 706 (2008)
74. E. Wertz et al., Nat. Phys. **6**, 860 (2010)
75. C. Mayoral et al., New J. Phys. **13**, 025007 (2011)
76. J.A. Wheeler, *Geometrodynamics* (Academic Press, New York, 1962)
77. M.S. Morris, K.S. Thorne, U. Yurtsever, Phys. Rev. Lett. **61**, 1446 (1988)
78. G. Malpuech et al., Appl. Phys. Lett. **88**, 111118 (2006)
79. G.E. Volovik, *The Universe in a Helium Droplet* (Clarendon Press, Oxford, 2003)

Chapter 6
Dynamics of Vortices and Dark Solitons in Polariton Superfluids

Benoit Deveaud, Gael Nardin, Gabriele Grosso, and Yoan Léger

Abstract In this chapter we describe some observations linked with turbulence in quantum fluids of polaritons. We imprint a given velocity and density to the polariton fluid by using an appropriate pulse intensity and wavevector. The flow is then perturbed by a natural defect or more interestingly, by engineered traps with a well defined potential change. The flow of the fluid is measured in a time resolved fashion through the use of homodyne detection. Both the intensity and the phase of the fluid can then be retrieved with a picosecond resolution. This allows observing the nucleation of quantized vortices, with the appropriate 2π phase shift around the core, or the growth of dark solitons in the wake of the obstacle. The dark solitons are observed to decay into vortex streets. Our results are compared to dynamical solutions of the Gross-Pitaevskii equation and a very good agreement is obtained allowing us to hold good confidence in our interpretation.

Hydrodynamics is an important field of physics with a wide range of well established results, and still some parts of the field under active investigation because of the importance of hydrodynamics, and in particular of hydrodynamical instabilities for major practical applications. Hydrodynamical instabilities have been studied experimentally at the beginning of the twentieth century with in particular the seminal papers of Bénard [1]. Such instabilities include many different possible cases, with in particular the convective Bénard-Rayleigh flows and Bénard-Von Kármán streets [2]. The flow around an obstacle is characterized, in conventional fluids, by the Reynolds number, a dimensionless parameter given by $R_e = vR/\upsilon$ where v represents the fluid velocity and υ its dynamical viscosity, R being the diameter of the obstacle. Upon increasing the Reynolds number, either through the size of the obstacle or the speed of the fluid, the following phenomenology is successively observed: laminar flow, stationary vortices, Bénard-Von Kármán streets of moving vortices and eventually fully turbulent regime [3]. Such phenomena are observed in various configurations and with a wide variety of classical fluids.

B. Deveaud (✉) · G. Nardin · G. Grosso · Y. Léger
Ecole Polytechnique Fédérale de Lausanne, CH 1015 Lausanne, Switzerland
e-mail: benoit.deveaud-pledran@epfl.ch

A. Bramati, M. Modugno (eds.), *Physics of Quantum Fluids*,
Springer Series in Solid-State Sciences 177, DOI 10.1007/978-3-642-37569-9_6,

Superfluids do not show turbulence in the low velocity regime, when their speed is sufficiently below the sound velocity in the fluid. This simplified view is valid when superfluids flow at a speed much smaller that the speed of sound in the fluid. However, quantum turbulence has been predicted to appear at the breakdown of superfluidity in quantum fluids, such as for example liquid helium [4] or atomic Bose-Einstein condensates [5, 6]. The absence of viscosity in superfluids, does not allow defining a Reynolds number as in classical fluids. In superfluids, the presence of an impenetrable obstacle leads to a local increase of the fluid velocity. In the vicinity of the obstacle however, quantum turbulence, in the form of quantized vortices, appears simultaneously with dissipation and drag on the obstacle once some critical velocity is exceeded. This critical velocity for the appearance of turbulence is predicted to be lower than the Landau criterion for superfluidity [7], far from the obstacle [8]. For larger speeds, turbulence occurs in a superfluid is the same way as they appear in a classical fluid, with major differences however in the fact that vortices are quantized, von Karman streets are made of quantized vortices and solitary waves are quantized and show a π phase shift, which is not observed in standard fluids. Quantized vortices and solitons have been observed in liquid Helium [9] as well as in atom condensates [10].

Since the realization of Bose-Einstein condensation in atom vapors in 1995 [11, 12], studies of first the superfluid behavior of such condensates through for example the stirring of the condensate allowing to create a network of quantized vortices [13] have been performed. Then, in a second step, the study of quantum turbulence with the observation for example of dark solitons [14], their decay into vortex rings [15] was realized. To conclude this incomplete list, vortex nucleation has been reported in the wake of a blue-detuned laser moving above a critical velocity through the condensate [16, 17].

In solids, the idea to use excitons in semiconductors for BEC derives from the observation, with BCS, that composite bosons could be very good candidates for condensation, in particular thanks to their mass similar to the mass of an electron. The idea was independently proposed by Moskalenko [18] and by Blatt [19] and both papers expose that, being composite bosons with very light mass, excitons should show BEC at reasonable temperatures. Such and idea has been pursued further by Keldysh [20], who described the possible transition from BEC to BCS of excitons. It soon became obvious that exciton condensates, if they are observed, should also evidence superfluidity [21]. Claims for condensation have been made by different groups in exciton physics, as early as in the late seventies [22, 23]. The different groups have in particular been using large band-gap semiconductors where the binding energy of excitons is larger and therefore the saturation density would be better suited for condensation. Such claims have however subsequently proved to be premature and have not been confirmed yet. Superfluidity has not been demonstrated either in such exciton systems.

In 1992, Claude Weisbuch and his coworkers pinned down the appearance of strong coupling between light and excitons in semiconductor microcavities therefore opening the whole field of microcavity polaritons [24]. Polaritons, half exciton and half photon quasiparticles, result form the coupling of two bosonic particles

and they inherit this double bosonic character. From the photon part, they get a very light mass, and from the excitonic part, they are strongly interacting at high densities. They also carry a spin, common to the exciton as well as to the photon part. Polaritons possess many interesting properties linked with their dispersion relation, in particular they possess a very light mass. Such a light mass should allow to observe Bose-Einstein condensation at rather high temperatures, and even possibly at room temperature. The observation of Bose-Einstein condensation of polaritons has been claimed in 2006 [25] in particular based on the observation of spontaneous long range ordering. Long range order has since then been observed in a number of other systems and in different labs around the world [26–28]. Subsequently, polariton condensation has also been claimed, without yet the demonstration of long range order, in different systems and in particular in GaN based cavities at room temperature [29, 30].

Following these demonstrations of the condensation of polaritons, and after the observation of quantized vortices pinned by the disorder existing in the sample, both single quantized vortices [31], half vortices [32] and vortex pairs [33]. Also, following the theoretical farseeing proposal by Carusotto and Ciuti [34], Alberto Amo and coworkers, using a clever "TOPO" configuration (triggered optical parametric oscillator), were able to give evidence of both the superfluidity of resonantly injected polaritons and the onset of turbulence in such a quantum fluid [35, 36]. Polaritons indeed clearly constitute a very advantageous tool to explore both superfluidity and quantum turbulence. Their dual light-matter nature gives them many advantages.

Thanks to a one-to-one coupling to the extra-cavity field, with conservation of in-plane momentum and energy, exciton polaritons can be easily optically injected, manipulated and detected [37, 38]. Thanks to their excitonic part, polaritons can interact with each other, leading to spectacular nonlinear behavior (see for example [39, 40]). At the same time, the interactions between polaritons may be tuned through the detuning between the exciton and the photon modes in the cavity. The scattering strength between polaritons is an easily adjustable parameter. The phase of the quantum fluid, and the changes in the phase around singularities, can be probed very directly with simple interferometric studies not accessible to the now standard condensates and superfluids: superfluid Helium, superconductors, cold atom condensates.

In the present work, we follow on the ideas of Carusotto and Ciuti [34] and image, in a time resolved way, the flow of a polariton quantum fluid around an obstacle. The light emitted by polaritons allows for homodyne detection of the emission and a very precise resolution of the coherence of the system. Our sample contains two dimensional polaritons and traps of well-defined geometry. We may excite polariton fluids of any density and peed by adjusting the excitation power and angle of incidence on the microcavity sample. Our technique has allowed evidencing the nucleation of vortex pairs in the wake of an obstacle. It has also allowed to observe dark solitons, and to study their stability and their break-up into vortex streets [41]. As the observations of superfluidity in the continuous regime are described in another chapter in this book [42], we will concentrate here on the observation of the dynamics of quantum turbulence in polariton superfluids.

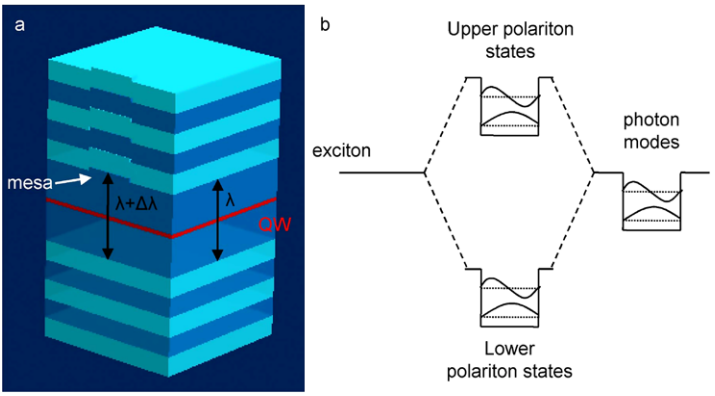

Fig. 6.1 *Polariton mesas*. Polariton mesas constitute potential obstacles with a size and depth that can be engineered at will. The mesa is realized by proper etching of the cavity spacer layer. (**a**) Giving rise to a modulation of the photon energy, which transfer to the polariton energy (**b**) Typical energy levels for confined polaritons in a trap. Figure adapted from the PhD of Gael Nardin [43]

6.1 Experimental Details

The sample that we use is a GaAs microcavity sandwiched between two distributed Bragg reflectors (DBR) with 22 (21) AlAs/GaAs pairs for the bottom (top) DBR. One single 8 nm thick InGaAs quantum well (QW) placed at the anti-node of the cavity field. The sample shows a Rabi splitting of 3.5 meV, in agreement with the exciton oscillator strength in the InGaAs QW and a cavity mode quality factor of 7000. A homodyne detection system (see Fig. 6.2) is used to probe the properties of the fluid.

Obstacles along the flow of the fluid consists either of a structural defect obtained randomly in the microcavity plane during the growth process, or of engineered defect, with a well known shape depth and position (polariton mesas [44], see Fig. 6.1). Both obstacles are penetrable. Their size can be estimated to be of the order of 5 μm in the direction perpendicular to the flow. The sample is placed in a cold-finger cryostat at liquid helium temperature.

The polariton population is generated using a pulsed Ti:sapphire laser. The laser pulse is spectrally shaped into 1 meV broad, 3 ps long pulses (we try to get the best out of the time energy uncertainty: we need a short enough pulse, and a precise enough energy). The laser is circularly polarized. The pulses are then split into one excitation pulse and one reference pulse. The reference pulse is directed through a telescope for spatial filtering and wavefront tuning, and incident at a small angle on the CCD, to serve as a phase reference [45]. The excitation pulse is passed through a delay line and focused on the back of the sample using a 25 cm focal length camera objective, providing a Fourier limited 25 μm diameter excitation spot. An oblique excitation angle is used to create a propagating polariton wave packet in the lower polariton branch with an initial adjustable in-plane momentum of 1.2 μm^{-1} (in most cases, see Fig. 6.3 for a schematics of the excitation).

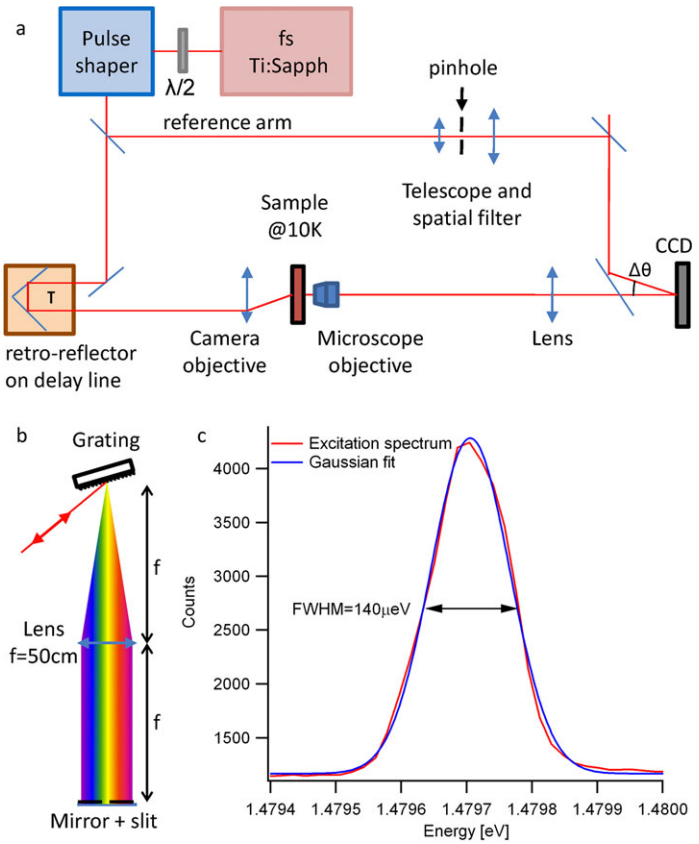

Fig. 6.2 *Homodyne detection system*. (**a**) Time and phase resolved imaging setup, based on a Mach-Zehnder interferometer. In order to obtain the time resolution, a mode-locked Ti:sapphire laser is used, and a delay line allows to scan the delay between excitation and reference pulses. A pulse shaper is added for the spectral tailoring of the laser pulse. It is preceded by a $\lambda/2$ waveplate, that allows for the rotation of the laser linear polarization, in order to maximize the output power of the polarization sensitive pulse shaper's grating. (**b**) Detail of the pulse shaper, containing a 1200 lines/mm blazed grating, a 50 cm focal length lens, a 75 μm wide slit and a mirror. (**c**) Spectrum of the laser pulse at the pulse shaper output, showing a nearly Gaussian 140 μeV broad pulse. Figure adapted from the PhD of Gael Nardin [43]

The coherent emission is collected by means of a 0.5 NA microscope objective in a transmission configuration. Real space or Fourier space images of the coherent emission are allowed to interfere, in a Mach-Zehnder configuration, with the reference pulse on the CCD. From the interferogram we numerically extract the amplitude and phase of the coherent emission at a time given by the delay between the excitation and reference pulses. Varying this delay allows us to probe the dynamics of the coherent polariton population in both real and momentum spaces. By acquiring data over 0.2 s, each measurement corresponds to the integration over millions of successive experimental realizations.

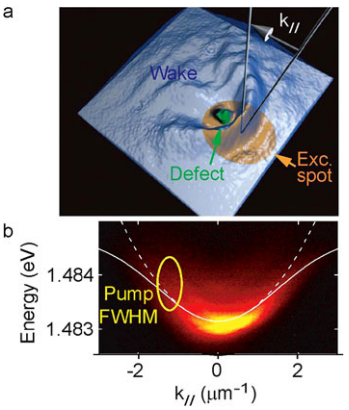

Fig. 6.3 *Schematics of the experiment*. (**a**) A polariton wavepacket is resonantly injected with an in-plane wavevector $k_{//}$ in front of a structural defect on which it scatters. (**b**) Experimental polariton dispersion curve, under non-resonant pumping. The *plain line* indicates the theoretical lower polariton (LP) dispersion, and the *dashed line* the standard small momentum parabolic approximation of the LP branch. During the experiment, polaritons are resonantly injected in the lower polariton branch: the *yellow circle* indicates the energy and momentum extension of the pulsed pump. Figure adapted from the PhD of Gael Nardin [43]

To extract the polariton amplitude and phase from the recorded interferogram, we use a technique known as digital off-axis holography [46]. The principle is to perform a two-dimensional Fourier transform of the interferogram. The fringes of the interferogram provide off-axis contributions in the Fourier plane, which can easily be differentiated from the cw contributions. Removing the cw contributions and performing an inverse Fourier transform allows one to isolate the fringes, from which the amplitude and phase are extracted. Such a procedure provides the full information on the coherent polariton field.

As a result of polariton-polariton interactions, resonantly pumping the polariton branch strongly modifies the excitation spectrum [34]. These interactions result in a blue-shift of the dispersion curve (interaction energy) and a linearization of the dispersion (Bogoliubov spectrum [47]) in the polariton gas. Such interactions are exemplified in Fig. 6.4, which allow understanding, in simplified terms, the transition form superfluidity towards turbulence when the speed of the fluid is larger than the sound speed in the fluid. In part (a) of the figure are sketched the transformation of the dispersion of polaritons as a function of density. This corresponds to the Bogoliubov transformation and should be accompanied by the appearance of a "*ghost branch*" [48, 49] that we will not discuss further in the present work. The linearized dispersion of the Bogoliubov dispersion explains the absence of scattering of a superfluid at rest. When the fluid is given some speed, the dispersion is modified as shown in Fig. 6.4b. If the speed is smaller than the speed of sound, we obtain the case in blue in Fig. 6.4b, where scattering stays impossible for moving polaritons. If, on the contrary, the speed is larger than the sound speed (see the red curve in Fig. 6.4b, where in fact the speed as been kept constant, but the sound speed has decreased because the density of the fluid has decreased), scattering becomes possible.

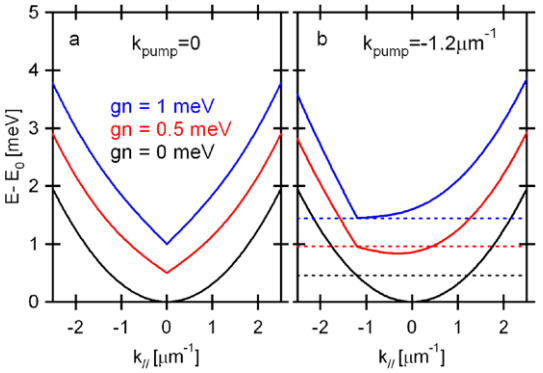

Fig. 6.4 *Bogoliubov excitation spectra*. (**a**) Plots of the excitation spectra, of the polaritons excited at $k = 0$, with the Bogoliubov transformation and the blueshift due to polariton-polariton interaction. (**b**) Same, with an excitation at 1.2 μm^{-1}. When the density is too small, scattering of the polariton flow is possible (*red curve*). Figure adapted from the PhD of Gael Nardin [43]

Frictionless flow of a polariton wave packet has been first reported in a triggered OPO scheme [35], and the superfluid regime has been demonstrated in a resonantly injected polariton fluid [36, 50]. In these last papers, depending on the fluid velocity, superfluid or Čerenkov regimes were observed when the polariton flow scatters on a defect. Additionally, quantized vortices have been optically imprinted in the optical parametric oscillator (OPO) configuration [51, 52].

6.2 Superfluidity and Turbulence in Microcavities

As explained above, at too large speeds, similarly to conventional superfluids, quantum turbulence is expected to appear in polariton fluids at the breakdown of superfluidity. When the sound velocity in the system is decreased, hydrodynamic nucleation of quantized vortices should occur when the local fluid velocity in the vicinity of the obstacle becomes larger than the sound velocity. A Čerenkov regime, accompanied by soliton lines, follows when the velocity of the fluid far from the obstacle becomes greater than the speed of sound

In our samples, the sound velocity c_s for the polariton fluid depends on the polariton density n, following $c_s = \sqrt{ng/m_{LP}}$ (where g is the polariton-polariton interaction constant and m_{LP} the lower polariton effective mass). The sound velocity can therefore be controlled simply by tuning the excitation power (see Fig. 6.4a). In the very low-density regime (black curve in Fig. 6.4b), the possibilities of elastic scattering due to disorder (the intersection with the dashed line) allow the formation of the so-called "*Rayleigh ring*" in the two-dimensional momentum space [53–55], see Fig. 6.5. Under high excitation density (blue curve), superfluidity arises because the dispersion no longer offers the possibility of Rayleigh scattering. This prevents any interaction of the polariton fluid with disorder. This collapse of the Rayleigh

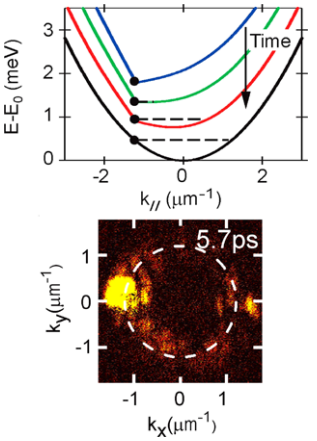

Fig. 6.5 *Time variation of the Bogoliubov excitation spectra*. *Upper panel*: Theoretical dispersion curves. Under low excitation density, the system is in the linear regime, and the dispersion is parabolic in the small momentum approximation (*black curve*). Polariton population is given by the *black dot*, and the intersection of the *dashed line* with the dispersion gives the possibility of scattering events, which conserve energy. When increasing the pump power, the excitation spectrum is modified, going from a Cerenkov regime (*red curve*) to a superfluid regime (*blue curve*). The *black arrow* schematically shows the time evolution of the dispersion curve during the decay of the polariton population. *Lower panel*: Rayleigh ring in the low intensity regime, at a delay of 5.7 ps after the excitation pulse: no relaxation is observed. Figure adapted from the PhD of Gael Nardin [43]

ring has been experimentally demonstrated by Amo et al. [35, 36]. In this case, the Landau criterion is fulfilled, as the fluid velocity is smaller than the sound velocity.

This case corresponds to a Mach number (defined as the ratio of the fluid velocity v over the sound speed c_s) smaller than one ($v/c_s < 1$). The red dispersion curve depicts a Čerenkov regime, where the fluid velocity is greater than the sound speed ($v/c_s > 1$). The green dispersion curve in Fig. 6.5 shows an intermediate regime, corresponding to a Mach number of $v/c_s = 1$. In such a case, the dispersion curve is flat on a finite distribution of wave vectors, offering a contiguous reciprocal space region in which Rayleigh scattering can occur. Using a pulsed excitation, we expect to pass through all these regimes (as schematically indicated by the black time arrow in Fig. 6.5, upper panel, after the polariton injection, leading to an extremely rich dynamics).

6.3 Momentum Space Dynamics

We first discuss the dynamics in momentum space. At low excitation pump power, the system is in the linear regime (black curve in Fig. 6.5). In this case, a Rayleigh ring (Fig. 6.5, lower panel) appears as the result of elastic scattering of polaritons on the disorder of the microcavity [56]. The Rayleigh ring disappears together with the

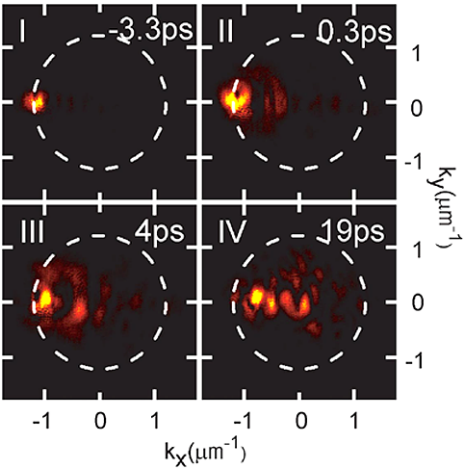

Fig. 6.6 *Disappearance of the Rayleigh ring*. Successive recordings of the reciprocal space emission of the microcavity. In the present case, where the excitation density is large enough to allow polariton-polariton scattering, and too small to allow a superfluid regime, a slow down of the fluid is obtained, evidenced by the concentration of polaritons around small wavevectors. Figure adapted from the PhD of Gael Nardin [43]

polariton decay time. At higher pump power, the time-dependent polariton density will make the dispersion curve vary with time, passing through the different cases depicted in Fig. 6.5. The four panels of Fig. 6.6 show different snapshots of this evolution.

At first the excitation laser creates a wave packet with an in-plane momentum defined by the excitation laser angle to the sample surface. Then, as time evolves, we observe the filling of the interior of the Rayleigh ring first due to inelastic scattering. This results in an average slowing down of the wave packet. At the same time, the density of the polariton fluid decays due to the short lifetime of polaritons.

This observation may be understood as follows: the decay of the polariton density is accompanied by a decrease of the sound velocity. When $v \approx c_s$ (green curve in Fig. 6.5), elastic scattering of the polariton wave packet on the disordered landscape fills a contiguous region inside the Rayleigh ring, relaxing the wave vector conservation rule. This is of crucial importance for the vortex nucleation mechanism, as vortices can appear only when a significant quantity of fluid has been slowed down behind the obstacle and a contiguous and sufficiently broad region of the reciprocal space provides the necessary wave vectors to form the rotating flow around the phase singularity.

The observed behavior can be qualitatively reproduced using the generalized Gross-Pitaevskii model previously introduced by Ciuti and Carusotto for exciton polaritons [34, 57]. We solve iteratively this generalized Gross-Pitaevskii equation with parameters adjusted to the experiment. We briefly summarize this model now. The time evolution of the quantum fluid can be obtained, in a simplified way by only considering the lower polariton mode ψ and can be described by:

$$i\hbar\frac{d}{dt}\psi(\boldsymbol{r},t) = \left(-i\frac{\gamma}{2} + \sum_k \hbar\omega_k |k\rangle\langle k| + g\left|\psi(\boldsymbol{r},t)\right|^2\right)\psi(\boldsymbol{r},t) + V\psi(\boldsymbol{r},t) + F_k(\boldsymbol{r},t)$$

The potential V is modeled as a 3 μm large and 1 meV high obstacle in the first series of experiments that we are describing here. Our model accounts for the dissipation

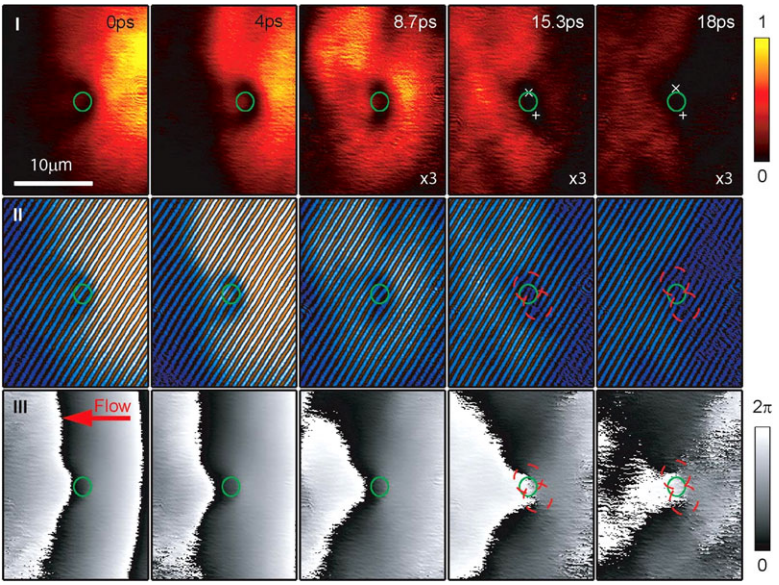

Fig. 6.7 *Superfluid behavior without turbulence*. The *three rows* show the polariton density (**I**), the fringes of the measured interferogram, in a saturated color scale (**II**), and the polariton phase (**III**). The estimated obstacle position is indicated with a *green circle*, and the polariton flow goes leftward (see the *red arrow* in the *third row*). At low speed, the wavepacket passes the obstacle without any turbulence. When the polariton population has significantly decayed (*last two columns*), a vortex pair is created at the boundary of the obstacle. The pair remains stitched to the defect for several picoseconds, and disappears in the noise when the polariton population has decayed. The density scale has been multiplied by 3 for the last 3 panels of the *first line*, for sake of visibility. Figure adapted from the PhD of Gael Nardin [43]

of polaritons, at rate $\gamma/\hbar$, after a 1 ps long initial excitation of the system through $F_k(\boldsymbol{r}, t)$. The polariton–polariton interaction is assumed to depend linearly on the polariton density $|\psi(\boldsymbol{r}, t)|^2$ through a phenomenological coefficient g. The lower polariton dispersion is approximated to a quadratic dispersion with effective mass m_{LP}. The parameters used in the simulations are: $\gamma = \hbar/15$ ps, $g = 0.01$ meV μm^2, $\hbar\omega_k = \hbar^2k^2/2m_{LP}$ with $m_{LP} = 0.7$ meV ps^2 μm^{-2}. The excitation intensity for the high excitation experiment corresponds to a maximal polariton density of 120 μm^{-2} on 20 μm large spot.

6.4 Real Space Dynamics, Superfluid Behavior

At low speed, as evidenced in Fig. 6.7, a very clear superfluid behavior is observed. This is in close agreement with the observations that have been performed by Alberto Amo and coworkers [35, 36, 42]. The three rows of Figs. 6.7 to 6.9 display experimental images of respectively (I) the normalized polariton density, (II) the

fringes of the interferogram (in a saturated color scale, to track the fork-like dislocations), and (III) the phase of the polariton gas, for different times after the excitation pulse. The estimated obstacle position is indicated with a green circle, and the polariton flow goes leftward (see the red arrow). The homodyne setup a not only allows to access the dynamics of the polariton fluid density, but also its phase, whose gradient provides the local in-plane momentum of the fluid.

This superfluid regime is straightforwardly observed in the high excitation density regime, giving a fast sound velocity, and small excitation angle, leading to a small speed of the polariton fluid. While the fluid density passes apparently unaffected over the defect, the phase structure allows to evidence a progressive bending of the phase front, corresponding to the slowing down of the flow behind the obstacle. Eventually, at long time, i.e. when the fluid density has decayed, a unique vortex pair is nucleated in the vicinity of the defect. at long time, when only a fraction of the polariton population is remaining. Interestingly, this low velocity regime provides the most accurate estimation of the obstacle effective size, given by the dark region in the third column of Fig. 6.7I. The defect shows transverse size of about 5 μm and a size in the direction of the flow of about 2 μm.

6.5 Real Space: Vortex Dynamics

Let us now discuss the dynamics of the vortex nucleation and migration. Figure 6.8 displays experimental images of (I) the normalized polariton density, (II) the fringes of the interferogram and (III) the phase of the polariton gas, for different times after the excitation pulse. In the first column ($t \sim -0.7$ ps), the phase structure imposed by the excitation laser is nicely observed. The phase gradient directly allows one to extract the flow velocity, which is homogeneous and measured to be $1.1 \pm 0.2\ \mu\text{m}\,\text{ps}^{-1}$, in agreement with the injected velocity of $1.1 \pm .3\ \mu\text{m}\,\text{ps}^{-1}$.

In the following, the fluid velocity will be specifically measured on two points of interest: behind the obstacle and on the equator of the obstacle perimeter. The corresponding measurement areas are indicated in Fig. 6.8 by a dashed white square and a plain white square, respectively. In the second column (1.3 ps), a low-density region appears in the wake of the defect, along with a curvature of the wavefront. The measurement of the phase gradient clearly shows that the polariton flow slows down in the wake of the obstacle. The flow velocity behind the obstacle is shown in Fig. 6.9a: a monotonous slowing down of the flow is observed.

In the third column of Fig. 6.8 (3.7 ps), the flow velocity is measured to be $0:9 \pm 0:2\ \mu\text{m}\,\text{ps}^{-1}$, dropping to $0:3 \pm 0:2\ \mu\text{m}\,\text{ps}^{-1}$ in the fifth column (9.3 ps), whereas the flow velocity measured on the obstacle perimeter, shown in Fig. 6.9b (cyan curve), remains above $0.95 \pm 0.35\ \mu\text{m}\,\text{ps}^{-1}$ on this time range. As expected in a quantum fluid, where the circulation is quantized, the phase accumulation between the very slow wave behind the obstacle and the main flow has to be accompanied by the nucleation of quantized vortices [58].

The fluid velocity vector field is extracted from the phase gradient of the polariton field. The values of Fig. 6.9a are obtained by fitting the slope of the phase profile

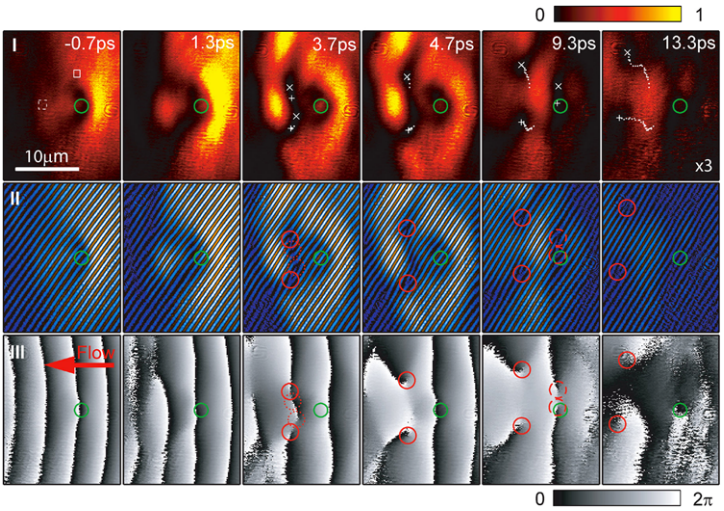

Fig. 6.8 *Experiment: vortex nucleation regime*. Experimental images for high excitation density ($P_{exc} = 2.1$ mW) and high fluid velocity. The wavepacket propagates towards the left, with an initial momentum of 1.2 μm^{-1}. The *three rows* show (**I**) the polariton density, (**II**) the fringes of the measured interferogram, (**III**) the polariton phase. In the *first column* (−0.7 ps), the phase structure is fully imposed by the excitation pulse. *Second column* (1.3 ps): the polariton fluid starts to feel the effect of the obstacle, resulting in a zone of low polariton density in the wake of the obstacle, and a bending of the polariton wavefront. *Third column* (3.7 ps): nucleation of vortices in the wake of the obstacle. Vortices are indicated with *white markers* (x for vortex, $+$ for anti-vortex) on the density plot and are circled in *red* on the interferogram and on the phase plots. *Dotted circles* indicate short-lived vortices. *Fourth*, *fifth* and *sixth columns* (from 4.7 to 13.3 ps): motion of the long-lived vortex pair. Previous vortex positions are indicated with *white dots* on the density plots, allowing us to follow the vortex motion. *Dashed circles* in the *fifth column* (9.3 ps) indicate the position of a new vortex pair, which moves on a few microns before disappearing due to the decay of the polariton population. For the sake of visibility, density values are multiplied by a factor three in the last density plot. Figure adapted from the PhD of Gael Nardin [43]

in the region of interest. The error bars take into account the standard deviation of the linear fit, as well as a systematic error coming from the determination of the phase gradient induced by the set-up alignment (see Ref. [40] for how this reference phase gradient can be determined). The value of the local sound velocity is determined from the density map, originally in arbitrary units, which needs to be scaled to the blue-shift ng. We have access only to the spatially and temporally averaged blue-shift in the polariton dispersion, which is measured to be 0.8 meV. Assuming that the major contribution to this blue-shift comes from the beginning of the dynamics, when the maximal population density is reached, we scale the density maps to the blue-shift. This allows us to extract a rough estimation for the local speed of sound along the dynamics (it more probably gives a lower bound to its value, as the averaging of the blue-shift yields an underestimation of its value). We consider an error in the local sound velocity, which takes into account the standard deviation on the averaging in the region of interest, as well as a systematic error on the scaling method, estimated to 25 %.

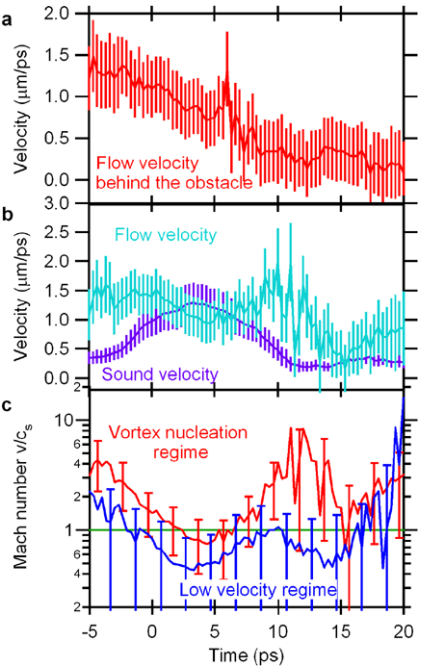

Fig. 6.9 *Quantitative velocity measurements*. (**a**) Flow velocity measured behind the defect (in the region delimited by the dashed white square in Fig. 6.8I), for the vortex nucleation regime. An almost constant slow down can be observed. The small jump observed at around 6 ps is due to a phase singularity passing in the vicinity of the region of interest. (**b**) Flow velocity and sound velocity measured on the obstacle perimeter (in the region delimited by the plain white square in Fig. 6.8I), for the vortex nucleation regime. The error bars on the velocity take into account the standard deviation of the linear fit of the phase gradient, as well as a systematic error coming from the determination of the phase gradient induced by the setup alignment. The error bars on the sound velocity take into account the standard deviation on the averaging in the region of interest, as well as the systematic relative error on the scaling method. (**c**) *Red curve*: Mach number on the obstacle perimeter, for the vortex nucleation regime. *Blue curve*: Mach number on the obstacle perimeter, for the low velocity regime. The *green line* at $M = 1$ indicates the limit between subsonic flow (*below the line*) and supersonic flow (*above the line*). Figure adapted from the PhD of Gael Nardin [43]

The third column of Fig. 6.8 (3.7 ps) exemplifies the nucleation of vortices. The ripping of the phase front is clearly visible (this needs good eyes at 3.7 ps, but is very clear at 4.7 ps). Vortices are unambiguously identified both by a minimum of density and a fork-like dislocation in the interferogram, accompanied by a phase singularity in the phase structure. They are indicated by white markers on the density map (x for a vortex and + for an anti-vortex) and red circles on the interferogram and phase maps. At the onset of vortex nucleation, four of them are observed in the wake of the defect. Rapidly, within less than 2 ps, two of them (circled with dotted lines) merge together and disappear.

In our experiments, the size of the obstacle is large enough to nucleate one vortex pair only: as discussed above, the defect size measured to be about 5 µm across the

direction of the flow. The defect size however appears to be too small to allow the nucleation of four vortices. The remaining vortex pair flows downstream, and we track its motion (white dots on the density map) for 10 μm, until the decay of the polariton population.

In atomic condensates, the vortex trajectories consist in closed loops because of the trapping potential [59]. In microcavities, the polariton vortices are free to propagate in the plane. The wandering nature of their tracks is presumably due to the disorder landscape. Their common change of direction with respect to the direction of the flow is attributed to the microcavity wedge, which indeed provides a potential gradient. Interesting also is to note the additional vortex pair created at a delay of 9 ps (visible in the fifth column, dashed circles). This pair propagates only a few micrometers and then disappears in the noise due to signal decay. This does not allow us to define a shedding frequency, as this latter is expected to depend on the fluid density [60] which varies with time in our experiment.

6.6 Real Space Dynamics, Čerenkov Case

Figure 6.10 now shows the scattering of a low-density polariton wavepacket on the same obstacle, for an excitation power of 15 μW and an excitation angle corresponding to a pump in-plane momentum of 1.2 μm^{-1}. As a result, because of the low polariton fluid density, the speed of sound in the system is low ($c_s = \sqrt{ng/m}$). We devised the excitation scheme so that the observe regime can be seen as strongly supersonic. In this regime, the polariton gas normally interact with disorder, and scatters elastically on the obstacle.

In the momentum space, a Rayleigh ring is visible, as shown in Fig. 6.5. In real space, a parabolic wavefront is created that corresponds to interference between the propagating polariton fluid and the scattered polaritons. In the first column (−0.7 ps), the phase structure is imposed by the excitation laser. The fluid density already shows the precursors of the parabolic wavefronts, though. These wavefronts are much more defined in the second column, where a nontrivial phase structure has developed: finite phase jumps can be seen between the successive wavefronts. In the third and fourth columns, the decay of the polariton population can be observed.

The Čerenkov case (or low density regime) has been observed in similar conditions in the experiments of Amo et al. [36, 42, 61] following the predictions of Carusotto and Ciuti [34]. The very high speed of the quantum fluid with respect to the speed of sound does not allow anymore for the creation of quantized vortices.

6.7 Conditions for Vortex Nucleation

In order to be able to determine the nucleation conditions in terms of polariton density and fluid velocity, we performed the same experiment with different excitation angles and powers. According to theoretical predictions [49, 58] different

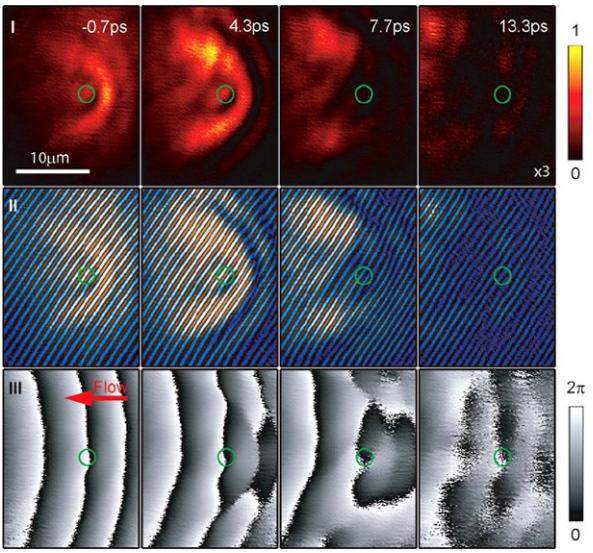

Fig. 6.10 *Experiment: low density/Čerenkov regime*. Experimental images of the scattering of the polariton wavepacket on the structural defect (indicated by a *green circle*), for the low-density regime ($P_{exc} = 15\ \mu W$). The pump in-plane momentum is $1.2\ \mu m^{-1}$. The *three rows* show the polariton density (**I**), the fringes of the measured interferogram, in a saturated color scale (**II**), and the polariton phase (**III**). With this low excitation density, the polariton wavepacket undergoes elastic scattering on the obstacle, leading to parabolic interference fringes between the propagating polariton and the backscattered ones. The phase resolution allows evidencing a finite phase jump between the different parabolic precursors. Density values are multiplied by a factor three in the last density plot, for the sake of visibility. Figure adapted from the PhD of Gael Nardin [43]

flow regimes are indeed observed, depending on the Mach number. Turbulence is expected in the wake of the obstacle when the local velocity on the perimeter of the impenetrable obstacle becomes supersonic. The original work of Frisch et al. [4] also predicts that this critical velocity is attained on the obstacle perimeter when $v/c_s \sim 0.4$ far from the defect, in a homogeneous and steady flow.

In our case, it is not possible to use such a criterion, as we have a finite-size, time-dependent population, and most likely a penetrable obstacle. The only way to determine the experimental conditions for vortex nucleation is therefore to look at the local fluid velocity and sound velocity on the obstacle perimeter. The fluid velocity vector field can be directly extracted from the polariton field phase gradient, the local speed of sound can be obtained from the density map. It is therefore possible to estimate the value of the local Mach number v/c_s on the obstacle perimeter along the dynamics. These values, computed in the area delimited by the plain white square in Fig. 6.8, are displayed in Fig. 6.9b (Cyan curve). This allows us to check that, indeed, a value of $v/c_s \sim 1$ is obtained on the obstacle perimeter at the onset of the vortex nucleation mechanism.

Reducing the excitation angle, we have probed different wavepacket momenta, and observed the nucleation of vortices in the wake of the obstacle down to a critical

initial fluid momentum of 0.6 μm^{-1}. Below this characteristic momentum, the wave packet passes the obstacle without any visible perturbation. The values of the Mach number on the obstacle perimeter for this regime are plotted in blue in Fig. 6.4b, for comparison with the vortex nucleation regime. Our measurements show that the flow remains mostly subsonic during the major part of its dynamics. Finally, we have also varied the average excitation power and observed a threshold (at 0.04 $\mu W\,\mu m^{-2}$) under which no vortices are nucleated in the wake of the obstacle.

Instead, parabolic backscattering standing waves are visible on the polariton density maps, and a Rayleigh ring is visible in the Fourier plane, as shown in Fig. 6.5. This corresponds to a standard elastic scattering process, where the flow is supersonic, as the polariton density and consequently the sound velocity is very low. In this low-density limit (also called the linear regime), the interaction energy is negligible with respect to the kinetic energy.

6.8 Insights from Numerical Simulations

The three typical behaviors that we have highlighted here are extremely well reproduced by our numerical simulations. This is true for vortex pair nucleation, the unperturbed flow and the standard Rayleigh scattering in the low-density flow. Our simulations take into account the pulsed excitation, the finite spot size and the exponential decay of the polariton population. The different simulations are highlighted in the three Figs. 6.11, 6.12 and 6.13, the main findings being summarized on Fig. 6.14.

Similarly to our experimental findings, the low-velocity regime remains subsonic for a longer time than the vortex nucleation regime (see Fig. 6.11). The simulation shows that the fluid passes around the obstacle without being affected. Only at longer times, when the density of the fluid has decayed, bringing the sound speed below the speed imposed on the fluid, do vortices appear. They appear at the backside of the obstacle, where the speed is the smallest. The vortex pair stays pinned on the obstacle for some time, and is then dragged away. Such an effect at long time has not been observed in our experiment, presumably hidden in the fluctuations of the phase at long times due to the low intensity of the signal.

The next simulation (Fig. 6.12) corresponds to the supersonic regime, where the injected density is kept small, and therefore the sound speed is quite slow. In such a case, in the simulation as in the experiments (see Fig. 6.10), no vortices are observed and the interaction with the defect created a parabolic wave due to the scattering on this defect. The Rayleigh ring is computed in the simulations, once again in very good agreement with the experiment.

Figure 6.13 now shows the simulation in a case where vortex nucleation is observed (see Fig. 6.8 for the experiment). There is a very nice qualitative agreement between the results of the simulation and the experimental observations. This allows us to go into more detail with the simulation where we can probe details difficult to attain in an experiment.

Consistently with the argument originally developed by Frisch et al. [4] for the transition to turbulence in a superfluid, we find in the simulation that the phase

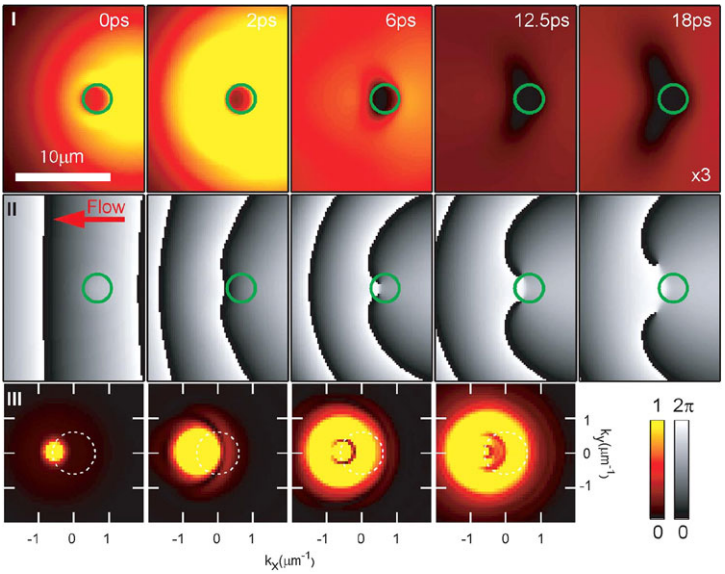

Fig. 6.11 *Simulations: low velocity regime*. Simulation of the low velocity regime, reproducing the features of the experimentally observed low velocity regime of Fig. 6.7. (**I**) and (**II**) density and phase profiles of the polariton fluid. A vortex pair is nucleated at long time, and stay on the defect for several picoseconds. Simulation show that the vortex pair is eventually dragged away form the defect at long time, when the fluid density is very low. This effect is not observed in experiment, as the low fluid density at long times hinder the measurement of the phase. Density values are multiplied by a factor three in the last density plot, for the sake of visibility. (**III**) Momentum space dynamics. The *white dashed circle* indicates the position that would be expected for a Rayleigh ring. The position and size of the defect are indicated by the *green circle*. Parameters: $k_{pump} = 0.6\ \mu m^{-1}$, excitation power 120 μm^{-2} on a 20 μm large spot. Figure adapted from the PhD of Gael Nardin [43]

accumulation resulting in vortex nucleation starts at the precise time when the fluid velocity becomes equal to the sound speed (when $v/c_s = 1$) on the obstacle equator. The nucleation of the vortex pairs occurs just after this event. The higher the initial velocity, the closer the vortex nucleation will occur to the initial phase accumulation. The vortices are then dragged away from the obstacle at later times, in a time range corresponding to the experimental findings.

A snapshot of the computed phase profile is displayed in Fig. 6.14, for the vortex nucleation regime, at the onset of the first vortex pair nucleation (this correspond to a time delay of 3.5 ps after the excitation, see the corresponding panel in the second column of Fig. 6.13). Local values of the Mach number are represented by colored lines. The thick green line corresponds precisely to a Mach number of 1.

In order to compare further the experimental findings of Fig. 6.9, with the simulations of Fig. 6.13, we plot in Fig. 6.14b the time evolution of the Mach number in a small region close to the equator of the obstacle (black circle at the center of Fig. 6.14a), using simulation parameters corresponding to the three flow regimes described previously (vortex nucleation regime, low velocity regime and low-density

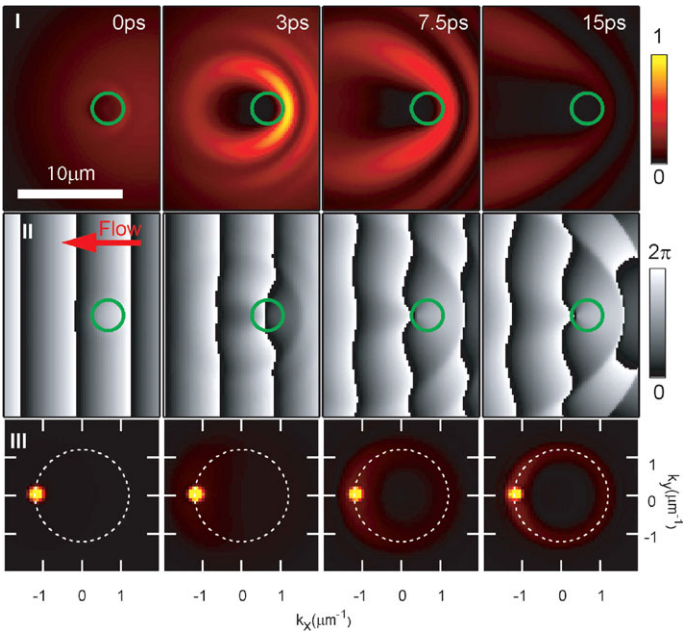

Fig. 6.12 *Simulations: low density regime*. Simulation of the low density, supersonic regime, reproducing the experimental features of the experimentally observed low density regime of Fig. 6.8. (**I**) and (**II**) density and phase profiles of the polariton fluid, displaying parabolic scattering wavefronts. (**III**) Momentum space dynamics, showing the appearance of a Rayleigh scattering ring. The *white dashed circle* indicates the expected position of the Rayleigh ring. Position and size of the defect are indicated by the *green circle*. Parameters: $k_{pump} = 1.2\ \mu m^{-1}$, excitation power $1.2\ \mu m^{-2}$ on a 20 μm large spot. Figure adapted from the PhD of Gael Nardin [43]

regime). Whereas the low-density experiment always lies in the supersonic region (black curve), the high-density experiments (blue and red curves) remain subsonic for a significant part of their dynamics.

To conclude this part, our Gross-Pitaevskii numerical simulations allow us to evidence the role of the polaritonic nonlinearities in the nucleation process of vortices. Indeed, no vortices are nucleated in the wake of the obstacle if the interaction constant is set to 0. The equations therefore allow us to differentiate clearly hydrodynamic nucleation process from linear optical processes, such as the generation of vortex lattices, whenever three or more plane waves interfere.

6.9 Dark Solitons and Vortex Streets

Aside from quantized vortices, perturbations of quantum fluids can also lead to the creation of solitary waves called solitons resulting from the compensation between dispersion and particle interaction [62, 63]. In fact, the Gross-Pitaevskii equations that we are using are closely related to the wave equations in nonlinear optics that

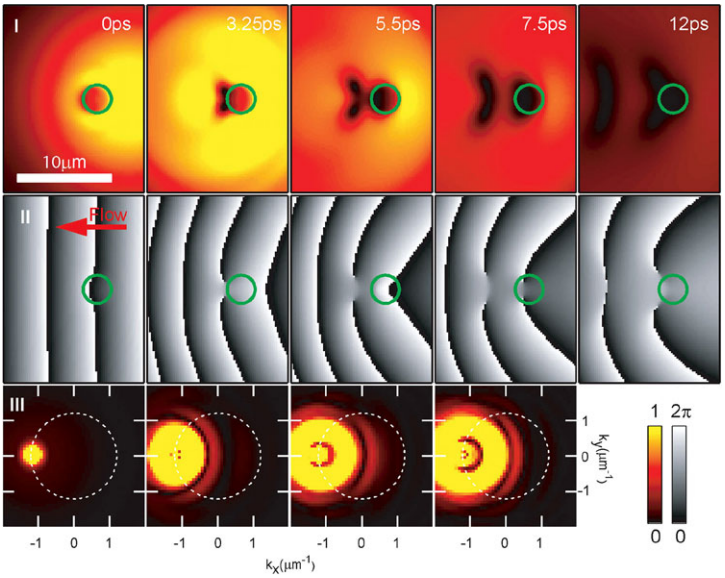

Fig. 6.13 *Simulations: vortex nucleation regime*. Simulation of the vortex nucleation regime, reproducing the features of the experimentally observed vortex nucleation regime of Figs. 6.7 and 6.8. (**I**) and (**II**) density and phase profiles of the polariton fluid, displaying the hydrodynamic nucleation of two vortex pairs. (**III**) Momentum space dynamics, showing a spreading into the interior of the Rayleigh ring. The *white dashed circle* indicates the position that would be expected for a Rayleigh ring. Position and size of the defect are indicated by the *green circle*. Parameters: $k_{pump} = 1.2\ \mu m^{-1}$, excitation power 120 μm^{-2} on a 20 μm large spot. Figure adapted from the PhD of Gael Nardin [43]

allow describing the propagation of light pulses in optical fibers. In the case of optical fibers, bright solitons are the result of a precise compensation between the self-phase modulation in the fiber and the chromatic dispersion [64]. Bright solitons propagate in fibers without changing their shape.

In condensates, in the particular case of repulsive interaction, dark solitons are expected. Dark solitons are density depressions move in the fluid while keeping a constant shape. They are characterized by a π phase jump across the density minimum. Since the first theoretical prediction [65], dark solitons have been observed in a variety of systems such as for example thin magnetic films [66]. They have recently attracted considerable interest in the field of atomic Bose-Einstein condensates [67] because they constitute excitations of the condensate that spontaneously occur upon the phase transition.

Dark solitons are often considered as the dispersive and nonlinear analog of shock waves of supersonic motion [68]. The production of dark solitons by phase imprinting in BEC has recently been reported [69, 70]. Such observations have triggered a clear interest towards their possible hydrodynamic formation and stability. In particular, dark solitons are known to be unstable with respect to transverse perturbations [71, 72] and to eventually decay into other more stable structures [73–75].

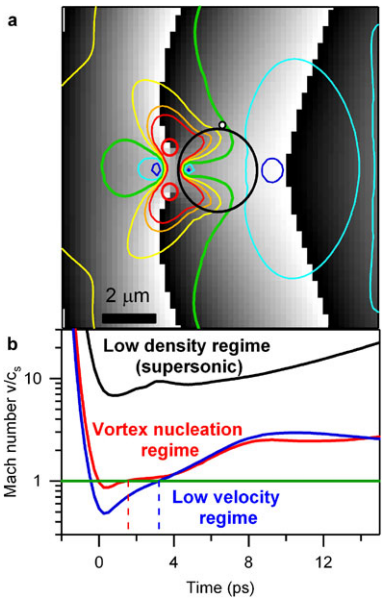

Fig. 6.14 *Nucleation criterion: numerical evidence*. (**a**) Numerical simulation of the phase profile, with simulation parameters corresponding to the vortex nucleation regime, at the onset of vortex nucleation. The obstacle is indicated with a *black circle*, and the flow is directed leftward. The *thick red circles* show the vortex positions. *Color lines* indicate lines of equal Mach number. The *green thick line* indicates a local Mach number of 1, *blue lines* indicate a local subsonic flow ($v/c_s < 1$), *yellow* to *red lines* indicate a local supersonic flow ($v/c_s > 1$). (**b**) Evolution of the Mach number at the equator of the obstacle (*small black and white circle* in (**a**)), using simulation parameters corresponding to the vortex nucleation regime (*red curve*), to the low velocity—mainly subsonic—regime (*blue curve*) and to the low density—linear—regime (*black curve*). The phase accumulation starts when the fluid velocity crosses the sound velocity ($v/c_s = 1$) on the obstacle equator (*dashed lines*) resulting in a systematic way in the nucleation of vortices. Figure adapted from the PhD of Gael Nardin [43]

In this paragraph, we follow on the previous experiments on turbulence, using the same homodyne detection system, with the same sample, however, this time, the defect is an engineered defect (mesa) that allows a better control on the experimental parameters [76]. Solitons are indeed predicted to appear for Mach numbers larger than 1 with values depending on the nature of the obstacle. Our experiments follow on observation of dark solitons in polariton fluids by Amo et al. [77], as well as of bright solitons using the TOPO technique [78].

Figure 6.15 shows an example of the scattering dynamics of a supersonic polariton wave packet against a 3 μm mesa (green solid circles at the center of the images). Polaritons are injected with a 1.5 μm^{-1} initial momentum and a pump power of 5 mW distributed over a laser spot of about 20 μm diameter (in all panels flow is from the bottom to the top). Using such conditions of density and speed of the polariton fluid allow us to set unambiguously the experiment in the supersonic regime. The position of the laser spot is indicated by a white dashed circle in the

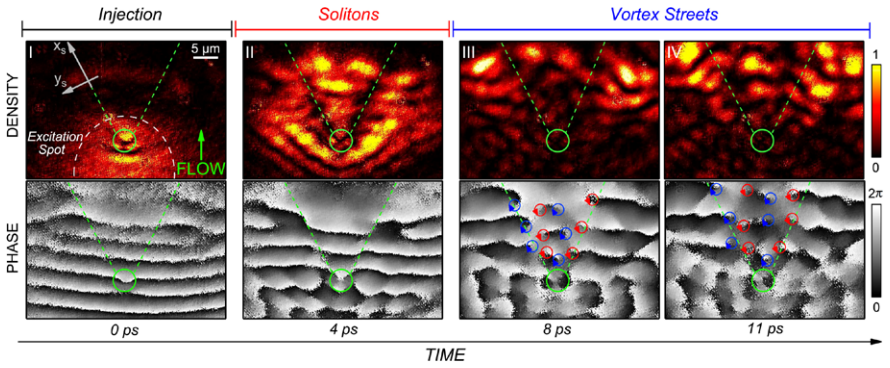

Fig. 6.15 *Dark solitons in polariton fluids*. Time evolution of density (*upper panel*) and phase (*lower panel*) of a polariton wave packet scattering on an engineered circular obstacle (*solid circles*) of 3 μm diameter. Polaritons are injected at t 1/4 0 ps with a 1.5 μm^{-1} initial momentum and a pump power of 5 mW in the vicinity of the mesa (column **I**). Solitons (**II**) are visible few picoseconds later and are characterized by low density straight lines and a phase shift. The soliton decay (**III**) comes along with the breaking of the phase fronts and the formation of vortex streets (*circular arrows*). The latter is pointed out by the apparition of several density minima coinciding with phase singularities. The motion of vortices is tracked along the flow during polariton lifetime (**IV**). Figure adapted from the PRL of Gabriele Grosso [76]

density profile of Fig. 6.15I. Looking carefully at the figure, it may be observed that our injection scheme allows to excite some excited states of the mesa, which are characterized by bright lobes (see [79] and [80] for details).

The mesa provides a continuous perturbation on the condensate in motion that allows an hydrodynamic formation of solitons. The dynamics of a 2D fluid passing an obstacle and the soliton formation can be analyzed in both the lab frame and the fluid reference frame. In the fluid frame, the mesa moves in a fluid at rest, leaving behind perturbations, which expand as circular waves. Positive interference between such waves occurs tangentially to the circular waves resulting in the oblique soliton formation. Solitons subsequently move with respect to the fluid frame in the y_s direction whereas they grow in x_s direction in the lab frame (see Fig. 6.15I and Fig. 6.16).

Dark solitons are clearly visible as linear density minima on Fig. 6.15II, and underlined by the white straight dashed lines. The phase map allows to measure the phase jumps across the amplitude minimum. A few picoseconds after the polariton injection, solitons decay into vortex streets and disappear. The linear phase front of the soliton transforms into a set of singularities associated with density minima in the intensity map: a clear evidence for quantized vortices. The vortices are highlighted in the phase map by clockwise (blue) and anticlockwise (red) circular arrows. The density profile and the phase map during the formation of vortex-antivortex pairs along the vortex streets are plotted in Fig. 6.15III. The motion of vortices can then be tracked in order to retrieve their dynamical movement.

In order to be able to come to a more quantitative vision on the behavior of solitons, it is interesting to look at things along the direction of one of the two

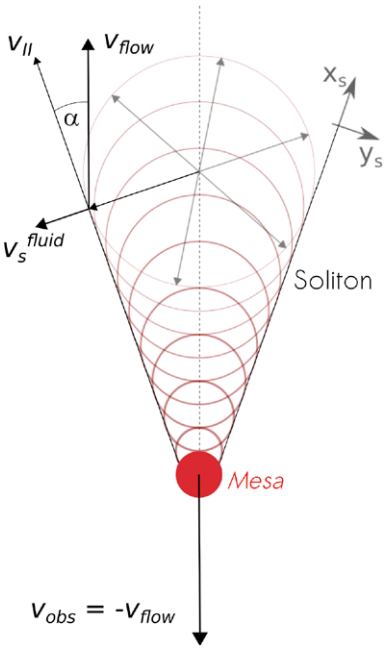

Fig. 6.16 *Solitons in the fluid frame*. Dynamics of a 2D fluid passing an obstacle in the fluid frame, showing the formation of dark solitons. The mesa moves with $\sim v_{flow}$ leaving behind perturbations which expand as circular waves. Positive interferences occur tangentially, resulting in the oblique soliton formation. The latter move in the y_s direction with respect to the fluid frame, whereas they grow along x_s direction in the lab frame

solitons in Fig. 6.15. In Fig. 6.16, we show, as a function of time, the intensity along the direction of one soliton line (x_s in Fig. 6.16). Figure 6.16 clearly show the pulse arrival at $t = 0$ and at the edge of the mesa. Immediately after the pulse arrival, solitons nucleate until about 4 ps after the initial pulse, and their presence is revealed by the long low-density region starting 5 μm away from the mesa. The soliton length has to be seen horizontally on this figure. The inset of Fig. 6.16 shows a characteristic soliton profile (black line) across its length. During the whole soliton lifetime, the soliton width has an almost constant value around 4.5 μm, independent of the laser pump power. The phase jump across the soliton line is shown in the inset. The phase jump, as expected, is close to the expected value of $\pi/2$.

Starting five picoseconds after their nucleation, solitons decay into vortex streets, in the present experimental conditions. The vortices may be visualized by the appearance of periodic modulations of the density. They are also revealed by sloping stripes of alternate density in Fig. 6.17. Low-density valleys represent the motion of the cores of quantized vortices. Once formed, vortices move with a constant velocity $v = 0.85$ μm/ps along the x_s axis, as demonstrated by the slope of the core trajectories in Fig. 6.17.

This velocity of the vortices must be compared with the projection of flow velocity over x_s, calculated by considering the ballistic propagation of polaritons with high momentum of injection [81]. As expected, vortices move along the flow with a velocity comparable to that of the fluid.

The same experiment has been repeated for a set of excitation powers ranging from 0.5 to 5 mW. Contrarily to what could come out from a naïve picture, we observe (see Fig. 6.17 lower panel (a)) that the solitons lines become less stable when

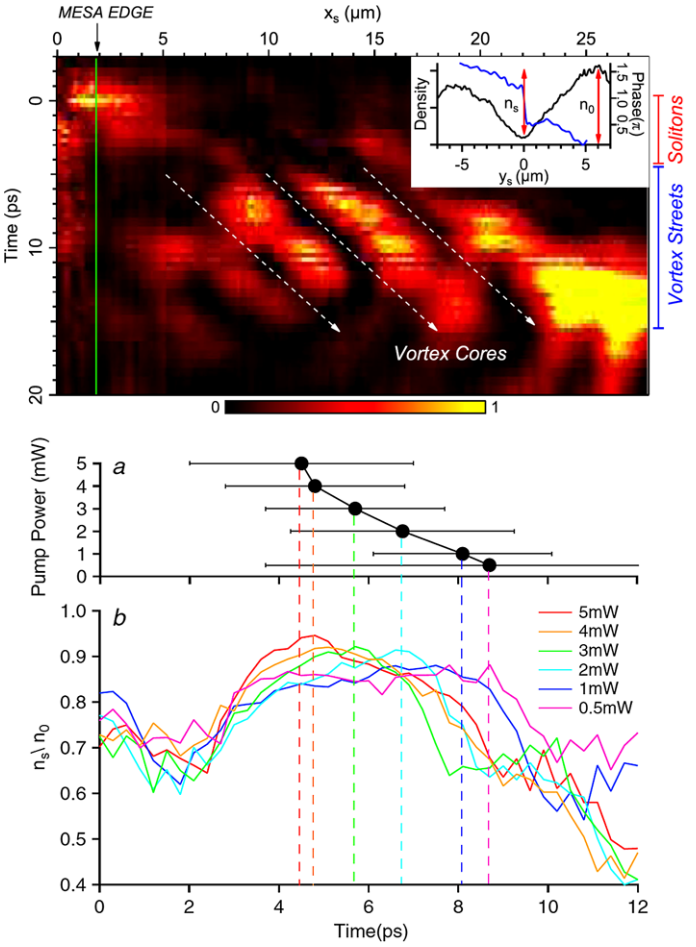

Fig. 6.17 *Decay of dark solitons into vortex streets*. *Upper panel*: Density map along the soliton direction x_s versus time. After the pulse arrival, the presence of a low density region stresses the nucleation of a soliton. Around 5 ps soliton decay occurs together with the formation of vortices is highlighted by the appearance of periodic modulation of the density in the region previously occupied by the soliton. The *inset plot* shows the density and the phase profile along y_s at $t = 3$ ps measured 7 μm away from the mesa center showing the characteristic soliton transversal shape and the phase jump across the minimum. *Lower panel*: (**a**) Pump power versus soliton lifetime. *Horizontal bars* show the time window at which vortex street formation occurs. *Central black spots* highlight that soliton lifetime increases while decreasing the pump power. (**b**) Time evolution of the soliton amplitude n_s over polariton fluid density n_0 for different pump powers. Maximum of the ratio is found in correspondence of the soliton decay into vortex streets (*dashed vertical lines*). Figure adapted from the PRL of Gabriele Grosso [76]

the excitation power is increased. The black dots in this figure show the average time delay for the vortex street formation. The horizontal bars represent the time window during which the soliton instability is observed, namely, the time between

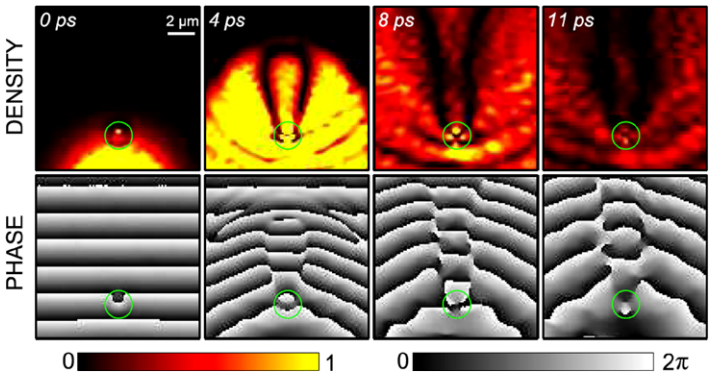

Fig. 6.18 Snapshots of the numerical simulations, based on the generalized Gross-Pitaevskii equations for the nucleation and the decay of dark solitons. The 2 μm diameter negative potential of 4 meV is indicated by a *green circle*. Flow direction is upstream. Random potential disorder is added in order to perturb solitons

the formation of the first and the last of the vortex pairs. Note that we consider the whole instability with vortices appearing progressively all along the solitons in region where the density and thus the fluid behavior could be at different stage of the soliton evolution.

Our observations are in agreement with previous studies on hydrodynamic nucleation of solitons and can be understood in terms of values of the Mach number in the obstacle perimeter. Solitons become more stable for higher values of M, which are obtained experimentally by decreasing the sound speed, namely, decreasing the polariton fluid density.

Our observations are supported by our theoretical investigations using the same Gross-Pitaevskii equation as before (see Fig. 6.18). Solitons nucleation in the wake of a negative potential and the subsequent decay into vortex streets is very well reproduced by the numerical simulations which take into account the pulsed excitation, the finite spot size of the laser, the exponential decay of the polariton population and the disorder potential. Snapshots of the simulated dynamics reproduce perfectly the time scale of the experiments. After the polariton injection, solitons are created almost instantly and transform in vortex streets after about 5 ps. After creation, vortices move along the flow as observed in the experiments. It is interesting to notice that, while keeping constant all the other parameters, no soliton decay is observed when the disorder potential amplitude is lowered to zero.

6.10 Conclusions

Quantum fluids of polaritons possess all interesting features of the more conventional condensates. Additionally, their very special character allows them to show adjustable interactions. Our experiments demonstrate here their great potential of

semiconductor for the study of turbulence in quantum gases. The key advantages of polaritons are the direct optical access to the polariton field (in both real and momentum spaces), the absence of a trapping potential and operation at easily achievable temperature (possibly even at room temperature in a very near future). This chapter, together with other chapters in this volume, has demonstrated first the superfluid behavior of the polariton fluid in appropriate conditions. We have also reported on the observation of the nucleation of vortices in the wake of an obstacle. The creation of dark solitons, and their decay into vortex streets has also been reported. All our observations have been compared with the dynamical solutions of Gross-Pitaevskii equations adapted to our system. The quality of the agreement, across a very wide range of experimental conditions is impressive.

Acknowledgements This work is inspired from the successive PhD works in my group (but not only as I integrate in this review the works of Pascale Senellart, Maxime Richard, Jacek Kasprzak and others), over the passed 15 years, starting from the PhD of Michele Saba, when we first envisaged the possibility of condensation of polaritons and designed an original way to produce efficient trapping of polaritons. It has been more particularly based on the PhD work of Gael Nardin, and on the ongoing work of Gabriele Grosso. The sample that we have used in the present study has been grown By François Morier-Genoud, with the very clever techniques allowing to prepare the mesas. This work has been made possible by what I call the dream team of LOEQ with, in order of appearance on stage, Stefan Kundermann, Jacek Kasprzak, Reda Idrissi Kaitouni, Ounsi El Daïf, Konstantinos Lagoudakis, Taofiq Paraïso, Gael Nardin, Roland Cerna, Verena Kohnle, Francesco Manni and Gabriele Grosso. It has also been supported very strongly by a group of extremely talented postdocs, that I wish to congratulate warmly for their outstanding work: Maxime Richard, Augustin Baas, Thierry Guillet, Barbara Pietka and, last but not least Yoan Léger. I also would like to convey my most sincere thanks to the theoreticians who allowed us to understand our results, by spending enough time with us, and by putting into simple words the results of their equations. In particular, Natalia Berloff, Michiel Wouters, Vincenzo Savona, Cristiano Ciuti, Alexei Kavokin and Yuri Rubo deserve very special acknowledgements. Antonio Quattropani and Paolo Schwendiman have also helped with many discussions and their indefectible support of theorist-experimentalist collaborations. Last, but not least, this work would not have been possible without the very close collaboration with the group of Dang in Grenoble, and in particular without the very high quality samples prepared by Régis André. The work has been carried out within the framework of the Quantum Photonics National Center of Competence in research financed by the Swiss National Science Foundation through the *Quantum Photonics* National Center of excellence in research and through successive SNF projects 2000020-135003, 200020-134789, 206021-128816, 206021-121496, 200020-107612. Complementary funding for conferences and meetings has been obtained through the Latsis Foundation, the Polatom network of the European Science Foundation. A King Saud University associate professorship is also deeply acknowledged.

References

1. H. Bénard, The cellular whirlpools in a liquid sheet transporting heat by convection in a permanent regime. Ann. Chim. Phys. **23**, 62–101 (1901)
2. M.C. Cross, P.C. Hohenberg, Pattern formation outside of equilibrium. Rev. Mod. Phys. **65**, 851–1112 (1993)
3. P. Bergé, Y. Pomeau, C. Vidal, *Order Within Chaos: Towards a Deterministic Approach to Turbulence* (Wiley, New York, 1986)
4. T. Frisch et al., Transition to dissipation in a model superflow. Phys. Rev. Lett. **69**, 1644–1647 (1992)

5. T. Winiecki, J.F. McCann, C.S. Adams, Pressure drag in linear and nonlinear quantum fluids. Phys. Rev. Lett. **82**, 5186–5189 (1999)
6. T. Winiecki et al., Vortex shedding and drag in dilute Bose-Einstein condensates. J. Phys. B **33**, 4069–4078 (2000)
7. L.D. Landau, The theory of superfluidity of helium II. J. Phys. USSR **5**, 71 (1941)
8. C.F. Barenghi, R.J. Donnelly, W.F. Vinen (eds.), *Quantized Vortex Dynamics and Superfluid Turbulence* (Springer, Berlin, 2001)
9. W.F. Vinen, J.J. Niemela, Quantum turbulence. J. Low Temp. Phys. **128**, 167 (2002)
10. P.C. Haljan, I. Coddington, P. Engels, E.A. Cornell, Driving Bose-Einstein-condensate vorticity with a rotating normal cloud. Phys. Rev. Lett. **87**, 210403 (2001)
11. M.H. Anderson, J.R. Ensher, M.R. Matthews, C.E. Wieman, E.A. Cornell, Observation of Bose-Einstein condensation in a dilute atomic vapor. Science **269**, 198–201 (1995)
12. K.B. Davis, M.O. Mewes, M.R. Andrews, N.J. van Druten, D.S. Durfee, D.M. Kurn, W. Ketterle, Bose-Einstein condensation in a gas of sodium atoms. Phys. Rev. Lett. **75**, 3969–3972 (1995)
13. J.R. Abo-Shaeer, C. Raman, J.M. Vogels, W. Ketterle, Observation of vortex lattices in Bose-Einstein condensates. Science **292**, 476–479 (2001)
14. S. Burger, K. Bongs, S. Dettmer, W. Ertmer, K. Sengstock, A. Sanpera, G.V. Shlyapnikov, M. Lewenstein, Dark solitons in Bose-Einstein condensates. Phys. Rev. Lett. **83**, 5198–5201 (1999)
15. B.P. Anderson, P.C. Haljan, C.A. Regal, D.L. Feder, L.A. Collins, C.W. Clark, E.A. Cornell, Watching dark solitons decay into vortex rings in a Bose-Einstein condensate. Phys. Rev. Lett. **86**, 2926–2929 (2001)
16. S. Inouye et al., Observation of vortex phase singularities in Bose-Einstein condensates. Phys. Rev. Lett. **87**, 080402 (2001)
17. T.W. Neely et al., Observation of vortex dipoles in an oblate Bose-Einstein condensate. Phys. Rev. Lett. **104**, 160401 (2010)
18. S.A. Moskalenko, Reversible optico-hydrodynamic phenomena in a nonideal exciton gas. Sov. Phys., Solid State **4**, 199–204 (1962)
19. J.M. Blatt, K.W. Böer, W. Brandt, Bose-Einstein condensation of excitons. Phys. Rev. **126**, 1691–1692 (1962)
20. L.V. Keldysh, A.N. Kozlov, Collective properties of excitons on semiconductors. Sov. Phys. JETP-USSR **27**, 521–528 (1968)
21. E. Fortin, S. Fafard, A. Mysyrowicz, Exciton transport in Cu_2O: Evidence for excitonic superfluidity? Phys. Rev. Lett. **70**, 3951–3954 (1993)
22. L.L. Chase, N. Peyghambarian, G. Grynberg, A. Mysyrowicz, Evidence for Bose-Einstein condensation of biexcitons in CuCl. Phys. Rev. Lett. **42**, 1231–1234 (1979)
23. D. Hulin, A. Mysyrowicz, C. Benoit à la Guillaume, Evidence for Bose-Einstein statistics of an exciton gas. Phys. Rev. Lett. **45**, 1970–1973 (1980)
24. C. Weisbuch, N. Nishioka, A. Ishikawa, Y. Arakawa, Observation of the coupled exciton–photon mode splitting in a semiconductor quantum microcavity. Phys. Rev. Lett. **69**, 3314–3317 (1992)
25. J. Kasprzak, M. Richard, S. Kundermann, A. Baas, P. Jeambrun, J.M.J. Keeling, F.M. Marchetti, M.H. Szymańska, R. André, J.L. Staehli, V. Savona, P.B. Littlewood, B. Deveaud, L.S. Dang, Bose-Einstein condensation of exciton polaritons. Nature **443**, 409–414 (2006)
26. R. Ballili, V. Hartwell, D. Snoke, L. Pfeiffer, K. West, Bose-Einstein condensation of microcavity polaritons in a trap. Science **316**, 1007–1010 (2008)
27. H. Deng, D. Press, S. Götzinger, G.S. Solomon, R. Hey, K.H. Ploog, Y. Yamamoto, Spatial coherence of a polariton condensate. Phys. Rev. Lett. **99**, 126403 (2007)
28. E. Wertz, L. Ferrier, D.D. Solnyshkov, R. Johne, D. Sanvitto, A. Lemaître, I. Sagnes, R. Grousson, A.V. Kavokin, P. Senellart, G. Malpuech, J. Bloch, Spontaneous formation and optical manipulation of extended polariton condensates. Nat. Phys. **6**, 860–864 (2010)
29. S. Christopoulos, G.B.H. von Högersthal, A.J.D. Grundy, P.G. Lagoudakis, A.V. Kavokin, J.J. Baumberg, G. Christmann, R. Butté, E. Feltin, J.-F. Carlin, N. Grandjean, Room-

temperature polariton lasing in semiconductor microcavities. Phys. Rev. Lett. **98**, 126405 (2007)
30. G. Christmann, R. Butté, E. Feltin, J.-F. Carlin, N. Grandjean, Room temperature polariton lasing in a GaN/AlGaN multiple quantum well microcavity. Appl. Phys. Lett. **93**, 051102 (2008)
31. K. Lagoudakis, M. Wouters, M. Richard, A. Baas, I. Carusotto, R. André, L.S. Dang, B. Deveaud-Plédran, Quantized vortices in an exciton–polariton condensate. Nat. Phys. **4**, 706–709 (2008)
32. K. Lagoudakis, T. Ostatnick, A.V. Kavokin, Y.G. Rubo, R. André, B. Deveaud-Plédran, Observation of half-quantum vortices in an exciton–polariton condensate. Science **326**, 974–977 (2009)
33. G. Roumpos, M.D. Fraser, A. Löffler, S. Höfling, A. Forchel, Y. Yamamoto, Single vortex–antivortex pair in an exciton–polariton condensate. Nat. Phys. **7**, 129–133 (2011)
34. I. Carusotto, C. Ciuti, Probing microcavity polariton superfluidity through resonant Rayleigh scattering. Phys. Rev. Lett. **93**, 166401 (2004)
35. A. Amo, D. Sanvitto, F.P. Laussy, D. Ballarini, E. del Valle, M.D. Martin, A. Lemaître, J. Bloch, D.N. Krizhanovskii, M.S. Skolnick, C. Tejedor, L. Vina, Collective fluid dynamics of a polariton condensate in a semiconductor microcavity. Nature **457**, 291–294 (2009)
36. A. Amo, J. Lefrère, S. Pigeon, C. Adrados, C. Ciuti, I. Carusotto, R. Houdré, E. Giacobino, A. Bramati, Superfluidity of polaritons in semiconductor microcavities. Nat. Phys. **5**, 805–810 (2009)
37. R. Cerna et al., Coherent optical control of the wave function of zero-dimensional exciton polaritons. Phys. Rev. B **80**, 121309(R) (2009)
38. G. Nardin et al., Selective photoexcitation of confined exciton–polariton vortices. Phys. Rev. B **82**, 073303 (2010)
39. P.G. Savvidis, J.J. Baumberg, R.M. Stevenson, M.S. Skolnick, D.M. Whittaker, J.S. Roberts, Angle-resonant stimulated polariton amplifier. Phys. Rev. Lett. **84**, 1547–1550 (2000).
40. M. Saba et al., High-temperature ultrafast polariton parametric amplification in semiconductor microcavities. Nature **414**, 731–735 (2001)
41. S. Pigeon, I. Carusotto, C. Ciuti, Hydrodynamic nucleation of vortices and solitons in a resonantly excited polariton superfluid. Phys. Rev. B **83**, 144513 (2011)
42. See Chap. 7 by Daniele Sanvitto
43. G. Nardin, Phase-resolved imaging of exciton polaritons. Thèse EPFL, no 5002 (2011). http://library.epfl.ch/theses/?nr= 5002
44. R.I. Kaitouni et al., Phys. Rev. B **74**, 155311 (2006)
45. G. Nardin et al., Phase-resolved imaging of confined exciton–polariton wave functions in elliptical traps. Phys. Rev. B **82**, 045304 (2010)
46. T. Kreis, *Holographic Interferometry-Principles and Methods* (Akademie Verlag, Berlin, 1996), 351 pp.
47. N.N. Bogoliubov, J. Phys. USSR **11**, 23 (1947)
48. L. Pitaevskii, S. Stringari, *Bose-Einstein Condensation* (Clarendon, Oxford, 2003), p. 56
49. V. Kohnle, Y. Léger, M. Wouters, M. Richard, M.T. Portela-Oberli, B. Deveaud-Plédran, From single particle to superfluid excitations in a polariton gas. Phys. Rev. Lett. **106**, 255302 (2011)
50. D. Sanvitto et al., Persistent currents and quantized vortices in a polariton superfluid. Nat. Phys. **6**, 527–533 (2010)
51. G. Roumpos et al., Single vortex–antivortex pair in an exciton–polariton condensate. Nat. Phys. **7**, 129–133 (2011)
52. D.N. Krizhanovskii et al., Effect of interactions on vortices in a nonequilibrium polariton condensate. Phys. Rev. Lett. **104**, 126402 (2010)
53. T. Freixanet, B. Sermage, J. Bloch et al., Annular resonant Rayleigh scattering in the picosecond dynamics of cavity polaritons. Phys. Rev. B **60**, R8509–R8512 (1999)
54. R. Houdre, C. Weisbuch, R.P. Stanley et al., Coherence effects in light scattering of two-dimensional photonic disordered systems: Elastic scattering of cavity polaritons. Phys. Rev. B **61**, 13333–13336 (2000)

55. W. Langbein, J.M. Hvam, Elastic scattering dynamics of cavity polaritons: Evidence for time-energy uncertainty and polariton localization. Phys. Rev. Lett. **88**, 047401 (2002)
56. S. Haacke, R.A. Taylor, R. Zimmermann et al., Resonant femtosecond emission from quantum well excitons: The role of Rayleigh scattering and luminescence. Phys. Rev. Lett. **78**, 2228–2231 (1997)
57. L. Pitaevskii, S. Stringari, *Bose-Einstein Condensation* (Oxford University Press, New York, 2003)
58. T. Winiecki, J.F. McCann, C.S. Adams, Pressure drag in linear and nonlinear quantum fluids. Phys. Rev. Lett. **82**, 5186–5189 (1999)
59. T.W. Neely et al., Observation of vortex dipoles in an oblate Bose-Einstein condensate. Phys. Rev. Lett. **104**, 160401 (2010)
60. T. Frisch et al., Transition to dissipation in a model superflow. Phys. Rev. Lett. **69**, 1644–1647 (1992)
61. D. Sanvitto, A. Amo, F.P. Laussy, A. Lemaître, J. Bloch, C. Tejedor, L. Vina, Polariton condensates put in motion. Nanotechnology **21**, 134025 (2010)
62. W. Zhang, D.F. Walls, B.C. Sanders, Phys. Rev. Lett. **72**, 60 (1994)
63. A.D. Jackson, G.M. Kavoulakis, C.J. Pethick, Solitary waves in clouds of Bose-Einstein condensed atoms. Phys. Rev. Lett. **83**, 5198–5201 (2007)
64. L.F. Mollenauer, R.H. Stolen, J.P. Gordon, Phys. Rev. Lett. **45**, 1095 (1980)
65. T. Tsuzuki, J. Low Temp. Phys. **4**, 441 (1971)
66. M. Chen, M.A. Tsankov, J.M. Nash, C.E. Patton, Microwave magnetic-envelope dark solitons in yttrium iron garnet thin films. Phys. Rev. Lett. **45**, 1095 (1980). Ming
67. D.J. Frantzeskakis, Dark solitons in atomic Bose-Einstein condensates: From theory to experiments. J. Phys. A, Math. Theor. **43**, 213001 (2010)
68. G.A. El, A. Gammal, A.M. Kamchatnov, Oblique dark solitons in supersonic flow of a Bose-Einstein condensate. Phys. Rev. Lett. **97**, 180405 (1980)
69. S. Burger, K. Bongs, S. Dettmer, W. Ertmer, K. Sengstock, A. Sanpera, G.V. Shlyapnikov, M. Lewenstein, Phys. Rev. Lett. **83**, 5198 (1999)
70. J. Denschlag, J.E. Simsarian, D.L. Feder, C.W. Clark, L.A. Collins, J. Cubizolles, L. Deng, E.W. Hagley, K. Helmerson, W.P. Reinhardt et al., Science **287**, 97 (2000)
71. B. Kadomtsev, V. Petviashvili, Sov. Phys. Dokl. **15**, 539 (1970)
72. V.E. Zakharov, JETP Lett. **22**, 172 (1975). http://www.jetpletters.ac.ru/ps/1526/article_23342.shtml
73. G. McDonald, K. Syed, W. Firth, Opt. Commun. **95**, 281 (1993)
74. B.P. Anderson, P.C. Haljan, C.A. Regal, D.L. Feder, L.A. Collins, C.W. Clark, E.A. Cornell, Phys. Rev. Lett. **86**, 2926 (2001)
75. V.A. Mironov, A.I. Smirnov, L.A. Smirnov, J. Exp. Theor. Phys. **110**, 877 (2010)
76. G. Grosso, G. Nardin, F. Morier-Genoud, Y. Léger, B. Deveaud-Plédran, Soliton instabilities and vortex street formation in a polariton quantum fluid. Phys. Rev. Lett. **83**, 5198 (1999)
77. A. Amo, S. Pigeon, D. Sanvitto, V.G. Sala, R. Hivet, I. Carusotto, F. Pisanello, G. Leménager, R. Houdré, E. Giacobino, C. Ciuti, A. Bramati, Polariton superfluids reveal quantum hydrodynamic solitons. Science **332**, 1167–1170 (2011)
78. M. Sich, D.N. Krizhanovskii, M.S. Skolnick, A.V. Gorbach, R. Hartley, D.V. Skryabin, E.A. Cerda-Méndez, K. Biermann, R. Hey, P.V. Santos, Observation of bright polariton solitons in a semiconductor microcavity. Nat. Photonics **6**, 50 (2012)
79. G. Nardin, Y. Léger, B. Pietka, F. Morier-Genoud, B. Deveaud-Plédran, Phys. Rev. B **82**, 045304 (2010)
80. R. Cerna et al., Phys. Rev. B **80**, 121309 (2009)
81. R. Cerna, T.K. Paraïso, Y. Léger, M. Wouters, F. Morier-Genoud, M.T. Portella-Oberli, B. Deveaud-Plédran, Phys. Rev. B **81**, 113306 (2010)

Chapter 7
Polariton Quantum Fluids and Devices

D. Ballarini, A. Amo, M. de Giorgi, and D. Sanvitto

Abstract In the following chapter we will review the first observations of fluid-dynamics of Bose Einstein condensates of polariton quasi-particles, from the propagation of single wavepackets to the continuous flow of steady polariton fluids. Photons, as intrinsic part of the polariton particle, are not only used as a mean to create polariton condensates but also to manipulate their quantum state giving specific momentum and energy, steering their steady state and controlling their flow velocity and trajectory. On the other hand light emitted from the cavity is also used as a convenient detection tool to reveal the complete quantum state of polariton fluids. Using the strong polariton non-linearities and spin dependence, we use different beams of light/polariton state to create ad hoc designed spatial potential landscapes which can be exploited as artificial defects, barriers and channels to impact with polariton quantum fluids and so revealing extremely interesting effects like superfluidity, oblique dark soliton formation, quantum turbulence, laminar flow and the effect on vortices of tailored energy barriers. Moreover, we will show that beyond fundamental turbulence studies, optically controlled polariton quantum fluids can be used as switches and amplifiers which could eventually be implemented in polariton chips for the next generation of all optical transistors and logics, which would make use of light-matter condensates to transport and manipulate quantum and classical information.

D. Ballarini · M. de Giorgi · D. Sanvitto
Istituto Italiano di Technologia, IIT-Lecce, Via Barsanti, 73010 Lecce, Italy

A. Amo
Laboratoire de Photonique et de Nanostructures, CNRS, Route de Nozay, 91460 Marcoussis, France

D. Ballarini · M. de Giorgi · D. Sanvitto (✉)
Istituto Nanoscienze – CNR, NNL, Via Arnesano, 73100 Lecce, Italy
e-mail: daniele.sanvitto@nano.cnr.it

A. Bramati, M. Modugno (eds.), *Physics of Quantum Fluids*,
Springer Series in Solid-State Sciences 177, DOI 10.1007/978-3-642-37569-9_7,

7.1 Introduction

When dealing with fluids and the study of their motion it is of fundamental importance the control, as accurate as possible, of many of their parameters, such as their density and momentum. In this respect, quantum fluids of condensed particles are as much intriguing as their phenomena are hard to study, given that a full control on the fluid state is not a trivial task.

One of the most important quantities describing a fluid is its velocity, which is classically associated to the kinetic energy of each particle moving in the liquid. In a quantum fluid, a fluid in which macroscopic numbers of particles occupy the same quantum state, it is the order parameter, the phase, which defines the state, including its motion, while the momentum of individual particles loses its meaning. Nonetheless, the access of the condensate phase both in space and in time can only be obtained via indirect interferometric measurements. Moreover, below a certain critical speed, bosonic condensates manifest superfluidity [1], which, if on the one hand it is a very interesting phenomenon to study, on the other could be seen as an obstacle to transfer a controlled quantity of speed to the fluid.

In this context, polaritons in microcavities are a very interesting and unique system in which bosonic condensates can be created. It offers huge advantages to the study of quantum fluid dynamics and its phenomenology thanks to the easy access to their quantum state and the possibility of complete control over their formation and motion [2–4]. In this chapter we will give an overview of the recent advances in the study of quantum fluids of polariton condensates which span from the observation of superfluidity to the dynamics of a turbulent flow of a bosonic condensate. All these observations, and the analysis of the vast phenomenology associated with polariton condensates, could only be possible thanks to the strong interconnection between coherent beams of light and polariton condensates inside the microcavity. In fact, photons, as intrinsic part of the polariton particle, are not only used as a mean to create polariton condensates but also to manipulate their quantum state giving specific momentum and energy, steering their steady state and controlling their flow velocity and trajectory. On the other hand light emitted from the cavity can also be used as a perfect detection tool to reveal the complete quantum state of polariton fluids.

7.1.1 Formation of a Polariton Condensate

Emission of a condensed polariton state can be obtained in different ways, each of which may show advantages and drawbacks. In this chapter we will concentrate on the generation of a polariton condensate either by the triggering of a parametric optical amplification process (TOPA) [5–7] or via direct resonant excitation of the polariton state along the low polariton branch. It is interesting to notice that such kind of condensate had already been experimentally studied at the beginning of the years 2000 with the first observation of strong non-linear response at the

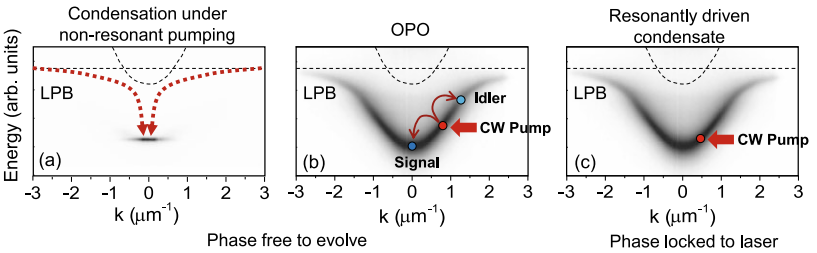

Fig. 7.1 Schematic representation of the three methods used to generate a state of coherent polariton in all similar to a Bose-Einstein condensate via non-resonant incoherent excitation (**a**), using a triggered OPO scheme (TOPA) (**b**) and via resonant laser excitation (**c**). All these cases have advantages and drawbacks, however in any circumstance the polariton condensate generated under any condition is always and out of equilibrium condensate and losses need to be compensated by a driving field

bottom of the LPB due to parametric scattering of a resonant laser pump (OPO) [8–10]. However, it is only after the observation of the formation of a coherent state with a non-resonant pumping scheme [11, 12], that the use of the word polariton condensation-yet with an ongoing debate about it-was associated to a macroscopic coherent occupation of a polariton state.

A schematic representation of the polariton dispersion and the different generation processes of a polariton condensate is described in Fig. 7.1 using non-resonant, TOPA and resonant excitation. In all these excitation schemes, which will be discussed one by one in the next sections, the created condensates of polaritons in microcavities present properties which depart from their atomic counterparts. This is mainly due to the intrinsic lossy nature of polariton quasi-particles, which, in the best of the cases, reach a dynamical equilibrium between the pumping and the decay processes.

Non-resonant Excitation Non-resonant pumping of the microcavity structure is the configuration to generate a polariton condensate which is closest to the conditions for the formation of an atomic BEC. In this case, the symmetry of the order parameter is spontaneously broken while a sort of thermalised population is present at the bottom of the low polariton branch (LPB) showing the coexistence of a condensed and a normal fluid.

However, in case of a standard BEC, the atomic density is fixed, and the temperature is reduced beyond a critical T_C to push De Broglie wavelength to a magnitude of the order of the inter-particle distance. In the polaritons case, instead, the De Broglie wavelength is dominated by the spatial size of the particle photonic component, which, in common GaAs structures, extends up to the micron size, independently of the polariton temperature. Thus, the parameter used to reach the critical interparticle distance is the polariton density, which is increased beyond a critical point at which condensation is achieved. Due to the constant escape of polaritons out of the cavity, a continuous pump needs to be provided to keep a constant population, which can then be described as being in a dynamical rather than in a thermal equilibrium. Very

interestingly, by changing the excitonic and photonic weight, the polariton-polariton interaction changes and the curvature of the LPB can be tuned almost at will. This allows the passage from a regime mostly dominated by the relaxation kinematics at negative detuning, which is far from thermal equilibrium, to a regime in which the dynamical equilibrium is close to be thermal at positive exciton-photon detuning [13, 14].

We should keep in mind that polaritons are formed by strong exciton-photon coupling and this can only hold if the electron-hole density does not screen the exciton in the active material. For high pumping powers, this situation can only be avoided either with very high finesse cavities or by using materials with very strong exciton binding energies. Under non-resonant excitation and good microcavity finesses condensation was obtained in a variety of materials, from CdTe to GaN based polaritons [11, 15] and more recently even in GaAs structures [12, 16]. In all cases, although polariton condensates are more prone to show a proper temperature, yet the phenomenology is strongly dominated by their non-equilibrium nature which, in case of confined systems, or inhomogeneous structures, can easily lead to a dynamical condensation in more than just the ground state [17]. Other very interesting examples are the observation of coherence, which is not just related to the number of particles, but it is also strongly affected by particle fluctuations in the condensate or in the exciton reservoir [18–21].

Resonant Excitation While a polariton condensate generated under non-resonant excitation has the advantage to appear spontaneously out of a non coherent population (typically in the excitonic reservoir), it lacks, though, of the possibility to be fully controlled: from the ratio between different polariton spin populations to the condensate position as well as its motion. In this respect the easiest way of generating a polariton state at a given point in the sample with a defined density, polarisation and specific momentum is via resonant excitation [22–24]. This is done by exciting directly with a laser, at a given energy and k-vector, the LPB. Photons are converted into polaritons straight away while entering the cavity region and any quantum number is then transferred into the polariton condensate with a one to one conversion relation. This method has the advantage of giving a complete control over the polariton state, including density and velocity, which is crucial in the study of quantum fluids. However, the phase of the condensate in space as much as in time is completely inherited from the laser field and many aspects of the condensate dynamics, including the appearance of vortices and correlations between different parts of the fluid, are suppressed or hidden by the incoming photonic radiation. Despite that, much interesting phenomenology [22–30], some of which will be discussed in the next section, has been observed using resonant polariton excitation.

Excitation via TOPA The problem of the polariton condensate to be locked to the phase of the pumping laser could be avoided by exploiting the peculiar polariton dispersion for which there is always a region around the inflection point where stimulated pair scattering can take place. This process, consist of parametric oscillations between two particles at the pump state with energy E_P and momentum k_P into a

signal state at the bottom of the LPB, $E_s, k_s = 0$, and an idler at E_i and k_i with the following conservation rules:

$$2E_P = E_s + Ei; \qquad 2k_P = k_s + k_i; \qquad 2\phi_P = \phi_s + \phi_i. \tag{7.1}$$

The last expression is particularly interesting since—considering the signal state as the polariton condensate we are interested to study—it leaves the system with a degree of freedom in the choice of the final phase. In other words there is no constrain or bound between the phase of the condensate at the signal and the phase of the laser, provided that the idler is free to carry the mismatch with the pump laser phase. No matter how weak this relation can appear, it has a strong conceptual meaning which actually changes considerably the physics of the condensate created under these conditions giving that, differently from the resonant case, here the symmetry of the choice in the order parameter has been broken spontaneously, similarly, on this, to the non-resonant excitation conditions. This peculiar character of the condensate created under OPO has been described in [31].

Such a condensate though, spontaneously generated by stimulated scattering, usually appears at the bottom of the LPB, similarly to the non-resonant excitation case. This is caused by the fact that it is in the lowest energy state where the stimulation of the process dominates over the spontaneous scattering in the whole LPB dispersion [32]. This, apparently, does not add any use compared to the non-resonant case. However, the stimulated process has the advantage to allow for the triggering of the final state with the use of an additional external laser source, which can undergo strong non-linear amplification both with pulse [9] as well as CW excitation (OPA) [33]. Therefore, using the combination of a CW pump, around the inflection point, and a laser pulse as trigger (either at the idler or the signal state), allows for the generation of a long living polariton condensate [5] having an initial position, momentum and polarisation given by the pulsed triggering laser, but lasting as long as the CW pump is *on*. This technique, which is a triggered optical parametric amplifier (TOPA) has the advantages of giving a good control over the polariton parameters and at the same time leaving the phase of the signal state free to evolve after the triggering pulse has passed. Clearly in this case, as well as in the case of direct resonant formation, the condensate is completely out of equilibrium and the system can be described fairly accurately by a standard Gross-Pitaevskii equation with the addition of one term that accounts for the pumping and another for dissipation.

7.1.2 Polaritons Put in Motion: Superfluidity

Frictionless Motion The dynamics of a polariton condensate in the presence of a potential barrier provides rich information on its quantum fluid state. This situation can be studied by direct observation of the fluid motion as well as via indirect detection of the effects of the barrier on the condensate compared to the unperturbed situation. In the latter it is sufficient to reach a steady state in which the condensate

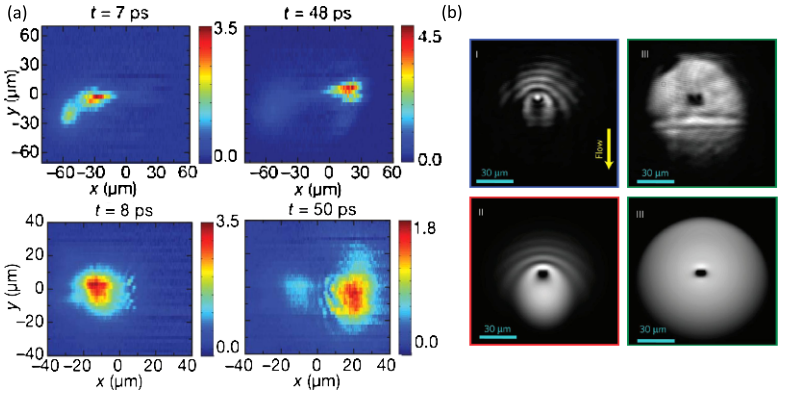

Fig. 7.2 (**a**) Real space emission of a polariton droplet, created under TOPA excitation, flowing inside the driving laser pump at a velocity of 1.2 μm/s (*upper panels*) and under similar experimental conditions but with a natural obstacle set in the droplet trajectory (*lower panel*). Figures taken from Ref. [6]. (**b**) Transition from supersonic (*left*) to superfluid (*right*) regime of a polariton condensate flowing against an obstacle. This time the steady state is observed and polaritons are created under CW resonant excitation at a k-vector of 0.335 μm^{-1}. The experimental images (*upper panels*) are compared with the theory (*lower panel*). Images taken from Ref. [24]

had a finite momentum while the pump and decay processes are compensated; this is easily reached under resonant excitation with a CW pump laser. In the former, instead, it is of fundamental importance to overcome the limits of very short polariton lifetime and to set the condensate in motion. For this purpose, the TOPA has shown to be quite effective in both, generating a controlled population with a finite wavevector and letting the condensate last for times which are orders of magnitude longer than the intrinsic cavity lifetime.

The first observation of a condensate put in motion using this technique is shown in Fig. 7.2a where a droplet of polariton condensate runs across a CW pump used for feeding the moving polariton state [6]. Under the same conditions it was possible to observe the unperturbed motion of this droplet across a natural defect present in the structure with no tangible sign of any scattering or energy relaxation (Fig. 7.2b). This is the first hint that frictionless motion, typical of superfluids, can be present even for the case of polariton condensates. Surprisingly the frictionless behaviour was observed under condensate velocities around 1/100 the velocity of light, many orders of magnitude higher than the velocity of sound in atomic BEC. However, a clear demonstration of the transition from superfluid to supersonic motion was subsequently shown only via resonant CW excitation and under steady state regime [24] as reproduced in Figs. 7.2c and 7.2d. Here the appearance of Cherenkov like waves was the smoking gun for a supersonic regime in which the fluid speed is larger than the speed of sound of the fluid. While the fluid speed can be controlled via the momentum of the injected polaritons, the speed of sound is fixed by the polariton density [22]. In this way the passage from a superfluid to a supersonic regime can be turned by simply playing with the excitation conditions.

If on the one hand, generating a condensate of polaritons via resonant excitation, has the disadvantage of fixing the phase by the pumping laser, on the other it has the benefit that the excitation spectrum of the condensate can be solved analytically assuming that the excitations, on top of the steady state, are small. In this way it is possible to compare how close polariton superfluidity is to the Landau criterion applied to atomic BEC. The spectrum of excitations, in the Landau theory, shows a linear dispersion at small momenta, with the tangent being the velocity of sound in the condensate, c_s. Thus, for a BEC moving at lower velocity than c_s no excitations are available for the system and the flow is superfluid, while for higher velocities the condensate becomes supersonic and recovers the behaviour of a classical fluid. However, in case of a single polariton fluid the system only partially shows to follow this criterion. Only for specific pumping conditions the excitation spectrum is Bogoliubov-like while, for sufficiently high density, the opening of a gap is observed [22, 34]. This situation resembles more that of a superconductor than an atomic BEC.

For the case of non-resonant excitation the excitation spectrum is significantly different, being diffusive and flat at small k-vectors, with a value of zero for the effective speed of sound [35, 36]. This means that by just looking at the real part of the excitation spectrum several states can be elastically accessible and no superfluidity would be possible for the polariton system when created by incoherent pumping. However, due to the dissipative nature of the polariton condensate, the imaginary part of the excitation spectrum is not vanishing and shows a negative component which gains importance for small wavenumbers. This negative imaginary part efficiently damps density perturbations and eventually allows for the superfluid behaviour to be recovered [37]. By now, though, there has been no experiment which could confirm this effect under such excitation condition.

Another case to mention is the one of two or more fluids, resonantly generated by external coherent light. From a theoretical point of view it is interesting to see that due to the new combined excitation spectra of the two fluids, the superfluid or supersonic properties of a single condensate are strongly affected by the presence of the second quantum fluid, depending on their relative coupling and densities [38].

Permanent Currents Other manifestations of superfluidity can be explored when considering a condensate in rotation. For atomic BEC this can be done by steering a laser which is tuned with specific atomic resonances. As a result the BEC shows the spontaneous formation of vortices carrying a quantum of angular momentum and typically forming a close packet lattice [39]. Noteworthy, a vortex state, corresponding to a circular motion of the condensate, has the property to keep the rotation for as long as the condensate persists [40]. This is a consequence of the superfluid motion of the condensate, in which no external drag forces can alter the circulation.

For a polariton condensate this operation can be done by imprinting a rotation via the external photonic field, as proposed and shown in Ref. [7]. In that work a single vortex state is observed to sustain rotation for times much longer than both the polariton intrinsic lifetime and the condensate coherence time. This result demonstrates that, due to the suppression of scattering and friction, a polariton fluid can

hold its rotation even in presence of defects and inhomogeneities of the photonic and excitonic potential. This behaviour is analogous to that of supercurrents in a toroidal superconductor.

The effects of a vortex in the steady state of a polariton condensate are a quite interesting and yet not completely understood phenomena. Their properties depend on many parameters. For instance it has been shown that the potential landscape, the presence of supercurrents flowing internally to the condensate, and the injected velocity [41–43] are all playing a fundamental role on the vortex dynamics and stability.

7.2 Beyond Superfluidity

The experiments described in Fig. 7.2 show that the motion of a polariton condensate through an obstacle provides an excellent system to study the fundamental problem of the onset of dissipation in quantum fluids. The transition from the supersonic to the superfluid regime takes place for velocities of the polariton fluid below the threshold v_c, usually associated with the speed of sound c_s. However, near the surface of an obstacle, additional friction mechanisms involving the nucleation of vortex pairs and solitons occur even below the critical velocity v_c, resulting in small energy dissipations [44–46]. This transient regime, characterised by a rich vortex dynamics, is one of the most interesting subjects in the field of quantum fluids, which can give us a deeper insight even in the still unsolved problem of turbulence in classical fluids. The onset of quantum turbulence in atomic condensates and quantum fluids will be addressed in detail in Chaps. 12, 13 and 14.

The link between the description of a Bose-Einstein condensate in terms of its macroscopic wavefunction $\psi_0(\mathbf{r})$, characterised by modulus and phase

$$\psi_0(\mathbf{r}) = \left|\psi_0(\mathbf{r})\right| e^{i\phi(\mathbf{r})} \tag{7.2}$$

and the equations describing its fluid dynamics, is the identification of the superfluid velocity v_s with the gradient of the phase of $\psi_0(\mathbf{r})$,

$$v_s = \frac{\hbar}{m}\nabla\phi, \tag{7.3}$$

where m is the mass of the condensed particle and $|\psi_0(\mathbf{r})| = \sqrt{\rho}$, being ρ the density of the condensate. Equation (7.3) shows the irrotationality of the superfluid motion, with the phase playing the role of a velocity potential. From this representation, follows one of the most striking quantum effects on the fluid dynamics: the quantisation of angular momentum (see Sect. 7.3).

The density, ρ, and phase, ϕ, completely define the macroscopic state of the polariton condensate in the absence of thermal excitations, and obey a set of two coupled equations [47]. The equation for the density is obtained from the conservation of mass, i.e. the continuity equation, which takes the form

$$\frac{\partial \rho}{\partial t} + \mathrm{div}(v_s \rho) = 0, \tag{7.4}$$

while the equation for the phase ϕ is

$$\hbar \frac{\partial}{\partial t}\phi + \left(\frac{1}{2} m \mathbf{v}_s^2 + V_{ext} + g\rho - \frac{\hbar^2}{2m\sqrt{\rho}} \nabla^2 \sqrt{n} \right) = 0, \tag{7.5}$$

where V_{ext} is the external potential and g expresses the interaction coupling between particles. The quantum effects are emphasised by the Planck constant present in the term containing the gradient of the density, which is called quantum pressure. Neglecting this term, the superfluid equations are formally identical to those for classical irrotational fluids. Anyhow, this approximation is limited to the study of macroscopic phenomena, where the density of the gas is varying slowly. In strongly nonuniform gases, the density gradients give rise to a non-negligible quantum pressure term which becomes important when the characteristic distance over which the density variations occur is of the order of the healing length ξ of the quantum fluid, defined by

$$\xi = \frac{\hbar}{\sqrt{2mg\rho}}. \tag{7.6}$$

From this equation we notice that the density variations of the superfluid are sharper than in dilute and weakly interacting gases. Note, however, that in the case of exciton-polaritons the stronger interactions are overcompensated by the extremely light mass of this particles, resulting in typical healing lengths of 1–10 μm, about two order of magnitude larger than in atomic systems.

In this scenario, the study of polariton fluids appears very promising in the understanding of many phenomena related to quantum hydrodynamics because of the easy access and control of all the relevant quantities of the polariton flow. Moreover, the strong polariton non-linearities allow generating tailored optical obstacles of defined shape and strength, as we will see below, thus offering an ideal test bed to study the polariton hydrodynamics.

In these systems, the critical value v_c can be associated to the speed of sound c_s in the uniform part of the polariton fluid,

$$c_s = \sqrt{\frac{\hbar g |\psi_X|^2}{m_{LP}}}; \tag{7.7}$$

where $|\psi_X|^2$ represents the exciton density and m_{LP} the effective mass of lower-branch polaritons. In the simplest case of a resonantly pumped polariton gas flowing against an obstacle, the transition from the frictionless flow typical of superfluid to the Cerenkov-like regime was predicted and observed for fluid speed respectively below and above the sonic threshold $v_c = c_s$ [22, 24]. However, under a monochromatic and spatially homogeneous pump, the local phase of the polariton field is fixed by the pump phase, inhibiting the appearance of topological defects such as vortices, which are indeed characterised by spatially localised phase singularities.

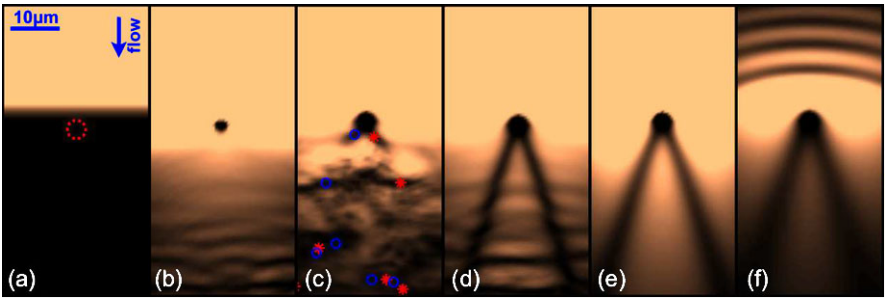

Fig. 7.3 Numerical simulation of a polariton flow (moving downstream in the figure) hitting a large defect for different values of the ratio $v_f > v_c$. The continuous wave pumping beam is restricted to an area which covers only half the plane, in order to follow the phase evolution after the defect. (**a**) Spatial profile of the pump intensity, with the red circle indicating the size and position of the defect. (**b**)–(**f**) Normalised real-space photonic density for different values of the exciting parameters, which correspond to increasing values of the flow speed with respect to the speed of sound, showing a variety of hydrodynamic regimes ranging from superfluidity (**b**) to dark solitons (**e**) and emission of sound waves (**f**), passing through the transient regime of vortex-antivortex formation and drift (**c**). The density patterns are stationary in time in all panels except (**c**). Taken from [48]

At this point, it is important to remind that the vortex appearance in the polariton condensate is only possible outside of the laser excitation spot, where the phase is free to evolve. Therefore, in all hydrodynamic experiments, given the direct relation between phase and velocity, it is crucial to let the system evolve without having its phase locked to the one of the laser.

As proposed in [48], and reported here in Fig. 7.3, one of the possible solution is to block the laser spot to half its size, leaving the space downstream of the defect without any external optical field. In this way, the phase of the polariton condensate is let free to evolve past the defect. The results of the numerical simulations, run with a defect size bigger than the healing length, show indeed a variety of hydrodynamic regimes which can be observed by changing the value of the speed of sound with respect to the flow speed. For $v_f \ll v_c$, the expected superfluid behaviour is reproduced (panel b)—here the fluid propagation is similar to that in the presence of a weak defect; for $v_f > 0.43 v_c$, vortex nucleation occurs from the defect surface (panel c)—in this case the vortex pairs are dragged away by the flow, making this turbulent regime accessible only in time-resolved experiments; for $v_f > v_c$ (panels d, e, f), straight pairs of dark solitons appear in the wake of the defect with an angle to the direction of the flow, accompanied by the emission of vortices (panel d) or precursor sound wave (panel f) depending on the local value of the ratio v_f/v_c.

In the next section we will focus on experiments exploring the turbulent regime of vortex-antivortex formation in the presence of a large defect, firstly under pulsed excitation, where the defect is artificially created and controlled by an optically-induced potential barrier, and secondly under cw excitation with a suitable shape of the pumping beam which allows for trapping the vortices nucleated past the defect.

In the last section the hydrodynamic formation of dark solitons will be treated in detail under cw excitation.

7.3 Vortex

In a superfluid, which is irrotational, the circulation around a closed loop simply connected is always zero. However, if the density ρ goes to zero in a small region (the vortex core), then the phase ϕ can change of 2π, or multiple s of 2π, around a closed loop which contains the vortex core. In order to ensure that the wavefunction is single valued at any point, s should be an integer and the circulation

$$\oint \mathbf{v}_s \cdot d\mathbf{l} = \oint \frac{\hbar}{m} \nabla\phi d\mathbf{l} = 2\pi s \frac{\hbar}{m}, \tag{7.8}$$

results quantised in units of $\frac{\hbar}{m}$.

For the conservation of angular momentum, the circulation around a closed contour does not change in time, which means that within the fluid only vortex-antivortex pairs can be created from a point. Nevertheless, this is not true at boundaries, where the density of the fluid goes to zero and no closed loop can be drawn.

Within polariton condensates, vortices can be generated by different mechanisms. For instance, an inhomogeneity of the pumping, or the presence of disorder potentials, form steady currents which may produce vortices. Experimentally, vortices have been observed to spontaneously appear in the disorder potential of the cavity [49] or in the minima of the excitation laser field [50], but in these cases they get pinned at the local minimum of such potentials and remain stationary, leaving unclear the conditions in which a turbulent state of matter can be obtained in exciton-polariton condensates. Only recently, two works have addressed the possibility to obtain the nucleation of vortices in polariton systems directly involving the hydrodynamic instabilities rising in the fluid density at the surface of a defect [51, 52]. In Chap. 6, we have already treated the effects of hydrodynamics in polariton quantum fluids: in this section, we will focus on the high level of control achievable on the vortex appearance and motion. To this scope, we will first describe an optical technique that allows us to generate potential barriers of engineered size, shape and height.

7.3.1 Optically Generated Potential Barriers

In order to study the vortex formation dynamics it is fundamental to have the full control over the parameters of the obstacle. The optical generation of potential barriers seems the most suitable technique, allowing the modification of the polariton potential landscape with the use of CW laser beams.

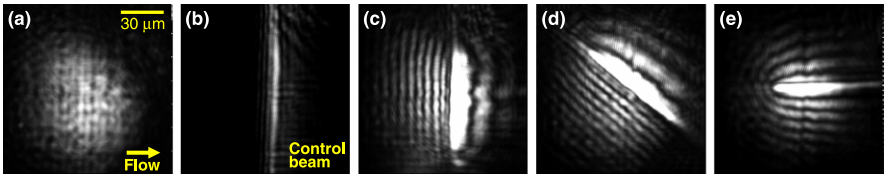

Fig. 7.4 (**a**) Real space emission of a dilute polariton gas resonantly injected in the lower polariton branch with a momentum of 0.35 μm^{-1} and linear polarisation. (**b**) Same for an intense control beam injected at *zero* momentum with perpendicular linear polarisation. The control beam creates a potential barrier with a linear shape, producing the retro-reflexion of the dilute polariton gas. This is shown in (**c**), where the stripped pattern arises from the interference between incident and scattered polaritons. (**d**), (**e**) Same as (**c**) for two different inclinations of the optically induced barrier. The excitation conditions are those of Ref. [55]

The main idea behind this technique is to use the strong polariton-polariton and polariton-exciton interaction to modify the potential. These interactions are dominated by exchange, and are strongly dependent on the spin of the considered particles. Polaritons posses two possible projections of their spin on the growth axis of the cavity: $S_z = \pm 1$, coupled, respectively, to right and left circularly polarised photons. The interaction between polaritons with parallel spins can be parametrised in the constant α_1 and it is repulsive, giving rise to an increase of the polariton energy (blueshift of the emission) equal to $\hbar\alpha_1 C_x^4 |\psi_\sigma|^2$, where $|\psi_\sigma|^2$ is the polariton density of the considered spin population σ, and C_x is the excitonic Hopfield coefficient [22]. On the other hand, the interaction between polaritons of opposite spins is attractive ($\alpha_2 < 0$), and gives rise to a decrease of the polariton energy. Note that while α_1 is a resonant interaction, α_2 involves an intermediate excitonic dark state ($S_z = \pm 2$) located at the energy of the uncoupled exciton. For this reason [53, 54] $\alpha_1 \gg |\alpha_2|$. If we optically create a very large accumulation of polaritons with a given spin in a certain region of the sample, we can modify the local polariton energy due to the blueshifts and/or redshifts induced by polariton interactions. A dilute polariton gas encountering this region of the sample will effectively feel the presence of the dense gas as a potential barrier or depression [55].

We illustrate this technique in Fig. 7.4, which shows real space images of an InGaAs/GaAs based microcavity for a transmission experiment under the configuration described in [55]. Figure 7.4a shows a resonantly injected dilute polariton gas at low excitation density, flowing from left to right in an area of the sample free from structural defects. Panel b, shows a strong resonant beam (control) designed in the form of a vertical line and injected at normal incidence. This beam is linearly polarised, and thus creates both polaritons with $S_z = +1$ and $S_z = -1$. As $\alpha_1 \gg |\alpha_2|$, this control beam induces a net blueshift of the polariton energy for both right and left polarisations. Therefore, it will give rise to a potential barrier that will be felt by the dilute polariton gas shown in Fig. 7.4a, independently of its polarisation. This is what is seen in Fig. 7.4c, where both dilute and control beams are simultaneously switched on. In this case we have injected the dilute gas with a linear polarisation perpendicular to that of the control. By selecting the polarisation of detection parallel to that of the dilute gas, we can minimise the impact of the strong control beam

in our detectors. Figure 7.4c shows that the dilute gas is retroreflected by the control barrier, resulting in the observed interference between incident and backscattered polaritons. The flexibility of this technique is demonstrated in Figs. 7.4d–e, where the line potential barrier is created at different inclinations with respect to the flow direction. Note that in these examples we can not only control the shape of the barrier, but also its height by tuning the polariton density. Moreover, due to the strong spin asymmetry of the polariton interactions, spin selective optical barriers could also be created.

As polariton interactions arise from their excitonic component, potential barriers can also be created by the direct excitation of excitons in the reservoir. This can be done via non-resonant pumping of the system. In this case the spin selectivity is lost as excitons loose their spin orientation extremely fast. If the excitation spot is small, the photogenerated exciton cloud can be confined to a few microns as the diffusion time of excitons out of the spot is much longer than their lifetime due to their very large mass. Reservoir induced potentials have been shown to be a very efficient tool to accelerate polariton condensates in 1D wires [56], to create optical confinements [56, 57] or to sculpt the polariton condensate in 2D [58, 59].

7.3.2 Vortex Nucleation in Optical Potentials

The technique we have just described can be used to create convenient potential barriers of controlled height and size, suitable for the hydrodynamic nucleation of vortices. We will now analyse the case of a barrier created by a CW laser with a Gaussian shape spot, in quasi-resonance with the lower polariton branch. Simultaneously, in order to study the eventual vortex hydrodynamics, a polariton condensate can be resonantly excited by another laser beam, with a pulse length of less than the cavity timescale (usually a few picoseconds). If the pulsed laser, incident on the sample, has a finite component of the momentum in the plane of the microcavity, it will result in a finite velocity of the polariton fluid v_f.

The fluid dynamics after the pulse is described in Fig. 7.5: in the upper row five snapshots of the polariton field are shown, while the corresponding phase patterns, obtained from the interference of the cavity emission with a reference beam of constant phase coming from the pulsed laser itself, are shown in the second raw.[1] Half of the laser spot is masked with a sharp metallic edge, so to induce a high density edge in the polariton density which allows to observe, within the polariton lifetime, the complete evolution of the injected fluid when encountering the potential barrier (rightward direction in the figure). The images plotted in Fig. 7.5 are the result of several billions of nominally identical single realisations: the fact that vortices are visible in the averaged images proves that they are formed at the same position and

[1] In order for the reference beam to temporally match the whole duration of the polariton dynamics in the cavity, the optical pulse in the reference beam has been stretched from a few hundred of femtoseconds (which is the typical laser pulse width) to a hundred of picoseconds.

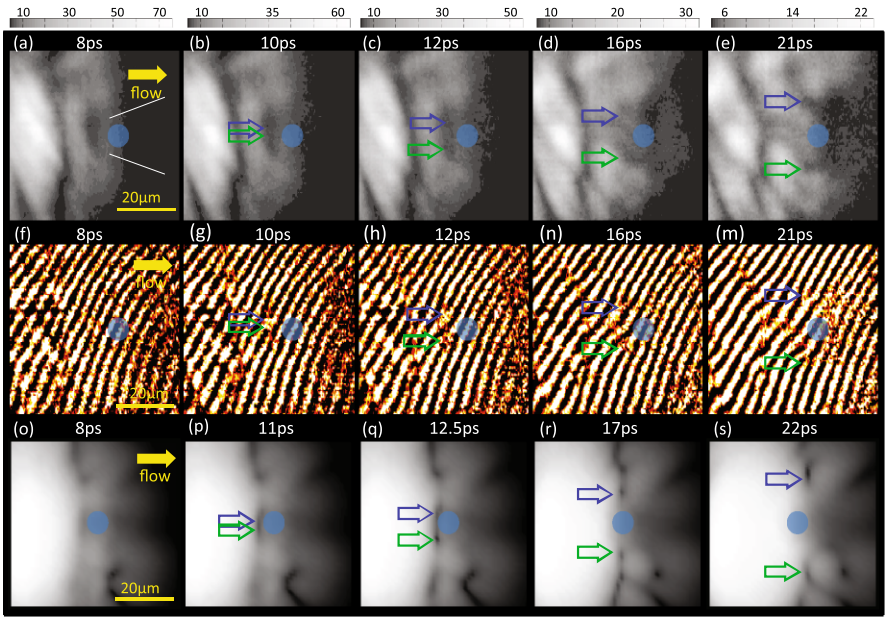

Fig. 7.5 Five temporal snapshots of the real space density (**a**)–(**e**) and phase profile (**f**)–(**m**) of a polariton condensate resonantly created in the cavity with a rightward velocity $v_f = 1.1$ m/ps. The shape of the barrier is Gaussian (10 m in diameter, 0.4 meV of mean height) and its position is indicated by a *blue circle* in the images. Vortex-antivortex pair, indicated in the images by *blue* and *green arrows*, are visible in (**b**)–(**e**) as density minima corresponding to their core, and as fork-like dislocations in the interferograms shown in (**g**)–(**m**). The results of the theoretical simulations run with the experimental parameters are reported in the bottom raw (**o**)–(**s**). Extracted from [52]

follow the same trajectory at each shot. Moreover, the good visibility of the fringes in the interference pattern proves that the polariton fluid preserves its coherence during the whole evolution.

Soon after the polariton flow has met the defect position, about 10 ps after the arrival of the pulse, a pair of vortices with opposite circulation is created in the center of the gas, as shown in Fig. 7.5b and Fig. 7.5g. Vortices are revealed as density minima corresponding to their core in Figs. 7.5b–e, and as fork-like dislocations in the interferograms shown in Figs. 7.5g–m. In the first 10 ps the vortex and the antivortex are pushed away from the center towards the equator of the obstacle (the equator axis being defined to be perpendicular to the flow direction). At this point, there is a clear deceleration of their motion and a small excursion in the direction orthogonal to the flow, which reveals the presence of transverse currents in the polariton fluid. After most of the polariton pulse has gone past the defect, the vortices localise at a distance of a few tenths of microns from the defect, and then disappear.

This exotic regime, characterised by the injection of a polariton fluid via a short laser pulse with an induced flow speed higher than the speed of sound, manifests in the creation of a turbulent motion in front of the obstacle and in the conical modulation of the density past the obstacle. It is important to point out here that,

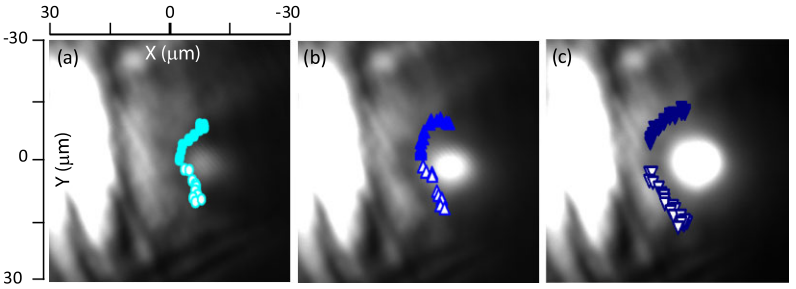

Fig. 7.6 Vortex-antivortex trajectories for different size of the barrier: (**a**)–(**c**) refer to a fixed pulse power, $P_{pulse} = 4$ mW, and different CW powers, $P_{cw} = 6$ mW, 26 mW and 52 mW respectively. The nucleation point shifts horizontally on the left, towards positions of higher polariton densities, and vertically further away from the defect axis, towards position of higher tangential flow speed. The background images are the corresponding time-integrated real space emission patterns

when the flow firstly hits the obstacle, the phase is totally free to evolve allowing the vortex-antivortex pair to nucleate where the fluid velocity is locally equal to the critical velocity, condition that in the experiment shown in Fig. 7.5 occurs up to more than 5 micrometers before the defect. This is confirmed by the solution of the time-dependent non-equilibrium Gross-Pitaevskii equations with the actual experimental excitation conditions, shown in the third row of Fig. 7.5.

In the present case, differently from the theoretical prediction shown in Fig. 7.3 which considers a stationary flow hitting a small and spatially abrupt potential, the optical barrier has a smooth profile and relatively shallow depth, allowing a small fraction of the condensate to penetrate it. Furthermore, polaritons are injected by a short pulse and their density swiftly decreases in time after the pulse has gone, being the situation far different from the steady state in which vortices are continuously dragged away.[2]

In the following, the conditions under which the nucleation of vortex-antivortex pairs can be generated in the polariton flow are further analysed by changing the parameters of the potential barriers, showing how the vortex formation and trajectories can be optically manipulated.

Increasing the Shape and Height of the Potential Barrier In Fig. 7.6, both the height and the effective width of the potential experienced by the moving polaritons has been changed, by increasing the CW power from $P = 6$ mW in Fig. 7.6a to $P = 26$ mW in Fig. 7.6b, and to $P = 52$ mW in Fig. 7.6c. Increasing the barrier size, the vortex-antivortex nucleation point is shifted simultaneously upstream and away from the horizontal axis. This behaviour can be understood considering that

[2] In the experimental conditions, when polaritons exit the area of the laser spot they acquire an extra velocity due to the conservation of energy, since the blueshifted energy inside the high density region of the spot is partially transformed in kinetic energy outside of the spot region, resembling the waterfall in a river.

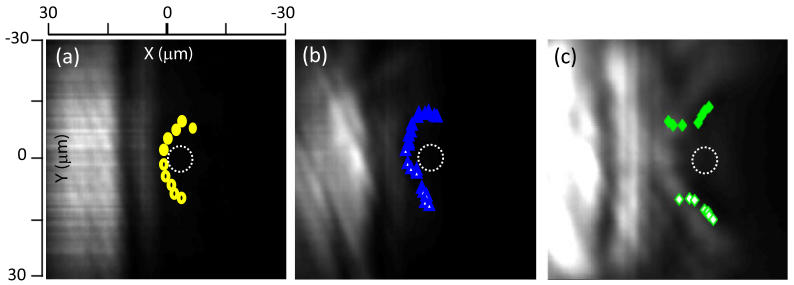

Fig. 7.7 Vortex-antivortex trajectories for different intensities of the pumping pulse: (**a**)–(**c**) refer to a fixed CW power, $P_{cw} = 26$ mW, and different pulse powers, $P_{pulse} = 1$ mW, 4 mW and 14 mW respectively. To higher pump intensities correspond higher polariton densities and therefore higher critical velocities: the nucleation of vortices takes place at positions where the local flow speed is higher, which occurs towards the equator of the defect. The background images are the corresponding time-integrated real space emission patterns

the fluid hits the barrier in regions where the polariton density is higher, which corresponds to higher critical velocities, going from Fig. 7.6a to Fig. 7.6c. Therefore, the local flow velocity matches with the critical velocity only at positions nearer to the equator of the obstacle, where the tangential velocity is higher [44], pushing the vortex formation away from the center of the polariton flow. This relation between changes in the local value of the critical velocities and positions of vortex nucleation has been indeed confirmed by direct measurements of the local changes in the polariton densities at the defect surface.

Increasing the Density of the Polariton Gas Conversely, the effect of increasing the polariton density can be measured by repeating the experiment with different powers of the pulsed laser with a given value of the barrier height and size. In Fig. 7.7, the barrier parameters are the same as in Fig. 7.6b, but the pulse power has been increased from $P_{pulse} = 1$ mW (Fig. 7.7a) to $P_{pulse} = 4$ mW (Fig. 7.7b) and $P_{pulse} = 14$ mW (Fig. 7.7c). The higher injected polariton density means an increase of the critical velocity, and manifests in a vertical shift of the nucleation points, as it is especially clear comparing the cases shown in Figs. 7.7b and 7.7c. The shift towards the equator of the obstacle, where the flow velocity is higher, is needed for compensating the higher sound speed experimented by the fluid. A rough estimation of the sound speed can be obtained from the aperture angle α of the Cerenkov-like conical density modulation, which forms past the defect, via the relation

$$\sin\left(\frac{\alpha}{2}\right) = \frac{c_s}{v_f}. \tag{7.9}$$

Consequently, to higher polariton densities correspond wider angles formed by the vortex trajectories with respect to the direction of the flow, as can be easily appreciated in Fig. 7.7.

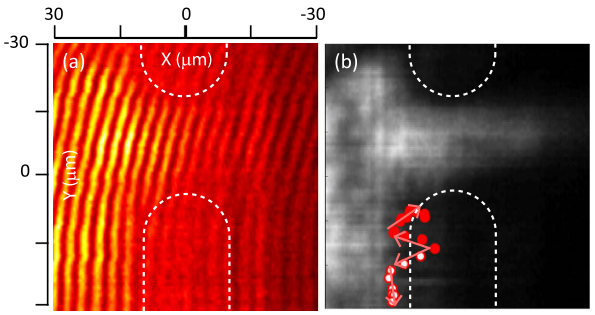

Fig. 7.8 (**a**) Interferograms taken 15 ps after the arrival of the pulse, showing the modification of the phase pattern induced by the presence of two shaped barriers separated by a channel of 20 micron which allows for the polariton flow to pass through. (**b**) shows the vortex-antivortex trajectories (*open and full red circle* respectively) plotted on the background image which is the time-integrated real-space emission of the polariton fluid while flowing through the barriers

Changing the Shape of the Potential Barrier The remarkable different phenomenology and dynamics of the vortex pairs can also be explored by simple manipulation of the shape of optical barriers. In Fig. 7.8, the shape of the CW laser beam has been changed by using convex lenses into a rectangular extended barrier with a channel of about 20 μm to allow polaritons to flow through. In Fig. 7.8a is shown an interferogram, taken 15 picoseconds after the arrival of the pulse, when the homogeneity of the phase is altered near the border of the barriers. In Fig. 7.8b, the time-integrated real space emission, modulated by the presence of the barriers, is shown as background, while the trajectories of the vortex and antivortex are plotted in the figure as open and full circle, respectively. When the fluid hits the barriers, a vortex pair forms near the boundary and then it is scattered back, reflected by the barrier itself. Subsequently, the flowing polaritons push the vortex towards the channel, and the antivortex along the barrier, showing the possibility to separate the vortex-antivortex pair in a controlled and stable way.

Creation/Annihilation of Vortices Around a Small Obstacle If the size and height of the obstacle are reduced to obtain only a shallow potential barrier, as shown in Fig. 7.9, the vortex-antivortex pair recombine right downstream of the obstacle, showing the ultrashort lifetime of a topological excitation created in the quantum fluid. In Fig. 7.9, the polariton fluid is moving in the rightward direction against a small circular barrier, indicated by a white open circle. From the interferograms of Fig. 7.9a, the vortex-antivortex pair formation can be appreciated as typical fork-like dislocations in front of the defect few picoseconds after the arrival of the pulse. The polariton fluid pushes the vortex and the antivortex to the opposite sides of the defect, but keeping a sort of ordered streamline flow, where the vortex pair follows the boundaries of the obstacle as evidenced in Figs. 7.9b–d. Indeed, the polariton density is not strongly reduced in the wake of the shallow potential barrier, allowing for the observation of vortex/antivortex annihilation once the flow has recovered its unperturbed pathway after passing the position of the obstacle. The coherence of

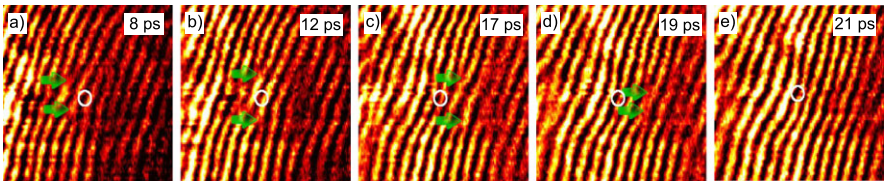

Fig. 7.9 Five snapshots of the phase pattern of the polariton fluid, flowing from the left to the right in the images, taken at different delays after the arrival of the pulse. The position of the shallow optical barrier is represented by the *white open circle* at the center of the panels. In (**a**), polaritons are mainly distributed before the obstacle, resulting in the higher visibility of the fringes in the *left part* of the image. After about 10 ps, a vortex pair nucleates in front of the obstacle and it is driven by the polariton flow around the obstacle itself (**b**). In (**c**), vortex and antivortex follow their ordered motion thanks to the absence of transverse currents. In (**d**), the fluid shows only a weak density deformation behind the barrier, keeping the coherent phase even in this region. Vortex and antivortex start to recombine. After 20 ps (**e**), when most of the fluid has passed the barrier, the homogeneous phase pattern of the fluid is recovered, showing a clean interferograms without phase singularities

the fluid at this stage is shown as a clean interferograms in Fig. 7.9e. The observation of this ordered dynamics around the potential barrier is due to the absence of cross currents perpendicular to the direction of motion and represents the quantum counterpart of the classical laminar flow.

7.3.3 Vortex Traps

We have seen that an artificial, optically induced, potential barrier is able to produce the hydrodynamic nucleation of vortices in a flowing polariton fluid. An alternative strategy is to work under CW excitation, modifying the intensity profile of the beam by a tailored mask to nucleate and then trap vortices as theoretically suggested in [48] and experimentally demonstrated in [52].

In Fig. 7.10a, polaritons are sent against a potential barrier formed by a natural defect present in the microcavity, in the absence of any mask: the phase of the polariton fluid is locked to the one of the pumping laser, so that vortices are prevented from nucleating even at supersonic speeds, as shown by the homogeneity of the interferograms in Fig. 7.10g. When a triangular metallic mask is used to create a dark region in the exciting laser field right downstream of the defect (dark triangle in Fig. 7.10b), a vortex-antivortex pair, nucleated in the proximity of the defect, gets trapped inside the dark area and can be observed as phase dislocations in Fig. 7.10h. Indeed, as the phase of the fluid is homogeneous outside the triangle, vortices cannot diffuse out and a steady state forms where they get permanently trapped within the triangle borders. Moving the dark region slightly away from the defect, we can still appreciate the presence of some trapped vortices within this area (Figs. 7.10c–d and Figs. 7.10i–j). On the other hand, if the dark trap is moved too far away from the defect (Fig. 7.10e and Fig. 7.10k), vortex nucleation is frustrated by the homogeneous

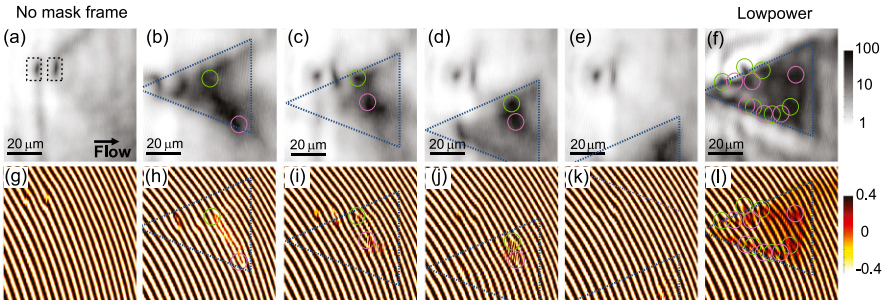

Fig. 7.10 Real space images (**a**)–(**f**) and corresponding interferograms (**g**)–(**l**) for polaritons injected by a CW laser beam and flowing rightward against a natural photonic defect present in the microcavity (black spots in (**a**), marked by *rectangular dotted contours*). In (**a**), (**g**), no mask is applied, so that the phase is pinned to that of the laser and the density is almost uniform behind the defect. In (**b**), a dark region is created behind the defect and a pair of vortices (*green and magenta solid circles*) nucleates and gets trapped inside the triangular area, as evidenced by the phase dislocations shown in the interferograms (**h**). In (**c**)–(**e**) and (**i**)–(**k**), the triangular mask is shifted with respect to the optical defect. In (**c**), (**d**), (**i**), (**j**), the lateral shift is small enough for vortices to still nucleate inside the triangular trap. In (**e**), (**k**), the mask has been shifted too far away from the defect and vortex nucleation is frustrated due to the homogeneous phase imprinted by the pump laser. In (**f**), (**l**) the pumping power of the laser is lowered to allow for many vortex pairs to get trapped

phase that is imprinted by the pump laser. As a result, no vortex is present. For sufficiently high intensities of the resonant CW laser, the amount of light diffracted by the edges of the metallic mask is sufficient to partially fix the laser phase in the inner region, as is the case of Figs. 7.10b, c, d, where only a pair of vortices is present. However, reducing the total laser power, the light field inside the triangle becomes negligible and the number of trapped vortices increases, as shown in Figs. 7.10f–l, demonstrating the possibility of storing different quantities of vortex pairs in an ordered lattice of vortex-antivortex pairs.

7.4 Oblique Dark Solitons

In the previous section, we have seen that the interplay between the local speed of sound and the fluid speed determines the nucleation point and trajectory of vortex-antivortex pairs around an obstacle. The presence of the potential barrier gives rise to transverse currents resulting in density and velocity gradients with an associated energy proportional to the gradients. This energy, which arises from the particle interactions and the quantum pressure, characteristic of inhomogeneous boson gases, is the analogous of the shear stress in classical fluids. When it is large enough (on the order of $\hbar g/(\pi\xi^2)$), it relaxes through the emission of a vortex-antivortex pair. In this way, a non-viscous fluid, like a superfluid, can dissipate its energy. This process is different to what is usually described in the Landau model, in which phonons

are, instead, the quasi-particles which account for the extra energy released by the fluid, and the process takes place at fluid velocities lower than the speed of sound.

In the case of the experiments on the turbulent dynamics described in Sect. 7.3, in which the fluid is injected in the form of a spatially and temporally localised packet, we have seen that just a pair of vortices is nucleated. We can now consider the situation in which a steady flow is continuously injected upstream from an obstacle. Also in this case, if the transverse currents induced by the obstacle are big enough, a sequence of vortex-antivortex pairs will nucleate. When the first pair is emitted, the transverse velocity is fully compensated by the circulation in the vortices, and the fluid becomes momentarily laminal. Very rapidly, new transverse currents are induced by the obstacle and a subsequent vortex-antivortex pair nucleates and is dragged away. In this way we expect a continuous formation of vortices around the obstacle, giving rise to vortex-antivortex streets [44, 46]. The generation rate is given by the ratio of fluid to sound speeds [46, 60]: the higher the ratio the higher the generation rate.

This situation is studied in the simulations shown in Fig. 7.3, in which the polariton flow is injected with a fixed speed, and the polariton density (i.e., the sound speed) is varied. The superfluid regime (Fig. 7.3b) is lost when the speed of sound is decreased below some threshold. Transverse currents appear and give rise to the continuous emission of vortex-antivortex pairs (Fig. 7.3c). If the speed of sound is decreased even further, the rate of vortex nucleation increases up to a point in which the vortex cores start to overlap, giving rise to the formation of oblique dark solitons, as seen in Figs. 7.3d–f.

Dark solitons are particular solutions of the Gross-Pitaevskii equation describing boson condensates subject to repulsive interactions. They are characterised by a notch in the density whose shape is not subject to dispersion thanks to the nonlinearity arising from particle interactions. One characteristic of solitons is that the phase of the fluid jumps up to π when crossing them [47]. The depth n_s/n, width w and phase jump δ are interrelated via the expression [30, 45, 61]:

$$\sin\left(\frac{\delta}{2}\right) = \left(1 - \frac{n_s}{n}\right)^{1/2} = \left(1 - \frac{\xi^2}{w^2}\right)^{1/2} = \frac{v_s}{c_s}, \tag{7.10}$$

where v_s is the soliton propagation speed in the fluid.

The specific phase structure of the fluid across the solitons has been used in one-dimensional atomic condensates to nucleate them, via the phase imprinting of the condensate using optical techniques [61, 62]. Here we will discuss the spontaneous hydrodynamic nucleation of solitons in the wake of an obstacle. As in the case of hydrodynamic nucleation of vortices, the phase of the fluid must be left free to evolve. This is what is done in the experiments [30] shown in Fig. 7.11. A mask as the one described for the experiments of Figs. 7.5 and 7.6 is used to inject polaritons with a resonant *cw* laser above the red line. In this case, as a potential barrier, we use a photonic defect naturally present during the growth of the microcavity structure. At high density (Fig. 7.11a), well in the subsonic regime, the polariton gas is superfluid, flowing around the obstacle without perturbation. This is also seen in

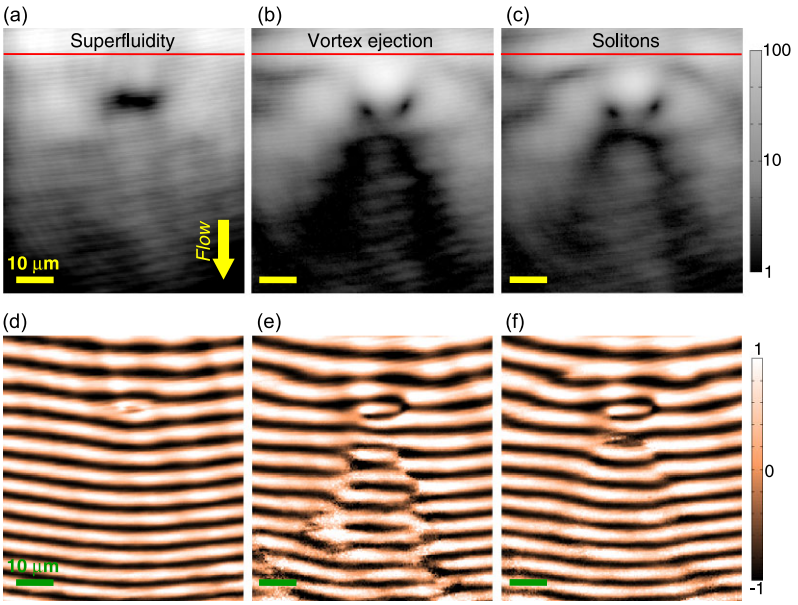

Fig. 7.11 (**a**) Real space image of the polariton fluid in the superfluid regime in the presence of a potential barrier formed by a photonic defect present in the microcavity. Injection takes place above the *red line* in order to leave the phase of the fluid free to evolve. In this regime, at high density, the fluid presents a homogeneous phase gradient, as observed in the interferometric image (**d**), formed from the superposition of the real space emission and a reference beam of constant phase. At lower density, the presence of the barrier gives rise to the formation of vortex streets, evidenced in the real space emission as low density traces in the wake of the obstacle (**b**), and with the formation of phase singularities in the interferometric images (**e**). Finally, at lower powers (supersonic regime), the vortex streets evolve into solitons (**c**), characterised by a phase shift of the wavefunction when crossing them. Extracted from [30]

the interferometric image depicted in Fig. 7.11d, where no phase dislocations are present, evidencing a thoroughly homogeneous flow.

When the density is decreased, the ratio v_s/c_s increases, and vortex-antivortex pairs are continuously nucleated and dragged away in the wake of the barrier. This is evidenced by the appearance of two low density channels in Fig. 7.11b, and by the phase dislocations in Fig. 7.11e.

As discussed above, if the ratio v_s/c_s is further increased by reducing the excitation density, the vortex nucleation regime gives way to the formation of oblique dark solitons. Dark solitons are evidenced in Fig. 7.11c as long dark traces starting in the potential barrier, with their characteristic phase jump as shown in the interferometric image displayed in Fig. 7.11f.

The hydrodynamic regime we have described, has been so far the only way to nucleate stable solitons in a two dimensional quantum fluid. The reason is that a dark soliton in a fluid at rest is unstable due to the fact that the soliton energy decreases when its depth decreases. A transverse perturbation to the soliton will then result in its collapse [63], and the dissipation of the soliton energy in the form of vor-

tices. This is the situation found when trying to nucleate solitons in two-dimensional atomic BEC at rest [64, 65]. El and coworkers showed theoretically in 2006 that stable dark solitons could be nucleated in the wake of an obstacle in a flowing atomic condensate [66]. In this case, if the fluid moves at sufficiently high velocity, instabilities are drifted away towards the end of the soliton, rendering it stable [67, 68]. In the case of polaritons, the additional damping, originated in the escape of photons out of the cavity, might result in an additional source of stability. Indeed, soliton nucleation in polaritons has been observed at subsonic speeds, much lower than the fluid speeds predicted for atomic condensates with quasi-infinite lifetimes [68].

The experimental examples we have provided above show that polariton quantum fluids are an excellent testbed for the study of the mechanisms of superflow. The break up of superfluidity can appear due to the onset of phonon-like excitations, as predicted by the Landau model, and via the nucleation of topological excitations like quantised vortices and oblique solitons. We have seen that the polariton dynamics is very rich, leading to different regimes which depend on the nature, size and shape of the obstacles, and on the density and speed of the quasi-particle flow. This results in unprecedented situations like the nucleation of vortices upstream from the barrier, or the observation of stable dark solitons.

7.5 All Optical Switching, Transistor Operation and Beyond

The fluid dynamics of exciton-polaritons in microcavities are not only interesting for their intrinsic phenomenology, as we have seen in the previous sections, but they also show very peculiar non-linear properties which make them very attractive for applications in the realm of optical devices and, eventually, as classical and quantum logic elements for optical integrated circuits. Semiconductor microcavities share many of the properties of an optical Kerr medium with a $\chi^{(3)}$ non-linearity. For instance, low threshold bi-stable behaviour has been observed and, in combination with the spin [69–71] and transport properties [6] of polaritons they can be exploited for the creation of novel spintronic devices [72]. One of their advantages is that, due to their photonic component, polaritons have a much longer coherence time than electrons in semiconductors. In the last part of this chapter we will review recent experiments which make use of the strong optical non-linear response in microcavities in view of new optical functionalities.

7.5.1 Propagating Spin Switch

Polariton interactions present a very strong spin asymmetry arising from their hybrid light matter nature. As discussed in Sect. 7.3.1 the optical selection rules in combination with the normal mode coupling results in interactions between polaritons with parallel spin (α_1) much stronger and of opposite sign than for polaritons with

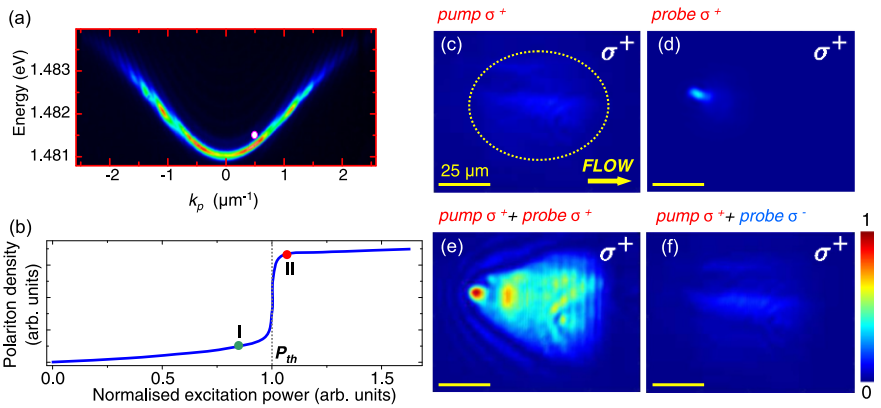

Fig. 7.12 Spin-switch operation. (**a**) Polariton dispersion where with a white spot the energy and momentum of the pump beam is shown. The slight blue-detuning from the lower polariton branch gives rise to the non-linear transmission curve schematised in (**b**), with a sharp threshold P_{th}. Point I corresponds to a low power "off" state while point II shows a high power "on" state. (**c**) Shows the σ^+ pump spot with a power corresponding to point I and extended over the area marked by the dashed line. (**d**) Image of the transmitted control beam in the same polarisation as the pump. When both beams arrive together at the sample the full pump spot is switched to the *on* regime (**e**). If the control is σ^- no switching takes place (**f**). Please note that panels (**c**)–(**f**) share the same intensity scale. Detection is performed in the σ^+ configuration. Extracted from [29]

opposite spins (α_2) [54]. The first give rise to a blueshift of the polariton energy, while the second results in a redshift. These properties can be used to induce spatial spin patterns by selecting the proper elliptical polarisation of excitation [73–75], or to enter a regime of multistability in which the system can emit either right-circular, left-circular or linearly polarised light for the same set of excitation conditions [76, 77]. In this case, indeed, the output polarisation can be selected not only by the parameters used for the generation of the coherent polariton state, but also with a specific choice of the path used to prepare the system. The spin interaction asymmetry along with the presence of a TE-TM splitting results also in polarisation inversion phenomena observed in the four-wave mixing [69, 71, 78, 79] and bosonic stimulation regimes [70, 80].

A fundamental and quite spectacular application of the spin dependent interactions in the configuration of quasi-resonant excitation is the propagating spin switch [29]. Its operation can be understood by looking at Fig. 7.12b. The sketched emission curve corresponds to polaritons with a given spin ($S_z = +1$) excited by a circularly polarised pump beam (σ^+) with an in-plane momentum of 0.5 μm^{-1}, and detuned by 0.16 meV from the lower polariton branch energy. As the pump beam is detuned from the polariton energy, optical injection is inefficient and the polariton population is very low at low power with no significant blueshift. This is the *off* state, characterised by a low transmission (point I in Fig. 7.12b). If now the laser power is increased, the polariton state, although still out of resonance, gets more and more populated. This corresponds to an increase of the polariton-polariton interactions which result in the renormalisation of the energy of the system. When the pump

power is raised above a certain threshold P_{th}, the polariton dispersion becomes in resonance with the pump laser, with a consequent change of the transmission response at the energy of the pump beam and an abrupt injection of a strong polariton population. This corresponds to the *on* state (point II in Fig. 7.12b), characterised by a high polariton population and a strong nonlinear emission.

If the system is pumped to point I (P_I), an additional control beam with a very low power $P_{th} - P_I$ will be able to switch the system to point II, with a high transmission. Due to the strong difference in absolute value and sign between α_1 and α_2, the passage from I to II is only possible if the weak control beam has the same circular polarisation as the strong pump beam. Otherwise it will not contribute to the blueshift of the polariton energy needed to overcome the non-linear threshold.

The rapid polariton motion induces the propagation of the switched signal. This effect is shown in Figs. 7.12c–f. The σ^+ cw pump beam with a polariton density corresponding to point I, is extended over a spot of 60 μm, Fig. 7.12c. A cw control beam of the same polarisation is turned on in a localised area of 4 μm, within the pump spot (Fig. 7.12d). Originally, only that area is switched to the *on* state, but polaritons move out (to the right) thanks to well-defined momentum of the pump given by the angle of incidence of the excitation laser. The passage to the *on* state rapidly propagates to the whole pump spot (Fig. 7.12e). If the control beam has a polarisation opposite to that of the pump, no switching takes place (Fig. 7.12f). Time resolved experiments using a pulsed control have confirmed this propagation mechanism, with a speed set by the momentum of the pump [81].

The device can also be operated as intensity switch whose polarisation state is set by the control beam. In order to do so we just need to pump the system with linear polarisation at a pump intensity corresponding to point I. In this case a circularly polarised control will induce the passage to point II of only the same circular polarisation component of the pump. In this way we can switch-on the whole pump spot with a weak control of the desired circular polarisation [29].

The spin-sensitive intensity-switch and the polarisation-controlled switch we have just described present extremely low values of the switching energy, estimated to be on the order of 1 fJ μm^{-2}. Additionally, the reduced polariton lifetime, set by the cavity decay, reduces the switch-on/switch-off operation to a few ps [81].

Apart from this state of the art values [82], one of the most interesting properties of the polariton switches is their propagation. While only engaged in a small point by the control beam, switching propagates all over the pump spot.

7.5.2 Polariton Transistor and Perspectives

The following logical next step, which is at present under study, is the use of polaritons as building blocks for an all-optical logic, of which the first element is the realisation of a polariton transistor [83]. In fact, optical logic and "switching" operation have already been demonstrated in many different cases with the use of non-linear optical elements and strong laser beams [84–87]. However, if a logical gate should be implemented in a circuit, it should satisfy some fundamental critical conditions

such as: cascadability, which is the compatibility of the input and output beams for serial interconnections of several devices; the logic level restoration; the isolation of the input/output, and, above all, the fact that with one output it should be possible to feed several devices, so to generate many input channels (fan-out/fan-in). All these conditions are hard to reach in standard optical devices and, so far, have not been simultaneously achieved in all the schemes proposed [88]. Nevertheless, using the combination of polariton fluids, which are very easy to manipulate, and their strong non-linear response to optical beams, it is possible to show that all these criteria can be fulfilled, under some conditions in an all-polaritonic device [83]. In combination with micro-structured patterns, as proposed in [72] for spin based logic gates, this opens the way to the realisation of polariton circuits, and eventually could work towards the realisation of a complex logic, based on all-optical elements.

References

1. A.J. Leggett, Superfluidity. Rev. Mod. Phys. **71**(2), S318 (1999)
2. C. Weisbuch, M. Nishioka, A. Ishikawa, Y. Arakawa, Observation of the coupled exciton-photon mode splitting in a semiconductor quantum microcavity. Phys. Rev. Lett. **69**(23), 3314 (1992)
3. A. Kavokin, J.J. Baumberg, G. Malpuech, F.P. Laussy, *Microcavities* (Oxford University Press, New York, 2007)
4. D. Sanvitto, V. Timofeev, *Exciton Polaritons in Microcavities: New Frontiers*. Springer Series in Solid-State Sciences (Springer, Berlin, 2012)
5. D. Ballarini, D. Sanvitto, A. Amo, L. Viña, M. Wouters, I. Carusotto, A. Lemaître, J. Bloch, Observation of long-lived polariton states in semiconductor microcavities across the parametric threshold. Phys. Rev. Lett. **102**, 056402 (2009)
6. A. Amo, D. Sanvitto, F.P. Laussy, D. Ballarini, E. del Valle, M.D. Martín, A. Lemaitre, J. Bloch, D.N. Krizhanovskii, M.S. Skolnick, C. Tejedor, L. Viña, Collective fluid dynamics of a polariton condensate in a semiconductor microcavity. Nature **457**(7227), 291 (2009)
7. D. Sanvitto, F.M. Marchetti, M.H. Szymanska, G. Tosi, M. Baudisch, F.P. Laussy, D.N. Krizhanovskii, M.S. Skolnick, L. Marrucci, A. Lemaitre, J. Bloch, C. Tejedor, L. Vina, Persistent currents and quantized vortices in a polariton superfluid. Nat. Phys. **6**(7), 527–533 (2010)
8. R.M. Stevenson, V.N. Astratov, M.S. Skolnick, D.M. Whittaker, M. Emam-Ismail, A.I. Tartakovskii, P.G. Savvidis, J.J. Baumberg, J.S. Roberts, Continuous wave observation of massive polariton redistribution by stimulated scattering in semiconductor microcavities. Phys. Rev. Lett. **85**(17), 3680 (2000)
9. P.G. Savvidis, J.J. Baumberg, R.M. Stevenson, M.S. Skolnick, D.M. Whittaker, J.S. Roberts, Angle-resonant stimulated polariton amplifier. Phys. Rev. Lett. **84**(7), 1547 (2000)
10. A.I. Tartakovskii, V.D. Kulakovskii, D.N. Krizhanovskii, M.S. Skolnick, V.N. Astratov, A. Armitage, J.S. Roberts, Nonlinearities in emission from the lower polariton branch of semiconductor microcavities. Phys. Rev. B **60**(16), R11293 (1999)
11. J. Kasprzak, M. Richard, S. Kundermann, A. Baas, P. Jeambrun, J.M.J. Keeling, F.M. Marchetti, M.H. Szymanska, R. André, J.L. Staehli, V. Savona, P.B. Littlewood, B. Deveaud, L.S. Dang, Bose-Einsten condensation of exciton polaritons. Nature **443**(7110), 409 (2006)
12. R. Balili, V. Hartwell, D. Snoke, L. Pfeiffer, K. West, Bose-Einsten condensation of microcavity polaritons in a trap. Science **316**(5827), 1007 (2007)

13. J. Kasprzak, D.D. Solnyshkov, R. André, L.S. Dang, G. Malpuech, Formation of an exciton polariton condensate: Thermodynamic versus kinetic regimes. Phys. Rev. Lett. **101**(14), 146404 (2008)
14. J. Levrat, R. Butté, E. Feltin, J.-F. Carlin, N. Grandjean, D. Solnyshkov, G. Malpuech, Condensation phase diagram of cavity polaritons in GaN-based microcavities: Experiment and theory. Phys. Rev. B **81**(12), 125305 (2010)
15. S. Christopoulos, G.B.H. von Hogersthal, A.J.D. Grundy, P.G. Lagoudakis, A.V. Kavokin, J.J. Baumberg, G. Christmann, R. Butte, E. Feltin, J.-F. Carlin, N. Grandjean, Room-temperature polariton lasing in semiconductor microcavities. Phys. Rev. Lett. **98**(12), 126405 (2007)
16. D. Bajoni, P. Senellart, E. Wertz, I. Sagnes, A. Miard, A. Lemaître, J. Bloch, Phys. Rev. Lett. **100**, 047401 (2008)
17. D. Sanvitto, A. Amo, L. Vina, R. André, D. Solnyshkov, G. Malpuech, Exciton-polariton condensation in a natural two-dimensional trap. Phys. Rev. B **80**(4), 045301 (2009)
18. A.P.D. Love, D.N. Krizhanovskii, D.M. Whittaker, R. Bouchekioua, D. Sanvitto, S. Al Rizeiqi, R. Bradley, M.S. Skolnick, P.R. Eastham, R. André, L.S. Dang, Intrinsic decoherence mechanisms in the microcavity polariton condensate. Phys. Rev. Lett. **101**(6), 067404 (2008)
19. D.N. Krizhanovskii, D. Sanvitto, A.P.D. Love, M.S. Skolnick, D.M. Whittaker, J.S. Roberts, Dominant effect of polariton-polariton interactions on the coherence of the microcavity optical parametric oscillator. Phys. Rev. Lett. **97**(9), 097402 (2006)
20. E. del Valle, D. Sanvitto, A. Amo, F.P. Laussy, R. André, C. Tejedor, L. Viña, Dynamics of formation and decay of coherence in a polariton condensate. Phys. Rev. Lett. **103**(9), 096404 (2009)
21. G. Nardin, K.G. Lagoudakis, M. Wouters, M. Richard, A. Baas, R. André, L.S. Dang, B. Pietka, B. Deveaud-Plédran, Dynamics of long-range ordering in an exciton-polariton condensate. Phys. Rev. Lett. **103**(25), 256402 (2009)
22. I. Carusotto, C. Ciuti, Probing microcavity polariton superfluidity through resonant Rayleigh scattering. Phys. Rev. Lett. **93**(16), 166401 (2004)
23. A. Baas, J.Ph. Karr, H. Eleuch, E. Giacobino, Optical bistability in semiconductor microcavities. Phys. Rev. A **69**(2), 023809 (2004)
24. A. Amo, J. Lefrère, S. Pigeon, C. Adrados, C. Ciuti, I. Carusotto, R. Houdré, E. Giacobino, A. Bramati, Superfluidity of polaritons in semiconductor microcavities. Nat. Phys. **5**, 805 (2009)
25. C. Leyder, M. Romanelli, J.Ph. Karr, E. Giacobino, T.C.H. Liew, M.M. Glazov, A.V. Kavokin, G. Malpuech, A. Bramati, Observation of the optical spin hall effect. Nat. Phys. **3**(9), 628–631 (2007)
26. R. Cerna, D. Sarchi, T.K. Paraïso, G. Nardin, Y. Léger, M. Richard, B. Pietka, O. El Daif, F. Morier-Genoud, V. Savona, M.T. Portella-Oberli, B. Deveaud-Plédran, Coherent optical control of the wave function of zero-dimensional exciton polaritons. Phys. Rev. B **80**(12), 121309 (2009)
27. R. Cerna, T. Paraïso, Y. Léger, M. Wouters, F. Morier-Genoud, M.T. Portella-Oberli, B. Deveaud-Plédran, Spatial dynamics of confined semiconductor microcavity polaritons. Phys. Rev. B **81**(11), 113306 (2010)
28. G. Nardin, K.G. Lagoudakis, B. Pietka, F. Morier-Genoud, Y. Léger, B. Deveaud-Plédran, Selective photoexcitation of confined exciton-polariton vortices. Phys. Rev. B **82**(7), 073303 (2010)
29. A. Amo, T.C.H. Liew, C. Adrados, R. Houdre, E. Giacobino, A.V. Kavokin, A. Bramati, Exciton-polariton spin switches. Nat. Photonics **4**(6), 361–366 (2010)
30. A. Amo, S. Pigeon, D. Sanvitto, V.G. Sala, R. Hivet, I. Carusotto, F. Pisanello, G. Lemenager, R. Houdre, E. Giacobino, C. Ciuti, A. Bramati, Polariton superfluids reveal quantum hydrodynamic solitons. Science **332**(6034), 1167–1170 (2011)
31. M. Wouters, I. Carusotto, Goldstone mode of optical parametric oscillators in planar semiconductor microcavities in the strong-coupling regime. Phys. Rev. A **76**(4), 043807 (2007)
32. D.M. Whittaker, Effects of polariton-energy renormalization in the microcavity optical parametric oscillator. Phys. Rev. B **71**(11), 115301 (2005)

33. D. Sanvitto, D.M. Whittaker, M.S. Skolnick, J.S. Roberts, Continuous wave pump-probe experiment on a planar microcavity. Phys. Status Solidi (a) **202**(3), 353 (2005)
34. C. Ciuti, I. Carusotto, Quantum fluid effects and parametric instabilities in microcavities. Phys. Status Solidi (b) **242**(11), 2224 (2005)
35. M. Wouters, I. Carusotto, Excitations in a nonequilibrium Bose-Einsten condensate of exciton polaritons. Phys. Rev. Lett. **99**(14), 140402 (2007)
36. M.H. Szymanska, J. Keeling, P.B. Littlewood, Nonequilibrium quantum condensation in an incoherently pumped dissipative system. Phys. Rev. Lett. **96**(23), 230602 (2006)
37. M. Wouters, I. Carusotto, Superfluidity and critical velocities in nonequilibrium Bose-Einstein condensates. Phys. Rev. Lett. **105**(2), 020602 (2010)
38. E. Cancellieri, F.M. Marchetti, M.H. Szymanska, C. Tejedor, Multistability of a two-component exciton-polariton fluid. Phys. Rev. B **83**(21), 214507 (2011)
39. J.R. Abo-Shaeer, C. Raman, J.M. Vogels, W. Ketterle, Observation of vortex lattices in Bose-Einsten condensates. Science **292**(5516), 476 (2001)
40. C. Ryu, M.F. Andersen, P. Clade, V. Natarajan, K. Helmerson, W.D. Phillips, Observation of persistent flow of a Bose-Einstein condensate in a toroidal trap. Phys. Rev. Lett. **99**(26), 260401 (2007)
41. M. Wouters, V. Savona, Creation and detection of vortices in polariton condensates, arXiv: 0904.2966v1 (2009)
42. F.M. Marchetti, M.H. Szymańska, C. Tejedor, D.M. Whittaker, Spontaneous and triggered vortices in polariton optical-parametric-oscillator superfluids. Phys. Rev. Lett. **105**, 063902 (2010)
43. G. Tosi, F.M. Marchetti, D. Sanvitto, C. Antón, M.H. Szymańska, A. Berceanu, C. Tejedor, L. Marrucci, A. Lemaître, J. Bloch, L. Viña, Onset and dynamics of vortex-antivortex pairs in polariton optical parametric oscillator superfluids. Phys. Rev. Lett. **107**, 036401 (2011)
44. T. Frisch, Y. Pomeau, S. Rica, Transition to dissipation in a model of superflow. Phys. Rev. Lett. **69**(11), 1644–1647 (1992)
45. A.D. Jackson, G.M. Kavoulakis, C.J. Pethick, Solitary waves in clouds of Bose-Einstein condensed atoms. Phys. Rev. A **58**(3), 2417–2422 (1998)
46. T. Winiecki, B. Jackson, J.F. McCann, C.S. Adams, Vortex shedding and drag in dilute Bose-Einstein condensates. J. Phys. B, At. Mol. Opt. Phys. **33**(19), 4069 (2000)
47. L. Pitaevskii, S. Strindgari, *Bose-Einsten Condensation*, 1st edn. (Clarendon Press, Oxford, 2003)
48. S. Pigeon, I. Carusotto, C. Ciuti, Hydrodynamic nucleation of vortices and solitons in a resonantly excited polariton superfluid. Phys. Rev. B **83**(14), 144513 (2011)
49. K.G. Lagoudakis, M. Wouters, M. Richard, A. Baas, I. Carusotto, R. André, L.S. Dang, B. Deveaud-Pledran, Quantized vortices in an exciton-polariton condensate. Nat. Phys. **4**(9), 706 (2008)
50. G. Roumpos, M.D. Fraser, A. Löffler, S. Höfling, A. Forchel, Y. Yamamoto, Single vortex-antivortex pair in an exciton-polariton condensate. Nat. Phys. **7**, 129–133 (2011)
51. G. Nardin, G. Grosso, Y. Leger, B. Pietka, F. Morier-Genoud, B. Deveaud-Pledran, Hydrodynamic nucleation of quantized vortex pairs in a polariton quantum fluid. Nat. Phys. **7**(8), 635–641 (2011)
52. D. Sanvitto, S. Pigeon, A. Amo, D. Ballarini, M. De Giorgi, I. Carusotto, R. Hivet, F. Pisanello, V.G. Sala, P.S. Soares-Guimaraes, R. Houdré, E. Giacobino, C. Ciuti, A. Bramati, G. Gigli, All-optical control of the quantum flow of a polariton superfluid. Nat. Photogr. **5**, 610 (2011)
53. A. Kavokin, P.G. Lagoudakis, G. Malpuech, J.J. Baumberg, Polarization rotation in parametric scattering of polaritons in semiconductor microcavities. Phys. Rev. B **67**(19), 195321 (2003)
54. P. Renucci, T. Amand, X. Marie, P. Senellart, J. Bloch, B. Sermage, K.V. Kavokin, Microcavity polariton spin quantum beats without a magnetic field: A manifestation of Coulomb exchange in dense and polarized polariton systems. Phys. Rev. B **72**(7), 075317 (2005)
55. A. Amo, S. Pigeon, C. Adrados, E. Giacobino, C. Ciuti, A. Bramati, Light engineering of the polariton landscape in semiconductor microcavities. Phys. Rev. B **82**, 081301 (2010)

56. E. Wertz, L. Ferrier, D.D. Solnyshkov, R. Johne, D. Sanvitto, A. Lemaitre, I. Sagnes, R. Grousson, A.V. Kavokin, P. Senellart, G. Malpuech, J. Bloch, Spontaneous formation and optical manipulation of extended polariton condensates. Nat. Phys. **6**(11), 860–864 (2010)
57. L. Ferrier, E. Wertz, R. Johne, D.D. Solnyshkov, P. Senellart, I. Sagnes, A. Lemaitre, G. Malpuech, J. Bloch, Interactions in confined polariton condensates. Phys. Rev. Lett. **106**(12), 126401 (2011)
58. G. Tosi, G. Christmann, N.G. Berloff, P. Tsotsis, T. Gao, Z. Hatzopoulos, P.G. Savvidis, J.J. Baumberg, Sculpting oscillators with light within a nonlinear quantum fluid. Nat. Phys. **8**, 190 (2012)
59. G. Christmann, G. Tosi, N.G. Berloff Panos Tsotsis, P.S. Eldridge, Z. Hatzopoulos, P.G. Savvidis, J.J. Baumberg, Polariton ring condensates and sunflower ripples in an expanding quantum liquid. Phys. Rev. B **85**, 235303 (2012)
60. K. Sasaki, N. Suzuki, H. Saito, Bernard-von Karman vortex street in a Bose-Einstein condensate. Phys. Rev. Lett. **104**(15), 150404 (2010)
61. J. Denschlag, J.E. Simsarian, D.L. Feder, C.W. Clark, L.A. Collins, J. Cubizolles, L. Deng, E.W. Hagley, K. Helmerson, W.P. Reinhardt, S.L. Rolston, B.I. Schneider, W.D. Phillips, Generating solitons by phase engineering of a Bose-Einstein condensate. Science **287**(5450), 97–101 (2000)
62. S. Burger, K. Bongs, S. Dettmer, W. Ertmer, K. Sengstock, A. Sanpera, G.V. Shlyapnikov, M. Lewenstein, Dark solitons in Bose-Einstein condensates. Phys. Rev. Lett. **83**(25), 5198–5201 (1999)
63. V.E. Zakharov, Instability and nonlinear oscillations of solitons. JETP Lett. **22**(7), 172–173 (1975)
64. B.P. Anderson, P.C. Haljan, C.A. Regal, D.L. Feder, L.A. Collins, C.W. Clark, E.A. Cornell, Watching dark solitons decay into vortex rings in a Bose-Einstein condensate. Phys. Rev. Lett. **86**(14), 2926–2929 (2001)
65. N.S. Ginsberg, J. Brand, L. Vestergaard Hau, Observation of hybrid soliton vortex-ring structures in Bose-Einstein condensates. Phys. Rev. Lett. **94**(4), 040403 (2005)
66. G.A. El, A. Gammal, A.M. Kamchatnov, Oblique dark solitons in supersonic flow of a Bose-Einstein condensate. Phys. Rev. Lett. **97**(18), 180405 (2006)
67. A.M. Kamchatnov, L.P. Pitaevskii, Stabilization of solitons generated by a supersonic flow of Bose-Einstein condensate past an obstacle. Phys. Rev. Lett. **100**(16), 160402 (2008)
68. A.M. Kamchatnov, S.V. Korneev, Condition for convective instability of dark solitons. Phys. Lett. A **375**, 2577 (2011)
69. P.G. Lagoudakis, P.G. Savvidis, J.J. Baumberg, D.M. Whittaker, P.R. Eastham, M.S. Skolnick, J.S. Roberts, Stimulated spin dynamics of polaritons in semiconductor microcavities. Phys. Rev. B **65**, 161310 (2002)
70. I. Shelykh, K.V. Kavokin, A.V. Kavokin, G. Malpuech, P. Bigenwald, H. Deng, G. Weihs, Y. Yamamoto, Semiconductor microcavity as a spin-dependent optoelectronic device. Phys. Rev. B **70**, 035320 (2004)
71. C. Leyder, T.C.H. Liew, A.V. Kavokin, I.A. Shelykh, M. Romanelli, J.Ph. Karr, E. Giacobino, A. Bramati, Interference of coherent polariton beams in microcavities: Polarization-controlled optical gates. Phys. Rev. Lett. **99**(19), 196402 (2007)
72. T.C.H. Liew, A.V. Kavokin, I.A. Shelykh, Optical circuits based on polariton neurons in semiconductor microcavities. Phys. Rev. Lett. **101**(1), 016402 (2008)
73. I.A. Shelykh, T.C.H. Liew, A.V. Kavokin, Spin rings in semiconductor microcavities. Phys. Rev. Lett. **100**(11), 116401 (2008)
74. D. Sarkar, S.S. Gavrilov, M. Sich, J.H. Quilter, R.A. Bradley, N.A. Gippius, K. Guda, V.D. Kulakovskii, M.S. Skolnick, D.N. Krizhanovskii, Polarization bistability and resultant spin rings in semiconductor microcavities. Phys. Rev. Lett. **105**(21), 216402 (2010)
75. C. Adrados, A. Amo, T.C.H. Liew, R. Hivet, R. Houdré, E. Giacobino, A.V. Kavokin, A. Bramati, Spin rings in bistable planar semiconductor microcavities. Phys. Rev. Lett. **105**(21), 216403 (2010)

76. N.A. Gippius, I.A. Shelykh, D.D. Solnyshkov, S.S. Gavrilov, Y.G. Rubo, A.V. Kavokin, S.G. Tikhodeev, G. Malpuech, Polarization multistability of cavity polaritons. Phys. Rev. Lett. **98**, 236401 (2007)
77. T.K. Paraïso, M. Wouters, Y. Leger, F. Mourier-Genoud, B. Deveaud-Plédran, Multistability of a coherent spin ensemble in a semiconductor microcavity. Nat. Mater. **10**(1), 80 (2011)
78. G. Dasbach, C. Diederichs, J. Tignon, C. Ciuti, Ph. Roussignol, C. Delalande, M. Bayer, A. Forchel, Polarization inversion via parametric scattering in quasi-one-dimensional microcavities. Phys. Rev. B **71**(16), 161308 (2005)
79. D.N. Krizhanovskii, D. Sanvitto, I.A. Shelykh, M.M. Glazov, G. Malpuech, D.D. Solnyshkov, A. Kavokin, S. Ceccarelli, M.S. Skolnick, J.S. Roberts, Rotation of the plane of polarization of light in a semiconductor microcavity. Phys. Rev. B **73**(7), 073303 (2006)
80. M.D. Martín, G. Aichmayr, L. Viña, R. André, Polarization control of the nonlinear emission of semiconductor microcavities. Phys. Rev. Lett. **89**(7), 077402 (2002)
81. C. Adrados, T.C.H. Liew, A. Amo, M.D. Martín, D. Sanvitto, C. Antón, E. Giacobino, A. Kavokin, A. Bramati, L. Viña, Motion of spin polariton bullets in semiconductor microcavities. Phys. Rev. Lett. **107**(14), 146402 (2011)
82. K. Nozaki, T. Tanabe, A. Shinya, S. Matsuo, T. Sato, H. Taniyama, M. Notomi, Subfemtojoule all-optical switching using a photonic-crystal nanocavity. Nat. Photonics **4**(7), 477–483 (2010)
83. D. Ballarini, M. De Giorgi, E. Cancellieri, R. Houdré, E. Giacobino, R. Cingolani, A. Bramati, G. Gigli, D. Sanvitto, All-optical polariton transistor. Nat. Commun. **4**, 1778 (2013)
84. B.P.J.C.P. Schmid, J.H. Lapointe, J. Janz, S. Glesk I, All-optical switching using nonlinear subwavelength Mach-Zehnder on silicon. Opt. Express (2011)
85. P.J.P. Smirl, A.L. Johnston W. J, Ultrafast all-optical polarization switching in Bragg-spaced quantum wells at 80 k. J. Appl. Phys. (2007)
86. C.A. Barrios, R.R. Panepucci, M. Lipson, V.R Almeida, All-optical control of light on a silicon chip. Nature **431**, 1081 (2004)
87. Y.Y. Kawaguchi, H. Mori T, Low-switching-energy and high-repetition-frequency all-optical flip-flop operations of a polarization bistable vertical-cavity surface-emitting laser. Appl. Phys. Lett. (2006)
88. D.A.B. Miller, Are optical transistors the logical next step? Nat. Photonics (2010)

Chapter 8
Exciton-Polariton Condensates in Zero-, One-, and Two-Dimensional Lattices

Na Young Kim, Yoshihisa Yamamoto, Shoko Utsunomiya, Kenichiro Kusudo, Sven Höfling, and Alfred Forchel

Abstract Microcavity exciton-polaritons are quantum quasi-particles arising from the strong light-matter coupling. They have exhibited rich quantum dynamics rooted from bosonic nature and inherent non-equilibrium condition. Dynamical condensation in microcavity exciton-polaritons has been observed at much elevated temperatures in comparison to ultracold atom condensates. Recently, we have investigated the behavior of exciton-polariton condensates in artificial trap and lattice geometries in zero-dimension, one-dimension (1D) and two-dimension (2D). Coherent π-state with p-wave order in a 1D condensate array and d-orbital state in a 2D square lattice are observed. We anticipate that the preparation of high-orbital condensates can be further extended to probe dynamical quantum phase transition in a controlled manner as quantum emulation applications.

8.1 Overview

All optical phenomena, whether visible or invisible, are ultimately resulting from an underlying mechanism: light-matter interaction. As a form of electromagnetic waves, the static and dynamical behavior of light and its interaction are well described within the classical electromagnetism framework, which was established more than 150 years ago [1]. Combined with quantum pictures, this fundamental physical knowledge conceptualized spontaneous and stimulated emission of radiations early 20th century, and the quest of engineering the light-matter interaction has been a driving force to invent novel and influential photonic devices. An optical cavity or optical resonator is an essential structure to confine the light and modify

N.Y. Kim (✉) · Y. Yamamoto
E. L. Ginzton Laboratory, Stanford University, Stanford, CA 94305, USA
e-mail: nayoung@stanford.edu

Y. Yamamoto · S. Utsunomiya · K. Kusudo
National Institute of Informatics, Hitotsubashi, Chiyoda-ku, Tokyo 101-8430, Japan

S. Höfling · A. Forchel
Technische Physik and Wilhelm-Conrad-Röntgen-Research Center for Complex Material Systems, Universität Würzburg, Am Hubland, Würzburg 97074, Germany

A. Bramati, M. Modugno (eds.), *Physics of Quantum Fluids*,
Springer Series in Solid-State Sciences 177, DOI 10.1007/978-3-642-37569-9_8,

its interaction. The simplest form of the cavity is a pair of mirrors, wherein resonant standing waves are formed from multiple reflections off the mirror surfaces. By locating the gain medium inside the cavity with respect to the light standing waves, light-matter coupling is readily manipulated, consequently enhancing or suppressing spontaneous and stimulated emission [2]. Recently, compact micron-size cavities, so-called microcavities, have been developed where the overlap between the light and matter is greatly increased. Numerous crafted microcavities of high quality factor Q are designed to incorporate with single or ensembles of solid-state light emitters, leading to influential optical applications and fundamental research activities in cavity quantum electrodynamics [3].

Among the ingenious designs of cavities, a planar Fabry-Perot resonator which consists of two mirrors enjoys simplicity and versatility to combine with different forms of matter. In particular, dielectric Fabry-Perot mirrors created by alternating two different refractive-index semiconductors can make monolithic structures combining with semiconductor gain media, for example, embedded quantum dots and quantum wells (QWs). When the gain media resides in a designated position, antinodes of the confined electromagnetic field distribution inside the cavity, the light and matter exchange energy reversibly, reaching the strong coupling regime. This chapter focuses on strongly coupled microcavity photons with QW excitons in III–V GaAs based semiconductors. In particular, it describes the recent research activities to investigate emergent quantum phases appearing in microcavity exciton-polariton condensates trapped in artificial lattice potentials.

8.1.1 Microcavity Exciton-Polaritons and Condensation

As cavity photons and QW excitons are strongly interacting through multiple reversible energy exchanges, new quantum quasi-particles, exciton-polaritons, emerge [4]. Mathematically, exciton-polaritons are eigenmodes of the coupled cavity photon-QW exciton Hamiltonian $\hat{H}$. The Hamiltonian is written as a second quantization format in terms of the cavity photon operator $\hat{a}_k$ with energy $\hbar\omega_{ph}$ and the QW exciton operator $\hat{C}_k$ with $\hbar\omega_{exc}$ and their inbetween interaction coupling constant g_k,

$$\hat{H} = \hbar \sum_k \left[\omega_{ph}\hat{a}_k^\dagger \hat{a}_k + \omega_{exc}\hat{C}_k^\dagger \hat{C}_k - i g_k \left(\hat{a_k}^\dagger \hat{C}_k - \hat{a}_k \hat{C}_k^\dagger\right)\right]. \tag{8.1}$$

This Hamiltonian is diagonalized with an exciton-polariton operator at a momentum k, $\hat{P}_k = u_k \hat{C}_k + v_k \hat{a}_k$, a linear superposition of cavity photon and QW exciton operators. The resulting Hamiltonian $\hat{H}_T$ is simplified to

$$\hat{H}_T = \sum_k \hbar\Omega_k \hat{P}_k^\dagger \hat{P}_k, \tag{8.2}$$

and exciton-polariton frequency relations are given by

$$\Omega_k = \frac{1}{2}(\omega_{exc} + \omega_{ph}) \pm \frac{1}{2}\sqrt{(2g_k)^2 + (\omega_{exc} - \omega_{ph})^2}. \tag{8.3}$$

This strong coupling manifests unequivocally as a pronounced energy doublet (upper polariton (UP) and lower polariton (LP) branches), whose energy separation indicates the coupling interaction strength ($2g$) denoted as vacuum Rabi splitting along the same spirit of the atom-cavity systems [5–7].

The dual nature of microcavity exciton-polaritons provides advantages to explore fundamental quantum Bose nature [5, 6] and to engineer potential photonic and optoelectronic devices [8, 9]. Elaborately, the partial photonic nature reduces the effective mass of this composite particle down to about 10^{-4}–10^{-5} of the electron mass and about 10^{-8} of the hydrogen atom mass. The extremely light effect mass of particles makes us to easily execute experiments at high operating temperatures. There are abundant photon flux leaked from the cavity structure owing to the finite lifetime of exciton-polaritons. These leaked photons carry out the energy-momentum distribution of exciton-polaritons under the energy and momentum conversation. Hence, capturing those leaked photons enables us to access polariton dynamics. On the other hand, electrons and holes, fermionic constituents of QW excitons, are Coulombically interacting and their repulsive interaction plays a significant role in scattering processes. These non-zero interactions among particles enrich the phase diagram of microcavity exciton-polaritons.

Being composite bosons of photons and excitons, exciton-polaritons in the low density limit and at low enough temperatures are predicted to reveal novel quantum Bose nature such as Bose-Einstein condensation (BEC) utilizing bosonic final state stimulation and stimulated scattering processes [10]. During last two decades since the discovery [4], the increased interest of microcavity exciton-polariton condensates has led to tremendous advancement both in theory and experiments, exploring unique BEC nature in microcavity exciton-polaritons. Several groups have reported strong evidences of exciton-polariton BEC in terms of macroscopic occupation in a ground state, thermal equilibrium to lattices, spontaneous long-range spatial and increased temporal coherence properties [11–17].

Exciton-polariton condensates have exhibited distinct features from atomic counterparts in several aspects. First, the reduced effective mass results in elevated BEC phase transition temperatures, which are inversely proportional to the mass. GaAs and CdTe systems undergo the phase transition around 4–10 K [11–13, 16], and large bandgap materials like GaN and organic systems show BEC at room temperatures [18–20], 10^8–10^9 times higher than the transition temperatures (tens of nK) of atomic BECs. Second, the macroscopic condensate population at the ground state can be accumulated by constant injection of particles in order to compensate leakages due to short quasi-particle lifetime. This open-dissipative nature is responsible for unique dynamics of exciton-polariton condensates.

Rigorously, owing to the fact that microcavity exciton-polaritons reside in two-dimension (2D), in the thermodynamical limit, infinite 2D systems cannot exhibit BEC at non-zero temperatures due to phase fluctuations in principle according to Hohenberg theorem [21, 22]. However, in finite 2D systems, long-range

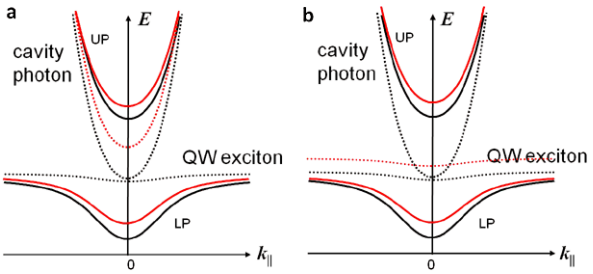

Fig. 8.1 Modified upper and lower polariton (UP, LP) energy dispersion relations (*red straight lines*) by shifting either cavity photon (**a**) or quantum well (QW) exciton modes (**b**) indicated by *red dotted lines*. *Black straight lines* draw the original UP and LP energy dispersions arising from the cavity photons and QW excitons drawn in the *black dotted lines*

off-diagonal coherence can still be preserved through the Berezinskii-Kosterlitz-Thouless (BKT) transition [23–25], where macroscopic quantum coherence would be stabilized by forming vortex-antivortex pairs. This fundamental inquiry has motivated to study trapped exciton-polariton condensates in spatial in-plane potentials since a well-defined trapping potential profile would guarantee single-mode BEC at discretized energy states. The following subsection summarizes attempts to create various types of trapping potentials in exciton-polariton systems.

8.1.2 Types of In-Plane Trapping Potential

Disorder, impurities and imperfections in semiconductor materials form locally isolated traps. While these natural traps are difficult to be controlled, several schemes to engineer local in-plane spatial traps have been attempted benefitting from the dual light-matter nature of exciton-polaritons. Figure 8.1 depicts how to modify the polariton branches correspondingly by influencing either the exciton mode energy or the cavity photon mode energy. The details of natural traps and engineered trapping potential are given in this subsection.

Natural Trap Natural spatial traps in semiconductors unavoidably exist due to semiconductor monolayer thickness fluctuations, defects and disorders. These local traps appear more often in II–VI semiconductors than GaAs materials since GaAs materials are relatively cleaner and purer. Although the controllability of these traps is absent, rather strong confinement potential (a few meV) profile leads to many interesting phenomena: to name a few, quantized vortex pinned at disorder [26] and half-quantum vortex [27]. Sanvitto and colleagues have identified exciton-polariton condensates populated in discrete modes only via time- and energy-resolved images [28]. These quantized states are from a ∼6 μm trap of ∼2 meV strength associated with one monolayer cavity thickness fluctuation.

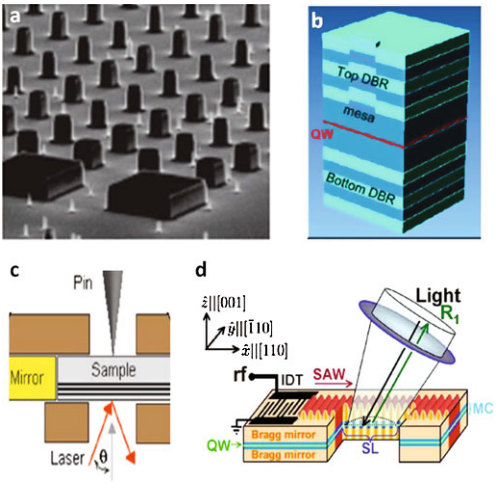

Fig. 8.2 (**a**) Image of pillar arrays adapted from Ref. [33]. (**b**) Partial etching and overgrowth technique developed in Professor B. Deveaud-Plédran group in Ref. [39]. (**c**) A schematic of a mechanical stress setup from Ref. [42]. (**d**) Illustration of an acoustic lattice in Ref. [46]. (**a**), (**b**), and (**d**) have acquired copyright permissions from America Physical Society journals. Copyright 2008, 2010, 2006, American Physical Society. (**c**) is reprinted with permission from Balili et al., Applied Physics Letters **88**, 031110. Copyright 2006, American Institute of Physics

Gain-Induced Trap Another effective confinement potential is formed due to the finite excitation laser spot size [29]. This implicit mechanism arises from the interlay of the finite lifetime and the spatial gain modulation bounded by the laser spot. Reservoir polaritons are rather short-lived to remain inside the finite laser spot region, building up the density and reaching the final state stimulation above quantum degeneracy threshold values. In this implicit effective trap, energy states are clearly quantized both in real- and momentum-spaces, and the Heisenberg-limited real- and momentum space distribution is observed. The experimental observations are consistent with the results of the infinite barrier circular trap model. Notwithstanding the successful description of the zero-dimensional confinement features, this method suffers from the limitation of the laser spot size control and cannot be readily scalable.

Etched Structures The aforementioned traps exist associated with material purity and the excitation scheme, lacking of controllability and scalability. To overcome the limitation, several schemes have been contrived. As a simplistic method, micro-sized pillars or photonic dots were fabricated by an etching method for a transverse spatial confinement [30–32]. Modifying the photonic component spatially, the large refractive index discontinuity is induced at the pillar sidewalls. Figure 8.2a images the array of pillars with varying sizes, which confirms that scalable polariton systems can be prepared in this etching technique. The micropillar structures clearly quantize photonic modes, consequently polariton modes as well. However, these earlier attempts failed to preserve the strong coupling regime at high

excitation powers. Recently, improved etching processes enable to show confined condensates in 2–20 μm-sized micropillar cavity structures [33, 34]. Not only is the quantized energy states observed as a zero-dimensional condensate confinement but also condensed polaritons reside near the pillar edges because of the strong repulsive interactions. In addition, 1D wire cavities [35] are patterned, where condensed polaritons are extended away from the excitation pump spot, manifesting strong correlation effects. Towards the 2D extension, two-by-two photonic molecules are prepared, where condensed states form bonding and antibonding states analogous to chemical molecule boding configurations [36].

Having a potential issue of the sidewall quality as a source of exciton loss and photon field leakage in micropillar structures, a slightly modified method has been implemented [37–39]. Instead of etching the whole structure, only the cavity space layer is partially etched by ∼6 nm. The height profile continues to be transferred to the subsequent layers after the overgrowth of the remaining structure (Fig. 8.2b). This physical cavity length spatial modulation produces strong confinement potential of ∼9 meV. The 3–20 μm-diameter mesa structures behave polariton quantum dots with discrete polaritonic energy spectra modified by confined photon modes. The nice thing of this alternative attempt lies in the fact that the partial etching does not touch QWs so that any spurious effect like surface recombination would be negligible. Incorporating with semiconductor processing techniques, this method would have flexibility to pattern arrays of mesa structures even in consideration of coupling control between nearest neighbor mesas.

Temperature and Electric Field Tuned Trap Whereas both the photonic disorder and the etching influence the cavity photon mode, there is another route to produce in-plane trapping potentials: shifting the QW exciton mode. Since the exciton mode is more sensitive to the environment temperatures through material lattice constant variations than the photon mode, temperature can tune the exciton energy and hence the polariton energy as well [40]. However, since temperature affects the whole device, it is not possible to engineer local trap potentials unless a delicate approach is introduced. Another tunable way is to apply electric fields through the quantum-confined Stark effect [41]. Basically, the non-zero electric fields reduce the overlap of electron and hole wavefunctions in QWs. As a result, the shifted exciton modes are mixed with cavity photons and the smaller oscillator strength is measured [40]. Electric-field tuned traps can be scalable by lithographic patterns and can be controlled in situ by varying the applied field values; however, to our best knowledge, trapped condensation inside the electrostatic traps has not been reported yet.

Stress Trap Another way to affect the exciton mode in the microcavity-QW structure is to apply mechanical stress. A strain harmonic potential of ∼3 meV with ∼1 N force is induced and its schematic sketch is drawn in Fig. 8.2c [16, 42, 43]. The harmonic potential alters the available density of states, and it assists to reduce the required particle density necessary for condensation. Since the stress-induced potential is rather large-sized 30–40 μm due to the rounded-tip pin size (radius 50 μm)

and the back substrate thickness (∼100 μm), no discrete modes have been observed yet in this manner. However, exciton-polariton condensates in this wide trap exhibit several clear BEC phenomena [16, 43, 44], and the trapped condensates would be a good candidate to explore BEC-BKT crossover in future. One concerns that it is difficult to imagine how to scale up the stress traps to arrays of them.

Acoustic Trap All above trapping potentials are time-independent and static, but dynamical traps would provide an interesting test-bed to explore condensate properties. A theoretical proposal envisages the acoustic lattices produced by strong exciton-phonon interaction [45]. Rayleigh surface acoustic waves (SAWs) launched in piezoelectric GaAs-based microcavity structures produce dynamical phonon superlattices [46] (Fig. 8.2d). The primary mechanisms of the acoustic lattices are the type I band-gap deformation and the in-phase cavity resonance energy modulation [46, 47]. The lattice constants of the phononic superlattices are determined by the SAW wavelength. The 5.6 μm and 8 μm SAWs are driven by a conventional GHz microwave technology [46, 47]. Microcavity exciton-polariton condensates are fragmented into arrays of 1D phonon traps located at the SAW minima, exhibiting the 1D band structures by a ∼160 μeV acoustic lattice [47]. Although dynamical acoustic lattices can be one- and two-dimensional and can be in-situ controllable, they face challenges: how to handle microwave heating for strongest traps and how to configure various lattice geometries beyond the simple 1D array or 2D square geometry.

Metal-Film Trap Finally, the concept of the metal-film traps is introduced as a new and simple way to create static in-plane potentials. A thin-metal film deposited on grown GaAs microcavity-QW wafers affects only the photonic mode [17, 48, 49]. Figure 8.3a and b compare the transfer matrix calculation result of the electromagnetic fields at the metal-semiconductor interface with that of the air-semiconductor interface [50]. The photon fields are extended rather smoothly at the air-semiconductor interfaces (Fig. 8.3a), but the confined electromagnetic components have to be zero at the metal-semiconductor interface (Fig. 8.3b). Therefore, the stiff boundary condition on the photonic mode due to the metal film gives rise to a locally squeezed cavity length, shifting the polariton energy upward in comparison to the polariton energy value under the air-semiconductor interfaces. With the 30 nm Au film, the cavity photon energy is blue shifted by ∼400 μeV, and the LP energy shift becomes half near the zero detuning area, where the photonic concentration is 50 %. In the calculation, we assume the wafer of the 16 top and 20 bottom distributed Bragg reflectors (DBRs).

Figure 8.3c explicitly draws the LP energy shift versus the metal film thickness at varying detuning parameters $\delta = E_{cav}(k_{//} = 0) - E_{exc}(k_{//} = 0)$, where $E_{cav(exc)}(k_{//} = 0)$ denote the energy of cavity (exciton) at the zero in-plane momentum $k_{//}$. The amount of LP energy shift becomes slowly saturated in cases with more than 30 nm thick metal layers. At a given metal thickness, the resulting LP energy shift is proportional to the photon concentration. The more negative δ is, the LP

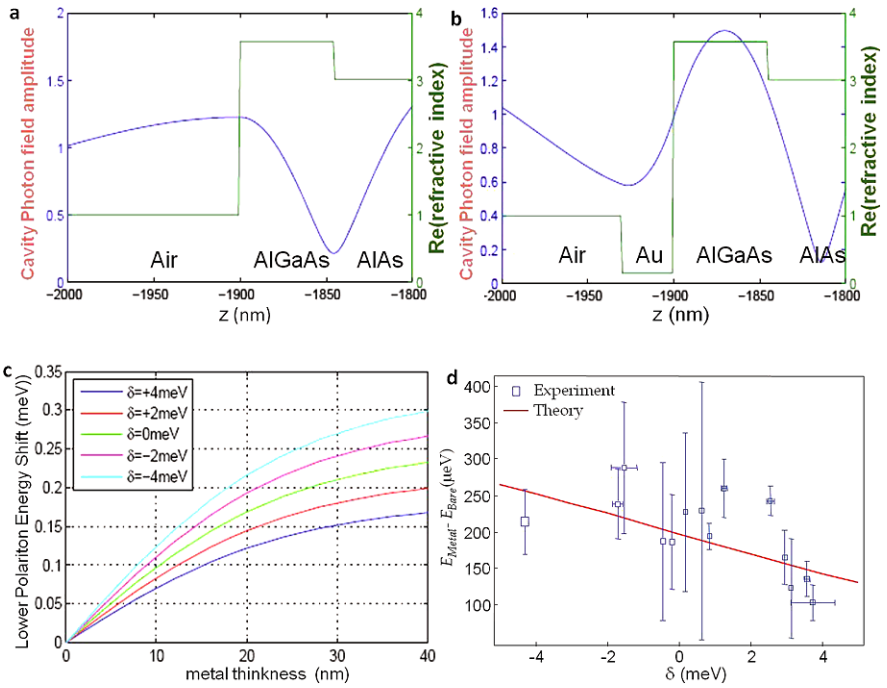

Fig. 8.3 The real part of refractive indices of materials (*green*) and the electromagnetic field amplitudes (*blue*) are plotted along the growth direction in z by the transfer matrix calculation for a standing wave at a resonance from the bare surface (**a**) and from the 30 nm Au metal layer (**b**). (**c**) Lower polariton (LP) energy shifts are shown as a function of the thin metal film thickness in the 16–20 top-bottom distributed Bragg reflector structure at varying detuning values δ. (**d**) The relation of the LP energy shift and the detuning values are measured with the a 24 nm–6 nm Au/Ti film deposited GaAs microcavity structure

energy shift is bigger. Suppose the metal film induces the cavity photon energy shift by ΔE_{cav}. Then, the overall LP energy at $k_{//} = 0$ below the metal film is written as

$$E_{metal,LP} = \frac{1}{2}\Big[E_{cav} + \Delta E_{cav} + E_{exc} - \sqrt{(2g)^2 + (E_{cav} - E_{exc})^2}\Big]. \tag{8.4}$$

In terms of the detuning δ, the LP energy difference between the metal and the bare surface is derived as

$$E_{metal,LP} - E_{bare,LP} = \frac{1}{2}\Big[\Delta E_{cav} - \sqrt{(2g)^2 + (\delta + \Delta E_{cav})^2} + \sqrt{(2g)^2 + \delta^2}\Big]. \tag{8.5}$$

We have measured the LP energy difference with the 26/4nm Au/Ti metal film on top of the 16/20 DBR structures in Fig. 8.3d, which matches qualitatively well with the computed results (red line) using $g \sim 6.97$ meV, $E_{exc} \sim 1.59241$ eV and $\Delta E_{cav} \sim 400$ μeV.

Although the trapping potential strength is much weaker than the above etched pillars and natural traps, this method possesses several advantages: (1) the non-

invasive in-plane potentials can be introduced on top of the fully grown wafer, which does not change the QW quality and exciton states; (2) the dimension of the in-plane potentials can be readily controlled even down to sub-microns by utilizing advanced lithographic techniques; and (3) the flexibility to design various geometries in 1D and 2D is very attractive, especially when many-body interaction effects among exciton-polaritons are explored in lattices.

The main body of the chapter is devoted to describe the detailed phenomena of the microcavity exciton-polariton condensates confined in a single trap, and 1D and 2D lattices prepared by the aforementioned thin metal-film technique.

8.2 Microcavity Exciton-Polariton Condensates in Lattices

Before delving into the indepth description of experimental signatures in trapped microcavity exciton-polaritons employing the metal film technique, the wafer structures, the abridged fabrication procedure and measurement setup are briefly discussed in Sect. 8.2.1.

8.2.1 Samples and Fabrication

8.2.1.1 GaAs Samples

Our $\lambda/2$ cavity contains three-stack of four GaAs QWs located at the central antinodes of the microcavity optical field. GaAs 6.8 nm-thick QWs are separated by 2.7 nm-AlAs barriers. The planar Fabry-Perot cavity is arranged by top and bottom DBRs from alternating $\lambda/4$ $Al_{0.15}Ga_{0.85}As$ and AlAs layers. A 16-layer top and 20-layer bottom DBR structure promises the microcavity quality factor $Q \sim 6000$ according to the transfer matrix calculation. The measured vacuum Rabi splitting energy $2g$ is around 15 meV near the zero-detuned area. A spatial inhomogeneity caused by a tapering in the layer thickness of the wafer allows us to tune the cavity resonance with respect to the exciton energy, which is relatively constant over the whole wafer.

8.2.1.2 Fabrication Procedure

On the top DBR surface of the grown microcavity wafer, we have designed circular traps, 1D metal strip gratings, and 2D square lattice. The 2D square lattice is patterned by arranging holes and we applied negative resist to the wafer followed by either electron-beam or photo-lithography depending on the feature sizes. The feature sizes vary from 1 to 10 μm. Then, a 24/6 nm Au/Ti metal film is deposited and finished with a lift-off in acetone.

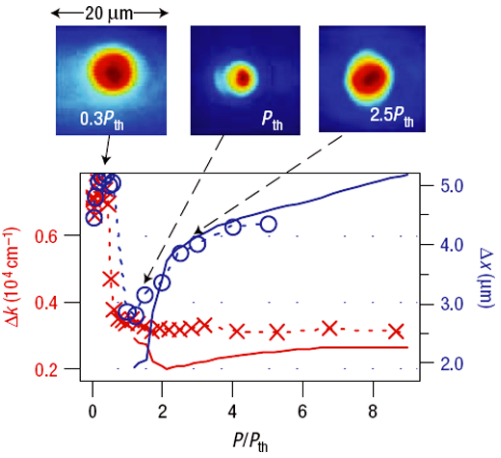

Fig. 8.4 Pump power-dependent near-field lower-polariton population distributions in a 8 μm-diameter single trap. The *bottom panel* summarizes the momentum and position standard deviations as a function of the normalized pump powers. Permission is acquired from Nature Physics

8.2.1.3 Photoluminescence Setup

Our primary measurements are to capture time-integrated photoluminescence (PL) signals of emitted LPs near 4 K in both near- and far-fields. Typically we excite our samples with a ∼3 ps pulse (∼0.5 meV spectral width) at ∼60 degree ($k_{//} \approx 7 \times 10^4$ cm^{-1} in air) by a mode-locked Ti:sapphaire laser at a 76 MHz repetition rate. The laser excitation wavelength is tuned to be near the exciton resonance energy near 768 nm. The excitation spot is focused on the sample surface, whose size is around typically 30×60 or 50×100 μm^2. The elliptical shape of the excitation spot is from the large angle side pumping scheme. The LP emission signals are collected in the normal direction by a high numerical aperture (NA = 0.55) objective lens. We built a standard micro-PL setup to access near-field (coordinate space) or far-field (momentum space) imaging and spectroscopy with a repositionable lens behind the objective lens. For spectroscopic information, the collected signals are fed into a 0.75 m spectrometer, dispersed by gratings and recorded on a liquid nitrogen cooled CCD camera.

8.2.2 Exciton-Polariton Condensates in a Single Trap

The isolated circular traps are displayed, whose trap diameters are chosen between 5 μm and 100 μm and whose LP trapping potential strength is approximately 200 μeV. Although the potential strength is compatible with the size of polariton kinetic energy (∼100–300 μeV) in relatively small diameter-traps (5–10 μm), exciton-polariton condensates remain in a single transverse mode over higher-order transverse modes shown in Fig. 8.4 [51].

To characterize trapped condensates, the standard deviations in momentum (Δk) and position (Δx) are recorded as a function of the excited laser pump power in

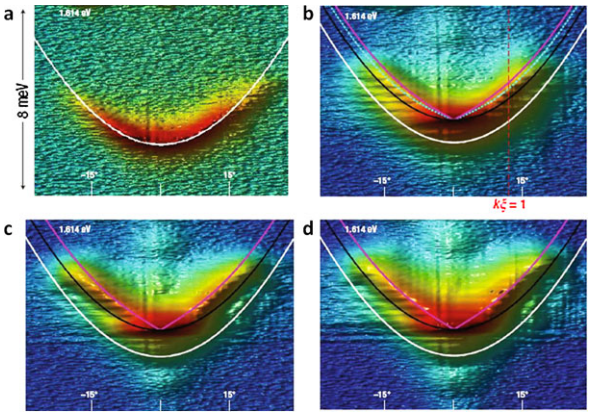

Fig. 8.5 Pump power-dependent energy dispersion and excitation spectra of trapped lower-polariton condensates at $P/P_{th} = 0.05$, 1.2, 4, and 6 from (**a**) to (**d**). The data were taken with a 8 μm-diameter single trap, and the energy axis in y spans 8 centered at 1.61 V. The *white line* indicates the free-polariton parabolic energy dispersion relations, the *black line* is the shifted parabolic curve at the condensed state, and the *pink line* draws the Bogoliubov excitation spectra computed using the homogeneous model. Permission of this figure is from Ref. [51] is acquired from Nature Physics

the main panel of Fig. 8.4. Both the momentum and the position fluctuations plummet abruptly at the quantum degeneracy threshold values ($P \approx P_{th}$). The measured uncertainty product $\Delta k \Delta x$ has a minimum value, 0.98 just above the threshold values. It is twice of the Heisenberg uncertainty product value ($\Delta k \Delta x \sim 0.5$) given by a minimum uncertainty wavefunction. Where Δk remains constant above P_{th}, the position uncertainty Δx significantly increases, hence the monotonic increase in $\Delta k \Delta x$. The increased condensate size directly manifests the repulsively interacting coherent LP condensates. The more polaritons are created by higher pump rates, the interaction energy among LPs increases, consequently LPs extends outward from the repelling one another. The experimental data show a consistent agreement with theoretical analysis using the Gross-Pitaevskii equation.

In addition, it is natural to search the influence of the inter-particle interaction on the condensates. The excitation spectra of condensates indeed reflect the signatures of superfluidity in terms of the population fluctuations and phase stabilization of condensates [52, 53]. Quantum and thermal depletions from the condensates excite the phonon-like spectrum. Clearly deviating from the free-particle quadratic dispersion curve, the linear Bogoliubov excitation spectrum of trapped condensates above the threshold pump powers is observed within the low-momentum regime $|k\xi| < 1$. ξ is the healing length given by $\xi = \hbar/\sqrt{2mU(n)}$ in terms of the effective mass m and the LP density (n) dependent interaction strength $U(n)$. It is one of superfluidity signatures shown in Fig. 8.5. The Bogoliubov energy relation E_B is written as $E_B = \sqrt{E_{free}(E_{free} + U(n))}$, where $E_{free} = \hbar^2 k^2/2m$ is the free-particle kinetic energy at $k_{//} = 0$. From the phonon-like linear dispersion relation, the extracted sound velocity is of the order of 10^8 cm/s, eight orders of magnitude faster than

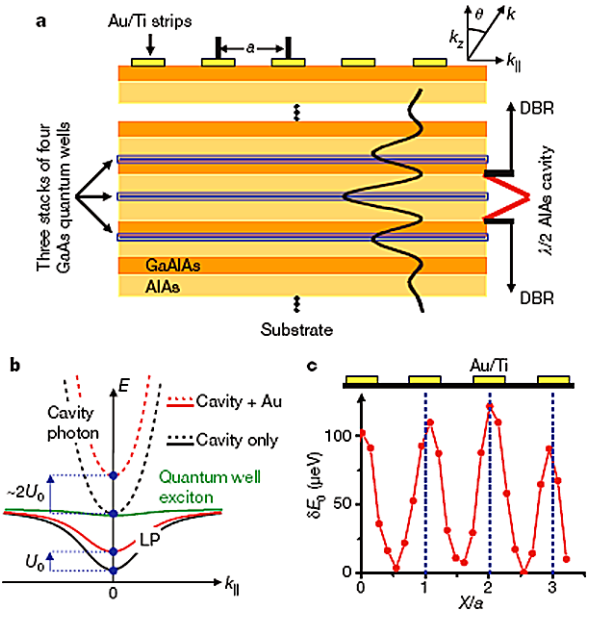

Fig. 8.6 (**a**) The cross-sectional view of the one dimensional grating film on a 12 GaAs quantum-well-microcavity structure. (**b**) Comparison of the polariton dispersions with two cases: the metal-cavity interface and the air-cavity interface. (**c**) Experimentally measured in-plane trapping potential for lower polaritons. The figure permission from Ref. [17] was given from Nature

that of atomic condensates. Again this large sound velocity value comes from the extremely light effective mass of LPs.

8.2.3 1D Condensate Arrays

In order to realize 1D condensate arrays, we have patterned a grating structure, where $a/2$-wide metal strips are equidistantly located with a $a/2$ wide gap. a represents the 1D lattice period illustrated in Fig. 8.6a, and the experimental data are taken with a device $a = 2.8$ μm. Below the metal strip, LPs encounter higher energy barriers caused by the locally squeezed cavity lengths, shifting the LP energy by $U_0 \sim 200$ μeV drawn in Fig. 8.6b. The Au/Ti metal film layer gives the spatial LP energy modulation δE_0 as 100 μeV measured by scanning the pinhole across the metal strips (Fig. 8.6c). The reduced LP energy shift measured in Fig. 8.6c is due to the diffraction-limited spatial resolution 1 μm, which is compatible to our device lattice constant. We have confirmed lower LP energy by 200 μeV under the bare surface independently.

The potential energy 200 μeV is of the same order of the kinetic energy $E_{free} = \hbar^2 k^2/2m$ at the 1D Brillouin zone (BZ) boundaries $k_{//} = \pm\pi/a$. The kinetic energy value is ~500 μeV with the effective mass m to be 9×10^{-5} of the electron mass. Therefore, this energy scaling comparison justifies us to treat our system as a single-particle in a weakly periodic 1D potential. We perform the 1D band structure calculation including a 200 μeV potential term. Figure 8.7b presents the theoretical

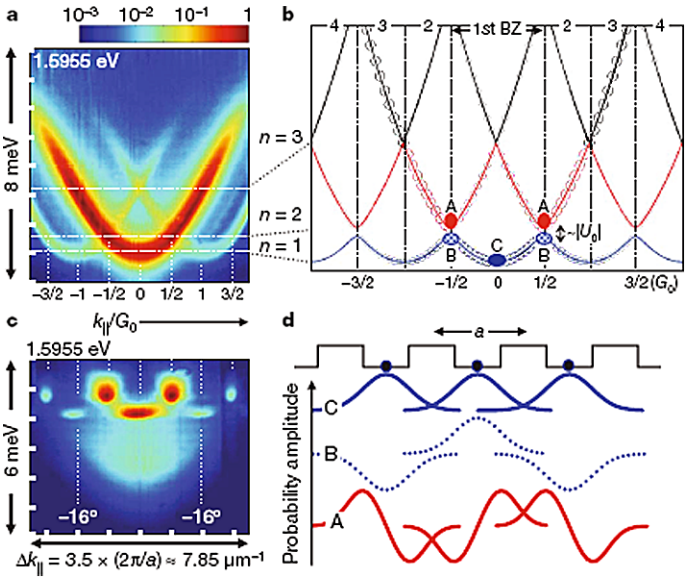

Fig. 8.7 (**a**) The measured angle-resolved spectroscopy of lower polaritons (LP) trapped in the $a = 2.8$ μm-period one-dimensional (1D) array taken at the below quantum degeneracy threshold values. G_0 is the reciprocal lattice vector, $2\pi/a$. (**b**) The single-particle 1D band structure in the extended zone scheme with the location of the first Brillouin zone. The *circles* represent the expected LP emission intensities. (**c**) The energy dispersion diagram above the quantum degeneracy threshold values. (**d**) The real-space wavefunction probability amplitudes in space. The figure is adapted from Ref. [17] with proper permission

band structures against the in-plane momentum in the unit of the 1D reciprocal lattice vector amplitude $G_0 = 2\pi/a$ in the extended zone scheme. The weak potential U_0 lifts the doubly degenerate energy states at the first BZ edges and the two energy states are denoted as A and B in Fig. 8.7b. Below threshold pump powers, the dominant parabolic dispersion curves together with two relatively weaker parabolas displaced by $\pm G_0$ are detected in Fig. 8.7a, which resemble the theoretical band structure calculation result. The spectral linewidth of the dispersion curves are bigger than the energy gap ($\sim|U_0|$) between two states A and B so that we were not able to directly measure the energy gap.

Above quantum degeneracy threshold values (Fig. 8.7c), the angle-resolved energy spectroscopy consists of narrow interference peaks at two different energy values as well as blurred emission from the thermal LPs below. The peaks are separated by G_0 (correspondingly, 16° in angles) at given energy values as a manifestation of diffraction from the 1D lattice. More important, the higher energy states occur at $\pm G_0/2$, the first BZ boundaries. The momentum distribution at this energy state is associated with the Bloch wavefunction at the A state, which has anti-phased relations between nearest-neighbor sites, whereas two other Bloch states B and C are in phase depicted in Fig. 8.7d. The anti-phased π-state in A exhibits the p-wave symmetry, and the in-phase 0-states in B and C show the s-wave symmetry. Even

though the state A is energetically higher than the state B, LPs are condensed in A since it is meta-stable protected by local bandstructure curvatures. The narrow emission lobes are evidences of the coherent condensates. At pump powers far above threshold values, the LP condensates indeed relax to the state C, which is the global ground state owing to the enhanced stimulated scattering processes among more LP particles.

Such dynamical relaxation and mode competition among multi-orbital states have been studied by the time-resolved spectroscopy. Near the threshold the condensates are easily trapped in high-momentum, meta-stable p-wave states initially, and the LPs in p-wave states decay rather faster than the ground s-wave state. Using the reasonable lifetime parameters for these energy states, the coupled rate equations with the s-, p- and reservoir states would well reproduce the observed dynamical behavior of s- and p-wave condensation. In comparison to the atomic condensate, the reason to create coherent condensates at non-zero momentum values readily with the LPs can be found in the fact that LPs are short-lived so that they leak out of the cavity before relaxation into the ground states at a certain particle density range. We have also shown that the off-diagonal long-range coherence preserves the entire LP condensate sizes bounded by the laser pump spot size $\sim 50 \times 100\ \mu m^2$. Hence, the LP system has a knob of excitation power, detuning parameters and the geometry to manipulate the condensate orbital symmetry and to search macroscopic quantum order. Next, we will describe a simple extension to the 2D square lattice using the advantage of the LP condensates.

8.2.4 2D Square Lattice

The dimensionality of 2D is very special in that many exotic physical phenomena in strongly correlated materials are closely tied to the high orbital electronic states arranged in 2D. High temperature superconductivity is one of the prime examples, and its properties would be owing to the d-orbital copper- and p-orbital oxide 2D planes. Utilizing the bottleneck condensate nature, exciton-polariton condensates can be engineered to form the excited state orbital symmetry in terms of the lattice constants and the excitation pumping condition.

A square lattice is one of the simplest 2D lattice structures with orthogonal real- and reciprocal-Bravais unit vectors. The Bravais lattice forms a square first BZ with a unit length $2\pi/a$, where a is the square lattice constant. The square lattice holds translational, rotational and reflection symmetries and three high symmetry points are denoted as Γ, X, M. Both Γ and M preserve the four-fold rotational symmetry, while X points exhibit two-fold rotational symmetry. The fabricated 2D square lattice device is shown in Fig. 8.8a [49].

The single-particle square lattice band structures are calculated using the plane-wave basis [54] by solving the Schrödinger equation,

$$-\frac{\hbar^2}{2m}\nabla^2\Psi(\mathbf{r}) + V(\mathbf{r})\Psi(\mathbf{r}) = E\Psi(\mathbf{r}). \tag{8.6}$$

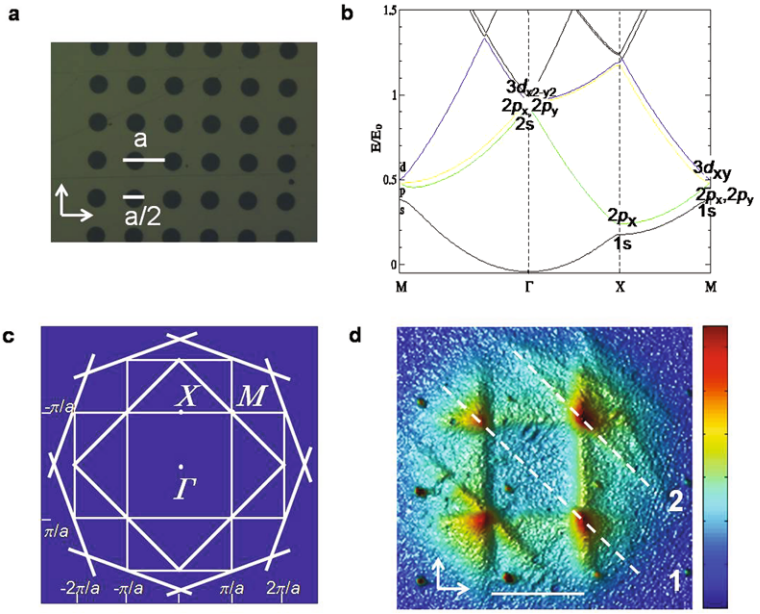

Fig. 8.8 (**a**) Photograph of a representative two-dimensional (2D) square lattice device with the lattice constant a. The *brighter area* is where the metal films are deposited and the darker holes with the diameter $a/2$ are artificial lattice sites. (**b**) The single-particle bandstructures along high symmetry points (Γ, X, M) in the presence of a weak square potential. (**c**) The multiple Brillouin zones (BZs) of the 2D square lattices. (**d**) Experimentally observed first and second BZs in the momentum space ($k_{//,x}, k_{//,y}$). Figure permission is acquired from Nature Physics

The 2D periodic potential $V(\mathbf{r})$ is modeled as $V(\mathbf{r}) = \sum_i l(\mathbf{r} - \mathbf{R_i})$ where $\mathbf{R_i}$ is the ith site center location, and the circular potential $l(\mathbf{r})$ is set to be $-V_0$ within the radius $r_0 = a/2$ and 0 otherwise. V_0 is the square lattice potential depth. Note that the bold symbols (e.g. $\mathbf{r}$) represent 2D vectors. We define the characteristic energy scale as $E_0 = \frac{\hbar^2}{2m}|\frac{2\pi}{a}|^2 \sim 1$ meV for the $a = 4$ μm device. Within the first BZ, the plane wave basis has a form of $|\mathbf{k} + \mathbf{G}_{mm}\rangle$ in terms of the 2D reciprocal lattice vectors $\mathbf{G}_{mn}$. Diagonalizing the Hamiltonian matrix $\langle \mathbf{k} + \mathbf{G}_{mm}|\hat{H}|\mathbf{k} + \mathbf{G}_{mm}\rangle$ with the operator $\hat{H} = -\frac{\hbar^2\hat{k}^2}{2m} + \hat{V}$ in the momentum space, the resulting bandstructures along Γ, X, M are plotted in Fig. 8.8b. Figure 8.8c draws the first four BZs with locations of Γ, X, M and the experimentally observed BZs are shown in Fig. 8.8d above threshold values. Because of the non-zero periodic potential, the degenerate eigenstates are lifted at the high symmetry points and classified according to the rotational group symmetry analogous to the atomic orbital denotations. For example, at Γ point, the lowest ground state exhibits the non-degenerate 1 s-wave symmetry, whereas the next quartet states exhibit $3d_{x^2-y^2}$, $2p_x$, $2p_y$, and $2s$-wave symmetries from the top to the bottom respectively. Similarly, at M point, the degenerate quartet states are split into $3d_{xy}$, $2p_x$, $2p_y$, and $1s$-wave symmetries.

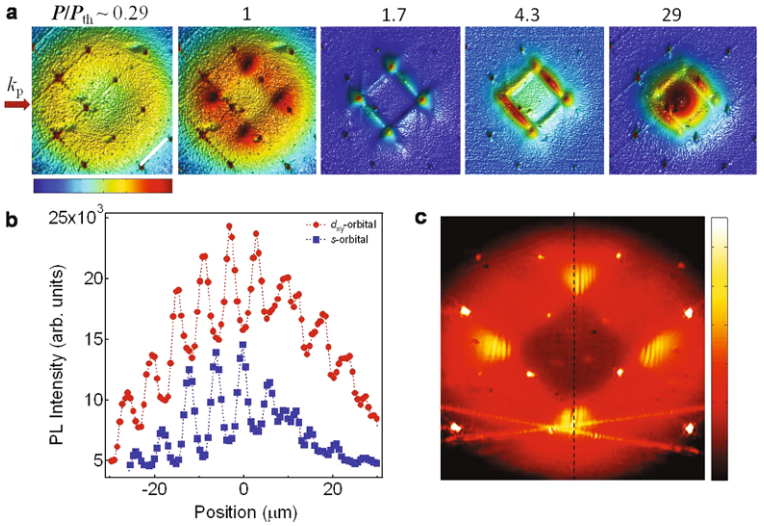

Fig. 8.9 (**a**) Power-dependent momentum space lower-polariton population distributions. (**b**) Anti-phased d- and in-phased s-wave near-space wavefunctions. (**c**) Michelson interference images of the d_{xy}-orbital condensates taken at $P/P_{th} = 1$, and the folding plane is denoted as the *dotted line* at the center. Figure is adapted from Ref. [49] with a proper permission

Figure 8.9a shows the evolution of the LP momentum space population distributions taken from the far-field (FF) images. The regular square-patterned sharp interference peaks come from the diffracted laser signals from the 2D square lattices, which are useful to calibrate the momentum space. Since the device sits around -3 meV detuned area, the donut shape,the bottleneck nature of the LP distribution in momentum space appears at $P/P_{th} \sim 0.29$. As the injected polaritons are increased, the emission intensity grows at the four M points, the corners of the first BZs. These peaks are further sharpened, and LP populations are further transferred to X points and ultimately relaxed to the inside of the first BZ. Furthermore, the states at M points are stronger emissions under the metal films (red circles) in comparison to the lower energy states which emit strongly through the holes (blue squares) from the near-field spectroscopy measurements above threshold (Fig. 8.9b). Similar to the p-wave symmetry in the previous 1D section, we can conclude that the M eigenstates are also anti-phased. And the coherence among M points produces the interference patterns by the self-folding in the Michelson interferometer shown in Fig. 8.9c.

Figure 8.10 summarizes the theoretical near-field (NF) and the FF distributions of $1s$, $2p_x$ and $3d_{xy}$ states in the 3-by-3 square lattice obtained by the previous single-particle calculation. Since the potential depth is relatively weak, the LP wavefunctions are rather extended in the 2D; however, it is still clear that both $2p_x$ and $3d_{xy}$ states are anti-phased in the NF space unlike the $1s$ state. Due to the orthogonal square lattice geometry, the interference peaks at M points emerge uniquely from the anti-phased $3d_{xy}$ states (Fig. 8.10c). Experimentally, we are able to access both

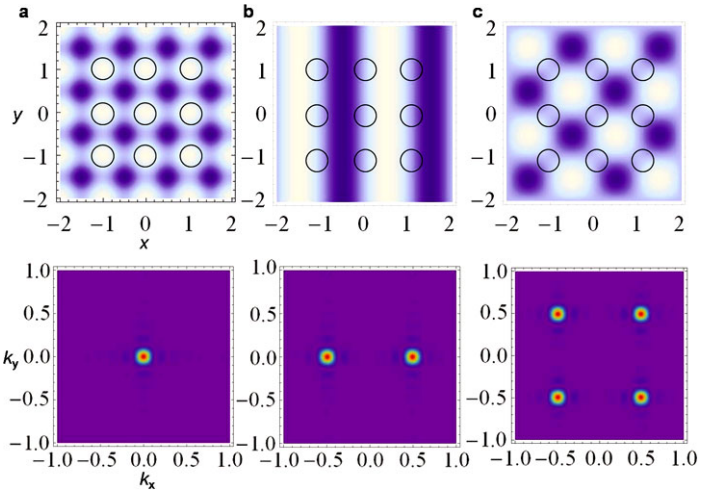

Fig. 8.10 Computed near-field lower polariton wavefunction (*upper panel*) and far-field intensities (*lower panel*) in the weak square lattice potential. $1s$- (**a**), $2p_x$- (**b**) and $3d_{xy}$- (**c**) orbital condensates are presented. The *black dotted circles* are where the circular apertures are located in the metal film pattern. Whereas the $1s$ wavefunction is in-phased (**a**), both $2p_x$ and $3d_{xy}$ orbitals are anti-phased, inducing the strong interference peaks at X and M points in the far-field images. Permission of figure from Ref. [49] is obtained from Nature Physics

NF and FF LP population information (Fig. 8.9) to nicely confirm the theoretical conjecture.

This is the first time to observe that the dynamic condensation takes place with the anti-phased d_{xy}-wave symmetry. Again, the advantages to create high-orbital condensate states in the exciton-polariton systems come from the competition between the leaked photons through the cavity mirrors and the thermal relaxation processes to the ground states. In addition, the compact photoluminescence setup using the Fourier optics allows to examine both the NF and FF images and spectroscopies. The high-orbital condensate state is the stepping stone to realize solid-state quantum simulators, which would explore macroscopic quantum order in designated solid-state systems with high-orbital electronic states.

8.3 Outlook

Solid-state microcavity exciton-polariton condensates are regarded as a promising physical system to explore the fundamental physical phenomena revealing quantum Bose nature at much elevated temperatures and in non-equilibrium situations. There are active research activities to engineer the trap potential for condensates in a controlled and systematic manner. Among numerous trapping schemes, our group has been using a simple metal-film deposition method to enjoy flexibility and scalability in multi-dimensions. We have observed high-orbital condensates in meta-

stable states formed by given lattice bandstructures and short polariton lifetimes in the cavity. The capability to manipulate condensate orbital states selectively is essential to emulate real material systems. For example, the 2D CuO plane of the high-temperature superconductors mixes with the d- and p-orbitals. Thus, we are equipped to arrange multi-orbital condensates in 2D. In addition, upon the successful demonstration in the 1D and 2D square lattices, it is straightforward to extend to other 2D lattices, for example, triangular, honeycomb and kagome geometries. The polariton-lattice system has shown a great potential to investigate exciting physical questions even including spin degrees of freedom, from which we would envision to grasp important clues towards the understanding of strongly correlated condensed matter systems.

References

1. J.D. Jackson, *Classical Electrodynamics*, 2nd edn. (Wiley, Hoboken, 1975)
2. S. Haroche, D. Kleppner, Phys. Today **42**, 24 (1989)
3. K.J. Vahala, Nature **424**, 839 (2003)
4. C. Weisbuch et al., Phys. Rev. Lett. **69**, 3314 (1992)
5. A. Kavokin, *Cavity Polaritons*, vol. 32 (Academic Press, San Diego, 2003)
6. Y. Yamamoto, F. Tassone, H. Cao, *Semiconductor Cavity Quantum Electrodynamics*, 1st edn. (Springer, Berlin, 2000)
7. H. Deng, H. Haug, Y. Yamamoto, Rev. Mod. Phys. **82**, 1489 (2010)
8. B. Deveaud-Plédran, Nature **453**, 297 (2008)
9. T.C.H. Liew, I.A. Shelykh, G. Malpuech, Physica E **43**, 1543 (2011)
10. A. Imamoglu et al., Phys. Rev. A **53**, 4259 (1996)
11. H. Deng et al., Science **298**, 199 (2002)
12. H. Deng et al., Proc. Natl. Acad. Sci. USA **100**, 15318 (2003)
13. J. Kapsrzak et al., Nature **443**, 409 (2006)
14. H. Deng et al., Phys. Rev. Lett. **97**, 146402 (2006)
15. H. Deng et al., Phys. Rev. Lett. **99**, 126403 (2007)
16. R.B. Balili et al., Science **316**, 1007 (2007)
17. C.-W. Lai et al., Nature **450**, 529 (2007)
18. S. Christopoulos et al., Phys. Rev. Lett. **98**, 126405 (2007)
19. G. Christmann et al., Appl. Phys. Lett. **93**, 051102 (2008)
20. S. Kena Cohen, S.R. Forrest, Nat. Photonics **4**, 371 (2010)
21. N.D. Mermin, H. Wagner, Phys. Rev. Lett. **17**, 1133 (1966)
22. P.C. Hohenberg, Phys. Rev. **158**, 383 (1967)
23. J.M. Kosterlitz, D.J. Thouless, J. Phys. C, Solid State Phys. **6**, 1181 (1973)
24. J.M. Kosterlitz, J. Phys. C, Solid State Phys. **7**, 1046 (1974)
25. V.L. Berezinskii, Zh. Èksp. Teor. Fiz. **61**, 1144 (1971) (Engl. Trans. Sov. Phys.-JETP **34**, 610 (1972))
26. K.G. Lagoudakis et al., Nat. Phys. **4**, 706 (2008)
27. K.G. Lagoudaki et al., Science **326**, 974 (2009)
28. D. Sanvitto et al., Phys. Rev. B **80**, 045301 (2009)
29. G. Roumpos et al., Phys. Rev. Lett. **104**, 126403 (2010)
30. J. Bloch et al., Physica E **2**, 915 (1998)
31. T. Gutbrod et al., Phys. Rev. B **57**, 9950 (1998)
32. M. Obert et al., Appl. Phys. Lett. **84**, 1435 (2004)
33. D. Bajoni et al., Phys. Rev. Lett. **100**, 047401 (2008)

34. L. Ferrier et al., Phys. Rev. Lett. **106**, 126401 (2011)
35. E. Wertz et al., Nat. Phys. **6**, 860 (2010)
36. M. Galbiati (2011). arXiv:1110.0359
37. O. El Daïf et al., Appl. Phys. Lett. **88**, 061105 (2006)
38. R. Idrissi Kaitouni et al., Phys. Rev. B **74**, 155311 (2006)
39. G. Nardin et al., Phys. Rev. B **82**, 045304 (2007)
40. T.A. Fisher et al., Phys. Rev. B **51**, 2600 (1995)
41. D.A.B. Miller et al., Phys. Rev. B **32**, 1043 (1985)
42. R.B. Balili et al., Appl. Phys. Lett. **88**, 031110 (2006)
43. R. Balili et al., Phys. Rev. B **79**, 075319 (2009)
44. B. Nelsen et al., J. Appl. Phys. **105**, 122414 (2009)
45. A.L. Ivanov, P.B. Littewood, Phys. Rev. Lett. **87**, 136403 (2001)
46. M.M. de Lima Jr. et al., Phys. Rev. Lett. **97**, 045501 (2006)
47. E.A. Cerda-Méndez et al., Phys. Rev. Lett. **105**, 116402 (2010)
48. N.Y. Kim et al., Phys. Status Solidi B **245**, 1076 (2008)
49. N.Y. Kim et al., Nat. Phys. **7**, 681 (2011)
50. P. Yeh, *Optical Waves in Layered Media* (Wiley, Hoboken, 2005)
51. S. Utsunomiya et al., Nat. Phys. **4**, 700 (2008)
52. N.N. Bogoliubov, J. Phys. **11**, 23 (1947)
53. L.P. Pitaevskii, S. Stringari, *Bose-Einstein Condensation* (Clarendon, Oxford, 2004)
54. N.W. Ashcroft, N.D. Mermin, *Solid State Physics* (Brooks Cole, New York, 1989)

Chapter 9
Polariton Condensates in Low Dimensional Cavities

Jacqueline Bloch

Abstract In the past few years, semiconductor microcavities have appeared to be a very attractive system for the exploration of the physics of interacting Bose condensates. In addition to the flexibility and richness of optical experiments that can be performed on polariton condensates in microcavities, the powerful tools offered by technological processes developed for opto-electronic devices can be used to fully engineer the potential landscape in which these half-light half-matter condensates evolve. In the present chapter, we will describe how polariton condensates can be confined in low dimensional microstructures. We will review some experiments performed in these geometries, highlighting the huge potential of microstructures for the development of innovative polaritonic devices.

We will first address experiments performed in wire cavities, which open the field of mesoscopic physics with polaritons. Propagation of polariton condensates over macroscopic distances has been demonstrated as well as the optical manipulation of these condensates (tunnel coupling and trapping). We will also discuss scattering by disorder in this one dimensional propagation.

Then we will describe experiments in fully confined systems like single or coupled micropillars. These 0D resonators allow proper investigation of the nature of interactions undergone by polariton condensates. To conclude we will mention several theoretical proposals which make use of the propagation and manipulation of polariton condensates in photonic circuits to develop new optical functionalities and reveal new physics.

9.1 Introduction

Cavity polaritons are now clearly identified as a powerful system to investigate the physics of Bose condensates [1–4]. They arise from the strong coupling regime between the optical mode of a Fabry-Perot cavity and excitons confined in quantum wells [5]. Because they are mixed exciton photon states, cavity polaritons possess

J. Bloch (✉)
Laboratoire de Photonique et de Nanostructures, LPN/CNRS, Route de Nozay, Marcoussis 91460, France
e-mail: jacqueline.bloch@lpn.cnrs.fr

A. Bramati, M. Modugno (eds.), *Physics of Quantum Fluids*,
Springer Series in Solid-State Sciences 177, DOI 10.1007/978-3-642-37569-9_9,

specific properties coming from this dual nature. Via their excitonic component they interact with their environment, namely with phonons [6], excitons [7, 8], polaritons [9–12], and electrons [13]. Their photonic character gives them a very small effective mass, typically three orders of magnitude smaller than the bare exciton. This is the key property which enables their condensation at very high temperatures (below 50 K for CdTe or GaAs based samples, room temperature for higher band gap semiconductors such as ZnO [14] (see Chap. 11) or GaN [13, 15–17] (see Chap. 10)). Cavity polaritons are coupled to the free space optical modes via the escape of their photonic part through the mirrors. These photons fully reflect the polariton quantum states they come from: their distribution in real space and momentum space, their energy, their degree of polarization, their spatial and temporal coherence can be measured and this allows the detailed investigation of the system via optical spectroscopy experiments. After the first demonstrations of polariton condensation [18–20], the quantum hydrodynamics of polariton condensates could be explored (see Chaps. 1–7 of the present book): superfluidity [21, 22], as well as the formation of quantized vortices [23, 24], bright solitons [25] have been reported. For the first time in any system, the formation of oblique dark solitons has been recently observed [26]. As described in other chapters of the present volume, these developments illustrate the huge potential of this non-linear system. Another advantage of semiconductor microcavities is that we can make use of the powerful technological techniques developed for opto-electronic devices to fully engineer the potential in which polariton condensates are created. In particular in materials such as GaAs/GaAlAs, dry etching techniques are particularly well mastered and allow fabricating low dimensional resonators with very good optical quality. The aim of the present chapter is to review some recent experiments performed with polariton condensates in low dimensional microstructures. We will first address how polariton states are discretized when the lateral dimensions of a microcavity are reduced. Different examples of resonator geometries will be described. We will then review experiments performed in one dimensional cavities, where extended polariton condensates have been generated. We will show how these condensates can propagate with strongly reduced scattering by disorder. Optical manipulation of these condensates is possible using interaction of the condensate with its environment. Controlled tunnel barrier can be created and optical trapping via optical means has been demonstrated. In the fourth part of this chapter, condensation in zero dimensional cavities will be shown. These structures are particularly interesting as they allow to distinguish the effect of the interaction of the condensate with the reservoir of uncondensed excitons from that of the interactions within the condensate itself.

9.2 Confining Polaritons in Low Dimensional Structures

9.2.1 Starting from the Planar Microcavity

Let us first recall the standard situation of a planar microcavity (embedded between two Bragg mirrors) containing a given number of quantum wells. A two dimensional

continuum of photon modes is coupled to a two-dimensional continuum of exciton states.

On the one hand, the optical cavity can be considered as a Fabry Perot, defining confined optical modes with a quantized in plane wavevector along the z direction, perpendicular to the (xy) plane of the layers given by $k_z = \frac{p\pi}{L_c}$. Here p denotes the order of the considered Fabry Perot optical mode and L_c the thickness of the cavity layer. Thus we can define a two dimensional continuum of photon modes, labeled by their in-plane wavevector $k_{//}$ and with energy $E_C(k_{//}) = \frac{\hbar c}{n_{cav}}\sqrt{k_z^2 + k_{//}^2}$, where n_{cav} is the cavity layer refractive index. Close to $k_{//} = 0$, the cavity mode energy has a parabolic dispersion, which enables defining an effective mass $M_{phot} = \frac{\hbar p \pi n_{cav}}{c L_c}$ for the cavity mode.

On the other hand, the lowest energy excited states of the quantum wells, which can be populated for instance via optical excitation, are excitonic states. They describe the quantum states of an electron hole pair bound by Coulombic interaction and free of motion in the plane of the quantum well. The 1s excitonic states can be labeled by their in-plane wavevector $k_{//}$, and have an energy of the form $E_x(k_{//}) = E_x + \frac{\hbar^2 k_{//}^2}{2M_X}$, where $M_X = m_e + m_h$ is the exciton effective mass and m_e (resp. m_h) the electron (resp. hole) effective mass. This energy dispersion describes the kinetic energy related to the exciton center of mass in-plane motion. Excitons and photons are coupled via dipolar interaction. Because of the in-plane translation invariance, each exciton of a given in-plane wave-vector $k_{//}$ is coupled to the photon mode of same $k_{//}$. As a result, for each $k_{//}$, the Hamiltonian describing the coupled system reads:

$$H(k_{//}) = \begin{pmatrix} E_x(k_{//}) & g \\ g & E_C(k_{//}) \end{pmatrix} \tag{9.1}$$

The eigenstates of the system are exciton-photon mixed states, which are called cavity polaritons [5]. The lower polariton branch has a peculiar s-shaped dispersion [27], with an effective mass M_{pol} close to $k_{//} = 0$ given by $\frac{1}{M_{pol}} = \frac{w_{exc}^2}{M_{exc}} + \frac{w_{phot}^2}{M_{phot}}$, where w_{exc} and w_{phot} are respectively the exciton and photon weight of the polariton state. Since M_{phot} is typically three orders of magnitude smaller than M_{exc}, a small photon weight in the polariton state is enough to give an effective mass to the polariton much smaller than that of the exciton. This small effective mass is expected to favor Bose condensation at high temperature [28, 29].

9.2.2 Lateral Confinement of the Polariton States

We will now consider cavities which have a lower dimensionality. This can be realized experimentally by several methods. One can induce a lateral potential barrier acting either on the exciton part of the polariton or on its photon part.

The polariton energy can be changed via the exciton part applying a local stress. Several methods to do that have been reported. For instance the stress can be applied

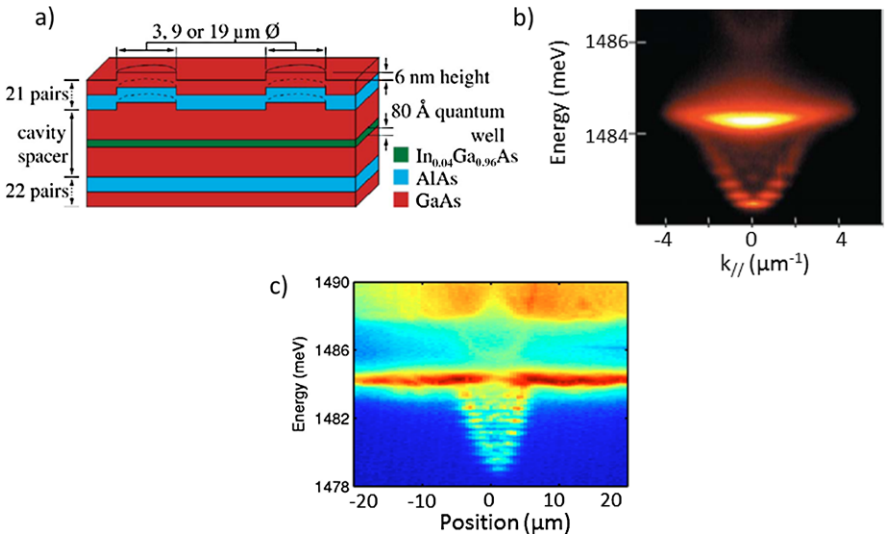

Fig. 9.1 (**a**) Schematic of the mesa sample developed by the group of B. Deveaud; (**b**) Far field emission and (**c**) spatially resolved emission of a single mesa structure showing the coexistence between laterally confined polaritons and two dimensional polaritons. This figure is adapted from Refs. [39] and [40]

locally with a tip pushing on the back side of the cavity sample: using this method a potential trap for the polariton states has been realized [20, 30]. Surface acoustic waves have also been used to modulate the polariton energy and confine them into 1D or 0D states [31, 32].

The alternative way of reducing the polariton dimensionality is to laterally confine the photon part. For instance one can deposit a patterned thin layer of metal on top of the cavity sample (see Chap. 8): metallic stripes or discs have been shown to induce a shallow potential on the polariton states, modulating the cavity mode energy [33, 34]. Similar methods have been theoretically proposed to laterally confine polariton surface states and guide their in-plane propagation. This approach can be applied to Tamm polariton states [35, 36] (confined at the interface between two mirrors) or to polariton Bloch surface waves [37] (localized close to the surface of a finite size Bragg mirror). Another very promising and versatile method has been pioneered by the group of B. Deveaud. It consists in defining mesa structures by etching of the cavity layer itself, before depositing the top Bragg mirror. The mesa region where the cavity thickness is larger defines a zero dimensional cavity in which the optical mode and thus the polariton states are fully confined into discrete states [38, 39]. This is illustrated in Fig. 9.1 where these polariton states have been imaged both in real and reciprocal space. A particularity of this technique is that the system offers the coexistence of 0D discrete polariton states with a continuum of two dimensional polariton states in the regions surrounding the mesas.

Another way of laterally confining the photon mode is simply to fully etch the planar cavity into wires, pillars or more complex microstructures. This is the geom-

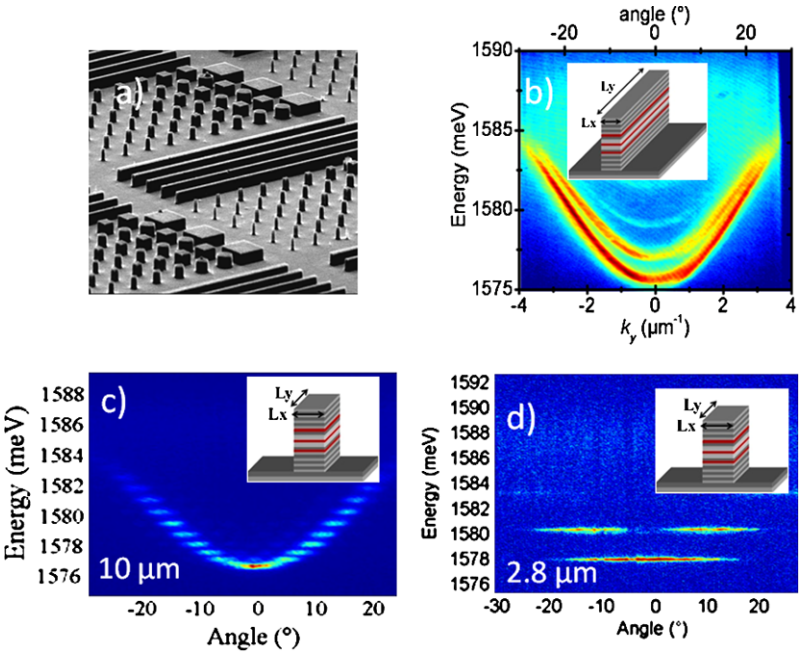

Fig. 9.2 (**a**) Scanning electron microscopy image of an array of wires and pillars etched starting from a planar microcavity; (**b**) Far field emission measured on a single wire cavity showing several 1D polariton subbands; (**c**) and (**d**) Same as (**b**) for a single squared micropillar of lateral dimension 10 µm for (**c**) and 2.8 µm for (**d**)

etry we describe in more details in the following and which is used in the condensation experiments we will review. Let us first consider the case of a one dimensional cavity with transverse dimension L_x. The in-plane translational invariance of the polariton states is lost and the in-plane wave-vector is quantized as: $k_x = \frac{p\pi}{L_x}$. As a result the polariton states are split into one-dimensional subbands describing the free motion of the polaritons along the y direction [41–43]. An example of such sub-bands measured by angle resolved photoluminescence is shown on Fig. 9.2.

One can also fully confine the polariton states into micropillars [44–46]. For instance if we consider a squared micropillar, both k_x and k_y are quantized as follows: $k_x = \frac{p_x\pi}{L_x}$ and $k_y = \frac{p_y\pi}{L_y}$ [47]. As a result, the polariton states in a micropillar are discrete states, which are spectrally more separated as the pillar size is reduced. This is illustrated on Fig. 9.2 where far field emission of single micropillars of various sizes is shown. If cylindrical micropillars are considered, the spherical symmetry has to be taken into account to find the polariton confined states and their degeneracy, as is well described in Ref. [48].

Note that a condition necessary to write a 2×2 matrix describing the coupling of each exciton and photon state with given wave vector is that exciton and photon states have the same dimensionality. This is the case for instance in planar cavity: both photons and excitons are two dimensional, excitons being confined in the quan-

tum wells while photons are confined in the cavity. Another example is the case of bulk semiconductor materials [49–52], where polaritons arise from the strong coupling of three dimensional excitons with three dimensional photons.

In laterally confined cavities such as those described above the situation is apparently different. Indeed the lateral dimensions of the cavities (a few microns) are typically 100 times larger than the exciton Bohr radius. As a result, the two dimensional character of the excitonic density of states is preserved, and there is no excitonic lateral quantum confinement. Therefore one dimensional photon modes in wire cavities (or zero dimensional photon modes in micropillars) are coupled to a continuum of two dimensional exciton states, a situation which may seem incompatible with the establishment of the strong coupling regime. As clearly explained in Ref. [53], when a quantum state is coupled to a continuum, the criterium for establishment of the strong coupling regime is the relative strength of the coupling interaction with respect to the spectral width ΔE of the continuum of emitting states. In our case, only excitons within the light cone can emit light. It is straightforward to show that ΔE is of the order of $\frac{E_x^2}{2M_{exc}c^2} \simeq 4$ μeV. This spectral width of the excitonic continuum is much smaller than the typical Rabi splitting of 15 meV in the sample we will consider in the following. Thus it is legitimate to consider that each photon state in microwires or micropillars, is coupled to a single exciton state and this is why the eigenstates of the system are exciton-photon mixed states with the dimensionality of the photon modes. It is therefore legitimate to describe the light-matter coupling in these system in the framework of the strong coupling regime.

9.3 Extended Polariton Condensates in 1D Cavities

9.3.1 Polariton Condensation Under Non-resonant Excitation

In the rest of the chapter we will review experiments performed under non-resonant excitation. This means that the sample is excited with a laser beam, which energy is tuned far above the polariton resonances (typically 100 meV above the lower polariton branch, tuned to the first reflectivity dip above the stop-band of the Bragg mirrors). As schematically represented on Fig. 9.3, hot electron-hole pairs are injected at the laser energy. They relax down to lower energy states via optical and acoustic phonon emission, and bind into excitons. Notice that the region in k-space indicated by blue circles is a region of very high density states and these states are excitonic-like states. For these two reasons, this region in k-space, called the excitonic reservoir is highly populated under such non-resonant excitation.

Excitons may also relax down to lower $k_{//}$ states to populate polariton states close to $k_{//} = 0$ on the lower polariton branch. Γ_{relax} describes the mean relaxation rate of excitons toward $k = 0$. This relaxation can occur via several scattering mechanisms. At low excitation powers, exciton phonon interaction is the dominant relaxation mechanism. This scattering mechanism is nevertheless not efficient for

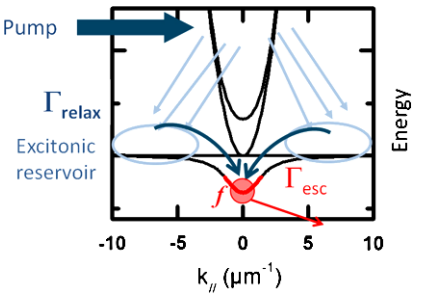

Fig. 9.3 Schematic of the polariton excitation scheme using non-resonant optical pumping. Γ_{relax} is the relaxation rate of excitons from the excitonic reservoir into $k_{//} \simeq 0$ polariton states while Γ_{esc} is the escape rate of photons out of the cavity. f is the occupancy of the polariton states close to $k_{//} = 0$

exchange energies larger than a few meV. Multiple phonon scatterings are necessary to populate the polariton states close to $k_{//} = 0$. These polariton states have a short lifetime, mostly because of the fast escape of the photon out of the cavity (typically Γ_{esc} lies between 1 to 30 ps depending of the quality factor of the considered sample). As a result at low excitation density, Γ_{relax} is smaller than Γ_{esc}^{-1}. Under steady state conditions, the resulting population of the lower branch is strongly out of equilibrium: excitons mainly populate the excitonic reservoir and the bottom of the lower polariton branch is depleted. This has been described as the relaxation bottleneck [6] and observed experimentally [54, 55]. Polariton electron scattering has been proposed as an alternative mechanism for efficient polariton thermalization [13]. This has been investigated experimentally: the bottleneck amplitude has been found to be reduced [56–59], but not enough to reach thermalization of the system.

Increasing the excitation power, exciton-exciton and polariton-polariton scattering become efficient relaxation mechanisms [54, 55, 60], which contribute to populate low energy polariton states close to $k_{//} = 0$. As a result Γ_{relax} increases. When it becomes larger than Γ_{esc}, a large occupancy of the lowest energy polariton states can start to develop. Once the occupancy of these states exceeds unity, the relaxation rate into these states becomes accelerated by bosonic stimulation and an exponential increase of the polariton occupancy close to $k_{//} = 0$ occurs. The regime of polariton condensation is achieved [29, 61–63].

This highly populated polariton state will be named in the following polariton condensate. Polariton condensates have been extensively studied in two dimensional cavities and some of their fascinating properties are described in the present volume. Here we want to emphasize a specificity of the non-resonant excitation condition, which will be crucial for the rest of the chapter. Because of its excitonic nature, a polariton condensate undergoes interaction with its environment. In particular in the case of non-resonant excitation, the interaction with the reservoir of uncondensed excitons present in the excitation area has to be taken into account. Let us consider the macroscopic wavefunction $\Psi(x, y, t)$ describing the time dependant probability

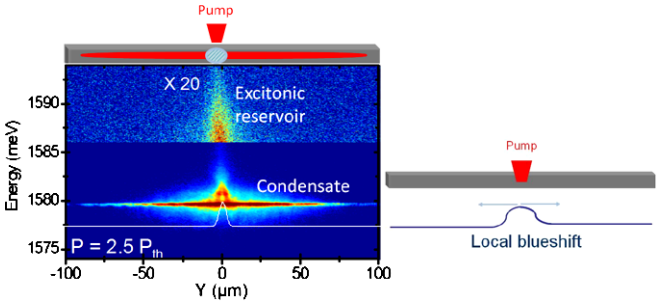

Fig. 9.4 Spatially resolved emission measured on a single wire cavity above condensation threshold. An extended polariton condensate is imaged. The high energy part of the graph has been magnified to observe the emission of the excitonic reservoir localized in the excitation area. On the *left* we have schematized the local blueshift of the polariton energy induced by the excitonic reservoir which tends to expulse polariton from the excitation region

density of the polariton condensate. It obeys the following Gross Pitaevski equation [64]:

$$i\hbar\frac{\partial\Psi(x,y,t)}{\partial t} = \left\{\frac{1}{2M_{pol}}\nabla^2 + V_{ext}(x,y) - i\frac{\hbar}{2}\left(\gamma_c - Rn_{res}(x,y,t)\right)\right.$$
$$\left. + g_{res}n_{res}(x,y,t) + g\left|\psi(x,y,t)\right|^2\right\}\psi(x,y,t) \qquad (9.2)$$

$V_{ext}(x,y)$ describes the potential defining the cavity geometry (wire, pillar or other); γ_c accounts for the loss due to photon escape rate out of the cavity while the term $Rn_{res}(x,y,t)$ is a gain term describing relaxation into the condensate from excitons from the reservoir which spatial density is $n_{res}(x,y,t)$. The term $g|\psi(x,y)|^2$ is due to polariton-polariton interaction within the condensate while the term $g_{res}n_{res}(x,y)$ comes from polariton interaction with the excitonic reservoir. These two interaction terms will be shown to strongly renormalize both the energy and the wavefunction of the polariton condensate. In particular the term due to interaction with the reservoir will have strong influence on the condensation process and is very specific to non-resonant excitation of the system.

9.3.2 Generation of an Extended Polariton Condensate

We describe here the generation of extended polariton condensates in 1D wire cavities [65]. In these experiments, a single wire is excited using a non-resonant laser beam focused down to a spot size of a few microns. The emission intensity of the excitation area presents an abrupt threshold in the excitation power above which the emission intensity increases exponentially. Figure 9.4 shows an example of the emission distribution measured above threshold along a 200 μm long wire. Surprisingly the emission at the energy of the condensate is spread all along the wire. This

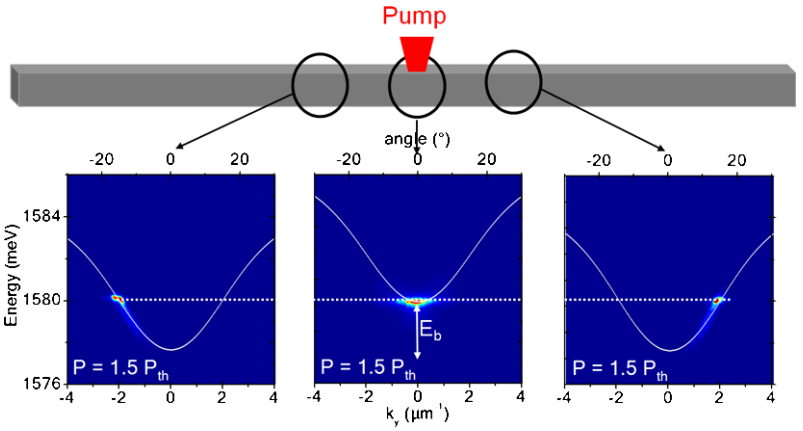

Fig. 9.5 Far field emission of a single wire cavity excited above the condensation threshold with a spatial selection of the excitation region in the *central panel*, and of the *left* (resp. *right*) side of the excitation area for *left* (resp. *right*) *panel*. Figure extracted from Ref. [65]

feature can be well understood when one looks at angle resolved emission with at the same time some spacial resolution. As shown in Fig. 9.5, where the far field emission of the excitation region is imaged, one clearly sees the formation of a condensate at $k_{//} = 0$, blueshifted by an energy E_B with respect to the polariton energy measured in the low density regime. This blueshift is induced by repulsive interaction with the reservoir of uncondensed excitons. Since excitons are quasi-particles much heavier than polaritons, they easily localize in the potential minima induced by disorder in the sample and remain in the excitation area. The emission of the reservoir visible at high energy in the upper part of Fig. 9.4 (which has been magnified) is indeed restricted to the excitation area. Thus the condensation generated in the excitation area stands at the top of a potential barrier induced by the optical excitation. This is why polaritons tends to be expelled from the excitation area, accelerated by this interaction energy with the reservoir and thus acquiring the corresponding kinetic energy. The far field imaging of the emission on both sides of the excitation area (see Fig. 9.5) evidences a beam of polaritons, at the same energy than the condensate in $k_{//} = 0$ and with a well defined finite in-plane wave-vector. Thus because of repulsive interaction with the excitonic reservoir, the condensate generated in the excitation tends to expand throughout the entire wire.

Analogy with the Atom Laser We want to mention here that there is a strong analogy between the present experiment and the realization of an atom laser [66–68]. Indeed in the atom laser experiments, a Bose Einstein condensate of atoms is generated in a confined region of space. Then a mechanism is able to extract atoms from the condensate, as if a little hole had been done in the box containing the condensate. A coherent beam of atom is thus extracted from the condensate, presenting coherence and directionality properties very similar to that of a laser beam. Here the excitation area is analogous to the box containing the condensate. The extraction

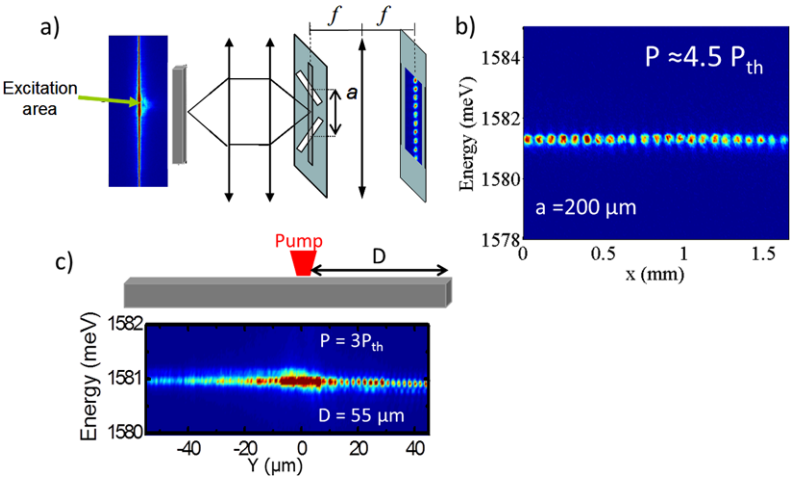

Fig. 9.6 (**a**) Experimental set-up to measure the spatial coherence of the polariton condensate; (**b**) Interference pattern obtained when interfering the emission of the two ends of a wire cavity (spatial separation of 200 µm). (**c**) Spatially resolved emission when a single wire cavity is excited 50 µm away from the right wire end. The observed modulation in the intensity reflects interferences between polaritons expelled from the excitation area and polaritons reflected at the wire end. Figure partly extracted from Ref. [65]

mechanism is provided by the repulsive interaction with the reservoir: a beam of polaritons which will be shown to be highly coherent is emitted within the cavity on each side of the excitation region. Our experiment can be considered as the demonstration of a polariton laser in the sense that coherent polaritons are emitted within the sample.

Spatial Coherence The extended polariton condensate which is formed in the wire cavity presents very high spatial coherence. This can be shown with a Young slit experiment. The set-up to do this experiment is schematically shown on Fig. 9.6a: an image of the wire emission is formed in a plane where a screen with two tilted slit is positioned. This set-up selects the emission from two small regions on the wire separated by a distance a. The mutual spatial coherence between these two regions can be probed looking at interference pattern arising from the emission of the selected zone. Figure 9.6b shows the fringe pattern arising from interfence between the emission of the two ends of the wire ($a = 200$ µm). The high fringe contrast indicates that the polariton condensate presents a spatial coherence over the entire wire. In this experiment interferences occur outside the sample. Signature of the high spatial coherence can also be seen in interferences occurring inside the sample. This is the case when the excitation spot is positioned close to one end of the wire cavity. Figure 9.6c shows the emission intensity measured along the wire when the excitation is located 50 µm from the wire end. Strong spatial modulation of the intensity is observed, due to interferences between polaritons escaping the excitation area and polaritons reflected by the end of the wire. These experiments

show that the condensates generated under non-resonant excitation propagate over large distances while preserving their spontaneous coherence. As a result one obtains polariton condensates with macroscopic spatial coherence.

9.3.3 Polariton Scattering by Disorder

One of the fascinating properties of Bose condensates is superfluidity, evidenced for instance with liquid helium [69, 70] and cold atoms [71, 72]. The characteristic signature of a superfluid propagation is the disappearance of all scattering by disorder. This friction-less propagation is due to a renormalization of the condensate excitation spectrum due to inter-particle interactions. A necessary requirement to reach the superfluid regime is that inter-particle interactions should be larger than the kinetic energy [73]. Polariton superfluidity has been reported in an experiment where the condensate was resonantly excited in a planar cavity [22]. To observe the superfluid regime [74], a small in-plane wave-vector was chosen for the propagating condensate so that the polariton kinetic energy could be smaller than interaction energy. On the contrary, if a large in-plane wave-vector was imprinted to the condensate, Cherenkov waves were observed, characteristic of the propagation of a supersonic condensate [22].

Scattering by disorder in the 1D propagation condensates has been investigated [75]. Since the in-plane wavevector of these condensates is given by the blueshift induced by the excitonic reservoir, it is not really controlled by the experimentalist, and always provides a large kinetic energy to the condensate of the order of 2–3 meV. In these experiments, the kinetic energy always remains larger than the interaction energy and therefore the polariton condensates, which spontaneously form, are always supersonic. Nevertheless a very strong suppression of the scattering by disorder (in a 1D geometry this is limited to backscattering) has been evidenced in this supersonic regime. This is illustrated on Fig. 9.7. A polariton condensate is generated via optical non-resonant excitation close to the right end of a microwire. The emission is probed from the left side of the excitation region. Below threshold a broad distribution of polariton traveling toward the left is measured in the far field emission. Polariton propagating in the opposite direction are also observed, which is the signature of polariton backscattering induced by disorder. Notice that because the probed region is always far from the left end of the wire, these polaritons traveling toward the right are not polaritons which have been reflected at the left end of the wire. As shown in the figure, when the excitation power is increased, the intensity of the backscattered signal is strongly reduced (by almost two orders of magnitude at the highest investigated excitation powers). Simultaneously to this non-linear effect, we observe signature of strong polariton-polariton scattering. Instead of a single polariton condensate generated at an energy related to the blueshift induced by the excitonic reservoir, we observe the formation of several condensates at lower energy. Simulation of the polariton propagation has been performed by the group of G. Malpuech. A photonic disorder is introduced to account for the observed backscattering at low density. These calculations show that

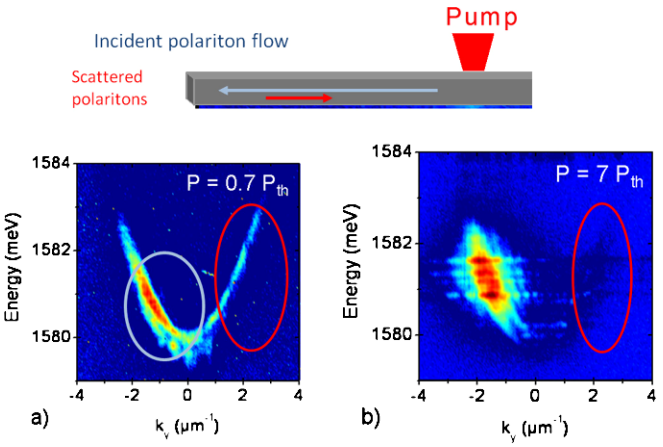

Fig. 9.7 *Upper part*: polariton are non-resonantly injected at the right end of a wire cavity; polariton far field emission (shown in logscale) is probed in the central part of the wire (**a**) below threshold and (**b**) above threshold

polariton-polariton scattering favors the propagation through the disorder potential and as a result the backscattering is reduced. This is a new mechanism which allows a quasi-frictionless propagation of a supersonic condensate [75].

9.3.4 Making Use of the Reservoir to Shape the Potential Landscape

The local blueshift induced by the reservoir can be used to shape the potential landscape of the polariton states. Two examples will be described below in experiments where a single non-resonant excitation beam is used. It is also possible to use several optical beams to modulate the potential. Such approach has been used to create a controlled localized defect or to confine vortices [76, 77].

Making Use of the Reservoir to Create a Tunnel Barrier In the regime described above where polariton-polariton interactions are responsible for the generation of several condensates, the blueshift induced by the excitonic reservoir creates a tunnel barrier. This is directly imaged by spatially resolved emission measurements, as illustrated in Fig. 9.8a. Several extended condensates are seen on each side of the excitation region while in the excitation region the absence of emission at low energy directly reflect the presence of a tunnel barrier. Polaritons close to the top of the barrier are coupled via tunneling through the barrier, while at low energy the barrier completely decouples the right and left side of the excitation region. This is further demonstrated by probing the mutual phase coherence between both sides of the excitation region performing young slit interferometry. As shown on Fig. 9.8b,

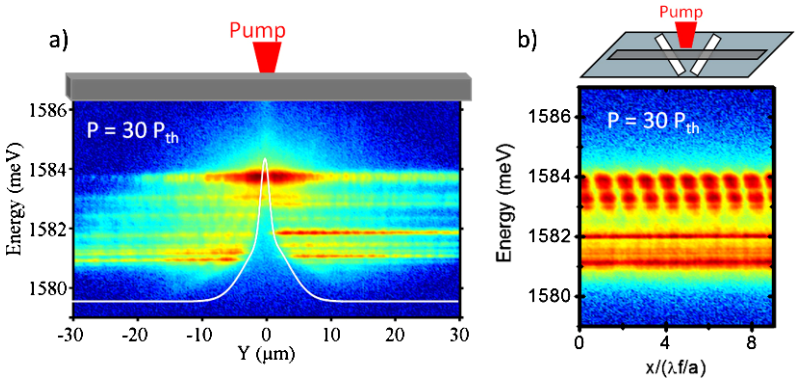

Fig. 9.8 (**a**) Spatially resolved emission of a single wire excited with a non-resonant laser beam: the tunnel barrier due to polariton interactions with the excitonic reservoir is directly imaged with extended polariton condensates on both sides. (**b**) Interference pattern using two slits located on each side of the excitation area. Figure adapted from Ref. [65]

pronounced fringes are observed for the highest energy polariton condensates. This shows that synchronization between left and right condensates occurs via tunnel coupling. On the opposite, no fringe is observed for the lowest energy states, where no signal is detected in the excitation region. Since, at this energy, the polariton condensates on each side of the excitation spot are fully decoupled by the tunnel barrier, no fixed phase relation exists between the two regions. Because the acquisition time of the measurements (typically of the order of 1s) is very large compared to the condensate coherence time (of the order of a few ns) the position of the fringes strongly fluctuates during the acquisition and as a result the fringe contrast is completely washed out. Of course it should be possible to recover a nice fringe contrast even for the low energy condensate if the experiment could be performed within the polariton coherence time.

Making Use of the Reservoir to Create an Optical Trap One can make use of the potential induced by the repulsive interaction with the excitonic reservoir to shape a potential trap. Figure 9.9a shows an example of such an experiment: a trap is formed between the excitation spot and the end of the wire. Its size is optically controlled by the position of the excitation spot. The spatially resolved photoluminescence allows direct imaging of the lobes of the polariton wavefunctions confined inside the optical trap. Both the energy level and the intensity distribution can be well reproduced using a Shrödinger equation describing the confinement inside the trap of a particle with the polariton effective mass. When the considered polariton modes have a strong photon content, relaxation into the trap is inhibited and a clear relaxation bottleneck is observed (see Fig. 9.9b). For more excitonic-like states, relaxation into the trap becomes efficient and polariton condensation into the trap can be achieved. It has been possible to observe the accumulation of more than 10^4 polaritons in the lowest energy state of the trap. Notice that in this configuration, the excitonic reservoir and the condensate are spatially separated. This is particularly

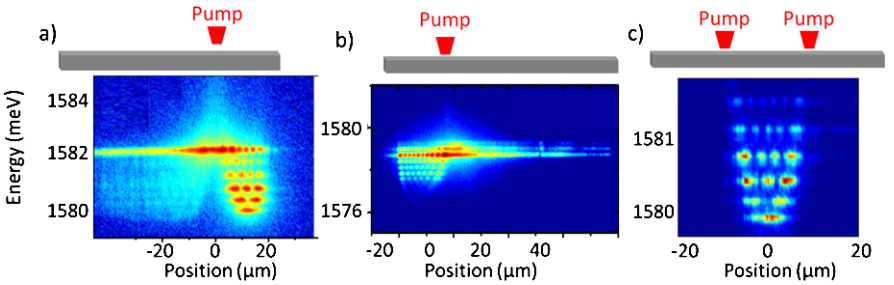

Fig. 9.9 Potential traps optically controlled by the excitonic reservoir: (**a**) The excitation spot is positioned close to one end of the wire and the trap is located between the excitation spot and the end of the wire; (**b**) same as (**a**) for a more negative detuning (more photon-like polariton) so that polariton relaxation into the trap is not efficient giving rise to a relaxation bottleneck; (**c**) Two pump spots are used to design the optical trap. The figure is partly adapted from Ref. [65]

favorable for the investigation of polariton interactions, as we will describe in the next section.

Finally using two non-resonant excitation spots it is possible to generate an optical trap which is fully optically controlled. This has been reported by the group of J.J. Baumberg in Ref. [78] and is illustrated in Fig. 9.9c in the case of a wire cavity.

9.4 Polariton Condensation in Zero-Dimensional Resonators

Polariton condensation can also be obtained on the discrete states of a micropillar [79]. In this system dramatic renormalization of the condensate wavefunction is observed, due to interaction with the reservoir. Also it is possible to investigate in detail both the interaction with the reservoir and interactions within the condensate itself [80, 81]. Finally micropillars have been the first system in which clear observation of both polariton condensation and photon lasing were reported [79]. The spatial emission patterns in both regimes differ drastically, which highlights the fact that they correspond to different physical lasing mechanisms.

9.4.1 Renormalization of the Polariton Wavefunction Induced by Interactions

We first consider polariton condensation in a single micropillar and are interested in the spatial emission pattern of the condensate in such zero-dimensional geometry. As in the wire cavity, polariton interaction with the excitonic reservoir tends to expel polaritons from the excitation area [80]. For instance when exciting a micropillar with a spot size much smaller than the pillar size, the reservoir creates a potential in the middle of the pillar which reshapes the polariton wavefunctions. This is illustrated on Fig. 9.10: as the excitation power is increased the polariton condensate

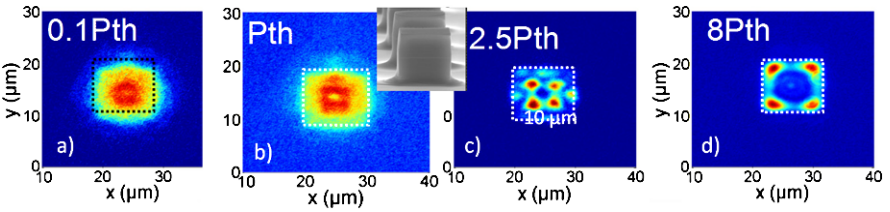

Fig. 9.10 Emission spatial distribution of a 10 µm square pillar excited at its center with a 2 µm excitation spot for several excitation powers. The potential induced by uncondensed excitons at the center of the pillar strongly modify the shape of the polariton wavefunction. The figure is partly adapted from Ref. [80]

tends to be expelled toward the four corners of the square micropillar. This behavior is fully reproduced when considering the confinement of a quasi-particle in a micropillar with a Gaussian potential at its center which increases linearly with excitation power. It has been carefully checked that the four lobe mode observed is not a high order mode of the pillar but really the lowest energy mode for the considered excitation power. So the observed behavior is characteristic of a polaritonic behavior, and different from a mode hoping in a standard laser. Further analysis of the difference with photon lasing will be presented in a next section.

Another illustration of the complex spatial properties of polariton condensation is found in photonic molecules (made of two coupled micropillars [82]). The condensation process under non-resonant excitation dramatically depends on the exact excitation conditions [83]. For instance the coupled system can be excited in a non-symmetric way, pumping with a small excitation spot only one of the two pillars. The excitonic reservoir creates a local potential in the excited pillar, which blueshift this micropillar with respect to the other. The spatial behavior of the condensation process in such excitation conditions is shown on Fig. 9.11. At threshold condensation occurs in the excited micropillar, even if this is not the lowest energy state of the system, which would be localized in the other pillar. Indeed the overlap between the lowest energy state and the states which are directly populated via interaction with the reservoir is too weak to allow for efficient scattering into the lowest energy state. As a result, condensation occurs in a metastable state located in the pumped pillar. As the excitation power is increased, further renormalization of the polariton wavefunction occurs, changing the relaxation rates between the different states. Eventually transfer of the condensate from the excited pillar into the lowest energy state of the other one becomes favorable. The condensate is then fully transferred into the pillar which is not optically excited. Such strong coherent emission from a region of the sample which is not pumped is another striking example of a condensation process, which would not be possible in a regular photon laser. To reproduce these results, it is not only necessary to consider the reservoir influence on the wavefunction space distributions, but also to recalculate the relaxation rates between these renormalized states. Indeed the change in the wavefunction dramatically modifies the overlap between the different states and thus the whole polariton relaxation mechanism [83].

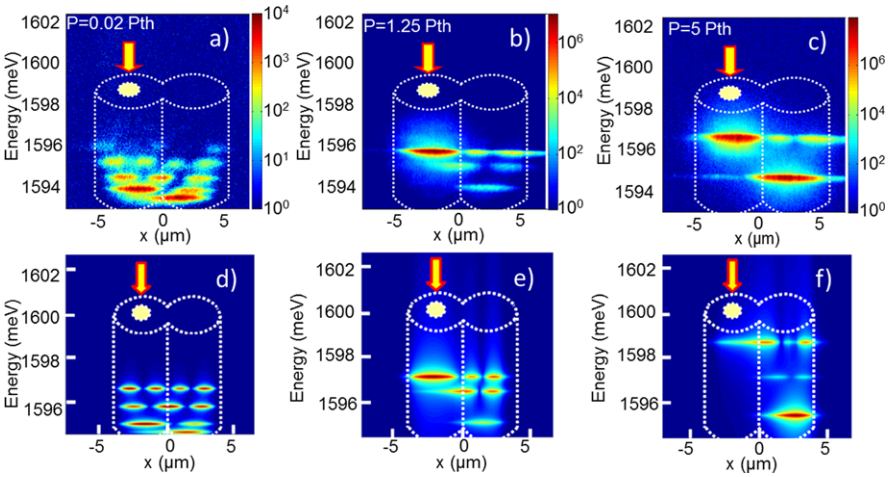

Fig. 9.11 (**a**)–(**c**) Spectrally resolved emission distribution measured for several excitation powers along a single molecule axis; The molecule is formed by two 3.5 μm diameter pillars separated by a center to center distance of 3.5 μm. (**d**)–(**f**) Calculated emission patterns for the corresponding excitation powers. The figure is extracted from Ref. [83]

9.4.2 Renormalization of the Polariton Energy Induced by Polariton-Polariton Interactions

We have seen above the strong effect of the excitonic reservoir on the polariton states and on the relaxation process. In particular, we have seen that both in an optical trap or in large micropillars, a spatial separation can be observed between the reservoir of uncondensed excitons and the condensate itself. In this configuration, because the spatial overlap between reservoir and polariton states is reduced, the blueshift due to the reservoir potential is smaller. This reveals another contribution to the energy renormalization, namely polariton-polariton interaction within the condensate itself. This is illustrated on Fig. 9.12, where the measured blueshift of the confined condensates is shown as a function of excitation power for several pillar sizes and for an optical trap. When the pillar size is very small (typically smaller than 3 μm), the condensate cannot be separated from the reservoir. The blueshift induced by the reservoir is strong and masks any other contribution to the energy renormalization. When the size of the pillar is reduced, the blueshift observed around condensation threshold decreases, due to the spatial separation from the reservoir. Then, above a given excitation level, an abrupt increase in the energy blueshift is observed. As shown on Fig. 9.12, this effect is simultaneous to the massive accumulation of polaritons in the considered quantum state. The population of the polariton state can be directly estimated considering its emission intensity normalized to the intensity at threshold: $N_{pol} = \langle |\psi(x, y)|^2 \rangle = \frac{I(P)}{I(Pth)}$. As shown on Fig. 9.12 polariton-polariton interaction when the polariton occupancy becomes large is indeed responsible for the strong increase in the polariton energy. This measurement allows quantitative

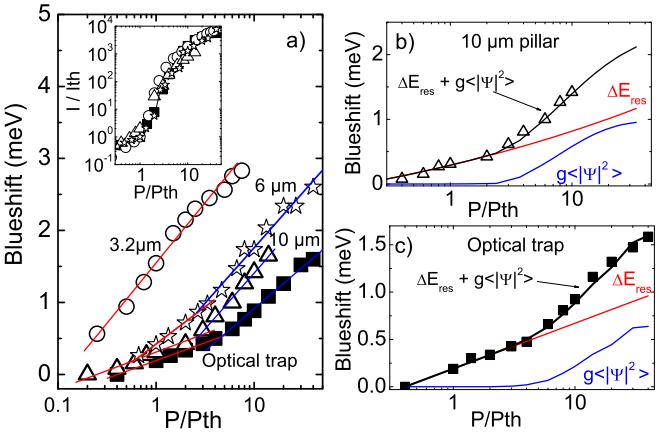

Fig. 9.12 (**a**) Blueshift measured in a 10, 6 and 3.2 µm micropillar and in the optical trap; the *red* (resp. *blue*) line shows the excitation range dominated by interactions with the reservoir (resp. within the condensate); the *inset* shows the measured intensity in the four systems. (**b**) (Symbols) Measured blueshift of the lowest energy polariton state in the 10 µm micropillar; Calculated blueshift induced (*red line*) by the excitonic reservoir or (*blue line*) by interactions within the condensate deduced from the measured polariton occupancy; (*black line*) Total calculated blueshift; (**c**) Same as (**b**) for the optical trap. The figure is extracted from Ref. [80]

estimate of the exciton-exciton interaction constant g, which is found to be of the order of 3 µeV cm^2, in accordance with theoretical calculation of exciton-exciton interactions [8]. Evaluation of the strength of polariton-polariton interaction is very important since this term is the non-linear term in the Gross Pitaevski equation responsible for many fascinating polaritonic features such as polariton bistability or superfluid behavior.

9.4.3 Polariton Condensation and Photon Lasing

There has been a long debate these last years in the scientific community about the understanding of the distinction between polariton condensation (or polariton lasing) and regular photon laser [84–88]. On a microscopic point of view, in a photon laser it is the emission of light that is stimulated whereas in a polariton laser, operating in the strong coupling regime, it is the polariton relaxation which is accelerated by bosonic stimulation. Nevertheless both devices emit coherent light and one could argue that these microscopic descriptions may be two different ways to describe the same physical mechanism. Here we want to show that it is possible to observe both regimes in the same cavity structure, either increasing the excitation density or increasing temperature. Very different spatial behaviors are observed in both cases, giving strong indication that indeed polariton lasers have very specific properties and are different from more conventional photon lasers.

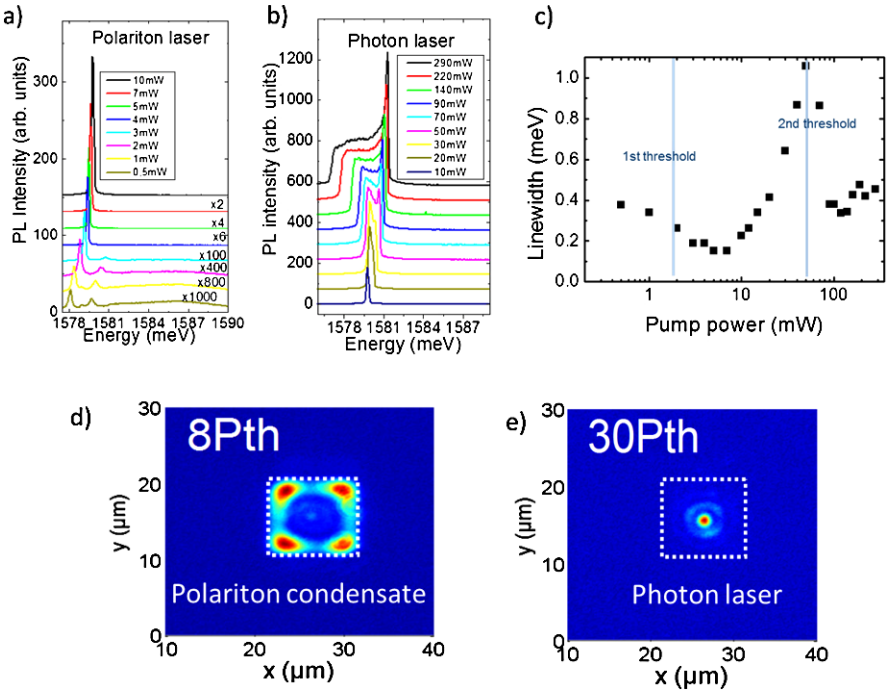

Fig. 9.13 (**a**) and (**b**) Emission spectra measured on a single 3 μm pillar for several excitation powers. Polariton condensation (photon lasing) is observed in (**a**) (resp. (**b**)); (**c**) Emission linewidth measured on a single 3 μm pillar as a function of the excitation power: pronounced spectral narrowing is observed both at polariton and photon lasing threshold. (**d**) and (**e**) Spatial emission distribution measured on a single 10 μm pillar in the polariton condensation regime and in the photon lasing regime. Figure partly extracted from Ref. [80]

Polariton and photon lasing can be successively observed in a single micropillar by increasing the excitation power, as illustrated in Fig. 9.13. A first threshold is primarily obtained, above which the emitted intensity strongly increases accompanied by a continuous blueshift of the emission due to polariton interactions. Further increasing the excitation density, the blueshift dramatically increases and then tend to saturate. Estimate of the exciton density shows that the system is pumped above the Mott density so that excitons are bleached. The system operate in the weak coupling regime and the emission comes from the uncoupled cavity mode (the energy of which may be slightly renormalized by the high pumping rate). Then a second threshold is seen, which is interpreted as the onset for photon lasing. Figure 9.13c shows that at both thresholds strong spectral narrowing of the lines is observed, further confirming the onset of two coherent regimes. A recent report of similar experiments in a planar cavity shows that the measure of the autocorrelation function $g^2(0)$ also confirms the onset of two coherent regimes. Nevertheless strong difference in the two regimes are evidenced when analyzing the emission pattern, for instance in the case of a large micropillar. We have seen that in the polariton conden-

sation regime, the emission comes from the four corners of the pillar. When passing through the second threshold, the emission abruptly arises from the very center of the excitation region and appears tightly focused. Thus going from polariton lasing into photon lasing, a completely different emission pattern is observed.

We want to mention also that the propagation features reported in 1D cavities completely vanish when operating the system at high enough temperature (above 50 K), such that the non-linear emission observed occurs in the weak coupling regime [65]. Indeed in this case, instead of observing long distance propagation, the emission only comes from a tightly focused region, within the excitation area.

So in all situations where lasing emission occurs in the weak coupling regime, the coherent emission is highly localized in the excitation region. Because of high pumping level, the index of refraction is modified and this creates a lateral confinement of the gain region. Such gain confinement was also reported in a cavity which was supposed to operate in the strong coupling regime [89], but this result needs to be confirmed.

To summarize, opposite spatial behaviors are observed in the weak and strong coupling regime. In the polariton condensation regime, repulsive interactions within the excitation area tend to expel polaritons from the excitation area. On the contrary, in the weak coupling regime, gain confinement induces a tight focus of the coherent emission. This clearly shows that the polariton device is not a standard laser and presents specific properties induced by interactions.

9.5 Conclusion

We have shown in this chapter that it is possible to spontaneously generate polariton condensates with a non-resonant optical excitation in semiconductor microcavities. The quality factor in GaAs based microcavities is now made large enough to enable ballistic propagation of these condensates over macroscopic distances, while preserving their spatial coherence. Via their excitonic part, polariton condensates undergo strong interactions with their environment. This is evidenced by strong renormalization of the condensate wavefunction and energy induced by polariton-polariton interaction within the condensate and also, by repulsive interactions with clouds of uncondensed excitons. Taking control of these interactions, it becomes possible to optically manipulate these condensates. Controlled trapping or tunnel coupling using interaction with a localized excitonic reservoir has been demonstrated. Finally it is possible to generate these polariton condensates in cavities etched into microstructures. We have shown the generation of macroscopically extended condensates in wire cavities or in fully confined resonators like micropillars or photonic molecules.

The very good control of the processing techniques and in particular of the dry etching of planar cavities now enables envisioning more complex photonic circuits to generate and manipulate polaritons. The experimental realization of several theoretical proposals for innovative circuits and new optical functionalities now becomes feasible. For instance very interesting physics is expected when considering

polaritons evolving in a periodic potential. Spatial Bloch oscillation of a polariton wavepacket could be revealed with interesting spin features [90, 91]. Polariton interactions could lead to localization of polariton condensates into gap solitons, as previously described for atomic condensates in an optical lattice [92] or in nonlinear optical fibers [93]. The use of spin dependant polariton bistability [94] in polaritonic circuits has been proposed to implement optical gates, analogous to a polariton neuron [95]. Also interesting could be the propagation and interaction of polariton bright solitons in photonic circuits [25]. Another very promising direction is the fabrication of a polariton interferometer, a ring shape polaritonic circuit [96]. In the presence of an external magnetic field, a polariton Berry phase is predicted in such device, resulting from competing effects of the longitudinal transverse splitting on one side and of the Zeeman splitting on the other side. Varying the magnetic field, strong modulation of the output polariton intensity is expected, in a similar way as for the Aharanov-Bohm effect in mesoscopic physics [97].

Finally following the implementation of photonic molecules composed of two coupled micropillars, one dimensional or two dimensional arrays of coupled pillars can be envisioned. This is the ideal system to investigate new quantum phases for a Bose Hubbard Hamiltonian in a dissipative system [98–100].

Acknowledgements I would like to warmly acknowledge all my collaborators who have been working so hard and with so much enthusiasm on polariton condensates over the last years. It has been a great pleasure to go through this adventure with them. I want to particularly thank the young people, PhD students, post-docs and master2 students, who have joined our team and did almost all the work: Esther Wertz, Dimitrii Tanese, Daniele Bajoni and Lydie Ferrier, Marta Galbiati and Emmanuel Bernet-Rollande. Special thanks to my collaborators at LPN who grew and processed these unique samples, and participated to optical spectroscopy experiments and active debate and discussions: Alberto Amo, Aristide Lemaître, Audray Miard, Elisabeth Galopin, Isabelle Sagnes, Rémy Braive, and Pascale Senellart. I want to also mention the strong and decisive collaboration we had with the theoretician group of Guillaume Malpuech and his collaborators Dmitri Solnishkov, Robert Johne and Hugo Flayac.

References

1. A. Kavokin, G. Malpuech, *Cavity Polaritons. Films and Nanostructures* (Academic Press, San Diego, 2003)
2. A. Kavokin, J.J. Baumberg, G. Malpuech, F.P. Laussy, *Microcavities* (Oxford University Press, New York, 2007)
3. B. Deveaud (ed.), *The Physics of Semiconductor Microcavities* (WILEY-VCH, Weinheim, 2007)
4. H. Deng, H. Haug, Y. Yamamoto, Rev. Mod. Phys. **82**, 1489 (2010)
5. C. Weisbuch, M. Nishioka, A. Ishikawa, Y. Arakawa, Phys. Rev. Lett. **69**(23), 3314 (1992)
6. F. Tassone, C. Piermarocchi, V. Savona, A. Quattropani, P. Schwendimann, Phys. Rev. B **56**, 7554 (1997)
7. F. Tassone, Y. Yamamoto, Phys. Rev. B **59**, 10830 (1999)
8. C. Ciuti, V. Savona, C. Piermarocchi, A. Quattropani, P. Schwendimann, Phys. Rev. B **58**(12), 7926 (1998)
9. C. Ciuti, V. Savona, C. Piermarocchi, A. Quattropani, P. Schwendimann, Phys. Rev. B **58**(16), R10123 (1998)

10. C. Ciuti, P. Schwendimann, A. Quattropani, Phys. Rev. B **63**(4), 041303 (2001)
11. M. Wouters, Phys. Rev. B **76**(4), 045319 (2007)
12. M.M. Glazov, H. Ouerdane, L. Pilozzi, G. Malpuech, A.V. Kavokin, A. D'Andrea, Phys. Rev. B **80**(15), 155306 (2009)
13. G. Malpuech, A. Kavokin, A. Di Carlo, J.J. Baumberg, Phys. Rev. B **65**, 153310 (2002)
14. M. Zamfirescu, A. Kavokin, B. Gil, G. Malpuech, M. Kaliteevski, Phys. Rev. B **65**, 161205 (2002)
15. J.J. Baumberg, A.V. Kavokin, S. Christopoulos, A.J.D. Grundy, R. Butte, G. Christmann, D.D. Solnyshkov, G. Malpuech, G.B.H. von Högersthal, E. Feltin, J.F. Carlin, N. Grandjean, Phys. Rev. Lett. **101**(13), 136409 (2008)
16. S. Christopoulos, G.B.H. von Högersthal, A.J.D. Grundy, P.G. Lagoudakis, A.V. Kavokin, J.J. Baumberg, G. Christmann, R. Butte, E. Feltin, J.F. Carlin, N. Grandjean, Phys. Rev. Lett. **98**(12), 126405 (2007)
17. G. Christmann, R. Butte, E. Feltin, J.F. Carlin, N. Grandjean, Appl. Phys. Lett. **93**, 051102 (2008)
18. J. Kasprzak, M. Richard, S. Kundermann, A. Baas, P. Jeambrun, J.M.J. Keeling, F.M. Marchetti, M.H. Szymanska, R. Andre, J.L. Staehli, V. Savona, P.B. Littlewood, B. Deveaud, L.S. Dang, Nature **443**(7110), 409 (2006)
19. H. Deng, G. Weihs, C. Santori, J. Bloch, Y. Yamamoto, Science **298**, 199 (2002)
20. R. Balili, V. Hartwell, D. Snoke, L. Pfeiffer, K. West, Science **316**(5827), 1007 (2007)
21. A. Amo, D. Sanvitto, F.P. Laussy, D. Ballarini, E. del Valle, M.D. Martín, A. Lemaitre, J. Bloch, D.N. Krizhanovskii, M.S. Skolnick, C. Tejedor, L. Viña, Nature **457**(7227), 291 (2009)
22. A. Amo, J. Lefrère, S. Pigeon, C. Adrados, C. Ciuti, I. Carusotto, R. Houdré, E. Giacobino, A. Bramati, Nat. Phys. **5**, 805 (2009)
23. K.G. Lagoudakis, M. Wouters, M. Richard, A. Baas, I. Carusotto, R. Andre, L.S. Dang, B. Deveaud-Pledran, Nat. Phys. **4**(9), 706 (2008)
24. K.G. Lagoudakis, T. Ostatnicky, A.V. Kavokin, Y.G. Rubo, R. Andre, B. Deveaud-Pledran, Science **326**(5955), 974 (2009)
25. M. Sich, D.N. Krizhanovskii, M. Skolnick, A.V. Gorbach, R. Hartley, D. Skryabin, E.A. Cerda-Méndez, K. Biermann, R. Hey, P. Santos, Nat. Photonics **6**, 50 (2012)
26. A. Amo, S. Pigeon, D. Sanvitto, V.G. Sala, R. Hivet, I. Carusotto, F. Pisanello, G. Lemenager, R. Houdre, E. Giacobino, C. Ciuti, A. Bramati, Science **332**(6034), 1167 (2011)
27. R. Houdré, C. Weisbuch, R.P. Stanley, U. Oesterle, P. Pellandini, M. Ilegems, Phys. Rev. Lett. **73**(15), 2043 (1994)
28. G. Malpuech, A.D. Carlo, A.V. Kavokin, J.J. Baumberg, M. Zamfirescu, P. Lugli, Appl. Phys. Lett. **81**(3), 412 (2002)
29. G. Malpuech, Y.G. Rubo, F.P. Laussy, P. Bigenwald, A.V. Kavokin, Semicond. Sci. Technol. **18**, S395 (2003)
30. R.B. Balili, D.W. Snoke, L. Pfeiffer, K. West, Appl. Phys. Lett. **88**(3), 031110 (2006)
31. E.A. Cerda-Méndez, D.N. Krizhanovskii, M. Wouters, R. Bradley, K. Biermann, K. Guda, R. Hey, P.V. Santos, D. Sarkar, M.S. Skolnick, Phys. Rev. Lett. **105**, 116402 (2010)
32. E.A. Cerda-Méndez, D.N. Krizhanovskii, K. Biermann, R. Hey, M.S. Skolnick, P.V. Santos, Phys. Rev. B **86**, 100301 (2012)
33. C.W. Lai, N.Y. Kim, S. Utsunomiya, G. Roumpos, H. Deng, M.D. Fraser, T. Byrnes, P. Recher, N. Kumada, T. Fujisawa, Y. Yamamoto, Nature **450**, 529 (2007)
34. N.Y. Kim, K. Kusudo, C. Wu, N. Masumoto, A. Loffler, S. Hofling, N. Kumada, L. Worschech, A. Forchel, Y. Yamamoto, Nat. Phys. **7**(9), 681 (2011)
35. M. Kaliteevski, I. Iorsh, S. Brand, R.A. Abram, J.M. Chamberlain, A.V. Kavokin, I.A. Shelykh, Phys. Rev. B **76**, 165415 (2007)
36. M. Kaliteevski, S. Brand, R.A. Abram, I. Iorsh, A.V. Kavokin, I.A. Shelykh, Appl. Phys. Lett. **95**(25), 251108 (2009)
37. M. Liscidini, D. Gerace, D. Sanvitto, D. Bajoni, Appl. Phys. Lett. **98**(12), 121118 (2011)

38. O.E. Daif, A. Baas, T. Guillet, J.P. Brantut, R.I. Kaitouni, J.L. Staehli, F. Morier-Genoud, B. Deveaud, Appl. Phys. Lett. **88**(6), 061105 (2006)
39. R.I. Kaitouni, O. El Daïf, A. Baas, M. Richard, T. Paraiso, P. Lugan, T. Guillet, F. Morier-Genoud, J.D. Ganière, J.L. Staehli, V. Savona, B. Deveaud, Phys. Rev. B **74**(15), 155311 (2006)
40. R. Cerna, T. Paraïso, Y. Léger, M. Wouters, F. Morier-Genoud, M.T. Portella-Oberli, B. Deveaud-Plédran, Phys. Rev. B **81**(11), 113306 (2010)
41. A. Kuther, M. Bayer, T. Gutbrod, A. Forchel, P.A. Knipp, T.L. Reinecke, R. Werner, Phys. Rev. B **58**, 15744 (1998)
42. A.I. Tartakovskii, V.D. Kulakovskii, A. Forchel, J.P. Reithmaier, Phys. Rev. B **57**, R6807 (1998)
43. G. Dasbach, M. Schwab, M. Bayer, D. Krizhanovskii, A. Forchel, Phys. Rev. B **66**(20), 201201 (2002)
44. J. Bloch, R. Planel, V. Thierry-Mieg, J. Gérard, D. Barrier, J.Y. Marzin, E. Costard, Superlattices Microstruct. **22**, 371 (1997)
45. T. Gutbrod, M. Bayer, A. Forchel, J.P. Reithmaier, T.L. Reinecke, S. Rudin, P.A. Knipp, Phys. Rev. B **57**, 9950 (1998)
46. M. Bayer, T. Gutbrod, J.P. Reithmaier, A. Forchel, T.L. Reinecke, P.A. Knipp, A.A. Dremin, V.D. Kulakovskii, Phys. Rev. Lett. **81**, 2582 (1998)
47. G. Dasbach, M. Schwab, M. Bayer, A. Forchel, Phys. Rev. B **64**(20), 201309 (2001)
48. G. Panzarini, L.C. Andreani, Phys. Rev. B **60**, 16799 (1999)
49. J.J. Hopfield, Phys. Rev. **112**(5), 1555 (1958)
50. C.H. Henry, J.J. Hopfield, Phys. Rev. Lett. **15**, 964 (1965)
51. D.D. Sell, S.E. Stokowski, R. Dingle, J.V. DiLorenzo, Phys. Rev. B **7**, 4568 (1973)
52. R.G. Ulbrich, C. Weisbuch, Phys. Rev. Lett. **38**, 865 (1977)
53. C. Cohen-Tannoudji, J. Dupont-Roc, *Processus d'interaction entre photons et atomes*, Savoirs Actuels. Série Physique (1996)
54. A.I. Tartakovskii, M. Emam-Ismail, R.M. Stevenson, M.S. Skolnick, V.N. Astratov, D.M. Whittaker, J.J. Baumberg, J.S. Roberts, Phys. Rev. B **62**(4), R2283 (2000)
55. P. Senellart, J. Bloch, B. Sermage, J.Y. Marzin, Phys. Rev. B **62**(24), R16263 (2000)
56. G. Ramon, R. Rapaport, A. Qarry, E. Cohen, A. Mann, A. Ron, L.N. Pfeiffer, Phys. Rev. B **65**, 085323 (2002)
57. A. Qarry, G. Ramon, R. Rapaport, E. Cohen, A. Ron, A. Mann, E. Linder, L.N. Pfeiffer, Phys. Rev. B **67**, 115320 (2003)
58. P.G. Lagoudakis, M.D. Martín, J.J. Baumberg, A. Qarry, E. Cohen, L.N. Pfeiffer, Phys. Rev. Lett. **90**(20), 206401 (2003)
59. M. Perrin, J. Bloch, A. Lemaitre, P. Senellart, Phys. Status Solidi C **2**(2), 759 (2005)
60. F. Tassone, Y. Yamamoto, Phys. Rev. B **59**(16), 10830 (1999)
61. A. Imamoglu, R.J. Ram, S. Pau, Y. Yamamoto, Phys. Rev. A **53**(6), 4250 (1996)
62. A. Kavokin, G. Malpuech, F.P. Laussy, Phys. Lett. A **306**(4), 187 (2003)
63. J. Keeling, P.R. Eastham, M.H. Szymanska, P.B. Littlewood, Phys. Rev. Lett. **93**(22), 226403 (2004)
64. L. Pitaevskii, S. Strindgari, *Bose-Einsten Condensation*, 1st edn. (Clarendon Press, Oxford, 2003)
65. E. Wertz, L. Ferrier, D.D. Solnyshkov, R. Johne, D. Sanvitto, A. Lemaitre, I. Sagnes, R. Grousson, A.V. Kavokin, P. Senellart, G. Malpuech, J. Bloch, Nat. Phys. **6**(11), 860 (2010)
66. M.O. Mewes, M.R. Andrews, D.M. Kurn, D.S. Durfee, C.G. Townsend, W. Ketterle, Phys. Rev. Lett. **78**, 582 (1997)
67. M.R. Andrews, C.G. Townsend, H.J. Miesner, D.S. Durfee, D.M. Kurn, W. Ketterle, Science **275**, 637 (1997)
68. I. Bloch, T.W. Hänsch, T. Esslinger, Phys. Rev. Lett. **82**, 3008 (1999)
69. P. Kapitza, Nature **141**, 74 (1938)
70. J.F. Allen, A.D. Misener, Nature **141**, 75 (1938)

71. C. Raman, M. Köhl, R. Onofrio, D.S. Durfee, C.E. Kuklewicz, Z. Hadzibabic, W. Ketterle, Phys. Rev. Lett. **83**(13), 2502 (1999)
72. R. Onofrio, C. Raman, J.M. Vogels, J.R. Abo-Shaeer, A.P. Chikkatur, W. Ketterle, Phys. Rev. Lett. **85**(11), 2228 (2000)
73. A.J. Leggett, Rev. Mod. Phys. **71**(2), S318 (1999)
74. I. Carusotto, C. Ciuti, Phys. Rev. Lett. **93**(16), 166401 (2004)
75. D. Tanese, D.D. Solnyshkov, A. Amo, L. Ferrier, E. Bernet-Rollande, E. Wertz, I. Sagnes, A. Lemaître, P. Senellart, G. Malpuech, J. Bloch, Phys. Rev. Lett. **108**, 036405 (2012)
76. A. Amo, S. Pigeon, C. Adrados, E. Giacobino, C. Ciuti, A. Bramati, Phys. Rev. B **82**, 081301 (2010)
77. D. Sanvitto, S. Pigeon, A. Amo, D. Ballarini, M.D. Giorgi, I. Carusotto, R. Hivet, F. Pisanello, V.G. Sala, P.S. Soares-Guimaraes, R. Houdré, E. Giacobino, C. Ciuti, A. Bramati, G. Gigli, Nat. Photonics **5**, 610 (2011)
78. G. Tosi, G. Christmann, N.G. Berloff, P. Tsotsis, T. Gao, Z. Hatzopoulos, P.G. Savvidis, J.J. Baumberg, Nat. Phys. **8**, 190 (2012)
79. D. Bajoni, P. Senellart, E. Wertz, I. Sagnes, A. Miard, A. Lemaître, J. Bloch, Phys. Rev. Lett. **100**, 047401 (2008)
80. L. Ferrier, E. Wertz, R. Johne, D.D. Solnyshkov, P. Senellart, I. Sagnes, A. Lemaitre, G. Malpuech, J. Bloch, Phys. Rev. Lett. **106**(12), 126401 (2011)
81. A.S. Brichkin, S.I. Novikov, A.V. Larionov, V.D. Kulakovskii, M.M. Glazov, C. Schneider, S. Höfling, M. Kamp, A. Forchel, Phys. Rev. B **84**, 195301 (2011)
82. S.M. de Vasconcellos, A. Calvar, A. Dousse, J. Suffczynski, N. Dupuis, A. Lemaitre, I. Sagnes, J. Bloch, P. Voisin, P. Senellart, Appl. Phys. Lett. **99**(10), 101103 (2011)
83. M. Galbiati, L. Ferrier, D.D. Solnyshkov, D. Tanese, E. Wertz, A. Amo, M. Abbarchi, P. Senellart, I. Sagnes, A. Lemaitre, E. Galopin, G. Malpuech, J. Bloch, Phys. Rev. Lett. **108**, 126403 (2012)
84. S. Pau, H. Cao, J. Jacobson, G. Bjørk, Y. Yamamoto, A. Imamoglu, Phys. Rev. A **54**(3), R1789 (1996)
85. M. Kira, F. Jahnke, S.W. Koch, J.D. Berger, D.V. Wick, T.R. Nelson, G. Khitrova, H.M. Gibbs, Phys. Rev. Lett. **79**, 5170 (1997)
86. H. Cao, S. Pau, J.M. Jacobson, G. Björk, Y. Yamamoto, A. Imamoğlu, Phys. Rev. A **55**, 4632 (1997)
87. R. Butté, G. Delalleau, A.I. Tartakovskii, M.S. Skolnick, V.N. Astratov, J.J. Baumberg, G. Malpuech, A. Di Carlo, A.V. Kavokin, J.S. Roberts, Phys. Rev. B **65**(20), 205310 (2002)
88. D. Bajoni, P. Senellart, A. Lemaître, J. Bloch, Phys. Rev. B **76**, 201305(R) (2007)
89. G. Roumpos, W.H. Nitsche, S. Höfling, A. Forchel, Y. Yamamoto, Phys. Rev. Lett. **104**, 126403 (2010)
90. H. Flayac, D.D. Solnyshkov, G. Malpuech, Phys. Rev. B **83**, 045412 (2011)
91. H. Flayac, D.D. Solnyshkov, G. Malpuech, Phys. Rev. B **84**, 125314 (2011)
92. B. Eiermann, T. Anker, M. Albiez, M. Taglieber, P. Treutlein, K.P. Marzlin, M.K. Oberthaler, Phys. Rev. Lett. **92**, 230401 (2004)
93. B.J. Eggleton, R.E. Slusher, C.M. de Sterke, P.A. Krug, J.E. Sipe, Phys. Rev. Lett. **76**, 1627 (1996)
94. N.A. Gippius, I.A. Shelykh, D.D. Solnyshkov, S.S. Gavrilov, Y.G. Rubo, A.V. Kavokin, S.G. Tikhodeev, G. Malpuech, Phys. Rev. Lett. **98**, 236401 (2007)
95. T.C.H. Liew, A.V. Kavokin, I.A. Shelykh, Phys. Rev. Lett. **101**, 016402 (2008)
96. I.A. Shelykh, G. Pavlovic, D.D. Solnyshkov, G. Malpuech, Phys. Rev. Lett. **102**(4), 046407 (2009)
97. D. Mailly, C. Chapelier, A. Benoit, Phys. Rev. Lett. **70**, 2020 (1993)
98. I. Carusotto, D. Gerace, H.E. Tureci, S.D. Liberato, C. Ciuti, A. Imamoglu, Phys. Rev. Lett. **103**(3), 033601 (2009)
99. M.J. Hartmann, Phys. Rev. Lett. **104**, 113601 (2010)
100. M. Leib, M.J. Hartmann, New J. Phys. **12**, 093031 (2012)

Chapter 10
Toward Quantum Fluids at Room Temperature: Polariton Condensation in III-Nitride Based Microcavities

Jacques Levrat, Georg Rossbach, Raphaël Butté, and Nicolas Grandjean

Abstract The combination of high exciton-binding energy and large coupling strength makes exciton-polaritons in wide bandgap semiconductor microcavities (MCs) eminently suitable to promote quantum effects up to ambient conditions. In this respect, the III-nitride material system is a very promising candidate owing to the recent observation of room temperature (RT) polariton condensation, which should even benefit further from rapid developments in the areas of growth and processing. This chapter deals with GaN-based planar MCs where the phase transition of exciton-polaritons to an out-of-equilibrium macroscopic quantum state has been demonstrated up to 340 K. A comprehensive study of the threshold of the polariton condensation phase transition as a function of temperature and detuning evidences the interplay between carrier kinetics and thermodynamics. It turns out that polariton relaxation is predominantly driven by thermodynamics at RT. The evolution of the order parameter, i.e., the wavefunction of the polariton condensate, can thus be confronted to Bose-Einstein theory. In particular, it is expected that spontaneous symmetry breaking leads to the observation of randomly-oriented linearly polarized light as the condensate acquires a different phase for each realization. This behavior is evidenced for the case of a bulk but not for a quantum-well based GaN MC as the dimensionality of the system is affecting the spin dependence of the polariton-polariton interactions. In particular, in the case of a two-dimensional system, interactions between polaritons with parallel and opposite spins are no longer equivalent causing the self-induced Larmor precession of the polariton pseudospin. This feature is evidenced by the progressive depinning of the order parameter above the polariton condensation threshold.

J. Levrat · G. Rossbach · R. Butté · N. Grandjean (✉)
Institute of Condensed Matter Physics, Ecole Polytechnique Fédérale de Lausanne, CH-1015 Lausanne, Switzerland
e-mail: nicolas.grandjean@epfl.ch

A. Bramati, M. Modugno (eds.), *Physics of Quantum Fluids*,
Springer Series in Solid-State Sciences 177, DOI 10.1007/978-3-642-37569-9_10,

10.1 Introduction

10.1.1 Polariton Condensation and Its Path Toward Room Temperature

After the first demonstration of the strong coupling regime (SCR) in planar GaAs-based microcavities (MCs) in 1992 [1] and the proposal of polariton condensation as a driving force for the realization of novel low-threshold coherent light emitters by A. Imamoğlu and co-workers in 1996 [2], the polaritonic field has grown at a fast pace. In particular, the first report of non-equilibrium Bose-Einstein condensation (BEC) of polaritons in a CdTe-based MC [3] and the subsequent observations of integer [4] and half-integer quantum vortices [5], superfluidity [6–8], and solitons [9] in polariton fluids, attracted a lot of attention. Cavity-polaritons exhibit unique characteristics inherited from their mixed light-matter nature. Thus, their photonic component confers them a very low effective mass, while their excitonic one allows them to interact causing non-linearities in polaritonic quantum systems.

From the point of view of integrated optoelectronics, cavity-polaritons are of high interest as they can carry information *via* their pseudospin **S**, their phase, their amplitude and their energy. When decaying, an exact copy of this information is transferred to the emitted photons allowing the readout of the polariton state. Another important aspect of cavity-polaritons is that the light-matter content can be controlled *via* the detuning δ between cavity-photons and excitons, e.g., by varying the cavity thickness or the lattice temperature. Thus, the way polaritons interact with each other can be modified: for negative δ values the lowest energy polariton state is mainly photon-like, while for positive ones the situation is reversed. Based on these unique properties, cavity-polaritons were proposed as promising candidates for several applications in optoelectronics and spinoptronics, including the generation of entangled photon pairs [10, 11], the realization of micro-optical parametric oscillators [12] and amplifiers [13, 14], ultrafast optical spin switches [15, 16], new coherent light sources [2, 17–20], mesoscopic optical Berry-phase interferometers [21], Sagnac interferometers [22], exciton-polariton BEC mediated high-temperature superconducting circuits [23], logic gates [24], polarization/spin-sensitive devices [25–29], THz emitters [30] and devices using spin-independent bistability [31]. Most of those phenomena or concepts have been proposed based on the properties of GaAs and CdTe MCs, which exhibit on the one hand an advanced structural and optical quality but on the other hand a limited exciton binding energy (E_X^b) restricting their experimental demonstrations to cryogenic temperatures and thus preventing the realization of devices. Indeed, despite the demonstration of an electrically-injected polariton light emitting diode, a system operating in the linear emission regime, at room temperature (RT) in a GaAs-based MC, it seems that the cut-off temperature T_{cut} for the observation of polariton related non-linearities is set by the thermal stability of excitons, i.e., $T_{cut} \approx E_X^b / k_B$ [14]. To overcome this issue E_X^b has to exceed the thermal energy at RT ($\sim$26 meV) and defines the main figure of merit to bring polariton non-linearities up to ambient conditions.

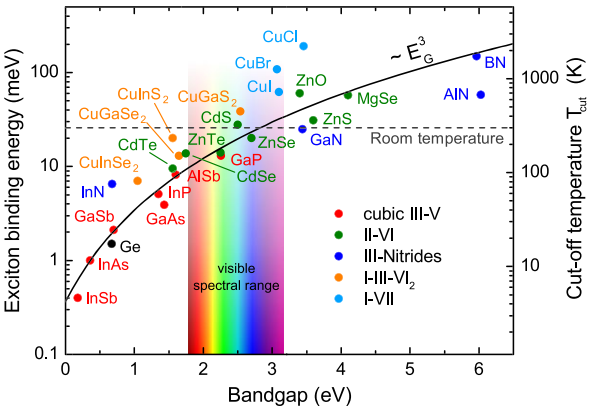

Fig. 10.1 Exciton binding energy for various inorganic bulk semiconductors: III–V (*red*), II–VI (*green*), I–VII (*light blue*), chalcopyrites I–III–VI_2 (*orange*), and III-nitrides (*blue*). The *right axis* corresponds to the cut-off temperature T_{cut} of excitons with binding energy E_X^b. A guide to the eye (*black solid line*) reproduces the power-law $E_X^b \propto E_G^3$ and the *horizontal dashed line* defines the room-temperature limit

Figure 10.1 shows E_X^b values for a variety of inorganic bulk semiconductor materials as a function of their bandgap energy E_G. Within the hydrogen-like approximation the relation $E_X^b \propto m_{eff}^*/\varepsilon_r^2$ holds, where m_{eff}^* is the reduced effective mass of the exciton and ε_r is the static dielectric constant of the material of interest. Both quantities are a function of E_G: as a first approximation $m_{eff}^* \propto E_G$ and $\varepsilon_r \propto 1/E_G$ [32]. The resulting power law $E_X^b \propto E_G^3$ is shown as a guide to the eye in Fig. 10.1 and highlights the limited number of bulk semiconductor MCs for high temperature exciton-based applications. This situation can be significantly improved if quantum-well (QW) based structures are considered instead of bulk ones. Indeed, due to carrier-confinement effects the value of E_X^b can theoretically be enhanced by a factor of up to four compared to the bulk case in perfectly two-dimensional (2D) QWs [33]. However, owing to deviations from the ideal 2D-symmetry real structures often exhibit a maximum enhancement factor of about two.

10.1.2 Systems Suitable for Room Temperature Polariton Condensation

Polariton condensation in semiconductor MCs under non-resonant excitation has been reported for the following material systems: GaAs [34, 35], CdTe [3], GaN [18, 19], anthracene [20], and very recently in ZnO [36]. Thus far, the critical temperature for this phase transition $T_c \leq T_{cut}$ amounts to ~40 K for GaAs [35] and ~50 K for CdTe [3]. A major breakthrough on the road toward higher temperatures occurred with the report of polariton condensation at RT in GaN-based MCs [18, 19]. These observations attracted a lot of interest and GaN is probably the most promising candidate to date for the realization of polariton-based devices operating under ambient conditions. However, ZnO and organic MCs are considered as alternative possibilities to GaN: their relevant characteristics are briefly discussed in this section and compared to the GaN ones in Table 10.1.

Table 10.1 Exciton binding energy E_X^b and vacuum Rabi-splitting Ω_{VRS} for the material systems exhibiting high temperature (RT, except $T_{ZnO} = 120$ K) polariton condensation in planar MCs

	GaN (bulk)	GaN (QW)	ZnO (bulk)	Organic (bulk)
E_X^b (meV)	26 [37]	48 [19]	60 [38]	∼1000 [20]
Ω_{VRS} (meV)	30 [18]	56 [19]	130 [36]	256 [20]

10.1.2.1 ZnO-Based Microcavities

Considering its high exciton binding energy (∼60 meV for bulk material [38]) and oscillator strength, ZnO has been proposed in 2002 as a candidate of choice for high temperature polariton condensation [39]. As a matter of fact, the SCR for a bulk cavity has been achieved in several geometries: in epitaxial cavities grown on top of a III-nitride bottom distributed Bragg-reflector (DBR) [36, 40, 41], in fully-hybrid microcrystalline ZnO structures relying on two dielectric DBRs [42, 43], and in other ZnO-based systems with vacuum Rabi-splittings as large as $\Omega_{VRS} \sim 280$ meV [44].[1] Although the SCR has been demonstrated up to 410 K in this system [45], non-linear emission in the SCR corresponding to polariton lasing has only been reported very recently at $T = 120$ K [36]. Despite a substantial research activity the insufficient material quality prevented more advanced studies on planar ZnO-based MCs so far and the lack of a highly reproducible and stable p-type doping might hamper the path toward devices.

10.1.2.2 Organic Microcavities

Optical excitations in organic semiconductors are preferentially described in the framework of Frenkel excitons [46], i.e., strongly bound and localized electron-hole pairs (E_X^b of up to 1 eV [20]) exhibiting a large oscillator strength and a transition energy commonly occurring in the visible spectral range. In combination with the ability of doping, organic MCs present serious advantages over inorganic ones and the potential low cost of device fabrication is a major trigger for this research activity. Until now the SCR has been demonstrated for various planar sample geometries and active media [47–53] up to RT. Nevertheless, polariton condensation has only been observed recently in an anthracene-based MC under non-resonant optical excitation by Kéna-Cohen and Forrest [20]. Despite obvious advantages, the limited thermal, mechanical and chemical stability of the most common organic compounds constitutes the major drawback of those MCs.

[1] Ω_{VRS} corresponds to the minimum mode splitting between the lower and the upper polariton branch (LPB and UPB, respectively) for zero detuning between cavity-photon and exciton eigenenergies.

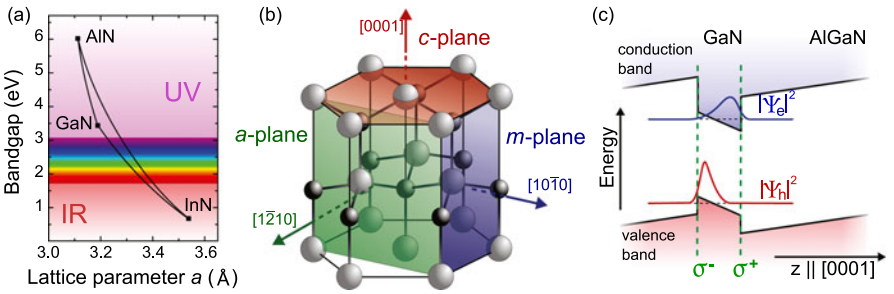

Fig. 10.2 (**a**) Bandgap of the common wurtzite III-nitride compounds *versus* lattice constant *a* emphasizing the possibility of bandgap engineering *via* alloying. (**b**) Wurtzite crystal structure with highlighted main planes. (**c**) Sketch of the quantum-confined Stark effect: polarization discontinuities at polar heterostructure interfaces lead to the formation of compensation charge planes and to a built-in electric field separating electron and hole wavefunctions

10.1.3 Basics on III-Nitrides

Recently III-nitrides became the second largest market in the semiconductor industry just after silicon. This development was mostly driven by the progress made by the III-nitride technology for numerous daily life applications relying on specific material properties. In the hexagonal phase all compounds provide a direct bandgap, which is continuously tunable from the ultraviolet down to the infrared spectral range *via* ternary alloying and thus also spans the whole visible spectrum (cf. Fig. 10.2(a)). Taking into account the well-established possibility of *p*-type doping for Ga-rich alloys, these characteristics make III-nitrides extremely suitable for optoelectronic applications. Besides the violet laser diodes used for optical data storage systems, the market of white light emitting diodes increases extremely rapidly. The latter provide record luminous efficacies and will progressively revolutionize general lighting. On the basis of their chemical and thermal robustness III-nitrides are further used for high-power and high-temperature electronics.

Basic characteristics of a material system can already be inferred from its crystal structure: III-nitrides preferably crystallize in the wurtzite phase, which is shown in Fig. 10.2(b). The hexagonal symmetry of the lattice causes uniaxial anisotropy to many material properties and in combination with the ionicity of the chemical bonding an intrinsic polarity along the *c*-axis. This so-called spontaneous polarization is specific for each binary compound and might be additionally modified by a strain related piezoelectric component. The discontinuity of the polarization vectors projected onto the growth axis z at the interfaces of heterostructures causes a large built-in electric field and leads to the so-called quantum-confined Stark effect (QCSE) [54]. Figure 10.2(c) displays the band profile of a *c*-plane ($z \parallel [0001]$) GaN QW embedded in an AlGaN matrix. The electric field generated by the sheet charge densities σ^+ and σ^- shifts the occupancy probability maximum of electrons and holes toward opposite sides of the well. Owing to the reduced wavefunction overlap the oscillator strength is decreased, which detrimentally affects the efficiency of

devices and in view of polaritons weakens the coupling strength between excitons and photons. This effect scales with the well thickness leading to a narrow optimum well width for nitride structures grown along the polar surface orientation, usually in the 1 to 2 nm range [55]. A way to completely circumvent the drawbacks of the QCSE consists in growing structures on non-polar surfaces, like the m- or a-planes (cf. Fig. 10.2(b)), where z and c-axis are orthogonal to each other and the projection of the polarization vectors onto z is thus equal to zero. However, due to the lack of adequate substrates crystal quality is still an issue for those structures and the well-controlled c-plane growth orientation is widely preferred.

The small Bohr radius of the exciton in a GaN QW ($\sim$2 nm) implies a high sensitivity of the latter to crystal defects, local lattice deformations and alloy composition fluctuations in the barriers, and leads in general to an increased inhomogeneous broadening γ_{inh} compared to semiconductors with lower exciton binding energy. Indeed it was shown that an increased inhomogeneous linewidth will decrease the polariton mode splitting and might potentially switch the system to the weak coupling regime [56, 57]. Therefore all design aspects of III-nitride MCs have to be carefully balanced with respect to their impact on the crystal quality. An important role is assigned to the bottom DBR: from the optical point of view it should provide a sufficient number of bilayer pairs exhibiting a refractive index contrast as large as possible to guarantee a high peak reflectivity, a broad stopband width and a small penetration depth. On the other hand it represents the template on which the active region of the MC will be grown. Thus a limited number of defects and a flat surface are required to reduce the inhomogeneous broadening of the exciton due to in-plane strain fluctuations, i.e., $\gamma_{\mathrm{inh}} \leq \Omega_{\mathrm{VRS}}$, and to have a low photonic disorder. The key to combine those features in a monolithic layer stack is the minimization of strain. Based on Fig. 10.2(a) a lattice-matched UV AlGaN/AlInN based bottom DBR has shown to be the best compromise [58, 59].

10.2 Polariton Condensation Phase Diagram in a GaN-Based Microcavity

The first demonstration of polariton lasing [18] and BEC of exciton-polaritons [60] at RT was achieved in a bulk GaN-based MC. However, with respect to Table 10.1 and the previous discussion, a lattice temperature of 300 K roughly corresponds to T_{cut} for this active material. Since device operating temperatures are usually exceeding the ambient one, a structure relying on a bulk GaN layer looks thus hardly probable. This intrinsic limitation can be effectively overcome by switching to appropriate multiple QW-based active regions. Quantum confinement enhances the exciton oscillator strength and the robustness of excitons: $E_{\mathrm{X}}^{\mathrm{b}}$ values of up to 50 meV have been obtained [59]. This approach also induces a reduction in the critical density for condensation n_{c} by at least one order of magnitude [61] and the observation of polariton condensation over a wider range of detunings δ and temperatures T [62, 63]. Note that the range of accessible δ directly scales with Ω_{VRS} and corresponds to

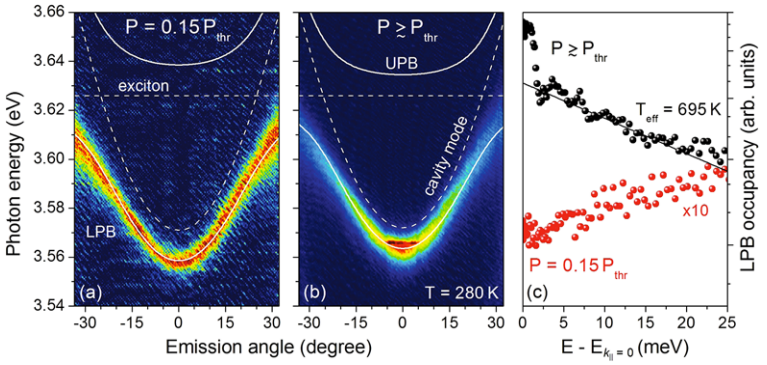

Fig. 10.3 LPB far-field emission spectra measured at 280 K (**a**) far below and (**b**) slightly above the threshold pumping power (P_{thr}), respectively. The macroscopic occupancy of the ground state is clearly seen at threshold and is associated with a blueshift of about 4.8 meV ($\delta \approx -56$ meV). (**c**) The deduced LPB occupancy shows the transition from a non-thermal distribution below threshold, i.e., a relaxation bottleneck is present [66], to a thermal one above

polariton states with a non-negligible excitonic fraction, i.e., $|\delta| < \Omega_{\mathrm{VRS}}$,[2] which explains why wide band gap semiconductors cover such a wide range of detunings. The situation is illustrated in Fig. 10.4(a) for the case of GaAs, CdTe and GaN quantum well-based structures (white dashed lines) together with bulk ZnO and organic microcavities (black dashed lines).

In the forthcoming section the phase diagram, i.e., the evolution of the polariton condensation threshold power density P_{thr} as a function of the independently tunable parameters δ and T will be presented and discussed for a multiple QW GaN-based MC. P_{thr} will be shown to be either governed by the carrier relaxation kinetics or by the thermodynamics depending on the set of δ and T investigated [64]. The sample studied is described in detail in Ref. [59]. Note that in the following sections the terminology *polariton condensation* encompasses both *polariton lasing* and *polariton BEC*. In the former case, the system transits from a metastable uncondensed phase to a condensed one and neither below nor above P_{thr} the system reaches thermal equilibrium, whereas for the polariton BEC the system exhibits a well defined temperature below and above the condensation threshold [64]. At this stage it is worth pointing out that a polariton BEC does not correspond to a BEC in the classical sense: polaritons rely on the strong coupling between photons and electronic excitations in the solid state and are thus short-living quasi-particles. This means that the condensate has to be continuously pumped to compensate for losses and as such it represents an intrinsically open system. Nevertheless, both phenomena share numerous essential characteristics leading to the denomination *non-equilibrium BEC* for exciton-polaritons [65].

[2]Note that this criterion sets an arbitrary frontier and the excitonic fraction at $k_{\parallel} = 0$ corresponds to 15 % for $\delta/\Omega_{\mathrm{VRS}} = -1$ and 85 % for $\delta/\Omega_{\mathrm{VRS}} = 1$. For $|\delta|/\Omega_{\mathrm{VRS}} = 2$, these ratios still amount to 5 and 95 %, respectively.

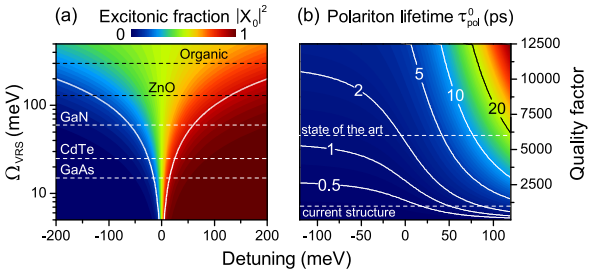

Fig. 10.4 (**a**) Excitonic fraction at $k_\parallel = 0$ as a function of δ and vacuum Rabi splitting Ω_{VRS}. The *horizontal dashed lines* represent the state-of-the art for different MCs. The *continuous white lines* are defined by the condition $\delta = \pm\Omega_{\mathrm{VRS}}$ and set the range where the polaritons significantly depart from the bare modes. (**b**) Polariton lifetime at $k_\parallel = 0$ as a function of the MC quality factor and the exciton cavity-photon detuning δ calculated for a GaN QW-based planar semiconductor microcavity operating in the SCR with an exciton transition at 3.65 eV at RT and $\Omega_{\mathrm{VRS}} = 60$ meV. The *horizontal dashed lines* illustrate the state-of-the-art for hybrid MC structures [73] and the sample investigated here, respectively

Typical far-field emission spectra of a GaN-based MC measured at 280 K are shown in Fig. 10.3. Far below the condensation threshold the LPB occupancy clearly appears non-thermal. With increasing polariton density, relaxation toward the ground state becomes more efficient resulting in a thermal carrier distribution when approaching P_{thr}. Note that for the transition region between both regimes the effective polariton temperature T_{eff} does not necessarily have to coincide with the lattice one and commonly exceeds the latter.

10.2.1 The Polariton Dispersion and Lifetime

When the coupling strength between excitons and cavity-photons exceeds the corresponding damping rates the SCR takes place, where lower and upper polaritons are the new eigenmodes of the system. Their energy evolves with the in-plane wavevector $k_\parallel$ according to:

$$E_{\mathrm{LPB/UPB}}(k_\parallel) = \frac{1}{2}\delta_{k_\parallel} + E_{\mathrm{X}}(k_\parallel) \mp \frac{1}{2}\sqrt{\delta_{k_\parallel}^2 + \Omega_{\mathrm{VRS}}^2}, \tag{10.1}$$

where the $-$ and $+$ signs stand for LPB and UPB, respectively, and $\delta_{k_\parallel}$ denotes the energy difference between the uncoupled cavity and exciton dispersion: $E_{\mathrm{cav}}(k_\parallel) - E_{\mathrm{X}}(k_\parallel)$. Since the momentum dependence of $\delta_{k_\parallel}$ is simply given by the different effective masses except for a constant offset, the detuning $\delta = \delta_{k_\parallel}(k_\parallel = 0)$ will be used as a characteristic quantity in the following. From (10.1) it appears that the detuning significantly influences the shape of the polariton dispersion. For the extreme case where $\delta \gg \Omega_{\mathrm{VRS}}$, the LPB dispersion reduces to the uncoupled exciton one, and in the opposite case where $\delta \ll \Omega_{\mathrm{VRS}}$, $E_{\mathrm{LPB}}(k_\parallel)$ converges to the cavity-photon dispersion around zero in-plane momentum. This asymptotic behav-

ior highlights the fact that the polariton description only holds in the region where $\delta_{k_\parallel}$ is small or of the order of the light-matter coupling strength, i.e., $|\delta| < \Omega_{\mathrm{VRS}}$. In this detuning range, whose extent critically depends on the system of interest, the polariton behavior can be continuously tuned from photon to exciton-like (see Fig. 10.4(a)). Thereby, the excitonic fraction along the LPB dispersion is strongly dependent on Ω_{VRS} and δ, and is given by:

$$\left|X(k_\parallel,\delta)\right|^2 = \hbar^2\Omega_{\mathrm{VRS}}^2/\left[\hbar^2\Omega_{\mathrm{VRS}}^2 + 4\left(E_{\mathrm{LPB}}(k_\parallel) - E_{\mathrm{X}}(k_\parallel)\right)^2\right], \tag{10.2}$$

while the evolution of the corresponding photonic fraction is set by the relation $|C(k_\parallel)|^2 = 1 - |X(k_\parallel)|^2$. Note that excitons and cavity-photons exhibit different lifetimes ($\tau_{\mathrm{X}} \neq \tau_{\mathrm{C}}$) resulting in a polariton lifetime τ_{pol} given by:

$$\frac{1}{\tau_{\mathrm{pol}}(k_\parallel)} = \frac{|C_{k_\parallel}|^2}{\tau_{\mathrm{C}}} + \frac{|X_{k_\parallel}|^2}{\tau_{\mathrm{X}}}. \tag{10.3}$$

All experiments reported in the following are performed using a non-resonant excitation scheme. Hence, the electronic population consists first of a hot electron-hole plasma with a very high kinetic energy excess, typically 1 eV. Despite the high temperature of the electronic gas, relaxation *via* longitudinal-optical (LO) phonon emission down to the exciton dispersion is very efficient in GaN and lasts for about a few 100 fs [67]. This high efficiency is attributed to both the high LO-phonon energy ($E_{\mathrm{LO}} = 92$ meV) and the intrinsic polarization field in the wurtzite crystal along the c-direction. As a consequence, the fast generation of a Boltzmann distribution of excitons with a temperature given by the LO-phonon energy can be reasonably assumed. Once this initial population is formed, it further thermalizes *via* interactions with acoustic phonons and the surrounding electronic population. This process is rather slow (scattering time ~10 ps [68]) and does not allow the exchange of a significant amount of energy, the latter typically amounting to 1 meV. However, the main limitation preventing thermalization of the polariton population is the decrease in τ_{pol} close to the center of the Brillouin zone according to (10.2) and (10.3). In addition, the increasing photonic content of lower polaritons inhibits those interactions and further promotes a non-thermal LPB occupancy characterized by the presence of a relaxation bottleneck [69]. This latter feature is commonly observed in semiconductor MCs whatever the material system [70–72].

For the achievement of a thermal carrier distribution and thus to minimize P_{thr} the relaxation bottleneck has to be overcome, which directly implies a relaxation timescale τ_{rel} smaller or at least comparable to the mean lifetime of the polariton ensemble:

$$\frac{1}{\langle\tau_{\mathrm{pol}}\rangle} = \left\langle \frac{1}{\tau_{\mathrm{pol}}(k_\parallel)} \right\rangle_{N_{\mathrm{tot}}} = \frac{1}{N_{\mathrm{tot}}} \sum_{\mathrm{k}_\parallel} \frac{n_{\mathrm{k}_\parallel}}{\tau_{\mathrm{pol}}(k_\parallel)}, \tag{10.4}$$

where $N_{\mathrm{tot}} = \sum_{\mathrm{k}_\parallel} n_{\mathrm{k}_\parallel}$ is the total number of particles in the system and $n_{\mathrm{k}_\parallel}$ is the occupancy number of a polariton state with in-plane momentum $k_\parallel$.

Since the exciton lifetime in (10.3) significantly exceeds the photon one, the lifetime of the polariton condensate, i.e., the lifetime at zero in-plane momentum

$\tau_{\mathrm{pol}}(k_{\parallel}=0)=\tau_{\mathrm{pol}}^{0}$, appears to be clearly limited by the photonic component and is well approximated by $\tau_{\mathrm{pol}}^{0}\sim\tau_C/|C_0|^2$. As a consequence, the MC quality factor $Q=E_C\tau_C/\hbar$, which mainly depends on the structural quality [74], is a key parameter to improve the relaxation efficiency as it directly sets the number of scattering events before polariton decay. The hybrid MC structure investigated in the following sections exhibits a Q-factor of ∼1000, but values in excess of 6000 have been demonstrated in similar nitride-based MCs [73]. Figure 10.4(b) illustrates the evolution of the polariton condensate lifetime as a function of detuning and quality factor. In the Q-factor range displayed, it is particularly visible that lifetimes longer than 5 ps are restricted to positive values of δ, even for full dielectric MCs that are expected to exhibit significantly larger Q-factors.

The majority of III-nitride based MCs feature a hybrid architecture, i.e., the bottom DBR and the overgrown cavity region consist of a monolithic III-nitride layer stack in order to ensure an optimum optical quality of the active medium. Thereby, the refractive index contrast of the DBR bilayer components $(\Delta n/n)_{\mathrm{nitride}}$ is strongly limited and amounts to about 10 % in the best cases [75]. Hence, a high number of pairs (typically >30) is required to reach a reflectivity as large as 99.5 % and a stopband width exceeding 200 meV [76]. This implies a significant penetration length of the light electric field into the DBR, which detrimentally affects the coupling strength in this geometry. The presence of propagating defects, interface roughness and residual absorption might further decrease the polariton lifetime. For all these reasons the full dielectric MC approach providing a high refractive index contrast: $(\Delta n/n)_{\mathrm{diel}}>30$ %, and low absorption looks better suited to achieve Q-factors exceeding 10 000 but they raise serious challenges in terms of fabrication and processing.

10.2.2 A Pedestrian Approach to the Phase Diagram: Kinetic vs. Thermodynamic Regimes

The polariton lasing threshold behavior crucially depends on how far the polariton gas is from thermal equilibrium, which in turn depends on the characteristic timescales involved in the system: the polariton ensemble lifetime $\langle\tau_{\mathrm{pol}}\rangle$ and the relaxation time τ_{rel}, i.e., the time required for the polaritons to thermalize with the lattice. As a consequence, a good figure of merit to understand the behavior of P_{thr} is the ratio $R=\langle\tau_{\mathrm{pol}}\rangle/\tau_{\mathrm{rel}}$ that can be naively understood as the ratio between the respective roles played by the thermodynamics and the kinetics. Intuitively, when R tends to zero, the polariton distribution cannot reach a thermal distribution and the final state of the system is fully governed by the relaxation kinetics. By contrast, when this ratio tends to large values, the polariton distribution approaches equilibrium and the threshold can be reasonably described within the BEC thermodynamic theory framework. The case $R\sim1$ defines an intermediate regime where both theories cannot be applied independently.

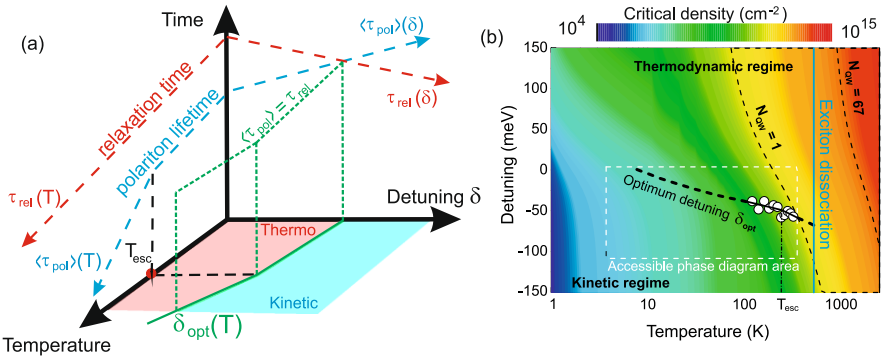

Fig. 10.5 (**a**) Schematic phase diagram representing the evolution of the characteristic times, $\langle\tau_{\rm pol}\rangle$ and $\tau_{\rm rel}$ as a function of δ and T (see text for details). Adapted from Ref. [63]; (**b**) Critical density for polariton condensation (*color scale*) as a function of δ and T. The saturation density for a GaN-based MC with 1 and 67 thin GaN QWs (corresponding to the investigated structure) is symbolized by the *thin black dashed lines*. The *vertical blue line* represents the dissociation temperature for QW excitons in the present structure. The *filled white circles* represent the experimental data for the optimum detuning corresponding to the minimum threshold power density required for condensation. This line separates the kinetic and thermodynamic regimes and the *thick black dashed line* represents the expected trend. The *dashed white rectangle* displays the experimentally accessible detunings and temperatures in the present MC

The following subsections will focus on the influence of the cavity-exciton detuning δ and the temperature T on the different timescales. As a result separate regions where the polariton relaxation is governed either by the thermodynamics ($R\to\infty$) or by the carrier kinetics ($R\to 0$) emerge in the (δ, T)-plane.

10.2.2.1 Effect of Detuning and Temperature on Polariton Relaxation

The role played by δ in semiconductor MCs operating in the SCR is essential as it allows to adjust the light-matter content of polaritons. According to (10.2) and Fig. 10.4(a), when δ is negative the LPB becomes photon-like and conversely exciton-like for positive detunings. More precisely, polaritons mimic the behavior of the closest bare mode and can be tuned from quasi non-interacting particles for $|X(0)|^2\to 0$ to strongly interacting ones when $|X(0)|^2\to 1$. As a consequence $\tau_{\rm rel}$ is a monotonically decreasing function of δ for a given temperature (cf. Fig. 10.5(a)):[3]

$$\left.\frac{\partial\tau_{\rm rel}(\delta,T)}{\partial\delta}\right|_{T={\rm cst}} < 0. \tag{10.5}$$

Hence, a higher excitonic content has been shown to favor relaxation processes bringing the system closer to the thermodynamic limit [72]. On the other hand in-

[3] This is true if one discards extra relaxation channels such as the LO-phonon assisted one [77].

creasing the temperature strongly affects the particles behavior. Even if polariton-polariton and polariton-acoustic phonon scattering rates decrease when the carrier temperature is increased [66], the overall dynamics is faster since the imbalance between income and escape rates for a given state with wave vector $k_\parallel$ increases with temperature. In particular, Porras and coworkers have shown that there is an approximately linear relation between the exciton reservoir temperature and the maximum energy loss in the relaxation process, i.e., the higher the temperature, the faster the relaxation dynamics [78]. The relaxation dynamics is further accelerated by the progressive apparition of free thermal electrons inducing additional polariton-electron scattering events. Consequently, a rising temperature promotes the relaxation efficiency (cf. Fig. 10.5(a)):

$$\left.\frac{\partial \tau_{\mathrm{rel}}(\delta, T)}{\partial T}\right|_{\delta=\mathrm{cst}} < 0. \tag{10.6}$$

This effect becomes more pronounced for positive detunings as the total scattering rate $W^{\mathrm{tot}}_{\mathrm{k}_\parallel \to \mathrm{k}'_\parallel}$ is proportional to the product of the excitonic fraction of the initial and final states. It is worth mentioning that the temperature also affects the exciton reservoir lifetime $\tau_{\mathrm{res}} = \tau_{\mathrm{X}}^{\mathrm{NR}}$. The latter decreases with rising lattice temperature resulting in an additional increase in P_{thr}. However, this effect is neglected in the present situation as it only occurs at high temperatures where the system is in the thermodynamic regime and thermal depopulation is then the predominantly limiting contribution affecting P_{thr} as described hereafter.

10.2.2.2 Impact of the Thermodynamics on the Threshold Power Density

In the previous section, the evolution of τ_{rel} has been qualitatively deduced depending on the weights of interactions for different regions in the phase diagram (δ, T)-plane (cf. Fig. 10.5(a)). However, so far the discussion has only accounted for the carrier kinetics. In order to get a complete picture of the P_{thr} evolution the role of thermodynamics has to be considered. Figure 10.5(b) displays the critical density $n_{\mathrm{c}}^{\mathrm{th}}(\delta, T)$ of polaritons, which corresponds to the total density of particles in the system at $P = P_{\mathrm{thr}}$. Even if this treatment is only valid for a perfect 2D non-interacting Bose gas, it provides basic understanding of the system behavior. For instance, it appears that for a given δ-value $n_{\mathrm{c}}^{\mathrm{th}}$ continuously increases with temperature due to the progressive population of the higher energy states:

$$\left.\frac{\partial n_{\mathrm{c}}^{\mathrm{th}}(\delta, T)}{\partial T}\right|_{\delta=\mathrm{cst}} > 0. \tag{10.7}$$

Note that for temperatures higher than a certain T_{esc}, the increase in $n_{\mathrm{c}}^{\mathrm{th}}$ is faster due to the onset of thermal detrapping. T_{esc} thus corresponds to the temperature where the thermal energy $k_{\mathrm{B}}T$ becomes comparable to the lower polariton trap depth in $k_\parallel$-space defined as the energy gap between the bottom of the branch and the onset of non parabolicity in the LPB. Indeed, it was shown that in our III-nitride MQW

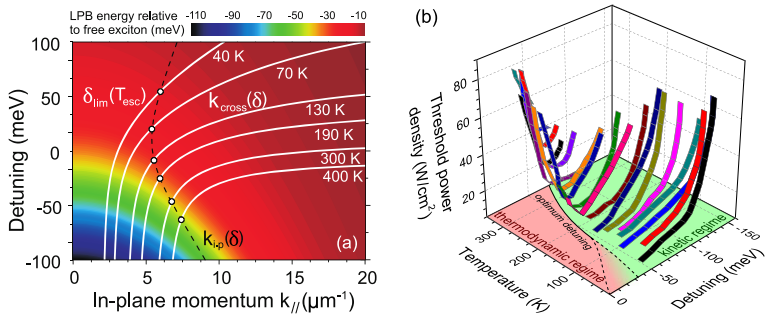

Fig. 10.6 (**a**) Color map of the lower polariton branch dispersion (LPB) relative to the free exciton line vs. in-plane momentum $k_{\|}$ for different δ values and $\Omega_{\mathrm{VRS}} = 60$ meV. The *continuous white lines* $k_{\mathrm{cross}}(\delta)$ define the maximum $k_{\|}$ occupied for different temperatures. The *black dashed line* $k_{\mathrm{i.p}}(\delta)$ corresponds to the position of the inflection point in the LPB. The transition detuning δ_{lim} is found when these two curves cross each other for each temperature. T_{esc} sets the onset of thermal detrapping for each detuning δ_{lim}. For less negative δ values, thermal depopulation is triggered; (**b**) Experimental condensation phase diagram: Evolution of the polariton lasing threshold as a function of temperature and detuning. Adapted from Ref. [62]

based MC thermal depletion is triggered when polaritons start populating the LPB beyond its inflection point [55]. This mechanism acts as an extra loss channel and hampers the polariton condensate formation. In Fig. 10.6(a) the LPB is shown for detunings ranging from -100 to 100 meV as a function of $k_{\|}$. The position of the inflection point $k_{\mathrm{i.p}}(\delta)$ is indicated and shown together with $k_{\mathrm{cross}}(\delta)$, which is given by the condition $E_{\mathrm{LPB}}(k = 0, \delta) + k_B T_{\mathrm{latt}} = E_{\mathrm{LPB}}(k_{\mathrm{cross}}, \delta)$ and denotes the highest accessible momentum for the polariton gas. The intersection of $k_{\mathrm{cross}}(\delta)$ and $k_{\mathrm{i.p}}(\delta)$ defines, for a given lattice temperature T_{esc}, the critical detuning δ_{lim} above which thermal depopulation becomes the dominant effect. In the region of the phase diagram where $\delta > \delta_{\mathrm{lim}}$ and $T > T_{\mathrm{esc}}$, the polariton condensation threshold undergoes a significant increase as illustrated in Figs. 10.5–10.7 [55]. This simple picture is in agreement with the experimental values extracted from the phase diagram (see Sect. 10.2.4), where $T_{\mathrm{esc}} \sim 260$ K and $\delta_{\mathrm{lim}} \sim -45$ meV.

To have a complete picture of the mechanisms ruling P_{thr}, the evolution of $n_{\mathrm{c}}^{\mathrm{th}}$ with δ should also be considered. From Fig. 10.5(b) it appears that $n_{\mathrm{c}}^{\mathrm{th}}$ increases with δ for the whole temperature range:

$$\left.\frac{\partial n_{\mathrm{c}}^{\mathrm{th}}(\delta, T)}{\partial \delta}\right|_{T=\mathrm{cst}} > 0. \tag{10.8}$$

This can be intuitively understood when considering that for more positive detunings the density of states at zero in-plane momentum increases due to the rising matter-like character of polaritons. Thus, more particles have to be brought to the bottom of the LPB to reach the degeneracy condition. Interestingly, at the same time τ_{rel} undergoes a significant decrease due to the enhancement of interactions. The system is therefore facing simultaneously two opposite constraints: the thermodynamic threshold is low in the region where R is small and the relaxation efficiency

is comparably low (kinetic regime) while it increases where R is large (thermodynamic regime) but τ_{rel} is short. As a consequence, for each temperature an optimum situation occurs where both kinetic and thermodynamic regimes are competing with each other and $\langle\tau_{\mathrm{pol}}\rangle$ and τ_{rel} become comparable. In this region, a minimum value for P_{thr} is expected and an optimum detuning δ_{opt} can be estimated by:

$$\tau_{\mathrm{pol}}(\delta_{\mathrm{opt}}, T) = \tau_{\mathrm{rel}}(\delta_{\mathrm{opt}}, T) \rightarrow R_{\mathrm{th/kin}}(\delta_{\mathrm{opt}}, T) = 1, \tag{10.9}$$

while satisfying:

$$\left.\frac{\partial P_{\mathrm{thr}}(\delta, T)}{\partial \delta}\right|_{T=\mathrm{cst}} = 0. \tag{10.10}$$

A calculation of $\delta_{\mathrm{opt}}(T)$ from (10.9) based on the knowledge of the average polariton lifetime $\langle\tau_{\mathrm{pol}}\rangle$ corresponding to (10.4) and the derivation of τ_{rel}, which requires a modeling of the polariton relaxation kinetics by solving semiclassical Boltzmann equations, is presented in the following section.

10.2.3 Theoretical Description of Polariton Relaxation

The calculation of the phase diagram requires the use of the correct formalism depending on the dominant regime, the kinetic or the thermodynamic one. Even if the kinetic approach can be applied to the whole phase diagram, it is of major importance to define the domain of validity of the thermodynamic one. This section provides a brief overview of the behavior of P_{thr} in the two regimes.

10.2.3.1 The Thermodynamic Limit

When polariton relaxation is predominantly driven by the thermodynamics, thus implying that R tends toward infinity, the polariton states are occupied according to the Bose-Einstein statistics [79]:

$$f_{\mathrm{BE}}\big(E_{\mathrm{LPB}}(k_{\parallel}), T, \mu\big) = \left[\exp\left(\frac{E_{\mathrm{LPB}}(k_{\parallel}) - E_{\mathrm{LPB}}(0) - \mu}{k_{\mathrm{B}}T}\right) - 1\right]^{-1}, \tag{10.11}$$

where $\mu < 0$ is the chemical potential and T is the polariton effective temperature which converges to that of the lattice in the thermodynamic limit [64]. The critical density for polariton condensation is then given by the total number of polaritons which can occupy all energy levels apart from the ground state. Considering that the sample is probed over a typical spot size r and calling $n^{\mathrm{th}}(\delta, T, \mu)$ the total polariton density, the critical density for polariton condensation is reached when the chemical potential μ vanishes. Beyond this point, each newly added particle to the system will

accumulate in the ground state. Thereby, the critical density can be derived *via* [80]:

$$n_{\mathrm{c}}^{\mathrm{th}}(\delta, T) = \lim_{\mu \to 0} n^{\mathrm{th}}(\delta, T, \mu) = \frac{1}{2\pi} \int_{k_{\parallel} > 2\pi/r} f_{\mathrm{BE}}\big(E_{\mathrm{LPB}}(k_{\parallel}), T, \mu = 0\big) k_{\parallel} dk_{\parallel}. \tag{10.12}$$

Figure 10.5(b) displays the calculated values for $n_{\mathrm{c}}^{\mathrm{th}}(\delta, T)$ over a wide range of detunings and temperatures for the investigated MC based on 67 thin GaN-QWs ($L_{\mathrm{QW}} = 1.2$ nm, $E_{\mathrm{X}}^{\mathrm{b}} \approx 48$ meV [59]) forming the active region, which theoretically allows the observation of the SCR up to ~540 K.

As already mentioned this discussion is only suitable for a perfect 2D ensemble of non-interacting bosonic particles. The non-idealities of the current system, namely the intrinsic interacting nature of polaritons and the non-equilibrium character arising from their finite lifetime, restrict its validity to regions of the phase diagram where the ratio $R(\delta, T)$ is significantly larger than unity. Since polariton condensation occurs far from thermodynamic equilibrium, it is important to keep in mind that the above-mentioned analysis can be considered as valid because a *quasi*-thermodynamic approximation is adopted.

10.2.3.2 The Kinetic Limit

The polariton relaxation kinetics, i.e., the time evolution of the occupancy number $n_{k_{\parallel}}(t)$, can be numerically solved through a semi-classical Boltzmann approach by using the following set of equations for $n_{k_{\parallel}}(t)$ for discrete values of $k_{\parallel}$:

$$\frac{\mathrm{d}n_{k_{\parallel}}}{\mathrm{d}t} = I_{k_{\parallel}} - \Gamma_{k_{\parallel}} n_{k_{\parallel}} - n_{k_{\parallel}} \sum_{k_{\parallel}} W_{k_{\parallel} \to k'_{\parallel}} (n_{k'_{\parallel}} + 1) + (n_{k_{\parallel}} + 1) \sum_{k'_{\parallel}} W_{k'_{\parallel} \to k_{\parallel}} n_{k'_{\parallel}}, \tag{10.13}$$

where $I_{k_{\parallel}}$ and $\Gamma_{k_{\parallel}}$ account for the pumping and decay rates (both of radiative and nonradiative origin) of the particles and $W_{k_{\parallel} \to k'_{\parallel}}$ is the total scattering rate between the initial state $k_{\parallel}$ and the final state $k'_{\parallel}$. The scattering rates are treated perturbatively and encompass all the interactions polaritons can undergo with their environment, namely exciton-phonon, exciton-exciton and exciton-electron interactions. Owing to strong piezoelectric effects in GaN-based systems attention has to be paid in particular to the treatment of the exciton-phonon interaction.

From the ensemble of solutions $n_{k_{\parallel}}$ various information can be deduced such as the polariton relaxation time τ_{rel}, defined as the characteristic time of the polariton temperature decay, or the critical density n_{c} for each temperature and detuning of the phase diagram accounting correctly for the system specificities *via* the total scattering rates. Note that the critical density calculated within the polariton kinetics approach is always larger compared to the ideal thermodynamic one $n_{\mathrm{c}}^{\mathrm{th}}$. However, R monotonically increases with δ and T bringing the system closer to the thermodynamic limit and the gap between $n_{\mathrm{c}}^{\mathrm{th}}$ and n_{c} can eventually vanish [61]. Finally, it is worth mentioning that the Boltzmann approach in the current form neglects the

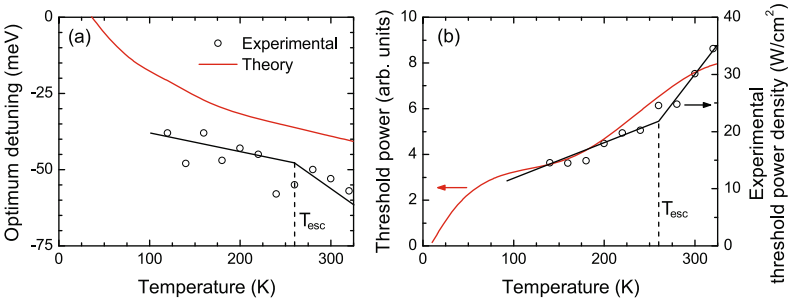

Fig. 10.7 (**a**) Optimum detuning $\delta_{opt}(T)$ as a function of the lattice temperature; (**b**) Evolution of P_{thr} at $\delta_{opt}(T)$. The *black solid lines* in (**a**) and (**b**) act as guide to the eye for the experimental values emphasizing T_{esc}. Adapted from Ref. [63]

spin state of polaritons. This approximation is expected to be correct under non-resonant excitation where the various processes of decoherence induce fast random changes of the phase of polaritons, which then nearly behave as classical particles. At and above the polariton condensation threshold, where the phase of the condensate is stabilized and amplified by the stimulated scattering process, the spin state has to be properly taken into account *via* the introduction of the two-component order parameter of the condensate (see Sect. 10.3).

10.2.4 Phase Diagram: Experimental Results vs. Theory

Figure 10.6(b) displays experimental values for the polariton condensation threshold power density for a wide range of detunings and temperatures. The accessible δ and T values are restricted by the sample geometry and the experimental setup. Nevertheless, for temperatures exceeding $\sim$100 K there is an obvious minimum of P_{thr} for a certain detuning corresponding to δ_{opt}. From there, P_{thr} increases in both directions according to the previous analysis: for $\delta < \delta_{opt}$ due to a decreased scattering efficiency and in the opposite case $\delta > \delta_{opt}$ because of a concomitant increase in n_c and thermal detrapping. Owing to the limited detuning range and the expected behavior of δ_{opt} in the low temperature range, only the kinetic regime is observable for $T < 100$ K. In summary, it can be stated that the experimental results qualitatively coincide with the predictions of the elementary theoretical discussion presented in Sect. 10.2.2.

The results of the numerical modeling introduced in Sect. 10.2.3 are confronted to the experimental values of δ_{opt} in Fig. 10.7(a). As expected from our intuitive approach δ_{opt} shifts toward more negative values with increasing temperature due to the larger weight played by thermal detrapping. The other interesting feature is that within the experimentally explored range of T and δ values (cf. Fig. 10.5(b)) the optimum detuning is always negative and especially for $T > 100$ K far from zero. This is in sharp contrast to the expected behavior for a vertical cavity surface emitting laser where the optimum situation corresponds to the maximum overlap

between the gain band and the cavity mode, i.e., for $\delta = 0$ [55], thereby highlighting the matter character of polaritons and the important role of interactions in the formation of the condensate. The position of δ_{opt}, at a given temperature, also sets the frontier between kinetics and thermodynamics and its absolute value is a characteristic of the system fixed by the relative weights of these two regimes. For instance, GaAs and CdTe-based systems are less dominated by the kinetics leading to δ_{opt} values much closer to zero compared to GaN-based MCs at low temperatures: $\delta_{\text{opt}}^{\text{GaAs}}(10\text{K}) \sim -3 \pm 1$ meV [35] and $\delta_{\text{opt}}^{\text{CdTe}}(4\text{K}) \sim 3 \pm 1$ meV [64]. However, hints for a shift toward more negative δ values with increasing temperatures due to enhanced thermodynamics is also observed in these two systems [35, 64]. Note that the discrepancy between experiments and theory seen in Fig. 10.7(a) is likely arising from the fact that the semiclassical Boltzmann approach is only accurate in the low density regime where renormalization effects of the LPB are negligible. Owing to the important impact of interactions and saturation on the LPB dispersion in GaN-based MCs [62], the currently applied modeling approach is restricted to a qualitative rather than a quantitative agreement with the experimental phase diagram.

10.3 Polarization Properties of III-Nitride Based MCs

10.3.1 Representation of the Polariton Spin State

Cavity polaritons result from the coupling between heavy- (hh) or light-hole (lh) excitons and a cavity photon.[4] Thereby, the exciton total angular momentum along the growth direction z consists of that of the electron $J_z^{\text{e}} = \pm\frac{1}{2}$ and that of the hole: $J_z^{\text{lh}} = \pm\frac{1}{2}$ or $J_z^{\text{hh}} = \pm\frac{3}{2}$, respectively. Consequently, the resulting spin projection reads $J_z^{\text{X}} \in \{\pm 1, \pm 2\}$ for hh-excitons and $J_z^{\text{X}} \in \{0, \pm 1\}$ for lh ones. As the photon carries a momentum $J_z^{\text{C}} = 1$ (right-circular polarized, σ^+) or $J_z^{\text{C}} = -1$ (left-circular polarized, σ^-), coupling of excitonic states with $J_z^{\text{X}} = 0$ and $J_z^{\text{X}} = \pm 2$ to the photonic mode is forbidden by spin selection rules. They are thus called *dark excitons*.

Referring to QW excitons, the dominant free-carrier relaxation channel is given by the Bir-Aronov-Pikus mechanism, which exclusively involves transitions between optically active states ensuring that the contribution of dark excitons for carrier relaxation can be neglected [82]. As there are only two possible spin projections, polaritons form a classical two-level system[5] whose spinor wavefunction $|\psi\rangle$ is expressed in the basis $\{|\psi_\downarrow\rangle, |\psi_\uparrow\rangle\}$ corresponding to the total angular momentum $J_z = -1$ and $+1$, respectively. Despite this natural geometric representation of $|\psi\rangle$ in the Bloch sphere, it is convenient to make use of the one-to-one correspondence

[4] This simple picture is valid for zincblende semiconductors such as GaAs or CdTe. In wurtzite compounds, the crystal-field and spin-orbit splitting lift the valence-band degeneracy at the Γ point: the A-exciton is equivalent to the heavy hole but B and C are mixed [81].

[5] This discussion is generally valid for any in-plane momentum $k_\parallel$. However, throughout the following discussion we only consider the pseudospin of the condensate.

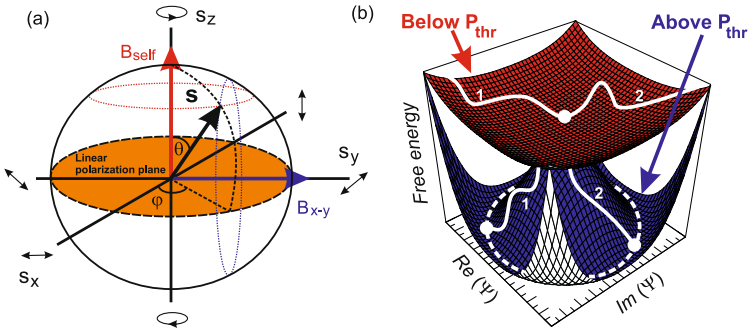

Fig. 10.8 In the Poincaré sphere, the pseudospin vector **S** describes the spin state of the polariton. The equatorial plane corresponds to a linear polarization while the poles correspond to circular polarization of the emitted light. B_{x-y} and B_{self} are the effective magnetic fields created by the static disorder splitting $\Delta E_{\text{x}-\text{y}}$ and polariton-polariton interactions ΔE_{self}, respectively. (**b**) Schematic representation of the polariton free energy as a function of the real and imaginary parts of the polariton wavefunction x_1 and x_2, respectively. Below threshold, the symmetric solution $\psi = 0$ is stable while above threshold, it spontaneously acquires a different phase for different realizations of the condensate (e.g., paths 1 and 2)

between the polarization of the emitted photons and the components of $|\psi\rangle$ to directly relate the polariton pseudospin **S**, which is a complex vector describing the quantum state of this 2-level system, to the Stokes-vector parameters [83, 84]. Thus, the linear (ρ_{l}), diagonal (ρ_{d}) and circular (ρ_{c}) polarization degrees of the emitted light and the polariton pseudospin components $S_{\text{x,y,z}}$ are directly linked *via* the relations $\rho_{\text{l,c,d}} = 2S_{\text{x,y,z}}/N$ where N denotes the occupancy number of the polariton condensate. As a consequence, the pseudospin **S** can be represented in the *Poincaré sphere* (cf. Fig. 10.8(a)) and is directly obtained from the polariton wavefunction components *via* the relations:

$$\begin{aligned} S_{\text{x}} &= \frac{1}{2}\left(\psi_{\downarrow}^{*}\psi_{\uparrow} + \psi_{\uparrow}^{*}\psi_{\downarrow}\right), \\ S_{\text{y}} &= \frac{i}{2}\left(\psi_{\downarrow}^{*}\psi_{\uparrow} - \psi_{\uparrow}^{*}\psi_{\downarrow}\right), \\ S_{\text{z}} &= \frac{1}{2}\left(|\psi_{\uparrow}|^{2} - |\psi_{\downarrow}|^{2}\right). \end{aligned} \tag{10.14}$$

Note finally that the norm of the pseudovector $|\mathbf{S}|$ is related to the degree of spin coherence: If $|\mathbf{S}|/2N < 1$ the polarization state contains a certain degree of incoherence whose limit $|\mathbf{S}| \to 0$ corresponds to a fully incoherent system, exhibiting totally unpolarized emitted light.

10.3.2 Spontaneous Symmetry Breaking and Polariton BEC

In a thermodynamic phase transition an order parameter x can be defined whose value is zero below the transition point, i.e., the condensation threshold, and acquires

a finite value above. In the Landau functional theory—providing a phenomenological description of the phase transition—the system free energy F is expanded in powers of the order parameter, which is small close to the transition point:

$$F[x] = F_0 + F_1 x + F_2 x^2 + F_3 x^3 + F_4 x^4 + O\left(x^5\right), \tag{10.15}$$

where F_0 can be ignored as it has no influence on the treatment and F_1 and F_3 vanish due to symmetry arguments. For a given temperature the value of x is determined by minimizing $F[x]$. Owing to the spinor nature of the order parameter for exciton-polaritons physically associated with the macroscopic wavefunction of the polariton condensate ψ, x has the form $\mathbf{x} = \{x_1, x_2\} = \{\mathrm{Re}(\psi), \mathrm{Im}(\psi)\}$ [85]. Once the expression of F is known, the state of the polariton condensate is defined by the minimum of $F[\psi]$. The situation is illustrated in Fig. 10.8(b). At the transition point the symmetric solution $x = 0$ is no longer stable and the whole system chooses a certain phase spontaneously. This remarkable effect is referred to as *spontaneous symmetry breaking*.

On the basis of in-plane translation invariance and 2D-character of cavity-polaritons, it is convenient to express the free energy in the MC (x, y)-plane with $\psi_{\downarrow,\uparrow} = \frac{1}{\sqrt{2}}(\psi_x \pm i\psi_y)$. The free energy then reads [68]:

$$F[S_z, N] = -\mu N + \frac{1}{4}(\alpha_1 + \alpha_2)N^2 + (\alpha_1 - \alpha_2)S_z^2, \tag{10.16}$$

where the occupancy number of the polaritons in the condensate is given by $N = \psi \cdot \psi^* = |\psi_x|^2 + |\psi_y|^2 = 4S^2$ (with $S^2 = S_x^2 + S_y^2 + S_z^2$). The non-linear terms in F account for the polariton-polariton interactions including a repulsion of polaritons with the same spin ($\alpha_1 > 0$) and a weak attraction of polaritons with opposite spins ($\alpha_2 < 0$). This spin anisotropy arises from the dominant role of the exchange term in the polariton-polariton interaction [86]. The chemical potential μ, i.e., the energy needed to add a particle in the system, is fixed by the imbalance between the escape rate $W_{\mathrm{out}} \sim 1/\tau_{\mathrm{pol}}(0)$ of polaritons limited by their short radiative lifetime and the income rate W_{in} into the condensate from the higher energy states. In this framework, μ is simply given by the minimum of the free energy with respect to N, which leads to:

$$\mu = \frac{(\alpha_1 + \alpha_2)}{2} N. \tag{10.17}$$

This expression shows that the injection-dependent blueshift observed in photoluminescence (PL) experiments depends on the interaction constants and allows an estimation of N above threshold. Similarly, minimization of F with respect to S_z leads to the polarization state at condensation threshold $S_z = 0$, i.e., the pseudospin $\mathbf{S}$ of the light emitted by the condensate lies in the equatorial plane of the Poincaré sphere, which corresponds to linearly polarized light. Note that the minimum of F is not unique and each realization of the condensate should result in a randomly-oriented linearly polarized state (see Fig. 10.8(b)). Thus, a true BEC requires the build-up of the order parameter which in turn can be considered as a necessary condition [60, 87].

Note that the presence of optical in-plane anisotropy of the cavity mode and/or the exciton will cancel the observation of spontaneous symmetry breaking. In this case F contains an extra term $-\Delta E_{\mathrm{x-y}} S_{\mathrm{x}}$, where $\Delta E_{\mathrm{x-y}}$ is the energy splitting between the two in-plane polarizations x and y [88]. Without loss of generality the lowest energy is assumed to lie along the x-axis in the following. In this case, the minimum of F is reached for $S_{\mathrm{y}} = S_{\mathrm{z}} = 0$. As a consequence, in the presence of optical anisotropy the order parameter is pinned to the x-direction and the same polarization is adopted by the condensate for each experimental realization. However, these considerations are only valid in the thermodynamic limit. Even if this situation is hardly realized in a polariton condensate, this thermodynamic approach gives a qualitative trend, at least in the region of the phase diagram where $R(\delta, T) > 1$. For this reason the measurements presented hereafter are performed at RT, i.e., at a temperature where quasi-thermal equilibrium is reached [89].

10.3.3 Polarization Behavior in III-Nitride-Based Microcavities

The formation dynamics of polariton condensates is still subject to intensive research. A deeper understanding of the build-up and the evolution of the condensate order parameter is thus of major interest. Due to the efficient polariton relaxation and the possibility of performing measurements at high temperatures, III-nitride based MCs appear as the system of choice to probe polariton condensation close to the thermodynamic limit. In the experiments presented below the structure already investigated in Sect. 10.2.2 is pumped non-resonantly ($\sim$1 eV above the condensate emission energy) in order to guarantee the memory loss of the laser polarization. Time-integrated polarization-resolved PL measurements are performed at RT under quasi-cw excitation ($\tau_{\mathrm{pulse}} = 500$ ps, repetition rate 8.52 kHz) and give access to the average linear polarization degree $\langle \rho_{\mathrm{l}} \rangle$ of the emitted light. The laser beam was focused down to a 50 μm diameter spot on a sample region and a power density range where the emission spectrum was unaltered by competing modes. Contrary to the bulk case, where the build-up of a stochastic linear polarization was observed at RT [60], the current GaN QW-based MC presents a pinning of the order parameter at threshold: $\langle \rho_{\mathrm{l}} \rangle$ does not average to zero. This pinning is commonly observed in all QW-based MCs investigated so far, i.e., in CdTe [3], GaAs [34] and GaN ones ([19] and Fig. 10.9(f)), and originates from the optical in-plane anisotropy $\Delta E_{\mathrm{x-y}}$ at zero in-plane momentum, $k_{\parallel} = 0$, of either the excitonic or the photonic component, or from both of them assuming a linear dependence on the excitonic and photonic fractions:

$$\Delta E_{\mathrm{x-y}} = |X_0|^2 \Delta E^{\mathrm{X}}_{\mathrm{x-y}} + |C_0|^2 \Delta E^{\mathrm{C}}_{\mathrm{x-y}}. \tag{10.18}$$

Since all the above-mentioned material systems are expected to exhibit isotropic optical properties,[6] $\Delta E^{\mathrm{X}}_{\mathrm{x-y}}$ likely originates from structural non-idealities such as

[6]Note that GaN is a uniaxial anisotropic material. However, for the c-plane structure investigated here the optical axis coincides with the surface normal and therefore no in-plane anisotropy is expected.

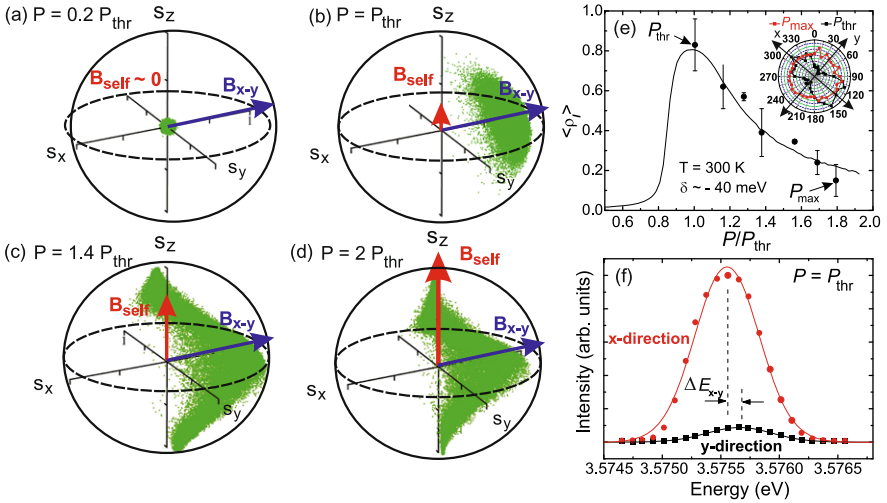

Fig. 10.9 All the figures correspond to room temperature conditions with a detuning of −40 meV. (**a**)–(**d**) Time-integrated simulation of the pseudospin components for different pumping regimes, equal to 0.2, 1, 1.4 and $2P/P_{\mathrm{thr}}$, respectively. The increasing role of the self-induced Larmor precession is indicated by the effective magnetic field B_{self} and that of the static influence of pinning by $B_{\mathrm{x-y}}$. (**e**) Evolution of the average linear polarization degree $\langle \rho_{\mathrm{l}} \rangle$ as a function of P/P_{thr}. The inset represents polar plots for the minimum (*black squares*) and the maximum power regimes (*red squares*). (**f**) Emission spectra at $P = P_{\mathrm{thr}}$ for the two orthogonal emission directions, corresponding to x- (*red circles*) and y-polarizations (*black squares*). Adapted from Ref. [89]

a reduced symmetry of the QWs (in or out of plane) as the exciton ground state splitting is forbidden in a perfectly symmetric QW [90]. Indeed, due to the vicinal growth of the III-nitride based MC on sapphire substrates with a slight miscut, the in-plane crystalline directions are not completely equivalent possibly resulting in a x–y splitting of the excitonic state. In polar QW-based MCs, the presence of a built-in electric field enhances this effect as it separates electrons and holes toward opposite sides of the QW, making the exciton more sensitive to interface and alloy disorder [91]. Note that $\Delta E^{\mathrm{C}}_{\mathrm{x-y}}$ is non-zero only if at least one of the MC building blocks exhibits some birefringence. However so far no experimental evidence allowed to firmly assess the origin of the mechanism involved in the pinning of the order parameter. The role of $\Delta E_{\mathrm{x-y}}$ on the polariton population is important since it acts as an effective magnetic field $\mathbf{B}_{\mathrm{x-y}}$ in the plane of the structure around which the pseudospin $\mathbf{S}$ can precess [84] (cf. Fig. 10.8(a)). Under resonant pumping, $\Delta E_{\mathrm{x-y}}$ can lead to time beats between circular-polarized components of the photoemission [92], or to a conversion between linear and circular light polarization [27]. However, in the non-resonant injection scheme, the polariton condensate is formed spontaneously and $\Delta E_{\mathrm{x-y}}$ causes the pinning of the order parameter as expected from the thermodynamic picture, where the energy relaxation brings the system to its lowest energy state which is a linearly polarized one. For the present GaN-based MC the ideal thermodynamic picture does not hold above the polariton condensation

threshold, where a rapid decrease in $\langle \rho_{\mathrm{l}} \rangle$ with injected carrier density is observed (cf. Fig. 10.9(e)). This behavior deviates from the one observed in CdTe-based MCs at low temperatures [88]. In this latter case, a fast increase in $\langle \rho_{\mathrm{l}} \rangle$ is followed by a saturation with no evidence of a decrease up to $5P_{\mathrm{thr}}$. Thus, for a reasonable description of the depinning behavior the stochastic formation of the polariton condensate in the time-domain has to be considered, while accounting for the relative weights of two antagonistic effects: the in-plane static polarization anisotropy that pins the order parameter and the spin dependent polariton-polariton interactions that tend to destroy it as demonstrated hereafter. The polarization behavior of the polariton condensate and its formation is described using a stochastic approach accounting for the spinor nature or the order parameter $\psi_\sigma(t)$ with $\sigma \in \{\downarrow, \uparrow\}$ [87]. An important role is played by the incoming flux of polaritons from the incoherent reservoir with random phases and polarizations, which is responsible for the stochastic nature of the condensate formation. The order parameter thus evolves following the Langevin-type equation [87]:

$$\frac{d\psi_\sigma}{dt} = \frac{1}{2}\big[W_{\mathrm{in}}(t) - W_{\mathrm{out}}(t)\big]\psi_\sigma + \frac{1}{2}\left[\gamma + \frac{i}{\hbar}\Delta E_{\mathrm{x-y}}\right]\psi_{-\sigma} - \frac{i}{\hbar}\big[\alpha_1|\psi_\sigma|^2 + \alpha_2|\psi_{-\sigma}|^2\big]\psi_\sigma + \theta_\sigma(t). \tag{10.19}$$

This equation consists of four terms: The first one describes the evolution of the order parameter due to a changing polariton condensate population, which is caused by the imbalance between the income rate from the reservoir $W_{\mathrm{in}}(t)$ and the depletion rate of polaritons at the Brillouin zone center $W_{\mathrm{out}}(t) \sim 1/\tau_{\mathrm{pol}}(0)$, which is set by the short radiative lifetime. $W_{\mathrm{in}}(t)$ is usually obtained by solving (10.13) for a two-level system formed by the condensate and the incoherent reservoir. The second term accounts for the spin relaxation rate $\gamma \gg W_{\mathrm{out}}$ and the in-plane polarization splitting $\Delta E_{\mathrm{x-y}}$ that is responsible for the pinning of the order parameter. The third term includes the effect of the anisotropic polariton-polariton interactions between polaritons with parallel ($\alpha_1 > 0$) and antiparallel spin orientations ($\alpha_2 < 0$). Its impact rises when the carrier density increases. The last term $\theta_\sigma(t)$ accounts for the shot noise originating from spontaneous scattering of polaritons out of the incoherent excitonic reservoir into the polariton condensate. It is a complex function with correlators $\langle \theta_\sigma(t)\theta_{\sigma'}(t')\rangle = 0$ and $\langle \theta_\sigma(t)\theta^*_{\sigma'}(t')\rangle = \frac{1}{2}W_{\mathrm{in}}(t)\delta_{\sigma\sigma'}\delta(t-t')$. The description of the noise is the central point in the stochastic description of the formation dynamics as it is responsible for the fluctuations of phase and polarization in the condensate. It depends on the pumping regime *via* the polariton income rate.

Formally, without $\theta_\sigma(t)$ and without the pinning term $\Delta E_{\mathrm{x-y}}$, (10.19) is perfectly isotropic and cannot explain the build-up of any preferential polarization. Due to spontaneous scattering modeled by the noise term, some random polarization appears that quickly vanishes below P_{thr} but is amplified above it due to the onset of stimulated scattering. Without energy relaxation pinning is inhibited since $\mathbf{S}$ would just precess around the effective in-plane magnetic field $\mathbf{B}_{\mathrm{x-y}}$ (cf. Fig. 10.8) and any polarization would occur with the same probability. Taking into account energy relaxation the system shifts toward the minimum of free energy resulting in

a linearly-polarized state with random orientation. This behavior has been observed in the experiments of Baumberg et al. on a bulk GaN MC [60]. The polarization is large for each experimental realization but as it has no preferential orientation, it averages to zero over many pulses. In the presence of a $\Delta E_{\mathrm{x-y}}$ value distinct from zero but without interactions (i.e., when the third term in (10.19) is set to zero), the lowest energy state would always be pinned along the same direction corresponding to that of $\mathbf{B}_{\mathrm{x-y}}$ (x-polarized in our case).

The role of interactions is of paramount importance as their contribution to the order parameter evolution increases together with the pump power density. As already mentioned the interactions between polaritons with equal and opposite spin are not equivalent. In the mean-field approximation the anisotropic interaction term reduces to an equation of precession of $\mathbf{S}$ along an effective magnetic field $\mathbf{B}_{\mathrm{self}}$ oriented in the z-direction with an absolute value given by [68]:

$$B_{\mathrm{self}} \propto (\alpha_1 - \alpha_2)(N_\downarrow - N_\uparrow), \tag{10.20}$$

where $(N_\downarrow - N_\uparrow)$ represents the population imbalance between the polariton populations with spin up and down. In the case of a spin-isotropic interaction, i.e., $\alpha_1 = \alpha_2$, B_{self} vanishes. Similarly, in the case where populations with opposite spins are balanced, B_{self} is also reduced to zero. This corresponds to the general case when θ_σ is neglected in (10.19) emphasizing the important role of statistical fluctuations in the process of the polariton condensate formation. Thus, the polariton ensemble experiences the contribution of two magnetic fields: one caused by the static disorder $\mathbf{B}_{\mathrm{x-y}}$ being completely power independent and that of $\mathbf{B}_{\mathrm{self}}$, which strongly depends on the injection regime. $\mathbf{B}_{\mathrm{self}}$ is responsible for the precession of the polariton pseudospin around the z-axis and tends to lift any asymmetry in the equatorial plane of the Poincaré sphere. This effect is referred to as self-induced Larmor precession [93, 94]. As a consequence, in the presence of interactions but without pinning, the phase of each condensate realization would exhibit a random polarization, so that $\langle \rho_{\mathrm{l}} \rangle$ would average to zero as for the bulk case. With $\Delta E_{\mathrm{x-y}} \neq 0$ both pinning and interactions compete with each other and the polarization degree continuously changes when the pump increases: the higher the injection the stronger the effect of depolarization due to the pseudospin precession.

Polarization-resolved PL studies allow to probe the components of the Stokes vector, which is directly related to the condensate pseudospin $\mathbf{S}$. The polarization degree of the emitted light can be traced out time-dependently [95] with high experimental effort. However, in the present case, it is integrated over several experimental realizations of the condensate (pulsed excitation in the quasi-cw regime, ~200 realizations per measurement). For a given realization, i.e., one specific value of $\theta_\sigma(t)$, the observed polarization corresponds to the normalized time-integrated components s_{i} with $i \in \{x, y, z\}$:

$$s_{\mathrm{i}} = \frac{\int S_{\mathrm{i}}(t)dt}{\int |\mathbf{S}(t)|dt} = 2\frac{\int S_{\mathrm{i}}(t)dt}{\int n(t)dt}, \tag{10.21}$$

where $n(t)$ is the instantaneous condensate occupancy number and the time-integration is performed over the whole condensate lifetime. The obtained value

of s_i gives precious information about the order parameter ψ as the role of the fluctuations is directly reflected by the build-up of the linear polarization degree. As the experimental data displayed in Fig. 10.9(e) represent an average over multiple pulses, it is necessary to average s_i over many realizations of the noise term $\theta_\sigma(t)$. This procedure is repeated for each pump power density of the investigated experimental range between 0 and 2 P_{thr} and the obtained normalized pseudospin values are reported in the Poincaré sphere illustrated in Figs. 10.9(a)–10.9(d) [89]. After this averaging procedure, it turns out that $\langle s_y \rangle \sim \langle s_z \rangle \sim 0$, which is consistent with the system symmetry, so that the only remaining contribution comes from $\langle s_x \rangle$. Thus, the experimentally determined degree of linear polarization $\langle \rho_l \rangle$ directly corresponds to $2 \cdot \langle s_x \rangle$. In Figs. 10.9(a)–10.9(d) four representative situations are displayed corresponding to:

- $P \ll P_{thr}$: Far below threshold, when the condensate occupation is low, the effect of pinning is not pronounced. ψ corresponds to an incoherent state and $\langle \rho_l \rangle = 0$.
- $P = P_{thr}$: At threshold, the condensate formation is fully dominated by the effect of static disorder and $\langle \rho_l \rangle$ is maximum.
- $P_{thr} < P < P_{max}$: Both pinning and self-induced Larmor precession compete to be the dominant effect. The resulting $\langle \rho_l \rangle$ is decreased with respect to the threshold case.
- $P = P_{max}$: For the highest injection regime the Larmor precession sets the tone and lifts any remaining asymmetry in the equatorial plane leading to a value of $\langle \rho_l \rangle$ approaching zero.

In conclusion, the progressive depinning observed experimentally is well described by the competition between the static disorder anisotropy, which dominates in the low density regime, and the Larmor precession at high excitation density, which successively breaks up the degree of linear polarization [89]. The efficiency of the pinning at threshold depends on δ in a non-monotonous way. Intuitively, one would expect that the pinning follows the behavior of (10.18), meaning that depending on the polariton character (light or matter-like), $\langle \rho_l \rangle$ reproduces the behavior of ΔE_{x-y} that changes with δ according to the excitonic and photonic fraction of the $k_\parallel = 0$ state. Experimentally, the situation looks more intricate and a minimum of $\langle \rho_l \rangle$ is observed at $\delta \sim -60$ meV (cf. Fig. 10.10). This peculiar feature can be qualitatively understood from the present model by comparing the evolution of $\langle \rho_l \rangle$ as a function of δ to that of the phase diagram, i.e., the evolution of $P_{thr}(\delta, T = 300\ \text{K})$ (cf. Fig. 10.10). What matters in the present theoretical description is the timescale of polariton relaxation from the reservoir to the condensate. As detailed in Sect. 10.2, both T and δ govern P_{thr}, an effect directly related to τ_{rel}. In the optimum case $\delta = \delta_{opt}$ the condensate builds-up quickly and the polariton relaxation time is short ($R = \tau_{pol}/\tau_{rel} = 1$) implying that there is no time for polaritons to relax to the lowest energy state, which would be linearly polarized. This results in an apparent decrease in $\langle \rho_l \rangle$ at $\delta = \delta_{opt}$.

The fact that the build-up of $\langle \rho_l \rangle$ is limited by the kinetics comes from the short lifetime of polaritons in GaN owing to the moderate Q-factor of the presently available samples ($Q \sim 1000$, cf. Fig. 10.4(b)). Thus, the difference between GaN [89]

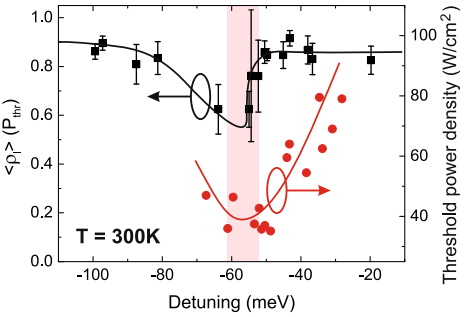

Fig. 10.10 Evolution of the average linear polarization degree $\langle \rho_l \rangle$ at the condensation threshold power density P_{thr} (*left axis*) and P_{thr} (*right axis*) as a function of δ at RT. The coincidence of the minima highlights the role of the relaxation dynamics in the polariton condensate formation. The *continuous lines* are guide to the eye. Adapted from Ref. [89]

and CdTe-based MCs [88] can be explained by the difference between $\langle \tau_{\text{pol}}^{\text{CdTe}} \rangle$ and $\langle \tau_{\text{pol}}^{\text{GaN}} \rangle$. In CdTe-base MCs any imbalance between circular polarization components is hardly achieved due to polariton interactions within the long cavity lifetime preventing the occurrence of self-induced Larmor precession. Hence, the free energy approaches its minimum and the polarization vector of the condensate lies in the equatorial plane of the Poincaré sphere along the preferential crystal direction.

10.4 Conclusion and Perspectives

In this chapter we highlighted that properly designed III-nitride QW based planar microcavities have been instrumental in bringing cavity polariton nonlinearities observed under incoherent excitation up to room temperature. Such samples clearly expand the opportunity to study the quantum phase-transition of interacting bosonic quasi-particles toward a condensate over a wide temperature range (here from 4 to 340 K) thanks to the large exciton binding energy and oscillator strength allowing for the formation of robust cavity polaritons. It turned out that the condensation threshold is governed by the interplay between the polariton lifetime (primarily governed by the cavity photon lifetime) and their relaxation efficiency toward the ground state, namely the very bottom of the lower polariton trap formed in $k_{\parallel}$-space. Both timescales critically depend on the light-matter content of polaritons at play. Thus for large negative detuning values condensation of polaritons can be hindered owing to their low excitonic fraction, which implies an inefficient carrier relaxation rate and a short lifetime—a limitation set by the carrier kinetics. On the other hand, for polaritons with a higher excitonic fraction their increased effective mass leads to a larger critical density for condensation and to an increasing role of thermal detrapping effects with rising temperatures—here carrier thermodynamics will govern the condensation threshold. Hence, when the timescales of polariton lifetime and relaxation time become similar there is an optimum detuning δ_{opt} for which the

condensation threshold power density is minimized. Contrary to the case of conventional lasers δ_{opt} is found to be negative, a feature that can be unambiguously ascribed to the admixed light-matter nature of cavity polaritons.

Furthermore, the investigation of the polarization properties of the emitted light as a function of carrier injection above the condensation threshold allowed gaining a deeper insight into the condensate formation, a process which is still the object of an intense research. Contrary to the bulk GaN MC case [60], the anisotropy induced by the static disorder potential in multiple QW-based GaN MCs pins the condensate order parameter at threshold. With increasing injection this effect competes with the self-induced Larmor-precession triggered by the stochastic nature of the condensate formation process and the anisotropic polariton interaction constants, which finally results in a depinning of the order parameter.

III-nitride compounds clearly demonstrate that they are not exclusively suitable for optoelectronic applications, where they dominate the semiconductor market nowadays, but also for studying light-matter coupling phenomena based on cavity-polaritons at room temperature. The ambient condition stability of such condensates should thus offer unprecedented opportunities to probe superfluidity-related properties at temperatures otherwise not accessible to the GaAs- and CdTe-based systems. In other words, exotic features of the quantum world should be made readily accessible in a condensed-matter system without the need for cooling. It would encompass various quantum hydrodynamic effects like the observation of quantized vortices, two-fluid hydrodynamics or solitary waves [6]. On a more prosaic level the demonstration of an electrically-injected polariton laser operating under ambient conditions appears as the next logical step. This would correspond to the realization of a room temperature operating quantum device based on interacting bosonic quasiparticles! Although this target might look quite close temporally some effort has still to be brought. The most promising design includes InGaN/GaN quantum wells [96], which are well suited for electrical injection and commonly exhibit high quantum efficiency. However, the latter are subject to a large disorder-induced inhomogeneous broadening, which could potentially prevent the strong coupling regime to take place. Finally note also that thanks to the recent progress made in the substrate fabrication and their expected better efficiency non-polar III-nitride heterostructures currently attract a lot of attention. Thus it is worth mentioning that strong coupling and polariton lasing have been recently demonstrated in an *m*-plane GaN-based microcavity [97, 98].

Acknowledgements G. Malpuech and D. Solnyshkov on the one hand and A.V. Kavokin, D. Read and Y.G. Rubo on the other hand are gratefully acknowledged for their respective theoretical investigation of the condensation phase diagram and the polarization properties of polariton condensates in III-nitride microcavities. The authors further wish to thank M. Glauser for careful proofreading. This work was supported by the NCCR Quantum Photonics, research instrument of the Swiss National Science Foundation (SNSF), by the SNSF (Grant No. 200020-113542) and by the EU-project Clermont4 (Grant No. FP7-235114).

References

1. C. Weisbuch, M. Nishioka, A. Ishikawa, Y. Arakawa, Phys. Rev. Lett. **69**, 3314 (1992)
2. A. Imamoğlu, R.J. Ram, S. Pau, Y. Yamamoto, Phys. Rev. A **53**, 4250 (1996)
3. J. Kasprzak, M. Richard, S. Kundermann, A. Baas, P. Jeambrun, J.M.J. Keeling, F.M. Marchetti, M.H. Szymanska, R. André, J.L. Staehli, V. Savona, P.B. Littlewood, B. Deveaud-Plédran, L.S. Dang, Nature (London) **443**, 409 (2008)
4. K.G. Lagoudakis, M. Wouters, M. Richard, A. Baas, I. Carusotto, R. André, L.S. Dang, B. Deveaud-Plédran, Nat. Phys. **4**, 706 (2008)
5. K.G. Lagoudakis, T. Ostatnický, A.V. Kavokin, Y.G. Rubo, R. André, B. Deveaud-Plédran, Science **326**, 5955 (2009)
6. A. Amo, D. Sanvitto, F.P. Laussy, D. Ballarini, E. del Valle, M.D. Martin, A. Lemaître, J. Bloch, D.N. Krizhanovskii, M.S. Skolnick, C. Tejedor, L. Viña, Nature (London) **457**, 291 (2008)
7. A. Amo, J. Lefrère, S. Pigeon, C. Adrados, C. Ciuti, I. Carusotto, R. Houdré, E. Giacobino, A. Bramati, Nat. Phys. **5**, 805 (2009)
8. S. Utsunomiya, L. Tian, G. Roumpos, C.W. Lai, N. Kumada, T. Fujisawa, M. Kuwata-Gonokami, A. Löffler, S. Höfling, A. Forchel, Y. Yamamoto, Nat. Phys. **4**, 700 (2008)
9. A. Amo, S. Pigeon, D. Sanvitto, V.G. Sala, R. Hivet, I. Carusotto, F. Pisanello, G. Leménager, R. Houdré, E. Giacobino, C. Ciuti, A. Bramati, Science **332**, 1167 (2011)
10. S. Savasta, O.D. Stefano, V. Savona, W. Langbein, Phys. Rev. Lett. **94**, 246401 (2005)
11. H. Oka, H. Ishihara, Phys. Rev. Lett. **100**, 170505 (2008)
12. R.M. Stevenson, V.N. Astratov, M.S. Skolnick, D.M. Whittaker, E. Emam-Ismail, A.I. Tartakovskii, P.G. Savvidis, J.J. Baumberg, J.S. Roberts, Phys. Rev. Lett. **85**, 3680 (2000)
13. P.G. Savvidis, J.J. Baumberg, R.M. Stevenson, M.S. Skolnick, D.M. Whittaker, J.S. Roberts, Phys. Rev. Lett. **84**, 1547 (2000)
14. M. Saba, C. Ciuti, J. Bloch, V. Thierry-Mieg, R. André, L.S. Dang, S. Kundermann, A. Mura, G. Bongiovanni, J.L. Staehli, B. Deveaud-Plédran, Nature (London) **414**, 731 (2001)
15. A.V. Kavokin, G. Malpuech, M. Glazov, Phys. Rev. Lett. **95**, 136601 (2005)
16. C. Leyder, M. Romanelli, J.P. Karr, E. Giacobino, T.C.H. Liew, M.M. Glazov, A.V. Kavokin, G. Malpuech, A. Bramati, Nat. Phys. **3**, 628 (2007)
17. L.S. Dang, D. Heger, R. André, F. Boeuf, R. Romestain, Phys. Rev. Lett. **81**, 3920 (1998)
18. S. Christopoulos, G.B.H. von Högersthal, A.J.D. Grundy, P.G. Lagoudakis, A.V. Kavokin, J.J. Baumberg, G. Christmann, R. Butté, E. Feltin, J.F. Carlin, N. Grandjean, Phys. Rev. Lett. **98**, 126405 (2007)
19. G. Christmann, R. Butté, E. Feltin, J.F. Carlin, N. Grandjean, Appl. Phys. Lett. **93**, 051102 (2008)
20. S. Kéna-Cohen, S.R. Forrest, Nat. Photonics **4**, 371 (2010)
21. I.A. Shelykh, G. Pavlovic, D.D. Solnyshkov, G. Malpuech, Phys. Rev. Lett. **102**, 046407 (2009)
22. L. Gu, H. Huang, Z. Gan, Phys. Rev. B **84**, 075402 (2011)
23. F.P. Laussy, A.V. Kavokin, I.A. Shelykh, Phys. Rev. Lett. **104**, 106402 (2010)
24. C. Leyder, T.C.H. Liew, A.V. Kavokin, I.A. Shelykh, M. Romanelli, J.P. Karr, E. Giacobino, A. Bramati, Phys. Rev. Lett. **99**, 196402 (2007)
25. I.A. Shelykh, A.V. Kavokin, Y.G. Rubo, T.C.H. Liew, G. Malpuech, Semicond. Sci. Technol. **25**, 013001 (2009)
26. T.K. Paraïso, M. Wouters, Y. Léger, F. Morier-Genoud, B. Deveaud-Plédran, Nat. Mater. **9**, 655 (2010)
27. I. Shelykh, K.V. Kavokin, A.V. Kavokin, G. Malpuech, P. Bigenwald, H. Deng, G. Weihs, Y. Yamamoto, Phys. Rev. B **70**, 035320 (2004)
28. A. Amo, T.C.H. Liew, C. Adrados, R. Houdré, E. Giacobino, A.V. Kavokin, A. Bramati, Nat. Photonics **4**, 361 (2010)
29. T.C.H. Liew, A.V. Kavokin, I.A. Shelykh, Phys. Rev. Lett. **101**, 016402 (2008)

30. K.V. Kavokin, M.A. Kaliteevski, R.A. Abram, A.V. Kavokin, S. Sharkova, I.A. Shelykh, Appl. Phys. Lett. **97**, 201111 (2010)
31. D. Bajoni, E. Semenova, A. Lemaître, S. Bouchoule, E. Wertz, P. Senellart, S. Barbay, R. Kuszelewicz, J. Bloch, Phys. Rev. Lett. **101**, 266402 (2008)
32. J. Robertson, Eur. Phys. J. Appl. Phys. **28**, 265 (2004)
33. G. Bastard, E.E. Mendez, L.L. Chang, L. Esaki, Phys. Rev. B **26**, 1974 (1982)
34. R. Balili, V. Hartwell, D. Snoke, L. Pfeiffer, K. West, Science **316**, 1007 (2007)
35. E. Wertz, L. Ferrier, D.D. Solnyshkov, P. Senellart, D. Bajoni, A. Miard, A. Lemaître, G. Malpuech, J. Bloch, Appl. Phys. Lett. **95**, 051108 (2009)
36. T. Guillet, M. Mexis, J. Levrat, G. Rossbach, C. Brimont, T. Bretagnon, B. Gil, R. Butté, N. Grandjean, L. Orosz, F. Réveret, J. Leymarie, J. Zúniga-Pérez, M. Leroux, F. Semond, S. Bouchoule, Appl. Phys. Lett. **99**, 161104 (2011)
37. K. Kornitzer, T. Ebner, K. Thonke, R. Sauer, C. Kirchner, V. Schwegler, M. Kamp, M. Leszczynski, I. Grzegory, S. Porowski, Phys. Rev. B **60**, 1471 (1999)
38. E.O. Kane, Phys. Rev. B **18**, 6849 (1978)
39. M. Zamfirescu, A. Kavokin, B. Gil, G. Malpuech, M. Kaliteevski, Phys. Rev. B **65**, 161205 (2002)
40. R. Shimada, J. Xie, V. Avrutin, U. Özgür, H. Morkoç, Appl. Phys. Lett. **92**, 011127 (2008)
41. J.R. Chen, T.C. Lu, Y.C. Wu, S.C. Lin, W.R. Liu, W.F. Hsieh, C.C. Kuo, C.C. Lee, Appl. Phys. Lett. **94**, 061103 (2009)
42. R. Schmidt-Grund, B. Rheinländer, C. Czekalla, G. Benndorf, H. Hochmuth, M. Lorenz, M. Grundmann, Appl. Phys. B **93**, 331 (2008)
43. M. Nakayama, S. Komura, T. Kawase, D. Kim, J. Phys. Soc. Jpn. **77**, 093705 (2008)
44. A. Trichet, L. Sun, G. Pavlovic, N.A. Gippius, G. Malpuech, W. Xie, Z. Chen, M. Richard, L.S. Dang, Phys. Rev. B **83**, 041302(R) (2011)
45. C. Sturm, H. Hilmer, R. Schmidt-Grund, M. Grundmann, New J. Phys. **11**, 073044 (2009)
46. J. Frenkel, Phys. Rev. **37**, 17 (1931)
47. D.G. Lidzey, D.D.C. Bradley, M.S. Skolnick, T. Virgili, S. Walker, D.M. Whittaker, Nature (London) **395**, 53 (1998)
48. P.A. Hobson, W.L. Barnes, D.G. Lidzey, G.A. Gehring, D.M. Whittaker, M.S. Skolnick, S. Walker, Appl. Phys. Lett. **81**, 3519 (2002)
49. L.G. Connolly, D.G. Lidzey, R. Butté, A.M. Adawi, D.M. Whittaker, M.S. Skolnick, R. Airey, Appl. Phys. Lett. **83**, 5377 (2003)
50. R.J. Holmes, S.R. Forrest, Phys. Rev. B **71**, 235203 (2005)
51. J. Wenus, R. Parashkov, S. Ceccarelli, A. Brehier, J.S. Lauret, M.S. Skolnick, E. Deleporte, D.G. Lidzey, Phys. Rev. B **74**, 235212 (2006)
52. S. Kéna-Cohen, S.R. Forrest, Phys. Rev. B **77**, 073205 (2008)
53. R. Brückner, M. Sudzius, S.I. Hintschich, H. Fröb, V.G. Lyssenko, K. Leo, Phys. Rev. B **83**, 033405 (2011)
54. M. Leroux, N. Grandjean, M. Laugt, J. Massies, B. Gil, P. Lefebvre, P. Bigenwald, Phys. Rev. B **58**, 13371 (1998)
55. J. Levrat, R. Butté, G. Christmann, E. Feltin, J.F. Carlin, N. Grandjean, Phys. Status Solidi C **6**, 2820 (2009)
56. R. Houdré, R.P. Stanley, M. Ilegems, Phys. Rev. A **53**, 2711 (1996)
57. G. Christmann, R. Butté, E. Feltin, J.F. Carlin, N. Grandjean, Phys. Rev. B **73**, 153305 (2006)
58. R. Butté, J.F. Carlin, E. Feltin, M. Gonschorek, S. Nicolay, G. Christmann, D. Simeonov, A. Castiglia, J. Dorsaz, H.J. Buehlmann, S. Christopoulos, G.B.H. von Högersthal, A.J.D. Grundy, M. Mosca, C. Pinquier, M.A. Py, F. Demangeot, J. Frandon, P.G. Lagoudakis, J.J. Baumberg, N. Grandjean, J. Phys. D, Appl. Phys. **40**, 6328 (2007)
59. G. Christmann, R. Butté, E. Feltin, A. Mouti, P.A. Stadelmann, A. Castiglia, J.F. Carlin, N. Grandjean, Phys. Rev. B **77**, 085310 (2008)
60. J.J. Baumberg, A.V. Kavokin, S. Christopoulos, A.J.D. Grundy, R. Butté, G. Christmann, D.D. Solnyshkov, G. Malpuech, G.B.H. von Högersthal, E. Feltin, J.F. Carlin, N. Grandjean, Phys. Rev. Lett. **101**, 136409 (2008)

61. D. Solnyshkov, H. Ouerdane, G. Malpuech, J. Appl. Phys. **103**, 016101 (2008)
62. R. Butté, J. Levrat, G. Christmann, E. Feltin, J.F. Carlin, N. Grandjean, Phys. Rev. B **80**, 233301 (2009)
63. J. Levrat, R. Butté, E. Feltin, J.F. Carlin, N. Grandjean, D. Solnyshkov, G. Malpuech, Phys. Rev. B **81**, 125305 (2010)
64. J. Kasprzak, D.D. Solnyshkov, R. André, L.S. Dang, G. Malpuech, Phys. Rev. Lett. **101**, 146404 (2008)
65. M. Wouters, I. Carusotto, Phys. Rev. Lett. **99**, 140402 (2007)
66. F. Tassone, Y. Yamamoto, Phys. Rev. B **59**, 10830 (1999)
67. M. Gallart, Private communication (2011)
68. A.V. Kavokin, J.J. Baumberg, G. Malpuech, F.P. Laussy, *Microcavities* (Oxford University Press, Oxford, 2007)
69. F. Tassone, C. Piermarocchi, V. Savona, A. Quattropani, P. Schwendimann, Phys. Rev. B **56**, 7554 (1997)
70. F. Stokker-Cheregi, A. Vinattieri, F. Semond, M. Leroux, I.R. Sellers, J. Massies, D. Solnyshkov, G. Malpuech, M. Colocci, M. Gurioli, Appl. Phys. Lett. **92**, 042119 (2008)
71. M. Müller, J. Bleuse, R. André, Phys. Rev. B **62**, 16886 (2000)
72. A.I. Tartakovskii, M. Emam-Ismail, R.M. Stevenson, M.S. Skolnick, V.N. Astratov, D.M. Whittaker, J.J. Baumberg, J.S. Roberts, Phys. Rev. B **62**, R2283 (2000)
73. R. Butté, G. Christmann, E. Feltin, A. Castiglia, J. Levrat, G. Cosendey, A. Altoukhov, J.F. Carlin, N. Grandjean, Proc. SPIE **7216**, 721619 (2009)
74. G. Christmann, D. Simeonov, R. Butté, E. Feltin, J.F. Carlin, N. Grandjean, Appl. Phys. Lett. **89**, 261101 (2006)
75. J.F. Carlin, M. Ilegems, Appl. Phys. Lett. **83**, 668 (2003)
76. E. Feltin, J.F. Carlin, J. Dorsaz, G. Christmann, R. Butté, M. Laügt, M. Ilegems, N. Grandjean, Appl. Phys. Lett. **88**, 051108 (2006)
77. F. Boeuf, R. André, R. Romestain, L.S. Dang, E. Péronne, J.F. Lampin, D. Hulin, A. Alexandrou, Phys. Rev. B **62**, R2279 (2000)
78. D. Porras, C. Ciuti, J.J. Baumberg, C. Tejedor, Phys. Rev. B **66**, 085304 (2002)
79. G. Malpuech, A.D. Carlo, A.V. Kavokin, J.J. Baumberg, P. Lugli, Appl. Phys. Lett. **81**, 412 (2002)
80. G. Malpuech, Y.G. Rubo, F.P. Laussy, P. Bigenwald, A.V. Kavokin, Semicond. Sci. Technol. **18**, S395 (2003)
81. J. Besbas, A. Gadalla, M. Gallart, O. Crégut, B. Hönerlage, P. Gilliot, E. Feltin, J.F. Carlin, R. Butté, N. Grandjean, Phys. Rev. B **82**, 195302 (2010)
82. M.Z. Maialle, A. de Andrada e Silva, L.J. Sham, Phys. Rev. B **47**, 15776 (1993)
83. R.I. Dzhioev, H.M. Gibbs, E.L. Ivchenko, G. Khitrova, V.L. Korenev, M.N. Tkachuk, B.P. Zakharchenya, Phys. Rev. B **56**, 13405 (1997)
84. K.V. Kavokin, I.A. Shelykh, A.V. Kavokin, G. Malpuech, P. Bigenwald, Phys. Rev. Lett. **92**, 017401 (2003)
85. Y.G. Rubo, Phys. Status Solidi A **201**, 641 (2003)
86. M. Vladimirova, S. Cronenberger, D. Scalbert, M. Nawrocki, A.V. Kavokin, A. Miard, A. Lemaître, J. Bloch, Phys. Rev. B **79**, 115325 (2009)
87. D. Read, T.C.H. Liew, Y.G. Rubo, A.V. Kavokin, Phys. Rev. B **80**, 195309 (2009)
88. J. Kasprzak, R. André, L.S. Dang, I.A. Shelykh, A.V. Kavokin, Y.G. Rubo, K.V. Kavokin, G. Malpuech, Phys. Rev. B **75**, 045326 (2007)
89. J. Levrat, R. Butté, T. Christian, M. Glauser, E. Feltin, J.F. Carlin, N. Grandjean, D. Read, A.V. Kavokin, Y.G. Rubo, Phys. Rev. Lett. **104**, 166402 (2010)
90. S.V. Gupalov, E.L. Ivchenko, A.V. Kavokin, JETP Lett. **86**, 388 (1998)
91. A.A. Toropov, E.L. Ivchenko, O. Krebs, S. Cortez, P. Voisin, J.L. Gentner, Phys. Rev. B **63**, 035302 (2000)
92. M.D. Martin, G. Aichmayr, L. Viña, R. André, Phys. Rev. Lett. **89**, 077402 (2002)
93. A.V. Kavokin, P.G. Lagoudakis, G. Malpuech, J.J. Baumberg, Phys. Rev. B **67**, 195321 (2003)

94. I.A. Shelykh, G. Malpuech, K.V. Kavokin, A.V. Kavokin, P. Bigenwald, Phys. Rev. B **70**, 115301 (2004)
95. E. del Valle, D. Sanvitto, A. Amo, F.P. Laussy, R. André, C. Tejedor, L. Viña, Phys. Rev. Lett. **103**, 096404 (2009)
96. R. Butté, N. Grandjean, Semicond. Sci. Technol. **26**, 014030 (2011)
97. G. Rossbach, J. Levrat, A. Dussaigne, G. Cosendey, M. Glauser, M. Cobet, R. Butté, N. Grandjean, H. Teisseyre, M. Bockowski, I. Grzegory, T. Suski, Phys. Rev. B **84**, 115315 (2011)
98. J. Levrat, G. Rossbach, A. Dussaigne, G. Cosendey, M. Glauser, M. Cobet, R. Butté, N. Grandjean, H. Teisseyre, M. Bockowski, I. Grzegory, T. Suski, Phys. Rev. B **86**, 165321 (2012)

Chapter 11
Toward Room Temperature One-Dimensional Quantum Fluid in the Solid State: Exciton Polaritons in Zinc Oxide Microwires

F. Médard, A. Trichet, Z. Chen, L.S. Dang, and M. Richard

Abstract Exciton-polaritons in semiconductor nanostructures constitute a model system of quantum fluid of ultra light Bose excitations in a driven-dissipative situation. Owing to recent progresses in the domain of nanofabrications, polaritons environment may now be tuned at will in terms of external potential and dimensionality. In this chapter we present a nanostructure of particular interest to generate and manipulate one dimensional polaritons with unusual properties: ZnO microwires. Within such a structure we show that polaritons are stable at room temperature and have the property of being strongly decoupled from the lattice thermal vibrations, therefore naturally protected from thermal decoherence. We also find that at cryogenic temperature, the 1D superfluid phase is surprising as polaritons are much heavier than usual and quasi purely excitonic in nature. At room temperature, another polariton superfluid phase is also observed, and several experimental facts indicate that the strong coupling is well preserved in spite of a much larger critical density.

11.1 Introduction

Upon tightening the confinement potential of a quantum fluid along one direction, the motional degree of freedom is getting quantized, and eventually frozen when the inter-level spacing exceeds the thermal energy. In this regime, the physical properties of the system are profoundly modified with respect to the unconfined case. It is a general trend that lowering the dimensionality of a quantum fluid results in enhanced quantum fluctuations and correlations.

The particular situation of 1-dimensional confined Bose liquid with repulsive interaction is of particular interest because it shows unique behavior which has no counterpart in 2D and 3D. For example, upon lowering the density or increasing the

F. Médard · A. Trichet · L.S. Dang · M. Richard (✉)
Institut Néel, CNRS-CEA, BP 166, F-38042 Grenoble, France
e-mail: maxime.richard@grenoble.cnrs.fr

Z. Chen
Surface Physics Laboratory, Department of Physics, Fudan University, Shanghai 200433, China

A. Bramati, M. Modugno (eds.), *Physics of Quantum Fluids*,
Springer Series in Solid-State Sciences 177, DOI 10.1007/978-3-642-37569-9_11,

interactions: the mean field shift $g_{1D}n_{1D}$ overcomes the characteristic kinetic energy $\hbar^2 n_{1D}^2/2m$ [1]. This situation results in a diluted highly correlated phase called "Tonks-Girardeau liquid" (TG), where the interactions result in a mutual exclusion between bosons, in rigorous analogy with Pauli's for fermions [2]. Also, the phenomenon of superfluidity—which is the most natural expectation in an interacting Bose system—is strongly affected in 1D due to umklapp-type of excitations in the superfluid. These excitations have increasing probability for increasing interactions and cost no energy; therefore, for non-zero interaction strength the usual Landau criterion for superfluidity cannot be rigorously verified [3].

From the experimental point of view, the actual realization of 1-dimensional confined system has been achieved with many different types of quantum fluids (see [4] for a comprehensive review). Superfluid ^{4}He for example has been successfully trapped in cylindrical capillaries of 1 nm diameter, and a linear increase of heat capacity versus temperature has been found as expected for phonons with 1D density of states [5]. With ultra-cold atom gas confined in 2D optical lattice, a lot of striking 1D physics has been reported already. Both limits of weak and strong interactions have been achieved and explored extensively [6–8], like for instance a direct demonstration of TG by spatial second order correlations measurement [9].

1D quantum fluids can also be created and studied in solid state system. Cooper pairs for example, may be confined into quasi 1-dimensional geometry using linear arrays of Josephson junctions. An insulating to superconducting phase transition has been reported in this system [10]. A completely different approach is offered with antiferromagnetic materials: indeed, elementary magnetic excitations—magnons—can be identified as a many-body Bose system [11] which has been observed to undergo Bose-Einstein condensation at room temperature [12]. In certain complex materials made of long molecular chains, magnons can be intrinsically 1-dimensional, with no degree of freedom between neighboring chains [13]. In such a system, the dimensionality reduction is accompanied by an interesting boson to fermion transition [11].

In this chapter, we are interested in a specific realization of quantum fluid in solid state environment which has been quite successful so far: exciton-polaritons in semiconductor nanostructures. As already explained in Chaps. 1, 5–10 of this book, exciton-polaritons are bosonic excitations which result from the strong coupling regime between photons confined in a cavity and excitonic excitations (bound electron-hole pair) of a semiconductor material embedded in the cavity [14]. Thus, in the strong coupling regime, polaritons have a mixed exciton and photon nature. This ubiquitous nature results in a very light mass of the order of $10^{-4}m_e$, as well as significant repulsive interactions mediated by Coulomb interaction. Owing to these properties, Bose-Einstein condensation [15] and superfluidity [16] are observed at cryogenic temperature. Recently, many fascinating effects of quantum hydrodynamics have been reported [17, 18]. One of the most important advantages of polaritons over other quantum fluids is the fact that the observables characterizing the polariton field can be fully accessed by optical measurements taking advantage of the radiative escape of polaritons through the mirrors of the cavity. Thus, coherence at any order, spin, energy and momentum can all be measured completely and in

real-time if needed. On the other hand, this fast escape (1 ps to 20 ps typical lifetime) constitutes a loss channel for the quantum fluid. Then, the system needs to be continuously replenished by optical excitations. This situation results in an unusual driven-dissipative situation, harder to describe theoretically than those at equilibrium, but physically richer.

In general, polaritons are studied in planar microcavities and their dimensionality is strictly 2. In Chap. 9, 1-dimensional polariton waveguides are fabricated by carefully etching a GaAs-based planar microcavity. In this chapter, we propose a different strategy to achieve one-dimensional confinement, using a large bandgap material (ZnO) and a design different from usual microcavities: microwires. Large bandgap materials are very interesting in this context due to the larger binding energy of the exciton and larger oscillator strength. Unlike polaritons in Arsenide-based material, this strategy results in a polariton fluid stable at room temperature and high density. Moreover the fabrication of microwires is a bottom-up technique, which is much simpler to implement than top-down techniques with microcavities.

After a brief introduction of the strong coupling regime in ZnO microwires, we will show that owing to an unusually large Rabi splitting, some polariton modes are decoupled from thermal fluctuations mediated by the lattice vibrations. This is a nice advantage to preserve the coherence at room temperature. On the other hand, this decoupling also makes it harder to reach quantum degeneracy of polaritons by stimulated relaxation of excitons. However, strong indications for polariton quantum degeneracy are observed at room temperature. Other interesting effects are observed at room temperature like parametric oscillation between several quantized transverse modes. At lower temperatures, quantum degeneracy is easier to reach and features original properties like polariton fluid with very excitonic character. This unexpected characteristic is favorable to reach stronger interactions as required for TG liquid. Prospects and future experiments involving large bandgap microwires will be discussed as a concluding section.

11.2 ZnO Microwires: Interest and Fabrication Technique

11.2.1 Why Microwires?

The realization of polariton quantum degeneracy at elevated temperature requires high quality photonic structures to achieve the strong exciton-photon coupling regime and strongly bound excitons to remain stable under high density and high temperature conditions. These excitons can be found in the wide band gap semiconductors ZnSe (zinc-blende structure; room temperature band gap of 2.82 eV; free exciton binding energy of 20 meV), GaN (wurtzite structure; 3.45 eV; 25 meV) or ZnO (wurtzite structure; 3.4 eV; 60 meV). Recently, it has been shown with GaAs materials that 1D photonic structures up to 200 μm long and 2–4 μm wide can be etched out of planar microcavities with quality factors Q exceeding 10000 [19]. Such top down approach to photonic wires is out of reach in the near future for

wide band gap semiconductors due to much less advanced growth and processing technologies combined with the very difficult strain management of heterostructures with large lattice mismatch.

On the other hand, it has been shown theoretically that the strong coupling of the light-matter interaction can be achieved also in cylindrical structures between whispering gallery modes, which are standing optical waves confined in the cross section plane of the cavity by total internal reflection at the lateral facets, and bulk excitons [20]. Furthermore, the resulting Rabi splitting is expected to be much larger than in planar microcavities embedding quantum wells thanks to a photon-exciton overlap integral close to unity. This regime is evidenced in ZnO wires 50 μm long and 1 μm wide [21] where 1-dimensional degree of freedom of polariton is found [22]. In this chapter we will mostly address the physics of these ZnO microwires.

11.2.2 Growth Technique

Single-crystalline (wurtzite) ZnO microwires are grown by a vapor-phase transport method under atmospheric pressure at ∼900 °C [23]. This method results in large microwires (diameters ranging from 100 nm to several microns and lengths ranging from 15 μm to 100 μm) with hexagonal cross section and the c-axis aligned with the wire axis. The air/semiconductor interface that is obtained is of high quality in terms of surface roughness and shape regularity. Indeed, hexagonal whispering gallery modes (HWGMs) of quality factor up to 1000 maybe sustained within the microwires. In these microwires, a very low photoluminescence inhomogeneous broadening (<1 meV) of bound as well as free excitons is observed, this is the footprint of an excellent crystalline quality.

Other techniques are possible like MOCVD (Metallo-Organic Chemical Vapor Deposition) epitaxial growth [24, 25]. Although more versatile (possibility of growing axial and radial heterostructures with more complex alloys) and accurate, these techniques result in general in microwires of smaller diameter and shorter length, thus lower quality factor.

These techniques are of "bottom-up" type, i.e. the microwire shape forms spontaneously during the growth when the right conditions are met. It is not the result of advanced etching processes which are realized after the growth.

11.3 ZnO Microwires Polaritons in the Low Density Limit

In this paragraph, we focus on the low density regime where polaritons behave like a dilute gas with negligible inter-particle interactions. It allows us to characterize the single particle properties: i.e. characteristics of the exciton-photon strong-coupling regime, dimensionality and interactions of polaritons with the solid-state environment.

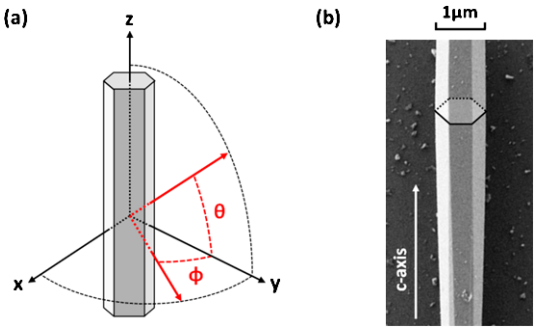

Fig. 11.1 (**a**) Definition of the main axis of the wire and the corresponding angles θ and ϕ used in the text; (**b**) SEM image of a typical ZnO microwire with a measured radius $\rho \approx 500$ nm; the *black solid* and *dashed line* materialize the microwire hexagonal cross section; the main axis of the wire is found to correspond to the crystallographic c-axis

11.3.1 Principle of the Strong Coupling Regime in ZnO Microwires

11.3.1.1 Photon Confinement Through Hexagonal Whispering Gallery Modes (HWGMs)

Our zinc oxide microwires exhibit typical diameters a few times larger than the wavelength of the visible light. Thus, these structures are suitable to confine photons in the direction perpendicular to the wire axis (referred as x and y axis, see Fig. 11.1) whereas these same photonic modes are free to propagate along the wire crystallographic c-axis (z-axis in the following) with a momentum k_z. An important consequence of this only degree of freedom is that for a given transverse mode, the confined photons have a ground state E_0 (i.e. non-zero energy at zero momentum along z-axis). The photon dispersion is an hyperbola parameterized by the dielectric function ϵ, which simplifies into a parabola for kinetic energy much lower than E_0:

$$E_c = \frac{\hbar c k}{\sqrt{\epsilon}} = \sqrt{E_0^2 + \left(\frac{\hbar c k_z}{\sqrt{\epsilon}}\right)^2} \approx E_0 + \frac{(\hbar k_z)^2}{2m^*} \tag{11.1}$$

According to this dispersion, confined photons behave as free particles of mass $m^* \approx 4 \cdot 10^{-5} m_e$, m_e being the mass of the electron. Thus, these quasi-particles are very light compared to atoms ($10^5 m_e$) or even excitons ($0.1 m_e$).

As the hexagonal shape of these wires tends to complicate the calculation of the photonic eigenstates, the system can be first considered, in a rough approximation, as a cylinder with a translational invariance along the z-axis. In such a system, the light is confined into the cross-section due to total reflections at the air-dielectric interface. It corresponds to Whispering Gallery Modes (WGMs) which are free to propagate along the wire axis. However, these kinds of modes are different in

essence from the guided modes exploited in optical fibers which cannot be confined for vanishing k_z. WGM energy and field distribution may be calculated using Maxwell equations: the electric $\boldsymbol{E}$ and magnetic $\boldsymbol{B}$ field inside the wire have to satisfy the wave equation [26]:

$$\left(\nabla^2 + \mu\boldsymbol{\epsilon}\frac{\omega^2}{c^2}\right)\left\{\begin{array}{c}\boldsymbol{E}\\ \boldsymbol{B}\end{array}\right\} = \mathbf{0} \tag{11.2}$$

where ω is related to the energy of the mode through $E = \hbar\omega$, $\boldsymbol{\epsilon}$ is the dielectric tensor accounting for the anisotropy of the crystal, and μ its permittivity. If the length of the wire is large compared to its diameter (translational invariance along the z-axis), the solution of (11.2) is the product of a radial function $R_j(\boldsymbol{r})$ (j is a positive integer) with an azimuthal phase term $e^{-im\phi}$ which accounts for the angular momentum of the mode (m is a signed integer), and a free propagation term $e^{-ik_z z}$. Hence, for $k_z \sim 0$, each WGM is defined by its azimuthal quantum number m (i.e. the number of half-wavelengths in one round-trip in the cross-section plane), its radial quantum number j (i.e. number of wavelengths along the radius) and its polarization *TE* or *TM* depending on the field whose component is non zero along the z-axis. Assuming a wire radius much larger than the photon wavelength, a simplified equation for the energy of these modes can be derived as [20]:

$$E_{j,m,\frac{TE}{TM}}(k_z \approx 0) = \frac{hc}{4\sqrt{\epsilon_0}\rho}\left(2j + |m| \pm 1/2\right) \tag{11.3}$$

where ρ is the radius of the wire and the plus or minus sign arises from the polarization dependent internal reflection dephasing. In this ideal case, in addition to be degenerated in $+m$ and $-m$, each mode is twofold degenerated into a (TE, m) mode and a $(TM, m+1)$ one. The radiative decay rate of such modes is only limited by the diffraction at the air-dielectric interface where their wave-functions spill over the wire cross-section. Theoretical calculations of the linewidth of WGMs [20] show an almost exponential decrease of the linewidth when the azimuthal quantum number m is increased. This can be seen in a simple point of view: the more the number of half-wavelengths needed to obtain a complete trip around the wire increases, the more the ray light model is relevant, and thus the mode becomes lossless.

A more elaborate model needs to account for both the hexagonal shape of the wire and the anisotropy of the wurtzite structure (C_6^v point group). As a consequence of the specific geometry of the system, the rotational invariance around the z-axis is broken. However, photons are still confined into the section of the wire by total internal reflections, leading to the so-called Hexagonal Whispering Gallery Modes (HWGMs). A wave-model has been developed specifically for hexagonal geometries [27, 28]. It takes advantage of the knowledge of the modes in cylindrical geometry, by expanding the modes in the hexagonal geometry on the basis of cylindrical harmonics:

$$\Psi_M^{hex}(r, \phi, z, t) = \sum_m A_m \Psi_m^{cyl}(r, \phi, z, t) \tag{11.4}$$

where in practice, a finite number of harmonics is considered. A_m may be obtained by introducing the hexagonal boundary conditions. The full calculation of the energy, linewidth and polarization has been carried out for HWGMs in ZnO microwires [27]. Due to the sharp corners of the hexagonal shape, HWGMs suffer from much larger losses than WGMs leading to a linewidth more than two orders of magnitude larger. However, in the context of the strong coupling regime, we will see that the losses are largely acceptable. Concerning the polarization degree of the modes, such a hexagonal shape strengthens the mixing of polarization for $k_z \neq 0$ in the case of *TM* modes (degree of polarization almost reversed) whereas the *TE* ones remain almost pure.

11.3.1.2 Excitonic States in Bulk Zinc Oxide Material

Since the typical diameter of our microwires is in the micron range, electronic confinement is not relevant. Thus, only purely three-dimensional electronic states are considered. Zinc oxide is a direct band-gap semiconductor with a threefold valence band [29, 30] of p-like character, whereas the conduction band is of s-like character. Both the spin-orbit interaction and the crystal field induced by the anisotropy of the wurtzite structure are responsible of the valence band splitting which lead to three bands of respective symmetries [31] A–Γ_7, B–Γ_9 and C–Γ_7. These different symmetries result in a set of polarization selection rules for the light-matter interaction.

In usual semiconductors, the lowest energy excited state is the exciton. In a simple picture, the exciton can be seen as an electron-hole pair attracted via electrostatic interaction. Its wavefunction satisfies a hydrogen-like Schrödinger equation [32] with an effective Rydberg constant R_y^*, and an effective Bohr radius a_b^* (respectively 60 meV, and 1.8 nm in ZnO [33]). The exciton behaves as a free particle characterized by its effective mass $M^*$and a parabolic dispersion relation $E_X(\boldsymbol{K})$ valid for low momentum K:

$$E_X = E_g - \frac{R_y^*}{n^2} + \frac{\hbar^2 |\boldsymbol{K}|^2}{2M^*} \tag{11.5}$$

where E_g is the band gap energy of the semiconductor and n the principal quantum number. As the mass M^* is much larger than that of confined photons, the dispersion of excitons is almost constant within the light-cone.

The light-matter interaction between excitons in semiconductors and photons can be described using a linear response theory, i.e. by assuming that the continuum of excitonic states behaves like a Lorentz oscillator driven by an electromagnetic field via their dipolar momentum. This semi-classical approach relies on the dielectric function $\epsilon(\omega)$ which characterizes the amount of excitonic polarization field generated by an electromagnetic field. Taking the electric displacement as a sum of the electric field and the polarization emitted by the dipoles, the dielectric function can be written as:

$$\boldsymbol{D} = \epsilon_\infty \boldsymbol{E} + \boldsymbol{P} = \epsilon_\infty \epsilon(\omega) \boldsymbol{E} = \epsilon_\infty \left(1 + \frac{f}{\omega_0^2 - \omega^2 + i\gamma\omega}\right) \boldsymbol{E} \tag{11.6}$$

Table 11.1 Brief summary of ZnO excitons properties: the group symmetry Γ_i refers to the wavefunction of each exciton; experimental data are taken from Chichibu and coworkers. [34]

Exciton band	Energy at 0 K (eV)	Oscillator strength (meV^2)	Polarization selection rules
A–Γ_5	3.3768	10130	mainly $E \perp c$
B–Γ_5	3.3830	75100	mainly $E \perp c$
C–Γ_1	3.4214	95100	mainly $E \parallel c$

where f is the oscillator strength per unit of volume and is linked to the dipole transition matrix element of the exciton and γ is the damping of the oscillation corresponding to the broadening of the transition due to dephasing or non-radiative losses. The main parameters of the three bright exciton states in ZnO are summarized below in Table 11.1.

11.3.1.3 Excitonic and Photonic Fraction of Polaritons

Since polaritons are mixed exciton-photon quasi-particles, it is necessary to characterize the balance between their light and matter parts. The quantity of interest is the amount of energy stored into the exciton field, which obviously depends on the eigen-energy of the polariton. Equation (11.7) gives an expression of the excitonic fraction $|X|^2$ in a classical point of view considering the photon mode as a plane electromagnetic wave and the exciton as a polarization described through the dielectric function. This result is equivalent to that obtains through a quantum calculation as developed by Hopfield [35]:

$$|X|^2 = \frac{\Omega^2}{\Omega^2 + 4(E_p - E_X)^2} \tag{11.7}$$

where Ω is the Rabi splitting, E_p and E_X the polariton and exciton energies, respectively. Firstly, this excitonic component will provide interactions within the polariton gas, and allow the achievement of thermal equilibrium, which is forbidden with pure photons. Secondly, the photon part decreases by several orders of magnitude the polariton mass with respect to the exciton and leads to a higher critical temperature for reaching quantum degeneracy and superfluid behavior.

11.3.1.4 One-Dimensional Degree of Freedom

Following Hopfield theory of the light-matter coupling [35], polaritons (i.e. a quasi-particle arising from the reversible exchange of energy between photon and exciton), and not excitons, are the true eigenstates of a semiconductor crystal. The polariton dispersion can be computed from the implicit equation (11.8) considering both the

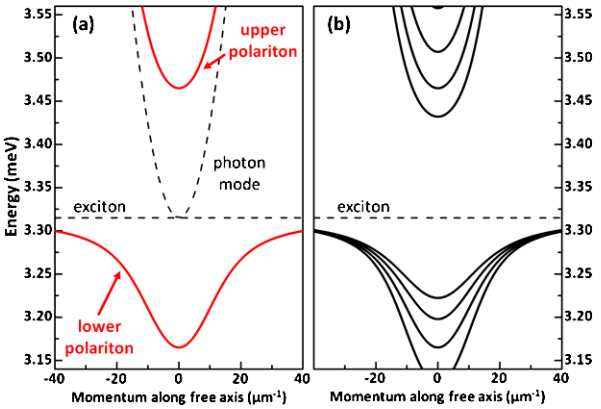

Fig. 11.2 (**a**) Theoretical dispersion of a polariton mode arising from the strong coupling of a confined photon mode and an exciton transition (*black dashed lines*); the lower and upper polariton branches (*red/dark gray lines*) are split in energy by a minimum value equals to the Rabi splitting (**b**) several polariton branches (*black lines*) are obtained when a single photon mode is replaced with a set of modes such as whispering gallery modes (WGM) in a wire

HWGM quadratic dispersion (11.1) and the complex dielectric function of zinc oxide (11.6).

$$\sqrt{\epsilon(E_p)}E_p = E_c \tag{11.8}$$

Although complicated, this equation may be solved analytically in a simple case of a single undamped excitonic transition without spatial dispersion. It results in two distinct polariton branches split by a minimal energy $\Omega = \sqrt{f}$, the Rabi splitting, as shown on Fig. 11.2.

An interesting issue concerns the dimensionality of the polariton modes arising from the strong coupling regime between bulk zinc oxide excitons and hexagonal whispering gallery modes. Usually, a textbook description will consider photons and excitons with the same dimensionality such as quantum wells in a planar microcavity [36]. However, in the case of ZnO microwires, a given state of the electromagnetic field $E_{j,m}(k_z)$ is coupled with a continuum of excitonic states described by their momentum in the cross section K_x and K_y as long as $\boldsymbol{K}$ remains within the light cone.

In fact it has been shown that equal dimensionality is a sufficient condition but not necessary to reach the strong coupling regime [37]. Indeed, as long as the continuum overall linewidth remains small as compared to the strength of the light-matter interaction, the strong coupling regime can be reached. This is the case in our microwires as well as in other microcavities with bulk active medium: it is a general situation that the linewidth of the exciton continuum contained within the light cone, is limited by its homogeneous linewidth, and not by its dispersion which is negligible. Thus, even in this situation, the strong coupling regime is reached as soon as the Rabi splitting exceeds the homogeneous linewidth of both excitons and photons.

But what is the dimensionality of the resulting polaritons? It is actually imposed by HWGMs, simply because they have a much lower density of states as compared to excitons. In other words, the polariton wavefunction is imposed by that of the photon. We demonstrate that fact experimentally for ZnO microwires in the next section.

11.3.2 Properties of One-Dimensional Polaritons in a Single ZnO Microwire

In this part we report on the measured optical properties of a single zinc oxide microwire using spatially resolved photoluminescence at room temperature. A small excitation spot (1 μm diameter) is chosen to both illuminate homogeneously the wire across its cross-section and select only a region of almost constant diameter. The photoluminescence intensity is also recorded in the Fourier plane to obtain a direct access to the spectral dispersion of the polaritons in momentum space.

11.3.2.1 Large Rabi Splitting at Room Temperature

Experimental data obtained at room temperature are shown in Fig. 11.3, the angles of emission are defined in the same way as in Fig. 11.1, i.e. θ is related to the photoluminescence emission direction with respect to the wire axis and ϕ is the angle in the plane of the wire cross-section. Left part of Fig. 11.3 displays the angle-resolved photoluminescence; the angle θ is connected to the momentum k_z along the free axis due to translational invariance. Several polariton modes are detected as maxima of emitted photoluminescence (yellow or white part of the color scale used in Fig. 11.3). Two families of polaritons can be selected with respect to the polarization of their photonic part as they arise from the coupling between polarized HWGMs and ZnO excitons. At k_z close to zero (i.e. $\theta \sim 0°$), one set of modes is mainly TE-polarized whereas the other one is TM-polarized. The respective quantum numbers of the corresponding HWGM are labeled according to theoretical calculations.

The dispersion of each mode demonstrates a specific behavior which unambiguously attests the strong coupling regime between excitons and photons. Firstly, modes of high energy (i.e. closer to the exciton transitions) show a dispersion shape much flatter than those at lower energy. And second, an inflexion point is clearly visible around $\theta \sim 45°$ which results from the anticrossing between HWGMs and exciton levels.

To fully characterize the strong coupling regime, the Rabi splitting is extracted from a simple modeling of the polariton dispersion as a function of the emission angle θ along the free axis. As we do not need to reproduce the eigenenergies of the modes but only their dispersions, we can directly link the energy of the polariton mode $E_p(\theta)$ at any given angle with its energy $E_p(0)$ at zero momentum along k_z

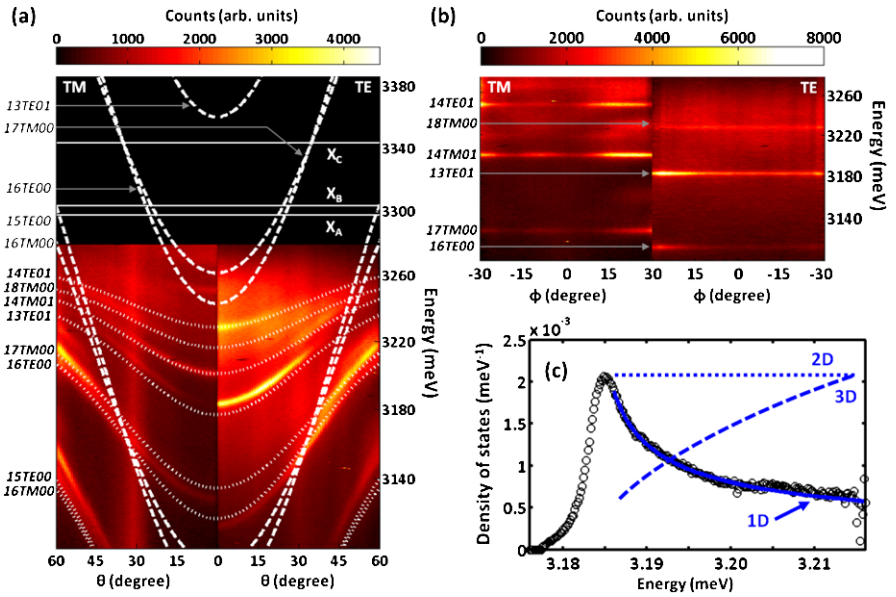

Fig. 11.3 (**a**) and (**b**) Angle-resolved and polarization-resolved (*right*: TE; *left*: TM) room-temperature PL of a single ZnO microwire; the emission intensity is color scaled and increases from black to white; angle θ resolution (**a**): the *white dashed lines* are the calculated dispersion of uncoupled HWGM modes; the *white dotted lines* represent the calculated exciton-polariton modes; angle ϕ resolution (**b**): the labels "mPn" on the *left-hand side* of the figure refer to the polariton mode quantum numbers (azimuthal m, and radial n) and polarization (P = TE or TM) according to the HWGM they derive from (calculated HWGM modes have their labels in italics) (**c**) measured density of states of the polariton labeled 13TE01; the *solid blue line* corresponds to the DOS for a 1D massive particle with a parabolic dispersion; *dashed blue lines* represent the shape of 2D and 3D DOS

through (11.9) where ϵ is the dielectric function and θ the detection angle.

$$E_p(\theta) = E_p(0)\left(1 - \frac{\sin(\theta)^2}{\epsilon(E_p)}\right)^{-1/2} \tag{11.9}$$

Following the linear response theory as developed in the previous section, the dielectric function $\epsilon(E)$ can be expressed using (11.10). This formula accounts for each exciton transition by its energy E_i and its bulk Rabi splitting Ω_i. In a first step, the exciton linewidth is set to 0 on purpose in this expression. The polariton linewidth will be properly accounted for in Sect. 11.3.3. In order to account for the finite fraction of the HWGM that lies outside of the wire, as well as in the outer shell of the wire where excitons are submitted to a strong electric-field [38], an exciton-photon overlap integral $\alpha < 1$ is considered:

$$\epsilon_\infty \epsilon(E) = \epsilon_\infty \left(1 + \sum_{i=A,B,C} \frac{\alpha^2 \Omega_i^2}{E_i^2 - E^2}\right) \tag{11.10}$$

Note that this procedure is not valid at large angles ($\theta \geq 30°$) due to mixing between the polarizations in the HWGM and the complicated selection rules of ZnO excitons. However, this modeling relies only on two free parameters (the spatial overlap integral α and the background dielectric function ϵ_∞) leading to an accurate value of the Rabi splitting without a-priori knowledge of the energies of the uncoupled modes. Using the above equations and the exciton parameters found in the literature (see for example Table 11.1), this model is applied to the set of polaritons observed in Fig. 11.3. It leads to a Rabi splitting of 320 ± 30 meV for TE-polarization [22], comparable to that of bulk zinc oxide and larger than the value obtained in other typical semiconductor systems, e.g. 15 meV in GaAs-based micropillar cavity [39], around 50 meV in bulk GaN microcavity [40], or 130 meV in bulk ZnO microcavity [41].

To fit the full angle scale dispersion of polariton modes and to attribute a set of quantum numbers to the corresponding HWGMs as shown on Fig. 11.3, it is necessary to solve a set of Maxwell equations for an anisotropic cylinder as introduced in the above part on WGMs. A detailed description of this model is beyond the scope of this chapter. We refer our readers to the work of Pavlovic and coworkers [22, 27].

11.3.2.2 Experimental Determination of the One-Dimensional Character

The polariton dispersion is also recorded versus the angle of emission ϕ as shown in the upper right part (b) of Fig. 11.3. The energy dispersion versus this angle reflects the possible dispersion of the radial and azimuthal part of the polariton wavefunction. Due to confinement, i.e. frozen degree of freedom in the cross-section plane, we observe no dispersion versus angle ϕ but a well defined constant energy (note that since we measure this dispersion over 60°, we know it also over 360° thanks to the hexagonal symmetry of the wire cross-section). This behavior is a direct evidence of the one-dimensional (1D) nature of the polaritons arising from the strong coupling in ZnO microwires. Such a clear demonstration of a confinement along two directions has been rarely achieved in other semiconductor systems and never at room temperature [19, 42].

From the experimental dispersion of a chosen polariton, it is also possible to compute the density of states (DOS) to assess the 1D character. Assuming a flat dispersion along the angle ϕ for every value of θ, the experimental DOS extraction is performed by numerically flattening the intensity in data of Fig. 11.3(a) over all angles of emission θ. Then, the data are reshaped in order to reflect k_z instead of θ for the abscissa and the sum over angles $\zeta(E)$ is performed. $\zeta(E)$ reflects the DOS $\rho(E)$ according to the relation

$$\rho(E) = \frac{L}{\pi}\left(\frac{\partial E}{\partial k}\right)^{-1} = \frac{L\zeta(E)}{\pi \mathcal{L}_0} \tag{11.11}$$

where L is the microwire length and $\mathcal{L}_0$ a normalization factor. The homogeneous broadening of the polariton is also taken into account in this numerical method. The result is shown in the lower right part of Fig. 11.3, and compared to the theoretical

DOS of a massive particle with a parabolic dispersion (proportional to $1/\sqrt{E}$ for a 1D system). The excellent agreement is found with the 1D DOS up to large energy where the polariton dispersion non-parabolicity becomes significant. This result is another way of demonstrating the one-dimensional character of polaritons in ZnO microwires.

11.3.2.3 Polariton Spin in ZnO Microwires

Polariton superfluid is a so-called spinor superfluid: it has a $1/2$-spin degree of freedom which results from both spin states of the bright heavy-hole exciton (of spin projection ± 1) coupled with both polarization states of light [43]. Thus the polariton condensate state may be represented by a two-component vector. In bi-dimensional polariton superfluids like in microcavities, this leads to peculiar properties such as half-vortices, which can be understood as a π*-shift* of the phase plus a π*-shift* of the polarization around the vortex core [18].

However, the polariton spin states are not always degenerate: for instance, at non-zero momentum, the TE/TM splitting acts as an effective field which rotates the spin. Moreover if the material exhibits anisotropy (e.g. due to crystalline properties), even zero-momentum polariton state is split. This results for example in a pinning of the condensate polarization state, and the condensate wavefunction becomes scalar [15].

In ZnO microwires, polaritons are subject to a strong TE/TM splitting plus a strong crystalline anisotropy. In Fig. 11.3, we clearly observe that TE and TM polarized polariton branches show up at completely different energies. Moreover, the measurement shows that the polarization state strongly depends also on θ: if we look at mode 13TE01, we observe a complete shift from a purely TE-polarized mode at $\theta \approx 0°$ to an almost TM one above $\theta \approx 30°$. Thus, the most frequent situation in ZnO microwires is to obtain a 1D polariton superfluid in a frozen linear polarization state. However, by carefully choosing the diameter of the microwire, it is in principle possible to bring a TE mode in resonance with a TM mode with a different orbital momentum. Then the degree of freedom of the spin could be restored and tuned in this way.

This control over the polarization degeneracy of our polariton condensate could lead to interesting 1D quantum hydrodynamic effects like half-solitons with spatial separation of the spin components as recently predicted theoretically by H. Flayac and coworkers [44].

11.3.3 Suppressed Coupling Between Polaritons and the Lattice Vibrations

In solid state environment, the lattice vibrations (i.e. phonons) constitute the thermostat to which is coupled the superfluid. Therefore the influence of the coupling between polaritons and lattice vibrations is important. A basic idea of this coupling strength is provided by the thermal polariton linewidth. Surprisingly, the

overall linewidth (including thermal broadening and photonic losses) of polaritons at room temperature is very low as compared to that expected from the strong interaction with phonons in zinc oxide [33]. Considering the polariton labeled 13TE01 in Fig. 11.3, a figure of merit (i.e. the ratio between Rabi splitting and linewidth) as high as 75 is measured. This broadening ($\Gamma_p \sim 4$ meV) is one order of magnitude smaller than the value reported for a high quality ZnO bulk sample ($\Gamma_x \sim 40$ meV) [45].

11.3.3.1 Evidence of an Unexpectedly Low Broadening

In the simplest approach, the polariton linewidth is estimated using a coupled oscillators model [46]. According to this naive picture, the lineshape of a polariton is given by the convolution of the respective lineshapes of the exciton and the photon. Thus, considering only homogeneous broadening (i.e. due to the photon escape and the exciton thermal broadening), the linewidth of the polariton Γ_p at room temperature is defined as an average of exciton and photon contributions (respectively Γ_x and Γ_c) following (11.12). The weighting term $|X|^2$ is the excitonic fraction of the considered polariton mode.

$$\Gamma_p = |X|^2 \Gamma_x + \left(1 - |X|^2\right) \Gamma_c \tag{11.12}$$

To estimate the lower bound of the linewidth of the observed polariton 13TE01, we neglect the linewidth of photonic origin, i.e. $\Gamma_c \sim 0$. According to (11.12), in this limit, the mode should have a FWHM larger than 25 meV. This result is obviously in contradiction with what is shown on Fig. 11.3. Indeed, the simple picture exposed above, is not correct in our situation because the exciton-photon interaction dominates over the exciton-phonon interaction by more than one order of magnitude [47].

11.3.3.2 Quenching of the Polariton-Phonon Interaction

The first indication of a peculiar coupling mechanism between polaritons and phonons is found by looking at the spatially resolved emission of a tapered ZnO microwire at two different temperatures. The result is shown in Fig. 11.4. Such a wire allows tuning the polariton energy along the wire axis (i.e. the HWGM eigenenergies are inversely proportional to the wire diameter as seen above). The black and white pictures in the left part of Fig. 11.4 are the luminescence spectra obtained at 70 K and 300 K along the wire axis. In the energy range referred as Δ in Fig. 11.4, an obvious change occurs between the two temperatures, as no more polaritons are visible at room temperature (modes labeled as $\mathcal{M}_3$, $\mathcal{M}_4$ and $\mathcal{M}_5$). However, below this range, polariton modes are not affected. This peculiar behavior is attributed to the interaction with LO-phonons.

At low temperature, LO-phonons are almost unpopulated and only acoustic phonons contribute slightly to the thermal broadening of polariton modes (see Fig. 11.4(a)). Then, at room temperature (Fig. 11.4(b)), the contribution of LO-phonons increases dramatically but only polaritons in the energy range $\Delta = [E_X;$

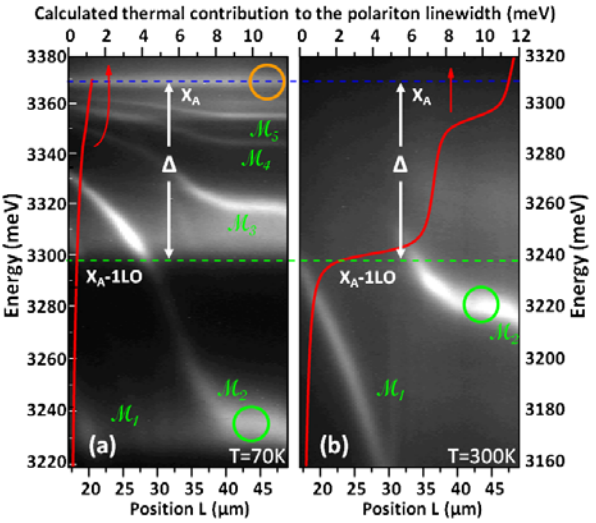

Fig. 11.4 Spatially resolved TE-polarized emission spectrum along a segment of a tapered ZnO microwire at temperature (**a**) $T = 70$ K and (**b**) $T = 300$ K; along this portion of the microwire, the inhomogeneous diameter (presently increasing from left to right) provides a natural way to continuously vary the exciton-photon detuning; $\mathcal{M}_i$ labels the five visible polariton modes at 70 K; the $\Delta = (E_X, E_X - E_{LO})$ energy range is shown by the *white arrows*; *red solid lines* show the calculation of the phonon contribution to the polariton linewidth vs energy

$E_X - E_{LO}$] are affected. This can be explained as follow: polaritons in the range Δ can be scattered by an acoustic or an optical phonon of the thermal bath, to the exciton reservoir (i.e. pure excitonic states with large momentum). The process is very efficient in ZnO because of the large interaction with optical phonons and the high density of states in the reservoir. Thus, at room temperature, polaritons whose energy lies within Δ are strongly scattered out.

The situation is very different for polariton states below Δ: there, regardless of the phonon involved, scattered polaritons can only end up in higher energy polariton states but not in the reservoir, as depicted in the sketch of Fig. 11.5(a). Because the density of states is four orders of magnitude lower in this part of the polariton dispersion than in the reservoir, this mechanism is very inefficient and hardly affects polaritons during their lifetime.

The exact amount of broadening due to polariton interaction with the thermal bath of optical and acoustic phonons can be computed using the Fermi golden rule. Because of the very low polariton density of states, the intrabranch scattering is neglected compared to the scattering toward the exciton reservoir. In this limit, the scattering rate of polaritons Γ_p with energy E_p is

$$\Gamma_p(E_p) = \pi V |X|^2 \int \frac{d^3\boldsymbol{q}}{(2\pi)^3} N(\boldsymbol{q}) \times \left[\left| M_{ac}(\boldsymbol{q}) \right|^2 \delta\left(E_p - E_X(\boldsymbol{q}) + E_{ac}(\boldsymbol{q})\right) + \left| M_{LO}(\boldsymbol{q}) \right|^2 \delta\left(E_p - E_X(\boldsymbol{q}) + E_{LO}\right) \right] \tag{11.13}$$

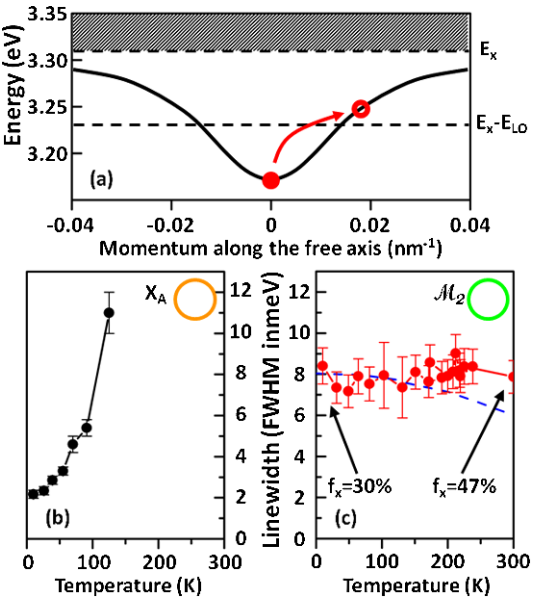

Fig. 11.5 (**a**) Sketch of the quenching of the interaction between LO-phonons and polaritons with a detuning greater than Δ; (**b**) Pure exciton linewidth vs temperature [energy and position shown by the *orange/gray circle* displayed at 3370 meV in the left panel of Fig. 11.4]; (**c**) Measured homogeneous linewidth of polariton mode M_2 of Fig. 11.4 vs temperature [*red/light gray round symbols*], when its energy lies below Δ; the *dashed blue/light gray line* plots the photon-escape contribution to the linewidth

where $|X|^2$ is the excitonic fraction (i.e. Hopfield coefficient) of the considered polariton state, V is the quantization volume, $\boldsymbol{q}$, $E_{ac}(\boldsymbol{q})$ and $E_{LO}$are the phonon momentum and energies and $M_{ac(LO)}(\boldsymbol{q})$ are the matrix elements for exciton and acoustic phonon (optical LO phonon) interaction. The polariton momentum is negligible as compared to $\boldsymbol{q}$. The phonons are assumed to be at thermal equilibrium, thus following a Bose distribution $N(\boldsymbol{q})$ at the lattice temperature. The results of this calculation are shown in Fig. 11.4(a) and (b) as red solid lines for temperatures $T = 70$ K and room temperature. It confirms indeed the weak contribution of phonons at low temperature and the quenching of polariton-phonon interaction at room temperature below Δ. To be more quantitative, the linewidth of bare excitons and a polariton modes below the Δ range are measured and compared in Fig. 11.5(b) and (c). Upon increasing temperature, the linewidth of polariton state labeled M_2 on Fig. 11.4 remains almost constant whereas the exciton is strongly broadened. Note that the excitonic fraction of polariton state M_2 changes by 17 % between $T = 10$ K and $T = 300$ K from which we can deduce a 3 meV maximum thermal broadening of polaritons at room temperature [22].

The quenching of the interaction between polaritons and optical phonons is usually not achieved with polaritons in other microcavity systems because the LO-phonon energy is larger than the Rabi splitting. Thus for polariton states with significant excitonic fraction, the "polariton trap" is not deep enough to prevent scattering. Nevertheless, in some cases, the scattering with acoustic phonons has been found quenched because of their lower energies as compared with optical phonons [48, 49] but the effect on the thermal broadening is less dramatic. Obviously, for zinc oxide microwires, a combination of a large Rabi splitting ($\Omega \sim 300$ meV) and a comparatively low optical phonon energy ($E_{LO} \sim 72$ meV) allows to observe polariton states

with significant excitonic fraction and negligible thermal broadening at room temperature. In the superfluid phase, at large polariton density, this decoupling with the lattice vibrations provides an efficient protection against thermal decoherence even at room temperature.

11.4 Properties of ZnO Microwires Polaritons in the High Density Limit

11.4.1 Polariton Lasing with a High Excitonic Fraction

A superfluid state of polaritons may be achieved at high density in different ways: upon non-resonant excitation, Bose-Einstein condensation [15] or polariton lasing [50] can occur, depending on the experimental conditions (thermal equilibrium achieved within the polariton lifetime or not). The polariton coherence can also be driven directly by a resonant laser [16] but then it is experimentally more difficult to distinguish between the laser and the polariton emission.

Reaching the polariton lasing regime at room temperature is at the moment quite challenging in every ZnO-based structures. Indeed, it is not clear yet whether the strong optical excitation required to achieve lasing destroys or not the strong coupling regime [41, 51]. This point will be discussed in Sect. 11.4.2. Thus, with ZnO microwires, we first focused our attention on cryogenic temperatures where a coherent polariton state with unusual characteristics is achieved upon non-resonant optical excitation orders of magnitude lower than at room temperature.

We characterized experimentally this polariton lasing mechanism at $T = 40$ K using a tapered microwire: The emission spectra in real space are recorded for various excitation power densities (gray color scale maps, Fig. 11.6). The shape of the wire allows to chose a short segment ($\sim$3 µm length, i.e. the laser spot size) of constant diameter, thus with almost constant polariton energies. The polariton modes are labeled M_i ($i = 1, \ldots, 5$ ordered in descending energy) as shown in Fig. 11.6(a). Since we are dealing with bulk material, optically active transitions other than polaritons are also visible like free A excitons and donor-bound excitons states (respectively labeled X_A and DBX on Fig. 11.6(a)). They show up as straight lines in the spatially resolved maps since unlike polaritons their energies do not depend on the wire diameter. Figure 11.6(a) is obtained at the lowest excitation density. Figure 11.6(b) and (c) are obtained respectively at and above the polariton lasing threshold which occurs in polariton state M_4. At threshold the M_4 mode population strongly increases as compared to the other modes due to onset of bosonic stimulation (i.e. the number of particles in the considered state is higher than one) and eventually dominates completely over all other modes (Fig. 11.6(c)).

To be more quantitative, the integrated intensity of polariton mode M_4 is plotted as a function of the incident power density on Fig. 11.7(b). At threshold, (corresponding to $P/P_{\text{th}} = 1$ on the plot), the slope of the intensity drastically increases from an almost linear part to a 3.3-power law. This is the consequence of stimulated

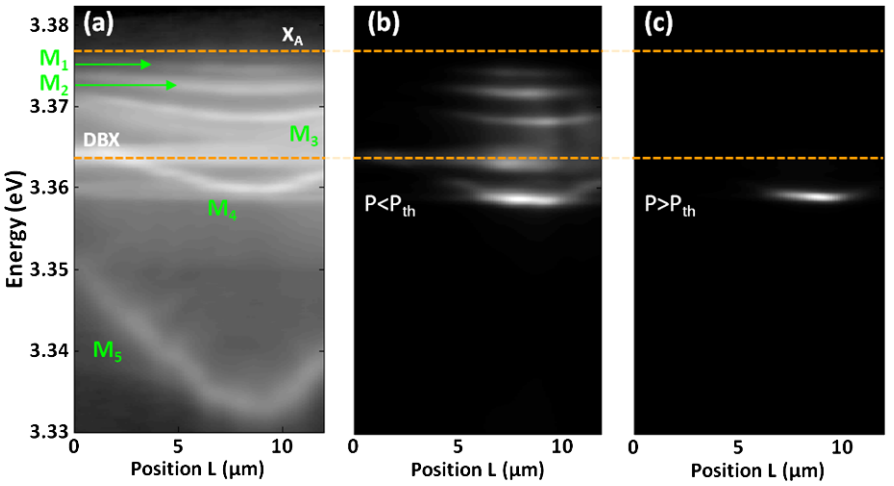

Fig. 11.6 Spatially resolved TE-polarized emission spectrum at $T = 40$ K along a segment of a tapered ZnO microwire at low temperature; in the range where L varies from 7 μm to 10 μm, the diameter of the wire is almost constant; (**a**) the whole wire is lit at very low power density; polariton modes are labeled as $M_{1,\ldots,5}$ and intrinsic zinc oxide transitions are positioned (free exciton X_A and donor-bound exciton *DBX*); (**b**) and (**c**) the same picture under (**b**) and above (**c**) polariton lasing threshold with a laser spot focused on the constant diameter part of the wire

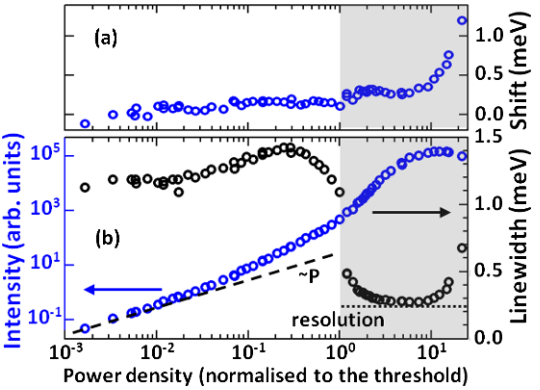

Fig. 11.7 (**a**) The blue-shift, (**b**) The emission intensity (*blue, on the left*) and the linewidth (*black, on the right*) of the M_4 polariton mode are plotted as a function of the incident power density (normalized to the threshold)

relaxation of polaritons into M_4 ground state. Due to its driven-dissipative character, the coherence dynamics of the polariton condensate is governed by laser physics. Indeed, we observe in Fig. 11.7(b) that the strong non-linearity is accompanied with a significant linewidth narrowing above threshold. This corresponds to a coherence time enhancement from $\tau_p = 0.5$ ps at low density to $\tau_p > 2.5$ ps above threshold.

Finally, we have to check whether this threshold occurs in the strong coupling regime, otherwise our polariton condensate would be instead a regular laser where a pure photon field is amplified. The conservation of the strong coupling regime is demonstrated Fig. 11.7(a) where a negligible blueshift (<0.5 meV for pumping

power 10 times above threshold) of the polariton mode is found over a large range of excitation density. Since the M_4 energy is 18 meV below the exciton energy, this blueshift correspond to 2.8 % of that required to break down the strong coupling regime.

One last important characteristic of this polariton condensate formed in mode M_4 is its large excitonic fraction. Indeed, due to the large Rabi splitting of 300 meV, the polariton/exciton energy difference of 18 meV corresponds to an excitonic fraction as high as 97 % for mode M_4. Interestingly, this 3 % photonic fraction is sufficient to reach polariton quantum degeneracy at low temperature. This is in contrast with most of the typical polariton systems where the polariton condensates are rather in the 50 % range of excitonic fraction. This high excitonic fraction confers original properties to the condensate. Since the polariton-polariton interactions scales like the square of the excitonic fraction, they are much larger than in other ZnO microcavities. Moreover the linewidth is not governed only by the photonic losses anymore but also by pure excitonic dephasing.

11.4.2 Room Temperature Operation

In this section, we discuss experimental studies of ZnO microwire polaritons under non resonant and high pumping conditions at room temperature. Evidence of polariton lasing and first observation of spontaneous interbranch parametric scattering will be examined. Hot carriers are injected in the microwire using the 355 nm (3.493 eV) line of a tripled Nd:YAG pulsed laser (10 Hz repetition rate and 3 ns pulse duration). The lowest stimulation threshold is usually obtained for TE modes since both A and B excitons are strongly TE polarized and more thermally populated than C excitons.

11.4.2.1 Polariton Lasing at Room Temperature

Figure 11.8(a) shows how the microwire far field emission around the TE modes $N = 46, 47, 48$, and 49 (3.10–3.25 eV) is modified with increasing excitation power. Strong stimulated emission can be clearly observed for mode $N = 48$ at angle $\theta = 0°$ for an average excitation power $P_{\text{th}} = 30$ nW. This stimulation is characterized by a strong nonlinearity above threshold shown in Fig. 11.8(b). These results raise again the question of polariton or photon lasing. First, the data in Fig. 11.8 have been acquired by time integrated photoluminescence measurements under pulsed excitation, and therefore could contain mixed information corresponding to both high and low excitation power due to the Gauss-like time profile $I(t)$ of the pulse. However, considering the strong nonlinearity between the excitation intensity and the polariton emission in the lasing regime, it is reasonable to say that the emission spectrum is dominated by the emission in the lasing regime. Moreover, the dynamics of the emission, dominated by the stimulation (time-scale of the order of 1 ps), is much faster than the pulse duration. Then, to confirm that the strong coupling regime

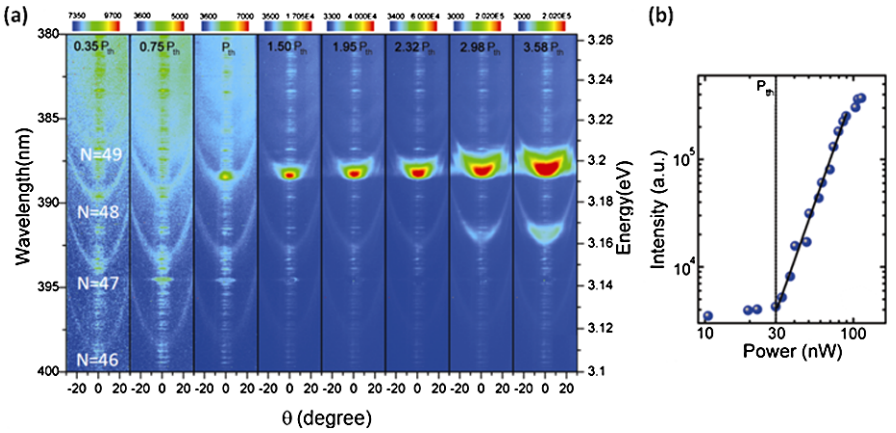

Fig. 11.8 (**a**) Angle-resolved emission intensity (TE polarized) at room temperature for increasing excitation power from left to right (10 nW to 100 nW average excitation power); P_{th} is the excitation power required to reach lasing threshold for mode $N = 48$ visible at 3.182 eV (*third panel from the left*); mode $N = 47$ (at 3.15 eV) starts lasing at 2.98 P_{th} on the *second panel from the right*; (**b**) Mode $N = 47$ emission intensity versus excitation power; the *vertical black line* marks the lasing threshold

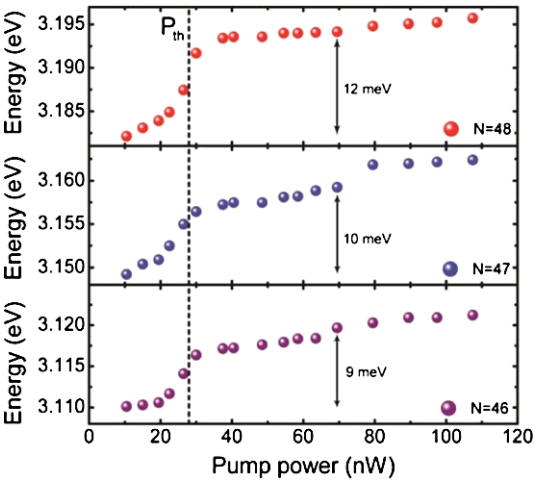

Fig. 11.9 Energy of the polariton modes $N = 46$, 47 and 48 from bottom to top panel versus average excitation power

is maintained throughout the threshold, Fig. 11.9 shows a detailed measurement of the blueshift of modes $N = 46$, 47 and 48.

As explained in the previous section the magnitude and behavior of the blueshift around threshold provides indication on the conservation of the strong coupling regime. In this room temperature experiment, the magnitude of the blueshift is larger and could be attributed to a jump to a pure photonic mode of different N in resonance with the gain peak. However, the magnitude of the blueshift of modes $N = 47$ and $N = 46$ is not consistent with this explanation. Indeed, the strong cou-

pling regime should be lost for them as well (they share the same reservoir as mode $N = 48$) and the blueshift magnitude should be larger (uncoupled modes of lower Ns should show up at unrelated spectral positions as compared to that of polariton modes $N = 46$ and 47) and not with decreasing magnitude for decreasing N. It can be explained instead within the polariton picture taking into account interactions with the exciton reservoir. This corresponds to what we observe on Fig. 11.9, where the blueshift is more important for polariton modes of higher energy, which are more exciton-like, and should interact more strongly with reservoir excitons. Beyond threshold, the shift is less pronounced since, like for regular lasers, additionally injected excitation would preferably participate in the on-going stimulation process. Further indication of the strong coupling regime above threshold is the mode dispersion which remains unchanged at the crossover (see Fig. 11.8).

Stimulation in the ground polariton state $k_z = 0$ would occur when the feeding rate to this state is faster than the polariton radiative lifetime (<1 ps). Feeding by the "standard" exciton-exciton scattering mechanism from the exciton reservoir would favor polariton modes at higher energy because of their higher excitonic fraction and their smaller energy to scatter (neglecting variation of density-of-states). In fact, in the studied microwire, stimulation is found to occur first for the $N = 48$ polariton mode at $\sim$3.19 eV, and then for the $N = 47$ mode at $\sim$3.16 eV, but not for the $N = 49$ mode at 3.22 eV. We have no clear explanation for this behavior yet. With additional unambiguous proof of strong coupling regime at threshold, these results will constitute a unique realization of a 1D-polariton superfluid at room temperature.

11.4.2.2 Interbranch Parametric Scattering

An interesting property of this superfluid state in the transverse mode N arises from the existence of the previous transverse modes $N - 1$ tens of meV below. This situation allows interbranch parametric scattering which leads to balanced signal and idler polariton states [52].

Some indications of this spontaneous scattering process are shown in Fig. 11.10: with increasing pump power beyond the lasing threshold for mode $N = 48$ ground state, we can observe strong polariton scattering towards a spectrally degenerate signal and idler in the $N = 47$ mode, followed by stimulation in the $N = 47$ ground state and scattering towards another degenerate pair in the $N = 46$ mode. In both cases, the signal and idler emissions are equally strong, which is desirable for practical applications. Furthermore they exhibit a non linear behavior, more marked for the $N = 47$ pair, which could be related to its stronger exciton character. Time and polarization correlation measurements are planned to confirm these promising observations.

11.5 Conclusion

ZnO microwires are strikingly simple objects: no heterostructures, just bulk semiconductor material, naturally shaped into a wire by setting the right thermodynamic

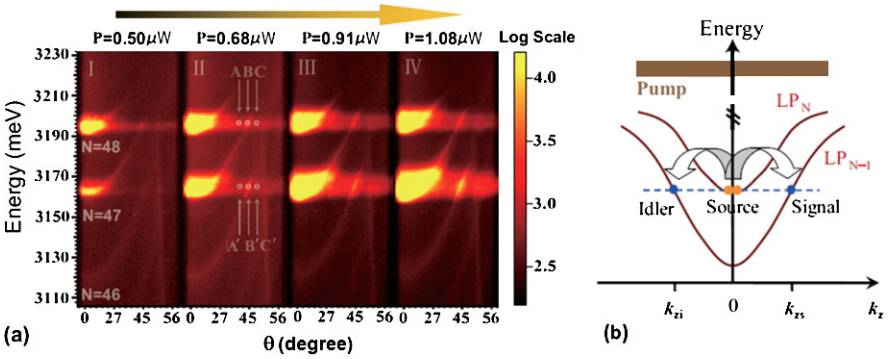

Fig. 11.10 (**a**) Angle-resolved emission intensity (TE polarized) at room temperature for increasing excitation power from left panel to right panel (500 nW to 1080 nW average excitation power); intensity in A and C feature a linear relationship with respect to intensity at $k_z = 0$ of mode $N = 48$; intensity in B taken on mode $N = 47$ at large angle is strongly non-linear as expected from parametric scattering; the same behavior is found for A', B' and C' and the pair of modes $N = 47$ and 46; (**b**) Schematic representation of interbranch polariton parametric scattering: two polaritons in $k_z = 0$, of mode N scatter into two polaritons of mode $N - 1$ and momenta $k_{zi} = -k_{zs}$

conditions into the growth chamber. And yet, they can sustain high quality polariton gases with surprising properties. We have shown so far that these polaritons have a 1-dimensional degree of freedom, that due to the large Rabi splitting, they are efficiently decoupled from the lattice vibrations even at room temperature, and that at cryogenic temperatures due to very low structural disorder, they can have a very large excitonic nature.

Obviously these characteristics are advantageous and original for the superfluid phase. The latter has not been rigorously demonstrated yet; however we have shown that a polariton condensate can be obtained spontaneously at cryogenic temperature by a polariton lasing mechanism. Its superfluid character is very likely as long as we have non-zero interactions. We also have encouraging results showing that the polariton condensate may subsist up to room temperature.

The characterization of the superfluid regime is a promising task where the polariton-polariton interaction plays a key role. Although the interactions should be weaker than in lower bandgap materials, the high excitonic character of polaritons counterbalances this fact. Moreover our condensate is very close to the biexcitonic resonance where significant enhancement of the interactions is expected [53], in complete analogy with Feshbach resonance in ultracold atom gases [54].

We have verified recently that the physics of polaritons described in this chapter for ZnO microwires is found qualitatively identical in GaN microwires [55]. However, the lasing regime has not been achieved yet due to a purely technical problem which should be sorted out soon. The major interest of working with GaN microwires is its potential in terms of electrical injection. Indeed unlike ZnO, fabricating a microwire featuring a *p–i–n* junction in the strong coupling regime is a technically feasible thing. This would open the way to electrically-pumped polari-

ton superfluid, interesting for an alternative coherent light emitter in the near UV with low threshold, and for opto-electronic applications.

Acknowledgements FM, AT, LSD and MR acknowledge financial support by the ERC starting grant No. 258608.

References

1. D.S. Petrov, G.V. Shlyapnikov, J.T.M. Walraven, Regimes of quantum degeneracy in trapped 1D gases. Phys. Rev. Lett. **85**, 3745 (2000)
2. M. Girardeau, Relationship between systems of impenetrable bosons and fermions in one dimension. J. Math. Phys. **1**, 516 (1960)
3. J. Brand, A.Y. Cherny, Dynamic structure factor of the one-dimensional Bose gas near the Tonks-Girardeau limit. Phys. Rev. A **72**, 033619 (2005)
4. M.A. Cazalilla, R. Citro, T. Giamarchi, E. Orignac, M. Rigol, One dimensional bosons: From condensed matter systems to ultracold gases. Rev. Mod. Phys. **83**, 1405 (2011)
5. N. Wada, J. Taniguchi, H. Ikegami, S. Inagaki, Y. Fukushima, Helium-4 Bose fluids formed in one-dimensional 18 Å diameter pores. Phys. Rev. Lett. **86**, 4322 (2001)
6. S. Richard, F. Gerbier, J.H. Thywissen, M. Hugbart, P. Bouyer, A. Aspect, Momentum spectroscopy of 1D phase fluctuations in Bose-Einstein condensates. Phys. Rev. Lett. **91**, 010405 (2003)
7. T. Kinoshita, T. Wenger, D.S. Weiss, A quantum Newton's cradle. Nature **440**, 900 (2006)
8. E. Haller, R. Hart, M.J. Mark, J.G. Danzl, L. Reichsöllner, M. Gustavsson, M. Dalmonte, G. Pupillo, H.-C. Nägerl, Pinning quantum phase transition for a Luttinger liquid of strongly interacting bosons. Nature **466**, 597 (2010)
9. T. Kinoshita, T. Wenger, D.S. Weiss, Local pair correlations in one-dimensional Bose gases. Phys. Rev. Lett. **95**, 190406 (2005)
10. E. Chow, P. Delsing, D.B. Haviland, Length-scale dependence of the superconductor-to-insulator quantum phase transition in one dimension. Phys. Rev. Lett. **81**, 204 (1998)
11. T. Giamarchi, C. Rüegg, O. Tchernyshyov, Bose-Einstein condensation in magnetic insulators. Nat. Phys. **4**, 198 (2008)
12. S.O. Demokritov, V.E. Demidov, O. Dzyapko, G.A. Melkov, A.A. Serga, B. Hillebrands, A.N. Slavin, Bose-Einstein condensation of quasi-equilibrium magnons at room temperature under pumping. Nature **443**, 430 (2006)
13. B.C. Watson, V.N. Kotov, M.W. Meisel, D.W. Hall, G.E. Granroth, W.T. Montfrooij, S.E. Nagler, D.A. Jensen, R. Backov, M.A. Petruska, G.E. Fanucci, D.R. Talham, Magnetic spin ladder $(C_5H_{12}N)_2CuBr_4$: High-field magnetization and scaling near quantum criticality. Phys. Rev. Lett. **86**, 5168 (2001)
14. C. Weisbuch, M. Nishioka, A. Ishikawa, Y. Arakawa, Observation of the coupled exciton-photon mode splitting in a semiconductor quantum microcavity. Phys. Rev. Lett. **69**, 3314 (1992)
15. J. Kasprzak, M. Richard, S. Kundermann, A. Baas, P. Jeambrun, J.M.J. Keeling, F.M. Marchetti, M.H. Szymańska, R. André, J.L. Staehli, V. Savona, P.B. Littlewood, B. Deveaud, L.S. Dang, Bose-Einstein condensation of exciton polaritons. Nature **443**, 409 (2006)
16. A. Amo, J. Lefrère, S. Pigeon, C. Adrados, C. Ciuti, I. Carusotto, R. Houdré, E. Giacobino, A. Bramati, Superfluidity of polaritons in semiconductor microcavities. Nat. Phys. **5**, 805 (2009)
17. K.G. Lagoudakis, M. Wouters, M. Richard, A. Baas, I. Carusotto, R. André, L.S. Dang, B. Deveaud-Plédran, Quantized vortices in an exciton-polariton condensate. Nat. Phys. **4**, 706 (2008)

18. K.G. Lagoudakis, T. Ostatnický, A.V. Kavokin, Y.G. Rubo, R. André, B. Deveaud-Plédran, Observation of half-quantum vortices in an exciton-polariton condensate. Science **326**, 974 (2009)
19. E. Wertz, L. Ferrier, D.D. Solnyshkov, R. Johne, D. Sanvitto, A. Lemaître, I. Sagnes, R. Grousson, A.V. Kavokin, P. Senellart, G. Malpuech, J. Bloch, Spontaneous formation and optical manipulation of extended polariton condensates. Nat. Phys. **6**, 860 (2011)
20. M.A. Kaliteevski, S. Brand, R.A. Abram, A. Kavokin, L.S. Dang, Whispering gallery polaritons in cylindrical cavities. Phys. Rev. B **75**, 233309 (2007)
21. L. Sun, Z. Chen, Q. Ren, K. Yu, L. Bai, W. Zhou, H. Xiong, Z.Q. Zhu, X. Shen, Direct observation of whispering gallery mode polaritons and their dispersion in a ZnO tapered microcavity. Phys. Rev. Lett. **100**, 156403 (2008)
22. A. Trichet, L. Sun, G. Pavlovic, N.A. Gippius, G. Malpuech, W. Xie, Z. Chen, M. Richard, L.S. Dang, One-dimensional ZnO exciton polaritons with negligible thermal broadening at room temperature. Phys. Rev. B **83**, 041302(R) (2011)
23. K. Yu, Y.S. Zhang, R.L. Xu, S.X. Ouyang, D.M. Li, L.Q. Luo, Z.Q. Zhu, J. Ma, S.J. Xie, S.H. Han, H.R. Geng, Efficient field emission from tetrapod-like zinc oxide nanoneedles. Mater. Lett. **59**, 1866 (2005)
24. I.C. Robin, B. Gauron, P. Ferret, C. Tavares, G. Feuillet, L.S. Dang, B. Gayral, J.M. Gérard, Evidence for low density of nonradiative defects in ZnO nanowires grown by metal organic vapor-phase epitaxy. Appl. Phys. Lett. **91**, 143120 (2007)
25. A. Marzouki, F. Falyouni, N. Haneche, A. Lusson, P. Galtier, L. Rigutti, G. Jacopin, M. Tchernycheva, M. Oueslati, V. Sallet, Structural and optical characterizations of N-doped ZnO nanowires grown by MOCVD. Mater. Lett. **64**, 2112 (2010)
26. J.D. Jackson, *Classical Electrodynamics* (Wiley, New York, 1999)
27. G. Pavlovic, G. Malpuech, N.A. Gippius, Dispersion and polarization conversion of whispering gallery modes in nanowires. Phys. Rev. B **82**, 195328 (2010)
28. J. Wiersig, Hexagonal dielectric resonators and microcrystal lasers. Phys. Rev. A **67**, 023807 (2003)
29. J.J. Hopfield, Finestructure in the optical absorption edge of anisotropic crystals. J. Phys. Chem. Solids **15**, 97 (1960)
30. D.G. Thomas, The exciton spectrum of zinc oxide. J. Phys. Chem. Solids **15**, 86 (1960)
31. M.R. Wagner, J.-H. Schulze, R. Kirste, M. Cobet, A. Hoffmann, C. Rauch, A.V. Rodina, B.K. Meyer, U. Röder, K. Thonke, Γ_7 valence band symmetry related hole fine splitting of bound excitons in ZnO observed in magneto-optical studies. Phys. Rev. B **80**, 205203 (2009)
32. P.Y. Yu, M. Cardona, *Fundamentals of Semiconductors* (Springer, Heidelberg, 2010)
33. C.F. Klingshirn, B.K. Meyer, A. Waag, A. Hoffmann, J.M.M. Geurts, *Zinc Oxide: From Fundamental Properties Towards Novel Applications* (Springer, Heidelberg, 2010)
34. S.F. Chichibu, T. Sota, G. Cantwell, D.B. Eason, C.W. Litton, Polarized photoreflectance spectra of excitonic polaritons in a ZnO single crystal. J. Appl. Phys. **93**, 756 (2003)
35. J.J. Hopfield, Theory of the contribution of excitons to the complex dielectric constant of crystals. Phys. Rev. **112**, 1555 (1958)
36. A.V. Kavokin, J.J. Baumberg, G. Malpuech, F. Laussy, *Microcavities* (Oxford University Press, London, 2007)
37. C. Cohen-Tannoudji, J. Dupont-Roc, G. Grynberg, *Atom-Photon Interactions: Basic Processes and Applications* (Wiley, New York, 1998)
38. Y. Li, F. Della Valle, M. Simonnet, I. Yamada, J.-J. Delaunay, Competitive surface effects of oxygen and water on UV photoresponse of ZnO nanowires. Appl. Phys. Lett. **94**, 023110 (2009)
39. D. Bajoni, P. Senellart, E. Wertz, I. Sagnes, A. Miard, A. Lemaître, J. Bloch, Polariton laser using single micropillar GaAs–GaAlAs semiconductor cavities. Phys. Rev. Lett. **100**, 047401 (2008)
40. S. Christopoulos, G.B.H. von Högersthal, A.J.D. Grundy, P.G. Lagoudakis, A.V. Kavokin, J.J. Baumberg, G. Christmann, R. Butté, E. Feltin, J.F. Carlin, N. Grandjean, Room-

temperature polariton lasing in semiconductor microcavities. Phys. Rev. Lett. **98**, 126405 (2007)
41. T. Guillet, M. Mexis, J. Levrat, G. Rossbach, C. Brimont, T. Bretagnon, B. Gil, R. Butté, N. Grandjean, L. Orosz, F. Reveret, J. Leymarie, J. Zúñiga-Perez, M. Leroux, F. Semond, S. Bouchoule, Polariton lasing in a hybrid bulk ZnO microcavity. Appl. Phys. Lett. **99**, 161104 (2011)
42. F. Manni, K.G. Lagoudakis, B. Pietka, L. Fontanesi, M. Wouters, V. Savona, R. André, B. Deveaud-Plédran, Polariton condensation in a one-dimensional disordered potential. Phys. Rev. Lett. **106**, 176401 (2011)
43. J.J. Baumberg, A. Kavokin, F. Laussy, G. Malpuech, *Microcavities* (Oxford University Press, New York, 2007)
44. H. Flayac, D.D. Solnyshkov, G. Malpuech, Oblique half-solitons and their generation in exciton-polariton condensates. Phys. Rev. B **83**, 193305 (2011)
45. C. Klingshirn, R. Hauschild, J. Fallert, H. Kalt, Room-temperature stimulated emission of ZnO: Alternatives to excitonic lasing. Phys. Rev. B **75**, 115203 (2007)
46. P. Kinsler, D.M. Whittaker, Linewidth narrowing of polaritons. Phys. Rev. B **54**, 4988 (1996)
47. V. Savona, C. Piermarocchi, Microcavity polaritons: Homogeneous and inhomogeneous broadening in the strong coupling regime. Phys. Status Solidi A **164**, 45 (1997)
48. J.J. Baumberg, A. Armitage, M.S. Skolnick, J.S. Roberts, Suppressed polariton scattering in semiconductor microcavities. Phys. Rev. Lett. **81**, 661 (1998)
49. P. Borri, J.R. Jensen, W. Langbein, J.M. Hvam, Direct evidence of reduced dynamic scattering in the lower polariton of a semiconductor microcavity. Phys. Rev. B **61**, R13377 (2000)
50. J. Kasprzak, D.D. Solnyshkov, R. André, L.S. Dang, G. Malpuech, Formation of an exciton polariton condensate: Thermodynamic versus kinetic regimes. Phys. Rev. Lett. **101**, 146404 (2008)
51. L. Sun, S. Sun, H. Dong, W. Xie, M. Richard, L. Zhou, L.S. Dang, X. Shen, Z. Chen, Room temperature one-dimensional polariton condensate in a ZnO microwire (2010). arXiv: 1007.4686v1
52. M. Abbarchi, V. Ardizzone, T. Lecomte, A. Lemaître, I. Sagnes, P. Senellart, J. Bloch, P. Roussignol, J. Tignon, One-dimensional microcavity-based optical parametric oscillator: Generation of balanced twin beams in strong and weak coupling regime. Phys. Rev. B **83**, 201310 (2011)
53. M. Wouters, Resonant polariton-polariton scattering in semiconductor microcavities. Phys. Rev. B **76**, 045319 (2007)
54. C. Chin, R. Grimm, P. Julienne, E. Tiesinga, Feshbach resonances in ultracold gases. Rev. Mod. Phys. **82**, 1225 (2010)
55. A. Trichet, F. Médard, J. Zuniga-Perez, B. Alloing, M. Richard, From strong to weak coupling regime in a single GaN microwire up to room temperature. New J. Phys. **14**, 073004 (2012)

Chapter 12
Superfluid Instability and Critical Velocity in Two and Three Dimensions

F. Piazza, L.A. Collins, and A. Smerzi

Abstract Using the mean-field GP equation, we study the dynamics of superfluid dilute Bose-Einstein condensates (BECs) in the regime where the flow velocity reaches a critical value above which stationary currents are impossible. We present results for two- and three-dimensional BECs in two different geometries: a toroidal and a waveguide configuration, and also discuss the behavior of the critical current, or critical velocity, establishing a general criterion for the breakdown of stationary superfluid flows.

12.1 Introduction

Macroscopic phase coherence allows superfluids to sustain a stationary flow between regions in which a constant phase difference is maintained. The existence of a finite critical current is due to interactions between particles, and is responsible for the characteristic absence of viscosity observed with superfluids since their discovery. For currents larger than this critical value, a stationary flow is no longer possible, even if a constant phase gradient is enforced. Superfluidity therefore loses one of his crucial features and is to some extent "dissipated".

As we shall discuss in detail, the superfluid dissipation dynamics reveals the nature and behavior of the excitations produced above the critical velocity, and depends on the dimensionality and geometry of the system. However, they share the same underlying mechanism: the phase-slip. This scenario for the slowdown of a su-

F. Piazza (✉) · A. Smerzi
INO-CNR, BEC Center and Dipartimento di Fisica, Università di Trento, Via Sommarive 14, 38123 Povo, Trento, Italy
e-mail: francesco.piazza@tum.de

A. Smerzi
e-mail: smerzi@science.unitn.it

L.A. Collins
Theoretical Division, Los Alamos National Laboratory, Mail Stop B214, Los Alamos, NM 87545, USA
e-mail: lac@lanl.gov

A. Bramati, M. Modugno (eds.), *Physics of Quantum Fluids*,
Springer Series in Solid-State Sciences 177, DOI 10.1007/978-3-642-37569-9_12,

perfluid was first introduced by Anderson [3]. In a phase-slip event, the phase difference across the system drops by 2π, and thereby the velocity is decreased by a quantized amount. Due to a phase-slip, the order parameter changes the total number of phase-windings across the system. Therefore, at some time during a phase-slip event, the order parameter must become zero at one point in space [24].

In the one-dimensional case, when the velocity is dynamically increased above the critical value, the density first forms a notch with increasing depth, which eventually touches zero at the center of the weak link. At this moment, the number of phase windings of the order parameter drops by one unit, and a dark soliton is created inside the weak link, having zero density at its center and a π phase difference across it. The dark soliton subsequently evolves into a gray soliton which drifts away from the weak link, carrying the energy subtracted from the superfluid flow.

In two- or three-dimensional cases, phase-slippage takes place through the nucleation of quantized vortices. As discussed by Anderson, since the total phase variation along any closed contour encircling a singly-quantized vortex core must be 2π, the total current drops by a quantized amount when a vortex crosses the system perpendicular to the flow direction.

The mechanism of phase-slippage based on vortex nucleation was proposed by Anderson in the context of superfluid helium. However, ultracold dilute atomic gases present some advantages for the study of superfluid dynamics in general, and in particular can shed new light on the physics of phase-slips. With these dilute atomic Bose-Einstein condensates (BECs) a weak link can be created by a laser beam generating a repulsive barrier for the atoms.

A distinctive feature of ultracold dilute quantum gases rests with the possibility of experimentally interrogating the response of the system in a wide variety of traps and dynamical configurations, exploiting powerful probing tools (see Chap. 18). Moreover, even if the dilute BEC is described by a Gross-Pitaevskii (GP) equation with a contact interaction potential [33, 34], and therefore lacks the rotonic part of the helium spectrum, its nonlinearity, together with the macroscopic phase coherence (see Chaps. 15 and 16), appears to be the only crucial ingredient needed to reveal the microscopic mechanisms underlying the vortex-induced phase-slips.

On the experimental side, the critical velocity for superfluid instability and some aspects of the dissipation dynamics have been already studied with dilute BECs. The superfluid critical velocity in a harmonically trapped cloud swept by a laser beam has been observed experimentally in [28] and associated with the creation of vortex phase singularities in [16], while solitons were observed in the effectively-one-dimensional geometry of [11]. Superfluid dissipation and critical velocity in a toroidal BEC is currently under investigation at NIST [36, 37]. Such problems have been the object of many theoretical efforts, mainly based on numerical simulations of the GP equation, starting from the seminal work of Frisch, Pomeau, and Rica, who examined the instability due to vortex nucleation in a two-dimensional flow past an impenetrable disk [13]. A two-dimensional flow inside a constricted waveguide with inpenetrable walls was explored in [41]. The already mentioned work [14] was devoted to the study of a one-dimensional flow past a repulsive barrier, as done later also in [29]. The phase-slip dissipation caused by a moving barrier inside both

a homogeneous and trapped condensate has been studied in two [17, 30, 46], and three [2, 46] dimensions, as well as the production of Cherenkov radiation [7].

In this chapter, using the mean-field GP equation, we will consider the dynamics of superfluid dilute BECs in the regime where the flow velocity reaches a critical value above which stationary currents are impossible. We will present results for two- and three-dimensional BECs in two different geometries: a toroidal and a waveguide configuration, and also discuss the behavior of the critical current, or critical velocity, in different geometries and dimensionalities, establishing a general criterion for the breakdown of stationary superfluid flows.

12.2 Phase-Slip Dissipation in Two Dimensions: Dilute BEC in a Toroidal Trap

In this section, we will treat a dilute BEC inside a toroidal trap, by which a constriction for the flow can also be created by an offset of the central hole of the torus. Broadly speaking, such multiply connected configurations allow for the observation of macroscopic phase coherence effects and can lead to a range of important technologies. While superconducting Josephson junctions are already employed in magnetic sensors and detectors, their superfluid counterparts can realize ultrasensitive gyroscopes to detect rotations [15]. For instance, a toroidally shaped superfluid weak link provides the building block of a d.c.-SQUID, which is a most promising sensing device based on superfluid interference.

Superfluid instability of a BEC confined in a torus has been experimentally observed at NIST [36, 37]. The BEC was initially stirred by transfer of quantized orbital angular momentum from a Laguerre-Gaussian beam and the rotation remained stable up to 20 seconds in the multiply connected trap. The breakdown of the superfluid flow was studied by raising a repulsive barrier across the annulus.

We theoretically study the dynamics of a dilute BEC flowing inside a toroidal trap at zero temperature and in the presence of a repulsive barrier [31]. This barrier is broader than the annulus width and extends over a few healing lengths along the flow direction. In this way, we create a constriction for the flow in the barrier region. In a toroidal trap, the constriction can also be created by an offset in the position of the central hole of the torus. In the latter situation, which will not be discussed in the following, the superfluid instability dynamics is qualitatively similar to the barrier case. The dynamics starts with the condensate flowing with a finite orbital angular momentum in the cylindrically symmetric torus. The critical regime is reached by adiabatically raising the standing repulsive barrier. The instability is characterized by singly-quantized vortex lines crossing the flow, thereby dissipating the superfluid flow through the phase slip mechanism introduced above. Due to the radial dependence of the superfluid velocity in the torus, which creates an asymmetry between the two edges of the annulus, two different critical barrier heights appear. At the smallest critical height, a singly-quantized vortex moves radially along a straight path from the center of the torus and enters the annulus, leaving behind a 2π phase

slip. The vortex keeps circulating without crossing completely the torus so that the total angular momentum decreases only by a fraction of unity. At the highest critical height, a singly-quantized anti-vortex enters the torus from the outward low density region of the system. Above the second critical barrier height, the vortex dynamics depends on the size of velocity asymmetry between the inner and the outer edge of the annulus as well as on the final barrier height and ramping time. For instance, a vortex and an anti-vortex can just circulate on separate orbits or can collide along a radial trajectory and annihilate. When they orbit on the same loop or annihilate, the system undergoes a global 2π phase slip with the decrease of one unit of total angular momentum. In general, after the penetration of a few vortices, the BEC flow can stabilize again in a lower angular momentum state. In the hydrodynamic regime, where the condensate healing length is smaller than all the other length scales in the system, a general criterion for the onset of the instability can be established. Namely, the latter occurs when the local superfluid velocity equals the average of the local sound speed along the transverse section of the annulus. In the presently discussed geometries, this happens inside the barrier region and close to the edges of the cloud. As we shall see in the next section, such a criterion applies also to fully three-dimensional flows.

The results discussed in this section are relevant for toroidal BECs in effectively two dimensional regimes so that the degrees of freedom along the axial direction do not come into play. Indeed, we will discuss the above scenario using numerical simulations of the two-dimensional time-dependent GP equation. Here we will also present results of calculations performed with the three-dimensional GP equation, but with a very tight axial confinement, employing the experimental parameters of a squashed toroidal trap created at NIST. However, experiments carried out in the latter setup proved not to be well described by a mean-field, and were actually performed to demonstrate the role of quantum fluctuations when dimensionality is reduced [8].

12.2.1 The Model

We numerically solve the two-dimensional time-dependent GP equation

$$i\hbar\frac{\partial\psi(\mathbf{r},t)}{\partial t}=\left[-\frac{\hbar^2\nabla^2}{2m}+V_{\rm tr}(\mathbf{r})+V_{\rm bar}(\mathbf{r},t)+g|\psi|^2\right]\psi(\mathbf{r},t). \tag{12.1}$$

The trapping potential is made by a harmonic potential plus a Gaussian repulsive core creating a hole in the trap center:

$$V_{\rm tr}(\mathbf{r})=V_{\rm ho}(\mathbf{r})+V_{\rm co}(\mathbf{r})=\frac{\hbar\omega_\perp}{2d_\perp^2}\left(x^2+y^2\right)+V_0e^{-(x^2+y^2)/\sigma_c^2}. \tag{12.2}$$

From now on, we express quantities in trap units of time $\omega_\perp^{-1}$ and length $d_\perp$. As an initial condition, we consider the numerical ground state obtained with $V_{\rm bar}=0$,

and transfer by linear phase imprinting a total angular momentum $L_z = N\ell$, with N the total number of particles and ℓ integer. The transferred angular momentum is low enough to have flow velocities in the torus region much smaller than the sound speed. Over each loop of radius $r = \sqrt{x^2 + y^2}$ the circulation is $C = 2\pi\ell$ and the modulus of the fluid velocity,

$$v(r) = \frac{C}{2\pi r}, \tag{12.3}$$

is constant and directed along the tangent of the same loop.

After angular momentum is transferred to the cloud, the barrier potential $V_{\rm bar}(\mathbf{r}, t)$ is adiabatically ramped up over a time $t_{\rm r}$ to a final height $V_{\rm s}$. We use a repulsive well with widths w_x centered at the maximum density, and w_y centered at $y = 0$. We always choose $w_x > d$, where $d \equiv R_2 - R_1$ is the width of the annulus. More precisely, the barrier potential is

$$V_{\rm bar}(\mathbf{r}, t) = f(t) V_{\rm s} V_{\rm bx}(x) V_{\rm by}(y), \tag{12.4}$$

with $f(t) = t/t_{\rm r}$ ($f(t) = 1$ for $t > t_{\rm r}$), and

$$V_{\rm bx} = \frac{1}{2}\left(\tanh\left(\frac{x - R_x + x_0}{b_{\rm s}}\right) + \tanh\left(\frac{-x + R_x + x_0}{b_{\rm s}}\right)\right). \tag{12.5}$$

Here R_x is the x-shift of the center of the barrier while its width is $w_x \sim 2x_0$. The other part of the barrier potential, $V_{\rm by}$, has the same shape as $V_{\rm bx}$, but with $R_y = 0$. The final height of the barrier is $V_{\rm s}$ as long as $x_0, y_0 \gg b_{\rm s}$.

We solved the two-dimensional GP equation numerically by a finite-difference real space product formula (RSPF) approach and employed a spatial grid of 300 to 600 points extending from -15 to $+15$ in both the x and y directions, with a time step of 1×10^{-5} (see [9] for details).

12.2.2 Vortex-Nucleation and Phase Slips

The ℓ quanta of circulation are carried by singly-quantized vortices confined within the low-density central hole of the torus [1, 10]. In our simulations, as soon as a finite angular momentum is transferred to the condensate, the vorticity field component perpendicular to the x–y plane,

$$v(\mathbf{r}, t) = \big(\nabla \times \mathbf{v}(\mathbf{r}, t)\big) \cdot \hat{z}, \tag{12.6}$$

shows a "sea" of positive and negative vorticity spots, corresponding to a mesh of vortices and anti-vortices, see Fig. 12.1(b). This is observed inside the two regions of very low density, close to the center and in the space surrounding the torus. The presence of the "vortex sea" is probably due to numerical noise acting inside very low density regions, possibly triggering an instability of GP equation. As we will

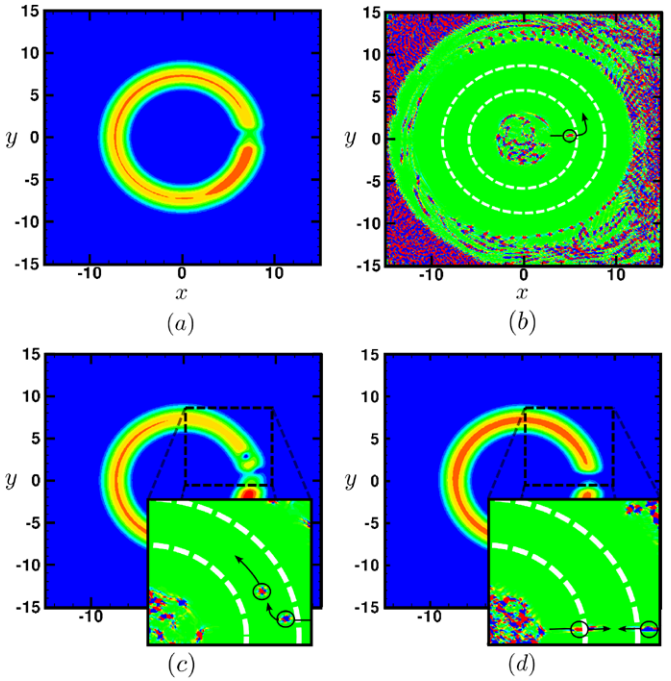

Fig. 12.1 Vortex nucleation and dynamics. (**a**), (**b**) and (**c**) $t_r = 10$, $L_z/N = 8$ and $V_s = 0.34\mu$. (**a**) $t = 7.6$. Density *contour plot* with no visible vortex core. (**b**) $t = 7.6$. The z component of the vorticity field $v(\mathbf{r})$. The *white dashed lines* indicates the Thomas-Fermi radii of the cloud. The *encircled dot* corresponds to a vortex about to enter the annulus from the inner edge. (**c**) $t = 11.6$. A vortex circulates along the annulus while the vorticity (*inset*) shows an anti-vortex about to enter. (**d**) $t_r = 10$, $L_z/N = 2$, $V_s = 0.61\mu$. Vortex anti-vortex annihilation

discuss in this and the following section, even though the above consideration seems to suggest that this vortex mesh is void of any physical meaning, it actually appears to be the reservoir from which the "physical" vortices, responsible for the superfluid dissipation, are generated.

Initially, if the repulsive barrier is raised slowly enough to preserve adiabaticity, the superfluid is able to adapt its density and velocity field and moves through neighboring stationary states at different barrier heights such that no excitation appears in the condensate. In the barrier region, where the density is depleted, the flow velocity increases mainly at the edges of the annulus. Meanwhile, as appears from the vorticity field, the two vortex seas are strongly fluctuating, with vortices and anti-vortices trying to escape but still being pushed back into the mesh.

However, when the barrier reaches a critical height V_{c1}, a vortex from the inner sea can successfully escape and enter the bulk of the density inside the annulus. The onset of instability at this stage is depicted in Fig. 12.1(a) and (b). In this example, before raising the barrier, the flow velocity at the maximum density, located at $r_m = 7.2$, is $v(r_m) = 0.67c_s$, where c_s is Thomas-Fermi estimate of the sound speed in the ground state. The corresponding value of the healing length at r_m is

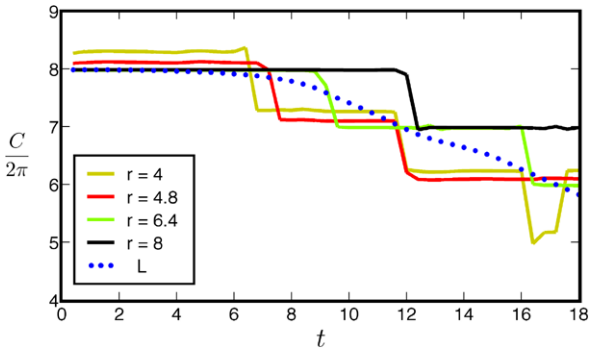

Fig. 12.2 Circulation (*solid lines*) for loops with different radii and total angular momentum (*dots*) as a function of time. The parameters are the same as in Fig. 12.1(a). The 2π drops in the circulation at $r = 4, 4.8, 6.4$ are due to a singly-quantized vortex moving outwards from the center. The drop at $r = 8$ and $t \sim 12$ is due to the passage of an anti-vortex entering the annulus from the outer edge. The oscillation in the circulation at $r = 4$ and $t \sim 16$–17 is due to a double crossing of a vortex trying to escape the inner region

$\xi \sim 1/\sqrt{2g\rho(r_{\rm m}, 0)} = 0.28$. The Thomas-Fermi width of the annulus is $d = 3.59$. In this case, the barrier widths are $w_x \sim 4$ and $w_y \sim 2$, and the observed critical barrier heights are $V_{\rm c1} \sim 0.14\mu$, and $V_{\rm c2} \sim 0.24\mu$.

The dissipation dynamics is better understood by combining the information coming from the superfluid density and vorticity field. In Fig. 12.1(a), we observe the depletion of the density but not a visible vortex core. However, if we inspect the vorticity field (12.6) plotted in Fig. 12.1(b), we clearly see an isolated red spot, corresponding to a positive vorticity, moving radially from the center of the torus towards the higher density region, indicating the presence of the core of a singly-quantized vortex. Such vortex cores inside low density regions which appear only as phase singularities have been referred to as "ghost vortices" [43].

As we discussed in the introduction, the passage of a vortex core between two points causes a 2π slip in the phase difference between them. In Fig. 12.2, we observe 2π sharp drops in the circulation C on a given loop of radius r, taking place when a vortex core crosses the latter. Consistently with the above discussed dynamics, the larger the loop radius r, the later the vortex core reaches it and creates the phase slip. The fact that the circulation at small (and large) radii is not exactly integer, but slightly larger, is due to numerical difficulties related to the calculation of the velocity field where the density is very small. However, even at $r = 4$, where the density is small, we see single 2π phase slips taking place at regular intervals and corresponding to (ghost) vortex core crossings. The behavior of circulation at small radii also provides further useful information. Indeed, close to the inner sea of vortices, the circulation shows spikes at which it decreases by 2π, then quickly goes back to its previous value. These are associated to the above mentioned events where a vortex moving out of the sea but is pushed back by a region of high density located slightly outwards. Indeed, in this way, a loop is crossed back and forth by

the same vortex. We have observed a similar effect with anti-vortices trying to enter the annulus from the outer vortex sea.

Due to phase slippage, the angular momentum is reduced, and eventually the system becomes stable again after a finite number of spawned vortices. The circulation is lowered by a few quanta, and the fluid velocity on vortex-crossed loops is brought back below the critical value. If the ramping is stopped at V_{c1}, vortices do not cross the torus completely and move on stable circular orbits. The vortices circulate on a fixed loop within our computational times. Vortices orbiting inside a two-dimensional toroidal trap have been studied with GP equation in [25, 26].

12.2.3 Instability Criterion and the Second Critical Velocity

The onset of the above instability can be understood, at least qualitatively, from energy considerations. A persistent flow in a toroidal geometry is possible because of the pinning of the vorticity in the low density regions near the center and outside of the torus. This can be explained with an effective energy barrier, arising from the nonlinearity of the GP equation, felt from a vortex core when trying to move towards a region of higher density [4, 6, 22, 42]. Within this interpretation, the obstacle raised across the annulus steadily decreases the density during the ramping process, suppressing the effective energy barrier and thereby unpinning a singly-quantized vortex.

This said, it must be however emphasized that the critical condition which quantitatively corresponds to the onset of instability observed here seems to have no direct connection to energy balance considerations. Indeed, in the hydrodynamic regime, when $\xi \ll d, w_x, w_y$ and $V_s \ll \mu$, we observe the onset of instability towards vortex penetration as soon as the local superfluid velocity reaches the "true" sound speed [47]. In this geometry, the latter corresponds to the velocity of propagation of phononic excitations along the direction of the flow and depends on the average density calculated on a line perpendicular to the flow. In particular, this is smallest inside the constriction, more precisely at the maximum of the repulsive well (at $y = 0$ in our case). The critical condition is thus first met inside the barrier region, at the Thomas-Fermi radius of the cloud where the superfluid velocity is highest.

It is important to mention at this point that for a one-dimensional flow through a constriction, a different criterion has been verified [23, 45]. Namely, in the hydrodynamic regime, the one-dimensional flow becomes unstable as soon as the local sound speed equals the superfluid velocity at the same point. This local instability criterion corresponds to the absence of stationary solutions of the classical inviscid and irrotational flow equation [21]. The present criterion is different from the local criterion verified in one dimension insofar as it involves the true sound speed and not the local sound speed, and the latter should be compared to the superfluid velocity at the Thomas-Fermi radius of the cloud.

The instability criterion appearing in two dimensions is neither connected to energetic arguments, nor corresponds to the local criterion, coming from classical hy-

drodynamics, verified for the one-dimensional GP equation. In the next section, we will return to the study of this instability criterion, giving quantitative results.

This general criterion also explains the existence of two different critical barrier heights. Indeed, as already mentioned above, if the barrier is stopped at V_{c1} only singly-quantized vortices penetrate the annulus from the inner edge, while nothing happens at the outer edge. According to the instability criterion, this is explained by the fact that only the inner edge of the annulus is unstable since there the fluid velocity is larger ($v(r) \propto \ell/r$) and can reach the true sound speed while at the outer edge the velocity is still small. If instead the barrier reaches a second critical height $V_{c2} > V_{c1}$, the outer part of the annulus also becomes unstable. Anti-vortices then enter from the outside while vortices enter from the inner edge. Anti-vortices move radially inwards and contribute to stabilize the outer part by phase slips. Indeed, an anti-vortex crossing a loop makes the circulation drop as a vortex crossing the opposite way.

In Fig. 12.1(c) we see a vortex already circulating inside the high density region of the annulus while an anti-vortex begins to enter. The separation between V_{c1} and V_{c2} is proportional to the velocity difference $\Delta v = \ell(R_1 - R_2)/(R_1 R_2)$ between the two edges. In general, depending on Δv, the dynamics at barrier heights larger than V_{c2} can vary. For instance, at lower angular momenta Δv becomes smaller, and a vortex and an anti-vortex enter the annulus almost simultaneously. They can then collide and annihilate, as shown in Fig. 12.1(d). When a vortex and an anti-vortex annihilate or separately orbit on the same loop, the system undergoes a global 2π phase slip, and the total angular momentum is decreased by one unit.

12.2.4 Three-Dimensional Calculations in a Squashed Torus

We extended our two-dimensional calculations into a three-dimensional configuration. The parameters of the squashed toroidal trap are those employed experimentally at NIST. To transfer angular momentum to the cloud, we use a Laguerre-Gaussian beam. We employ an harmonic trapping with $\omega_\perp = 2\pi \times 20$ Hz (such that $d_\perp = 4.69$ μm) and $\omega_z = 48\omega_\perp$. The Laguerre-Gaussian beam is modeled by a proper external potential term in the GP equation [40]. The core repulsive potential is $V_{co}(r, z) = -V_c(r/\sigma_c)^2 e^{-2(r/\sigma_c)^2}$, and the resulting condensate has a shape close to a hollow disk. We add a repulsive well potential of the same kind used in two dimensions, whose shape, however, is not crucial in determining the qualitative features of the dissipation, as long as w_x is larger than the width of the annulus. We solve the three-dimensional GP equation numerically by a finite-element discrete variable representation in the spatial coordinates and a RSPF in time. The x and y coordinates were divided into boxes of span $[-20.0, +20.0]$ with 160 elements and order 5 Gauss-Legendre bases while the z-direction covered a box $[-10.0, +10.0]$ with 80 elements of order 5 bases. The time step was 1×10^{-5} (see [38] for details).

Since the healing length is of the order of the harmonic length along z, we found, as expected, that the nucleation of singly-quantized vortex lines and their dynamics

resemble those observed in two-dimensional calculations. In particular, we have two critical values for the barrier height V_{c1} and V_{c2} connected respectively with the nucleation of vortices or both vortices and anti-vortices.

The study of the instability scenario in fully three dimensional cases, where the degrees of freedom along all the three directions play a role, represents a necessary extension of the above results. Indeed, understanding how the phase-slippage dynamics changes from two to three dimensions is also experimentally relevant, since the first demonstration of persistent currents at NIST has been achieved in a fully three-dimensional torus [37], while the recent experimental study of the current decay in a weak link has been performed much more squashed toroidal trap [36].

Another interesting observation which deserves further investigation, is the discovery of a new instability criterion, different from the local hydrodynamic criterion verified with one-dimensional GP equation. These issues will be the object of the next section.

12.3 Phase-Slip Dissipation in Three Dimensions: The Role of Confinement Asymmetry and the Instability Criterion

In this section, we will study the critical velocity and superfluid dissipation mechanism in a three-dimensional constricted flow configuration, where the size of the cloud along all the three directions is much larger than the healing length ξ [32]. We consider a subsonic flow of a zero-temperature dilute BEC, and numerically solve the GP equation in two different geometries: (i) a wave guide with periodic boundary conditions, which can mimic an elongated cloud along the flow direction as created in the experiments of [11, 39], and (ii) a torus, already introduced in the previous section. Again, the unstable regime is reached by raising a repulsive penetrable barrier, which is broader than the cloud size transverse to the flow, and extends over typically 5 to 10 healing lengths along the direction of flow, as shown in Fig. 12.3. As in the previously described two-dimensional study, we start from a stationary flow with a given velocity and adiabatically raise the barrier during the dynamical evolution until the instability sets in. In three dimensions, the latter corresponds to the nucleation of vortex rings penetrating the cloud and taking energy from the superfluid flow by the same phase-slip mechanism described in the previous section.

The two geometries under study present significative differences in the phase slip dynamics. We will show that vortex rings, which can find a stationary configuration after entering an axially symmetric waveguide, are instead always transient in the torus, and, more generally, as soon as the axial symmetry about the direction of flow is broken.

In this section, we will also present more quantitative results regarding the general criterion determining the critical velocity for superfluid instability, which we already introduced for the two-dimensional case described earlier. In both of the

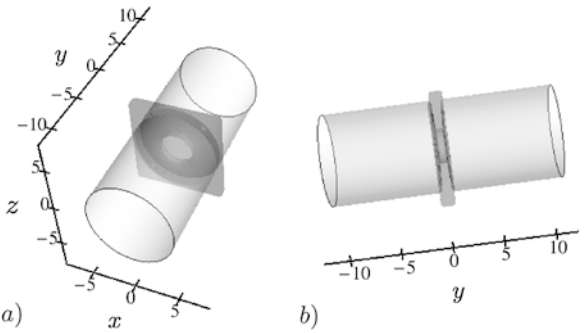

Fig. 12.3 Constriction configuration. The *light-gray surface* corresponds to the classical (Thomas-Fermi) surface of the cloud. The *dark-gray surface* shows an isosurface of the barrier potential used to create the constriction

three-dimensional geometries studied here, in the hydrodynamic regime of the GP equation, the instability criterion, which determines the critical velocity, is not given by the local hydrodynamics condition, according to which the flow breaks down as soon as in any point the local sound speed equals the superfluid velocity. Instead, consistently with the criterion verified in the two-dimensional case treated in the previous section, the instability sets in as soon as the fluid velocity at the Thomas-Fermi surface of the cloud equals the true sound speed, which in this case is the local sound speed averaged over the transverse plane of the waveguide/annulus.

12.3.1 The Model

In order to study these various configurations, we solve the time-dependent GP equation (12.1) for three spatial dimensions in scaled form as

$$i\hbar\frac{\partial\psi(\mathbf{r},t)}{\partial t}=\left[-\frac{1}{2}\nabla^2+V(\mathbf{r},t)+g|\psi|^2\right]\psi(\mathbf{r},t) \tag{12.7}$$

where length, time, and energy are given in units of $d_o=[\frac{\hbar}{m\omega_o}]^{\frac{1}{2}}$, $1/\omega_o$, and $\hbar\omega_o$ respectively for a representative harmonic frequency ω_o that characterizes the trap. $V(\mathbf{r},t)$ is the external potential. The condensate wavefunction $\psi(\mathbf{r},t)$ is normalized to the total number of particles N. The external potential has components associated with the trapping and the barrier potentials of the form

$$V(\mathbf{r},t)=V_{\rm tr}(\mathbf{r})+V_{\rm bar}(\mathbf{r},t). \tag{12.8}$$

In both cases, we find the ground state of the system with $V_{\rm bar}=0$.

The waveguide geometry is implemented by choosing the trapping potential

$$V_{\rm tr}(\mathbf{r})=\frac{1}{2}\left[x^2+\gamma^2z^2\right], \tag{12.9}$$

with $\omega_o\equiv\omega_x=30\times2\pi$ Hz, $\gamma=\omega_z/\omega_x$, and periodic boundary conditions along the flow direction y. We considered three different values of the γ, namely 1,

1.05, and 1.2, which correspond, respectively, to a ground state chemical potential $\mu = 11.7, 12.0, 16.5$ with $N = 3 \times 10^5$ ^{87}Rb atoms and a nonlinear scaling value $gN = 10134$.

The toroidal geometry is implemented by choosing the trapping potential

$$V_{\rm tr}(\mathbf{r}) = \frac{1}{2}\left[\alpha^2 x^2 + \beta^2 y^2 + z^2\right] + V_c e^{-2(\rho/\sigma_c)^2}, \tag{12.10}$$

where $\alpha = \omega_x/\omega_z$ and $\beta = \omega_y/\omega_z$. We take $\alpha = \beta = 0.5$ with $\omega_o \equiv \omega_z = 25 \times 2\pi$ Hz and form the torus by including a core potential with parameters $V_c = 144$, and $\sigma_c = 1.88$ with $\rho^2 = x^2 + y^2$. The ground state chemical potential is $\mu = 7.6$ for $N = 2.5 \times 10^5$ ^{23}Na atoms, corresponding to a nonlinear scaling value $gN = 2028$.

During the dynamical evolution, we use a time-dependent barrier potential of the same kind used in the two-dimensional calculations of the previous section (see (12.4)):

$$V_{\rm b}(\mathbf{r}, t) = f(t) V_{\rm s} V_{\rm bx}(x) V_{\rm by}(y) V_{\rm bz}(z)/8, \tag{12.11}$$

with $f(t) = t/t_{\rm r}$ ($f(t) = 1$ for $t > t_{\rm r}$) and $V_{\rm bx} = \tanh(\frac{x - R_x + x_0}{b_{\rm s}}) + \tanh(\frac{-x + R_x + x_0}{b_{\rm s}})$. Here R_x is the x-shift of the center of the barrier while its width is $w_x \sim 2x_0$. $V_{\rm by}(y)$ and $V_{\rm bz}(z)$ have the same form as $V_{\rm bx}$. The final height of the barrier is $V_{\rm s}$ as long as $x_0, y_0, z_0 \gg b_{\rm s}$.

As done in the two-dimensional study, before starting the dynamics, we put the condensate in motion by imprinting an appropriate spatially dependent phase $\theta(\mathbf{r})$ on the wavefunction. In the waveguide case, $\theta(\mathbf{r}) = mvy/\hbar$ generates a uniform flow of velocity v along the y direction. In the torus, $\theta(\mathbf{r}) = ml\phi/\hbar$, with l integer, generates a tangential flow of speed $v(r) = l/\rho$, where $\phi = \arctan(y/x)$.

The numerical solution of the GP equation used to obtain the results presented here can be sketched as follows. After finding the ground state with an imaginary-time propagation, the dynamical evolution is performed in real time. All the simulations rely on a finite-element discrete variable representation (DVR)[38]. In the waveguide geometry, a split-operator method was employed, with a Fast-Fourier-Transform algorithm used for the kinetic part of the evolution, while the simulations in the torus use a Real Space Product Formula [38]. The spatial grid for the waveguide calculations is $n_x = 60$, $n_y = 120$, $n_z = 60$ (or $n_x = 180$, $n_y = 120$, $n_z = 180$ for Figs. 12.6 and 12.7) with box sizes $L_x = 12$, $L_y = 24$, $L_z = 12$ for the axially symmetric case (see below), $n_x = 90$, $n_y = 120$, $n_z = 80$ with box sizes $L_x = 18$, $L_y = 24$, $L_z = 16$ for the axially asymmetric case, while the time-step is $dt = 10^{-4}$. In the torus simulations, the spatial grid consists of 80 elements in each dimension with 4 DVR Gauss-Legendre functions in each element spanning cubic box lengths of $[-12, 12]$, $[-12, 12]$, and $[-10, 10]$ in the x, y, and z-directions respectively. This choice gives 241 grid points in each direction. The convergence has also been tested with 5 basis functions and 321 points with only a few percent change in basic quantities such as energies, momentum, and positions.

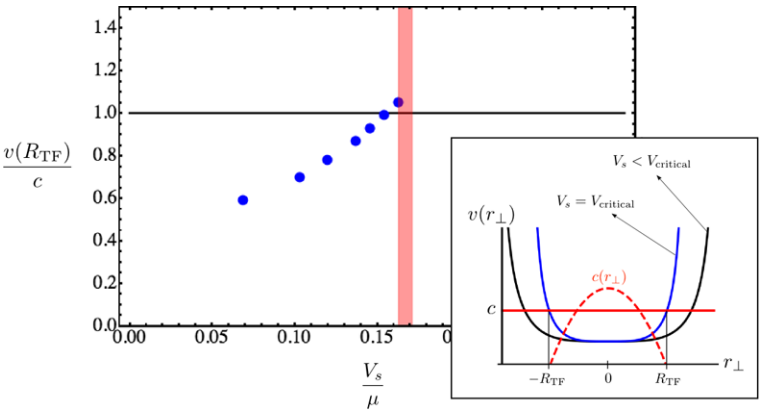

Fig. 12.4 Ratio of the higher local fluid velocity at the Thomas-Fermi radius, $v(R_{TF})$, to the sound speed c inside the barrier, as a function of the barrier height. The *red-shaded area* correspond to the critical point plus uncertainty. The results are obtained for the cylindrically symmetric waveguide $\gamma = 1$ and initial flow velocity $v = 1.05$. The *inset* shows a sketch of the behavior of the local fluid velocity along a radial cut inside the barrier region. The *red solid line* indicates the value of the sound speed c, which with transverse harmonic confinement is just the average of the local sound speed, $c(r_\perp)$ (*red dashed line*) over the transverse plane. The *black* (*blue*) *solid line* corresponds to a subcritical (critical) condition

12.3.2 Criterion for Instability in Three-Dimensions

Let us start by presenting a quantitative study of the instability criterion, that is, the general condition which determines the critical velocity above which the superfluid flow starts being dissipated. We shall see that the following results for three-dimensional GP equation provide a criterion which is consistent with the one verified in the two-dimensional geometry discussed in the previous section.

Indeed, in the hydrodynamic regime, that is, when the healing length ξ is much smaller than all other length scales (the smallest of which is the barrier width along the flow direction), it can be verified that the onset of instability coincides with the simple condition, $v_{TF} = c$: inside the barrier region, the local fluid velocity at the classical (Thomas-Fermi) surface of the cloud, v_{TF}, equals the sound speed c, as depicted in the inset of Fig. 12.4. Again, the sound speed which sets the threshold for the critical velocity is the Bogoliubov sound speed, calculated inside the barrier region, for the low-lying modes propagating along the flow, taken as if the system was homogeneous in this direction. In the present case of a harmonic transverse confinement, and within the Thomas-Fermi approximation, this sound speed is simply the average of the local sound speed on a plane perpendicular to the flow $c = c(0)/\sqrt{2}$, where $c(0)$ is the local sound speed at the center of the transverse harmonic trap [47]. Notice that in two-dimensions exactly the same expression for the criterion can be used, with the only difference that the integration is on a line and not a plane, which turns into a different numerical factor relating c with $c(0)$.

In Fig. 12.4, quantitative results for the three-dimensional waveguide geometry are presented. In a waveguide with cylindrical symmetry, the condition $v_{\mathrm{TF}} = c$ is verified simultaneously at points on a circle perpendicular to the flow, from where a vortex ring will then enter. Instead, as discussed in Sect. 12.2.3, in the torus, due to a higher flow speed at the inner edge of the annulus, the critical condition is reached first on the interior of the cloud, with the consequence here that vortex rings, if ever formed, must be asymmetric, as we discuss below.

We again see that this criterion allows for a simple understanding of the details of vortex penetration dynamics, based on the observation that vortex cores enter first where the critical condition is first reached.

Before going on with the study of the three-dimensional phase slip dissipation dynamics, it is interesting to return to the discussion of "ghost" vortices and of "vortex sea", already encountered in the previous section. As already seen in the two-dimensional torus case, below the critical point, we also observe in the present three-dimensional calculations vortices getting closer to the edges of the cloud but failing to enter. The presence of these "ghost" vortices detaching from the "vortex sea" located at the boundaries of the system suggests that a pre-instability is triggered at the edges of the condensate, but, since the vortices do not enter the bulk region, it is not sufficient to dissipate the superflow. This observation can help to build a connection between the present criterion and the local criterion coming from classical hydrodynamics. As anticipated, the latter is clearly not valid here, since it would predict the flow to be always unstable for the simple reason that the local sound speed goes to zero at the edges of the waveguide (see Fig. 12.4). Therefore the condition is always met, even before raising the obstacle. However, even though not giving the condition for the real instability, the local criterion can be signaling the onset of the above pre-instability. Indeed, the "vortex sea" is present as soon as the fluid moves, providing a source for the ghost vortices which try to enter the cloud before the critical velocity.

12.3.3 Phase Slip Dynamics in the Three-Dimensional Waveguide

The first geometry we will discuss consists of a waveguide with periodic boundary conditions along the flow direction y. This configuration can be realized experimentally with a BEC inside an elongated trap along the flow direction. As stated above, before raising the barrier in the simulations, a stationary flow is created by imprinting a phase $mvy/\hbar$ on the condensate wavefunction, where v is the constant flow speed. In the experiment, such situation can be for instance realized by sweeping the barrier across the cloud at a constant velocity. We consider a harmonic confinement in the transverse x–z plane, such that $d_x = \sqrt{\hbar/m\omega_x}$ and $d_z = \sqrt{\hbar/m\omega_z}$ are both sufficiently larger than the bulk healing length. The effect of transverse degrees of freedom comes thus into play, giving rise to a fully three-dimensional dynamics. A recent experiment which would be relevant for the present study has been described in [39]. In the latter, the possibility of creating a penetrable repulsive barrier across

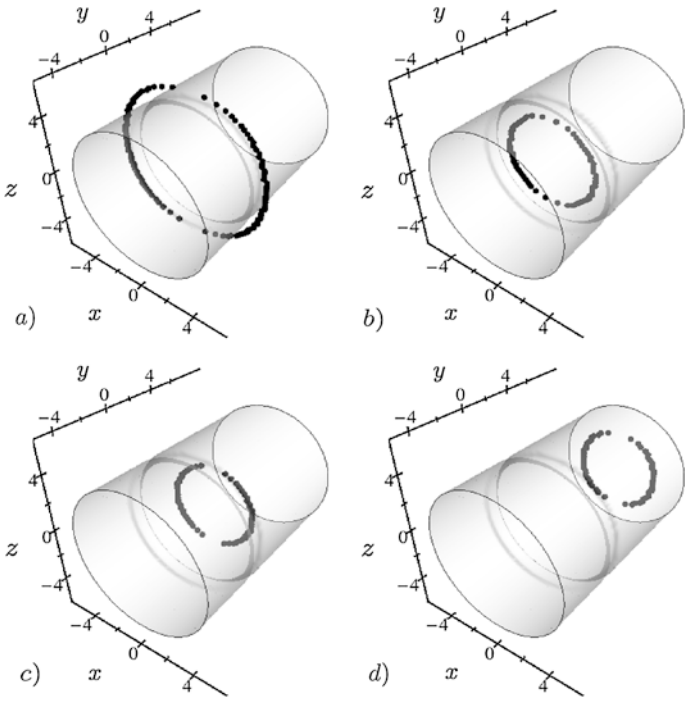

Fig. 12.5 Four subsequent stages of the vortex ring penetration in the waveguide. The *gray surface* indicates the position of the Thomas-Fermi surface of the condensate. *Black dots* show the position of the vortex cores. Here the waveguide is axially symmetric $\gamma = 1$, the initial flow velocity is $v = 1.05$, and the final barrier height is $V_s = 0.17\mu$. (**a**) The ring is shrinking around the cloud in barrier region, still outside the Thomas-Fermi borders of the cloud. (**b**) The ring has just entered the cloud. (**c**) The ring has shrunk to its final size and is already outside the barrier region, moving along the flow direction. (**d**) The ring has moved far from the constriction region, with a constant speed and radius

an elongated three-dimensional condensate, with a control over a length comparable to the healing length, has been demonstrated.

When the waveguide is axially symmetric, as soon as the critical barrier height is reached, a vortex ring detaches from the system boundaries and starts shrinking into the cloud inside the barrier region, as shown in Fig. 12.5(a), (b). In the figure, black points indicate the position of vortex cores while the gray surface corresponds to the Thomas-Fermi surface of the cloud. Detection of vortex cores is performed using a plaquette method, described in [12].

We observe that a vortex ring shrinking into the cloud is the three-dimensional analogue of the penetration of a vortex-anti-vortex pair in two dimensions, shown in Fig. 12.1(d). Indeed, vortex cores located at opposite sides of a circular vortex ring carry opposite vorticity.

Depending on the initial flow velocity, waveguide transverse section, and barrier height at the critical point, the ring attains a certain radius and velocity with which

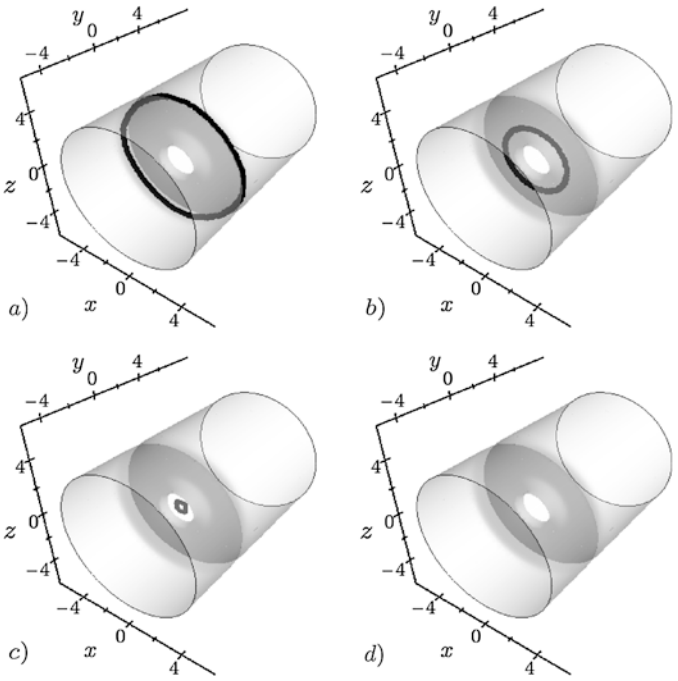

Fig. 12.6 Four subsequent stages of the vortex ring annihilation in the waveguide. The gray surface indicates the position of the Thomas-Fermi surface of the condensate. *Black dots* show the position of the vortex cores. Here the waveguide is axially symmetric $\gamma = 1$, the initial flow velocity is $v = 0.52$, and the final barrier height is $V_s = 0.94\mu$. (**a**) The ring is shrinking around the cloud in the barrier region, still outside the classical borders of the cloud. (**b**) The ring has entered the cloud. (**c**) The ring is about to shrink completely and annihilate. (**d**) The ring has annihilated and no vortex core is now inside the Thomas-Fermi surface

it propagates in the flow direction in a stable fashion, as long as axial symmetry is preserved, as depicted in Fig. 12.5(c) and (d). Here the vortex ring eventually propagates at the speed $u_r = 0.65$, and a radius $R = 2.9$.

12.3.4 Motion of Vortex Rings

Both in Figs. 12.5 and 12.6, we see that, at least initially, the vortex cores are subjected to an essentially radial motion, corresponding to the shrinking of the vortex ring. This behavior can be understood by considering what contributes to the motion of vortex cores in non-homogeneous systems [27]. Let us consider a single vortex core located at some position x_c. Its velocity is the sum of two terms: (i) the background flow velocity at x_c, and (ii) a term perpendicular to the gradient of the density at x_c. Both contributions must be calculated as if the vortex was not present. Since the relative weight of term (ii) is proportional to the value of the healing length cal-

culated at x_c, in high density regions, a vortex core will move mainly with the background superfluid velocity, while in low density regions, it will move mainly due to the gradient of the density. Therefore, when the vortex ring is inside the constriction, where the density is low, and especially when it is close to the Thomas-Fermi surface, it will principally move perpendicular to the gradient of the density, whose main contribution comes from the density modulation induced by the barrier along the flow direction. This results in an essentially radial motion of the cores, and thus into the shrinking of the ring.

12.3.5 The Full Phase Slip Event: Vortex Ring Self-annihilation

In analogy to what happens to vortex-anti-vortex pairs in a two-dimensional geometry (see Fig. 12.1(d)), for sufficiently strong barriers, the ring shrinks to a point, thereby annihilating and completing a full single phase-slip, as shown in Fig. 12.6. After this process, the velocity has dropped everywhere by the same quantized amount. Again, such an event is the three-dimensional analogue of vortex-anti-vortex annihilation in two dimensions.

Let us now analyze the full phase slip event in more detail, since vortex ring self-annihilation contains interesting information about the properties of the solutions of the GP equation [35].

In Fig. 12.7(a) and (b), respectively, we show the position of the vortex cores together with the density on a plane parallel to the flow direction, at a time just before and just after the ring has shrunk to a point. In Fig. 12.7(c), the density on the same plane is plotted at four subsequent times after the annihilation. If we consider the position of the vortex cores, we see that the points of phase singularity form a loop which shrinks inside the constriction, Fig. 12.7(a), and whose radius eventually becomes zero, Fig. 12.7(b). At this moment, we see the zero-density core being filled with atoms, thereby transforming into a density depression, which further propagates out of the constriction as a rarefaction pulse, as shown in Fig. 12.7(c). Finally, this rarefaction pulse decays into sound. The details of self-annihilation process which we observe are consistent with the previous studies of axisymmetric vortex ring solutions [5, 18–20]. Namely, an analysis of stationary solutions of the GP equations shows that the vortex ring branch, for decreasing momentum (or equivalently ring radius), meets a rarefaction pulse solution branch. The two branches merge into a cusp at a given momentum.

12.3.6 Phase Slip Dynamics in the Three-Dimensional Torus

We now consider the study of the phase-slip dynamics in the torus. As we learned in the previous section, here the scenario is richer since the tangential flow velocity at a given total angular momentum decreases like $1/r$, where r is the distance from the

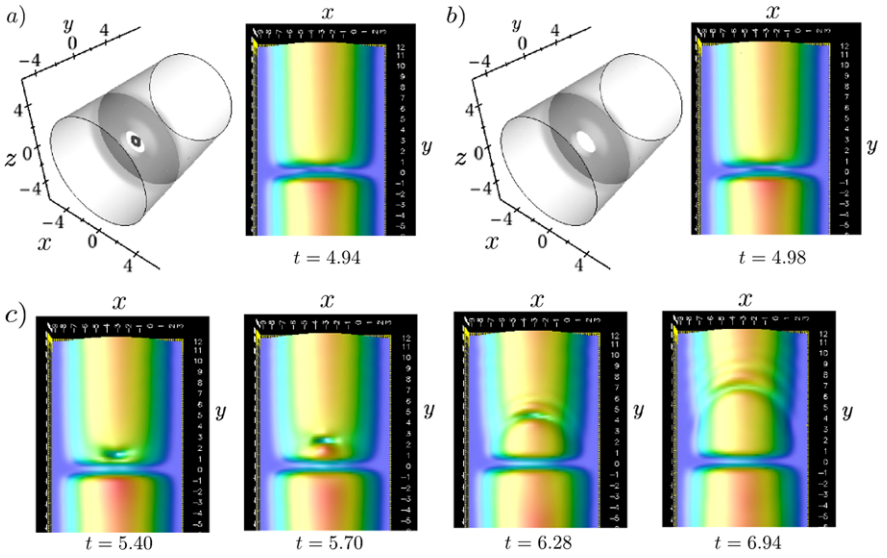

Fig. 12.7 Details of the ring self-annihilation event studied in Fig. 12.6, at six subsequent times. In (**a**) and (**b**), *left panel*, *the gray surface* indicates the position of the Thomas-Fermi surface of the condensate, while *black dots* show the position of the vortex cores. In (**a**) and (**b**), *right panel*, and (**c**), the density on a $z = 0$ plane parallel to the flow direction is shown. A very small loop structure of vortex cores, in (**a**), shrinks to a point and has disappeared in (**b**). The ring has transformed into a rarefaction pulse, whose propagation and decay into sound appears in (**c**)

center of the torus. This introduces an asymmetry between the inner and the outer edges of the cloud, which is not present in the waveguide case. In three-dimensional configurations, this implies that vortex rings are transient features in a toroidal geometry. As we shall see, vortex rings either break or self-annihilate, or even not be formed at all.

As observed in the two dimensional torus (see Fig. 12.1), for a sufficiently small asymmetry between the inner and the outer edge of the annulus, which is typically achieved with low angular momentum, at the critical barrier height, a vortex ring can enter the cloud and shrink down to a point and self-annihilate. The self-annihilation process, shown in Fig. 12.8, is very similar to the one taking place in the waveguide (see Sect. 12.3.5), with the only difference that in the torus the ring is never axially symmetric.

However, the difference between the toroidal and waveguide geometry is more clearly demonstrated by the vortex ring breaking process we will describe next. As shown in Fig. 12.9, after entering the cloud, the ring is strongly deformed since the inner part moves faster (the velocity of a vortex core, when the healing length is much smaller than the length scale of density variation, is essentially given by the background flow velocity, see Sect. 12.3.4). The deformation increases in time up to the point at which the ring bends in on itself, forming a right angle with a kink at its vertex, as shown in Fig. 12.9(b). Meanwhile, a vortex line coming from the inner core of the torus approaches the vertex, and also forms a kink in correspondence

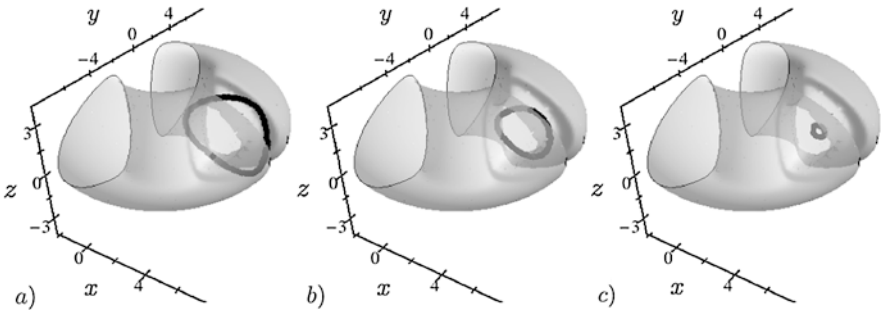

Fig. 12.8 Three subsequent stages of the vortex ring annihilation in the torus. The *gray surface* indicates the position of the Thomas-Fermi surface of the condensate. *Black dots* show the position of the vortex cores. Here the initial circulation is $l = 1$, and the final barrier height is $V_s = 0.5\mu$. (**a**) The ring is shrinking around the cloud in barrier region, still outside the classical borders of the cloud. (**b**) The ring has entered the cloud. (**c**) The ring is about to shrink completely and annihilate

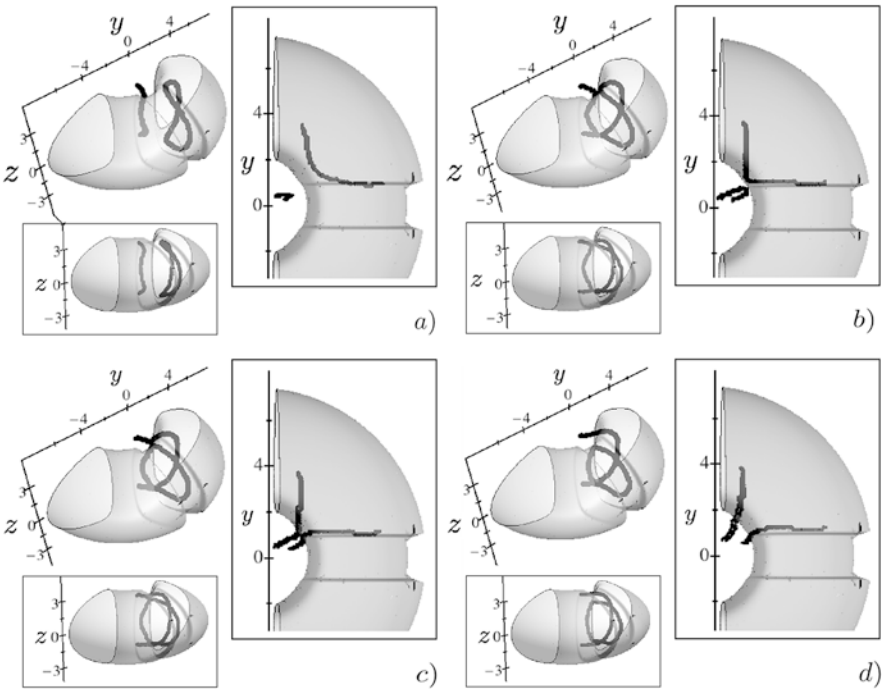

Fig. 12.9 Four subsequent stages of the vortex ring breaking in the torus. The *gray surface* indicates the position of the Thomas-Fermi surface of the condensate. *Black dots* show the position of the vortex cores. *Insets* show the top and side views. Here the initial circulation is $l = 4$, and the final barrier height is $V_s = 0.2\mu$. (**a**) The vortex ring is bending to form a right angle. (**b**) The vortex ring has formed a right angle whose vertex is close to a vortex line coming from the center of the torus. (**c**) The vortex ring and line have just reconnected: a vortex line and a portion of a ring vortex are now inside the Thomas-Fermi surface. (**d**) The vortex line and the ring have moved apart

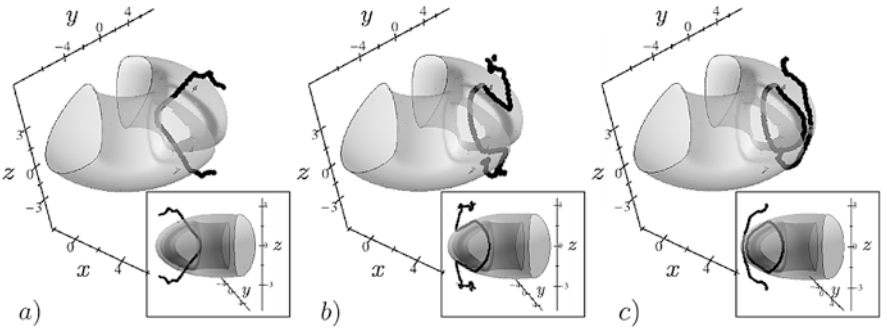

Fig. 12.10 Three subsequent stages of the vortex ring formation in the torus. The *gray surface* indicates the position of the Thomas-Fermi surface of the condensate. *Black dots* show the position of the vortex cores. *Insets* show the side view. Here the initial circulation is $l = 4$, and the final barrier height is $V_s = 0.2\mu$. (**a**) The vortex line is bending around the cloud in barrier region, partially outside the Thomas-Fermi borders of the cloud. (**b**) The vortex line has developed two kinks. (**c**) The vortex ring has just formed

to the latter. Eventually, the line and the ring connect, joining each other at the position of the kinks. Such an event produces a vortex line plus a new ring vortex, appearing in Fig. 12.9(c). Therefore, we can understand the vortex ring breaking as a vortex reconnection. These reconnections between vortex lines or rings play an important role in turbulent scenarios since they provide a very efficient mechanism for increasing the number of vortices in the system [44], see also Chaps. 13 and 14.

In the two-dimensional torus, we observed a single vortex entering the cloud and circulating (see Fig. 12.1(b)), when the barrier was not strong enough to make both the edges of the annulus unstable. We observe the corresponding case in three dimensions, when the ring is not formed at all, and a strongly bent vortex line enters the cloud from its inner edge, to circulate around the torus. As already discussed, the fact that the vortex line enters the inner edge of the annulus is due to the asymmetry in the velocity field which makes the instability set in there first, according to the criterion discussed in Sects. 12.2.3 and 12.3.2.

To conclude the study of the phase slip dynamics in the three-dimensional torus, let us discuss the formation of a vortex ring in this geometry. It is interesting to see that the latter event is nothing more than a reconnection of a vortex line with itself. Indeed, as shown in Fig. 12.10, a bended vortex line is always present at first. While the bending increases, the vortex line develops two sharp kinks whose tips get closer to each other, up to when they join, thereby cutting the original line into a vortex ring plus a yet another line. The latter is then reabsorbed at the system's boundary.

12.3.7 Crossover from Two to Three Dimensions

In the final part of this chapter, we will study how the phase slip dynamics change when the effective dimensionality of the system crosses from two to three. When

the condensate is effectively in two dimensions, i.e. the cloud size along the third direction is comparable with the healing length ξ, vortex lines oriented along the direction of tighter confinement become the preferred excitations with respect to vortex rings, as we learned in the previous section, by studying a condensate inside an effective two-dimensional toroidal trap (the system's size along the axis of the torus was about one healing length). We indeed observed that superfluid dissipation took place through the formation of vortex lines entering the cloud.

On the other hand, for the three-dimensional trap configurations considered in this section, we have shown that phase slip dissipation can happen through vortex rings. More precisely, at first we observed vortex rings in the very low density regions outside the condensate classical Thomas-Fermi surface, the so called "ghost" vortices, not visible from the condensate density profile. In some cases, these "ghost" vortex rings are able to enter completely the classical surface of the cloud, transforming into what we should then call "real" ring vortices. Now, in the crossover between effective two- and three-dimensional regimes, moving from a scenario in which only vortex lines are present to one in which real vortex rings come into play, it is reasonable to expect an intermediate regime in which ghost vortex rings are formed, but the condensate is sufficiently squashed along the third dimension that the full vortex loop is not able to enter the cloud's classical surface. In this regime, superfluid would be dissipated by vortex rings, which are partly real and partly ghost, appearing as simple bent vortex lines in the density profile. As we shall see next, this is only partially true, since the breaking of axial symmetry about the flow direction, which is necessary to move from three- to two-dimensional regimes, introduces a more complex dynamics with respect to the axially-symmetric case.

In what follows, we will use the waveguide geometry, and break the symmetry of the trap along the flow direction. An example of such situation is given in Fig. 12.11, where the waveguide asymmetry parameter is $\gamma = 1.2$. After the instability sets in, a ghost vortex ring forms and shrinks around the cloud in the barrier region up to when we observe a full-fledged ring vortex, which is only partially inside the Thomas-Fermi surface of the condensate (Fig. 12.11(a)). This is indeed the partially real and partially ghost ring vortex mentioned above.

However, since the part of the ring which is inside the Thomas-Fermi surface moves with a larger speed along the flow direction with respect to the part which remains outside, the ring vortex is soon deformed (Fig. 12.11(b)), and eventually breaks up (Fig. 12.11(c)). Indeed, as already discussed in Sect. 12.3.4, the vortex cores located inside the Thomas-Fermi surface of the cloud move, to a good approximation, along with the background velocity field. On the other hand, cores in the low density region outside the surface of the cloud essentially do not feel the background velocity and move along the flow direction only because of the presence of transverse density gradients. After the vortex ring breaks up, the two lines move downstream and continue to deform, and eventually re-join to form a vortex ring (Fig. 12.11(d)). The latter undergoes the same deformation described above, leading to another break up.

We also verified that, even in a very slightly non-axially symmetric waveguide, ring vortices eventually break up. With $\gamma = 1.05$, the deformation is created more

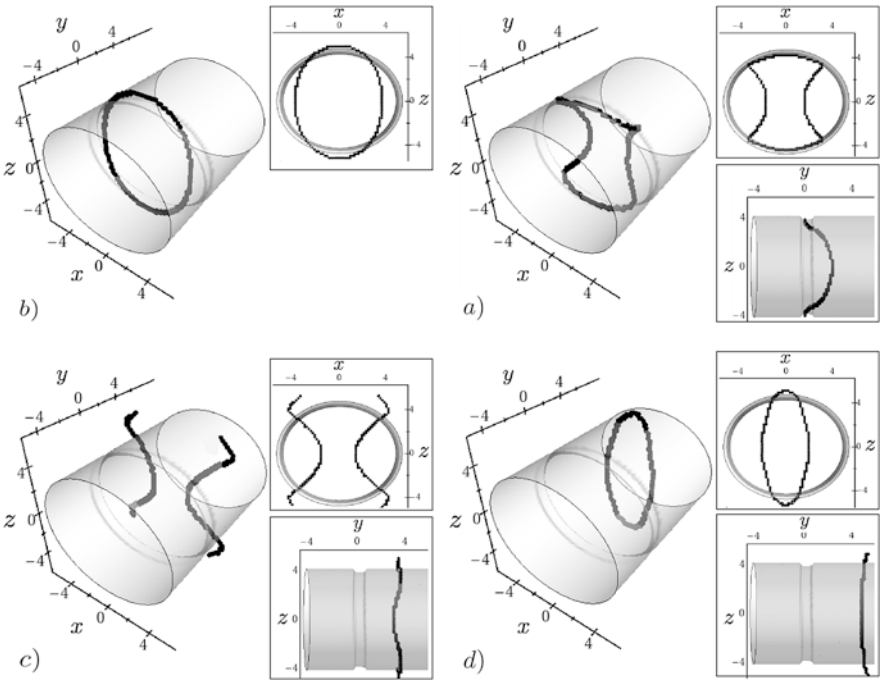

Fig. 12.11 Four subsequent stages of the vortex ring dynamics in the axially asymmetric waveguide. The *gray surface* indicates the position of the Thomas-Fermi surface of the condensate. *Black dots* show the position of the vortex cores. *Insets* show the front and side view. Here the waveguide is non-axially symmetric $\gamma = 1.2$, the initial flow velocity is $v = 1.05$, and the final barrier height is $V_s = 0.13\mu$. (**a**) A partially-ghost ring vortex has formed. (**b**) The ring vortex is strongly deformed. (**c**) The ring vortex has broken up leaving two vortex lines. (**d**) The vortex lines have joined back to form a new ring vortex

slowly with respect to the $\gamma = 1.2$ case, but the ring breaks up anyway, though at a later time.

We thus see how the partially real and partially ghost ring vortices which come into play due to the trapping asymmetry are unstable toward deformation and breaking, giving rise to a very rich phase slip dissipation dynamics.

12.4 Conclusions

In these chapter, we have seen that the excitations which show up above the critical velocity, when the superfluid is flowing through a weak link in two and three dimensions, are always vortices: inside the cloud there are cores of zero density around which the circulation is quantized. These cores are connected with each other to form lines ending at the boundaries of the system, or to form loops. The nature

and dynamics of these vortex structures are very rich, and dependent on the system geometry.

The phase slip instability studied here is a superfluid dissipation mechanism since, as already discussed; it subtracts energy from the flow of the superfluid. However, the GP equation does not include the dissipative processes which bring the system to thermal equilibrium. In a realistic situation, the vortices, carrying the energy subtracted from the superfluid, are supposed to eventually thermalize, with the result of heating the system. The role of finite temperature on the superfluid instability scenario presented here deserves further study.

We also showed that there exists a general criterion which determines the critical velocity for superfluid dissipation in one-, two-, and three-dimensional GP equation. Remarkably, we found that this criterion coincides with the local criterion coming from classical hydrodynamics only in one-dimension, and the latter fails to predict the critical velocity in two- and three-dimensional cases.

The study of the critical velocity for phase slip dissipation based on the mean-field Gross-Pitaevskii equation provides a simple theoretical model containing the fundamental ingredients for the understanding of general superfluidity properties. Moreover, the GPE dynamics is of direct (and quantitative) experimental relevance for ultracold atoms. In particular, the recent experiments with BECs in a toroidal geometry are mostly interesting since they provide an ideal setup both for testing models for superfluidity and also for building an ultracold atomic SQUID.

References

1. A. Aftalion, I. Danaila, Giant vortices in combined harmonic and quartic traps. Phys. Rev. A **69**(3), 033608 (2004)
2. A. Aftalion, Q. Du, Y. Pomeau, Dissipative flow and vortex shedding in the Painlevé boundary layer of a Bose-Einstein condensate. Phys. Rev. Lett. **91**(9), 090407 (2003)
3. P.W. Anderson, Considerations on the flow of superfluid helium. Rev. Mod. Phys. **38**(2), 298–310 (1966)
4. M. Benakli, S. Raghavan, A. Smerzi, S. Fantoni, S.R. Shenoy, Macroscopic angular-momentum states of Bose-Einstein condensates in toroidal traps. Europhys. Lett. **46**(3), 275–281 (1999)
5. N.G. Berloff, P.H. Roberts, Motions in a Bose condensate: X. new results on the stability of axisymmetric solitary waves of the Gross-Pitaevskii equation. J. Phys. A, Math. Gen. **37**(47), 11333 (2004)
6. F. Bloch, Superfluidity in a ring. Phys. Rev. A **7**(6), 2187–2191 (1973)
7. I. Carusotto, S.X. Hu, L.A. Collins, A. Smerzi, Bogoliubov-Čerenkov radiation in a Bose-Einstein condensate flowing against an obstacle. Phys. Rev. Lett. **97**(26), 260403 (2006)
8. P. Cladé, C. Ryu, A. Ramanathan, K. Helmerson, W.D. Phillips, Observation of a 2d Bose gas: From thermal to quasicondensate to superfluid. Phys. Rev. Lett. **102**(17), 170401 (2009)
9. L.A. Collins, J.D. Kress, R.B. Walker, Excitation and ionization of molecules by a single-mode laser field using a time-dependent approach. Comput. Phys. Commun. **114**(1-3), 15–26 (1998).
10. M. Cozzini, B. Jackson, S. Stringari, Vortex signatures in annular Bose-Einstein condensates. Phys. Rev. A **73**(1), 013603 (2006)
11. P. Engels, C. Atherton, Stationary and nonstationary fluid flow of a Bose-Einstein condensate through a penetrable barrier. Phys. Rev. Lett. **99**(16), 160405 (2007)

12. C.J. Foster, P.B. Blakie, M.J. Davis, Vortex pairing in two-dimensional Bose gases. Phys. Rev. A **81**(2), 023623 (2010)
13. T. Frisch, Y. Pomeau, S. Rica, Transition to dissipation in a model of superflow. Phys. Rev. Lett. **69**(11), 1644–1647 (1992)
14. V. Hakim, Nonlinear Schrödinger flow past an obstacle in one dimension. Phys. Rev. E **55**(3), 2835–2845 (1997)
15. E. Hoskinson, Y. Sato, I. Hahn, R.E. Packard, Transition from phase slips to the Josephson effect in a superfluid ^{4}He weak link. Nat. Phys. **2**, 23–26 (2006)
16. S. Inouye, S. Gupta, T. Rosenband, A.P. Chikkatur, A. Görlitz, T.L. Gustavson, A.E. Leanhardt, D.E. Pritchard, W. Ketterle, Observation of vortex phase singularities in Bose-Einstein condensates. Phys. Rev. Lett. **87**(8), 080402 (2001)
17. B. Jackson, J.F. McCann, C.S. Adams, Vortex formation in dilute inhomogeneous Bose-Einstein condensates. Phys. Rev. Lett. **80**(18), 3903–3906 (1998)
18. C.A. Jones, P.H. Roberts, Motions in a Bose condensate. IV. Axisymmetric solitary waves. J. Phys. A, Math. Gen. **15**(8), 2599 (1982)
19. C.A. Jones, S.J. Putterman, P.H. Roberts, Motions in a Bose condensate. V. Stability of solitary wave solutions of non-linear Schrödinger equations in two and three dimensions. J. Phys. A, Math. Gen. **19**(15), 2991 (1986)
20. V.V. Konotop, L. Pitaevskii, Landau dynamics of a grey soliton in a trapped condensate. Phys. Rev. Lett. **93**(24), 240403 (2004)
21. L.D. Landau, E.M. Lifshitz, *Fluid Mechanics* (Pergamon, Oxford, 1987)
22. A.J. Leggett, Bose-Einstein condensation in the alkali gases: Some fundamental concepts. Rev. Mod. Phys. **73**(2), 307–356 (2001)
23. A.M. Leszczyszyn, G.A. El, Y.G. Gladush, A.M. Kamchatnov, Transcritical flow of a Bose-Einstein condensate through a penetrable barrier. Phys. Rev. A **79**(6), 063608 (2009)
24. W.A. Little, Decay of persistent currents in small superconductors. Phys. Rev. **156**(2), 396–403 (1967)
25. J.-P. Martikainen, K.-A. Suominen, L. Santos, T. Schulte, A. Sanpera, Generation and evolution of vortex-antivortex pairs in Bose-Einstein condensates. Phys. Rev. A **64**(6), 063602 (2001)
26. P. Mason, N.G. Berloff, Dynamics of quantum vortices in a toroidal trap. Phys. Rev. A **79**(4), 043620 (2009)
27. H.M. Nilsen, G. Baym, C.J. Pethick, Velocity of vortices in inhomogeneous Bose-Einstein condensates. Proc. Natl. Acad. Sci. **103**(21), 7978–7981 (2006)
28. R. Onofrio, C. Raman, J.M. Vogels, J.R. Abo-Shaeer, A.P. Chikkatur, W. Ketterle, Observation of superfluid flow in a Bose-Einstein condensed gas. Phys. Rev. Lett. **85**(11), 2228–2231 (2000)
29. N. Pavloff, Breakdown of superfluidity of an atom laser past an obstacle. Phys. Rev. A **66**(1), 013610 (2002)
30. C.-T. Pham, C. Nore, M.-É. Brachet, Boundary layers and emitted excitations in nonlinear Schrödinger superflow past a disk. Phys. D, Nonlinear Phenom. **210**(3–4), 203–226 (2005)
31. F. Piazza, L.A. Collins, A. Smerzi, Vortex-induced phase-slip dissipation in a toroidal Bose-Einstein condensate flowing through a barrier. Phys. Rev. A **80**(2), 021601 (2009)
32. F. Piazza, L.A. Collins, A. Smerzi, Instability and vortex ring dynamics in a three-dimensional superfluid flow through a constriction. New J. Phys. **13**(4), 043008 (2011)
33. E.P. Pitaevskii, Nuovo Cimento **20**, 454 (1961)
34. L.P. Pitaevskii, Sov. Phys. JETP **13**, 451 (1961)
35. L.P. Pitaevskii, S. Stringari, *Bose-Einstein Condensation* (Oxford University Press, Oxford, 2003)
36. A. Ramanathan, K.C. Wright, S.R. Muniz, M. Zelan, W.T. Hill, C.J. Lobb, K. Helmerson, W.D. Phillips, G.K. Campbell, Superflow in a toroidal Bose-Einstein condensate: An atom circuit with a tunable weak link. Phys. Rev. Lett. **106**(13), 130401 (2011)
37. C. Ryu, M.F. Andersen, P. Cladé, V. Natarajan, K. Helmerson, W.D. Phillips, Observation of persistent flow of a Bose-Einstein condensate in a toroidal trap. Phys. Rev. Lett. **99**(26), 260401 (2007)

38. B.I. Schneider, L.A. Collins, S.X. Hu, Parallel solver for the time-dependent linear and nonlinear Schrödinger equation. Phys. Rev. E **73**(3), 036708 (2006)
39. I. Shomroni, E. Lahoud, S. Levy, J. Steinhauer, Evidence for an oscillating soliton/vortex ring by density engineering of a Bose-Einstein condensate. Nat. Phys. **5**, 193–197 (2009)
40. T.P. Simula, N. Nygaard, S.X. Hu, L.A. Collins, B.I. Schneider, K. Mølmer, Angular momentum exchange between coherent light and matter fields. Phys. Rev. A **77**(1), 015401 (2008)
41. M. Stone, A.M. Srivastava, Boundary layer separation and vortex creation in superflow through small orifices. J. Low Temp. Phys. **102**, 445–459 (1996). doi:10.1007/BF00755123
42. J. Tempere, J.T. Devreese, E.R.I. Abraham, Vortices in Bose-Einstein condensates confined in a multiply connected Laguerre-Gaussian optical trap. Phys. Rev. A **64**(2), 023603 (2001)
43. M. Tsubota, K. Kasamatsu, M. Ueda, Vortex lattice formation in a rotating Bose-Einstein condensate. Phys. Rev. A **65**(2), 023603 (2002)
44. W.F. Vinen, J.J. Niemela, Quantum turbulence. J. Low Temp. Phys. **128**, 167–231 (2002). doi:10.1023/A:1019695418590
45. G. Watanabe, F. Dalfovo, F. Piazza, L.P. Pitaevskii, S. Stringari, Critical velocity of superfluid flow through single-barrier and periodic potentials. Phys. Rev. A **80**(5), 053602 (2009)
46. T. Winiecki, B. Jackson, J.F. McCann, C.S. Adams, Vortex shedding and drag in dilute Bose-Einstein condensates. J. Phys. B, At. Mol. Opt. Phys. **33**(19), 4069 (2000)
47. E. Zaremba, Sound propagation in a cylindrical Bose-Condensed gas. Phys. Rev. A **57**(1), 518–521 (1998)

Chapter 13
Quantized Vortices and Quantum Turbulence

Makoto Tsubota and Kenichi Kasamatsu

Abstract We review recent important topics in quantized vortices and quantum turbulence in atomic Bose–Einstein condensates (BECs). They have previously been studied for a long time in superfluid helium. Quantum turbulence is currently one of the most important topics in low-temperature physics. Atomic BECs have two distinct advantages over liquid helium for investigating such topics: quantized vortices can be directly visualized and the interaction parameters can be controlled by the Feshbach resonance. A general introduction is followed by a description of the dynamics of quantized vortices, hydrodynamic instability, and quantum turbulence in atomic BECs.

13.1 Introduction

Bose–Einstein condensation is often considered to be a macroscopic quantum phenomenon because bosons occupy the same single-particle ground state below the critical temperature for Bose–Einstein condensation so that they have a macroscopic wave function (order parameter) $\Psi(\boldsymbol{r}, t) = |\Psi(\boldsymbol{r}, t)|e^{i\theta(\boldsymbol{r},t)}$ that extends over the entire system. Here, the absolute squared amplitude $|\Psi|^2 = n$ gives the condensate density and the gradient of the phase $\theta(\boldsymbol{r}, t)$ gives the superfluid velocity field $\boldsymbol{v}_s = (\hbar/m)\nabla\theta$ with boson mass m as the potential flow. Since the macroscopic wave function should be single-valued for the space coordinate $\boldsymbol{r}$, the circulation $\Gamma = \oint \boldsymbol{v}_s \cdot d\boldsymbol{\ell}$ for an arbitrary closed loop in the fluid will be quantized with the quantum $\kappa = h/m$. A vortex with such quantized circulation is known as a quantized vortex. Any rotational motion of a superfluid is sustained only by quantized vortices. Hydrodynamics dominated by quantized vortices is called *quantum hy-*

M. Tsubota (✉)
Department of Physics, Osaka City University, Osaka, Japan
e-mail: tsubota@sci.osaka-cu.ac.jp

K. Kasamatsu
Department of Physics, Kinki University, Higashi-Osaka, Japan
e-mail: kenichi@phys.kindai.ac.jp

A. Bramati, M. Modugno (eds.), *Physics of Quantum Fluids*,
Springer Series in Solid-State Sciences 177, DOI 10.1007/978-3-642-37569-9_13,

drodynamics (QHD), and turbulence comprised of quantized vortices is known as *quantum turbulence* (QT).

A quantized vortex is a stable topological defect that is a characteristic of a Bose–Einstein condensate (BEC). It differs from a vortex in a classical viscous fluid in the following three ways. First, unlike a classical vortex that can have an arbitrary circulation, the circulation of a quantized vortex is quantized. Second, since a quantized vortex is a vortex of inviscid superflow it cannot decay by viscous diffusion of vorticity, which occurs in classical fluids. Third, the core of a quantized vortex is very thin, being of the order of the coherence length (i.e., only a few angstroms in superfluid ^{4}He and submicrometer in atomic BECs). Since the vortex core is very thin and does not decay by diffusion, the position of a quantized vortex in the fluid can always be identified.

Since any rotational motion of a superfluid is sustained by quantized vortices, QT usually takes the form of a disordered tangle of quantized vortices. QT is currently the most important research topic in QHD, which is an area in the field of low-temperature physics. The turbulence in a classical fluid, which is known as classical turbulence (CT), has been extensively studied in a number of fields, but it is still not well understood [1]. This is mainly because turbulence is a complicated dynamical phenomenon that is highly nonlinear. Vortices may represent the key for understanding turbulence, but they are not well defined for a classical viscous fluid. They are unstable and appear and disappear repeatedly. The circulation is not conserved and varies between vortices. Comparison of QT and CT reveals definite differences, which demonstrates the importance of studying QT. QT consists of a tangle of quantized vortices that have the same conserved circulation. Thus, QT can be easier to study than CT and it offers a much simpler model of turbulence than CT.

Quantized vortices and QT have historically been studied in superfluid helium. However, the realization of Bose–Einstein condensation in trapped atomic gases in 1995 provided another important system for studying quantized vortices and QT. The existence of superfluidity has been confirmed by creating and observing quantized vortices in atomic BECs and a lot of effort has been devoted to studying lots of fascinating problems. Atomic BECs have several advantages over superfluid helium, the most important being that modern optical techniques can be used to directly control their properties and to visualize quantized vortices.

In a weakly interacting Bose system at zero temperature, the macroscopic wave function $\Psi(\boldsymbol{r}, t)$ obeys the Gross–Pitaevskii (GP) equation [2, 3]:

$$i\hbar\frac{\partial\Psi(\boldsymbol{r},t)}{\partial t} = \left(-\frac{\hbar^2}{2m}\nabla^2 + U(\boldsymbol{r}) + g\left|\Psi(\boldsymbol{r},t)\right|^2 - \mu\right)\Psi(\boldsymbol{r},t). \tag{13.1}$$

Here, $U(\boldsymbol{r})$ represents the external potential (trapping potential, obstacle potential, etc.), $g = 4\pi\hbar^2 a/m$ denotes the strength of the interaction characterized by the s-wave scattering length a, and μ is the chemical potential. The only characteristic length scale of the GP model is the coherence length. It is defined by $\xi = \hbar/(\sqrt{2mg}|\Psi|)$ and gives the vortex core size. The GP equation has been used to interpret many properties of BECs in a dilute atomic gas [4, 5]. It can explain both vortex dynamics and vortex core phenomena, such as reconnection and nucleation.

This chapter is organized as follows. Section 13.2 describes the dynamics of quantized vortices. It is very difficult to directly observe their dynamics in superfluid ^{4}He and ^{3}He, which is one important advantage of atomic BECs over superfluid helium. In Sect. 13.3, we discuss hydrodynamic instability and QT in atomic BECs. The last section presents the conclusions.

13.2 Dynamics of Quantized Vortices

Since the realization of atomic BECs, many researchers have formed vortices by stirring a condensate or phase engineering. The details of these studies have been reviewed in other articles [6, 7]. This chapter describes some recent contributions to this topic.

13.2.1 Dynamics of a Single Vortex and Vortex Dipoles

To gain insight into diverse superfluid phenomena, it is essential to understand the dynamics of a single vortex or vortex dipoles (i.e., vortex–antivortex pairs). A few important observations have recently been made. Neely et al. nucleated vortex dipoles in an oblate BEC by forcing superfluid flow around a repulsive Gaussian obstacle generated by a focused blue-detuned laser beam [8]. The nucleated vortex dipole propagates in a BEC cloud for many seconds; its continuous trajectory was found to be consistent with a numerical simulation of the GP model. Freilich et al. observed the real-time dynamics of vortices by repeatedly extracting, expanding, and imaging small fractions of the condensate to visualize the motion of the vortex cores [9]. They nucleated vortices via the Kibble–Zurek mechanism [10, 11] in which rapid quenching of a cold thermal gas through the BEC phase transition causes topological defects to nucleate [12]. This produces single-vortex precesses in the cloud, whose frequency is in good agreement with a simple theoretical analysis [13]. Freilich et al. also nucleated vortex dipoles and observed their real-time dynamics. This new technique enables quantitative comparisons to be performed between experiment and theory for vortex dynamics [14, 15].

Vortex dipole generation has been investigated theoretically and numerically in some recent studies based on the GP model. Sasaki et al. studied vortex shedding from an obstacle potential moving in a uniform BEC [16]. The flow around the obstacle is laminar when the velocity of the potential is sufficiently low. When the velocity exceeds a critical velocity of the order of the sound velocity, the potential commences to emit vortex trains. The manner in which vortices are emitted depends on the velocity and the width of the potential. The first pattern is the emission of the alternately inclined vortex pairs in a V-shaped wake, as shown in Fig. 13.1(a). The second pattern is produced by sequential shedding of two vortices having the same circulation. The two vortices rotate about their center without varying their separation, forming a train of vortices similar to a Bénard–von Kármán vortex street, as

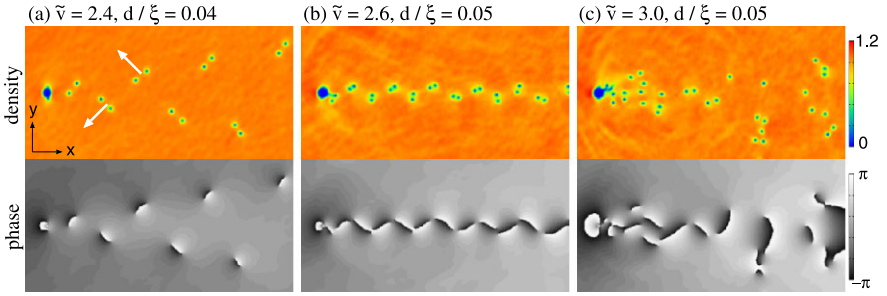

Fig. 13.1 Density and phase distributions of a condensate past an obstacle potential. The velocity and potential width are (**a**) $(\tilde{v}, d/\xi) = (2.4, 0.04)$, (**b**) $(2.6, 0.05)$, and (**c**) $(3.0, 0.05)$, where $\tilde{v} = v(10^3 m/gn_0)^{1/2}$ and $\xi = \hbar(10^3/(mgn_0))^{1/2}$ with n_0 the atom density without perturbation. The *white arrows* in (**a**) indicate the directions in which the vortex pairs move. The field of view is $6\xi \times 3\xi$. [Sasaki, Suzuki and Saito: Phys. Rev. Lett. **104**, 150404 (2010), reproduced with permission. Copyright 2010 by the American Physical Society]

shown in Fig. 13.1(b). For a wide potential with a high velocity, the periodicity disappears, as shown in Fig. 13.1(c). Aioi et al. subsequently proposed controlled generation and manipulation of vortex dipoles by using several Gaussian beams from a red (attractive potential) or blue (repulsive potential) detuned laser [17]. For example, when a red-detuned beam moves through a BEC cloud above a critical velocity, a vortex dipole nucleates at the head of the potential. In contrast, a blue-detuned beam generates vortex dipoles on both sides of the potential. Double beams can generate various kinds of dipole wakes depending on the velocity and the distance of the two beams. The trajectory of emitted vortices can be modified by another potential.

13.2.2 Dynamics of Vortices Generated by an Oscillating Obstacle Potential

Recently, in the field of superfluid ^{4}He and ^{3}He, several groups have experimentally studied QT generated by oscillating structures such as wires, spheres, and grids [18]. Despite significant differences between the structures used, their responses with respect to the alternating drive have revealed some surprising common phenomena. The response was laminar at low driving rates, whereas it became turbulent at high driving rates.

This strategy can also be applied to trapped atomic BECs. Fujimoto and Tsubota numerically investigated the two-dimensional dynamics of trapped BECs induced by an oscillating repulsive Gaussian potential [19, 20] and found a strong dependence on the amplitude and frequency of the potential. Unlike a potential with constant velocity [16], an oscillating potential continually sheds vortex pairs with alternating impulses, a typical example of which is shown in Fig. 13.2. The nucleated pairs form new vortex pairs through reconnections that move away from the obstacle potential and toward the condensate surface. The BEC cloud eventually

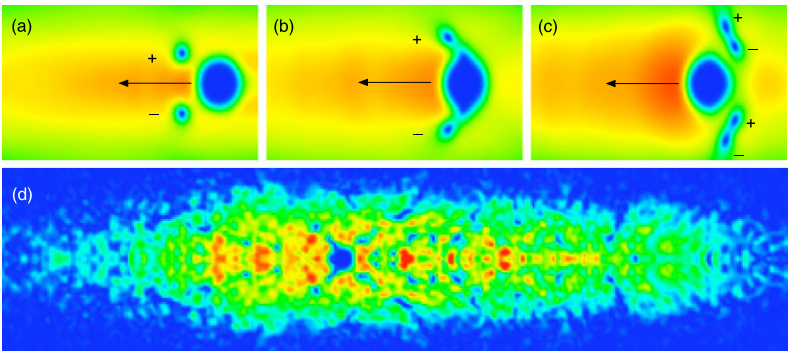

Fig. 13.2 Reconnection of vortex pairs about an oscillating potential. The symbols − and + indicate vortices with clockwise and counterclockwise circulations, respectively. The *black arrows* indicate the direction in which the potential moves. The horizontal and vertical dimensions of (**a**), (**b**) and (**c**) are 27.0 and 14.0 micrometer, while those of (**d**) are 145 and 34.0 micrometer. When the potential moves to the right, it generates a vortex pair with an impulse in the same direction as the potential. When the potential (**a**) ($t = 31.4$ ms) changes direction and moves to the left, (**b**) ($t = 38.3$ ms) it collides with the pair and (**c**) ($t = 43.2$ ms) emits another pair. These two pairs reconnect to form new pairs that move away from the potential. (**d**) The BEC cloud eventually becomes filled with such vortices. [Fujimoto and Tsubota: Phys. Rev. A **83**, 053609 (2011), reproduced with permission. Copyright 2011 by the American Physical Society]

becomes full with such vortices, as shown in Fig. 13.2(d). An oscillating potential is thus a useful tool for generating QT in a trapped BEC.

13.2.3 Kelvin Wave Dynamics

Kelvin waves are three-dimensional excitations along a vortex line. Kelvin waves play an important role in dissipation in superfluid helium at very low temperatures in which the normal fluid component is negligible [21]. Kelvin waves have been experimentally demonstrated in a trapped BEC [22] by exciting a collective quadrupole mode to a single-vortex state that subsequently decays to Kelvin modes by a nonlinear Beliaev process. This was supported by numerical analysis based on the Bogoliubov–de Gennes equation [23] and the GP equation [24]. Rooney et al. recently studied the dynamics of Kelvin waves using the stochastic projected GP equation [25]. They showed that Kelvin waves can be suppressed by tightening the confinement of the trap along the vortex line, which drastically reduces the vortex decay rate as the system becomes two-dimensional. This behavior is consistent with observations of the decay of vortex dipoles [8].

13.3 Hydrodynamic Instability and Quantum Turbulence

Some theoretical ideas for achieving QT in trapped BECs have been proposed. The turbulent state may be generated during the formation of a condensate from

a nonequilibrium non-condensed Bose gas by rapid quenching [26]. Conversely, turbulence is expected to be generated during the *destruction* process from the equilibrium condensed state. This subsection describes recent studies on hydrodynamic instability and the resulting nonlinear dynamics that may lead to QT. These instabilities are formed by applying an external driving force to condensates or by complicated interactive phenomena between multicomponent BECs (some of which are analogs of well-known phenomena in classical hydrodynamics).

13.3.1 Methods to Produce Turbulence in Trapped BECs

A major problem when investigating QT in atomic BECs is the difficulty in applying a dc velocity field in superfluid helium. Here, we summarize some proposals for and a recent experimental realization of QT generation in a trapped single-component BEC.

Simple Rotation An important way for generating vortices in trapped BECs is to rotate the external potential [27–29]. However, rotation alone cannot lead to QT because it generates an ordered vortex lattice along the rotational axis [30], which is the equilibrium state in the corresponding rotating frame. Nevertheless, Parker and Adams suggested the emergence and decay of turbulence in a BEC under a simple rotation, starting from a vortex-free equilibrium BEC [31]. A numerical simulation based on the energy-conserving GP equation suggests the existence of a turbulent regime that contains many vortices and high-energy-density fluctuations (sound field) on a route to the ordered vortex lattice.

Two-Axis Rotation Since the above turbulence is generated during the ordering process, it is not steady turbulence. Kobayashi and Tsubota suggested performing rotations about two axes [32], as shown in Fig. 13.3(a). When the spinning and precessing rotational axes are perpendicular, the two rotations do not commute and thus cannot be represented by their sum. This situation can be modeled by simulations based on the GP equation:

$$i\hbar\frac{\partial\Psi}{\partial t} = \left(-\frac{\hbar\nabla^2}{2m} + U + g|\Psi|^2 - \boldsymbol{\Omega}\cdot\boldsymbol{L}\right)\Psi, \tag{13.2}$$

where $\boldsymbol{L}$ is the angular momentum and the rotation vector is written as $\boldsymbol{\Omega}(t) = (\Omega_x, \Omega_z \sin\Omega_x t, \Omega_z \cos\Omega_x t)$ with frequencies of Ω_z and Ω_x for the first and second rotations, respectively. The inclusion of these non-commuting rotations and phenomenological dissipation which is effective only at scales smaller than the healing length successfully generate steady turbulence [32].

Donnelly–Glaberson Instability When both rotation and a linear velocity are applied to the system, the right-hand side of the GP equation (13.2) will have the term $-\boldsymbol{V}\cdot\boldsymbol{p}$ in the corresponding *helically* moving frame. For $\boldsymbol{V} = V\hat{\boldsymbol{z}}$ the dispersion

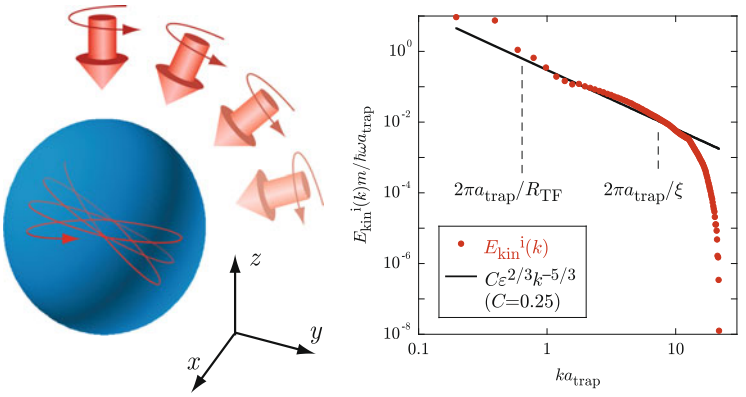

Fig. 13.3 QT in atomic BECs. (**a**) A method for realizing steady turbulence in an atomic BEC subject to precession. A BEC is trapped in a weakly elliptical harmonic potential. A rotation is applied along the z-axis followed by a rotation along the x-axis. (**b**) Energy spectrum of steady QT obtained by two-axis rotation. The *dots* represent the numerically obtained spectrum for an incompressible kinetic energy, while the *solid line* is the Kolmogorov spectrum. Here, $R_{\rm TF}$ is the Thomas–Fermi radius and $a_{\rm trap} = \sqrt{\hbar/m\omega}$ is the characteristic length scale of the trap [Kobayashi and Tsubota: Phys. Rev. A **76**, 045603 (2007), reproduced with permission. Copyright 2007 by the American Physical Society]

of the vortex waves (Kelvin waves) on a straight vortex line parallel to the z-axis behaves as $\omega - Vk_z$ and its frequency will become negative above a certain critical velocity. This is known as the Donnelly–Glaberson instability in superfluid helium and it amplifies Kelvin waves [33]. If the rotating BEC contains a vortex lattice, the amplified Kelvin wave induces reconnections of adjoining vortex lines, eventually leading to a turbulent state [34].

Combined Rotation and Oscillating Excitation As a method that enables better control of turbulence, Henn et al. introduced an external oscillatory potential to an ^{87}Rb BEC [35, 36]. This oscillatory field induced a successive coherent mode excitation in a BEC. They observed that increasing the amplitude of the oscillating field and the excitation period increased the number of vortices and eventually lead to the turbulent state [36]. In the turbulent regime, they observed a rapid increase in the number of vortices followed by proliferation of vortex lines in all directions, where many vortices with no preferred orientation formed a vortex tangle. The oscillatory excitation (which mainly consists of oscillation, rotation, and deformation) nucleated vortices. However, it is still not known theoretically how the turbulence is generated.

13.3.2 Signature of Quantum Turbulence

It is important to determine whether the highly excited state is really QT. Several methods are used to identify the turbulent state; they are discussed in this subsection.

In most numerical simulations, apart from observing a random configuration of vortices, the turbulent regime has been identified by checking if its incompressible kinetic energy spectrum obeys Kolmogorov's $-5/3$ law [1]. When the condensate wave function is written in the form $\Psi(\boldsymbol{r},t)=\sqrt{n(\boldsymbol{r},t)}e^{i\theta(\boldsymbol{r},t)}$, the kinetic energy is expressed by the sum $E_{\rm kin}=E_k+E_q$, where $E_k=(\hbar^2/2m)\int d\boldsymbol{r}|\sqrt{n}\nabla\theta|^2$ denotes the superfluid kinetic energy and $E_q=(\hbar^2/2m)\int d\boldsymbol{r}|\nabla\sqrt{n}|^2$ is the quantum pressure energy. The vector field $\sqrt{n}\nabla\theta$ can be divided into incompressible (solenoidal) and compressible (irrotational) components: $\sqrt{n}\nabla\theta=(\sqrt{n}\nabla\theta)^i+(\sqrt{n}\nabla\theta)^c$, where $\nabla\cdot(\sqrt{n}\nabla\theta)^i=0$ and $\nabla\times(\sqrt{n}\nabla\theta)^c=0$. Thus, the incompressible and compressible kinetic energies are defined by $E_k^{i,c}=(\hbar^2/2m)\int d\boldsymbol{r}|(\sqrt{n}\nabla\theta)^{i,c}|^2$. They correspond to the kinetic energies in the vortices and the sound waves, respectively. Since the compressible and incompressible fields are mutually orthogonal, it follows that $E_k=E_k^i+E_k^c$. The kinetic energy spectrum as a function of wave number k is defined by

$$\epsilon_k^{i,c}(k)=\frac{\hbar^2}{2m}\int k^2\sin\theta d\theta d\phi\left|\int e^{i\boldsymbol{k}\cdot\boldsymbol{r}}(\sqrt{n}\nabla\theta)^{i,c}\frac{d\boldsymbol{r}}{(2\pi)^3}\right|, \tag{13.3}$$

such that $E_k^{i,c}=\int_0^\infty\epsilon_k^{i,c}(k)dk$. The Kolmogorov law states that the incompressible energy spectrum obeys the power law $\epsilon_k^i(k)\sim k^\nu$ where $\nu=-5/3$ over the inertial range of k. For a trapped BEC, the inertial range that follows the Kolmogorov law is determined by the Thomas–Fermi radius $R_{\rm TF}$ and the coherence length $\xi=\hbar/2m\mu$ [32] [see the right panel of Fig. 13.3].

The structure of QT is reflected in the time dependence of the decay of the total vortex line density L after turning off the excitation that sustains the turbulence. Correlations of vortex tangles can be classified into two kinds [37]: correlated and uncorrelated tangles. In a correlated tangle, turbulent energy is concentrated in the "classical" length scale range that is larger than the intervortex distance l, where the correlated tangle exhibits a Kolmogorov spectrum. The energy is then transferred to smaller scales by a Richardson cascade and L decays as $t^{-3/2}$. In an uncorrelated tangle, the turbulent energy is associated with a random vortex tangle with spacing l and it is concentrated in the "quantum" range of length scales smaller than l. Then, L decays as t^{-1}. Thus, observing the scaling behavior of L on t provides useful information about QT.

In addition, White et al. [38] showed that QT is characterized by a power-law behavior of the probability density function of the velocity field $\boldsymbol{v}_s(\boldsymbol{r})=(\hbar/m)\nabla\theta(\boldsymbol{r})$, whereas classical turbulence obeys Gaussian velocity statistics. This non-Gaussian behavior originates from the singular nature of a quantized vorticity with a $1/r$ velocity field, which appears in the high-velocity region determined by the intervortex distance $v\sim\kappa/\pi l$ [39].

It is difficult to measure the above statistical or scaling properties experimentally. Henn et al. observed another remarkable feature of turbulent condensates: suppression of aspect ratio inversion during free expansion after turning the trapping potential off [36]. Despite the asymmetric expansion (from a cigar shape to a pancake

shape) of a conventional BEC or isotropic expansion of a thermal cloud, the turbulent state exhibited a self-similar expansion that preserved the initial aspect ratio. Although a quantitative theoretical understanding of this effect has yet to be fully realized [40], it represents a remarkable new effect in the turbulent regime.

13.3.3 Hydrodynamic Instability in Multicomponent BECs

Multicomponent atomic BECs can be created in cold-atom systems with, for example, multiple hyperfine spin states or a mixture of different atomic species. Such systems yield a rich variety of superfluid dynamics due to the intercomponent interaction. Two-component BECs are the simplest multicomponent system. Schweikhard et al. experimentally investigated the vortex-lattice dynamics of two interacting and rotating condensates by transferring some of the initial population of ^{87}Rb BECs with a vortex lattice to its other hyperfine state via a coupling pulse [41]. They observed the ordering dynamics change from a triangular lattice structure to a stable square lattice through the transient turbulent regime.

Recent experimental advances have provided more controllable ways to study the rich dynamics of two-component BECs. External potentials can be prepared that can act independently on both components; this enables initial conditions to be prepared that are suitable for studying a particular problem. In addition, the intra- and inter-component interactions can be tuned with the help of the Feshbach resonance [42–44]. This allows phase separation to be performed and interface phenomena between two superfluids to be studied in a well-controlled manner.

In the mean-field theory, a two-component BEC is described by macroscopic wave functions Ψ_i, where the subscript i refers to each component ($i = 1, 2$). The Lagrangian for this system is given by

$$L = \int d\boldsymbol{r}\left(P_1 + P_2 - g_{12}|\Psi_1|^2|\Psi_2|^2\right), \tag{13.4}$$

where

$$P_i = i\hbar\Psi_i^* \frac{\partial \Psi_i}{\partial t} + \frac{\hbar^2}{2m_i}\Psi_i^* \nabla^2 \Psi_i - U_i|\Psi_i|^2 - \frac{g_{ii}}{2}|\Psi_i|^4 \tag{13.5}$$

with m_i and U_i being the atomic mass and the external potential of the ith component, respectively. The intra- and inter-component interaction parameters have the form

$$g_{ij} = 2\pi\hbar^2 a_{ij}\left(m_i^{-1} + m_j^{-1}\right), \tag{13.6}$$

where a_{ij} is the s-wave scattering length between the ith and jth components; we assume $a_{ij} > 0$ in the following. For homogeneous condensates, the condensates are miscible and immiscible when $g_{11}g_{22} > g_{12}^2$ and $g_{11}g_{22} < g_{12}^2$, respectively. Below, we review the characteristic hydrodynamic instability that occurs in each condition.

13.3.3.1 Counter-Superflow Instability

When two-component BECs coexist with a relative velocity, they exhibit dynamic instability above a critical relative velocity [45]. This phenomenon is known as a counter-*superflow* instability (CSI). Takeuchi et al. suggested that the nonlinear dynamics triggered by the CSI generates a binary QT composed of coreless vortices and that thus has a continuous velocity field [46, 47]. Hamner et al. realized the CSI experimentally for quasi-1D geometry and observed the generation of shock waves and dark–bright solitons [48].

The CSI can be understood from the Bogoliubov spectrum for a system of a uniform two-component BEC with a relative velocity [45]. The functional derivative of $\int dt L$, where L is the Lagrangian in (13.4), with respect to Ψ_i^* gives the GP equation,

$$i\hbar\frac{\partial\Psi_i}{\partial t} = \left(-\frac{\hbar^2}{2m_i}\nabla^2 + \sum_{j=1,2} g_{ij}|\Psi_j|^2\right)\Psi_i. \tag{13.7}$$

In this subsection, we assume $U_i = 0$ and the miscible condition $g_{11}g_{22} > g_{12}^2$. The wave functions $\Psi_i = \Psi_{i0}$ in a stationary state can be written as

$$\Psi_{i0} = \sqrt{n_{i0}}e^{i(m_i \boldsymbol{V}_i\cdot\boldsymbol{r}-\mu_i t)/\hbar} \tag{13.8}$$

with the velocity $\boldsymbol{V}_i$ and the chemical potential μ_i of the ith component. Counter superflow occurs when $\boldsymbol{V}_1 \neq \boldsymbol{V}_2$. We consider a small excitation above the stationary state as $\Psi_i = \Psi_{i0} + \delta\Psi_i$, where we write the excitation of the wave functions $\delta\Psi_i$ in the form

$$\delta\Psi_i = e^{i(m_i \boldsymbol{V}_i\cdot\boldsymbol{r}-\mu_i t)/\hbar}\left[u_i e^{i(\boldsymbol{k}\cdot\boldsymbol{r}-\omega t)} - v_i^* e^{-i(\boldsymbol{k}\cdot\boldsymbol{r}-\omega t)}\right]. \tag{13.9}$$

By linearizing the GP equation (13.7) with respect to $\delta\Psi_i$, we obtain the Bogoliubov–de Gennes equations ($i \neq j$):

$$\left(\frac{\hbar^2k^2}{2m_i} + \hbar\boldsymbol{k}\cdot\boldsymbol{V}_i + g_{ii}n_{i0}\right)u_i - g_{ii}n_{i0}v_i + g_{ij}\sqrt{n_{i0}n_{j0}}(u_j - v_j) = \hbar\omega u_i, \tag{13.10}$$

$$\left(\frac{\hbar^2k^2}{2m_i} - \hbar\boldsymbol{k}\cdot\boldsymbol{V}_i + g_{ii}n_{i0}\right)v_i - g_{ii}n_{i0}u_i - g_{ij}\sqrt{n_{i0}n_{j0}}(u_j - v_j) = -\hbar\omega v_i. \tag{13.11}$$

Diagonalizing the eigenvalue equations (13.10) and (13.11), we obtain the Bogoliubov excitation spectrum. For simplicity, we set $m_1 = m_2 \equiv m$, $g_{11} = g_{22} \equiv g$, and $n_{10} = n_{20} \equiv n_0$, and neglect the center-of-mass velocity of the two condensates. The eigenvalue of (13.10) and (13.11) then has the simple form:

$$\hbar^2\omega^2 = \epsilon^2 + \frac{1}{4}\hbar^2k_{||}^2V_R^2 \pm \sqrt{\epsilon^2\hbar^2k_{||}^2V_R^2 + 4g_{12}^2n_0^2\epsilon_0^2}, \tag{13.12}$$

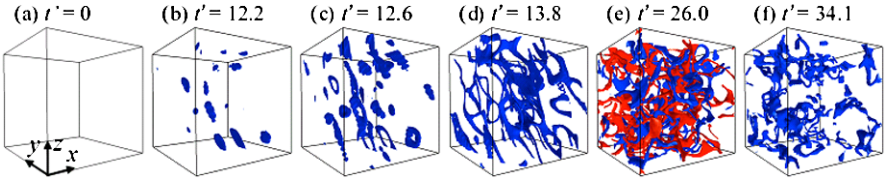

Fig. 13.4 Characteristic nonlinear dynamics of CSI of two-component BECs. The parameters are set to $m_1 = m_2 = m$, $g_{11} = g_{22} = g$, and $g_{12} = 0.9g$, similar to those in experiments. In the numerical simulation, the initial state is prepared by adding small random noise to the stationary wave function Ψ_{i0} with $n_{10} = n_{20} = n_0$ and $\boldsymbol{V}_1 = -\boldsymbol{V}_2$. The panels show the time development of low-density isosurfaces with $n_1(\boldsymbol{r}) = 0.05n_0$ for $\boldsymbol{V}_1 = \frac{1}{2}V_R\hat{\boldsymbol{x}}$. Because of the symmetric parameter setting, the second component behaves in a similar manner to the first component (not shown) [Takeuchi et al.: Phys. Rev. Lett. **105**, 205301 (2010), reproduced with permission. Copyright 2010 by the American Physical Society]

where $\boldsymbol{V}_R = \boldsymbol{V}_1 - \boldsymbol{V}_2$ is the relative velocity and we denote $\epsilon^2 = \epsilon_0(\epsilon_0 + 2gn_0)$, $\epsilon_0 = \hbar^2k^2/2m$, and $k^2 = k_{||}^2 + k_\perp^2$ with $k_{||} = (\boldsymbol{k}\cdot\boldsymbol{V}_R)/V_R$ and $k_\perp \geq 0$. The system is dynamically unstable when the excitation frequency ω becomes imaginary (i.e., $\omega^2 < 0$), which reduces to $\epsilon_- < \hbar k_{||}V_R/2 < \epsilon_+$ with $\epsilon_\pm = \sqrt{\epsilon_0[\epsilon_0 + 2(g \pm g_{12})n_0]}$. This inequality determines the unstable region in wavenumber space $(k_{||}, k_\perp)$, where V_R exceeds the critical relative velocity $V_c = V_-$ with $V_\pm = 2\sqrt{gn_0/m}\sqrt{1 \pm g_{12}/g}$. The total momentum density $\delta\boldsymbol{J}$ carried by the excitation can be defined as $\delta\boldsymbol{J} = \delta\boldsymbol{J}_1 + \delta\boldsymbol{J}_2$ with a change in the momentum density $\delta\boldsymbol{J}_j \equiv \hbar\boldsymbol{k}(|u_i|^2 - |v_i|^2)$ of the ith component. The unstable modes, which trigger CSI, should satisfy the condition $\delta\boldsymbol{J} = 0$ with $\delta\boldsymbol{J}_1 = -\delta\boldsymbol{J}_2 \neq 0$ due to the law of momentum conservation. Since the CSI is the dynamic instability triggered by unstable modes with an imaginary part $\mathrm{Im}\,\omega \neq 0$ [45], the amplification of the unstable modes will exponentially enhance the momentum exchange.

Figure 13.4 depicts the characteristic nonlinear dynamics of the CSI in an uniform two-component BEC obtained by numerically solving the GP equation (13.7). In the early stage of the dynamics, amplification of the unstable modes creates disk-shaped low-density regions that are orientated in the x direction [Fig. 13.4(b)]. The lowest density inside the disk region reaches zero, creating a local dark soliton. The soliton in the ith component transforms into a vortex ring via snake instability [49] with a momentum antiparallel to the initial velocity $\boldsymbol{V}_i$ [Fig. 13.4(c)]. The vortex ring distribution can be determined by the characteristic wavenumber of the unstable mode $k_{||} \sim mV_R/\hbar$ and $k_\perp \sim mV_R/2\hbar$ for a large relative velocity $V_R > V_+$. The length scale $\sim \kappa/V_R$ with $\kappa = 2\pi\hbar/m$ then characterizes both the radii of the vortex rings and the intervals between the rings along $\boldsymbol{V}_R$ immediately after vortex nucleation. Thus, the vortex line density l_v after the instability is roughly estimated to be $l_v \sim V_R^2/\kappa^2$, which can be controlled by varying the relative velocity V_R.

Momentum exchange accelerates after vortex ring nucleation. The vortex motion then dominates the exchange. Since the momentum carried by a vortex ring increases with increasing radius, the radii of the nucleated vortex rings increase with time for momentum exchange. This dynamics resembles that of quantized vortices under thermal counterflow of liquid helium [50], where the vortices are dragged

by the mutual friction between the superfluid and normal fluid components. When the vortex rings become large, the interaction between the vortex rings deforms the rings and vortex reconnections occur, which depresses the momentum exchange [Fig. 13.4(d)]. These effects make the vortex dynamics very complicated, leading to binary QT in which the vortices of both components are tangled with each other [Fig. 13.4(e)]. The momentum exchange almost terminates and each component has an average momentum of nearly zero.

The relative motion of two-component BECs and the resulting CSI can be experimentally realized by employing the Zeeman shift of atomic hyperfine states. Hamner et al. [48] initially prepared overlapping two-component BECs of ^{87}Rb in the hyperfine states $|F, m_F\rangle = |1, 1\rangle$ and $|2, 2\rangle$, which satisfy the miscible condition $g_{11}g_{22} > g_{12}^2$. When a magnetic field gradient was applied along the longer axis of the trap, the gradient generated forces in opposite directions for the two components due to the Zeeman shifts. Counter superflow then occurred and its relative velocity was controlled by the magnetic field gradient [48, 51].

13.3.3.2 Interface Instability

Next, we consider the interface instability of phase-separated two-component BECs. The interaction parameters satisfy the immiscible condition $g_{11}g_{22} < g_{12}^2$. We assume that components 1 and 2 are phase separated at the interface near the $y = 0$ plane, which is sustained by the external potential $U_i(y)$. The density distributions $n_i(y)$ are also assumed to depend only on y and $n_1 = 0$ for $y > \eta$ and $n_2 = 0$ for $y < \eta$, where $y = \eta(x, z, t)$ is the interface position. Here, we neglect the interface thickness for simplicity. The Lagrangian of (13.4) can then be rewritten as

$$L = \int dxdz \left(\int_{-\infty}^{\eta} dy P_1 + \int_{\eta}^{\infty} dy P_2 \right) - \alpha S, \tag{13.13}$$

where α is the interface tension coefficient α [52–54], which originates from the excess energy at the interface, and $S = \int dxdz[1 + (\partial\eta/\partial x)^2 + (\partial\eta/\partial z)^2]^{1/2}$ is the interface area. Taking the functional derivative of the action $\int dt L$ with respect to $\eta(x, z, t)$ and setting it to zero, we obtain

$$P_1(y = \eta) - P_2(y = \eta) + \alpha \left(\frac{\partial^2 \eta}{\partial x^2} + \frac{\partial^2 \eta}{\partial z^2} \right) = 0, \tag{13.14}$$

which corresponds to the Bernoulli equation in hydrodynamics.

We consider a stationary state in which the ith component flows with a velocity $\boldsymbol{V}_i = V_i \hat{\boldsymbol{x}}$ as $\Psi_{i0} = \sqrt{n_i(y)} e^{i(m_i V_i x - \mu_i t)/\hbar}$, which is similar to (13.8) except that the density depends on y. Substituting this into (13.14) with $\eta = 0$ gives the equilibrium condition for the pressure, $g_{11}n_1(0)^2/2 = g_{22}n_2(0)^2/2$.

To analytically derive the dispersion relation for the interface wave, we apply the discussion of the surface modes for a single-component BEC; see Sect. 7.4 in

Ref. [4]. We consider the small phase fluctuation $\Psi_i = \Psi_{i0} e^{i\delta\theta_i}$ and the interface mode $\eta = \delta\eta$ as

$$\delta\theta_i = A_i e^{-(-1)^i ky} \cos(kx - \omega t), \tag{13.15}$$

$$\delta\eta = a \sin(kx - \omega t), \tag{13.16}$$

where A_i and a are infinitesimal parameters. From the kinematic boundary condition, the interface velocity in the y direction $(\partial/\partial t + V_i \partial/\partial x)\eta$ must be equal to $\hbar/(im_i n_i)\Psi_i^* \partial\Psi_i/\partial y|_{y=\eta}$, giving

$$-(-1)^i \frac{\hbar}{m_i} A_i k e^{-(-1)^i k\eta} = (V_i k - \omega)a. \tag{13.17}$$

Substituting (13.15)–(13.17) into (13.14) and neglecting second and higher orders of A_i and a, we obtain

$$\frac{\rho_1}{k}(\omega - V_1 k)^2 - f_1 n_{s1} = -\frac{\rho_2}{k}(\omega - V_2 k)^2 - f_2 n_{s2} + \alpha k^2, \tag{13.18}$$

where $n_{s1} = n_1(\eta - 0)$, $n_{s2} = n_2(\eta + 0)$, $\rho_i = m_i n_{si}$, and $f_i = dU_i/dy|_{y=\eta}$. Equation (13.18) gives the dispersion relation,

$$\omega = V_G k \pm \sqrt{-\frac{\rho_1\rho_2 V_R^2 k^2}{(\rho_1 + \rho_2)^2} + \frac{Fk + \alpha k^3}{\rho_1 + \rho_2}}, \tag{13.19}$$

where $\boldsymbol{V}_G = (\rho_1 \boldsymbol{V}_1 + \rho_2 \boldsymbol{V}_2)/(\rho_1 + \rho_2)$ is the center-of-mass velocity and $F = n_{s1} f_1 - n_{s2} f_2$ is the force due to the gradient of the external potential. We note that (13.19) has the same form as the dispersion relation for an interface wave in classical incompressible and inviscid fluids. In fluid dynamics, the gradient of the potential is equivalent to gravity.

Rayleigh–Taylor Instability First, we consider the case $V_1 = V_2 = 0$. For $F < 0$, the system is always dynamically unstable in the wavenumber range $0 < k < \sqrt{|F|/\alpha}$, which is known as a Rayleigh–Taylor instability [55, 56]. This situation corresponds to a layer of a lighter fluid under a heavier fluid layer in a classical fluid, where the translation symmetry of the interface is spontaneously broken.

Sasaki et al. [55] proposed a system of two immiscible BECs with different hyperfine spins (e.g., $|F, m_F\rangle = |1, -1\rangle$ and $|1, 1\rangle$ of ^{87}Rb atoms) placed in an external magnetic field gradient $B' \equiv dB/dz$. Such condensates experience the potentials $+\mu_B B' z/2$ and $-\mu_B B' z/2$, where μ_B is the Bohr magneton. The force generated by this potential can realize $F < 0$ so that the two condensates are pushed in opposite direction. Numerical simulations of the GP equations reveal that this gradient modulates the interface so that it grows in a mushroom pattern. Vortex rings then nucleate due to atoms near the center flowing upward and atoms at the periphery of the cap of the mushroom shape flowing downward. Gautam and Angom [56] considered a system of a ^{85}Rb–^{87}Rb BEC mixture and the Rayleigh–Taylor instability

caused by tuning the interspecies interaction through a Feshbach resonance. The signature of the instability should appear in the damping behavior of the collective shape oscillation.

Richtmyer–Meshkov Instability The Richtmyer–Meshkov instability occurs when an interface between fluids with different densities is impulsively accelerated (e.g., by the passage of a shock wave). For atomic BECs, this instability can be caused by a magnetic field gradient pulse $B'(t) \propto \delta(t)$ [57]. The nonlinear stage of this evolution is qualitatively similar to that of the Rayleigh–Taylor instability. However, the instability dynamics differs considerably from that of classical fluids. The main difference originates from the quantum surface tension and capillary waves, which suppress perturbation growth and droplet detachment from an elongated perturbation finger. The instability for more general time-dependent forces has been discussed in Ref. [58].

Kelvin–Helmholtz Instability Finally, we consider a system with the shear flow $V_1 \neq V_2 \neq 0$ ($V_R \neq 0$). The dispersion relation (13.19) implies that, for $V_R^2 > 2\sqrt{F\alpha}(\rho_1 + \rho_2)/\rho_1\rho_2 \equiv V_{\rm KH}^2$, the imaginary part $\mathrm{Im}(\omega)$ becomes nonzero and the shear-flow states are dynamically unstable against excitation of the interface modes with $k_- < k < k_+$, as in classical Kelvin–Helmholtz instability, where $k_\pm = k_0 \pm \sqrt{k_0^2 - F/\alpha}$ with $k_0 = \rho_1\rho_2 V_R^2/2\alpha(\rho_1 + \rho_2)$. When $F = 0$, $V_{\rm KH}$ vanishes and the system is always dynamically unstable for $V_R > 0$. In addition to dynamic instability, thermodynamic instability can occur due to dissipation when $\omega < 0$ [59]. Here, we restrict ourselves to dynamic instability in nondissipative systems.

Figure 13.5 demonstrates the Kelvin–Helmholtz instability for $V_R > V_{\rm KH}$ [59]. In the linear stage of the instability, the sine wave corresponding to the most unstable mode with the maximum imaginary part $\max_k\{\mathrm{Im}[\omega(k)]\}$ is predominantly amplified. As the amplitude increases, the sine wave is distorted by nonlinearity [Fig. 13.5(b)], and deforms into a sawtooth wave [Fig. 13.5(c)]. The vorticity $\omega_{\rm eff}$ increases on the edges of the sawtooth waves and creates singular peaks [Fig. 13.5(d)]. Subsequently, each singular peak is released into each bulk, becoming a singly quantized vortex [Fig. 13.5(e)]. The release of vortices reduces the vorticity of the vortex sheet and therefore reduces the relative velocity across the interface. The released vortices drift along the interface and the system never recovers its initial flat interface. These nonlinear dynamics differ considerably from those in classical KHI, where the interface wave grows into roll-up patterns.

The above discussion is valid when the interface thickness $\sim \xi\sqrt{g_{12}/g - 1}$ (for the case $g_{11} = g_{22} = g$) is much smaller than the wavelength of the unstable interface mode, typically given by $\sim \hbar/mV_R$. In the opposite case, the CSI becomes the dominant instability of the flowing state. The crossover relative velocity between the two instabilities is evaluated as $V_R^c \sim \hbar\sqrt{g_{12}/g - 1}/m\xi$ [60].

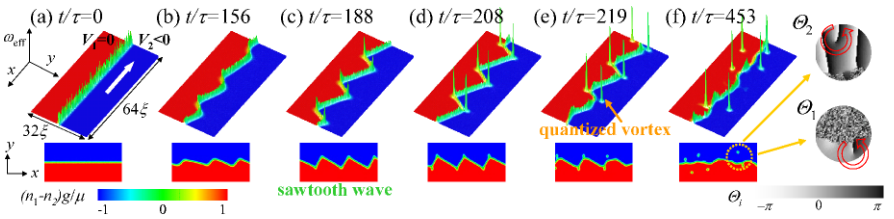

Fig. 13.5 Nonlinear dynamics of Kelvin–Helmholtz instability in phase-separated two-component BECs with a relative velocity $V_R = V_1 - V_2 > V_{\rm KH}$. The numerical simulation of the GP equation was performed with a period $L = 64\xi$ along the x-axis and the Neumann boundary condition with $L = 32\xi$ in the y-direction, where ξ is the healing length. The unit of time is ξ/c, where c is the sound velocity. The initial state (**a**) is Ψ_i^0 with a small random seed to trigger the instability. (*Upper panels*) The height and color show the vorticity $\omega_{\rm eff} = (\nabla \times \boldsymbol{V}_G)_z$ and the density difference $n_1 - n_2$ between the two condensates, respectively. (*Lower panels*) Two-dimensional plots of $n_1 - n_2$. [Takeuchi et al.: Phys. Rev. B **81**, 094517 (2010), reproduced with permission. Copyright 2010 by the American Physical Society]

13.4 Conclusions

Since the realization of BEC in a dilute atomic gas in 1995, most studies on its QHD have been limited to vortex lattices under rotation or motion of a few vortices. However, as research on superfluid helium has shown, there are many other interesting problems on QHD in atomic BECs, some of which have been discussed in this paper. Important topics are quantum hydrodynamic instability and QT beyond this instability. Unlike classical fluid dynamics, most QHD phenomena can be reduced to the motion of quantized vortices. For example, for QT in atomic BECs, the cascade process of quantized vortices, which transfer energy from large to small scales, can be visualized. The observation of Kolmogorov spectra could confirm the cascade process in wavenumber space. The observation of QT in atomic BECs enables us to combine cascade processes in real and wavenumber spaces. Such investigations are almost impossible in superfluid helium and in classical turbulence. We anticipate that this research field will develop rapidly in the near future.

References

1. U. Frisch, *Turbulence* (Cambridge University Press, Cambridge, 1995)
2. E.P. Gross, Nuovo Cimento **20**, 454 (1961)
3. L.P. Pitaevskii, Zh. Eksp. Teor. Fiz. **40**, 646 (1961). [Sov. Phys. JETP **13**, 451 (1961)]
4. C.J. Pethick, H. Smith, *Bose-Einstein Condensation in Dilute Gases*, 2nd edn. (Cambridge University Press, Cambridge, 2008)
5. L.P. Pitaevskii, S. Stringari, *Bose-Einstein Condensation* (Oxford University Press, Oxford, 2003)
6. A.L. Fetter, Rev. Mod. Phys. **81**, 647 (2009)
7. K. Kasamatsu, M. Tsubota, in *Progress in Low Temperature Physics*, vol. XVI, ed. by W.P. Halperin, M. Tsubota (Elsevier, Amsterdam, 2009), pp. 351–403

8. T.W. Neely, E.C. Samson, A.S. Bradley, M.J. Davis, B.P. Anderson, Phys. Rev. Lett. **104**, 160401 (2010)
9. D.V. Freilich, D.M. Bianchi, A.M. Kaufman, T.K. Langin, D.S. Halls, Science **329**, 1182 (2010)
10. T.W.B. Kibble, J. Phys. A **9**, 1387 (1976)
11. W.H. Zurek, Nature **317**, 505 (1985)
12. C.N. Weiler, T.W. Neely, D.R. Scherer, A.S. Bradley, M.J. Davis, B.P. Anderson, Nature (London) **455**, 948 (2008)
13. A.L. Fetter, A.A. Svidzinsky, J. Phys. Condens. Matter **13**, R135 (2001)
14. P. Kuopanportti, J.A.M. Huhtamäki, M. Möttönen, Phys. Rev. A **83**, 011603(R) (2011)
15. S. Middelkamp, P.J. Torres, P.G. Kevrekidis, D.J. Frantzeskakis, R. Carretero-González, P. Schmelcher, D.V. Freilich, D.S. Hall, Phys. Rev. A **84**, 011605(R) (2011)
16. K. Sasaki, N. Suzuki, H. Saito, Phys. Rev. Lett. **104**, 150404 (2010)
17. T. Aioi, T. Kadokura, T. Kishimoto, H. Saito, Phys. Rev. X **1**, 021003 (2011)
18. L. Skrbek, W.F. Vinen, in *Progress in Low Temperature Physics*, vol. XVI, ed. by W.P. Halperin, M. Tsubota (Elsevier, Amsterdam, 2009), pp. 195–246
19. K. Fujimoto, M. Tsubota, Phys. Rev. A **82**, 043611 (2010)
20. K. Fujimoto, M. Tsubota, Phys. Rev. A **83**, 053609 (2011)
21. M. Tsubota, M. Kobayashi, in *Progress in Low Temperature Physics*, vol. XVI, ed. by W.P. Halperin, M. Tsubota (Elsevier, Amsterdam, 2009), pp. 1–43
22. V. Bretin, P. Rosenbusch, F. Chevy, G.V. Shlyapnikov, J. Dalibard, Phys. Rev. Lett. **90**, 100403 (2003)
23. T. Mizushima, M. Ichioka, K. Machida, Phys. Rev. Lett. **90**, 180401 (2003)
24. T.P. Simula, T. Mizushima, K. Machida, Phys. Rev. Lett. **101**, 020402 (2008)
25. S.J. Rooney, P.B. Blakie, B.P. Anderson, A.C. Bradley, Phys. Rev. A **84**, 023637 (2011)
26. N.G. Berloff, B.V. Svistunov, Phys. Rev. A **66**, 013603 (2002)
27. K.W. Madison, F. Chevy, W. Wohlleben, J. Dalibard, Phys. Rev. Lett. **84**, 806 (2000)
28. J.R. Abo-Shaeer, C. Raman, J.M. Vogels, W. Ketterle, Science **292**, 476 (2001)
29. E. Hodby, G. Hechenblaikner, S.A. Hopkins, O.M. Maragó, C.J. Foot, Phys. Rev. Lett. **88**, 010405 (2002)
30. M. Tsubota, K. Kasamatsu, M. Ueda, Phys. Rev. A **65**, 023603 (2002)
31. N.G. Parker, C.S. Adams, Phys. Rev. Lett. **95**, 145301 (2005)
32. M. Kobayashi, M. Tsubota, Phys. Rev. A **76**, 045603 (2007)
33. M. Tsubota, T. Araki, C.F. Barenghi, Phys. Rev. Lett. **90**, 205301 (2003)
34. H. Takeuchi, K. Kasamatsu, M. Tsubota, Phys. Rev. A **79**, 033619 (2009)
35. E.A.L. Henn, J.A. Seman, E.R.F. Ramos, M. Caracanhas, P. Castilho, E.P. Olímpio, G. Roati, D.V. Magalhães, K.M.F. Magalhães, V.S. Bagnato, Phys. Rev. A **79**, 043618 (2009)
36. E.A.L. Henn, J.A. Seman, G. Roati, K.M.F. Magalhães, V.S. Bagnato, Phys. Rev. Lett. **103**, 045301 (2009)
37. W.F. Vinen, J. Low Temp. Phys. **161**, 419 (2010)
38. A.C. White, C.F. Barenghi, N.P. Proukakis, A.J. Youd, D.H. Wacks, Phys. Rev. Lett. **104**, 075301 (2010)
39. H. Adachi, M. Tsubota, Phys. Rev. B **83**, 132503 (2011)
40. M. Caracanhas, A.L. Fetter, S.R. Muniz, K.M.F. Magalhães, G. Roati, G. Bagnato, V.S. Bagnato, J. Low Temp. Phys. **166**, 49 (2012)
41. V. Schweikhard, I. Coddington, P. Engels, S. Tung, E.A. Cornell, Phys. Rev. Lett. **93**, 210403 (2004)
42. G. Thalhammer, G. Barontini, L. De Sarlo, J. Catani, F. Minardi, M. Inguscio, Phys. Rev. Lett. **100**, 210402 (2008)
43. S.B. Papp, J.M. Pino, C.E. Wieman, Phys. Rev. Lett. **101**, 040402 (2008)
44. S. Tojo, Y. Taguchi, Y. Masuyama, T. Hayashi, H. Saito, T. Hirano, Phys. Rev. A **82**, 033609 (2010)
45. C.K. Law, C.M. Chan, P.T. Leung, M.-C. Chu, Phys. Rev. A **63**, 063612 (2001)
46. H. Takeuchi, S. Ishino, M. Tsubota, Phys. Rev. Lett. **105**, 205301 (2010)

47. S. Ishino, M. Tsubota, H. Takeuchi, Phys. Rev. A **83**, 063602 (2011)
48. C. Hamner, J.J. Chang, P. Engels, M.A. Hoefer, Phys. Rev. Lett. **106**, 065302 (2011)
49. B.P. Anderson, P.C. Haljan, C.A. Regal, D.L. Feder, L.A. Collins, C.W. Clark, E.A. Cornell, Phys. Rev. Lett. **86**, 2926 (2001)
50. H. Adachi, S. Fujiyama, M. Tsubota, Phys. Rev. B **81**, 104511 (2010)
51. M.A. Hoefer, J.J. Chang, C. Hamner, P. Engels, Phys. Rev. A **84**, 041605 (2011)
52. R.A. Barankov, Phys. Rev. A **66**, 013612 (2002)
53. B. Van Schaeybroeck, Phys. Rev. A **78**, 023624 (2008)
54. B. Van Schaeybroeck, Phys. Rev. A **80**, 065601 (2009)
55. K. Sasaki, N. Suzuki, D. Akamatsu, H. Saito, Phys. Rev. A **80**, 063611 (2009)
56. S. Gautam, D. Angom, Phys. Rev. A **81**, 053616 (2010)
57. A. Bezett, V. Bychkov, E. Lundh, D. Kobyakov, M. Marklund, Phys. Rev. A **82**, 043608 (2010)
58. D. Kobyakov, V. Bychkov, E. Lundh, A. Bezett, V. Akkerman, M. Marklund, Phys. Rev. A **83**, 043623 (2011)
59. H. Takeuchi, N. Suzuki, K. Kasamatsu, H. Saito, M. Tsubota, Phys. Rev. B **81**, 094517 (2010)
60. N. Suzuki, H. Takeuchi, K. Kasamatsu, M. Tsubota, H. Saito, Phys. Rev. A **82**, 063604 (2010)

Chapter 14
Characteristics and Perspectives of Quantum Turbulence in Atomic Bose-Einstein Condensates

V.S. Bagnato, R.F. Shiozaki, J.A. Seman, E.A.L. Henn, G. Telles, P. Tavares, G. Roati, G. Bagnato, K.M.F. Magalhães, S.R. Muniz, and M. Caracanhas

Abstract In spite of being a phenomenon studied over centuries, turbulence remains an intriguing phenomenon of nature. In the low temperature regime, turbulence has been investigated in superfluid helium during the last decades. Due to the quantum nature of superfluids, this phenomenon is named Quantum Turbulence and it is characterized by a particular configuration of quantized vortices in the sample. Recently, this topic started to be investigated in a different kind of superfluids, namely, trapped atomic Bose-Einstein condensates (BEC). In this text we review the first experimental evidences of Quantum Turbulence in a BEC of ^{87}Rb. We describe our most important observations and discuss possible research perspectives.

14.1 Introduction

Turbulent processes are everywhere on Earth and beyond. It is crucial to life support from microscopic scale, inside the human body, to the macroscopic scale of the Earth's rotating core. There are many familiar examples of turbulent processes taking place in the everyday life as they are natural phenomena occurring on airplane flights, or on the sky's clouds motion, forming characteristic patterns.

Despite of being commonly observed, turbulence is known to be difficult to treat and study. The interplay from small to large scale in turbulent fields makes it difficult to study due to the need to resolve spatial and temporal ranges over several orders of magnitude. This often requires large experimental samples and the need to measure

V.S. Bagnato · R.F. Shiozaki · E.A.L. Henn · G. Telles (✉) · P. Tavares · G. Bagnato · K.M.F. Magalhães · S.R. Muniz · M. Caracanhas
Instituto de Física de São Carlos, Universidade de São Paulo, C.P. 369, 13560-970 São Carlos, SP, Brazil
e-mail: gugs@ursa.ifsc.usp.br

V.S. Bagnato
e-mail: vander@ifsc.usp.br

J.A. Seman · G. Roati
LENS and Dipartimento di Fisica, Università di Firenze, and INFM-CNR, Via Nello Carrara 1, 50019 Sesto Fiorentino, Italy

A. Bramati, M. Modugno (eds.), *Physics of Quantum Fluids*,
Springer Series in Solid-State Sciences 177, DOI 10.1007/978-3-642-37569-9_14,

fast fluctuations on microscopic (or mesoscopic) scales. The nonlinear equations (Navier-Stokes) of motion are difficult to handle because of the large span of scales involved in turbulence. As a result, many terms in the equations cannot be neglected because their contribution may change over the relevant scales.

Quantum fluids, such as superfluids, superconductors, and Bose-Einstein condensates, may present turbulent states that are different from classical due to long-range quantum order, which poses constraints to their dynamics. All vorticity, in the case of superfluids and Bose-Einstein condensates is restricted to topological defects in the order parameter of the system. The resulting linear structures are named quantized vortices because continuity in the order parameter quantizes the circulating flow around each topological defect. As such, turbulence in a quantum fluid displays a tangle of interacting quantized vortices, as first pointed by Feynman [1] and others [2–6], that is very different from the continuous distributions of vorticity observed in classical turbulence.

Since then many studies have investigated the distinct characteristics of this phenomenon (for a comprehensive and complete review, please see Ref. [7]). Recently the experimental realization of Bose-Einstein Condensation (BEC) in trapped atomic samples [8–10] and its relation with superfluidity [11–13] opened up new possibilities to investigate Quantum Turbulence (QT). A series of published papers by M. Tsubota and collaborators [14, 15] presented a possible mechanism for inducing QT in atomic superfluids. Using a model based on the Gross-Pitaevskii equation, they have successfully derived the Kolmogorov spectrum for QT in atomic superfluids, analogous to the previous observations made on superfluid ^{4}He. See Chap. 13 for details.

There are a few advantages when using BECs of trapped atoms to investigate QT. A first clear advantage is the fact that BECs are weakly interacting systems, hence, its theoretical description is simpler. Second, the number density is much smaller than in liquid ^{4}He, therefore, the vortex cores will be much larger, making their observation easier. Finally, these systems present a larger variety of controllable parameters such as the density, temperature, geometry and even the interatomic interactions. This controllability allows a vast exploration of the phenomena.

During last years, our group have observed the first clear evidences of QT emerging in a BEC of ^{87}Rb atoms, produced by an external oscillating magnetic field [16]. Also, several peculiarities of QT in this system have been investigated. First, the generation of clusters of vortices and anti-vortices when the oscillatory excitation is introduced [17] represents an essential ingredient to reach QT. Second, effects due to the finite size of the sample are related to the existence of a definite boundary region in between the turbulent and non-turbulent regimes [18]. Finally, the different levels of excitation produced in the BEC can be summarized in a diagram of the excitation parameters [19]. This diagram shows the evolution of the number and distribution of vortices nucleated in the condensed sample.

In the next section we give a general introduction to the phenomenon of QT in atomic trapped BECs. In Sect. 14.3, we briefly describe our experimental setup and present our first results on the vortex nucleation in a BEC sample. The evolution from regular vortices to the turbulent state is explained in Sect. 14.4. We then present

a simple model to help understanding the role of the BEC finite size in the transition to quantum turbulence. Then, in Sect. 14.5, a very important characteristic of the turbulent cloud is explained: the peculiar dynamics of the system when expands freely. In this section we also present a new analysis of the turbulent state in terms of the Reynolds number of the system. Finally, in Sect. 14.6, we discuss the current directions of our research and introduce our future perspectives.

14.2 Turbulence in Trapped Bose-Einstein Condensates

Superfluid BECs have some important characteristics. Since BEC samples comprise condensed and thermal fractions, these systems must be described by a two-fluid model. BECs must also obey certain constraints imposed by quantum mechanics. For instance, the vortices inside a condensate are quantized, with integer number of fundamental circulation (see, for instance, Ref. [20]). There are many ways to produce a collection of vortices in the condensate, Ref. [21] is a review on this topic. Rotating condensates normally results in a collection of vortices presenting the same circulation and spatially distributed forming a lattice [22], equivalent to the Abrikosov lattice in superconductors [23, 24]. Rotating condensate is not the only way to introduce vortices. A phase imprinting technique recently demonstrated [25] is another alternative.

However the simple presence of vortices in the condensate does not fulfill the conditions to obtain QT. Following the concepts introduced by R. P. Feynman, QT is a phenomenon characterized by a spatial distribution of quantized vortices in a tangled way. Therefore, simple rotation does not take the trapped superfluid to QT. To generate such a tangle configuration, one can imagine the introduction of rotation in two orthogonal axes as suggested by M. Tsubota and co-workers [14]. Another alternative is the introduction of periodic density modulation either by trap oscillations [16] or by oscillating the s-wave scattering length near Feshbach resonances [26]. We have applied in our system the oscillation of the trap by the introduction of an external oscillating magnetic field [16, 27].

14.3 Generation and Proliferation of Vortices

We start with a ^{87}Rb condensate whose experimental setup has been described in details elsewhere [28]. The basic system is composed of a QUIC trap with frequencies given by $\omega_z = \omega_0$ and $\omega_x = \omega_y = 9\omega_0$, with $\omega_0 = 2\pi \times 23$ Hz, and produce a condensate with about 2×10^5 atoms in the $|2, 2\rangle$ hyperfine state.

Superimposed to the trap coils are two extra coils as shown in Fig. 14.1. The symmetry axis of these coils is slightly tilted with respect to the symmetry axis of the trap itself. Through these coils runs a small sinusoidal current which causes a combination of rotation and translation on the trap bottom. Such motions take place

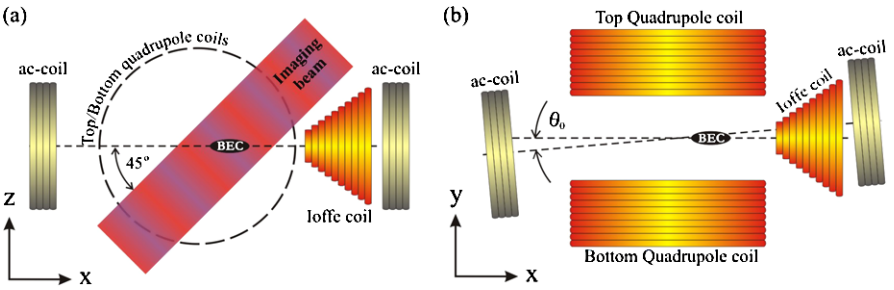

Fig. 14.1 Schematics of the (**a**) above and (**b**) side view of the coils configuration. Superimposed to the QUIC trap coils, there are two ac-coils slightly misaligned from the Ioffe coil axis

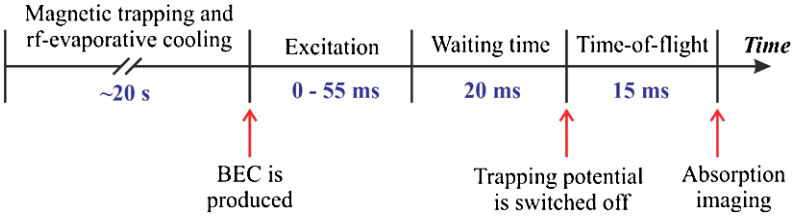

Fig. 14.2 Experimental time sequence. Once in the QUIC trap, the atoms are evaporatively cooled for 20 s to form a BEC. Then, for a time ranging from 0 to 55 ms, the ac-coils excite the sample which, later, rests in the trap for 20 ms. Subsequently, the trap coils are turned off and the cloud freely falls for 15 ms before an absorption image is taken

for an oscillation frequency Ω close to 207 Hz, the highest trapping frequency. Amplitude and time of the excitation are the main parameters controlled for the vortices production. A typical time sequence for the experiment is presented in Fig. 14.2. Once the Bose condensate is produced, the excitation by the oscillatory field is applied during a time interval that can range from 0 to 55 ms. After this excitation period, there is a waiting time in the trap followed by a time-of-flight (TOF) measurement using the absorption on a CCD camera.

The result of this excitation is the generation of collective modes in the condensate cloud. A typical sequence of TOF images is reported in Fig. 14.3. A clear composition of dipole, quadrupole and breathing modes is present in the condensate cloud. We believe that such excitations are essential to couple energy and angular momentum into the cloud to further generate other excitations. Besides the collective modes, the long axes of the condensate (after 15 ms of TOF) shows an angular oscillation (scissors mode) due to the superfluid nature of the condensate [13, 29].

As the excitation amplitude increases we start to nucleate vortices in the cloud. As recently reported [30], those vortices are first nucleated at the edge of the cloud where a low density cloud of excited atoms (probably originated from the whole excitation process) surrounds the dense condensate cloud. Figure 14.4 highlights the vortices being nucleated at the edges. It seems that many of the nucleated vortices

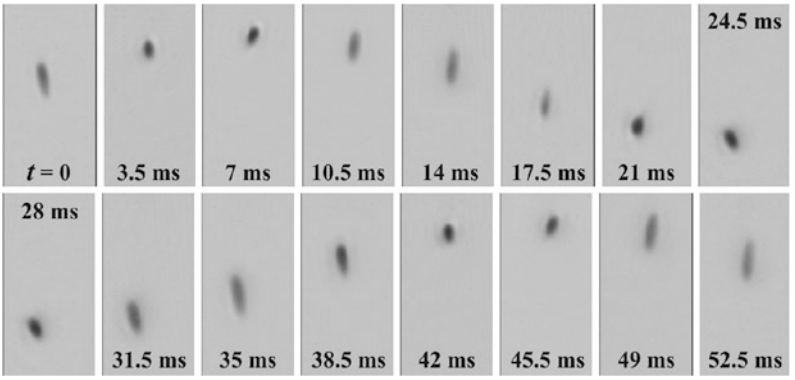

Fig. 14.3 Sequence of absorption images for different wait times showing the presence of collective modes of excitation in the sample

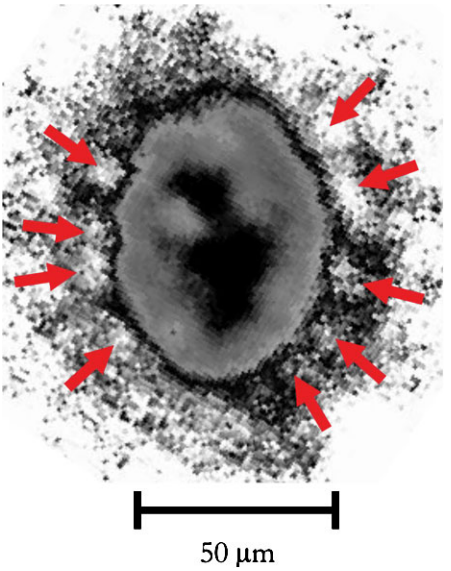

Fig. 14.4 Absorption image of the cloud showing the nucleation of vortices at the edges

do not survive to the interior of the cloud. In fact, in Ref. [30] we have presented evidences that vortices and anti-vortices are all produced together, and they undergo dynamical processes after which only few of them survive.

The final number of vortices observed in the sample is strongly dependent on the combination of time and amplitude of excitation. Smaller amplitudes or shorter times produce only the bending mode already discussed. To observe vortices within the cloud, a compromise between amplitude and time is necessary. In Fig. 14.5 (extracted from Ref. [19]) we show the evolution for the average number of vortices as a function of the amplitude of excitation for two different times (17 ms and 33 ms). Figure 14.6 shows pictures for the observed vortices distribution. While for both

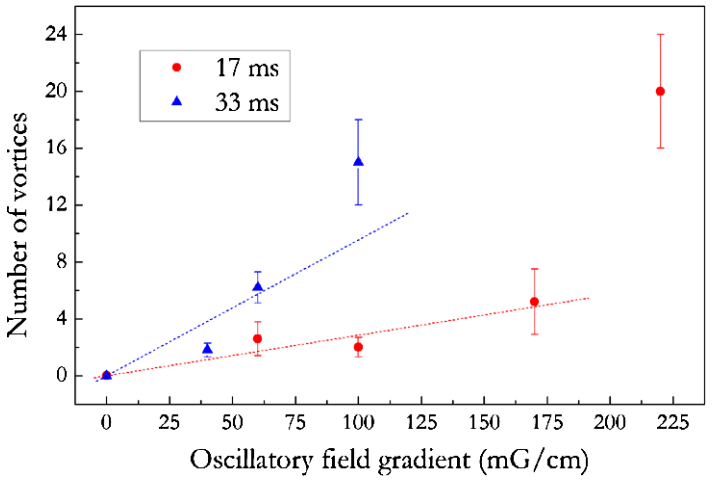

Fig. 14.5 Average number of vortices formed as a function of the excitation amplitude for two fixed excitation times. The behavior is roughly linear for few vortices, and shows a strong proliferation later

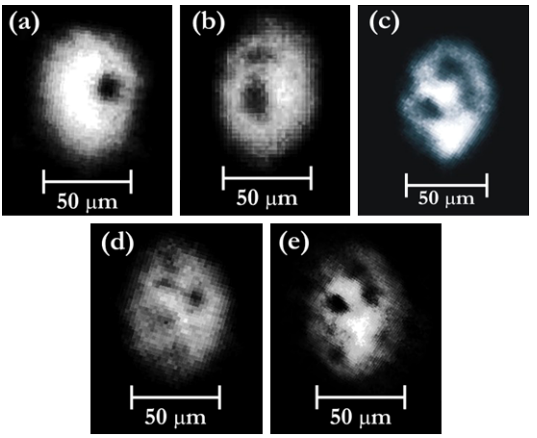

Fig. 14.6 Absorption images of the cloud showing different number of vortices formed within the sample

times, the number strongly increases with the amplitude, longer excitation times take the system to higher number of vortices for a given amplitude. The strong proliferation for the number of vortices soon starts to cover the full sample with dark spots observed in the probe laser description. The peculiar way we excite the sample, through oscillations, results in vortex nucleation in different directions. We believe that this technique is similar to the combination of rotations proposed by Kobayashi and Tsubota [14]. The production of vortex filaments along different directions builds up the necessary ingredients for the evolution of the configuration of vortices to a tangle configuration characterizing QT in the system.

14.4 Observation of Tangled Vortex Configuration

From the graphic of Fig. 14.5, one can imagine that as the energy is pumped into the system part of it is coupled to the superfluid resulting in the vortex formation. Following Ref. [20] the energy of each vortex line within the cloud is given by:

$$E_{vort} = \frac{\hbar^2}{m l_0^2} \ln \frac{l_0}{\xi}, \tag{14.1}$$

where l_0 is the typical harmonic oscillator length for the trap ($l_0 = \sqrt{\frac{\hbar}{m\omega_{ho}}}$), $\omega_{ho} = (\omega_x \omega_y \omega_z)^{1/3}$, $\xi = \frac{1}{\sqrt{8\pi n a_s}}$ is the healing length, n is the peak atomic density, and a_s is the s-wave scattering length. In writing (14.1), we have considered that the vortex line crosses the cloud diametrically.

When the cloud volume is saturated with vortex lines, the energy to create additional vortices starts to be very high and a turn over in the evolution of the vortices number with increasing amplitude should appear. However a change in overall cloud behavior is observed. Although the additional coupled energy to the cloud is not enough to generate more vortices, it is certainly sufficient to accelerate the dynamics, promoting a fast movement of the vortex lines. The final result is the production of a tangled configuration of vortices, characterizing the turbulent state. Considering the total rate of pumped energy into the cloud as R_{pump}, the energy coupled to the cloud in the form of vortices can be written as

$$E_{pump} = \eta R_{pump}(t - t_0), \tag{14.2}$$

where t is the time of excitation, η is the fraction of energy converted into rotation. The time t_0 corresponds to the mean time to form the first vortex. Elapsed the excitation time t, the number of vortices accumulated must be N_{vort}. In a first approximation where annihilations of vortex-anti-vortex pairs are not considered, one can write:

$$\eta R_{pump}(t - t_0) = N_{vort} E_{vort}, \tag{14.3}$$

or

$$N_{vort} = \frac{\eta R_{pump}}{E_{vort}}(t - t_0). \tag{14.4}$$

This shall be the number of vortices in the atomic cloud for an excitation time t. A graphic showing the evolution of the observed number of vortices in the cloud as a function of time for different energy pump rates (here produced using different amplitudes of excitation) is presented in Fig. 14.7.

Considering the simple model represented by (14.2) and (14.4) we find that in this experimental conditions $t_0 \approx 15$ ms. Times shorter than that shall be very inefficient to produce vortices. Considering that the saturation number of vortices in the cloud must be on the order of $N_{vort} \approx l_0/\xi$, a limiting relation between the pumped energy

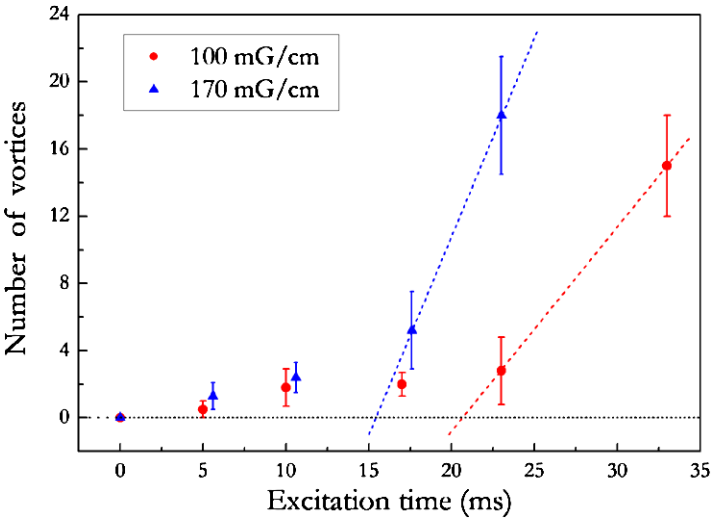

Fig. 14.7 Average number of vortices formed as a function of the excitation time for two fixed excitation amplitudes. A strong proliferation of vortices takes place after a certain excitation time

and the excitation time, before the occurrence of turbulence can be obtained

$$R_{pump} = \frac{l_0 E_{vort}}{\xi \eta} \frac{1}{t - t_0}. \tag{14.5}$$

And since R_{pump} is proportional to the amplitude of excitation (for a fixed excitation frequency), the relation between amplitude and time of excitation to generate QT must be on the type:

$$A(t)(t - t_0) \cong C. \tag{14.6}$$

The existence of this limiting condition to generate turbulence is a consequence of the finite size of the atomic superfluid [18]. QT develops for the atomic superfluid densely filled with vortices. After this point the energy pumped into the system transforms not only into the formation of vortices but mostly into their motion, with the evolution to a tangle configuration. Such configuration is believed to produce reconnections and the formation of many oscillations into the vortex filaments. Sooner the rotation field is all distributed in the sample. At this point the absorption image becomes hazy, which can be considered as a first manifestation of the presence of turbulence. Figure 14.8 shows a typical transition between a regular cloud, proliferation and QT.

The distributed vortices in our sample do not reveal any regular pattern as reported in other experiments [22]. We strongly believe that this a consequence of the excitation process generating vortex and anti-vortex all together, and covering many spatial directions.

As stated before, the generation of QT is a consequence of a compromise between amplitude and time of the excitation. The diagram of Fig. 14.9 shows this

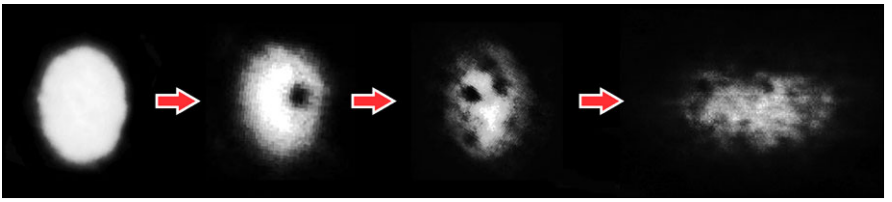

Fig. 14.8 Absorption images showing the transition from a regular BEC with no vortices, to one vortex, to many vortices, and to a turbulent state

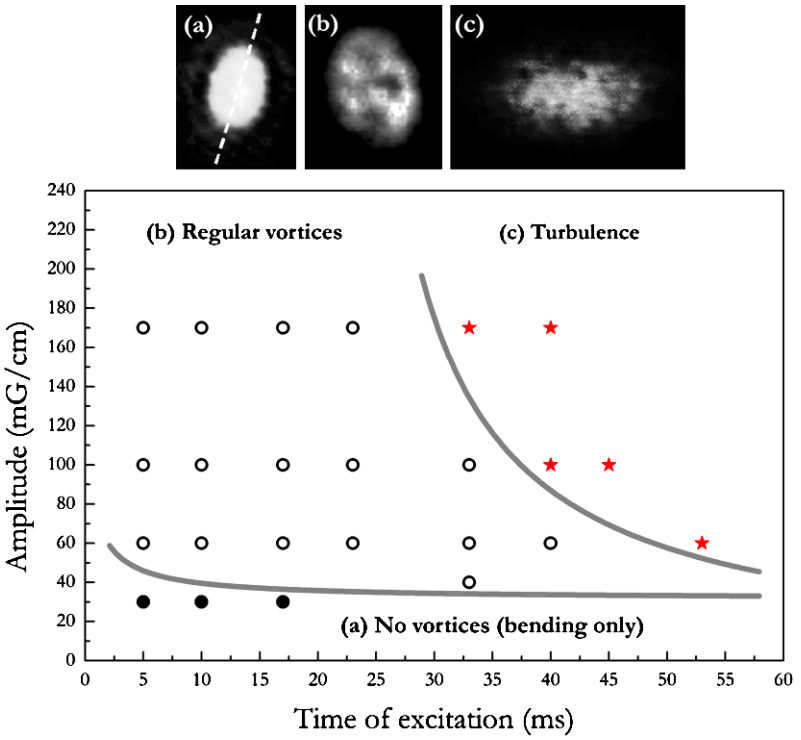

Fig. 14.9 Diagram of the amplitude × time of excitation showing three domains: (**a**) no vortices, only bending is observed; (**b**) well defined vortices are formed; and (**c**) QT takes place. *Figures on the top* show typical observations for each regime, and *grey guide lines* on the diagram separate the domains

compromise through the existence of domains in the amplitude × time space. This diagram was presented before in Ref. [19] and for the simplicity we have omitted the granulation domain of the diagram which will not be discussed in this paper. Three regimes presented in the diagram of Fig. 14.9 are useful in the understanding of the QT formation in a trapped atomic superfluid and the routes to achieve such regime.

As mentioned before, after reaching QT, increasing even further the excitation time and/or amplitude takes the sample to a distribution where pieces of condensate are spread in space characterizing a configuration named as granulation. There are many questions and many observations related to this regime which we are still considering and must be reported after we reach a conclusive understanding.

14.5 Characteristics Observed on the Turbulent Cloud

One of the fingerprints of QT in a BEC is the change of the expansion behavior during time-of-flight. Quantum degenerate Bose gas when confined by an anisotropic potential will present asymmetric velocity distribution. An excess of kinetic energy is liberated on the most confined direction causing an inversion of the cloud aspect ratio after a certain time of flight. This effect was well investigated by many authors (see Ref. [20]). Typically, for a cigar type condensate cloud, the aspect ratio $\frac{R_\rho(t)}{R_z(t)}$ grows with time-of-flight, reaching an asymptotic value which has a strong dependence with the initial aspect ratio for the *in situ* cloud. For a typical elongated cloud, there will be a faster expansion along the most compressed direction, and vice-versa, which causes an aspect ratio inversion. In contrast, a cloud with only thermal atoms liberates its energy during expansion, in a way that the asymptotic behavior tends to a unitary value for the aspect ratio. The thermal cloud always ends its expansion in an isotropic way.

A quite different behavior is observed for a turbulent cloud during free expansion. The aspect ratio is observed to stay constant from the beginning to the end of the expansion. This complete suppression of the aspect ratio change was well reported in Ref. [16]. We refer to this as a self-similar expansion during the time-of-flight for the turbulent cloud [27]. Similarly to the fact that the inversion ratio is a macroscopic evidence for the condensate, the self-similar expansion seems to be a good evidence for the presence of random distribution of vortex lines within the sample, fact that is associated with QT. Figure 14.10 from Ref. [16] shows the expansion behavior comparing the evolution of the aspect ratio for a thermal cloud, the pure condensate and the turbulent condensate. To explain this observation, we have recently produced a theoretical analysis where the effect of vorticity in the behavior of free expansion was investigated using a hydrodynamic approach [31] in a rotational version. Due to the presence of vortices, we considered a rotational component in the cloud velocity field, such that $|\nabla \times \mathbf{v}| = 2\Omega$, where $\Omega = \frac{hn_v}{2m}$. The vortex density, n_v, is derived considering a uniform distribution of a large number of equally oriented vortices [20]. That leads to the modified Euler equation:

$$m\frac{d\mathbf{v}}{dt} + \nabla\left(\frac{1}{2}mv^2 + V_{trap} + gn(\mathbf{r},t)\right) = m\mathbf{v}\times\nabla\times\mathbf{v}, \tag{14.7}$$

with $g = \frac{4\pi\hbar^2 a_s}{m}$ while a_s is the s-wave scattering length. Together with the continuity equation, the free expansion of the cloud was calculated starting with an Ansatz for the density $n(\mathbf{r},t)$ equivalent to the TF profile.

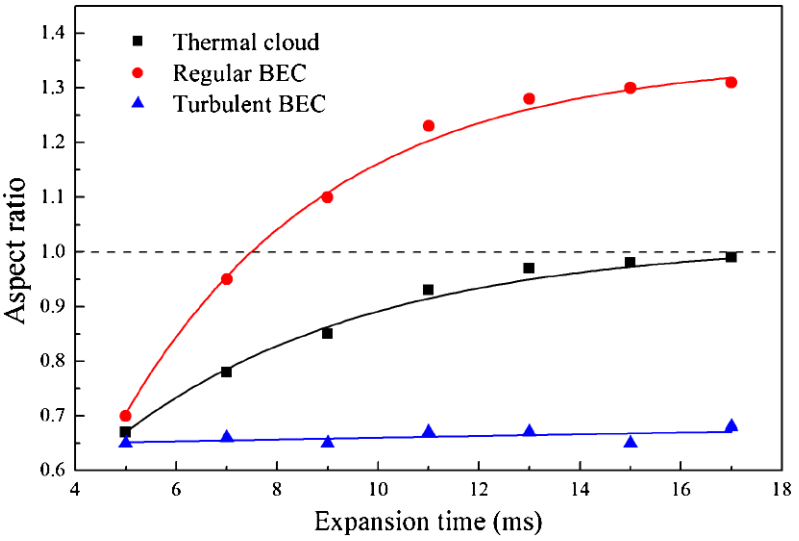

Fig. 14.10 Aspect ratio as a function of expansion time for a thermal cloud, a regular BEC and a turbulent BEC. The thermal cloud aspect ratio tends to 1, the regular BEC expansion shows an aspect ratio inversion, and the turbulent BEC aspect ratio does not change during expansion. The *lines* are guides to the eye

We have demonstrated that the extra kinetic contribution due to the vorticity not only produces a larger initial cloud, but also introduces an extra acceleration for the expansion in the plane perpendicular to Ω. For large values of Ω, this term becomes dominant and the presence of angular momenta in many directions promotes an expansion with insignificant time variation of the aspect ratio. Even being a "toy model" calculation, it provides the main physical insights towards the understanding of the experimental behavior.

As described previously, the oscillatory excitation of the condensate is always accompanied by the excitation of collective modes including the dipole mode. In this mode the condensate cloud as a whole travels inside the potential at the excitation frequency. One could think that such a motion is "like" a flow of the superfluid. Considering that this is truth, one can make a Reynolds type of analysis. For a classical fluid, flowing with velocity v under the influence of a lateral confinement of dimension D, the Reynolds number is defined as $R_e = \frac{Dv}{\eta}$ with η the viscosity. This non dimensional quantity indicates if the flow will remain as laminar or if the turbulence will take place. Conventionally, for $R_e \approx 1000$ turbulence starts to appear.

For superfluids, the viscosity is replaced by the quantum of circulation h/m, and the quantum Reynolds number is given by $R_e^Q = \frac{Dv}{h/m}$ [32]. For the oscillating cloud as indicated in Fig. 14.11, the condensate is always embedded in a thermal cloud, since our experiment is done at finite temperature. Considering $D = 2R_{TF}$, i.e., the flow dimension as twice the Thomas-Fermi radius, and $v = \omega A$, where A is the oscillatory amplitude and ω the frequency, we can evaluate R_e^Q for many different amplitudes of oscillation, which corresponds to different velocities for the cloud

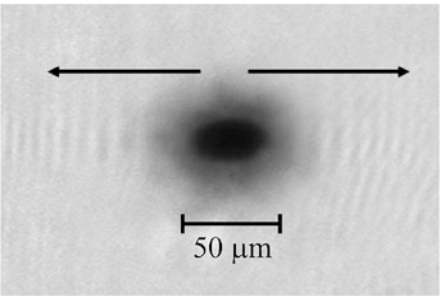

Fig. 14.11 Absorption image of a cloud showing a BEC embedded in a thermal cloud

center of mass. The quantification of R_e^Q for many excitation conditions shows that for $R_e^Q < 0.5$ there was no turbulence. On the other hand, for the cases where turbulence was observed, $R_e^Q > 2$. In the region going from $0.5 < R_e^Q < 2$, the experimental observations shows that in those conditions of oscillation sometimes QT is observed and sometimes not.

In Ref. [32], G.E. Volovik proposes an interesting diagram relating R_e^Q with a frictional parameter (q). There, the transition between QT and laminar flow, for $q \leq 1$ (low frictional parameter for the sample), takes place for $R_e^Q \approx 1$. At this point we cannot present yet all the arguments that guarantee the validity of taking the oscillatory motion of the superfluid sample in the potential as a flow experiment. But it certainly produce numbers that are not far from the existing theoretical predictions for flow experiments with ^{4}He-superfluid.

14.6 Present Stage of Investigation

In classical viscous fluids, the change in the viscosity distribution during the development of turbulence represents an intrinsic problem to characterize the turbulent flow. Therefore it is more convenient to determine statistical laws instead of the dynamics of individual variables. In a turbulent regime fully developed in its steady state, the injected energy is transferred to smaller scales without dissipation and the energy spectrum is given by:

$$E(k) = C\epsilon^{2/3}k^{-5/3}, \tag{14.8}$$

known as Kolmogorov Law [33, 34]. The energy spectrum is defined as $E(k)$, such that $E = \int d\mathbf{k}E(\mathbf{k})$, where k is the wavenumber originated from the Fourier transform of the velocity field. Kolmogorov law is well verified in classical turbulence. In QT, it was first experimentally demonstrated in ^{4}He [35]. Many other experiments follow this one and much theoretical work was developed in order to understand the similarities between the energy spectrum of classical and quantum turbulence [7, 36–39]. In the case of atomic BECs, a work conducted by M. Tsubota and coworkers [14, 15] has demonstrated theoretically that QT can be developed in a BEC, and the originated energy spectrum is related to the Kolmogorov law. The research

in this direction is quite important since it may allow us to directly observe the relation between real-space and reciprocal-space.

To obtain the energy spectrum of our experimental turbulent samples, we are performing measurements and calculations using time-of-flight images of the turbulent cloud obtained by absorption after time-of-flight. A normal cloud in time-of-flight is actually a momentum distribution. Considering $n(x, y, z)$ as the density profile, after a time-of-flight τ, $x = \frac{hk_x}{m}\tau$, $y = \frac{hk_y}{m}\tau$ and $z = \frac{hk_z}{m}\tau$. So the distribution $n(x, y, z)$ turns into $\rho(k_x, k_y, k_z)$ which can be used to determine $n(k)$ such that $E = \frac{\hbar^2 k^2}{2m} n(k)$. The only problem is that the absorption image provide us with $\int n(x, y, z)dx$ rather than $n(x, y, z)$. We are therefore processing our images in order to obtain information about the energy spectrum. The preliminary results seem very promising and may allow us to investigate $n(k)$ which, according to the Kolmogorov discussion, is expected to be proportional to k^{-3}.

References

1. R.P. Feynman, Prog. Low Temp. Phys. **1**, 17 (1955)
2. H.E. Hall, W.F. Vinen, Proc. R. Soc. Lond. A **238**, 204 (1956)
3. W.F. Vinen, Proc. R. Soc. Lond. A **240**, 114 (1957)
4. W.F. Vinen, Proc. R. Soc. Lond. A **240**, 128 (1957)
5. W.F. Vinen, Proc. R. Soc. Lond. A **242**, 493 (1957)
6. W.F. Vinen, Proc. R. Soc. Lond. A **243**, 400 (1958)
7. W.F. Vinen, J.J. Niemela, J. Low Temp. Phys. **128**, 167 (2002)
8. M.H. Anderson et al., Science **269**(5221), 198 (1995)
9. K.B. Davis et al., Phys. Rev. Lett. **75**(22), 3969 (1995)
10. C.C. Bradley et al., Phys. Rev. Lett. **75**(9), 1687 (1995)
11. M.R. Matthews et al., Phys. Rev. Lett. **83**, 2498 (1999)
12. K.W. Madison et al., Phys. Rev. Lett. **84**, 806 (2000)
13. O.M. Maragò et al., Phys. Rev. Lett. **84**, 2056 (2000)
14. M. Kobayashi, M. Tsubota, Phys. Rev. A **76**, 045603 (2007)
15. M. Tsubota, J. Phys. Condens. Matter **21**, 164207 (2009)
16. E.A.L. Henn et al., Phys. Rev. Lett. **103**, 045301 (2009)
17. J.A. Seman et al., Phys. Rev. A **82**, 033616 (2010)
18. R.F. Shiozaki et al., Laser Phys. Lett. **8**(5), 393 (2011)
19. J.A. Seman et al., Laser Phys. Lett. **8**(9), 691 (2011)
20. C.J. Pethick, H. Smith, *Bose-Einstein Condensation in Dilute Gases*, 2nd edn. (Cambridge University Press, Cambridge, 2001)
21. K. Kasamatsu, M. Tsubota, Prog. Low Temp. Phys. **16**, 349 (2008)
22. J.R. Abo-Shaeer et al., Science **292**(5516), 476 (2001)
23. A.A. Abrikosov, Sov. Phys. JETP **5**, 1174 (1957)
24. U. Essmann, H. Trauble, Phys. Lett. **24A**, 526 (1967)
25. A.E. Leanhardt et al., Phys. Rev. Lett. **89**, 190403 (2002)
26. S.E. Pollack et al., Phys. Rev. A **81**, 053627 (2010)
27. E.A.L. Henn et al., J. Low Temp. Phys. **158**, 435 (2010)
28. E.A.L. Henn et al., Braz. J. Phys. **38**, 279 (2008)
29. E.A.L. Henn et al., Phys. Rev. A **79**(4), 043618 (2009)
30. J.A. Seman et al., J. Phys. Conf. Ser. **264**, 012004 (2011)
31. M. Caracanhas et al., J. Low Temp. Phys. **170**, 133 (2013)

32. G.E. Volovik, *The Universe in a Helium Droplet* (Oxford University Press, New York, 2003)
33. A.N. Kolmogorov, Dokl. Akad. Nauk SSSR **30**, 299 (1941)
34. A.N. Kolmogorov, Dokl. Akad. Nauk SSSR **32**, 16 (1941)
35. J. Maurer, P. Tabeling, Europhys. Lett. **43**(1), 29 (1998)
36. S.R. Stalp, L. Skrbek, R.J. Donnelly, Phys. Rev. Lett. **82**, 4831 (1999)
37. C. Barenghi, R.J. Donnelly, W.F. Vinen (eds.), *Quantized Vortex Dynamics and Superfluid TURBULENCE* (Springer, New York, 2001)
38. M. Kobayashi, M. Tsubota, J. Phys. Soc. Jpn. **74**, 3248 (2005)
39. M. Tsubota, W.P. Halperin (eds.). *Progress in Low Temperature Physics: Quantum Turbulence*, vol. 16 (2009)

Chapter 15
Spatial and Temporal Coherence of a Bose-Condensed Gas

Yvan Castin and Alice Sinatra

Abstract The central problem of this chapter is temporal coherence of a three-dimensional spatially homogeneous Bose-condensed gas, initially prepared at finite temperature and then evolving as an isolated interacting system. A first theoretical tool is a number-conserving Bogoliubov approach that allows to describe the system as a weakly interacting gas of quasi-particles. This approach naturally introduces the phase operator of the condensate: a central actor since loss of temporal coherence is governed by the spreading of the condensate phase-change. A second tool is the set of kinetic equations describing the Beliaev-Landau processes for the quasi-particles. We find that in general the variance of the condensate phase-change at long times t is the sum of a ballistic term $\propto t^2$ and a diffusive term $\propto t$ with temperature and interaction dependent coefficients. In the thermodynamic limit, the diffusion coefficient scales as the inverse of the system volume. The coefficient of t^2 scales as the inverse volume squared times the variance of the energy of the system in the initial state and can also be obtained by a quantum ergodic theory (the so-called eigenstate thermalization hypothesis).

15.1 Description of the Problem

We consider a single-spin state Bose gas prepared in equilibrium. To extract the relevant physics, we avoid the complication of harmonic trapping present in real experiments [1–3] and we consider a spatially homogeneous system in a parallelepipedic quantization volume V with periodic boundary conditions. In all the chapter except Sect. 15.4.3 the total particle number is fixed and equal to N. In all the chapter except in Sect. 15.3.2 the system is three-dimensional. We restrict to the deeply Bose-condensed regime where the non-condensed fraction is small. This implies that the temperature T is much lower than the critical temperature T_c

Y. Castin (✉) · A. Sinatra
Laboratoire Kastler Brossel, Ecole normale supérieure, CNRS and UPMC, Paris, France
e-mail: yvan.castin@lkb.ens.fr

A. Sinatra
e-mail: alice.sinatra@lkb.ens.fr

A. Bramati, M. Modugno (eds.), *Physics of Quantum Fluids*,
Springer Series in Solid-State Sciences 177, DOI 10.1007/978-3-642-37569-9_15,

and that the system is weakly interacting. Interactions between the cold bosons are characterized by the s-wave scattering length a, that we take positive for repulsive interactions. The microscopic details of the interaction potential are irrelevant here since the interaction range is much smaller than the typical de Broglie wavelength of the particles. The weakly interacting regime, in the considered low temperature regime, is then defined by $(\rho a^3)^{1/2} \ll 1$ where $\rho = N/V$ is the mean density.

We assume that the gas is prepared in thermal equilibrium at negative times with some unspecified experimental procedure generally implying a coupling with the outer world. For clarity we consider first that the system is prepared either in the canonical or the microcanonical ensemble, then we apply our theory to a more general ensemble: a statistical mixture of microcanonical ensembles with weak relative energy fluctuations. After the preparation phase, at positive times, the system is supposed to be *totally isolated* in its evolution. This implies that the total particle number N and the total energy E are exactly conserved in time evolution. This assumption is realistic for ultra-cold atom experiments: the atoms are hold in conservative immaterial traps and the three-body loss rates are very low in the weak density limit. As we shall see, this has important consequences for the temporal coherence of the gas.

A first property that we discuss in this chapter is the spatial coherence of the gas. This is determined by the first-order coherence function

$$g_1(\mathbf{r}) \equiv \left\langle \hat{\psi}^\dagger(\mathbf{r}) \hat{\psi}(\mathbf{0}) \right\rangle \tag{15.1}$$

where the bosonic field operator $\hat{\psi}(\mathbf{r})$ annihilates a particle in position $\mathbf{r}$. The g_1 function has been measured using atomic interferometric techniques [4]. In the thermodynamic limit, $g_1(\mathbf{r})$ tends to the condensate density $\rho_0 > 0$ at large distances r. One refers to this property as long-range order.

A second, more subtle property, that we discuss in detail is the temporal coherence of the gas. We define the temporal coherence function of the condensate as

$$\left\langle \hat{a}_0^\dagger(t) \hat{a}_0(0) \right\rangle \tag{15.2}$$

where $\hat{a}_0$ is the annihilation operator in the condensate mode that is the plane wave with $\mathbf{k} = \mathbf{0}$. Contrarily to the case of g_1, here the operators appear in the Heisenberg picture at different times. The temporal coherence function of the condensate is measurable (as we argue in Sect. 15.4.1) but it was not measured yet. The closest analog that has been measured is the relative coherence of two condensates in different external or internal states at equal times [5, 6]. The coherence time of the condensate is simply the half width of the temporal coherence function. Remarkably at zero temperature it was shown that the coherence function does not decay at long times, it rather oscillates [7]

$$\left\langle \hat{a}_0^\dagger(t) \hat{a}_0(0) \right\rangle \sim \langle \hat{n}_0 \rangle e^{i\mu(T=0)t/\hbar} \tag{15.3}$$

where $\langle \hat{n}_0 \rangle$ is the mean number of particles in the condensate and $\mu(T=0)$ is the ground state chemical potential of the gas. This implies an infinite coherence time.

At finite temperature however one expects a finite coherence time for a finite size system. We find that in the thermodynamic limit this coherence time diverges with a scaling with the system volume V that depends on the statistical ensemble in which the system is prepared.

This chapter is based on our works [8–10].[1] It is organized as follows. We give a pedagogical presentation of the number conserving Bogoliubov theory, a central tool for our problem, in Sect. 15.2. We apply this theory to the spatial coherence in Sect. 15.3. The more involved issue of temporal coherence is treated in Sect. 15.4. In Sect. 15.4.1 we discuss how to measure $\langle \hat{a}_0^\dagger(t)\hat{a}_0(0)\rangle$ with cold atoms. General considerations are given in 15.4.2, showing the central role of condensate phase-change spreading, that is then studied for different initial states of the gas. First for a single-mode model in 15.4.3 and for the canonical ensemble Sect. 15.4.4, where one of the conserved quantities (the particle number N or the energy E) has fluctuations in the initial state. Then for the microcanonical ensemble Sect. 15.4.5, where none of these conserved quantities fluctuates. Finally in the already mentioned more general statistical ensemble within a unified theoretical framework in Sect. 15.4.6.

15.2 Reminder of Bogoliubov Theory

The central result of Bogoliubov theory [11] is that our system can be described as an ensemble of weakly interacting *quasi-particles*. The necessity to go from a particle to a quasi-particle picture to obtain weakly interacting objects is due to the presence of the condensate that provides a large bosonic enhancement of particle scattering processes in and out of the condensate mode. In the initial work of Bogoliubov the quasi-particles are non-interacting. We will need to include the interactions among quasi-particles that give them a finite lifetime through the so-called Beliaev-Landau mechanism [7, 12]. Here we present a powerful formulation of Bogoliubov ideas introducing the phase operator $\hat{\theta}$ for the condensate mode [13]: in addition to making the theory number conserving [14–16], $\hat{\theta}$ will play a crucial role for the study of temporal coherence.

15.2.1 Lattice Model Hamiltonian

Commonly a zero range delta potential $V_{12} = g\delta(\mathbf{r}_1 - \mathbf{r}_2)$ is used to model particle interactions with an effective coupling constant

$$g = \frac{4\pi\hbar^2 a}{m} \tag{15.4}$$

[1] Particle losses are not discussed in this chapter. Their effect on temporal coherence is weak at relevant times as explicitly shown in [10] for one-body losses in the canonical ensemble.

(here the s-wave scattering length is $a > 0$ and m is the mass of a particle). This however does not lead to a mathematically well defined Hamiltonian problem, even for two particles. As explained in [17] a convenient way to regularize the theory while keeping the simplicity of contact interactions is to discretize the coordinate space on a cubic lattice with lattice spacing b. This automatically introduces a cut-off in momentum space, since single particle wave vectors are restricted to the first Brillouin zone (FBZ) of the lattice $[-\frac{\pi}{b}, \frac{\pi}{b})^3$. Then

$$V_{12} = g_0 \frac{\delta_{\mathbf{r}_1,\mathbf{r}_2}}{b^3} \tag{15.5}$$

where now δ is a discrete Kronecker δ. The bare coupling constant g_0 is adjusted to reproduce the true s-wave scattering length on the lattice [17],

$$g_0 = \frac{g}{1 - Ca/b} \tag{15.6}$$

where $C = 2.442\,749\ldots$ is a numerical constant.[2] The Bogoliubov method is applicable when the zero energy scattering problem is treatable in the Born regime [18] which requires here that $a \ll b$. In this limit $g_0 \simeq g$. For the lattice model to well describe continuous space physics the lattice spacing b should be smaller than the macroscopic length scales ξ and λ of the gas. The healing length ξ is defined as

$$\frac{\hbar^2}{2m\xi^2} = \rho g \tag{15.7}$$

and the thermal de Broglie wavelength as

$$\lambda^2 = \frac{2\pi\hbar^2}{mk_BT} \tag{15.8}$$

Note that in the weakly interacting and degenerate limit one has $\xi \gg a$ and $\lambda \gg a$.

The system Hamiltonian in second quantized form is

$$\hat{H} = \sum_{\mathbf{r}} b^3 \left[\hat{\psi}^\dagger h_0 \hat{\psi} + \frac{g_0}{2} \hat{\psi}^\dagger \hat{\psi}^\dagger \hat{\psi} \hat{\psi} \right] \tag{15.9}$$

where h_0 is the one-body Hamiltonian reduced here to the kinetic energy term, $h_0 = -\frac{\hbar^2}{2m}\Delta_{\mathbf{r}}$, with a discrete Laplacian reproducing the free wave dispersion relation $E_k = \hbar^2 k^2/2m$ when applied over a plane wave. The bosonic field operator $\hat{\psi}(\mathbf{r})$ obeys the discrete commutation relation

$$\left[\hat{\psi}(\mathbf{r}_1), \hat{\psi}^\dagger(\mathbf{r}_2)\right] = \frac{\delta_{\mathbf{r}_1,\mathbf{r}_2}}{b^3} \tag{15.10}$$

[2] This results from the formula $g_0^{-1} = g^{-1} - \int_{\mathrm{FBZ}} \frac{d^3k}{(2\pi)^3} \frac{m}{\hbar^2 k^2}$.

15.2.2 Bogoliubov Expansion of the Hamiltonian

We split the field operator into the condensate field and the non-condensed field $\hat{\psi}_\perp(\mathbf{r})$ orthogonal to the condensate wave function $\phi(\mathbf{r})$:

$$\hat{\psi}(\mathbf{r}) = \phi(\mathbf{r})\hat{a}_0 + \hat{\psi}_\perp(\mathbf{r}) \tag{15.11}$$

where $\hat{a}_0$ is the annihilation operator of a particle in the condensate mode. For the homogeneous system that we consider, $\phi(\mathbf{r}) = 1/V^{1/2}$. The main idea of the Bogoliubov approach is to use the fact that the non-condensed field is much smaller than the condensate field to expand the Hamiltonian in powers of $\hat{\psi}_\perp(\mathbf{r})$. This becomes truly operational if one succeeds in eliminating the amplitude $\hat{a}_0$ of the field on the condensate mode. For the modulus of $\hat{a}_0$ we can use the identity

$$\hat{n}_0 = \hat{N} - \hat{N}_\perp \tag{15.12}$$

with $\hat{N}$ the total particle number operator, $\hat{n}_0 = \hat{a}_0^\dagger \hat{a}_0$ the condensate particle number operator and $\hat{N}_\perp = \sum_{\mathbf{r}} b^3 \hat{\psi}_\perp^\dagger \hat{\psi}_\perp$ the non-condensed particle number operator. The elimination of the phase of $\hat{a}_0$ at the quantum level is more subtle, and it was not performed in the original work of Bogoliubov. We introduce the modulus-phase representation [13]

$$\hat{a}_0 = e^{i\hat{\theta}} \hat{n}_0^{1/2} \tag{15.13}$$

with the hermitian phase operator $\hat{\theta}$, conjugate to the condensate particle number:

$$[\hat{n}_0, \hat{\theta}] = i \tag{15.14}$$

It is known that the introduction of a phase operator in quantum mechanics is a delicate matter [19]. As we explain below, our formulation is not exact but it is extremely accurate in the present case of a highly populated condensate mode. As it appears from (15.14), there is a formal analogy with the position operator $\hat{x}$ and the momentum operator $\hat{p}$ of a fictitious particle in one spatial dimension. For the fictitious particle $\hat{p}$ is the generator of spatial translations so that

$$\begin{aligned} [\hat{x}, \hat{p}] = i\hbar \quad &\Longrightarrow \quad e^{i\hat{p}/\hbar}|x\rangle = |x-1\rangle \\ [\hat{n}_0, \hat{\theta}] = i \quad &\Longrightarrow \quad e^{i\hat{\theta}}|n_0 : \phi\rangle = |n_0 - 1 : \phi\rangle \end{aligned}$$

where $|x\rangle$ represents the fictitious particle localized in position x and $|n_0 : \phi\rangle$ is the Fock state with n_0 particles in the condensate mode. As a consequence the representation (15.13) of $\hat{a}_0$ has the correct matrix elements in the Fock basis. The operator $\exp(i\hat{\theta})$ is a respectable unitary operator... except when the condensate mode is empty where one gets the meaningless result:

$$e^{i\hat{\theta}}|0 : \phi\rangle \stackrel{?!}{=} |-1 : \phi\rangle \tag{15.15}$$

This is in practice not an issue if, in the physical state of the system, the probability for the condensate mode to be empty is negligible. For a finite size system the probability distribution of n_0 was calculated using the Bogoliubov approach and even an exact numerical approach [20, 21]. In the thermodynamic limit we expect that the probability of having an empty condensate vanishes exponentially with the system size at $T < T_c$.

In order to eliminate the condensate phase we introduce the number conserving operator [14, 15]

$$\hat{\Lambda}(\mathbf{r}) = e^{-i\hat{\theta}}\hat{\psi}_\perp(\mathbf{r}) \tag{15.16}$$

The success of the elimination procedure is guaranteed since the Hamiltonian conserves the particle number: Injecting the splitting of the field (15.11) in the Hamiltonian and expanding, generates a series of terms in which $\hat{a}_0$ appears either with $\hat{a}_0^\dagger$ or with $\hat{\psi}_\perp^\dagger(\mathbf{r})$. Expanding $\hat{H}$ to second order in $\hat{\psi}_\perp$ and using (15.12) we obtain the Bogoliubov Hamiltonian

$$\boxed{\hat{H}_{\rm Bog} = \frac{g_0 N^2}{2V} + \sum_{\mathbf{r}} b^3 \left[\hat{\Lambda}^\dagger (h_0 - \mu_0)\hat{\Lambda} + \mu_0 \left(\frac{1}{2}\hat{\Lambda}^2 + \frac{1}{2}\hat{\Lambda}^{\dagger 2} + 2\hat{\Lambda}^\dagger \hat{\Lambda} \right) \right]} \tag{15.17}$$

We have assumed that the total particle number is fixed and equal to N and we have replaced $\hat{N}$ by N. Still, one obtains a grand canonical ensemble for the non-condensed modes, with a chemical potential $\mu_0 = g_0\rho$. The condensate indeed acts as a reservoir of particles for the non-condensed modes. The expression $\mu_0 = g_0\rho$ is in fact the zeroth order approximation (in the non-condensed fraction) to the gas chemical potential. In what follows we shall take

$$\mu_0 = g\rho \tag{15.18}$$

which is consistent with the Bogoliubov theory at this order. The terms $\hat{\Lambda}^\dagger\hat{\Lambda}$ in (15.17) represent elastic interactions between the condensate and the non-condensed particles. They also appear in the simple Hartree-Fock theory. The terms $\hat{\Lambda}^{\dagger 2}$ and hermitian conjugate represent inelastic interactions where two condensate particles collide and are both scattered into non-condensed modes with opposite momenta. They are absent in the Hartree-Fock theory and they play a crucial role in explaining the superfluidity of the gas.

15.2.3 An Ideal Gas of Quasi-particles

To extract the physics contained in the Bogoliubov Hamiltonian one has to identify the eigenmodes of the system putting the quadratic Hamiltonian in a normal form. We present here a brief overview, a more detailed discussion was given in [16, 22].

In the Heisenberg picture the equations of motion of the field operators are linear, provided one collects $\hat{\Lambda}$ and $\hat{\Lambda}^\dagger$ into a single unknown:

$$i\hbar\partial_t \begin{pmatrix} \hat{\Lambda} \\ \hat{\Lambda}^\dagger \end{pmatrix} = \begin{pmatrix} h_0+\mu_0 & \mu_0 \\ -\mu_0 & -(h_0+\mu_0) \end{pmatrix} \begin{pmatrix} \hat{\Lambda} \\ \hat{\Lambda}^\dagger \end{pmatrix} \equiv \mathscr{L} \begin{pmatrix} \hat{\Lambda} \\ \hat{\Lambda}^\dagger \end{pmatrix} \tag{15.19}$$

The matrix $\mathscr{L}$ is not hermitian for the usual scalar product, but it is "hermitian" for a modified scalar product of signature $(1,-1)$. It has moreover a symmetry property ensuring that its eigenvalues come in pairs $\pm\varepsilon_k$.

We now expand the field operators over the eigenvectors of $\mathscr{L}$:

$$\begin{pmatrix} \hat{\Lambda}(\mathbf{r}) \\ \hat{\Lambda}^\dagger(\mathbf{r}) \end{pmatrix} = \sum_{\mathbf{k}\neq\mathbf{0}} \frac{e^{i\mathbf{k}\cdot\mathbf{r}}}{V^{1/2}} \begin{pmatrix} U_k \\ V_k \end{pmatrix} \hat{b}_{\mathbf{k}} + \frac{e^{-i\mathbf{k}\cdot\mathbf{r}}}{V^{1/2}} \begin{pmatrix} V_k \\ U_k \end{pmatrix} \hat{b}^\dagger_{\mathbf{k}} \tag{15.20}$$

with $U_k^2 - V_k^2 = 1$ (this is the normalization condition for the modified scalar product). An explicit calculation gives

$$U_k + V_k = \frac{1}{U_k - V_k} = \left(\frac{\hbar^2k^2/2m}{2\mu_0 + \hbar^2k^2/2m} \right)^{1/4} \tag{15.21}$$

The coefficients $\hat{b}_{\mathbf{k}}$ and $\hat{b}^\dagger_{\mathbf{k}}$ obey the usual bosonic commutation relations e.g. $[\hat{b}_{\mathbf{k}}, \hat{b}^\dagger_{\mathbf{k}'}] = \delta_{\mathbf{k},\mathbf{k}'}$. Injecting the modal decomposition (15.20) in the Bogoliubov Hamiltonian (15.17) one obtains a Hamiltonian of non-interacting bosons called quasi-particles:

$$\boxed{\hat{H}_{\mathrm{Bog}} = E_0(N) + \sum_{\mathbf{k}\neq\mathbf{0}} \varepsilon_k \hat{b}^\dagger_k \hat{b}_{\mathbf{k}} \quad \text{with } \varepsilon_k = \left[\frac{\hbar^2k^2}{2m} \left(\frac{\hbar^2k^2}{2m} + 2\mu_0 \right) \right]^{1/2}} \tag{15.22}$$

The quantity $E_0(N)$ is the Bogoliubov approximation of the ground state energy. It reads

$$E_0(N) = \frac{g_0 N^2}{2V} - \sum_{\mathbf{k}\neq\mathbf{0}} \varepsilon_k V_k^2 \tag{15.23}$$

In the continuous space limit $b/\xi \to 0$, the sum over $\mathbf{k}$ has an ultraviolet ($k \to \infty$) divergence. If one replaces g_0 by its expression (15.6) expanded to first order in a/b, $g_0 \simeq g(1 + Ca/b)$, this exactly compensates the ultraviolet divergence and one recovers the Lee-Huang-Yang result

$$E_0(N) = \frac{gN^2}{2V} \left[1 + \frac{128}{15\pi^{1/2}} \left(\rho a^3 \right)^{1/2} \right] \tag{15.24}$$

The Bogoliubov spectrum ε_k starts linearly at low k: the quasi-particles are then phonons. At high k one recovers the free particle spectrum shifted upwards by μ_0:

quasi-particles in this limit are just particles. At thermal equilibrium in the canonical ensemble for the original system the Bogoliubov density operator is

$$\hat{\sigma} = \frac{1}{Z_{\rm Bog}} e^{-\beta \hat{H}_{\rm Bog}} \quad \text{with } \beta = 1/k_B T \tag{15.25}$$

where $Z_{\rm Bog}$ is the partition function in the Bogoliubov approximation. This density operator in the canonical ensemble for *particles*, corresponds in fact to a grand canonical ensemble, with zero chemical potential, for the *quasi-particles* whose number is not conserved.

15.3 Spatial Coherence

In this section we discuss the spatial coherence properties of a weakly interacting Bose-condensed gas, using the Bogoliubov theory. As expected one finds long range order in the thermodynamic limit. To complete the discussion we briefly address the case of a low-dimensional system where long range order is in general lost (except for the $2D$ gas at zero temperature) but where the ideas of the Bogoliubov method can be adapted for quasi-condensates [17, 23].

15.3.1 Non-condensed Fraction and g_1 Function

In a spatially homogeneous gas, the non-condensed fraction is the ratio of the non-condensed density $\langle \hat{\Lambda}^\dagger \hat{\Lambda} \rangle$ and the total density ρ. Using the modal decomposition (15.20) and the thermal equilibrium state (15.25), one obtains in the thermodynamic limit in $3D$:

$$\frac{\langle \hat{N}_\perp \rangle}{N} = \frac{\langle \hat{\Lambda}^\dagger \hat{\Lambda} \rangle}{\rho} = \frac{1}{\rho} \int \frac{d^3k}{(2\pi)^3} \left[\frac{U_k^2 + V_k^2}{e^{\beta \varepsilon_k} - 1} + V_k^2 \right] \tag{15.26}$$

This integral has no ultraviolet ($k \to \infty$) divergence since $V_k^2 = O(1/k^4)$. One can thus take the continuous space limit $b \to 0$ and integrate over the whole Fourier space. The integral has no infrared ($k \to 0$) divergence either, since $U_k^2, V_k^2 = O(1/k)$. In order for the Bogoliubov theory to be applicable, the non-condensed fraction should be small. From the result (15.26) one can check that this is indeed the case for the degenerate $\rho\lambda^3 \gg 1$ and weakly interacting $(\rho a^3)^{1/2} \ll 1$ regime.

The first-order coherence function (15.1) in the thermodynamic limit is given in the Bogoliubov theory by

$$g_1^{\rm Bog}(\mathbf{r}) = \rho - \int \frac{d^3k}{(2\pi)^3} (1 - \cos \mathbf{k} \cdot \mathbf{r}) \left[\frac{U_k^2 + V_k^2}{e^{\beta \varepsilon_k} - 1} + V_k^2 \right] \tag{15.27}$$

where we used the exact relation $\langle \hat{a}_0^\dagger \hat{\psi}_\perp \rangle = 0$. In the large r limit, the contribution of the oscillating term $\cos \mathbf{k} \cdot \mathbf{r}$ vanishes and g_1 tends to the condensate density. This implies that spatial coherence extends over the whole system size.

15.3.2 In Low Dimensions

In a straightforward generalization of (15.26) to low dimensions, the non-condensed fraction is infrared divergent in $2D$ for $T > 0$, and in $1D$ for all T: there is no Bose-Einstein condensate in the thermodynamic limit in agreement with the Mermin-Wagner-Hohenberg theorem [24, 25]. Nevertheless, in the weakly interacting and degenerate regime there are weak density fluctuations and weak phase gradients. This is the so called quasi-condensate regime [23, 26]. The main ideas of the Bogoliubov approach can still be applied after the introduction of a modulus-phase representation of the field operator $\hat{\psi}$ in each lattice site [27]:

$$\hat{\psi}(\mathbf{r}) = e^{i\hat{\theta}(\mathbf{r})} \sqrt{\hat{\rho}(\mathbf{r})} \tag{15.28}$$

where $\hat{\rho}(\mathbf{r}) b^d$ and $\hat{\theta}(\mathbf{r})$ are conjugate variables similarly to (15.14) and d is the spatial dimension. As we discussed in Sect. 15.2.2 and in [17], the modulus-phase representation of the annihilation operator in a given field mode is accurate if this mode has a negligible probability to be empty. This in particular requires that the mean number of particles per lattice site is large, $\rho b^d \gg 1$. In the weakly interacting $\rho \xi^d \gg 1$ and degenerate $\rho \lambda^d \gg 1$ regime, one can adjust b to satisfy this condition while keeping $b \ll \xi, \lambda$ so as to well reproduce the continuous space physics. In this regime one also finds that the probability distribution of the number of particles on a given lattice site is strongly peaked around the mean value $\rho b^d \gg 1$, with a width much smaller than the mean value, which legitimates the representation (15.28).

If one blindly applies the plain Bogoliubov result (15.27) in the absence of a condensate,[3] one finds that the first-order coherence function $g_1^{\mathrm{Bog}}(\mathbf{r}) \to -\infty$ at infinity, logarithmically with r in $2D$ ($T > 0$) and in $1D$ ($T = 0$), and even linearly in r in $1D$ at $T > 0$. One may believe at this stage that $g_1^{\mathrm{Bog}}(\mathbf{r})$ is simply meaningless in those cases. The extension of the Bogoliubov theory to quasi-condensates however produces the remarkable result [27]:

$$g_1^{\mathrm{QC}}(\mathbf{r}) = \rho \exp\left[\frac{g_1^{\mathrm{Bog}}(\mathbf{r})}{\rho} - 1 \right] \tag{15.29}$$

The quasi-condensate first-order coherence function $g_1^{\mathrm{QC}}(\mathbf{r})$ tends to zero for $r \to \infty$ as a power law in $2D$ ($T > 0$) and in $1D$ ($T = 0$), and exponentially for $T > 0$ in $1D$, as expected [23]. The gas has then a finite coherence length l_c (e.g. the

[3] One may wonder in $2D$ about the value of $\mu_0 = g_0 \rho$, since g_0 logarithmically depends on the lattice spacing b [27], and dimensionality reasons prevent from forming a coupling constant g (such that $g\rho$ is an energy) from the quantities $\hbar$, m and a, where a is now the $2D$ scattering length, given in [26, 28]. According to [27] one simply has to take for μ_0 the gas chemical potential $\mu(T)$.

half-width of g_1) much larger than ξ or λ in the weakly interacting and degenerate regime. Over distances $r \ll l_c$, phase fluctuations are small, and the system gives the illusion of being a condensate: one can linearize the exponential in (15.29), to obtain $g_1^{\rm QC}(\mathbf{r}) \simeq g_1^{\rm Bog}(\mathbf{r})$. The phase and density fluctuation properties of the quasi-condensates at nonzero temperature have been studied experimentally with cold atoms in $1D$ [29–31] and in $2D$ [32, 33] and confirm the theoretical picture.

15.4 Temporal Coherence

In this section we discuss the temporal coherence properties of a finite size Bose-condensed gas, defined by the coherence function $\langle \hat{a}_0^\dagger(t)\hat{a}_0(0)\rangle$ already introduced in (15.2). Although, strictly speaking, this coherence function was not measured yet with cold atoms, we argue in Sect. 15.4.1 that it is in principle measurable. In Sect. 15.4.2 we show that the condensate coherence function (15.2) can be related to the condensate phase-change during the time interval t. The loss of temporal coherence is thus due to the spreading in time of this phase-change, which is the quantity that we actually calculate. Whenever one of the conserved quantities (total particle number N or total energy E) fluctuates in the initial state from one realization to the other, the phase-change spreads ballistically. Once the effect of fluctuations of N is understood (Sect. 15.4.3), the more involved effect of energy fluctuations for fixed N can be understood by analogy. The resulting guess for the phase-change spreading can be justified within the quantum ergodic theory (Sect. 15.4.4). The only case in which pure phase diffusion is found is when the conserved quantities N and E are fixed, that is in the microcanonical ensemble (Sect. 15.4.5). For fixed N and a general statistical ensemble for energy fluctuations, we finally give in Sect. 15.4.6 the expression for the variance of the phase-change in the long time limit, that includes both a ballistic term and a diffusive term.

15.4.1 How to Measure the Temporal Coherence Function

We give here an idea of how to measure the condensate temporal coherence function $\langle \hat{a}_0^\dagger(t)\hat{a}_0(0)\rangle$ in a cold atom experiment [10]. The scheme uses two long-lived atomic internal states $|a\rangle$ and $|b\rangle$ and it is a Ramsey experiment as in [5], with the notable difference that the pulses are arbitrarily weak instead of being $\pi/2$ pulses.

The Bose-condensed gas is prepared in equilibrium in the internal state $|a\rangle$ and the state $|b\rangle$ is initially empty. At time zero one applies a very weak electromagnetic pulse, of negligible duration, coherently coupling the two internal states. After the pulse, the system evolves during a time t in presence of interactions only among atoms in $|a\rangle$: we assume no interactions between a and b components[4] and neg-

[4]This can be realized experimentally either using a Feshbach resonance [34] or spatially separating the two components [35].

ligible interactions within the b component due to the very weak density in that component. At time t one applies a second pulse of the same amplitude, and one measures the particle number in state $|b\rangle$ in the plane wave $\mathbf{k} = \mathbf{0}$.

The scheme can be formalized as follows. The first pulse, at $t = 0$, coherently mixes the two bosonic fields $\hat{\psi}_a$ and $\hat{\psi}_b$ with a real amplitude η so that

$$\hat{\psi}_a(\mathbf{r}, 0^+) = \sqrt{1-\eta^2}\,\hat{\psi}_a(\mathbf{r}, 0^-) + \eta\hat{\psi}_b(\mathbf{r}, 0^-) \tag{15.30}$$

$$\hat{\psi}_b(\mathbf{r}, 0^+) = \sqrt{1-\eta^2}\,\hat{\psi}_b(\mathbf{r}, 0^-) - \eta\hat{\psi}_a(\mathbf{r}, 0^-) \tag{15.31}$$

In between time 0^+ and time t^- the two fields evolve independently. Field $\hat{\psi}_a$ evolves in presence of kinetic and interaction terms as in (15.9). Field $\hat{\psi}_b$ evolves with kinetic and internal energy terms so that its amplitude on the $\mathbf{k} = \mathbf{0}$ mode obeys

$$\hat{b}_0(t^-) = e^{i\delta t}\hat{b}_0(0^+) \tag{15.32}$$

where δ is the detuning between the electromagnetic field and the $a - b$ atomic transition (the calculation is performed in the rotating frame). The second pulse at time t mixes again the two fields with the same mixing amplitudes as in (15.30), (15.31). After the second pulse one measures $N_{b0}(t) = \langle(\hat{b}_0^\dagger\hat{b}_0)(t^+)\rangle$. Using the mixing relations and (15.32) one expresses $\hat{b}_0(t^+)$ as a function of $\hat{b}_0(0^-)$, $\hat{a}_0(0^-)$ and $\hat{a}_0(t^-)$. Since the initial state for component b is the vacuum, the contribution of $\hat{b}_0(0^-)$ vanishes and one obtains the exact relation:

$$\begin{aligned} N_{b0}(t) = \eta^2\big\{&(1-\eta^2)\big\langle(\hat{a}_0^\dagger\hat{a}_0)(0^-)\big\rangle + \big\langle(\hat{a}_0^\dagger\hat{a}_0)(t^-)\big\rangle_{\text{pulse}} \\ &+ \sqrt{1-\eta^2}\big[e^{i\delta t}\big\langle\hat{a}_0^\dagger(t^-)\hat{a}_0(0^-)\big\rangle_{\text{pulse}} + \text{c.c.}\big]\big\} \end{aligned} \tag{15.33}$$

that we expand for vanishing η:

$$N_{b0}(t) = 2\eta^2\big\{\langle\hat{n}_0\rangle + \text{Re}\big[e^{i\delta t}\big\langle\hat{a}_0^\dagger(t)\hat{a}_0(0)\big\rangle\big]\big\} + O(\eta^4) \tag{15.34}$$

In particular, the subscript $\langle\ldots\rangle_{\text{pulse}}$ on the expectation values, indicating that they are taken for a system having experienced the first pulse, was removed.[5] The desired correlation function $\langle\hat{a}_0^\dagger(t)\hat{a}_0(0)\rangle$ can be extracted from the contrast of the fringes obtained by varying the electromagnetic field frequency. The signal $N_{b0}(t)$ itself is small (it is proportional to η^2) but the contrast of the fringes is independent of η in the small η limit, and it starts at unity at $t = 0$.

[5]The expectation values $\langle\ldots\rangle_{\text{pulse}}$ differ from the original ones $\langle\ldots\rangle$ in the absence of pulse by $O(\eta^2)$: To first order in η, the perturbation of $\hat{\psi}_a$ due to the pulse is linear in $\hat{\psi}_b(0^-)$ and has a zero contribution to the expectation values since component b is initially in vacuum.

15.4.2 General Considerations About $\langle \hat{a}_0^\dagger(t)\hat{a}_0(0)\rangle$

15.4.2.1 Phase-Change Spreading

Here we go through a sequence of transformations that relates the temporal coherence function $\langle \hat{a}_0^\dagger(t)\hat{a}_0(0)\rangle$ to the variance of the condensate phase-change $\hat{\theta}(t)-\hat{\theta}(0)$. We use the modulus-phase representation (15.13) of the annihilation operator $\hat{a}_0$. Since the non-condensed fraction is very small, we simply neglect the fluctuations of the modulus of $\hat{a}_0$ i.e. we replace $\hat{n}_0$ with its mean value in (15.13). We then obtain[6]

$$\left\langle \hat{a}_0^\dagger(t)\hat{a}_0(0)\right\rangle \simeq \langle \hat{n}_0\rangle \left\langle e^{-i[\hat{\theta}(t)-\hat{\theta}(0)]}\right\rangle \tag{15.35}$$

If the phase-change $\hat{\theta}(t)-\hat{\theta}(0)$ has a Gaussian distribution, which may be checked *a posteriori*, the application of Wick's theorem yields

$$\boxed{\left\langle \hat{a}_0^\dagger(t)\hat{a}_0(0)\right\rangle \simeq \langle \hat{n}_0\rangle e^{-i\langle \hat{\theta}(t)-\hat{\theta}(0)\rangle} e^{-\mathrm{Var}[\hat{\theta}(t)-\hat{\theta}(0)]/2}} \tag{15.36}$$

This remarkable formula quantitatively relates the loss of temporal coherence in an isolated Bose-condensed gas to the spreading of the condensate phase-change.

The operational way to determine the condensate phase-change spreading is to work with the phase derivative: contrarily to $\hat{\theta}$, $\dot{\hat{\theta}}$ is a *single-valued* hermitian operator that has a simple expression within the Bogoliubov approach. The correlation function of the phase derivative

$$C(t) = \left\langle \dot{\hat{\theta}}(t)\dot{\hat{\theta}}(0)\right\rangle - \langle \dot{\hat{\theta}}\rangle^2 \tag{15.37}$$

gives access to the variance of the phase-change by simple integration:

$$\boxed{\mathrm{Var}\left[\hat{\theta}(t)-\hat{\theta}(0)\right] = 2t\int_0^t d\tau\, C_R(\tau) - 2\int_0^t d\tau\, \tau\, C_R(\tau)} \tag{15.38}$$

where C_R is the real part of C. One obtains a single integral (rather than a double integral) using the fact that the real part of $\langle \dot{\hat{\theta}}(t_1)\dot{\hat{\theta}}(t_2)\rangle$ is a function of $|t_1-t_2|$ only, for a system at equilibrium. The long-time behavior of C_R determines how the phase-change spreads at long times as summarized in Fig. 15.1.

At finite temperature, one might expect that $\dot{\hat{\theta}}(t)$ decorrelates from $\dot{\hat{\theta}}(0)$ at long times so that $C_R \to 0$ and the phase-change spreading is diffusive. As we will see, this is however not the case, except if the system is prepared in the microcanonical ensemble. This is a consequence of energy conservation between times 0 and t in our isolated system. This point was overlooked in the early studies of [36–38] where

[6] Here we have neglected the non-commutation of $\hat{\theta}(t)$ and $\hat{\theta}(0)$. From the Baker-Campbell-Hausdorff formula, and to zeroth order in the non-condensed fraction, see (15.45), the correction is a factor $e^{-\frac{Ht}{2\hbar}\mu'(N)+O(N^{-2})}$ which is irrelevant for our discussion.

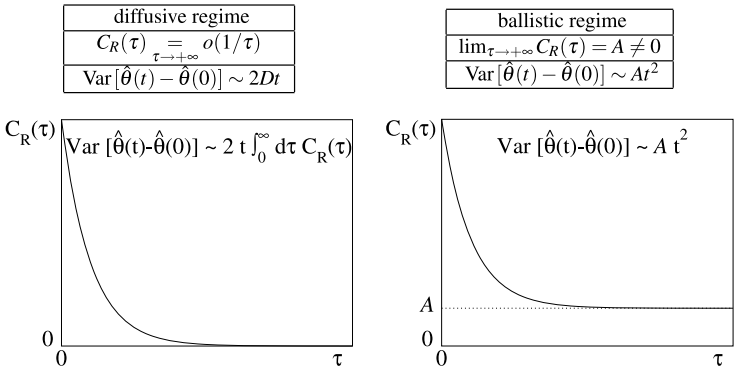

Fig. 15.1 Different regimes of the condensate phase-change spreading at long times. C_R is the real part of the correlation function C defined in (15.37)

the non-condensed modes were treated as a Markovian reservoir and phase diffusion was predicted. A subsequent study [39] based on a many-body Hamiltonian approach showed that phase-change spreading is ballistic for a system prepared in the canonical ensemble. The coefficient of t^2 in [39] was however calculated within the pure Bogoliubov approximation, neglecting the interactions between the Bogoliubov quasi-particles, which is illegitimate in the long time limit as we shall see.

15.4.2.2 Key Ingredients of the Theory

In order to correctly determine the phase-change spreading in the long time limit, we shall use two key ingredients in our theoretical treatment: an accurate expression of the phase derivative and the inclusion of the interactions among Bogoliubov quasi-particles, to which we add the constraint of strict energy conservation during the system evolution.

Time Derivative of Condensate Phase Operator The commutator of $\hat{\theta}$ with $\hat{H}$ given by (15.9) is calculated exactly using

$$\left[\hat{\theta}, \hat{\psi}(\mathbf{r})\right] = -\hat{a}_0 \frac{i\phi(\mathbf{r})}{2\hat{n}_0} \tag{15.39}$$

and its hermitian conjugate, with the condensate wave function $\phi(\mathbf{r}) = 1/V^{1/2}$. The exact result is given in (67) of [8]. Expanding up to second order in the non-condensed field $\hat{\Lambda}$ and using the modal decomposition (15.20), one obtains for fixed N:[7]

[7] We have neglected oscillating terms in $\hat{b}\hat{b}$ and $\hat{b}^\dagger\hat{b}^\dagger$: after time integration of $\dot{\hat{\theta}}$ they give a negligible contribution to $\hat{\theta}(t) - \hat{\theta}(0)$.

$$\dot{\hat{\theta}} = \frac{1}{i\hbar}[\hat{\theta}, \hat{H}] \simeq -\frac{1}{\hbar}\mu(T=0) - \frac{g_0}{\hbar V}\sum_{\mathbf{k}\neq\mathbf{0}}(U_k + V_k)^2\hat{n}_{\mathbf{k}} \tag{15.40}$$

We have introduced the zero-temperature chemical potential $\mu(T=0) = \frac{d}{dN}E_0(N)$, where $E_0(N)$ is given in (15.23), and the quasi-particle number operators

$$\hat{n}_{\mathbf{k}} = \hat{b}^\dagger_{\mathbf{k}}\hat{b}_{\mathbf{k}} \tag{15.41}$$

The expression (15.40) of the phase derivative differs from the one heuristically introduced in [37, 38]: $\dot{\hat{\theta}}$ is not simply equal to $-g\hat{n}_0/\hbar V$.

Interactions Between Quasi-particles Pushing one step further the Bogoliubov expansion of Sect. 15.2, that is including terms up to third order in the non-condensed field, one obtains

$$\hat{H} \simeq \hat{H}_{\text{Bog}} + \hat{H}_3 \tag{15.42}$$

where $\hat{H}_{\text{Bog}}$ is the Bogoliubov Hamiltonian (15.22) and

$$\hat{H}_3 = g_0\rho^{1/2}\sum_{\mathbf{r}} b^3\hat{\Lambda}^+\big(\hat{\Lambda} + \hat{\Lambda}^\dagger\big)\hat{\Lambda} \tag{15.43}$$

The Hamiltonian $\hat{H}_3$ is cubic in the field $\hat{\Lambda}$ and it corresponds to interactions between quasi-particles. While $\hat{H}_{\text{Bog}}$ is integrable (all the $\hat{n}_{\mathbf{k}}$ are conserved quantities), the Hamiltonian $\hat{H}_{\text{Bog}} + \hat{H}_3$ is not integrable, which plays a central role in condensate dephasing. By replacing $\hat{\Lambda}$ with its modal decomposition (15.20) in $\hat{H}_3$, two types of resonant processes appear, that do not conserve the total number of quasi-particles: the $\hat{b}^\dagger\hat{b}^\dagger\hat{b}$ Beliaev process and the $\hat{b}^\dagger\hat{b}\hat{b}$ Landau process. In the Beliaev process one quasi-particle decays into two quasi-particles, while in the Landau process two quasi-particles merge into another quasi-particle. The processes involving $\hat{b}^\dagger\hat{b}^\dagger\hat{b}^\dagger$ and $\hat{b}\hat{b}\hat{b}$ are non-resonant (they do not conserve the Bogoliubov energy) and they cannot induce real transitions at the present order.

15.4.3 If N Fluctuates

In this subsection we allow fluctuations of the total number of particles and we investigate their effect on temporal coherence. The effect is already present in the case of a pure condensate, so that we restrict to a one-mode model in this subsection: identifying the condensate particle number $\hat{n}_0$ with the total particle number $\hat{N}$, we obtain the model Hamiltonian

$$\hat{H}_{\text{one mode}} = \frac{g}{2V}\hat{N}^2 \tag{15.44}$$

The condensate phase derivative is

$$\dot{\hat{\theta}}(t) = \frac{1}{i\hbar}[\hat{\theta}, \hat{H}_{\text{one mode}}] = -\mu(\hat{N})/\hbar \tag{15.45}$$

where the chemical potential for the system with N particles is simply $\mu(N) = gN/V$ for the one-mode model. Since $\hat{N}$ is a constant of motion, temporal integration is straightforward:

$$\hat{\theta}(t) - \hat{\theta}(0) = -\mu(\hat{N})t/\hbar \tag{15.46}$$

If N is fixed there is no phase-change spreading. If the initial state is prepared with fluctuations in N then the phase-change spreads ballistically [40, 41]:

$$\text{Var}\big[\hat{\theta}(t) - \hat{\theta}(0)\big] = (t/\hbar)^2 \left(\frac{d\mu}{dN}\right)^2 \text{Var}\,\hat{N} \tag{15.47}$$

Correspondingly the temporal coherence function $\langle \hat{a}_0^\dagger(t)\hat{a}_0\rangle$ decays as a Gaussian in time[8] [42, 43]. A similar phenomenon was observed experimentally [44–46] not for the temporal correlation of a single condensate but for equal-time coherence $\langle \hat{a}_0^\dagger(t)\hat{b}_0(t)\rangle$ between two condensates prepared in different modes or internal states with a well defined relative phase and fluctuations in the relative particle number.

15.4.4 N Fixed, E Fluctuates: Canonical Ensemble

We assume in this subsection that the gas is prepared in equilibrium at finite temperature T in the canonical ensemble with N particles. We first treat this case by analogy with the previous subsection, and then we expose a systematic derivation of the result based on quantum ergodicity.

15.4.4.1 Using an Analogy with the Case of Fluctuating $\hat{N}$

Similarly to $\hat{N}$ in the previous subsection, here $\hat{H}$ is a conserved quantity that fluctuates in the initial state. Indeed the canonical ensemble is a statistical mixture of energy eigenstates with different eigenenergies. By analogy with (15.46) we expect that

$$\hat{\theta}(t) - \hat{\theta}(0) \sim -\mu_{\text{mc}}(\hat{H})t/\hbar \tag{15.48}$$

where $\mu_{\text{mc}}(E)$ is the chemical potential of the microcanonical ensemble of energy E. As relative energy fluctuations are vanishingly small for a large system, we

[8] The phase revivals at macroscopic times multiples of $2\pi\hbar V/g$ [42, 43] are absent here due to the Gaussian hypothesis used to obtain (15.36).

can linearize $\mu_{\rm mc}(E)$ around the mean energy $\bar{E}$ to obtain a *ballistic* phase-change spreading

$$\mathrm{Var}\big[\hat{\theta}(t)-\hat{\theta}(0)\big] \sim (t/\hbar)^2 \left[\frac{d\mu_{\rm mc}}{dE}(\bar{E})\right]^2 \mathrm{Var}\,\hat{H} \tag{15.49}$$

The coefficient of t^2 is proportional to the variance of the energy in the initial state and scales as the inverse of the system volume in the thermodynamic limit. For convenience, one can reexpress this coefficient in terms of canonical ensemble quantities using $\mu_{\rm mc}[\bar{E}(T)]=\mu(T)$ (for a large system) so that $\frac{d}{dE}\mu_{\rm mc}(\bar{E})=\frac{d}{dT}\mu/\frac{d}{dT}\bar{E}$, where $\mu(T)$ and $\bar{E}(T)$ are the chemical potential and mean energy in the canonical ensemble at temperature T. An explicit expression of the coefficient of t^2 is given in (73) of [8] using Bogoliubov theory to evaluate the partition function, $\bar{E}(T)$ and $\mu(T)$. The obtained formula for $\mu(T)$ also gives the intuitive and interesting side result

$$\langle\dot{\hat{\theta}}\rangle = -\mu(T)/\hbar \tag{15.50}$$

15.4.4.2 From Quantum Ergodic Theory

In the previous analogy leading to (15.49) there is a strong implicit hypothesis. The fact that the phase-change is a function of the Hamiltonian only, see (15.48), is in general true only for an ergodic system in the long time limit. For example if the Hamiltonian was truly equal to $\hat{H}_{\rm Bog}$, $\hat{\theta}(t)-\hat{\theta}(0)$ would depend on the set of all occupation number operators $\hat{n}_{\mathbf{k}}$ and (15.48), (15.49) would not apply.

We now derive (15.49) using quantum ergodic theory. To this end we calculate the asymptotic value of the correlation function $C(t)$. To eliminate oscillations of $C(t)$ we evaluate its time average. By inserting a closure relation over exact eigenstates $|\Psi_\lambda\rangle$ with eigenenergies E_λ of the interacting many-body system, we obtain

$$\frac{1}{t}\int_0^t d\tau\, C(\tau) \underset{t\to\infty}{\to} \sum_\lambda p_\lambda \big|\langle\Psi_\lambda|\dot{\hat{\theta}}|\Psi_\lambda\rangle\big|^2 - \left(\sum_\lambda p_\lambda \langle\Psi_\lambda|\dot{\hat{\theta}}|\Psi_\lambda\rangle\right)^2 \tag{15.51}$$

where p_λ is the probability to find the system in the eigenstate $|\Psi_\lambda\rangle$. In the canonical ensemble $p_\lambda=\exp(-\beta E_\lambda)/Z$. In (15.51) we have assumed that there are no degeneracies consistently with the non-integrability of the system.[9] For a classical system, ergodicity implies that the time average over a trajectory of energy E coincides with the microcanonical average at that energy. The extension of this concept to a quantum system is the so-called eigenstate thermalization hypothesis [47–49]:

[9] For a large system the level-spacing δE vanishes exponentially with the system size, and one may fear that an exponentially long time $t>\hbar/\delta E$ is needed to reach the limit (15.51). However, the corresponding off-diagonal matrix elements of $\dot{\hat{\theta}}$ also vanish exponentially with the system size in the eigenstate thermalization hypothesis [47].

the mean value of a few-body observable $\hat{O}$ in a *single* eigenstate $|\Psi_\lambda\rangle$ is very close to the microcanonical average at the same energy:

$$\langle\Psi_\lambda|\hat{O}|\Psi_\lambda\rangle \simeq \bar{\hat{O}}_{\rm mc}(E = E_\lambda) \tag{15.52}$$

We apply this hypothesis to the operator $\hat{O} = \dot{\hat{\theta}}$. The last step is to realize that within the Bogoliubov theory, the microcanonical average of $\dot{\hat{\theta}}$ is proportional to the microcanonical chemical potential[10]

$$\bar{\dot{\hat{\theta}}}_{\rm mc}(E) = -\mu_{\rm mc}(E)/\hbar \tag{15.53}$$

One then obtains

$$\boxed{\mathrm{Var}\big[\hat{\theta}(t) - \hat{\theta}(0)\big] \underset{t\to\infty}{\sim} \frac{t^2}{\hbar^2}\,\mathrm{Var}\,\mu_{\rm mc}(\hat{H})} \tag{15.54}$$

Linearizing $\mu_{\rm mc}(\hat{H})$ in (15.54) for small relative energy fluctuations around $\bar{E}$ one recovers (15.49).

15.4.4.3 Physical Implications

A consequence of (15.49) is that, for a system prepared in the canonical ensemble, the correlation function $C(\tau)$ of $\hat{\theta}$ *does not* tend to zero when $\tau \to +\infty$. The same conclusion is reached for the correlation function of $\hat{n}_0$, whose long time limit can be calculated with the quantum ergodic theory [8]. This qualitatively contradicts [36–38]. It only qualitatively agrees with [39] since the system Hamiltonian $\hat{H}$ in [39] was eventually replaced by the integrable Hamiltonian $\hat{H}_{\rm Bog}$.

In [36–38] the non-condensed modes were treated as a Markovian reservoir. This approximation is excellent to calculate temporal correlation functions of "microscopic" observables such as the quasiparticle numbers. For example, this gives for $\mathbf{k}, \mathbf{k}' \neq \mathbf{0}$ [8]:

$$\big\langle \hat{n}_{\mathbf{k}}(t)\hat{n}_{\mathbf{k}'}(0)\big\rangle - \langle\hat{n}_{\mathbf{k}}\rangle\langle\hat{n}_{\mathbf{k}'}\rangle \overset{\rm Markov}{=} \delta_{\mathbf{k},\mathbf{k}'}\langle\hat{n}_{\mathbf{k}}\rangle\big(1 + \langle\hat{n}_{\mathbf{k}}\rangle\big)e^{-\Gamma_{\mathbf{k}}t} \tag{15.55}$$

where the damping rate $\Gamma_{\mathbf{k}}$ is due to the Beliaev-Landau processes. However quantum ergodic theory shows that the exact long time limit of this correlation function is nonzero (even for $\mathbf{k} \neq \mathbf{k}'$) but rather a quantity of order $1/N$. In the double sum over $\mathbf{k}$ and $\mathbf{k}'$ that appears in $C(\tau)$, this introduces a macroscopic correction of order N missed by the Markovian approximation.

We illustrate this discussion in Fig. 15.2 with a classical field model [8]. The exact numerical result (black squares linked by a solid line) confirms the ergodic

[10] See Ref. [45] of [8]. In fact for a large system it is sufficient to prove the equality in the canonical ensemble of mean energy E, as already given by (15.50).

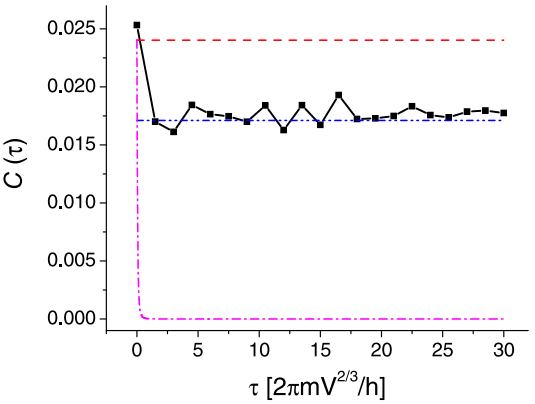

Fig. 15.2 For a gas prepared in the canonical ensemble, correlation function of $\dot{\theta}$ for the classical field model. The equation of motion is the non-linear Schrödinger equation. This corresponds to Fig. 6 in [8]. V is the volume. See text for the meaning of the various curves and symbols

result (dash-dot-dotted blue curve). The flat red dashed line is the Bogoliubov theory where the $n_{\mathbf{k}}$ are constants of motion. It is close to the numerical result only at short times. The dash-dotted violet curve that tends rapidly to zero is a Markovian model based on (15.55).

15.4.5 N Fixed, E Fixed: Microcanonical Ensemble

In this section we assume that the gas is prepared in the microcanonical ensemble of energy E. According to (15.54) the coefficient of the ballistic spreading of the phase-change is zero. It was found in [10] that $C(\tau) = O(1/\tau^3)$ at long times, so that the phase-change spreads diffusively, with a diffusion coefficient defined by

$$\mathrm{Var}\big[\hat{\theta}(t) - \hat{\theta}(0)\big] \sim 2Dt \quad \text{with } D = \int_0^\infty d\tau\, C_R(\tau) \tag{15.56}$$

To determine D we thus need the whole time dependence of $C(\tau)$. From (15.40), $C(\tau)$ can be deduced from all the correlation functions $\langle \hat{n}_{\mathbf{k}}(\tau)\hat{n}_{\mathbf{k}'}(0)\rangle$ of the quasi-particle number operators. Within the Bogoliubov approximation for the initial equilibrium state, the gas is prepared in a statistical mixture of Fock states $|\{n^0_{\mathbf{q}}\}\rangle$ of *quasi-particles* where, in any given Bogoliubov mode of wave vector $\mathbf{q}$, there are exactly $n^0_{\mathbf{q}}$ quasi-particles ($n^0_{\mathbf{q}}$ is an integer). One can then calculate the correlation functions for an initial Fock state $|\{n^0_{\mathbf{q}}\}\rangle$ and average over the microcanonical probability distribution for the $\{n^0_{\mathbf{q}}\}$.

For a given initial Fock state, one then simply needs

$$n_{\mathbf{k}}(\tau) \equiv \big\langle \{n^0_{\mathbf{q}}\} \big| \hat{n}_{\mathbf{k}}(\tau) \big| \{n^0_{\mathbf{q}}\} \big\rangle \tag{15.57}$$

In the thermodynamic limit, the evolution of such mean numbers of quasi-particles are given by quantum kinetic equations including the Beliaev-Landau processes due

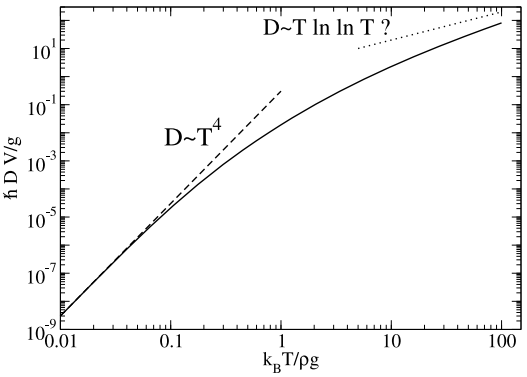

Fig. 15.3 *Solid line*: Universal result for the phase diffusion coefficient in the Bogoliubov limit $(\rho a^3)^{1/2} \ll 1$, $T \ll T_c$. *Dashed line*: Low-T analytical result (15.60). The high-T behavior is only conjectured, and the *dotted line* is an arbitrary linear function of T to guide the eye. V is the volume and g the effective coupling constant (15.4)

to $\hat{H}_3$ [50]:

$$\dot{n}_{\mathbf{k}} = -\frac{g^2\rho}{\hbar\pi^2}\int d^3q\big[n_{\mathbf{k}}n_{\mathbf{q}} - n_{\mathbf{k}+\mathbf{q}}(1+n_{\mathbf{q}}+n_{\mathbf{k}})\big]\big(\mathscr{A}_{q,k}^{|\mathbf{k}+\mathbf{q}|}\big)^2\delta(\varepsilon_k+\varepsilon_q-\varepsilon_{|\mathbf{k}+\mathbf{q}|}) - \frac{g^2\rho}{2\hbar\pi^2}\int d^3q\big[n_{\mathbf{k}}(1+n_{\mathbf{q}}+n_{\mathbf{k}-\mathbf{q}})-n_{\mathbf{q}}n_{\mathbf{k}-\mathbf{q}}\big]\big(\mathscr{A}_{q,|\mathbf{k}-\mathbf{q}|}^{k}\big)^2\delta(\varepsilon_q+\varepsilon_{|\mathbf{k}-\mathbf{q}|}-\varepsilon_k) \tag{15.58}$$

with the Beliaev-Landau coupling amplitudes:

$$\mathscr{A}_{k,k'}^{q} = U_qU_kU_{k'} + V_qV_kV_{k'} + (U_q+V_q)(V_kU_{k'}+U_kV_{k'}) \tag{15.59}$$

The first line in (15.58) describes Landau processes and the second line describes Beliaev processes. In practice we linearize the kinetic equation (15.58) around the equilibrium solution $\bar{n}_{\mathbf{k}}$ [11] and we solve the resulting linear system numerically. We refer to [10] for technical details.

The phase diffusion coefficient is shown in Fig. 15.3 as a function of the temperature T such that the mean canonical energy $\bar{E}(T)$ is equal to the microcanonical energy E. Remarkably, when D and T are properly rescaled (as in the figure), the curve is universal. In particular this shows that D vanishes as the inverse of the system volume in the thermodynamic limit. Interestingly, at low temperature, D vanishes with the same power-law T^4 as the normal fraction of the gas:

$$\frac{\hbar DV}{g} \sim 0.3036\left(\frac{k_BT}{\rho g}\right)^4 \tag{15.60}$$

We performed classical field simulations in the microcanonical ensemble [9]. As expected we found that the phase-change has a diffusive behavior: its variance

[11] For an infinite system, the stationary solution of (15.58) is ensemble independent and corresponds to the Bose formula $\bar{n}_{\mathbf{k}}(E) = 1/(\exp\beta\varepsilon_k - 1)$, where β is adjusted to give the mean energy E. Finite size effects on the $\bar{n}_{\mathbf{k}}$, that can be calculated from (61) of [8], are here not relevant.

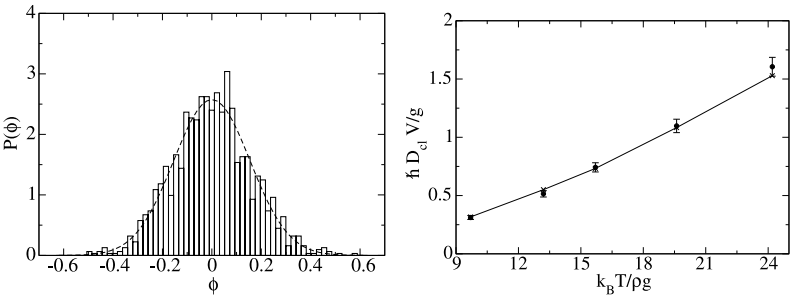

Fig. 15.4 Classical field simulations in the microcanonical ensemble. *Left panel* (taken from [9]): Probability distribution $P(\phi)$ of the condensate phase-change fluctuations $\phi = \theta(t) - \theta(0) - \langle \theta(t) - \theta(0) \rangle$ at a large time t. The *dashed line* is the expected Gaussian. *Right panel* (taken from [10]): Diffusion coefficient as a function of the temperature, extracted from the numerics (bullets with error bars) and calculated by the classical field version of the kinetic equations (15.58) (crosses linked by segments)

increases linearly in time at long times (not shown) and the phase-change probability distribution is well adjusted by a Gaussian as we show in the left panel of Fig. 15.4. In the right panel Fig. 15.4 we show that the diffusion coefficient is well reproduced by a classical field version of the kinetic theory.

15.4.6 A General Statistical Ensemble

We now consider a generalized ensemble at fixed N that includes both the microcanonical and the canonical ensembles as particular cases. This is a statistical mixture of microcanonical ensembles with a probability distribution $P(E)$ of the system energy E that depends on the particular experimental procedure to prepare the initial state of the gas. Remarkably the approach of the previous subsection based on kinetic equations can be extended to this case.

15.4.6.1 General Result for the Phase-Change Spreading

Provided that the relative energy fluctuations vanish in the thermodynamic limit, we find the long time limit [10]

$$\boxed{\mathrm{Var}\big[\hat{\theta}(t) - \hat{\theta}(0)\big] \underset{t\to+\infty}{=} \mathrm{Var}(E)\left[\frac{d\mu_{\mathrm{mc}}}{\hbar\, dE}(\bar{E})\right]^2 t^2 + 2D(t - t_{\mathrm{off}}) + O\left(\frac{1}{t}\right)} \tag{15.61}$$

For the coefficient A of the ballistic t^2 term we recover the *form* of the quantum ergodic result (15.49). This is not surprising as the reasoning of Sect. 15.4.4 does not

rely on the fact that the system is prepared in the canonical ensemble. On the other hand the *value* of the coefficient does depend on the statistical ensemble through the mean energy $\bar{E}$ and the variance of the energy. A physical derivation of this result within kinetic theory is given in the next subsection.

A remarkable result is that, in the general ensemble, the phase derivative correlation function $C(\tau)$ is the sum of its long time limit A and of the correlation function $C_{\rm mc}(\tau)$ in the microcanonical ensemble of energy $\bar{E}$:

$$C(\tau) = A + C_{\rm mc}(\tau) \tag{15.62}$$

As a consequence the diffusion coefficient D of (15.61) is the same as the one for the microcanonical ensemble of energy $\bar{E}$. The same conclusion holds for the constant time offset $t_{\rm off}$:[12]

$$D = \int_0^\infty d\tau\, C_{R,\rm mc}(\tau) \tag{15.63}$$

$$t_{\rm off} = \frac{\int_0^\infty d\tau\, \tau\, C_{R,\rm mc}(\tau)}{\int_0^\infty d\tau\, C_{R,\rm mc}(\tau)} \tag{15.64}$$

where $C_{R,\rm mc}$ is the real part of $C_{\rm mc}$. The physical origin of the time offset $t_{\rm off}$ is apparent in (15.64): it is due to the finite width of the phase derivative correlation function. As $C_{R,\rm mc}(\tau)$ is found to be positive, $t_{\rm off}$ can be simply interpreted as the correlation time of the phase derivative in the microcanonical ensemble. The formal expressions for D and $t_{\rm off}$, in terms of the matrix of the linearized kinetic equations, are given in [10].

These results are made more concrete by Fig. 15.5: for a quantum system in the thermodynamic limit, we show the microcanonical correlation function $C_{\rm mc}(t)$ as a function of time, and the variance of the phase-change either in the canonical ensemble of temperature $k_B T = 10\rho g$ or in the microcanonical ensemble with the same mean energy. This reveals in particular that the asymptotic expression (15.61) becomes rapidly accurate.

15.4.6.2 Recovering the Ballistic Spreading from Kinetic Theory

Due to energy conservation, the linearized kinetic equations have a zero-frequency undamped mode. We will show that, in presence of energy fluctuations in the initial state, the amplitude over this mode is nonzero, so that the phase derivative correlation function $C(\tau)$ does not tend to zero at long times and the phase-change variance shows a t^2 term as in (15.61). The derivation presented here was significantly simplified with respect to the original one of [10].

[12] This is true to leading order in the system size since our linearized kinetic approach cannot access the subleading terms.

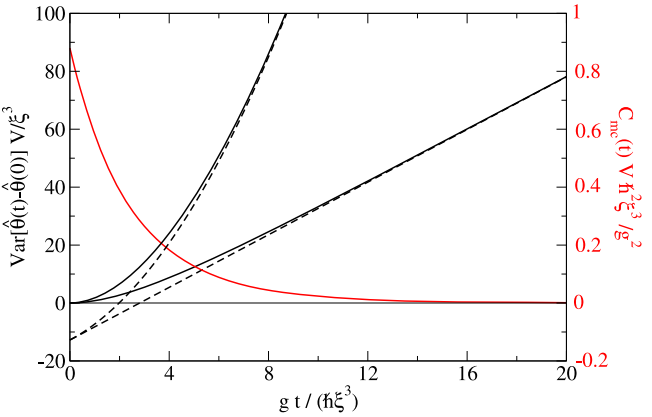

Fig. 15.5 For a quantum system in the thermodynamic limit, the microcanonical phase derivative correlation function $C_{\rm mc}(t)$ (*red solid line*, *right vertical axis*) and the variance of the phase-change (*black lines*, *left vertical axis*) are shown as functions of time. For the variance, the *upper* (*lower*) *solid line* is for the canonical (microcanonical) ensemble, and the *dashed lines* are the corresponding asymptotic forms of (15.61). $k_BT = 10\rho g$, V is the system volume, g is the effective coupling constant (15.4) and ξ is the healing length (15.7). This is Fig. 3 of [10]. In atomic condensates ξ is in the μm range and the time unit of the figure is in the ms range

We introduce the notation

$$\bar{n}_{\mathbf{k}}(E) = \bar{\hat{n}}_{\mathbf{k}\,\rm mc}(E) \tag{15.65}$$

for the average number of quasi-particles in mode $\mathbf{k}$ in the microcanonical ensemble of energy E. The kinetic equations (15.58), linearized around the stationary solution $\{\bar{n}_{\mathbf{q}}(\bar{E})\}$, can be put in the form

$$\dot{\vec{x}}(\tau) = M\vec{x}(\tau) \tag{15.66}$$

where we have collected all the unknowns $n_{\mathbf{k}}(\tau) - \bar{n}_{\mathbf{k}}(\bar{E})$ in a single vector $\vec{x}(\tau)$ and M is a matrix. The existence of a zero-frequency mode can be understood in two different ways that we explain.

First Reasoning Consider an energy E close to $\bar{E}$. In the same way as $\{\bar{n}_{\mathbf{k}}(\bar{E})\}$, the set of occupation numbers $\{\bar{n}_{\mathbf{k}}(E)\}$ constitutes a stationary solution of the full kinetic equations (15.58). Since the solutions are close, their difference $\{\bar{n}_{\mathbf{k}}(E) - \bar{n}_{\mathbf{k}}(\bar{E})\}$ obeys the linear system (15.66) so that the vector $\vec{e}_0$ of components

$$e_{0,\mathbf{k}} = \frac{d}{dE}\bar{n}_{\mathbf{k}}(\bar{E}) \tag{15.67}$$

is a zero-frequency eigenmode of M.

Second Reasoning The Bogoliubov energy $\sum_{\mathbf{k}\neq\mathbf{0}} \varepsilon_k n_{\mathbf{k}}(\tau)$ is conserved by the kinetic equations. An a consequence $\vec{\varepsilon}\cdot\vec{x}(\tau)$ is a constant (the vector $\vec{\varepsilon}$ has compo-

nents ε_k) and its time derivative is zero. This holds for all initial values of $\vec{x}$, and thus implies that $\vec{\varepsilon}$ is a left eigenvector of M with zero eigenvalue. A basic theorem of linear algebra then implies the existence of a right eigenvector of M with zero eigenvalue. Actually we already found it: it is $\vec{e}_0$ of components (15.67). Such left and right eigenvectors are called adjoint vectors. For our normalization choice, their scalar product $\vec{\varepsilon} \cdot \vec{e}_0 = \frac{d}{dE} E = 1$ as it should be.

We now go back to the correlation function $C(\tau)$. We introduce the (zero-mean) fluctuation operators

$$\hat{\delta n}_{\mathbf{k}} = \hat{n}_{\mathbf{k}} - \bar{n}_{\mathbf{k}}(\bar{E}) \tag{15.68}$$

where we have neglected the difference between $\langle \hat{n}_{\mathbf{k}} \rangle$ and $\bar{n}_{\mathbf{k}}(\bar{E})$ in the large system size limit. The correlation function $C(\tau)$ is then obtained as

$$C(\tau) = \vec{A} \cdot \vec{x}(\tau) \quad \text{with } x_{\mathbf{k}}(\tau) = -\left\langle \delta \hat{n}_{\mathbf{k}}(\tau) \dot{\hat{\theta}}(0) \right\rangle \tag{15.69}$$

where we have collected in a vector $\vec{A}$, the coefficients in $\dot{\hat{\theta}}$ given by (15.40):

$$A_{\mathbf{k}} \equiv \frac{g_0}{\hbar V} (U_k + V_k)^2 \tag{15.70}$$

Following the reasoning of Sect. 15.4.5 on finds that $\vec{x}(\tau)$ obeys (15.66). Splitting $\vec{x}(\tau) = \gamma \vec{e}_0 + \vec{X}(\tau)$ we have in the long time limit that $\vec{X}(\tau) \to 0$ due to the Beliaev-Landau damping processes whereas $\gamma = \vec{\varepsilon} \cdot \vec{x}(0)$ is a constant. At long times one then has

$$C(\tau) \underset{\tau \to \infty}{\to} \left[\vec{\varepsilon} \cdot \vec{x}(0) \right] (\vec{A} \cdot \vec{e}_0) \tag{15.71}$$

Taking the microcanonical average of (15.40) and using (15.53) on obtains the Bogoliubov expression for the microcanonical chemical potential:

$$\mu_{\mathrm{mc}}(E) = \mu(T = 0)(N) + \sum_{\mathbf{k} \neq \mathbf{0}} \hbar A_{\mathbf{k}} \bar{n}_{\mathbf{k}}(E) \tag{15.72}$$

Using the expression of $\vec{e}_0$ this leads to $\vec{A} \cdot \vec{e}_0 = \frac{d}{dE} \mu_{\mathrm{mc}}(\bar{E})/\hbar$. We now evaluate the expectation value $\langle \ldots \rangle$ appearing in $\vec{\varepsilon} \cdot \vec{x}(0)$ in two steps. We first take the expectation value in the microcanonical ensemble of energy E: one can then replace the operator $\sum_{\mathbf{k}} \varepsilon_k \hat{\delta n}_{\mathbf{k}}(0)$ with $E - \bar{E}$, since the total Bogoliubov energy is fixed to E. One is left with a microcanonical average of $\dot{\hat{\theta}}(0)$ at energy E, an average already given by (15.53), and that one can expand around $\bar{E}$ to first order in $E - \bar{E}$. The last step is to average over E with the probability distribution $P(E)$ defining the ensemble, to obtain

$$\vec{\varepsilon} \cdot \vec{x}(0) = \mathrm{Var}(E) \frac{d\mu_{\mathrm{mc}}}{\hbar\, dE}(\bar{E}) \tag{15.73}$$

Collecting all the results, we exactly recover the coefficient of t^2 in (15.61).

After this last reasoning, it becomes apparent that, contrarily to the zero-frequency component $\gamma \vec{e}_0$, the contribution of the damped component $\vec{X}(\tau)$ of $\vec{x}(\tau)$

can be treated to zeroth order in the energy fluctuations: one can directly take $E = \bar{E}$ without getting a vanishing contribution to $C(\tau)$ and to (15.61). This explains why both the diffusion coefficient D and the time offset $t_{\rm off}$, that purely originate from $\vec{X}(\tau)$, are essentially ensemble independent.

15.5 Conclusion

After a reminder of the spatial coherence properties, we focused on the temporal coherence of a homogeneous interacting Bose-Einstein condensed gas at finite temperature. We assumed that the system, prepared at thermal equilibrium at time zero, is isolated in its further evolution. As expected, the coherence time of the condensate is finite for a finite interacting system and diverges in the thermodynamic limit.

The loss of temporal coherence of the condensate is due to a spreading in time of the condensate phase-change induced in particular by the non-linear coupling to the thermally populated non-condensed modes. Using quantum kinetic equations describing the Landau and Beliaev interaction processes among the Bogoliubov quasiparticles, we found that the variance of the condensate phase-change at long times t includes both a ballistic term $\propto t^2$ and a diffusive term $\propto t$ with temperature and interaction dependent coefficients. For a large system, with vanishing relative energy fluctuations, the diffusion coefficient is independent of the statistical ensemble and scales as the inverse of the system volume. On the contrary, the coefficient of t^2 strongly depends on the ensemble: it scales as the inverse volume squared times the variance of the system energy. This result, implying that paradoxically some correlation functions in the system do not tend to zero at infinite time, can also be obtained by a quantum ergodic theory (the so-called eigenstate thermalization hypothesis).

Finally, we sketched a possible scheme to measure the condensate coherence time and test our predictions in cold atoms experiment.

References

1. M.H. Anderson, J.R. Ensher, M.R. Matthews, C.E. Wieman, E.A. Cornell, Science **269**, 198 (1995)
2. K. Davis, M.O. Mewes, M.R. Andrews, N.J. van Druten, D.S. Durfee, D.M. Kurn, W. Ketterle, Phys. Rev. Lett. **75**, 3969 (1995)
3. C.C. Bradley, C.A. Sackett, J.J. Tollett, R.G. Hulet, Phys. Rev. Lett. **75**, 1687 (1995)
4. I. Bloch, T.W. Hänsch, T. Esslinger, Nature **403**, 166 (2000)
5. D.S. Hall, M.R. Matthews, C.E. Wieman, E.A. Cornell, Phys. Rev. Lett. **81**, 1543 (1998)
6. G.-B. Jo, Y. Shin, S. Will, T.A. Pasquini, M. Saba, W. Ketterle, D.E. Pritchard, M. Vengalattore, M. Prentiss, Phys. Rev. Lett. **98**, 030407 (2007)
7. S.T. Beliaev, Zh. Eksp. Teor. Fiz. **34**, 417 (1958) [Sov. Phys. JETP **34**, 289 (1958)]
8. A. Sinatra, Y. Castin, E. Witkowska, Phys. Rev. A **75**, 033616 (2007)
9. A. Sinatra, Y. Castin, Phys. Rev. A **78**, 053615 (2008)
10. A. Sinatra, Y. Castin, E. Witkowska, Phys. Rev. A **80**, 033614 (2009)
11. N.N. Bogoliubov, J. Phys. USSR **11**, 23 (1947)

12. S. Giorgini, Phys. Rev. A **57**, 2949 (1998)
13. M. Girardeau, R. Arnowitt, Phys. Rev. **113**, 755 (1959)
14. Y. Castin, R. Dum, Phys. Rev. A **57**, 3008 (1998)
15. C.W. Gardiner, Phys. Rev. A **56**, 1414 (1997)
16. Y. Castin, Bose-Einstein condensates in atomic gases, in *Coherent Atomic Matter Waves*, ed. by R. Kaiser, C. Westbrook, F. David. Lecture Notes of 1999 Les Houches Summer School (EDP Sciences and Springer, Les Ulis/Berlin, 2001), pp. 1–136
17. Y. Castin, Simple theoretical tools for low dimension Bose gases, in *Quantum Gases in Low Dimensions*, ed. by M. Olshanii, H. Perrin, L. Pricoupenko. Lecture Notes of the 2003 Les Houches Spring School. J. Phys. IV **116**, 89–132 (2004)
18. E.H. Lieb, W. Liniger, Phys. Rev. **130**, 1605 (1963)
19. P. Carruthers, M.M. Nieto, Rev. Mod. Phys. **40**, 411 (1968)
20. A. Sinatra, C. Lobo, Y. Castin, J. Phys. B **35**, 3599 (2002)
21. I. Carusotto, Y. Castin, Phys. Rev. Lett. **90**, 030401 (2003)
22. J.-P. Blaizot, G. Ripka, *Quantum Theory of Finite Systems* (MIT Press/Bradford, Cambridge, 1986)
23. V.N. Popov, *Functional Integrals in Quantum Field Theory and Statistical Physics*, Chap. 6 (Reidel, Dordrecht, 1983)
24. N.D. Mermin, H. Wagner, Phys. Rev. Lett. **17**, 1133 (1966)
25. P.C. Hohenberg, Phys. Rev. **158**, 383 (1967)
26. D.S. Petrov, M. Holzmann, G.V. Shlyapnikov, Phys. Rev. Lett. **84**, 2551 (2000)
27. C. Mora, Y. Castin, Phys. Rev. A **67**, 053615 (2003)
28. L. Pricoupenko, M. Olshanii, J. Phys. B **40**, 2065 (2007)
29. D.S. Petrov, G.V. Shlyapnikov, J.T.M. Walraven, Phys. Rev. Lett. **87**, 050404 (2001)
30. S. Richard, F. Gerbier, J.H. Thywissen, M. Hugbart, P. Bouyer, A. Aspect, Phys. Rev. Lett. **91**, 010405 (2003)
31. J. Esteve, J.-B. Trebbia, T. Schumm, A. Aspect, C.I. Westbrook, I. Bouchoule, Phys. Rev. Lett. **96**, 130403 (2006)
32. Z. Hadzibabic, P. Krüger, M. Cheneau, B. Battelier, J. Dalibard, Nature **441**, 1118 (2006)
33. C.-L. Hung, X. Zhang, L.-C. Ha, S.-K. Tung, N. Gemelke, C. Chin, New J. Phys. **13**, 075019 (2011)
34. C. Gross, T. Zibold, E. Nicklas, J. Estève, M.K. Oberthaler, Nature **464**, 1165 (2010)
35. M.F. Riedel, P. Böhi, Y. Li, T.W. Hänsch, A. Sinatra, P. Treutlein, Nature **464**, 1170 (2010)
36. D. Jaksch, C.W. Gardiner, K.M. Gheri, P. Zoller, Phys. Rev. A **58**, 1450 (1998)
37. R. Graham, Phys. Rev. Lett. **81**, 5262 (1998)
38. R. Graham, Phys. Rev. A **62**, 023609 (2000)
39. A.B. Kuklov, J.L. Birman, Phys. Rev. A **63**, 013609 (2000)
40. F. Sols, Physica B **194**, 1389 (1994)
41. M. Lewenstein, L. You, Phys. Rev. Lett. **77**, 3489 (1996)
42. E.M. Wright, D.F. Walls, J.C. Garrison, Phys. Rev. Lett. **77**, 2158 (1996)
43. Y. Castin, J. Dalibard, Phys. Rev. A **55**, 4330 (1997)
44. M. Greiner, O. Mandel, T.W. Hänsch, I. Bloch, Nature **419**, 51 (2002)
45. G.-B. Jo, J.-H. Choi, C.A. Christensen, Y.-R. Lee, T.A. Pasquini, W. Ketterle, D.E. Pritchard, Phys. Rev. Lett. **99**, 240406 (2007)
46. K. Maussang PhD Thesis of Université Pierre et Marie Curie, Paris, 2010. http://tel.archives-ouvertes.fr/tel-00589713
47. M. Rigol, M. Srednicki, Phys. Rev. Lett. **108**, 110601 (2012)
48. J.M. Deutsch, Phys. Rev. A **43**, 2046 (1991)
49. M. Rigol, V. Dunjko, M. Olshanii, Nature **452**, 854 (2008)
50. E.M. Lifshitz, L.P. Pitaevskii, *Physical Kinetics*, Landau and Lifshitz Course of Theoretical Physics, vol. 10, Chap. VII (Pergamon, Elmsford, 1981)

Chapter 16
Effects of Interactions on Bose-Einstein Condensation of an Atomic Gas

Robert P. Smith and Zoran Hadzibabic

Abstract The phase transition to a Bose-Einstein condensate is unusual in that it is not necessarily driven by inter-particle interactions but can occur in an ideal gas as a result of a purely statistical saturation of excited states. However, interactions are necessary for any system to reach thermal equilibrium and so are required for condensation to occur in finite time. In this chapter we review the role of interactions in Bose-Einstein condensation, covering both theory and experiment. We focus on measurements performed on harmonically trapped ultracold atomic gases, but also discuss how these results relate to the uniform-system case, which is more theoretically studied and also more relevant for other experimental systems.

We first consider interaction strengths for which the system can be considered sufficiently close to equilibrium to measure thermodynamic behaviour. In particular we discuss the effects of interactions both on the mechanism of condensation (namely the saturation of the excited states) and on the critical temperature at which condensation occurs. We then discuss in more detail the conditions for the equilibrium thermodynamic measurements to be possible, and the non-equilibrium phenomena that occur when these conditions are controllably violated by tuning the strength of interactions in the gas.

16.1 Introduction

Virtually all thermodynamic phase transitions are driven by interactions between particles, which promote symmetry breaking into an ordered state. The phase transition comes about as a result of the competition between the energy, which favours the ordered state, and the entropy, which favours the disordered state. In contrast, Bose-Einstein condensation (BEC) is a purely statistical phase transition, which at least in principle should not rely on interactions. The transition is instead a direct consequence of the finite-temperature saturation of the number of particles in the excited states of the system [1–4]. While this statistical argument does not explicitly

R.P. Smith · Z. Hadzibabic (✉)
Cavendish Laboratory, University of Cambridge, J.J. Thomson Avenue, Cambridge, CB3 0HE, UK
e-mail: zh10001@cam.ac.uk

A. Bramati, M. Modugno (eds.), *Physics of Quantum Fluids*,
Springer Series in Solid-State Sciences 177, DOI 10.1007/978-3-642-37569-9_16,

invoke interactions between the particles, it does assume that the gas is in thermal equilibrium, which is impossible to attain in a completely noninteracting system.[1] This makes it challenging to experimentally observe ideal-gas behaviour and disentangle the role of interactions on the thermodynamics and dynamics of condensation.

In this chapter we review our recent experiments on this topic [6–8], performed with an ultracold Bose gas of ^{39}K atoms with tuneable interactions. We were able to identify the interaction regime in which the gas may be considered to be in thermal equilibrium and also to extrapolate our results to the noninteracting limit where direct equilibrium measurements are not possible. This allowed us to verify the statistical-saturation BEC mechanism in the noninteracting limit, and to accurately determine the deviations from ideal-gas behaviour due to interactions; these are seen both in the non-saturation of the excited states and in the shift of the critical point. Before presenting the experimental results we briefly review some background theory that will be useful for our discussion.

16.1.1 Noninteracting Bosons

We start by considering an ideal, noninteracting Bose gas. We first derive the key results for a uniform system, which we then apply to the trapped gas using the local density approximation (LDA). This "local" approach will be useful later when we consider the effects of interactions, and in particular for the comparison of a uniform Bose gas with one that is harmonically trapped.

The equilibrium momentum distribution of noninteracting bosons with mass m at a temperature T is given by the Bose distribution function

$$f_p = \frac{1}{\mathrm{e}^{(p^2/2m-\mu)/k_\mathrm{B}T} - 1}, \tag{16.1}$$

where p is the momentum and $\mu \leq 0$ the chemical potential. The total particle density n can be found by integrating over all momentum states:

$$n = \int \frac{\mathrm{d}\mathbf{p}}{(2\pi\hbar)^3} \frac{1}{\mathrm{e}^{(p^2/2m-\mu)/k_\mathrm{B}T} - 1} = \frac{g_{3/2}(\mathrm{e}^{\mu/k_\mathrm{B}T})}{\lambda^3}, \tag{16.2}$$

where $g_{3/2}(x) = \sum_{k=1}^{\infty} x^k/k^{3/2}$ is a polylogarithm function and $\lambda = [2\pi\hbar^2/(mk_\mathrm{B}T)]^{1/2}$ is the thermal wavelength. We can re-express this result in terms of the phase space density D as

$$D \equiv n\lambda^3 = g_{3/2}\left(\mathrm{e}^{\mu/k_\mathrm{B}T}\right). \tag{16.3}$$

[1] In the recently observed Bose-Einstein condensation of a photon gas [5], there is no direct interaction between the light particles. However the interaction with the material environment, which ensures thermalisation, leads to a second-order interaction between the photons.

Equation (16.3) shows that there is a maximum value that D can take. This critical value is reached when $\mu = 0$ and is given by $D_c = g_{3/2}(1) = \zeta(3/2) \approx 2.612$ (where ζ is the Riemann function). At a given temperature this corresponds to a maximum density. If this density is reached all the excited states saturate and any additional particles must accumulate in the ground state, forming a Bose-Einstein condensate.[2] At a given density n the BEC transition temperature is given by

$$k_{\mathrm{B}} T_c^0 = \frac{2\pi\hbar^2}{m}\left(\frac{n}{\zeta(3/2)}\right)^{2/3}, \tag{16.4}$$

where the superscript ^{0} refers to the fact this is an ideal gas result.

For a gas in a potential $V(\mathbf{r})$ we may apply LDA to (16.2). This amounts to having a local chemical potential

$$\mu(\mathbf{r}) = \mu - V(\mathbf{r}). \tag{16.5}$$

Specifically for a harmonic trap, $V(\mathbf{r}) = \sum(1/2)m\omega_i^2 r_i^2$, where ω_i (with $i = 1, 2, 3$) are the trapping frequencies along three spatial dimensions.

The local density is then

$$n(\mathbf{r}) = \frac{g_{3/2}(\mathrm{e}^{(\mu - V(\mathbf{r}))/k_{\mathrm{B}}T})}{\lambda^3}, \tag{16.6}$$

and the local phase space density $D(\mathbf{r}) = n(\mathbf{r})\lambda^3$. The total number of particles in the excited states can be found by integrating over all space:

$$N' = \int \frac{g_{3/2}(\mathrm{e}^{(\mu - V(\mathbf{r}))/k_{\mathrm{B}}T})}{\lambda^3} \mathrm{d}\mathbf{r}. \tag{16.7}$$

The critical point for a trapped gas is the point at which the maximal local D reaches the critical value of $\zeta(3/2)$. For a fixed T it makes sense to define the critical point in terms of the critical total particle number N_c. For a harmonic trap, with the geometric mean of the three trapping frequencies $\bar{\omega}$, the integral in (16.7) for $\mu = 0$ gives

$$N_{\mathrm{c}}^0 = \zeta(3)\left(\frac{k_{\mathrm{B}}T}{\hbar\bar{\omega}}\right)^3, \tag{16.8}$$

[2] The singular ground-state contribution to the total density is implicitly excluded from the integral in (16.2). As μ approaches zero from below the ground state occupation can become arbitrarily large, as can be seen by inspecting (16.1).

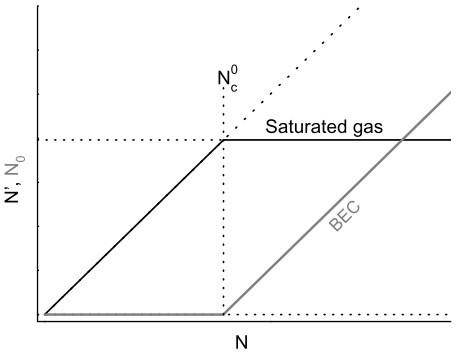

Fig. 16.1 Ideal Bose gas condensation. Number of thermal atoms N' (*black line*) and number of condensed atoms N_0 (*grey line*) are plotted versus the total atom number N, at a fixed temperature. As atoms are added to trap $N' = N$ and $N_0 = 0$ until the critical atom number N_c^0 is reached. At this point the excited states of the system saturate, and for $N > N_c^0$ we have $N' = N_c^0$ and $N_0 = N - N_c^0$

where $\zeta(3) \approx 1.202$. The equivalent expression for the transition temperature at a fixed particle number is given by[3]

$$k_B T_c^0 = \hbar\bar{\omega}\left(\frac{N}{\zeta(3)}\right)^{1/3}. \tag{16.9}$$

The ideal-gas picture of Bose-Einstein condensation driven by the purely statistical saturation of the excited states is simply summarised graphically in Fig. 16.1. Here we plot the number of atoms in the excited states, N', and in the condensate, N_0, as the total atom number N is increased at constant temperature. For $N < N_c^0$ no condensate is present and $N' = N$. However for $N > N_c^0$ the thermal component is saturated at $N' = N_c^0$ and the number of condensed atoms is simply given by $N_0 = N - N_c^0$. In Sects. 16.3 and 16.4 we will examine the effects of interactions both on the saturation of the excited states and on the value of the critical atom number.

16.1.2 Interacting Bosons

The dominant effects of interactions on Bose-Einstein condensation are quite different in a uniform system and in the experimentally pertinent case of a harmonically trapped atomic gas. This complex problem has a long history and for reviews we

[3]Finite-size corrections slightly reduce the ideal-gas critical temperature, by $k_B \Delta T_c^0 = -\zeta(2)/(2\zeta(3))\hbar\omega_m \approx -0.684\hbar\omega_m$, where ω_m is the algebraic mean of the trapping frequencies [9].

refer the reader to, for example, [3, 4, 9, 10]. Here we just briefly introduce some key points.

The simplest theoretical framework to address the effects of interactions in a Bose gas is the Hartree-Fock approximation [9]. In this mean-field (MF) model one treats the thermal atoms as a "noninteracting" gas of density $n'(\mathbf{r})$ that experiences a self-consistent MF interaction potential $g[2n_0(\mathbf{r}) + 2n'(\mathbf{r})]$, where $g = 4\pi\hbar^2 a/m$, a is the s-wave scattering length, and $n_0(\mathbf{r})$ the condensate density. We can then define an effective total potential

$$V_{\text{eff}}(\mathbf{r}) = V(\mathbf{r}) + 2g\big[n_0(\mathbf{r}) + n'(\mathbf{r})\big], \tag{16.10}$$

and apply the LDA by replacing $V(\mathbf{r})$ with $V_{\text{eff}}(\mathbf{r})$ in (16.6). Meanwhile the condensed atoms feel an interaction potential $g[n_0(\mathbf{r}) + 2n'(\mathbf{r})]$, where the factor of two difference in the condensate self-interaction comes about due to the lack of the exchange interaction term for particles in the same state.[4]

In a uniform system, the MF potential gives just a spatially uniform energy offset and the most interesting effects arise due to beyond-MF quantum correlations.

On the other hand, in a harmonically trapped gas (with repulsive interactions) the inhomogeneous density results in a mean-field repulsion of atoms from the central high-density region. This geometrical effect often dominates and makes it harder to experimentally observe the more interesting beyond-MF physics.

16.1.3 Chapter Outline

In Sect. 16.2 we briefly outline our experimental procedure for performing precision measurements of the effects of interactions on Bose-Einstein condensation of an atomic gas.

In Sects. 16.3 and 16.4 we discuss the effects of interactions on the thermodynamics of a Bose gas with tuneable interactions. Here the range of interaction strengths we explore experimentally is such that the gas can always be assumed to be in thermal equilibrium. In Sect. 16.3 we scrutinise the concept of saturation as the driving mechanism for Bose-Einstein condensation, and in Sect. 16.4 we focus on the interaction shift of the critical point for condensation. We compare the experimental results to both MF and beyond-MF theories and discuss how they relate to the case of a uniform Bose gas.

In Sect. 16.5 we discuss the conditions required for equilibrium measurements, and non-equilibrium effects that are observed when they are violated.

[4] This approach does not take into account the modification of the excitation spectrum due to the presence of the condensate, which is included in more elaborate MF theories such as those of Bogoliubov [11] and Popov [12] (see also [9]). However, it is often sufficient to give the correct leading order MF results.

16.2 Precision Measurements on a Bose Gas with Tuneable Interactions

All the results presented here were obtained by performing conceptually simple experiments which are close in spirit to the ideal-gas theoretical plots of Fig. 16.1, but are performed for various strengths of repulsive interatomic interactions, characterised by the positive s-wave scattering length a.

Our experiments start with a partially condensed gas of ^{39}K atoms, produced in an optical dipole trap [13] with $\bar{\omega}/2\pi$ varying between 60 and 80 Hz for data taken at different temperatures. The strength of interactions in the gas can be tuned by applying a uniform external magnetic field in the vicinity of a Feshbach scattering resonance centred at 402.5 G [14].

In each experimental series we fix a by choosing the value of the Feshbach field, and keep the temperature constant by fixing the depth of the optical trap. The total number of trapped atoms N is then varied by holding the gas in the trap for a variable time t, up to tens of seconds. During this time N, initially larger than the critical value N_c, slowly decays and eventually drops below N_c. Meanwhile elastic collisions between the atoms act to redistribute the particles between the condensed and thermal components of the gas.

In each experimental run within a given series, corresponding to a particular hold-time t, the thermal atom number N' and the condensate atom number N_0 are extracted from fits to the absorption images of the gas after 18–20 ms of free time-of-flight (TOF) expansion from the trap [15, 16]. The interactions are rapidly turned off at the beginning of TOF, by tuning the Feshbach field to the $a = 0$ point. This minimises the condensate expansion and allows us to home in on the critical point by reliably measuring condensed fractions as low as 0.1 %.

For accurate measurements of the small interaction shift of the critical point it is particularly important to minimise various systematic errors, e.g. due to finite-size effects [9], uncertainties in the absolute calibration of N and $\bar{\omega}$, and small anharmonic corrections to the trapping potential [13]. We achieve this by performing "differential measurements", always concurrently running two experimental series which are identical in every respect except for the choice of the scattering length [7].

16.3 Non-saturation of the Excited States

In this section, we focus on the concept of the saturation of the excited states as the underlying mechanism driving the BEC transition. In superfluid ^{4}He, which is conceptually associated with BEC, strong interactions preclude direct observation of purely statistical effects postulated by Einstein for an ideal gas. On the other hand it is generally accepted that a close-to-textbook BEC is observed in the weakly interacting atomic gases. Therefore, one might expect that the saturation inequal-

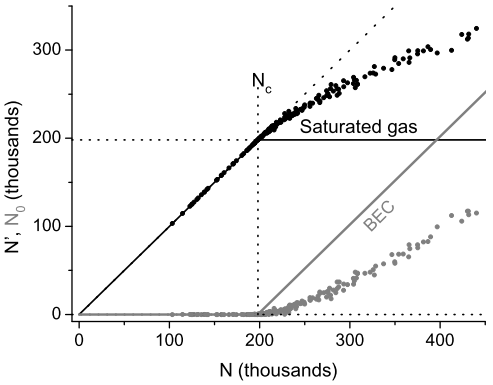

Fig. 16.2 Lack of saturation of the thermal component in a quantum degenerate atomic Bose gas. N' (*black points*) and N_0 (*grey points*) are plotted versus the total atom number N at $T = 177$ nK and $a = 135a_0$. The corresponding predictions for a saturated gas are shown by *black and grey solid lines*. The critical point $N = N_c$ is marked by a *vertical dashed line*. (Figure adapted from [6])

ity $N' \leq N_c^0$ is essentially satisfied in these systems, with just the value of the bound on the right-hand side slightly modified by interactions. However, as shown in Fig. 16.2, this is far from being the case under typical conditions of an ultracold gas experiment. Here, in an experimental series taken with $a = 135a_0$ (where a_0 is the Bohr radius) and $T = 177$ nK, the measured critical atom number is $N_c \approx 200\,000$; if the total number of atoms is increased to 450 000, only half of the additional atoms accumulate in the condensate.

In order to explore the relationship between the experimentally observed non-saturation of the thermal component and the interatomic interactions, we first identify the relevant interaction energy. As a BEC is formed and then grows, the change in the average density of the condensed atoms is much larger than the change of the thermal density. Therefore one expects the non-saturation of the thermal component to result primarily from its interaction with the condensate (the $2gn_0(\mathbf{r})$ term in (16.10)). The relevant energy scale is then provided by [9]

$$\mu_0 = gn_0(\mathbf{r} = 0) = \frac{\hbar\bar{\omega}}{2}\left(15N_0\frac{a}{a_{\rm ho}}\right)^{2/5}, \tag{16.11}$$

where $a_{\rm ho} = (\hbar/m\bar{\omega})^{1/2}$ is the spatial extension of the ground state of the harmonic oscillator. The energy μ_0 is the MF result for the chemical potential of a gas with N_0 atoms at zero temperature in the Thomas-Fermi limit [9].

Guided by this scaling, for the data shown in Fig. 16.2 we plot N' as a function of $N_0^{2/5}$ in Fig. 16.3. The growth of N' with $N_0^{2/5}$ is not perfectly linear, so we quantify the non-saturation effect with two linear slopes: (1) the initial slope S_0 for $N_0 \to 0$, and (2) the course grained slope $S = \Delta[N']/\Delta[N_0^{2/5}]$ for $0.1 < \mu_0/k_{\rm B}T < 0.3$ [6]. The data shown in Fig. 16.3 can also be described by a second-order polynomial fit, as described later.

The initial slope S_0 may be compared with the HF model. In order to obtain the non-saturation effect to first order within the HF approach, we only consider the

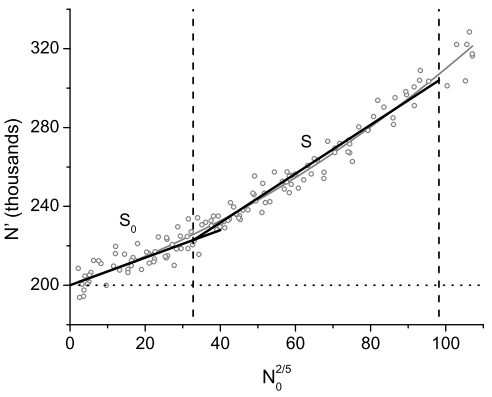

Fig. 16.3 Quantifying the lack of saturation. Here N' is plotted as a function of $N_0^{2/5}$ for the same series as in Fig. 16.2. The *horizontal dotted line* is the saturation prediction $N' = N_c$. The *two black lines* show the initial slope S_0 and the slope S for $0.1 < \mu_0/k_B T < 0.3$. The *solid grey line* is a guide to the eye based on a second-order polynomial fit. (Figure adapted from [6])

repulsive interaction of the thermal atoms with the condensate and not with other thermal atoms. From (16.10) this leads to an effective potential[5]

$$V_{\text{eff}}(\mathbf{r}) = V(\mathbf{r}) + 2gn_0(\mathbf{r}) = \left|V(\mathbf{r}) - \mu_0\right| + \mu_0. \tag{16.12}$$

Note that within this theory $N_c = N_c^0$ since $V_{\text{eff}}(\mathbf{r}) = V(\mathbf{r})$ when $N_0 = 0$. By integrating (16.7) with the effective potential of (16.12) one can predict a linear variation of N'/N_c^0 with the small parameter $\mu_0/k_B T$:

$$\frac{N'}{N_c^0} = 1 + \alpha \frac{\mu_0}{k_B T}, \tag{16.13}$$

with $\alpha = \zeta(2)/\zeta(3) \approx 1.37$. This first order non-saturation result is identical to that obtained in more elaborate MF approximations, which only modify higher order terms.

The origin of the non-saturation effect can be qualitatively understood by noting that interactions with the condensate modify the effective potential seen by the thermal atoms from a parabola into the "Mexican hat" shape of (16.12); this effectively allows the thermal component to occupy a larger volume, which grows with increasing N_0.

From (16.11) and (16.13) we define the HF non-saturation slope

$$S_{\text{HF}} = \frac{dN'}{d(N_0^{2/5})} = \frac{\zeta(2)}{\zeta(3)} X \tag{16.14}$$

where X is the dimensionless parameter

$$X = \frac{\zeta(3)}{2} \left(\frac{k_B T}{\hbar\bar{\omega}}\right)^2 \left(\frac{15a}{a_{\text{ho}}}\right)^{2/5}. \tag{16.15}$$

The measured S_0 is found to agree with S_{HF} for a range of a and T values [6].

[5] Note that $gn_0(\mathbf{r}) = \max\{\mu_0 - V(r), 0\}$.

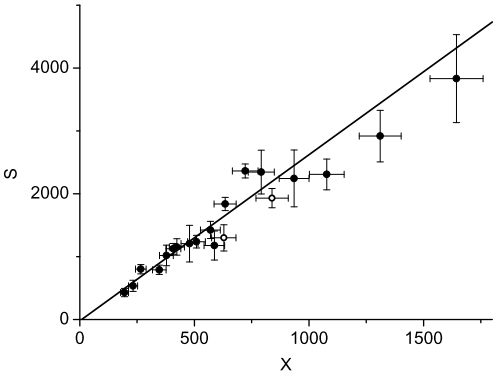

Fig. 16.4 Deviation from the saturation picture at a range of interaction strengths and temperatures. The non-saturation slope S is plotted versus the dimensionless interaction parameter $X \propto T^2 a^{2/5}$ (see text). A linear fit (*black line*) gives $dS/dX = 2.6 \pm 0.3$ and an intercept $S(0) = -20 \pm 100$, consistent with complete saturation in the ideal-gas limit. The data points are based on measurements with the ^{39}K gas (*closed circles*) at a range of scattering lengths ($a = 40$–$356a_0$) and temperatures ($T = 115$–284 nK), and two additional experimental series taken with a ^{87}Rb gas (*open circles*). (Figure adapted from [6])

We now consider the non-saturation at higher N_0 values, where the data is not well described by (16.14). Figure 16.4 summarises the non-saturation slopes $S(a, T)$ for a wide range of interaction strengths and temperatures. Within experimental error all data points fall onto a straight line with gradient 2.6 ± 0.3 and intercept $S(0) = -20 \pm 100$ when plotted against the dimensionless interaction parameter X.

The first and most important thing to notice is that both non-saturation slopes, S_0 and S, tend to zero for $X \to 0$. These experiments thus confirm the concept of a saturated Bose gas, and Bose-Einstein condensation as a purely statistical phase transition in the non-interacting limit.

A question that is still open is the deviation of S from the first order HF result S_{HF}, i.e. $dS/dX \approx 2.6$ versus $\zeta(2)/\zeta(3) \approx 1.37$ predicted from HF theory. This discrepancy can partially be explained by higher order terms in the mean-field theory, either directly from using (16.12) in (16.7), or using more elaborate MF theories such as the Popov approximation [3]. However the effect is far stronger in the experimental results than any of these MF theories predict. To see this we consider the next order term in (16.13), writing $N'/N_{\mathrm{c}}^0 = 1 + \alpha(\mu_0/k_{\mathrm{B}}T) + \alpha_2(\mu_0/k_{\mathrm{B}}T)^2$ with $\alpha = 1.37$. Experimentally, by identifying S with the gradient of this quadratic function evaluated at $\mu_0/k_{\mathrm{B}}T = 0.2$, we get $\alpha_2 = 3 \pm 0.7$. For comparison the Popov approximation gives $\alpha_2 \approx 0.6$. At present the reason for this discrepancy and the possible role of beyond-MF effects are unclear, and require further investigation.

In summary, we can quantify the non-saturation of the thermal component in a harmonically trapped gas by writing the number of thermal atoms in a partially condensed cloud as

$$N' = N_c + S_0 N_0^{2/5} + S_2 N_0^{4/5}, \tag{16.16}$$

where

$$S_0 = \frac{\zeta(2)}{2}\left(\frac{k_B T}{\hbar\bar{\omega}}\right)^2 \left(\frac{15a}{a_{ho}}\right)^{2/5} \tag{16.17}$$

and

$$S_2 = (3 \pm 0.7)\frac{\zeta(3)}{4}\frac{k_B T}{\hbar\bar{\omega}}\left(\frac{15a}{a_{ho}}\right)^{4/5}. \tag{16.18}$$

We have seen that in a harmonic trap the dominant non-saturation effect is "geometric", arising from an interplay of the mean-field repulsion and the inhomogeneity of the condensate density. It is then interesting to consider the case of a uniform system, where this geometric effect is absent. Within MF theory, as the total density of a uniform Bose gas is increased past the critical value the thermal density n' actually decreases. This is due to the fact that the atoms in the condensate have less interaction energy, as discussed in Sect. 16.1.2. In addition, close to the transition, beyond-MF effects are expected to play an important role. This would make measurements in a uniform system (or of the local density in a trapped system) particularly interesting.

16.4 Interaction Shift of the Transition Temperature

Having considered the effect of interactions on the saturation of the thermal component we now consider the location of the critical point itself.

It is generally accepted that in a uniform system there is no interaction shift of the critical temperature T_c at the level of mean-field theory. However, the beyond-MF correlations between particles which develop near the critical point are expected to shift T_c [10, 17–28]. For several decades there was no consensus on the functional form, or even on the sign of this T_c shift (for an overview see e.g. [10, 23, 26, 28]). It is now generally believed that the shift is positive and to leading order given by [23, 24]:

$$\frac{\Delta T_c}{T_c^0} \approx 1.3 a n^{1/3} \approx 1.8\frac{a}{\lambda_0}, \tag{16.19}$$

where $\Delta T_c = T_c - T_c^0$ and λ_0 is the thermal wavelength at temperature T_c^0. Equivalently, the n_c shift at constant T is $\Delta n_c/n_c^0 \approx -(3/2)\Delta T_c/T_c^0$. The positive ΔT_c implies that condensation occurs at a phase space density below the ideal-gas critical value of 2.612.

The problem of the T_c shift in a harmonically trapped gas is even more complex. In this case, at least for weak interactions, the shift is dominated by an opposing effect that reduces the critical temperature [29]. This negative T_c shift is due to the broadening of the density distribution by repulsive interactions (see Fig. 16.5).

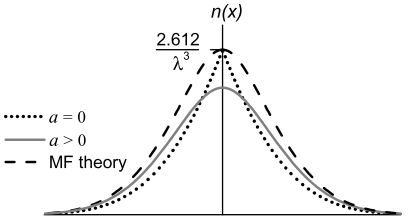

Fig. 16.5 Opposing effects of interactions on the critical point of a trapped Bose gas. We sketch the density distribution in a harmonic potential $V(r)$ at the condensation point. Compared to an ideal gas (*dotted line*) at the same temperature, repulsive interactions reduce the critical density, but also broaden the density distribution (*solid line*). Mean-field theory (*dashed line*) captures only the latter effect, and predicts an increase of the critical atom number N_c at fixed T, equivalent to a decrease of T_c at fixed N. (Figure adapted from [7])

To leading order it can be calculated analytically using MF theory [29], by self-consistently solving (16.6) with $V_{\text{eff}} = V(\mathbf{r}) + 2gn'(\mathbf{r})$:

$$\frac{\Delta T_c}{T_c^0} \approx -3.426 \frac{a}{\lambda_0}. \tag{16.20}$$

For the experimentally relevant range of interaction strengths, $0 < a/\lambda_0 < 0.05$, we numerically obtain the second-order MF shift, $\approx 11.7(a/\lambda_0)^2$ [8].

The two opposing effects of repulsive interactions on the critical point of a trapped gas are visually summarised in Fig. 16.5, where we sketch the density distribution at the condensation point for an ideal and an interacting gas at the same temperature.[6] In the spirit of LDA, the critical density should be reduced by interactions. However, interactions also broaden the density distribution. For weak interactions the latter effect is dominant, making the overall interaction shift $\Delta N_c(T)$ positive, or equivalently $\Delta T_c(N)$ negative.

The dominance of the negative MF shift of T_c over the positive beyond-MF one goes beyond the difference in the numerical factors in (16.19) and (16.20). In a harmonic trap, at the condensation point only the central region of the cloud is close to criticality;[7] this reduces the net effect of critical correlations so that they affect T_c only at a higher order in a/λ_0. The MF result of (16.20) should therefore be exact at first order in a/λ_0. The higher-order beyond-MF shift is still expected to be positive, but the theoretical consensus on its value has not been reached [30–34].

[6] The shift of the critical point can be equivalently expressed as $\Delta T_c(N)$ or $\Delta N_c(T)$, with $\Delta N_c(T)/N_c^0 \approx -3\Delta T_c/T_c^0$.

[7] The size of the central critical region is $r_c \sim (a/\lambda_0)R_T$, where $R_T = \sqrt{k_B T/m\omega^2}$ is the thermal radius of the cloud [30].

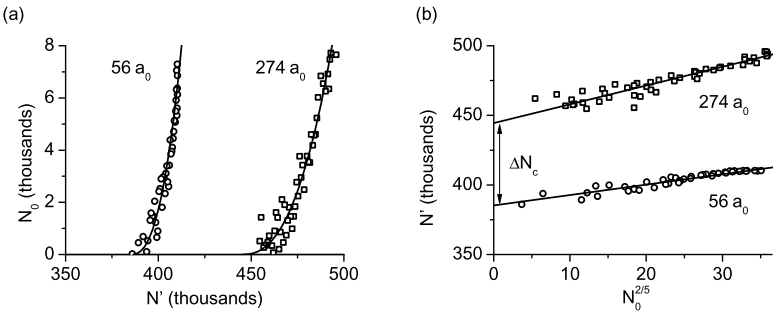

Fig. 16.6 Determination of the critical point and the differential interaction shift. (**a**) Condensed (N_0) versus thermal (N') atom number for two concurrently taken data series with $a = 56a_0$ (*circles*) and $a = 274a_0$ (*squares*). Note that all points correspond to condensed fractions below 2 %. The data is scaled to the same temperature ($T = 240$ nK) and shows the shift of the critical point in the form $\Delta N_c(T)$. *Solid lines* show the extrapolation to $N_0 = 0$, necessary to accurately determine N_c. (**b**) N' is plotted versus $N_0^{2/5}$ for the same data as in (**a**), showing more clearly the extrapolation procedure. (Figure adapted from [7])

16.4.1 Measurements on a Harmonically Trapped Bose Gas

Since the early days of atomic BECs there have been several measurements of the interaction T_c shift in a harmonically trapped gas [35–37]. These experiments, performed at a/λ_0 ranging from 0.007 [37] to 0.024 [36], nicely confirmed the theoretical prediction for the linear MF shift of (16.20), but could not discern the beyond-MF effects of critical correlations.

The recent measurements [7] presented here provided the first clear observation of the beyond-MF T_c shift in a trapped atomic gas. Several improvements contributed to making this possible. First, we explored slightly higher interaction strengths, up to $a/\lambda_0 \approx 0.04$. Second, by performing precision measurements outlined in Sect. 16.2, and directly accessing the small differential T_c shift due to the variation in a/λ_0, we significantly reduced the experimental error bars. Third, understanding the non-saturation effects discussed in Sect. 16.3 was also essential for accurately determining the critical point from the measurements performed *close* to it (see Fig. 16.6).

Figure 16.6 illustrates a differential measurement with $a = 56a_0$ and $a = 274a_0$. The rise of N_0 in Fig. 16.6(a) is not simply vertical because the thermal component is not saturated at N_c (see Sect. 16.3). It is therefore essential to carefully extrapolate N' to the $N_0 = 0$ limit in order to accurately determine N_c. For small N_0 the extrapolation is done using $N' = N_c + S_0 N_0^{2/5}$, with the non-saturation slope $S_0(T, \bar{\omega}, a)$ given by (16.17).

In Fig. 16.7 we summarise our measurements of $\Delta T_c / T_c^0$ [7]. The data taken with different atom numbers, $N \approx (2\text{–}8) \times 10^5$, fall onto the same curve, confirming that the results depend only on the interaction parameter a/λ_0. The MF prediction agrees very well with the data for $a/\lambda_0 \lesssim 0.01$, but for larger a/λ_0 there is a clear deviation from this prediction. All the data are fitted well by a second-order polynomial

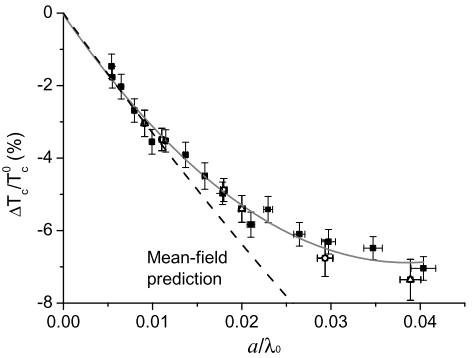

Fig. 16.7 Interaction shift of the critical temperature. Data points were taken with $N \approx 2 \times 10^5$ (*open circles*), 4×10^5 (*black squares*), and 8×10^5 (*open triangles*) atoms. The *dashed line* is the MF prediction. The *solid line* shows a second-order polynomial fit to the data (see text). Vertical error bars are statistical, while systematic errors in $\Delta T_c/T_c^0$ are assessed to be <1 % [7]. (Figure adapted from [7])

$$\frac{\Delta T_c}{T_c^0} \approx b_1 \frac{a}{\lambda_0} + b_2 \left(\frac{a}{\lambda_0}\right)^2, \tag{16.21}$$

with $b_1 = -3.5 \pm 0.3$ and $b_2 = 46 \pm 5$. The value of b_1 is in agreement with the MF prediction of -3.426. The b_2 value strongly excludes the MF result of $b_2^{\mathrm{MF}} \approx 11.7$ and its sign is consistent with the expected effect of beyond-MF critical correlations. Fixing $b_1 = -3.426$ (which is expected to be exact even including beyond-MF effects) gives an improved estimate of $b_2 = 42 \pm 2$.

16.4.2 Connection with a Uniform Bose Gas

In order to make a connection between the experiments on trapped atomic clouds and the theory of a uniform Bose gas we also need to consider the effect of interactions on the critical chemical potential μ_c.

In a uniform gas the interactions differently affect T_c (or equivalently n_c) and μ_c at both MF and beyond-MF level. The simple MF shift $\beta\mu_c^{\mathrm{MF}} = 4\zeta(3/2)a/\lambda_0$ (where $\beta = 1/k_{\mathrm{B}}T$) has no effect on condensation. To lowest beyond-MF order we have:[8]

$$\beta\mu_c \approx \beta\mu_c^{\mathrm{MF}} + B_2 \left(\frac{a}{\lambda_0}\right)^2. \tag{16.22}$$

[8]Note that B_2 is not just a constant but contains logarithmic corrections in a/λ_0 [23]. We neglect these in our discussion since they are not discernible at the current level of experimental precision.

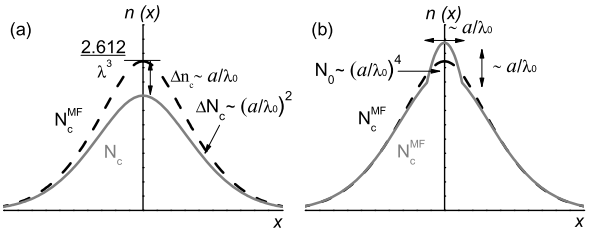

Fig. 16.8 Beyond-MF effects near the critical point in a harmonically trapped Bose gas. (**a**) For a fixed T, the density distribution at the critical point $N = N_c < N_c^{\mathrm{MF}}$ (*solid grey line*) is compared with the MF prediction (*dashed line*). In the trap centre we expect $n_c^{\mathrm{MF}} - n_c \propto a/\lambda_0$, characteristic of a uniform system. However the experimentally measured $N_c^{\mathrm{MF}} - N_c \propto (a/\lambda_0)^2$ is dominated by the density shift *outside* the central critical region, and is not directly related to the n_c shift. (**b**) If N is increased to $N_c^{\mathrm{MF}} > N_c$, a condensate induced by critical correlations forms within the critical region of size $\propto a/\lambda_0$. The condensed atom number $N_0 \propto (a/\lambda_0)^4$ directly relates to the critical density shift $\Delta n_c \propto a/\lambda_0$. (Figure adapted from [8])

We see that there is a qualitative difference between (16.19) and (16.22). Specifically, we have $n_c^{\mathrm{MF}} - n_c \propto a/\lambda_0$, but $\mu_c^{\mathrm{MF}} - \mu_c \propto (a/\lambda_0)^2$. This difference highlights the fact that the problem of the T_c shift is non-perturbative; near criticality the equation of state does not have a regular expansion[9] in μ, otherwise one would get $\Delta n_c \propto \mu_c - \mu_c^{\mathrm{MF}}$. For a harmonic trap, within LDA the uniform-system results for n_c and μ_c apply in the centre of the trap, and elsewhere local μ is given by (16.5). The result for the T_c shift however does not carry over easily to the non-uniform case. As illustrated in Fig. 16.8(a), in the centre of the trap we expect $\Delta n_c \propto a/\lambda_0$, but the measured beyond-MF $\Delta N_c \propto (a/\lambda_0)^2$ (see (16.21)).

In fact, the experimentally observed T_c shift (16.21) qualitatively mirrors (16.22), with the MF term linear in a/λ_0 and the beyond-MF one quadratic in a/λ_0 (to leading orders). This similarity can be understood as follows: The interaction shift of μ_c affects the density everywhere in the trap; outside the small critical region the equation of state is regular in μ and the local density shift is simply proportional to the local μ shift; the contribution to the total N_c shift from the non-critical region greatly outweighs the contribution from within the critical region and therefore one qualitatively expects $N_c - N_c^{\mathrm{MF}} \propto \mu_c - \mu_c^{\mathrm{MF}}$. More quantitatively, this connection is given by[10] [23]

$$-3\left(b_2 - b_2^{\mathrm{MF}}\right) = \frac{\zeta(2)}{\zeta(3)} B_2. \tag{16.23}$$

The key conclusion of this discussion is therefore that the beyond-MF T_c shift observed in a trapped gas is directly related to the beyond-MF μ_c shift (in either

[9]The non-interacting equation of state (16.3) cannot be expanded about D_c in $\beta\mu$, but rather in $\sqrt{-\beta\mu}$; up to first order this expansion gives $D = D_c - 2\sqrt{\pi}\sqrt{-\beta\mu}$. This scaling goes some way in explaining the qualitative difference between (16.19) and (16.22) although it cannot be used quantitatively.

[10]Note that this relationship is closely related to (16.13).

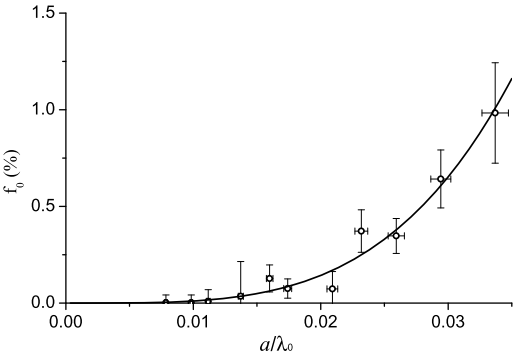

Fig. 16.9 Condensed fraction of an atomic gas induced by critical correlations. The condensed fraction $f_0 = N_0/N$ is measured for $N = N_c^{\mathrm{MF}} > N_c$. A fit to the data (*solid line*) with the function $f_0 \propto (a/\lambda_0)^x$ gives an exponent $x = 3.9 \pm 0.4$, in agreement with the predicted $x = 4$. (Figure adapted from [8])

trapped or uniform system). It does not however directly reveal the expected linear n_c shift and the theoretically most intriguing non-perturbative connection between μ_c and n_c shifts. In fact one could say that the historically puzzling (theoretical) connection between n_c and μ_c is just replaced by the puzzling connection between (expected) n_c and (measured) N_c.

This problem can be partly overcome by studying the condensed fraction f_0 in a trapped atomic cloud at the MF-predicted critical point [8]. By definition f_0 vanishes within MF theory, and so directly measures the effect of critical correlations which shift T_c above T_c^{MF}. At a fixed T we consider the condensed fraction of a gas, N_0/N, at the point where $N = N_c^{\mathrm{MF}} > N_c$, as illustrated in Fig. 16.8(b). The analogous quantity for a uniform gas was first theoretically studied by Holzmann and Baym [38], who showed that[11] $n_0/n \propto \Delta n_c \propto a/\lambda_0$. The condensate density n_0 vanishes at the point where the local $\mu = \mu_c$, so from (16.5) and (16.22) we get that the spatial extension of the condensate is also $\propto a/\lambda_0$, and hence $f_0 \propto (a/\lambda_0)^4$.

The quartic scaling of f_0 with a/λ_0 is thus directly related to the expected linear scaling of Δn_c with a/λ_0; the two scalings are simply connected by the volume of the critical region, $\propto (a/\lambda_0)^3$. This scaling is indeed confirmed experimentally [8], as shown in Fig. 16.9.

One can take the comparison with theory beyond just the scaling of f_0 with a/λ_0, and quantitatively compare the measured N_0 at the MF critical point with the Monte-Carlo (MC) calculations [39] for a uniform gas. This also works out very well, with the measured and predicted N_0 agreeing within a few percent [8]. It is however important to carefully summarise the conceptual steps involved in this comparison:

(i) On the one hand, the measurements of the T_c shift [7] experimentally provide (up to logarithmic corrections) the value of $\mu_c^{\mathrm{MF}} - \mu_c \propto (a/\lambda_0)^2$, via (16.21), (16.22), and (16.23) [8].

[11] This scaling holds for any distance from the critical point given by $(\mu - \mu_c)(\lambda_0/a)^2 = \text{const}$. By applying it to the MF critical point we neglect the logarithmic corrections to $\mu_c^{\mathrm{MF}} - \mu_c$, which are so far not experimentally observable.

(ii) On the other hand, the MC calculations [24, 39] that predict the n_c shift of (16.19) also provide tabulated values of the uniform-system condensate density n_0 for any $\mu - \mu_c \propto (a/\lambda_0)^2$.

(iii) Combining these two results and the LDA (16.5) we calculate the expected N_0 in a trapped gas with $N = N_c^{\mathrm{MF}}$ and find excellent agreement with the measurements shown in Fig. 16.9 [8].

Overall this provides strong cross-validation of theory and experiment. However it is important to note that the two different measurements of beyond-MF effects (i.e. of the T_c shift and f_0) do not provide two *independent* quantitative tests of the uniform-system theory. Instead, what we have shown is that they are consistently connected via the MC calculations for a uniform system. Finally it is also important to stress that we are still lacking a direct measurement of the n_c shift, which would explicitly test the historically most debated theoretical result of (16.19). This goal remains open for future measurements, either of the local density in a harmonically trapped gas or on a uniformly trapped atomic gas.

16.5 Equilibrium Criteria and Non-equilibrium Effects

Finally, we discuss the criteria for the measurements on a trapped Bose gas to faithfully represent its equilibrium properties, and the non-equilibrium effects revealed when they are violated. It is helpful to distinguish two types of non-equilibrium behaviour, transient and intrinsic.

Transient non-equilibrium effects are more familiar, and occur whenever some system parameter, such as the interaction strength, is rapidly changed (quenched). After such a quench the system relaxes towards its new equilibrium. Classically, one can estimate the relaxation time to be several elastic scattering times $1/\gamma_{\mathrm{el}}$, where γ_{el} is the elastic scattering rate [40–43].

However a system with continuous dissipation can only be "close to" thermodynamic equilibrium and is to some extent always intrinsically out of equilibrium. The proximity to equilibrium broadly depends on the competition between relaxation and dissipation. For an atomic gas, this leads to a criterion based on the dimensionless parameter $\gamma_{\mathrm{el}}\tau$, where τ is some characteristic dissipation time, e.g. for atom loss. In practice, the relevant τ and the criteria for equilibrium measurements depend on the required measurement precision.

In the case of the T_c measurements presented in Sect. 16.4, N_c is determined to about 1 %, so we require that the gas continuously (re-)equilibrates on a timescale τ corresponding to only 1 % atom-loss. This requires about 100 times higher γ_{el} than one would naively conclude by taking the $1/e$ lifetime of the cloud as the relevant timescale.

An interesting question is then what happens if we violate these stringent equilibrium criteria. In Fig. 16.10(a) we show measurements extending beyond the equilibrium region shown in Fig. 16.7, and in Fig. 16.10(b) we plot the corresponding

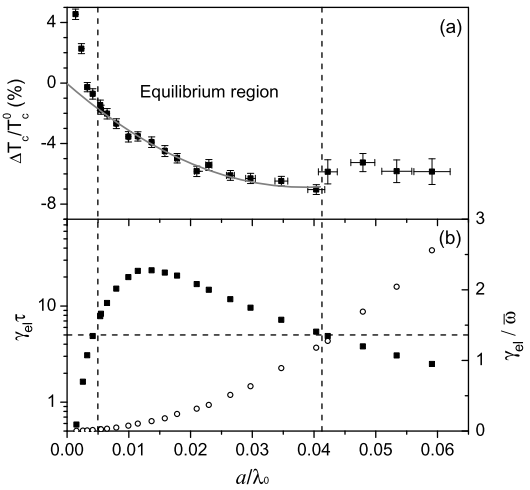

Fig. 16.10 Non-equilibrium effects. (**a**) $\Delta T_c / T_c^0$ is determined assuming equilibrium, as in Fig. 16.6. At both very low and very high a the apparent T_c deviates from the equilibrium curve. (**b**) Equilibrium criteria (see text): $\gamma_{el}\tau$ (*solid squares*) is the number of elastic collisions per particle during 1 % atom-loss; $\gamma_{el}/\bar{\omega} = 1$ (*open circles*) marks the onset of the hydrodynamic regime. (Figure adapted from [7])

$\gamma_{el}\tau$. Individually, γ_{el} and τ vary vastly as a function of a (γ_{el} increasing and τ decreasing) [7], but the breakdown of equilibrium appears to occur at $\gamma_{el}\tau \approx 5$ in both the low- and high-a limit.

In the small-a limit the apparent T_c is significantly above the equilibrium curve. We can qualitatively understand this effect within a simple picture. In this regime, losses are dominated by one-body processes which equally affect N_0 and N'. The net effect of equilibrating elastic collisions would therefore be to transfer atoms from the condensate to the thermal cloud. However the dissipation rate is too high compared to γ_{el}, and so N_0 remains non-zero even after the total atom number drops below the equilibrium critical value N_c.

In the large-a limit the initial breakdown of equilibrium again appears to result in condensates surviving above the equilibrium T_c. However the physics in this regime is much richer, with several potentially competing effects requiring further investigation. For example, three-body decay affects N_0 and N' differently, the thermal component is far from saturation, and the thermal component of the gas also enters the hydrodynamic regime, $\gamma_{el}/\bar{\omega} > 1$.

16.6 Conclusions and Outlook

In this chapter we reviewed the recent advances in the experimental observation and theoretical understanding of the effects of interactions on Bose-Einstein condensation (BEC) of harmonically-trapped ultracold atomic gases.

These systems are generally considered weakly interacting, but still display intricate deviations from the textbook picture of ideal-gas condensation. Even very weak interactions, necessary to maintain thermal equilibrium, lead to a strong deviation from the purely statistical picture of condensation driven by the saturation of the excited states in the system. The condensation temperature T_c is also affected

by interactions; recently it became possible to measure beyond-mean-field effects of interactions on T_c and quantitatively relate the experiments on trapped atomic gases with the theoretical literature on spatially uniform systems. Based on precision measurements of the non-saturation effects and the T_c shift, it is now possible to construct a simple effective equation of state describing a weakly interacting Bose gas in the vicinity of the BEC critical point.

Most of the experimental research so far focused on the equilibrium properties of an interacting gas. However these studies also led to an improved understanding of the conditions necessary for the system to be in thermal equilibrium, and first observations of non-equilibrium effects that emerge when those conditions are violated. Further study of these non-equilibrium phenomena promises to become a particularly exciting new research direction. Ultracold atomic gases are very well suited for such a study because non-equilibrium dynamics occur on easily resolvable timescales of milliseconds to seconds. Ultimately this research could improve our understanding of condensation in intrinsically out-of-equilibrium quantum systems, such as polariton gases.

References

1. A. Einstein, Sitz.ber./Phys. Kl. Preuss. Akad. Wiss. **1**, 3 (1925)
2. K. Huang, *Statistical Mechanics* (Wiley, New York, 1987)
3. C. Pethick, H. Smith, *Bose–Einstein Condensation in Dilute Gases* (Cambridge University Press, Cambridge, 2002)
4. L. Pitaevskii, S. Stringari, *Bose–Einstein Condensation* (Oxford University Press, Oxford, 2003)
5. J. Klaers, J. Schmitt, F. Vewinger, M. Weitz, Nature **468**, 545 (2010)
6. N. Tammuz, R.P. Smith, R.L.D. Campbell, S. Beattie, S. Moulder, J. Dalibard, Z. Hadzibabic, Phys. Rev. Lett. **106**, 230401 (2011)
7. R.P. Smith, R.L.D. Campbell, N. Tammuz, Z. Hadzibabic, Phys. Rev. Lett. **106**, 250403 (2011)
8. R.P. Smith, N. Tammuz, R.L.D. Campbell, M. Holzmann, Z. Hadzibabic, Phys. Rev. Lett. **107**, 190403 (2011)
9. F. Dalfovo, S. Giorgini, L.P. Pitaevskii, S. Stringari, Rev. Mod. Phys. **71**, 463 (1999)
10. J.O. Andersen, Rev. Mod. Phys. **76**, 599 (2004)
11. N.N. Bogoliubov, J. Phys. (USSR) **11**, 23 (1947)
12. V.N. Popov, *Functional Integrals and Collective Modes* (Cambridge University Press, Cambridge, 1987)
13. R.L.D. Campbell, R.P. Smith, N. Tammuz, S. Beattie, S. Moulder, Z. Hadzibabic, Phys. Rev. A **82**, 063611 (2010)
14. M. Zaccanti, B. Deissler, C. D'Errico, M. Fattori, M. Jona-Lasinio, S. Mueller, G. Roati, M. Inguscio, G. Modugno, Nat. Phys. **5**, 586 (2009)
15. W. Ketterle, D.S. Durfee, D.M. Stamper-Kurn, Bose–Einstein condensation in atomic gases, in *Proceedings of the International School of Physics Enrico Fermi*, vol. CXL (IOS Press, Amsterdam, 1999)
16. F. Gerbier, J.H. Thywissen, S. Richard, M. Hugbart, P. Bouyer, A. Aspect, Phys. Rev. A **70**, 013607 (2004)
17. T.D. Lee, C.N. Yang, Phys. Rev. **105**, 1119 (1957)
18. T.D. Lee, C.N. Yang, Phys. Rev. **112**, 1419 (1958)

19. M. Bijlsma, H.T.C. Stoof, Phys. Rev. A **54**, 5085 (1996)
20. G. Baym, J.P. Blaizot, M. Holzmann, F. Laloë, D. Vautherin, Phys. Rev. Lett. **83**, 1703 (1999)
21. M. Holzmann, W. Krauth, Phys. Rev. Lett. **83**, 2687 (1999)
22. J.D. Reppy, B.C. Crooker, B. Hebral, A.D. Corwin, J. He, G.M. Zassenhaus, Phys. Rev. Lett. **84**, 2060 (2000)
23. P. Arnold, G. Moore, Phys. Rev. Lett. **87**, 120401 (2001)
24. V.A. Kashurnikov, N.V. Prokof'ev, B.V. Svistunov, Phys. Rev. Lett. **87**, 120402 (2001)
25. M. Holzmann, G. Baym, J.P. Blaizot, F. Laloë, Phys. Rev. Lett. **87**, 120403 (2001)
26. G. Baym, J.P. Blaizot, M. Holzmann, F. Laloë, D. Vautherin, Eur. Phys. J. B **24**, 107 (2001)
27. H. Kleinert, Mod. Phys. Lett. B **17**, 1011 (2003)
28. M. Holzmann, J.N. Fuchs, G.A. Baym, J.P. Blaizot, F. Laloë, C. R. Phys. **5**, 21 (2004)
29. S. Giorgini, L.P. Pitaevskii, S. Stringari, Phys. Rev. A **54**, R4633 (1996)
30. P. Arnold, B. Tomášik, Phys. Rev. A **64**, 053609 (2001)
31. M. Houbiers, H.T.C. Stoof, E.A. Cornell, Phys. Rev. A **56**, 2041 (1997)
32. M. Holzmann, W. Krauth, M. Naraschewski, Phys. Rev. A **59**, 2956 (1999)
33. M.J. Davis, P.B. Blakie, Phys. Rev. Lett. **96**, 060404 (2006)
34. O. Zobay, Laser Phys. **19**, 700 (2009)
35. J.R. Ensher, D.S. Jin, M.R. Matthews, C.E. Wieman, E.A. Cornell, Phys. Rev. Lett. **77**, 4984 (1996)
36. F. Gerbier, J.H. Thywissen, S. Richard, M. Hugbart, P. Bouyer, A. Aspect, Phys. Rev. Lett. **92**, 030405 (2004)
37. R. Meppelink, R.A. Rozendaal, S.B. Koller, J.M. Vogels, P. van der Straten, Phys. Rev. A **81**, 053632 (2010)
38. M. Holzmann, G. Baym, Phys. Rev. Lett. **90**, 040402 (2003)
39. N. Prokof'ev, O. Ruebenacker, B. Svistunov, Phys. Rev. A **69**, 053625 (2004)
40. C.R. Monroe, E.A. Cornell, C.A. Sackett, C.J. Myatt, C.E. Wieman, Phys. Rev. Lett. **70**, 414 (1993)
41. M. Arndt, M.B. Dahan, D. Guéry-Odelin, M.W. Reynolds, J. Dalibard, Rev. Mod. Phys. **79**, 625 (1997)
42. N.R. Newbury, C.J. Myatt, C.E. Wieman, Phys. Rev. A **51**, R2680 (1995)
43. G.M. Kavoulakis, C.J. Pethick, H. Smith, Phys. Rev. A **61**, 053603 (2000)

Chapter 17
Universal Thermodynamics of a Unitary Fermi Gas

Takashi Mukaiyama and Masahito Ueda

Abstract A Fermi gas at the unitarity limit, where the scattering length diverges, is believed to exhibit universal thermodynamics. Recently, it has become possible to derive thermodynamic properties of a uniform system from those of a harmonically trapped system, enabling one to directly compare experimental results with many-body theories. In this chapter, we provide an overview of theories and experiments on the thermodynamics of a unitary Fermi gas.

17.1 Introduction

Strongly interacting Fermi systems offer a universal testbed for several subfields of physics such as atomic physics, condensed-matter physics, and nuclear physics. The interatomic interactions can be tuned simply by changing the strength of an external magnetic field. In an ultralow-temperature regime, a two-component Fermi gas of atoms shows superfluidity in various ways. In the positive s-wave scattering-length side of a Feshbach resonance, where interatomic interactions are repulsive, a two-component Fermi gas of atoms behaves as a gas of diatomic molecules and exhibits Bose-Einstein condensation of molecules. In the negative side, where the interactions are attractive, atoms form Cooper pairs and show BCS-type superfluidity. These two different regimes are considered to be the opposite extremes of a single phase and cross over to each other across the Feshbach resonance.

The superfluid phase diagram in the BCS-BEC crossover regime was theoretically predicted by Sa de Melo et al. in 1993 [1]. Back in those days, it was not clear whether a strongly-interacting Fermi gas would show superfluidity at very low temperatures or whether the system would be stable at all. In 2002, the Duke group experimentally demonstrated that a system of fermionic lithium atoms in the

T. Mukaiyama
Institute for Laser Science, University of Electro-Communications, 1-5-1 Chofugaoka, Chofu, Tokyo 182-8585, Japan

M. Ueda (✉)
Department of Physics, University of Tokyo, Hongo, Bunkyo-ku, Tokyo 113-0033, Japan
e-mail: ueda@phys.s.u-tokyo.ac.jp

A. Bramati, M. Modugno (eds.), *Physics of Quantum Fluids*,
Springer Series in Solid-State Sciences 177, DOI 10.1007/978-3-642-37569-9_17,

unitary regime is stable [2]. They also found a hydrodynamic behavior in the expansion of the gas [3] which is analogous to the elliptic flow in quark-gluon plasmas. In 2004, the Innsbruck group observed a smooth change in the atomic density distribution across the Feshbach resonance, which indicates that the system crosses over from the BEC to BCS regimes without undergoing a phase transition [4]. The Innsbruck group also measured the pairing gap in this crossover region by using RF spectroscopy [5]. In the same year, the JILA group and the MIT group observed the emergence of condensation in ultracold Fermi gases in the BCS-BEC crossover regime [6, 7]. However, the entire superfluid phase diagram in the BCS-BEC crossover regime has not yet been determined, because of the difficulty in determining the thermodynamic quantities including the temperature due to the strong interatomic interaction. Understanding the thermodynamic behavior of a Fermi gas at the unitarity limit is among the most important problems in the strongly interaction Fermi system.

At the unitarity limit, thermodynamics is expected to become universal. In 1999, Bertsch raised the question about the ground state of dilute spin-1/2 particles when the scattering length diverges and the range of interaction is negligible [8]. He envisaged such a situation as an extreme case of the inner crust of neutron stars in which the range of interaction R, neutron density n, and the scattering length a_s satisfy $R \sim 1$ [fm] $< n^{-1/3} < |a_s| \sim 18.5$ [fm]. When the scattering length diverges and the zero-range approximation is valid, the interaction parameter drops out of the thermodynamic description and therefore we may expect the same thermodynamic behavior at unitarity, regardless of the atomic species of constituent particles. This is called the universal hypothesis. In this chapter, we present an overview of the universal properties of a unitary Fermi gas.

17.2 Universality in a Unitary Fermi Gas

17.2.1 Universal Thermodynamics

We consider s-wave collisions in a two-component Fermi gas of atoms. The scattering amplitude is described as $f(k) = 1/(-1/a_s + r_e k^2/2 - ik)$, where k is the relative wavenumber, a_s is the scattering length, and r_e is the range of the interactions. At the unitarity and zero-range limits, where $k|a_s| \to \infty$ and $k|r_e| \to 0$, the scattering amplitude reaches the maximum $f(k) = -1/ik$. The characteristic length scale of fermionic atoms is the Fermi wavenumber k_F, which is on the order of a typical interatomic distance $n^{-1/3}$. The condition of the unitarity limit is $|r_e| \ll n^{-1/3} \ll |a_s|$. In the case of fermionic lithium-6 (^{6}Li) near quantum degeneracy, a typical interatomic distance $n^{-1/3}$ is on the order of a few hundred nanometers and the range of interaction r_e is 5 nm. By tuning the s-wave scattering length to infinity using a Feshbach resonance, the unitarity limit can be realized experimentally.

Since the divergent scattering length and the negligibly small range of interaction do not enter the thermodynamic description, the thermodynamics of a unitary

Fermi gas depends only on the Fermi energy ε_{F} and the temperature $k_{\mathrm{B}}T$ [9, 10]. According to this universal hypothesis, the internal energy, which is the sum of the kinetic energy and the interaction energy, is described by the following universal thermodynamic function:

$$E = NE_{\mathrm{F}} f_E(k_B T/E_{\mathrm{F}}) = NE_{\mathrm{F}} f_E(T/T_{\mathrm{F}}). \tag{17.1}$$

Here, T_{F} is the Fermi temperature and f_E is a dimensionless universal function. Other thermodynamic functions can also be described in similar universal forms; for example, the chemical potential μ, Helmholtz free energy F, and entropy S are described as

$$\mu = E_{\mathrm{F}} f_\mu(T/T_{\mathrm{F}}), \tag{17.2}$$

$$F = NE_{\mathrm{F}} f_F(T/T_{\mathrm{F}}), \tag{17.3}$$

$$S = Nk_{\mathrm{B}} f_S(T/T_{\mathrm{F}}). \tag{17.4}$$

According to the universal hypothesis, the internal energy of a unitary Fermi gas at $T = 0$ is given by $E_0^{\mathrm{unitary}}/N = E_0^{\mathrm{ideal}}(1+\beta)$, where $E_0^{\mathrm{ideal}} = \frac{3}{5}\varepsilon_{\mathrm{F}}N$ is the internal energy of an ideal Fermi gas, and β is a dimensionless universal parameter. The ratio of the ground-state energy of a unitary Fermi gas to that of an ideal Fermi gas $E_0^{\mathrm{unitary}}/E_0^{\mathrm{ideal}} = 1+\beta = \xi$ is called the Bertsch parameter, where β has been measured to be $-0.64(15)$ [11], $-0.68(^{+0.15}_{-0.10})$ [12], $-0.49(4)$ [13], $-0.54(^{+0.05}_{-0.12})$ [14], $-0.54(5)$ [15], $-0.50(7)$ [16], $-0.61(2)$ [17], $-0.565(15)$ [18]; at the time of writing, the latest experimental result gives $\xi = 0.376(4)$ [19]. The fact $\beta < 0$ shows that the effective interatomic interaction is attractive at unitarity. This can be confirmed by the experimental fact that the size of the cloud of a unitary Fermi gas in a harmonic trap is smaller than that of an ideal Fermi gas with the same number of atoms.

17.2.2 Pressure-Energy Relation and Virial Theorem

A unitary Fermi gas features several key properties that can be derived from the form of the universal thermodynamic functions in (17.1)–(17.4). One is the relation between the pressure P and the energy density E/V [20, 21]. We consider N atoms in a volume V. The pressure of the gas is determined from the relation $P = -(\partial E/\partial V)_{N,S}$. Equation (17.4) shows that the constant entropy implies constant T/T_{F}. Therefore, the pressure can be described as

$$P = -(\partial E/\partial V)_{N,T/T_{\mathrm{F}}} = -Nf_E(T/T_{\mathrm{F}})\partial E_{\mathrm{F}}/\partial V = Nf_E(T/T_{\mathrm{F}})\frac{2}{3}\frac{E_{\mathrm{F}}}{V} = \frac{2}{3}\frac{E}{V}, \tag{17.5}$$

where we used $E_{\mathrm{F}} \propto V^{-2/3}$. This relation is the same as the one for a uniform ideal Fermi gas.

Another key property of a unitary Fermi gas is the virial theorem [21]. The virial theorem can be derived from (17.5) and the equation of force balance of a gas. At mechanical equilibrium, an inward force due to a trapping potential and an outward force due to the gas pressure balance everywhere inside the gas:

$$\nabla P(\boldsymbol{r}) + n(\boldsymbol{r})\nabla U_{\mathrm{trap}}(\boldsymbol{r}) = 0. \tag{17.6}$$

Taking the inner product of this equation with $\boldsymbol{r}$ and performing the volume integration, the first term yields

$$\begin{aligned}\int \boldsymbol{r}\cdot\nabla P(\boldsymbol{r})\mathrm{d}\boldsymbol{r} &= \int \nabla\cdot\big(\boldsymbol{r}P(\boldsymbol{r})\big)\mathrm{d}\boldsymbol{r} - \int P(\boldsymbol{r})\nabla\cdot\boldsymbol{r}\mathrm{d}\boldsymbol{r}\\ &= -3\int P(\boldsymbol{r})\mathrm{d}\boldsymbol{r}\\ &= -2N\cdot E_{\mathrm{internal}}.\end{aligned} \tag{17.7}$$

Here E_{internal} is the internal energy per particle. The first term on the right-hand side of the first equality vanishes and (17.5) is used in deriving the last equality. In a harmonic trapping potential which gives $\boldsymbol{r}\cdot\nabla U_{\mathrm{trap}}(\boldsymbol{r}) = 2U_{\mathrm{trap}}(\boldsymbol{r})$, the second term in (17.6) is transformed by taking the inner product with $\boldsymbol{r}$ and performing the volume integration to

$$\int \boldsymbol{r}\cdot n(\boldsymbol{r})\nabla U_{\mathrm{trap}}(\boldsymbol{r})\mathrm{d}\boldsymbol{r} = \int 2n(\boldsymbol{r})U_{\mathrm{trap}}(\boldsymbol{r})\mathrm{d}\boldsymbol{r} = 2NE_{\mathrm{pot}}. \tag{17.8}$$

Thus, (17.7) and (17.8) give

$$E_{\mathrm{pot}} = E_{\mathrm{internal}}. \tag{17.9}$$

This is the same as the one for an ideal Fermi gas since the derivation starts from (17.5) and (17.6), which hold for both a unitary Fermi gas and an ideal Fermi gas. The experimental verification of (17.9) is reported in [21]. Since E_{pot} is proportional to the mean square size of the cloud $\langle x^2\rangle$, (17.9) can be verified by checking the relation $\langle x^2(E)\rangle/\langle x^2(E_0)\rangle = E/E_0$, where E_0 denotes the ground-state energy. To measure the energy of the gas, Thomas et al. first prepared the gas in the ground state and then added the energy to the gas by turning off the optical trap for a short time and recapturing the atoms. By recapturing the atoms after the expansion, a controlled amount of energy was added to the gas in the form of a potential energy. Since the unitary Fermi gas is strongly interacting, the expansion of the unitary Fermi gas can be well described by hydrodynamics. By calculating the energy that is added to the gas due to the hydrodynamic expansion, they found the precise energy of the gas after thermalization. Figure 17.1 shows the experimental result of $\langle x^2(E)\rangle/\langle x^2(E_0)\rangle - 1$ vs. $E/E_0 - 1$. The dashed line in Fig. 17.1 shows $\langle x^2(E)\rangle/\langle x^2(E_0)\rangle = 1.03(0.02)E/E_0$, which is consistent with the virial theorem. Equation (17.9) is quite useful in experiments because the total energy of the gas is derived from the potential energy, which can be measured directly from the density profile.

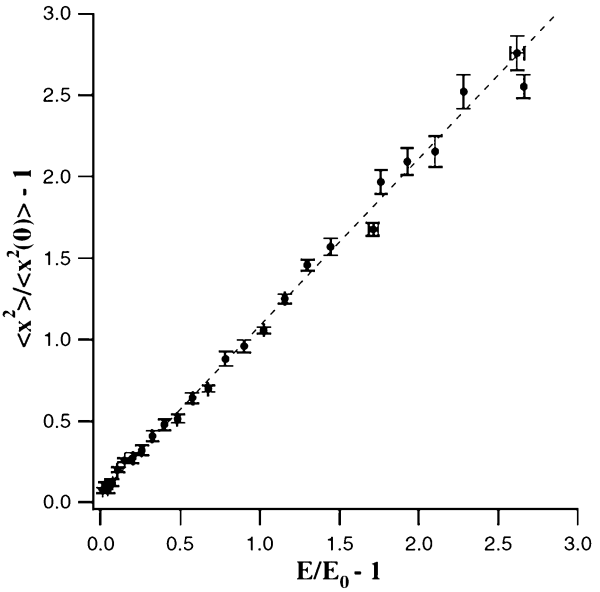

Fig. 17.1 Experimental verification of the virial theorem in a unitary Fermi gas. The linear dependence shows $\langle x^2(E)\rangle/\langle x^2(E_0)\rangle = E/E_0$. Reproduced from [21] with permission

17.2.3 Measurement of Trap-Averaged Thermodynamic Quantities

The first thermodynamic quantity that was measured experimentally was the ground-state energy of a unitary Fermi gas in a harmonic trap. The ground-state energy is described as $(1+\beta)E_{\mathrm{F}}$, and several measurements of β have been reported from the measurement of the size of the cloud [11–14, 17] and the measurement of the first sound velocity [9] at the low-temperature limit.

Kinast et al. measured the heat capacity of a unitary Fermi gas using the optically trapped ^{6}Li atoms [13]. They measured the trap-averaged energy of the gas as a function of temperature and observed a clear change in the temperature dependence of the heat capacity upon the emergence of superfluidity. To determine the energy, they applied the energy input technique [13]. In this experiment, they determined the temperature by using the calibration curve from an empirical temperature estimated by applying the Thomas-Fermi profile to a unitary Fermi gas. Although the change in the heat capacity due to superfluidity was clearly observed, the accuracy of the estimation of the critical temperature was limited by the empirical temperature calibration. Later, they invented a new scheme to determine the temperature of a unitary Fermi gas more accurately from the measurement of the total energy and entropy [17, 22]. The entropy of the gas can be determined from the density profile at a magnetic field where the scattering length is small enough to guarantee that the entropy versus cloud size curve is to a good approximation given by that for an ideal gas. From the energy and entropy measurements, they determined the relation between energy and temperature by applying the thermo-

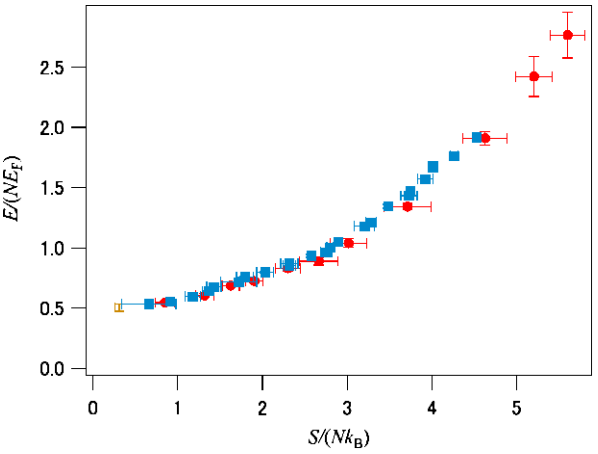

Fig. 17.2 Universal thermodynamics of a unitary Fermi gas. Three experimental results of the trap-averaged energy are plotted as a function of entropy. *Blue*, *red* and *yellow markers* show the experimental result from the Duke, JILA, and Rice groups, respectively

dynamic relation $1/T = \partial S/\partial E$ to the entropy vs. energy data. Therefore, once we know any one of the energy, entropy or temperature, we can find the other quantities from the relations obtained by the Duke group. This is quite useful because the total energy can easily be obtained from the potential energy which is calculated from the absorption image and the information about the trapping potential.

Stewart et al. measured the potential energy of a unitary Fermi gas of ^{40}K [14]. They investigated the temperature dependence of the potential energy of a gas in a harmonic trap and determined β at the low-temperature limit. Their result is consistent with that obtained from experiments using ^{6}Li [11–13, 15–18], which indicates the universality of the thermodynamics.

Hu et al. analyzed the data of the trap-averaged energy vs. entropy measured at Duke and Rice using ^{6}Li and at JILA using ^{40}K (Fig. 17.2) [23]. All the experimental data are consistent with each other, which indicates that the thermodynamics of a unitary Fermi gas is universal independent of the atomic species and trapping condition over a wide range of temperature.

However, these results are obtained from trap-averaged quantities, and they do not provide direct information on the universal thermodynamic functions. The universal thermodynamic functions for a unitary Fermi gas have $k_B T/E_F$ as an argument. Since the scattering between atoms occurs so frequently that the thermal equilibrium is always achieved, implying that $k_B T$ is constant over the entire atomic cloud. However, since an atomic gas in a harmonic trap has a nonuniform density profile, the Fermi energy E_F, which depends on the density n, becomes position-dependent. Therefore $k_B T/E_F$ is also position-dependent, which makes it difficult to derive the thermodynamic functions from the trap-averaged thermodynamic quantities and to compare experimental results with theoretical ones [24–28]. To determine the detailed shape of the thermodynamic functions, it is necessary to measure both the thermodynamic quantities and $k_B T/E_F$ at the same position.

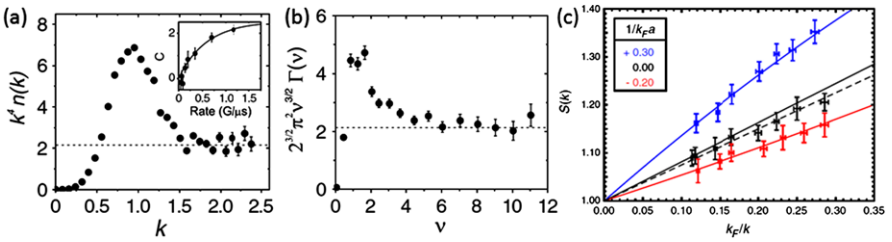

Fig. 17.3 Experimental confirmation of the universal behavior of a strongly interacting Fermi gas. (**a**) Momentum distribution of a unitary Fermi gas measured at JILA using ^{40}K. The high-momentum tail shows the k^{-4} dependence. (**b**) RF spectrum showing the $\nu^{-3/2}$ dependence at the high-frequency region. (**c**) Static structure factor measured by the Swinburne group, showing the $1/k$ dependence. (**a**) and (**b**) are taken from [34] and (**c**) is taken from [35] with permissions

17.2.4 Tan Relations

In 2008, Tan predicted several remarkable relations between the momentum distribution and thermodynamic quantities [29–31]. These relations, known as Tan relations, hold quite generally for interacting gases in the sense that they can be applied to any system that satisfies

$$r_0 \ll a_s,\ n^{-1/3},\ \lambda,\ (\hbar/m\omega)^{1/2}, \tag{17.10}$$

where r_0 is the range of interaction, $n^{-1/3}$ is the mean interparticle distance, $\lambda = h/\sqrt{2\pi m k_B T}$ is the thermal de Broglie length, and $(\hbar/m\omega)^{1/2}$ is the size of the harmonic potential with the energy separation $\hbar\omega$. In typical cold atom experiments near quantum degeneracy, r_0 is much smaller than any of $n^{-1/3}$, λ, and $(\hbar/m\omega)^{1/2}$. At the unitarity limit where a_s diverges, the Tan relations become exact. When the condition (17.10) is met, it is known that the momentum distribution of a Fermi gas over the range

$$a_s^{-1},\ n^{1/3},\ \lambda^{-1},\ (\hbar/m\omega)^{-1/2} \ll k \ll r_0^{-1} \tag{17.11}$$

can be described as $n(k) = C/k^4$ [32], and Tan dubbed C as contact. Since the number of atoms with the wavenumber larger than K_C is given by $N(|k| > K_C) = C/2\pi^2 K_C$, the contact may be interpreted as a measure of the number of high-momentum atoms [33]. The contact is also related to the density-density correlation of atoms and can be considered as a measure of the number of pairs of atoms in a small volume [33].

The universal properties of interacting fermions have been experimentally confirmed by several groups. Figure 17.3(a) shows the measurement of the momentum distribution of a unitary Fermi gas performed at JILA [34]. The magnetic field was tuned quickly to switch off the atomic interaction when the atoms were released to measure the momentum distribution. The JILA group confirmed that the high-momentum tail of the distribution has the predicted k^{-4} dependence and obtained the contact from the asymptotic behavior of the rf spectrum. Figure 17.3(b) shows the frequency dependence of the transition rate in the RF spectroscopy [34]. The

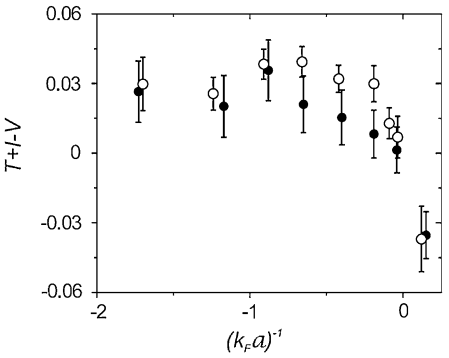

Fig. 17.4 The left- and right-hand sides of (17.12) are plotted as *closed* and *open circles*, respectively. Those two quantities agree within the experimental uncertainty. Figure is taken from [34] with permission

$\nu^{-3/2}$ dependence of the line shape of the RF spectrum at the high-frequency region is another consequence of the universal behavior. Since the static structure factor is the Fourier transform of the density-density correlation which can be described in terms of the contact [33], the static structure factor $S(k)$ can also be used to test the universal behavior. Figure 17.3(c) shows the measurement of $S(k)$ using the Bragg spectroscopy performed by the Swinburne group [35]. The $1/k$ dependence of $S(k)$ shows the predicted universal behavior.

Although the contact depends on the scattering length, atomic density and temperature, the relations between thermodynamic quantities and the contact are universal. A prime example that has been verified experimentally is the virial theorem [34]. For interacting particles in a harmonic trap, the kinetic energy T, the interaction energy I and the potential energy V satisfy the following equation:

$$T + I - V = -C/4\pi k_{\mathrm{F}} a. \tag{17.12}$$

The virial theorem for the unitary gas mentioned in the previous section is $T + I - V = 0$, which is given as the special case of $(k_{\mathrm{F}}a)^{-1} = 0$. Figure 17.4 shows the experimental verification of the virial theorem over a range of the scattering length. The left- and right-hand side of (17.12) are plotted as closed and open circles. Those two quantities agree within the uncertainty, showing the universality of the system. The JILA group also tested the adiabatic sweep theorem [34]. Tan relations show that many thermodynamic quantities are related to one another through the contact, and it will therefore be useful to derive thermodynamic quantities which cannot be measured directly from the experiment.

17.3 Experimental Determination of Universal Thermodynamics

17.3.1 Determination of Universal Energy Function $E(T)$

One way to determine the universal thermodynamic functions is to measure the local energy density [36]. As mentioned in Sect. 17.2.2, the local pressure of a trapped

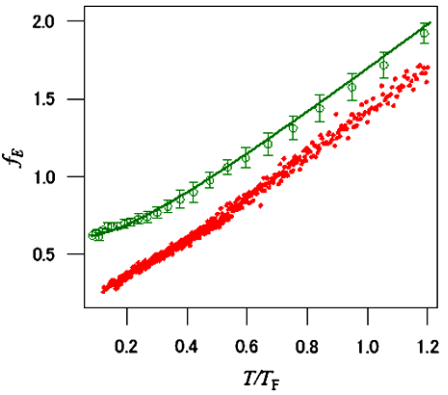

Fig. 17.5 Universal functions of the internal energy ($f_E(T/T_F) = E/NE_F$) for an ideal Fermi gas (*green open circles*) and for a unitary Fermi gas (*red dots*). The green curve shows the theoretical universal function for an ideal Fermi gas

gas is related to the internal energy through (17.5) at the unitarity limit. Therefore, we can determine the local energy by measuring the local pressure in a gas. At thermal equilibrium, (17.6) can be used to determine the local pressure $P(\boldsymbol{r})$ from the information of the trapping potential $U_{\rm trap}(\boldsymbol{r})$ and the atomic density profile $n(\boldsymbol{r})$. By relating $f_E(\boldsymbol{r}) = 3P(\boldsymbol{r})/2n(\boldsymbol{r})E_F(\boldsymbol{r})$ to the reduced temperature T/T_F at the same position, we determine the universal energy function $f_E(T/T_F)$. In fact, we can determine $f_E(T/T_F)$ over a wide range of temperature from a single density profile because it contains the information of the universal functions ranging from $f_E(T/T_F^0)$ at the cloud center to $f_E(\infty)$ at the edge of the cloud, where T_F^0 is the Fermi temperature at the center of the cloud.

The degenerate Fermi gas of ^{6}Li are prepared in the two lowest spin states in an optical dipole trap, and the magnetic field of 834 gauss is applied to realize the unitary gas condition. The temperature of the gas is controlled by the final trap depth of evaporative cooling, and the gas is held until the system reaches thermal equilibrium. The atomic density distribution $n(\boldsymbol{r})$ is determined from the absorption image taken perpendicular to the axial direction after a 3 ms free expansion at the same magnetic field. From the image, we construct an *in situ* three-dimensional atomic density distribution under the assumption of local density approximation (LDA) and hydrodynamic expansion. The temperature T is determined by using thermometry for the trapped unitary Fermi gas, which allows us to estimate $T/T_{F,\rm trap}$ from $E_{\rm total}/E_{F,\rm trap}$ [17, 37]. Here, $E_{F,\rm trap} = k_B T_{F,\rm trap} = \hbar\overline{\omega}(3N)^{1/3}$ is the Fermi energy in the trap and $E_{\rm total} = 3m\omega_z^2\langle z^2\rangle$ is the total energy per particle. The absolute temperature T is obtained by multiplying the given $T/T_{F,\rm trap}$ by $T_{F,\rm trap}$.

Since the thermodynamic function of an ideal Fermi gas also has the universal form and obeys (17.5) and (17.6), we first applied the measurement scheme mentioned above to an ideal Fermi gas to check the validity of the scheme. 50 profiles taken at 526 gauss, where the scattering length is zero, are analyzed according to the above procedure. The green open circles in Fig. 17.5 show the experimentally obtained thermodynamic function of the internal energy for an ideal Fermi gas $f_E^{\rm ideal}(T/T_F)$. The experimental data show excellent agreement with the theoretical curve (green curve), which indicates that we have successfully determined the thermodynamic function for an ideal Fermi gas.

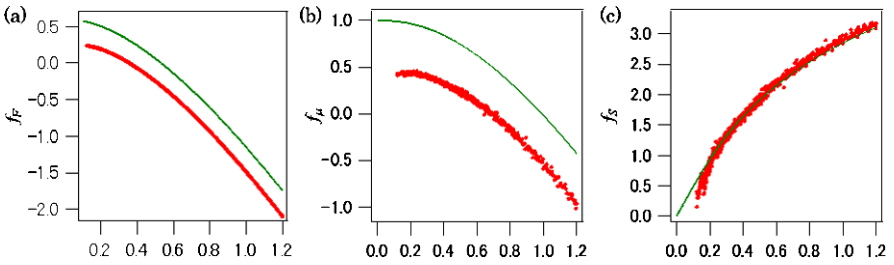

Fig. 17.6 Universal functions for (**a**) the Helmholtz free energy, (**b**) chemical potential, and (**c**) entropy. The *red dots* show the measured data for a unitary Fermi gas, and the *green solid curves* show the corresponding functions for an ideal Fermi gas

Next, the same scheme is applied to the unitary Fermi gas. By analyzing 800 measured profiles, we determined $f_E(T/T_F)$ for various trap geometries and temperatures, and confirmed that $f_E(T/T_F)$ determined by this method is independent of the trap geometry. The red dots in Fig. 17.5 show the experimentally determined $f_E(T/T_F)$ for the unitary Fermi gas. Because of the effective attractive interaction at the unitarity limit, $f_E(T/T_F)$ for the unitary Fermi gas is smaller than $f_E^{\text{ideal}}(T/T_F)$.

Now that the universal function of the internal energy is determined, other thermodynamic functions for the unitary gas can also be determined from the energy function. The universal function of the Helmholtz free energy, chemical potential, and entropy are derived from the standard thermodynamic relations as $f_E(T/T_F) = f_F(T/T_F) - T/T_F f_F'(T/T_F)$, $f_\mu(T/T_F) = \{5f_F(T/T_F) - 2T/T_F f_F'(T/T_F)\}/3$, and $f_S(T/T_F) = -f_F'(T/T_F)$, respectively, and plotted in Fig. 17.6.

17.3.2 Determination of the equation of state $P(\mu, T)$

Nascimbène et al. determined the equation of state $P(\mu, T)$ for a unitary Fermi gas of ^{6}Li [38]. They determined the local pressure of the gas from the *in situ* absorption images, following the proposal by Ho and Zhou [39] who showed that the local pressure is related to the doubly-integrated density profiles:

$$P\big(0, 0, z; \mu(0, 0, z), T\big) = \frac{m\omega_x\omega_y}{2\pi}\overline{n}(z), \tag{17.13}$$

where $P(0, 0, z; \mu, T)$ is the local pressure in the gas on the z-axis, m is the atomic mass, ω_x and ω_y are the angular frequencies of the trap in the x and y directions, and $\overline{n}(z) = \int n(x, y, z)\mathrm{d}x\mathrm{d}y$ is the doubly-integrated density with $n(x, y, z)$ being the atomic density. They trapped a small number of ^{7}Li atoms together with ^{6}Li, made both atomic species thermally equilibrated with each other, and determined the temperature of ^{6}Li from that of ^{7}Li which was measured by the time-of-flight measurement. To determine the chemical potential, they started with the data at a high-temperature region, where the second-order virial expansion can be used as a

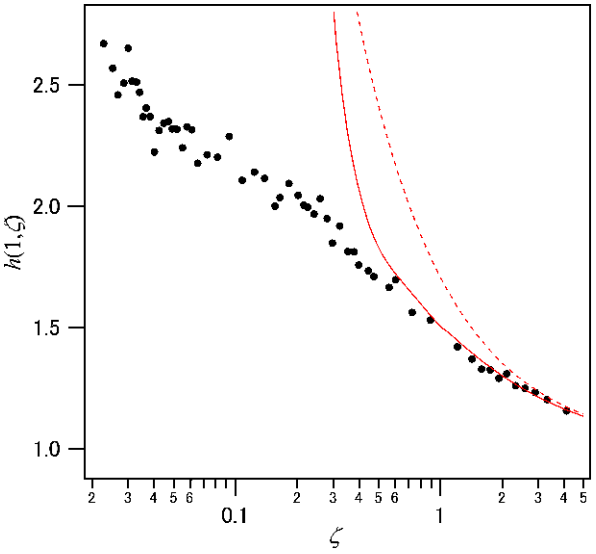

Fig. 17.7 Equation of state for a unitary Fermi gas $h(1, \zeta)$ measured by the ENS group [38]. *Black dots* show the experimental data, and the *red dashed and solid curves* show the result of the second- and fourth-order virial expansion

reference. Once the equation of state for the high-temperature cloud is determined, it can be used as a new reference for a colder gas in determining the chemical potential. By iterating this procedure, they were able to determine the equation of state over a wide range of temperature.

The pressure of the gas can be described as

$$P(\mu_1, \mu_2, T) = P_{\text{ideal}}(\mu_1, T) h\left(\eta = \frac{\mu_1}{\mu_2}, \zeta = \exp\left(-\frac{\mu_1}{k_{\text{B}} T}\right)\right), \tag{17.14}$$

where μ_1 and μ_2 are the chemical potentials for two different species and $P_{\text{ideal}}(\mu_1, T)$ is the pressure of an ideal Fermi gas. The equation of state for a spin-balanced gas $h(1, \zeta)$ is plotted as black dots in Fig. 17.7. From this data, they derived the third and fourth virial coefficients and compared them with theoretical predictions. They analyzed the data to focus on the temperature dependence of the pressure by plotting $P(\mu, T)/P_{\text{ideal}}(\mu, 0)$ as a function of $(k_{\text{B}} T/\mu)^2$. The data show the T^2 dependence of the pressure from the high-temperature side down to $(k_{\text{B}} T/\mu)^2 \sim 0.1$. The T^2 dependence of the pressure above the critical temperature is consistent with the Fermi liquid behavior. By fitting the data with Fermi liquid theory, they determined the Fermi liquid parameters. They observed the deviation of the data from the T^2 dependence at $(k_{\text{B}} T/\mu)^2 \sim 0.1$, and interpreted it as a signature of the superfluid phase transition.

Now that there are two independent sets of experimental results on the thermodynamics, we can compare them and check the consistency between them. The result discussed in Sect. 17.3.1 is the canonical equation of state $E(n, T)$ and the result mentioned in this section is the grand-canonical equation of state $P(\mu, T)$. By converting $P(\mu, T)$ obtained by the ENS group to $E(n, T)$ [40], we can directly compare these two results. Figure 17.8 shows the thermodynamic function

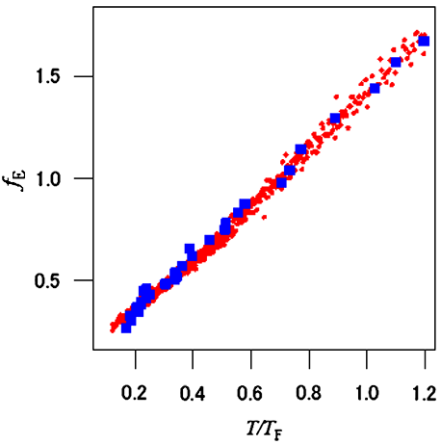

Fig. 17.8 Comparison of $f_E[T/T_F]$. *Red dots* show $f_E[T/T_F]$ measured by the Tokyo group [36] and *blue squares* show $f_E[T/T_F]$ measured by the ENS group [38, 40]

$f_E[T/T_F] = E/NE_F$ obtained by the Tokyo group (red dots) and the ENS group (blue squares). The two data sets are consistent with each other.

17.4 Signatures of the Superfluid Phase Transition

17.4.1 Detection of the Phase Superfluid Transition

To detect an emergence of a condensate, we release an atomic cloud from a trap to measure its momentum distribution and observe the bimodal distribution which is composed of a zero-momentum component at the center and a thermal component surrounding it. This technique can be used to probe the condensation of Bose gases but cannot be used for a fermion pair condensate except in the deep BEC regime. This is because the fermion pairs are formed due to the many-body effect and therefore pairs are broken as the density of atoms decreases during the expansion. Therefore, to detect a condensation in a Fermi gas, it is necessary to measure the center-of-mass momentum distribution of the pairs. In 2004, Regal et al. demonstrated a new scheme to detect the condensation of fermions using ^{40}K [6]. When they release the Fermi gas, they sweep the magnetic field from the BCS-BEC crossover region to the deep BEC regime to convert correlated fermion pairs into tightly-bound molecules. When the magnetic field sweep is slow enough to satisfy the adiabatic condition for the atom pairs to follow the two-body bound state, and fast enough to ensure that collisions between atoms can be neglected within the sweep time, atom pairs are efficiently converted into tightly-bound dimers (Fig. 17.9(a)). By applying the magnetic field sweep just before expansion of the gas, we are able to measure the center-of-mass momentum distribution of atom pairs. Figure 17.9(b) shows a typical center-of-mass momentum distribution of atom pairs obtained in the actual experiment. An emergence of the condensate can clearly be seen when the temperature is lower than the critical temperature. The onset of superfluidity can

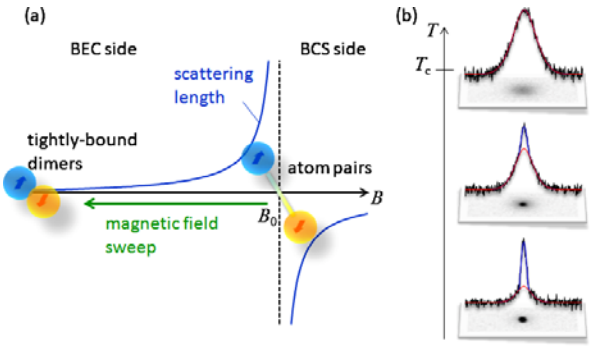

Fig. 17.9 Schematic illustration of converting pairs of fermions into tightly-bound dimers. (**a**) To measure the center-of-mass momentum of correlated atom pairs at the Feshbach resonance B_0, the magnetic field is swept to the BEC side of the resonance as indicated by the *green arrow*. (**b**) Time-of-flight images taken after the magnetic field sweep. *Top image* shows the center-of-mass momentum of atom pairs at T_c, and the *lower* ones were taken at lower temperatures, where the central peak shows the condensate

be identified by observing a sudden change in the thermodynamic properties. The changes in the frequency and damping rate of collective excitations were extensively studied to observe a superfluid hydrodynamic behavior. However, since the atoms near a Feshbach resonance are strongly interacting, they show collisional hydrodynamic behavior even at temperature higher than T_c. It was difficult to distinguish between superfluid and collisional hydrodynamics. In 2005, the Duke group determined the superfluid transition point as a change in the heat capacity of a unitary Fermi gas [13]. More recently, the ENS group measured the pressure as a function of $(k_B T/\mu)^2$ and observed the deviation from a Fermi liquid behavior at T_c. Very recently, the MIT group measured the compressibility and the specific heat as a function of temperature for a homogeneous gas and observed the superfluid lambda transition at T_c [19].

17.4.2 Measurements of Critical Parameters

Figure 17.10 shows the condensate fraction as a function of the ratio of the total energy to the Fermi energy $E_{F,trap}$ in a harmonic trap [36]. The condensate fraction was determined by fitting the momentum distribution of molecules measured after the magnetic-field sweep with a bimodal distribution. In this measurement, the sweep time required to leave the strongly interacting regime is 2 μs. This time scale is much shorter than the typical relaxation time of 500 μs. Therefore, the condensate fraction is not likely to change noticeably during the sweep.

In our experiment [36], the critical total energy is determined to be $E_c/E_{F,trap} = 0.76(1)$ and the reduced temperature is determined to be $T_c/T_F = 0.17(1)$ from the peak atomic density and the cloud temperature. The universal functions have the

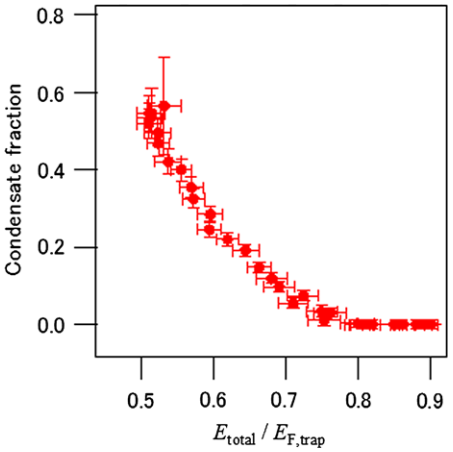

Fig. 17.10 Condensate fraction plotted against the ratio of the total energy to the Fermi energy in a harmonic trap. The critical point is identified as the point where the condensate fraction starts to increase from zero

critical values of $f_E[T_c/T_F] = 0.32(2)$, $f_F[T_c/T_F] = 0.21(1)$, $f_\mu[T_c/T_F] = 0.42(2)$, and $f_S[T_c/T_F] = 0.7(2)$. The experimental and theoretical results of the critical temperature, energy, chemical potential and entropy obtained by several groups are listed in Table 17.1.

17.4.3 Fermi Liquid vs. Non-Fermi Liquid

In high-T_c materials, a gap structure in the single-particle density of states has been observed above the critical temperature. This phenomenon is known as a pseudo-gap, the origin of which has long been debated. Among the possible scenarios for explaining the pseudo-gap phenomenon is pre-formed pairing which implies that formation of pairs and emergence of the superfluidity occur at different temperatures. Identification of the microscopic mechanism of pairing and characterization of the pseudo-gap phase are important for understanding the superfluidity in a strongly-interacting Fermi gas.

The JILA group conducted a photoemission spectroscopy of ^{40}K atoms in a strongly-interacting regime [42, 43]. By resolving momentum and energy at the same time, which is analogous to the angle-resolved photoemission spectroscopy, they observed a change in the dispersion relation of a strongly-interacting Fermi gas from above to below the superfluid critical temperature. An RF field was applied to drive one of the two components of the Fermi gas to a third state that has negligible interactions with the original two states. The dispersion relation of atoms in the third state is then the same as the one for a free particle, and therefore it is possible to measure the energy of a unitary Fermi gas from the resonant frequency of the applied RF field. Furthermore, they released the atoms at the same time and measure the momentum of atoms in the third state by reconstructing the three-dimensional momentum distribution from the time-of-flight images. This technique cannot be

Table 17.1 Experimental and theoretical superfluid critical parameters of a unitary Fermi gas

		T_c/T_F	$E(T_c)/NT_F$	$\mu(T_c)/T_F$	$S(T_c)/Nk_B$
Experimental results	Horikoshi et al. [36]	0.17(1)	0.32(2)	0.42(2)	0.7(2)
	Nascimbène et al. [38]	0.157(15)		0.49(2)	
	Ku et al. [19]	0.167(13)			0.73(13)
Calculated values	Bulgac et al. [24]	0.23(2)	0.41	0.45	0.99
	Burovski et al. [25]	0.152(7)	0.31(1)	0.493(14)	0.16(14)
	Hu et al. [26]	0.225	0.4	0.459	0.91
	Haussmann et al. [27]	0.16	0.304	0.394	0.71
	Nishida [41]	0.249	0.212	0.18	0.698

applied to ^{6}Li atoms because there is no useful third state with negligible interactions with the initial states. The JILA group measured the temperature dependence of the dispersion relation by the photoemission spectroscopy and observed the back-bending of the dispersion around $k \sim k_F$, which is a characteristic behavior of the BCS-type dispersion relation even above the critical temperature. They concluded that the pseudo-gap theory based on the existence of a finite excitation gap due to preformed pairs describes the properties of a strongly-interacting Fermi gas.

On the other hand, Nascimbène et al. observed the T^2 dependence of the pressure, which is a characteristic feature of the Fermi liquid above the critical temperature [38]. The MIT group also measured the temperature dependence of the magnetic susceptibility of a unitary Fermi gas and showed that their result is consistent with no excitation gap above the critical temperature, which is consistent with Fermi liquid theory [44]. It seems that the fundamental understanding of the unitary Fermi gas above T_c is still elusive, as in high-T_c superconductivity.

17.5 Summary and Outlook

In this chapter, we have reviewed the recent developments on the thermodynamics of a unitary Fermi gas. Experimental studies on the thermodynamics using ultracold atoms had been conducted through trap-averaged thermodynamic quantities. Recently, it has become possible to determine local thermodynamic quantities of harmonically trapped gases. Universal thermodynamic functions and the equation of state of a unitary Fermi gas have thus been quantitatively determined. Such experimental advances have enables us to study thermodynamics of a homogeneous gas and to directly compare experimental results with theories.

A future challenge is to improve the accuracy of the measurement of the thermodynamics. In this direction, Ku et al. recently performed the measurement of the equation of state of a unitary Fermi gas without any external data input [19]. In their work, clear thermodynamic signatures of the superfluid phase transition have been identified via high precision measurement of the compressibility and specific

heat. Another challenge will be to extend the measurement of the thermodynamics to a Fermi gas away from unitarity. ENS reported the experimental determination of the thermodynamics of a Fermi gas in the BCS-BEC crossover regime at the low-temperature limit. Measurements of thermodynamic properties over a broad temperature range in the crossover regime will be the next challenge. New schemes that can be applied at finite temperature need to be developed.

As for thermodynamic measurements on a Bose gas near unitarity, Papp et al. measured the excitation spectra of a strongly-interacting Bose gas of ^{85}Rb using Bragg spectroscopy, and observed the beyond mean-field effect in the spectra [45]. More recently, the ENS group observed the equation of state of a Bose gas of ^{7}Li with the scattering length of $2000a_0$ [46]. The same group also determined the upper bound of the universal parameter for a Bose gas in a non-equilibrium condition. However, the thermodynamics of bosons at the unitarity limit is not yet fully understood because of the strong inelastic loss near Feshbach resonances.

References

1. C.A.R. Sa de Melo, M. Randeria, J.R. Engelbrecht, Phys. Rev. Lett. **71**, 3202 (1993)
2. M.E. Gehm, S.L. Hemmer, S.R. Granade, K.M. O'Hara, J.E. Thomas, Phys. Rev. A **68**, 011401(R) (2003)
3. K.M. O'Hara, S.L. Hemmer, M.E. Gehm, S.R. Granade, J.E. Thomas, Science **298**, 2179 (2002)
4. M. Bartenstein, A. Altmeyer, S. Riedl, S. Jochim, C. Chin, J. Hecker Denschlag, R. Grimm, Phys. Rev. Lett. **92**, 120401 (2004)
5. C. Chin, M. Bartenstein, A. Altmeyer, S. Riedl, S. Jochim, J. Hecker Denschlag, R. Grimm, Science **305**, 1128 (2004)
6. C. Regal, M. Greiner, D.S. Jin, Phys. Rev. Lett. **92**, 040403 (2004)
7. M.W. Zwierlein, C.A. Stan, C.H. Schunck, S.M.F. Raupach, A.J. Kerman, W. Ketterle, Phys. Rev. Lett. **92**, 120403 (2004)
8. The *Many-Body Challenge Problem* (mbx) formulated by G.F. Bertsch in (1999)
9. H. Heiselberg, Phys. Rev. A **63**, 043606 (2001)
10. T.-L. Ho, E.J. Mueller, Phys. Rev. Lett. **92**, 160404 (2004)
11. T. Bourdel, L. Khaykovich, J. Cubizolles, J. Zhang, F. Chevy, M. Teichmann, L. Tarruell, S.J.J.M.F. Kokkelmans, C. Salomon, Phys. Rev. Lett. **93**, 050401 (2004)
12. M. Bartenstein, A. Altmeyer, S. Riedl, S. Jochim, C. Chin, J. Hecker Denschlag, R. Grimm, Phys. Rev. Lett. **92**, 120401 (2004)
13. J. Kinast, A. Turlapov, J.E. Thomas, Q. Chen, J. Stajic, K. Levin, Science **307**, 1296 (2005)
14. J.T. Stewart, J.P. Gaebler, C.A. Regal, D.S. Jin, Phys. Rev. Lett. **97**, 220406 (2006)
15. G.B. Partridge, W. Li, R.I. Kamar, Y.A. Liao, R.G. Hulet, Science **311**, 503 (2006)
16. Y.I. Shin, C.H. Schunck, A. Schirotzek, W. Ketterle, Phys. Rev. Lett. **99**, 090403 (2007)
17. L. Luo, J.E. Thomas, J. Low Temp. Phys. **154**, 1 (2009)
18. J. Joseph, B. Clancy, L. Luo, J. Kinast, A. Turlapov, J.E. Thomas, Phys. Rev. Lett. **98**, 170401 (2007)
19. M.J.H. Ku, A.T. Sommer, L.W. Cheuk, M.W. Zwierlein, Science **335**, 563 (2012)
20. T.-L. Ho, Phys. Rev. Lett. **92**, 090402 (2004)
21. J.E. Thomas, J. Kinast, A. Turlapov, Phys. Rev. Lett. **95**, 120402 (2005)
22. C. Cao, E. Elliott, H. Wu, J.E. Thomas, New J. Phys. **13**, 075007 (2011)
23. H. Hu, P.D. Drummond, X.-J. Liu, Nat. Phys. **3**, 469 (2007)
24. A. Bulgac, J.E. Drut, P. Magierski, Phys. Rev. Lett. **96**, 090404 (2006)

25. E. Burovski, N. Prokof'ev, B. Svistunov, M. Troyer, Phys. Rev. Lett. **96**, 160402 (2006)
26. H. Hu, X.-J. Liu, P.D. Drummond, Phys. Rev. A **73**, 023617 (2006)
27. R. Haussmann, W. Rantner, S. Cerrito, W. Zwerger, Phys. Rev. A **75**, 023610 (2007)
28. K. Van Houcke, F. Werner, E. Kozik, N. Prokof'ev, B. Svistunov, M. Ku, A. Sommer, L.W. Cheuk, A. Schirotzek, M.W. Zwierlein, arXiv:1110.3747 (2011)
29. S. Tan, Ann. Phys. **323**, 2952 (2008)
30. S. Tan, Ann. Phys. **323**, 2971 (2008)
31. S. Tan, Ann. Phys. **323**, 2987 (2008)
32. L. Viverit, S. Giorgini, L.P. Pitaevskii, S. Stringari, Phys. Rev. A **69**, 013607 (2004)
33. E. Braaten, arXiv:1008.2922
34. J.T. Stewart, J.P. Gaebler, T.E. Drake, D.S. Jin, Phys. Rev. Lett. **104**, 235301 (2010)
35. E.D. Kuhnle, H. Hu, X.-J. Liu, P. Dyke, M. Mark, P.D. Drummond, P. Hannaford, C.J. Vale, Phys. Rev. Lett. **105**, 070402 (2010)
36. M. Horikoshi, S. Nakajima, M. Ueda, T. Mukaiyama, Science **327**, 442 (2010)
37. Thermometer that was used in [36] turned out to be not accurate and has been updated [22, p. 38]. The data presented in this chapter are the results analyzed using the updated thermometer
38. S. Nascimbène, N. Navon, K.J. Jiang, F. Chevy, C. Salomon, Nature **463**, 1057 (2010)
39. T.-L. Ho, Q. Zhou, Nat. Phys. **6**, 131 (2010)
40. S. Nascimbène, N. Navon, F. Chevy, C. Salomon, New J. Phys. **12**, 103026 (2010)
41. Y. Nishida, Phys. Rev. A **75**, 063618 (2007)
42. J.T. Stewart, J.P. Gaebler, D.S. Jin, Nature **454**, 744 (2008)
43. J.P. Gaebler, J.T. Stewart, T.E. Drake, D.S. Jin, A. Perali, P. Pieri, G.C. Strinati, Nat. Phys. **6**, 569 (2010)
44. A. Sommer, M. Ku, G. Roati, M.W. Zwierlein, Nature **472**, 201 (2011)
45. S.B. Papp, J.M. Pino, R.J. Wild, S. Ronen, C.E. Wieman, D.S. Jin, E.A. Cornell, Phys. Rev. Lett. **101**, 135301 (2008)
46. N. Navon, S. Piatecki, K. Günter, B. Rem, T.C. Nguyen, F. Chevy, W. Krauth, C. Salomon, Phys. Rev. Lett. **107**, 135301 (2011)

Chapter 18
High Resolution Electron Microscopy of Quantum Gases

Giovanni Barontini and Herwig Ott

Abstract The complete understanding of the properties of ultracold and degenerate samples requires the ability to probe and manipulate such systems with extremely high resolution and precision. The introduction of the scanning electron microscopy (SEM) techniques on ultracold atoms provides the necessary tool for such purposes, thus allowing the observation of several fundamental phenomena with unprecedented clarity. Thanks to its extremely high resolution ($<$100 nm) and to the single-atom sensitivity the SEM method permitted the first observation of *in situ* profiles of trapped Bose-Einstein condensates of ^{87}Rb and of ultracold clouds in one- and two-dimensional optical lattices. Moreover the single lattice sites were selectively addressed and manipulated thus demonstrating the possibility to create arbitrary patterns of occupied sites. In addition to the spatial characteristics of ultracold samples the SEM technique allows for the investigation of their dynamical processes. Moreover, exploiting the single atom sensitivity of the method, second and higher order correlation functions can be measured as well.

18.1 Introduction

The density distribution of a many-body wave function of an ultracold quantum gas can be visualized by various techniques. Absorption imaging [1] the workhorse in most experiments and is typically applied in time of flight in order to increase the cloud size and reduce the optical density. To date, it is possible to image a single atom in absorption [2]. Fluorescence imaging [3–10] also allows for single atom detection with almost 100 % efficiency. It can be applied in time of flight or *in situ*. The success of this technique is best reflected in the studies of the properties of two-dimensional Mott-insulators where single atom sensitivity was combined with single site resolution [9, 10]. One fundamental aspect of fluorescence imaging is that the atoms have to be hold in a trap during the imaging procedure in order to accumulate enough scattered photon. The available resolution of optical imaging

G. Barontini (✉) · H. Ott
Research Center OPTIMAS and Fachbereich Physik, Technische Universität Kaiserslautern, 67663 Kaiserslautern, Germany
e-mail: g.barontini@gmail.com

A. Bramati, M. Modugno (eds.), *Physics of Quantum Fluids*,
Springer Series in Solid-State Sciences 177, DOI 10.1007/978-3-642-37569-9_18,

techniques is limited by the wavelength of the used light field. In practice, the best reported resolution is about 400 nm [2].

Direct particle detection, e.g. of metastable atoms [11, 12] or of ionized atoms, is an alternative way which allows for the detection of the particle in a single instant. It does not require the accumulation of scattered photons from the sample and no trap is needed. However, as only one single interaction process is involved, the detection efficiency can be limited. Especially attractive are such techniques which allow for the time-resolved *in situ* observation of ultracold atoms. Scanning electron microscopy is a versatile *in situ* detection technique of single atoms in a quantum gas [13]. It combines high spatial resolution with single atom sensitivity and can be applied to bulk and lattice systems. The range of possible applications spans from density measurements over correlation measurements up to density engineering and dissipation effects. By the basic principle, this method can reach an unprecedented spatial resolution. In standard scanning electron microscopy, the current record in resolution is below 1 nm and has reached atomic distances.

Here, we describe how the principles of scanning electron microscopy can be applied to the investigation of ultracold atoms. The structure of the article is as follows: in the first section we review some technical aspects of our experimental approach. They cover the preparation of the ultracold quantum gases, the details of the electron column and a review of the relevant electron-atom scattering mechanisms. The working principle of the microscope is slightly different from standard electron microscopy and is also explained. The reader might skip this technical part and directly continue with the second part. There, we show results on the bimodal distribution of a Bose-Einstein condensate in a harmonic trap and the density distribution in a one- and two-dimensional optical lattice. We also discuss the possibilities to manipulate the atoms by precise density engineering of a BEC in an optical lattice. We close the article by a study of the pair correlation function in a thermal gas—an example for the measurement of an intrinsically time-dependent observable.

18.2 The Scanning Electron Microscopy Technique

18.2.1 Experimental Setup

Our experiment combines an apparatus for the production of Bose-Einstein ^{87}Rb condensates with the setup of a scanning electron microscope. We limit the presence of inhomogeneous magnetic fields that can distort the electron beam by making the BEC in an optical way, by employing amagnetic materials and by shielding the main chamber with μ-metal plates. Except for these additional cares, the setup is exactly the one of a standard BEC experiment. The electron column is mounted on top of the main chamber and completely occupies its vertical axis. The lower part of the column, ion optics and detection devices are placed directly inside the vacuum chamber. In the following we will give a brief description of the typical experimental sequence and we will concentrate our attention on the description of

the electron column. A detailed explanation of the interaction mechanisms between the electrons and the ions will be also given.

Production of the Degenerate Samples In a pre-cooling chamber, atoms from the vapor pressure of a solid Rb sample are cooled and trapped by a 2D-MOT scheme which combines the action of two counterpropagating laser beams, along two orthogonal spatial directions, and a quadrupolar magnetic field. A push beam, resonant on an atomic transition force the precooled atoms to enter the science chamber through a differential pumping stage. There the atoms are first trapped in a 3D-MOT. After a dark-MOT stage of a few tens of ms the atoms are loaded in a single beam CO_2 dipole trap. The CO_2 trap is already on when the MOT is active and a fraction of typically 4×10^6 atoms with a temperature of 170 μK remains trapped once the MOT is completely extinguished. To perform evaporative cooling the power of the CO_2 laser is decreased from the starting value of 10 W according to an experimentally optimized exponential ramp. The critical temperature for condensation is reached at 160 nK with typically 3×10^5 atoms. A pure BEC with 10^5 atoms is obtained at a final power of ∼50 mW, corresponding to trapping frequencies of $\omega_{ax} = 2\pi \times 13$ Hz and $\omega_{rad} = 2\pi \times 170$ Hz. In our optical dipole trap all magnetic substates of the $F = 1$ manifold are trapped, which results in a spinor condensate [14].

The Electron Column There are several requirements that the electron column itself has to fulfill in order to build an electron microscope that is able to image ultracold atoms. It should provide an electron beam that can be focused to a diameter of a few hundred nanometers and below. Furthermore, the current of the electron beam should be as high as possible since the probability for a scattering event between the electron beam and the atomic sample is proportional to it. Finally, the electron column has to be UHV compatible. The electron column that we have chosen to satisfy these requirements is a custom made column with thermal ZrO-Schottky emitter, which provides an electron beam with an energy up to 6 keV (for more details see [15]). The upper part of the column consists of three different vacuum chambers: the gun chamber which holds the electron emitter, the aperture chamber in which a movable stage with several apertures is mounted and the so called intermediated chamber which mainly consists of a pneumatic isolation valve connected to the main vacuum chamber. This valve, that is open during normal operation, is necessary to isolate the main chamber from the electron column when this one is vented to substitute the emitter, which has a lifetime of roughly 12000 hours. The lower part of the column, consisting of a pole piece made of an iron-nickel alloy extends into the main chamber (see Fig. 18.1). The current of the electron beam is measured with a Faraday cup, which is placed 5 cm underneath the tip. The electron column has two magnetic lenses to focus the beam at a working distance of 13 mm below the tip. The magnetic field produced inside the second lens, the closest to the atoms, reaches 2000 G and is guided in the μ-metal pole piece of the tip. However due to the self-shielding of the pole piece, the magnetic field rapidly decreases to 1 G at the position of the atoms, resulting in a negligible perturbation. The size of

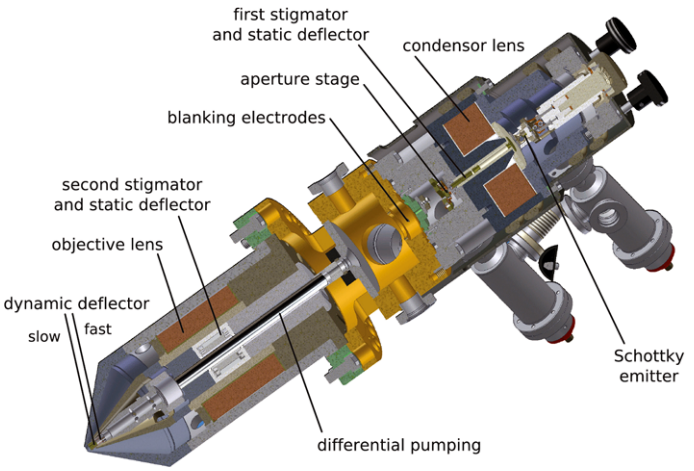

Fig. 18.1 Technical drawing of the electron column

the actual probe is enlarged due to spherical aberrations, which can be reduced by inserting apertures into the electron beam. Astigmatic aberrations and displacement of the electron beam, caused by the lenses, are corrected respectively by stigmators and by electrostatic deflectors, which are placed in a combined unit behind each lens [16]. The movable aperture strip with apertures of 300 µm, 250 µm, 150 µm, 100 µm, 50 µm and 20 µm is placed underneath the first deflector and stigmator stage in the aperture chamber together with an electrostatic blanking unit, which allows for the dumping of the electron beam inside the column with a frequency up to 5 MHz. Two physically separated scanning units, consisting of electrostatic quadrupoles, can move the electron beam over the atomic cloud. The fast scan unit has a field of view of 200 µm × 200 µm and can be moved with a bandwidth of 10 MHz. The slow scan unit provides scans up to 20 kHz and a field of view of 1 mm × 1 mm.

Alignment and Characterization The current value and the beam aperture are chosen according to the peculiar measurement we want to perform on the atoms. The alignment and the characterization of the electron beam is done prior to any application of the column. To this purpose, we use two different test targets mounted on a movable holder. The first target is a copper mesh and the second is a hole with a diameter of 200 µm. Furthermore, a Multi Channel Plate (MCP) is placed on the holder to detect secondary and backscattered electrons from the test targets. The alignment consists in adjusting the two lenses, deflectors and stigmators to maximize the resolution of the image in a convenient field of view. Typically we use the mesh target for a first alignment and we fine adjust the settings with the hole target, which is at a slightly different vertical position. The hole target is then used to obtain the beam diameter by taking a line scan over the edge of the hole. The measured scan is fitted with an error function, from which we derive the beam waist. Finally

we remove the targets holder and we perform the alignment at the real atoms position by adjusting the second lens and stigmator to maximize the visibility when scanning a two dimensional lattice realized by trapping the atoms in a strong 2D periodic optical potential with spacing 600 nm [15, 17, 18]. The smallest beam waist, i.e. the highest spatial resolution that we can obtain for a typical current of 20 nA is $\sim$100 nm. The depth of focus is derived by measuring the FWHM of the electron beam at different vertical positions without refocusing. This is achieved by moving the hole target along the beam axis by a micrometrical translational stage. Assuming a Gaussian shaped electron beam to fit the data, the Rayleigh length is obtained. We measured a value of 35 μm for a beam waist of 130 nm. Being the vertical extension of the atomic cloud 6 μm at most, with the optical traps we have in use, a depth of focus of 35 μm guaranties a constant electron beam diameter over the atomic sample.

Ion Optics and Detection Once the atoms are ionized by electron impact, they are attracted by the high negative voltage of -4.8 kV of a conversion dynode. On their way to the dynode, the ions are guided by a series of different electrodes. Once they hit the dynode, secondary electrons are produced, which are then accelerated towards the channeltron. The input of the channeltron has a voltage of -2.2 kV and is grounded at the end. The conversion efficiency of the conversion dynode is almost 100 %. A detected ion produces a negative voltage peak at the anode of the channeltron of 10 to 60 mV. This signal is then converted into a TTL pulse by a discriminator and amplified. To each ion is thus associated a single TTL pulse, which is recorded into a channel scaler card (MCS). The card has 65536 channels with a variable bin length and allows for time-resolved recorded signals.

18.2.2 Electron-Atom Interaction Mechanisms

The interaction between atoms and electrons can be elastic or inelastic. The electron impact ionization of atoms is a special case of inelastic scattering which we consider here as an independent process. In an elastic scattering event, the internal state of the target atom remains unchanged. The scattered atom carries some energy and momentum of the incident electron and the transferred energy depends on the scattering angle. For all angles except an extremely narrow (and therefore negligible) window of scattering angles around zero degrees, the atom gains enough kinetic energy to escape from the trapping potential. Note that the potential depth of an optical dipole trap holding a Bose-Einstein condensate corresponds to a kinetic energy of 10^{-11} eV. As the atom remains in its ground state it is not seen by the ion detector. Elastic scattering therefore constitutes a loss channel. In an inelastic scattering event, the target atom is excited to a higher lying state. The energy transfer to the atom is accompanied by a momentum transfer, which occurs even under a scattering angle of zero degree. Again, the atoms escape from the trap and will not be detected as no ion is created. In electron impact ionization, the incident electron knocks out

one or more bound electrons from the target atom and promotes it to the continuum. The resulting ions are then extracted by a continuously applied electrostatic field and are guided towards the detector.

The applicability of this scheme for the imaging of ultracold quantum gases depends on several questions: (i) Is there enough signal? (ii) How fast and efficient is the detection process? (iii) What is the role of multiple scattering and secondary processes? (iv) Can the ion be assigned to the position of the electron beam? The last question is answered quickly. The initial cold temperature of the atoms and the fact that the majority of the ionization processes occurs at small momentum transfer to the remaining ion (the collision are almost pure electron-electron scattering processes) ensure that the created ions have a negligible initial velocity. The time of flight to the detector is therefore identical for all ions and the detection time of the ion can be unambiguously assigned to the position of the electron beam. Only multiply charged ions are wrongly assigned. We can avoid this by either reducing the scanning speed or by subsequent post processing [19].

The magnitude of the signal is a crucial point. Electron impact ionization does not only produce an ion but also one or even more electrons. For typical beam currents of several nA the background of primary electrons is very large so that the discrimination of electrons stemming from impact ionization is a challenge. We therefore exclusively detect the ions. As a consequence, the maximum signal we can get is given by the number of atoms in the gas. To calculate the ratio of electron impact ionization events to elastic and inelastic scattering processes, we can rely on the first Born approximation as the incident electron energy is very high (6 keV). In first Born approximation, all particles are described by plane waves and the scattering process is described by a single matrix element. For elastic and inelastic scattering processes, the differential cross section is given by

$$\frac{d\sigma}{d\Omega}(0 \to n) = \frac{4m^2 Z^2 e^4}{\hbar^4 q^4}\left(\frac{k'}{k}\right)\left|F_n(\mathbf{q}) - \delta_{n0}\right|^2, \tag{18.1}$$

where δ_{nm} denotes the Kronecker symbol and F_n is a modified form factor defined as follows:

$$Z F_n(\mathbf{q}) = \langle \varphi_n | \sum_j e^{i\mathbf{q}\cdot\mathbf{x_j}} | \varphi_0 \rangle. \tag{18.2}$$

Here, $\mathbf{q} \equiv \mathbf{k} - \mathbf{k}'$ is the momentum change of the incoming electron ($\mathbf{k}$ is the incoming and $\mathbf{k}'$ the outgoing wave vector). The charge of the nucleus is given by Z, the initial ground state of the atom is given by $|\varphi_0\rangle$ and the state after the collision is denoted by $|\varphi_n\rangle$. The case $n = 0$ corresponds to the elastic scattering. The total cross section is given by the integral over the solid angle. Analytical and approximative results can be found in [20]. Note that the total inelastic cross section scales at high but non-relativistic energies as $E^{-1} \log E$, where E is the energy of the incident electron [20]. For the case of electron impact ionization, the cross section is triply

differential and reads for single ionization processes

$$\frac{d^3\sigma_{(e,2e)}}{d\Omega d\Omega'' dE''} = \frac{4m^2e^4}{\hbar^4 q^4}\left(\frac{k'k''}{k}\right)\left|\left\langle\varphi^*(\mathbf{x})\left|e^{\frac{i\mathbf{K}\cdot\mathbf{r}''}{\hbar}}\right|\varphi_0(\mathbf{x})\right\rangle\right|^2, \tag{18.3}$$

Here, $\mathbf{k}''$ and $\mathbf{r}''$ are the wave vector and the coordinate of the second outgoing electron and $-\hbar\mathbf{K} = \hbar\mathbf{k} - \hbar(\mathbf{k}' + \mathbf{k}'')$ is the recoil momentum of the residual ion. For a more detailed description of electron impact ionization we refer to [21]. The total ionization cross section is again retrieved by integration. The sum of all three contributions gives the total scattering cross section. The total scattering cross section amounts to $(1.78 \pm 0.14) \times 10^{-17}$ cm^2 and the fraction for ionization is around 40 % [22]. From the total scattering cross section one can also deduce the lifetime of an atom against a collision. We assume a Gaussian shaped electron beam with a full width half maximum (FWHM) of 100 nm and a beam current of 20 nA which are typical beam parameters in our experiment. When an atom is exactly in the center of this beam, its lifetime is given by

$$\tau = \frac{e}{j_0\sigma_{\text{tot}}}, \tag{18.4}$$

where j_0 is the current density in the beam center and σ_{tot} is the total scattering cross section. For the given numbers we find $\tau = 5$ µs. This time gives an estimate for a reasonable dwell time per pixel. If the chosen dwell time is smaller, only a fraction of the atoms is detected. In fact, most of our experiments are done with a dwell time of one or two microseconds per pixel. This allows for a faster scanning procedure. As the atoms inside the quantum gas move with a speed of a few mm per second we can do scans that proceed faster than the motion of the atoms. This ensures that we can scan a cloud of atoms fast enough to effectively interact with an unperturbed cloud. Electron impact ionization represents about 40 % of all scattering events. Given a full transmission of the ion to the detector and assuming a well adjusted ion detector with 90 % overall detection efficiency, about 35 % of the atoms can be detected. This signal is enough to extract all relevant quantities from the quantum gas.

In scanning electron microscopy, multiple scattering and secondary scattering processes often pose a problem for the proper interpretation of the signal. In our approach, the scattering cross sections are so small and the atomic cloud is so dilute, that only a fraction of 10^{-5} of the incident electrons undergoes a collision. All other electrons pass through the gas without any interaction. Multiple scattering is therefore completely negligible. As to secondary processes however, ion atom collisions are of some importance. As the ions are created inside the gas, they can scatter with other atoms on their way out of the gas. As the potential between an ion and an atom scales as r^{-4}, where r is the relative distance, the scattering cross section can become very large when low temperatures are approached [23]. Depending on the specific imaging mode or investigation these processes have to be taken into account. They can be suppressed by reducing the transverse extension of the atomic gas or by increasing the electrostatic extraction field as the cross section rapidly drops with the ion energy [23].

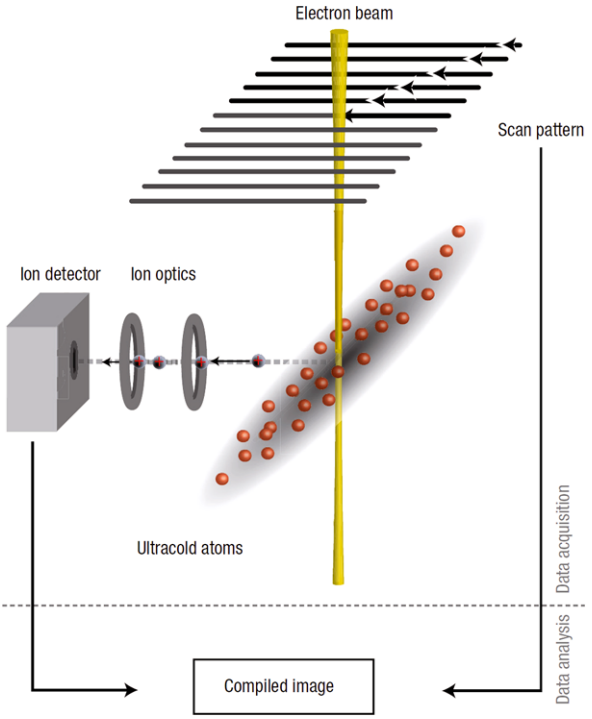

Fig. 18.2 Schematics of the working principle. Electron impact ionization produces ions, which are guided with an ion optical system towards a channeltron detector. The ion signal together with the scan pattern is used to compile the image

18.3 Probing and Imaging Ultracold Quantum Gases

In order to acquire an image of the trapped BEC we can, in principle, move the electron beam following any arbitrary scan pattern. A fraction of the atoms which undergo collisions with the electrons is ionized and the produced ions are then extracted and detected. The knowledge of the scan pattern and the obtained ion signal allows to reconstruct the image of the atom cloud. A standard image is taken by using a rectangular scan pattern and synchronizing it with the signal from the ion detector: an illustration of the working principle is depicted in Fig. 18.2. The voltages for the scanning unit are produced by using two waveform generators, one for each imaging axis. The first generator provides the deflection along the x-axis using a saw tooth voltage form. The second generator sets the deflection along the y-axis and uses a repetition of several identical saw tooth voltage waveforms. The electron beam is therefore continuously moved and not in discrete steps. The lower limit for the dwell time is given by the smallest time bin of the MCS card which is 100 ns. The ion signal intensity is, in case of small depletion, proportional to the dwell time.

Figure 18.3 shows such an image of a Bose-Einstein condensate. Even though the cloud contains about 10^5 atoms, only a fraction of the atoms has been detected in order to get an unperturbed image of the cloud. From this image one can already retrieve substantial information on the density distribution; as an example the size

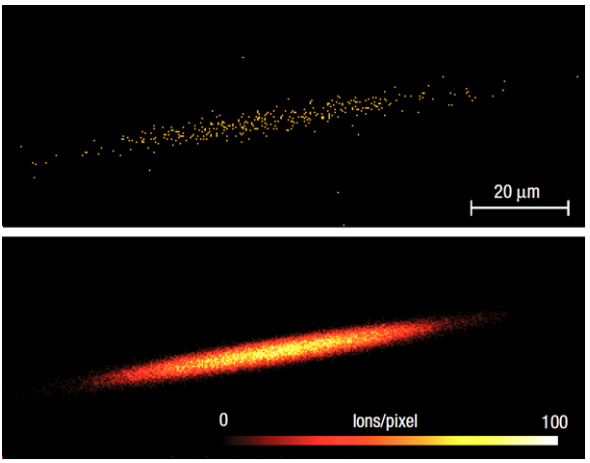

Fig. 18.3 *Top*: An image of a trapped ^{87}Rb condensate. The image has 400 × 150 pixels with a pixel size of 300 nm × 300 nm. Each pixel was illuminated for 2 µs with the electron beam (140 nm FWHM beam diameter). Every dot corresponds to a detected atom. In total, 350 ions were collected during the exposure. The condensate contains about 10^5 atoms. *Bottom*: The sum over 300 images. Each image was taken in a separate experimental run

of the cloud can be determined within a precision of 5 %, (see Fig. 18.4). In order to obtain a more precise picture of the trapped sample in Fig. 18.3 we can sum over many individual images, corresponding to an overall number of processed events that is comparable to the total number of atoms in the condensate. This picture shows how accurately the shape of the condensate would be determined if all atoms were detected in an idealized experiment. For each run, which lasts roughly 15 s, the condensate has to be produced again. Essentially no energy is deposited in the cloud, as we observe an additional heating of merely 5 nK after exposure to the electron beam, as shown in Fig. 18.4. Thus, the perturbation caused by the detection process is very small. This, in combination with a high detection efficiency could make it possible to take several images of the same condensate, thus allowing for a direct observation of the dynamical evolution of an individual system.

Notably, the extremely high resolution ensured by our detection technique allows a direct quantitative comparison with the theory. This is a great advantage with respect to those techniques which need the cloud to expand before being imaged. We have indeed compared the experimental density profiles with those obtained solving the Gross-Pitaevskii equation (GPE). The solution of the GPE, Ψ, is then used to model an effective potential for the thermal component $V = V_{ho} + 2g|\Psi|^2$, where $g = 4\pi\hbar^2 a/m$, being a the s-wave scattering length and m the Rb mass. From this we obtain the density distribution of the thermal component as $\rho = g_{3/2}(\exp(-(V - \mu)/k_B T))$, where μ is the chemical potential, k_B the Boltzmann constant and $g_{3/2}(z)$ the 3/2 polylogarithmic function of z. As reported in Fig. 18.4 this approach allows us to reproduce the measured profiles, matching their bimodal nature.

It is obvious that the spatial resolution of a scanning electron microscope exceeds that of an optical microscope by far. However, the high resolution is achieved at the cost of beam current. In order to get a decent signal we cannot go to beam currents below 5 nA. In fact, many experiments even require higher beam currents. As all characteristic length scales in a quantum gas are in the order of a few hundred nanometers a too high resolution is of no great use. We therefore have working

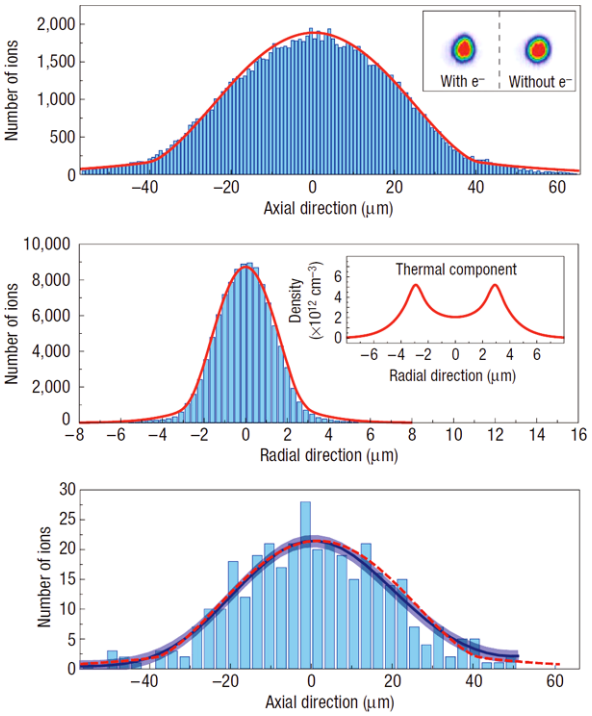

Fig. 18.4 *Top*: The axial distribution of the condensate shown in Fig. 18.3, integrated in the radial direction. The experimental data (*blue columns*, 900 nm bin size) are compared with a bimodal distribution (*red line*) calculated for a temperature of 80 nK. The condensate fraction is 80 %. The *inset* shows absorption images of the condensate after 15 ms time of flight with and without exposure to the electron beam. The number of atoms after exposure is reduced by 7 % on average. *Center*: The distribution in the radial direction (300 nm bin size). In the *inset* we have plotted the radial density of the thermal component in the trap center as calculated from the model. The minimum is due to the repulsion from the condensate fraction. *Bottom*: The estimated density distribution in the axial direction for the single-shot image in Fig. 18.3 (*blue line*). The data (columns) have been binned over 3 μm. The *blue shaded area* indicates the uncertainty of the estimated distribution. For comparison, the *red dashed line* shows the solution of the theoretical model

Table 18.1 Electron beam characteristics. Typical working points of our experiment

Beam diameter (FWHM)	Beam current
90 nm	12 nA
250 nm	100 nA
400 nm	180 nA
5000 nm	800 nA

points that are rather unusual for scanning electron microscope and are optimized for our experimental needs. Table 18.1 summarizes the different combinations of beam current and beam diameter we can realize.

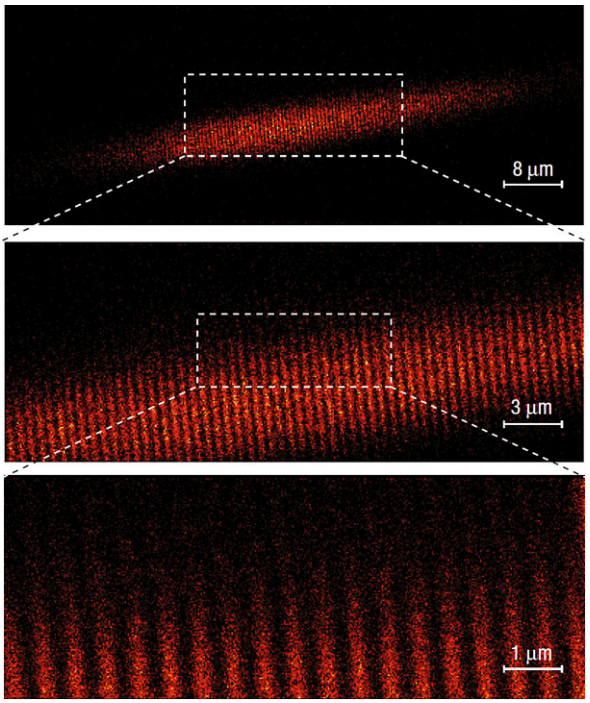

Fig. 18.5 The lattice has a period of 600 nm. Each image is the sum of 50 individual images. The pixel size is 200 nm × 200 nm. The lattice depth is 20 recoil energies and the FWHM diameter of the electron beam was 95 nm

18.3.1 Single Site Addressability in Optical Lattices

In order to demonstrate the high spatial resolution of our approach, we have imaged a Bose-Einstein condensate in a one-dimensional and in a two-dimensional optical lattice (Figs. 18.5 and 18.6). With a lattice constant of 600 nm we can clearly resolve individual lattice sites. This possibility opens up many future studies as it is possible to observe the tunneling dynamics and the behavior of taylored quantum systems in periodic potentials.

Furthermore we have demonstrated the single-site addressability of a quantum gas in such optical lattices with 600 nm lattice spacing. After loading a Bose-Einstein condensate in the lattice potential, we selectively remove atoms from individual sites by means of the dissipative interaction with the focused electron beam. In this way, arbitrary patterns of occupied lattice sites can be produced, as shown in Figs. 18.7 and 18.8. The addressing of individual sites in the optical lattice works as follows: the electron beam is pointed at selected sites for a dwell time of 1–3 ms per site (35 ms for 1D lattice) in order to remove the atoms. Immediately after the preparation, the imaging procedure is started. Four elementary examples of this patterning technique are presented in Fig. 18.8. A single defect in the lattice structure is shown in the first panel. The structure resembles a Schottky defect in a solid and is an ideal starting point to study the tunneling dynamics close to a defect. The opposite situation corresponds to an isolated lattice site and is shown in the second panel. Such a mesoscopic ensemble provides, for instance, the possibility to study

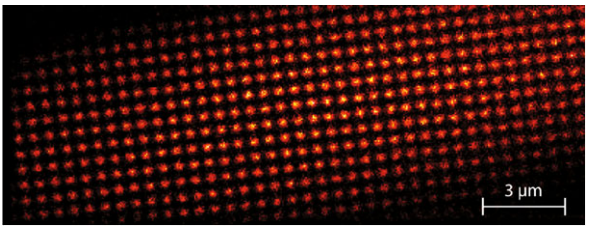

Fig. 18.6 Image of a Bose-Einstein condensate in a 2D optical lattice with 600 nm lattice spacing (sum obtained from 260 individual experimental realizations). Each site has a tubelike shape with an extension of 6 μm perpendicular to the plane of projection. The central lattice sites contain about 80 atoms

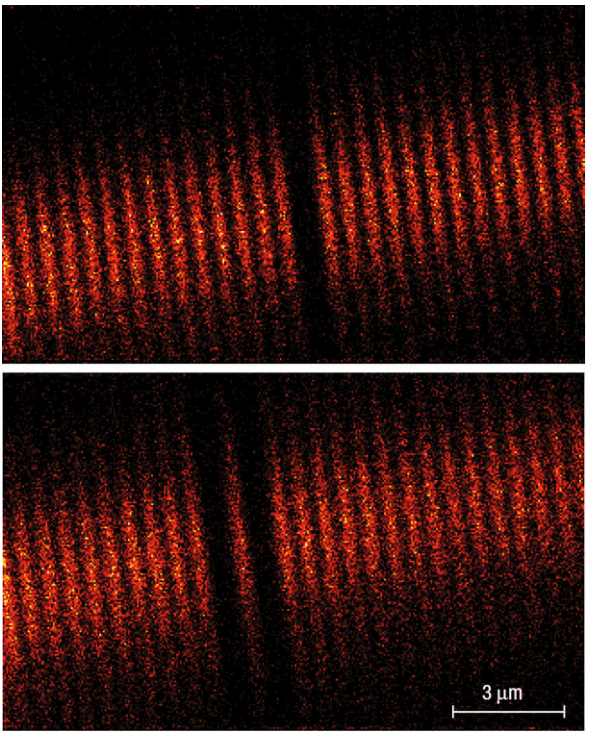

Fig. 18.7 We first remove atoms from the optical lattice, pointing the electron beam at the specific sites for 35 ms. Thereafter the image is taken (200×325 pixels, 50 nm pixel size, 2 μs pixel dwell time)

the transition from few-body systems to the thermodynamic limit. It can also act as a paradigm for Rydberg blockade studies as the spatial extension of the ensemble is very small. A chain and a ring of lattice sites are shown in the lower panels in order to illustrate the large variety of achievable geometries. We remark that our approach allows for any arbitrary pattern that fits to the underlying quadratic one. Notably, in terms of writing time, a lattice site can be prepared in about 1 ms, provided that the site is hit in the center. Imperfect addressing leads indeed to longer depletion times. The dependence of the depletion time constant on the position of the electron beam

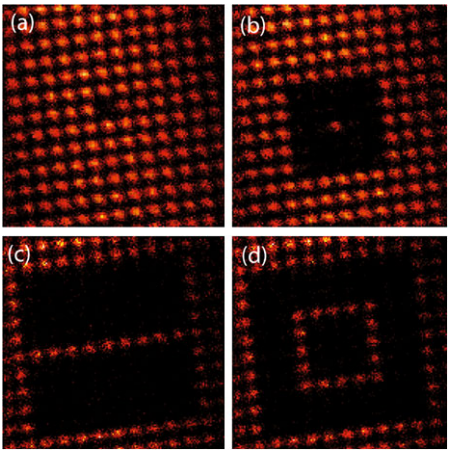

Fig. 18.8 Patterning a Bose-Einstein condensate in a 2D optical lattice with a spacing of 600 nm. Every emptied site is illuminated with the electron beam (7 nA beam current, 100 nm FWHM beam diameter) for a few ms. The imaging time is 45 ms. Between 150 and 250 images from individual experimental realizations have been summed for each pattern

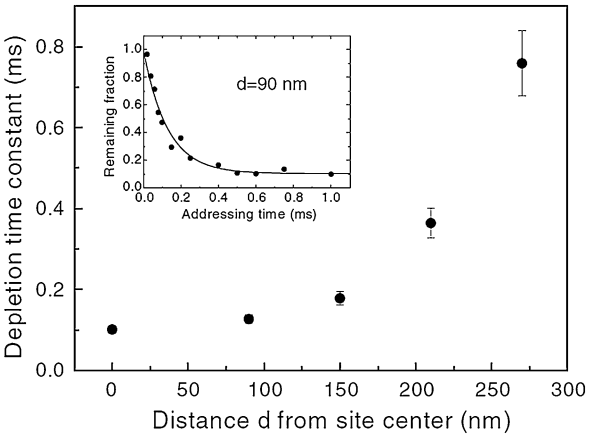

Fig. 18.9 Depletion time constant for different positions of the electron beam with respect to the lattice site. At all distances we find an exponential decay. For central hits, the population decays with a time constant of 100 µs. The *inset* shows the depletion at a distance of 90 nm. The *solid line* is a fit with an exponential decay. The offset of 10 % represents atoms that are refilling the lattice site between the end of the preparation and the instant of imaging

is shown in Fig. 18.9. Whereas for central hits we find a time constant of 100 µs, it is more than 10 times larger if the electron beam points at the edge of a site. For all positions we find an exponential decay of the atom number. In conclusion, if we allow for a preparation time of 100 ms, a total of 100 sites can be emptied. This is in general sufficient to tailor a large part of the gas.

18.3.2 Temporal Correlation Functions

A peculiarity of our approach is the fact the a scanning probe technique also allows for an *in vivo* study of the atoms. In the case of a gaseous target this gives access to dynamical investigations on the temporal evolution of the gas. In this context, we have measured temporal correlation functions of ultracold thermal bosons in

equilibrium [24]. As outlined above, the interaction with the electron beam leads to almost no heating of the system. As quantum objects are imaged, the detection of an atom is intrinsically connected with a change of its external and internal state. Therefore, after the detection, the atom is no longer part of the many-body quantum system and its ionization and subsequent extraction is no problem. Consequently, despite the removal of atoms from the system, the probing technique can nevertheless be considered as minimal invasive.

While first order correlations are often accessible via interference experiments, higher order correlations require in general the recording of density or atom number fluctuations by a probe sensitive enough to detect single particles (counting techniques) or, at least, atomic shot-noise (absorption imaging). In order to have a good statistical description, an average over many realizations of the system (in theory all possible realizations) is needed. Consequently correlations, especially at orders higher than two, are usually difficult to measure because of the huge statistics required for a reliable signal. Using scanning electron microscopy as time-resolved local detection method, our measurements directly yield the second and third order time correlation functions. Notably, our approach is not complicated by the time of flight expansion and directly manifest the properties of the many-body system.

The general form of the normalized spatio-temporal correlation function of n particles at position $\mathbf{r}_i$ at time t_i, with $i = 1, \ldots, n$, is given by:

$$g^{(n)}(\mathbf{r}_1, t_1; \ldots; \mathbf{r}_n, t_n) = \frac{\langle \widehat{\Psi}^\dagger(\mathbf{r}_1, t_1) \cdots \widehat{\Psi}^\dagger(\mathbf{r}_n, t_n) \widehat{\Psi}(\mathbf{r}_n, t_n) \cdots \widehat{\Psi}(\mathbf{r}_1, t_1) \rangle}{\langle \widehat{\Psi}^\dagger(\mathbf{r}_1, t_1) \widehat{\Psi}(\mathbf{r}_1, t_1) \rangle \cdots \langle \widehat{\Psi}^\dagger(\mathbf{r}_n, t_n) \widehat{\Psi}(\mathbf{r}_n, t_n) \rangle} \quad (18.5)$$

where $\widehat{\Psi}$ are the bosonic operators and $\langle \cdots \rangle$ indicates the ensemble average. We first derive an analytical expression of $g^{(1)}(\mathbf{r}_1, t_1; \mathbf{r}_2, t_2)$ for an ideal Bose gas at temperature T above the critical temperature T_c, trapped in a harmonic potential $V(\mathbf{r}) = m\omega^2 r^2/2$, with average trapping frequency ω, extending the approach of Ref.[25] to take into account also the temporal evolution. Given $\tau = t_2 - t_1$ and $\mathbf{r} = \mathbf{r}_2 - \mathbf{r}_1$ and assuming $\omega\tau, \hbar\omega/(k_B T) \ll 1$, we obtain:

$$g^{(1)}(\mathbf{r}, \tau) = \frac{1}{(1 + i\frac{\tau}{\tau_c})^{3/2}} \exp\left(-\frac{mr^2}{2\hbar\tau_c^2} \frac{\tau_c + i\tau}{1 + (\frac{\tau}{\tau_c})^2} \right) \quad (18.6)$$

where $\tau_c = \frac{\hbar}{k_B T}$ is defined as the correlation time. From the above expression we can derive any higher order correlation function for thermal bosons and, in particular, the second order correlation can be easily calculated as $g^{(2)}(\mathbf{r}, \tau) = 1 + |g^{(1)}(\mathbf{r}, \tau)|^2$.

From (18.5), integrating on the absolute time and averaging on the different repetitions of the experiment, we calculate the correlation function $g^{(2)}(\tau)$ for a cold thermal cloud, analyzing the time-resolved signal from the ion detector. In Fig. 18.10 we report the measurements for two different temperatures $T = 45$ nK and $T = 100$ nK. Averaging over several experimental cycles, fluctuations in the total number of detected ions affect the normalization of the correlation function. As a result, an offset shifts the uncorrelated signal to a value 1 % above 1. To compensate for these fluctuations we normalize $g^{(2)}(\tau)$ by the factor $1 + \sigma^2/\langle N \rangle^2$, where σ^2 and

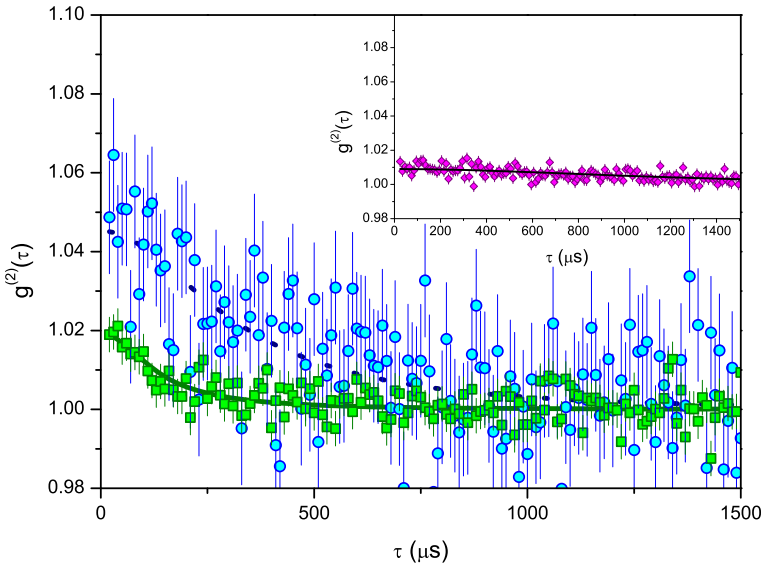

Fig. 18.10 Normalized second order temporal correlation function. Data (*dots*) acquired at different temperatures (*circles* for 45 nK, *squares* for 100 nK) are plotted together with the fitting functions (*lines*) explained in the text. The *inset* displays the data (*diamonds*) acquired for a BEC and the corresponding fit (*line*). Please note that even well below the critical temperature (the thermal fraction cannot be detected in time of flight absorption imaging) we are able to measure a small residual bunching induced by the thermal component

$\langle N \rangle$ are respectively the variance and the mean value of the total number of detected ions in the different experimental realizations. A measurement with a BEC is also presented in the inset of Fig. 18.10. Notably, we can still detect a small correlation signal due to a residual thermal fraction present well below the critical temperature T_c. The $g^{(2)}(\tau)$ data points are fitted with the function we derived for an ideal non interacting gas of bosons integrated over the volume, leaving the amplitude and τ_c as free parameters (lines in Fig. 18.10). In the inset of Fig. 18.11 we show the fitted amplitude of the normalized second order correlation functions at different temperatures together with the values expected from the volume integration of the non-interacting model and of its extension to the interacting case [25]:

$$g^{(2)}_{int}(\mathbf{r}, 0) = 1 + \frac{2a^2}{r^2} + \left|g^{(1)}(\mathbf{r}, 0)\right|^2 \left(1 - \frac{4a}{r}\right), \tag{18.7}$$

being a the s-wave scattering length. As expected, repulsive interactions play a role for *in situ* measurements since they induce short-range anti-bunching that reduces or overcomes the bunching signal of bosons. The inclusion of interactions in our model contributes in shifting the theoretical prediction towards the range of compatibility with the experimental results.

In addition, we also calculate the third order correlation function, extracting it from the same data sets for which we derived the $g^{(2)}(\tau)$. The results are reported

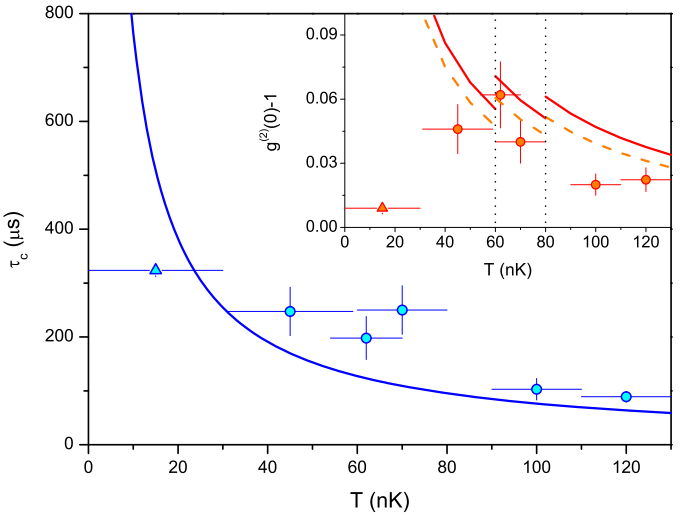

Fig. 18.11 Correlation time τ_c as a function of the temperature. The values obtained fitting the experimental data (*circles*) are compared with the function $\tau_c = \hbar/(k_B T)$ (*line*). The *inset* shows the fitted bunching enhancements (*circles* for thermal gases and a *triangle* for the BEC) and the corresponding theoretically expected values for the non-interacting (*solid line*) and the interacting (*dashed line*) model. Each curve segment refers to a different power of the dipole trap ($P = 3, 4, 5$ mW)

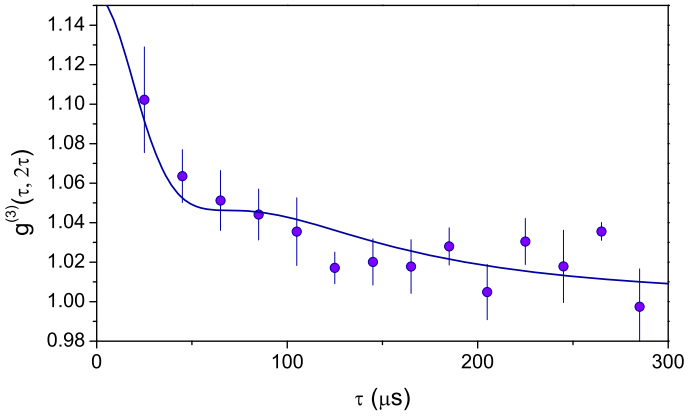

Fig. 18.12 Normalized third order correlation function (*dots*) along the axis ($\tau_1 = t_2 - t_1$, $\tau_2 = t_3 - t_1 = 2\tau_1$) for a thermal cloud with $T = 100$ nK. The *solid line* is the fitting function explained in the text

in Fig. 18.12. Bunching is expected to be more pronounced at higher orders n as a consequence of the factorial law $n!$ that regulates the dependence of the correlated to the uncorrelated amplitudes. For this reason higher order correlations can be employed as a highly sensitive test for coherence, with the only drawback

represented by the need of high statistics, as proved by the very few experiments reporting correlations at orders higher than 2. The solid line in the picture is a fit made with the volume integration of the non interacting model $g^{(3)}(\tau_1, \tau_2) = 1 + |g^{(1)}(\tau_1)|^2 + |g^{(1)}(\tau_2)|^2 + |g^{(1)}(\tau_2 - \tau_1)|^2 + 2\Re(g^{(1)}(\tau_1)g^{(1)}(-\tau_2)g^{(1)}(\tau_2 - \tau_1))$, along the same axis, leaving the amplitude as the only free parameter.

18.3.3 Perspectives and Outlook

We expect that scanning electron microscopy applied to ultracold quantum gases will add new aspects on the research with ultracold atoms. The detection of pair correlations in the spatial and temporal domain is an ideal tool to investigate strongly correlated quantum system which currently pose a challenge to their theoretical description. One-dimensional quantum gases are promising candidates for this. The strong correlations that appear require sophisticated numerical and analytical tools to predict and calculate the measured quantities [26–28]. Another interesting field of research is connected to the fact that the atoms are removed from the trap *locally*. This can be considered as a localized dissipative defect that acts back on the remaining atoms. Theoretical simulations [29] have shown that intriguing phenomena such as quantum Zeno like dynamics should be observable. The system has also promising perspectives in connection with Rydberg atoms. These highly excited atoms have recently attracted a lot of attention due to their unique interaction properties [30–34]. A direct detection via electron impact ionization seems to be feasible as the total ionization scattering cross section scales quadratically with the principal quantum number. If successful, intriguing quantum phases such as crystalline structure of Rydberg atoms are detectable [35]. Finally, the technique is also ideally suited to study mixtures of different atomic species [36–39]. The different mass can be easily separated in the analyzing channel and a full time-, spatial- and mass-resolved detection is possible which can be even extended to ultracold molecules [40, 41]. This short list of applications gives only a first glance of the potential of this technique which we plan to further exploit in the future.

References

1. W. Ketterle, D. Durfee, D. Stamper-Kurn, Making, probing and understanding Bose-Einstein condensates, in *Bose-Einstein Condensation in Atomic Gases, Proceedings of the International School of Physics Enrico Fermi* (IOS Press, Amsterdam, 1999)
2. E.W. Streed, A. Jechow, B.G. Norton, D. Kielpinski, Absorption imaging of a single atom. arXiv:1201.5280
3. Z. Hu, H. Kimble, Observation of a single atom in a magneto-optical trap. Opt. Lett. **19**, 1888–1890 (1994)
4. N. Schlosser, G. Reymond, I. Protsenko, P. Grangier, Sub-poissonian loading of single atoms in a microscopic dipole trap. Nature **411**, 1024–1027 (2001)
5. S. Kuhr, W. Alt, D. Schrader, M. Müller, V. Gomer, D. Meschede, Deterministic delivery of a single atom. Science **293**, 278–280 (2001)

6. D. Schrader, I. Dotsenko, M. Khudaverdyan, Y. Miroshnychenko, A. Rauschenbeutel, D. Meschede, Neutral atom quantum register, Phys. Rev. Lett. **93**, 150501 (2004)
7. I. Teper, Y. Lin, V. Vuletic, Resonator-aided single-atom detection on a microfabricated chip. Phys. Rev. Lett. **97**, 023002 (2006)
8. K. Nelson, X. Li, D. Weiss, Imaging single atoms in a three-dimensional array. Nat. Phys. **3**, 556–560 (2007)
9. W.S. Bakr, A. Peng, M.E. Tai, R. Ma, J. Simon, J.I. Gillen, S. Fölling, L. Pollet, M. Greiner, Probing the superfluid-to-Mott insulator transition at the single-atom level. Science **329**, 547 (2010)
10. J.F. Sherson, C. Weitenberg, M. Endres, M. Cheneau, I. Bloch, S. Kuhr, Single-atom-resolved fluorescence imaging of an atomic Mott insulator. Nature **467**, 68 (2010)
11. M. Schellekens, R. Hoppeler, A. Perrin, J. Viana Gomes, D. Boiron, A. Aspect, C.I. Westbrook, Hanbury Brown Twiss effect for ultracold quantum gases. Science **310**, 648–651 (2005)
12. T. Jeltes, J.M. McNamara, W. Hogervorst, W. Vassen, V. Krachmalnicoff, M. Schellekens, A. Perrin, H. Chang, D. Boiron, A. Aspect, C.I. Westbrook, Comparison of the Hanbury Brown-Twiss effect for bosons and fermions. Nature **445**, 402–405 (2007)
13. T. Gericke, P. Würtz, D. Reitz, T. Langen, H. Ott, High resolution scanning electron microscopy of an ultracold quantum gas. Nat. Phys. **4**, 949–953 (2008)
14. T. Gericke, P. Würtz, D. Reitz, C. Utfeld, H. Ott, All-optical formation of a Bose-Einstein condensate for applications in scanning electron microscopy. Appl. Phys. B **89**, 447–451 (2007)
15. T. Gericke, A scanning electron microscope for ultracold quantum gases. PhD thesis, Johannes Gutenberg Universität, Mainz, 2010
16. P.W. Hawkes, E. Kasper, *Principles of Electron Optics* (Academic Press, San Diego, 1996)
17. P. Würtz, T. Gericke, T. Langen, A. Koglbauer, H. Ott, Probing Bose-Einstein condensates by electron impact ionization. J. Phys. Conf. Ser. **141**, 012020 (2008)
18. P. Würtz, T. Langen, T. Gericke, A. Koglbauer, H. Ott, Experimental demonstration of single-site addressability in a two-dimensional optical lattice. Phys. Rev. Lett. **103**, 080404 (2009)
19. P. Würtz, T. Gericke, A. Vogler, F. Etzold, H. Ott, Image formation in scanning electron microscopy of ultracold atoms. Appl. Phys. B **98**, 641–645 (2010)
20. M. Inokuti, Inelastic collisions of fast charged particles with atoms and molecules-the Bethe theory revisited. Rev. Mod. Phys. **43**, 297–347 (1971)
21. M.A. Coplan, J.H. Moore, J.U.P. Doering, $(e, 2e)$ spectroscopy. Rev. Mod. Phys. **66**, 985–1014 (1994)
22. P. Würtz, T. Gericke, A. Vogler, H. Ott, Ultracold atoms as a target: Absolute scattering cross-section measurements. New J. Phys. **12**, 065033 (2010)
23. R. Côté, A. Dalgarno, Ultracold atom-ion collisions. Phys. Rev. A **62**, 012729 (2000)
24. V. Guarrera, P. Würtz, A. Ewerbeck, A. Vogler, G. Barontini, H. Ott, Observation of local temporal correlations in trapped quantum gases. Phys. Rev. Lett. **107**, 160403 (2011)
25. M. Naraschewski, R.J. Glauber, Phys. Rev. A **59**, 4595 (1999)
26. K.V. Kheruntsyan, D.M. Gangardt, P.D. Drummond, G.V. Shlyapnikov, Pair correlations in a finite-temperature 1D Bose gas. Phys. Rev. Lett. **91**, 040403 (2003)
27. J. Caux, P. Calabrese, Dynamical density-density correlations in the one-dimensional Bose gas. Phys. Rev. A **74**, 031605 (2006)
28. D. Muth, M. Fleischhauer, Dynamics of pair correlations in the attractive Lieb-Liniger gas. Phys. Rev. Lett. **105**, 150403 (2010)
29. V.A. Brazhnyi, V.V. Konotop, V.M. Perez-Garcia, H. Ott, Dissipation-induced coherent structures in Bose-Einstein condensates. Phys. Rev. Lett. **102**, 144101 (2009)
30. R. Heidemann, U. Raitzsch, V. Bendkowsky, B. Butscher, R. Löw, L. Santos, T. Pfau, Evidence for coherent collective Rydberg excitation in the strong blockade regime. Phys. Rev. Lett. **99**, 163601 (2007)
31. M. Reetz-Lamopur, T. Amthor, J. Deiglmayr, M. Weidemüller, Rabi oscillations and excitation trapping in the coherent excitation of a mesoscopic frozen Rydberg gas. Phys. Rev. Lett. **100**, 253001 (2008)

32. E. Urban, T.A. Johnson, T. Henage, L. Isenhower, D.D. Yavuz, T.G. Walker, M. Saffman, Observation of Rydberg blockade between two atoms. Nat. Phys. **5**, 110–114 (2009)
33. A. Gaëtan, Y. Miroshnychenko, T. Wilk, A. Chotia, M. Viteau, D. Comparat, P. Pillet, A. Browaeys, P. Grangier, Observation of collective excitation of two individual atoms in the Rydberg blockade regime. Nat. Phys. **5**, 115–118 (2009)
34. M. Saffman, T.G. Walker, K. Molmer, Quantum information with Rydberg atoms. Rev. Mod. Phys. **82**, 2313–2363 (2010)
35. H. Weimer, R. Löw, T. Pfau, H.P. Büchler, Quantum critical behavior in strongly interacting Rydberg gases. Phys. Rev. Lett. **101**, 250601 (2008)
36. S. Inouye, J. Goldwin, M.L. Olsen, C. Ticknor, J.L. Bohn, D.S. Jin, Observation of heteronuclear Feshbach resonances in a mixture of bosons and fermions. Phys. Rev. Lett. **93**, 183201 (2004)
37. B. DeMarco, D.S. Jin, Onset of Fermi degeneracy in a trapped atomic gas. Science **285**, 1703–1706 (1999)
38. G. Modugno, G. Ferrari, G. Roati, R.J. Brecha, A. Simoni, M. Inguscio, Bose-Einstein condensation of potassium atoms by sympathetic cooling. Science **294**, 1320–1322 (2001)
39. G. Thalhammer, G. Barontini, L. De Sarlo, J. Catani, F. Minardi, M. Inguscio, Double species Bose-Einstein condensate with tunable interspecies interactions. Phys. Rev. Lett. **100**, 210402 (2008)
40. S. Ospelkaus, A. Pe'er, K.-K. Ni, J.J. Zirbel, B. Neyenhuis, S. Kotochigova, P.S. Julienne, J. Ye, D.S. Jin, Efficient state transfer in an ultracold dense gas of heteronuclear molecules. Nat. Phys. **4**, 622–626 (2008)
41. J.G. Danzl, E. Haller, M. Gustavsson, M.J. Mark, R. Hart, N. Bouloufa, O. Dulieu, H. Ritsch, H.-C. Nägerl, Quantum gas of deeply bound ground state molecules. Science **321**, 1062–1066 (2008)

Index

A. Bramati, M. Modugno (eds.), *Physics of Quantum Fluids*,
Springer Series in Solid-State Sciences 177, DOI 10.1007/978-3-642-37569-9,